APPLICATIONS OF ULTRA-HIGH PERFORMANCE FIBER-REINFORCED CONCRETE ON FLEXURAL STRUCTURAL AND ARCHITECTURAL MEMBERS

by

VENKATESH BABU KAKA

Presented to the Faculty of the Graduate School of

The University of Texas at Arlington in Partial Fulfillment

of the Requirements

for the Degree of

MASTER OF SCIENCE IN CIVIL ENGINEERING

THE UNIVERSITY OF TEXAS AT ARLINGTON

May 2017

Acknowledgements

This investigation was carried out as a part of the requirements for a Master of Science degree in Civil Engineering. The author was motivated to conduct this investigation because of numerous discussions with Dr. Shih-Ho Chao, Associate Professor at the University of Texas, Arlington, TX. Under Dr. Chao's supervision and guidance, and with his constant assistance and encouragement, the purpose of this investigation has been accomplished. It is hoped that this investigation will contribute to the knowledge and state-of-the-art of reinforced concrete design with new construction materials. In addition to an expression of gratitude to Dr. Chao, the author also wishes to express his appreciation to the other members of his committee, Professor Bradley Bell, Associate Professor/Interim director at School of Architecture and Dr. Suyun Ham, Assistant Professor at University of Texas at Arlington.

Gratifying acknowledgement must also be expressed to Mr. Jean Gamarra, Program Manager/Civil Engineer at Federal Aviation Administration, Mr. Varthan Babakhanian, Technical Services Lab Manager at Forterra Pipe & Precast in Grand Prairie, TX for providing cement, fly ash and construction materials, Mr. Larry Rowland, Manager Marketing and Technical services at Lehigh White Cement Company for providing white cement, Mr. Antonio Gallovich, Export Area Manager Americas Region at Fiori Group for providing the concrete mixing truck.

Special thanks to graduate students Santhosh Maney, Akshay Suryawanshi, Santhosh Gurjar and Rasoul Adnan Abbas for their significant contributions to the manual labor needed for this study. The author also would like to sincerely thank all members of the research group Dr. Jinsup Kim, Dr. Sanputt Simasathien, Chatchai Jiansinlapadamrong, Young-Jae Choi, Poorya Hajy Alikhani, Natawut Chaiwino, Shi He, Shuveksha Tuladhar, Dr. Kyoung-Sub Park, Mohammadreza Zarrinpour, Guillermo

Palacios, Ashish Karmacharya, Ghassan Almasabha, Ra'ed Al-Mazaidh, Brandon Boehme, Lindsay Lafferty, Nga Thuy Phan and Carlos Leyva. The author would like to acknowledge the UTA CELB technician Dr. Oleh Kinash and Timothy Andrew Kruzic for all of their help throughout this research.

Finally, all of this would not have been possible without the unconditional love and limitless support of the author's family and friends.

April 24, 2017

Abstract

APPLICATIONS OF ULTRA-HIGH PERFORMANCE FIBER-REINFORCED CONCRETE ON FLEXURAL STRUCTURAL AND ARCHITECTURAL MEMBERS

Venkatesh Babu Kaka, MS

The University of Texas at Arlington, 2017

Supervising Professor: Shih-Ho Chao

This thesis presents the test results of a study on flexural and shear behavior of Ultra-High-Performance Fiber-Reinforced concrete (UHP-FRC) beams, reinforced with Grade 60 steel (ASTM A615/A615M), Grade 100 steel (ASTM A1035/A1035M) and Basalt fiber reinforced polymer (BFRP) bars. Ultra-high-performance fiber-reinforced concrete (UHP-FRC) has high compressive strength (> 22 ksi (150 MPa)) and exceptional compressive ductility. The use of UHP-FRC provides new opportunities for future infrastructure. However, structural design criteria have not been developed to fully utilize UHP-FRC's excellent mechanical properties. Maximum useable compressive strain, ε_{cu}, specified in the current design codes (ACI 318 Building Code and AASHTO LRFD Bridge Design Specifications) are limited to 0.003 for conventional plain concrete with little ductility and a maximum compressive strength of about 15 ksi (103 MPa). This maximum concrete compressive strain directly limits the amount of longitudinal reinforcement that could be used in flexural members, which in turn limits the flexural capacity of the members. Since the maximum useable strains of UHP-FRC are 5 to 10 times of that of plain concrete, it is apparent that the maximum compressive strain used for the current design needs to be reevaluated for UHP-FRC. In addition, unlike plain

concrete, the tensile strength of UHP-FRC can also contribute to its bending capacity. The large amount of reinforcement also significantly affected the tensile behavior of UHP-FRC due to the tension-stiffening effect.

Ability of UHP-FRC to lend itself in to very complex shapes and thin elements make it well-suited to contemporary architectural needs. Columns articulated by non-Euclidean geometries offer a new type of architecture with formal and structural possibilities. Specifically, branching concrete columnar structures offer a unique opportunity to merge biomimetic structural geometry with new computationally controlled performance criteria. Typical plain concrete does not willingly lend itself to these types of geometries due to its brittle nature and sensitivity to stress concentration. The non-Euclidean geometries also make the conventional reinforcing methodology difficult to be practically implemented. In the work shown in this research, the introduction of ultra-high-performance fiber reinforced concrete (UHP-FRC) allows for a new way of advancing beyond some of the limitations of conventional construction methods which use reinforced concrete. The formwork used for these columns presents a unique solution for assembling 2D materials in complex 3D forms. In this research, the two-legged and three-legged branching and twisting scaled columns all rely upon developable geometry that has been cut via a CNC machine out of 1/16th inch polypropylene. The parts are seamed together by hand via a ‘zipper’ connection that is the result of running an algorithmic script on the edge geometry of each edge of adjoining parts.

The physical properties of UHP-FRC give significant advantages to design and develop structurally and thermally optimized precast cladding system. UHP-FRC is used for developing stronger, thinner and more durable concrete sandwich panels and to fabricate more detailed geometry that can create self-shading surface using UHP-FRC. Thickness of UHP-FRC required for minimum thermal heat transfer though the building

envelope has also been investigated. This thesis discusses the progress of this novel UHP-FRC application and the experimental testing results of flexural structural members, columns designed with non-Euclidean geometries and also thin sandwich panels designed and developed with UHP-FRC.

Table of Contents

List of Illustrations

List of Tables

Chapter 1

Organization of Thesis

This thesis is comprised of two different research projects and thus organized into two major parts. Chapter 1 will discuss the organization of the report.

Part I will be covered in Chapter 2 through Chapter 5, and will discuss the behavior of UHP-FRC in flexural structural members. Chapter 2 will present a literature review on UHP-FRC, ASTM A1035 rebar and Fiber reinforced polymer reinforcing bars. Chapter 3 will discuss the experimental testing program including material test data, casting process of beam specimens, test setup and procedures, instrumentations, and data acquisition for the experimental test program. Chapter 4 will present the test results and the response of the specimens. Finally, the summary and conclusions, of the part I of the research project will be summarized in Chapter 5.

Part IIa and part IIb will be covered in Chapter 6 and Chapter 7, describing Architectural applications of UHP-FRC. Background of biomimicry, unconventional semi rigid formwork development and experimental program with UHP-FRC in non-Euclidian shaped columnar branches will be presented in Chapter 7 (Part IIa). Chapter 8 will discuss the process of using UHP-FRC for designing and develop structurally and thermally optimized precast cladding system. Chapter 8 also includes the experimental program of sandwich panels cast with UHP-FRC.

Chapter 2

Part I: Literature Review

2.1 Ultra-High Performance Fiber-Reinforced Concrete

2.1.1 UHP-FRC Definition

Ultra-high performance fiber-reinforced concrete (UHP-FRC) is an advanced reinforced cementitious material, with improved mechanical properties, fractural toughness, and durability properties compared to normal or high-performance concrete. Typical uniaxial compressive behavior of UHP-FRC in comparison to other concretes is illustrated in Figures 2-3 and 2-4. Currently there is no commonly accepted definition for UHP-FRC in the U.S, in addition nationally accepted test methods to evaluate the material performance has yet to be established. According to the French Recommendations on UHP-FRC [AFGC 2013], UHP-FRC is a material with a cement matrix having:

1. A characteristic compressive strength more than 150 MPa and a maximum of 250 MPa.
2. Sufficient fiber content to achieve ductile behavior under tension, with high post-cracking tensile strength.
3. High binder content which decreases capillary porosity that improves durability of the fibers inside UHP-FRC.

Same limits for strength and ductility were imposed by the Japanese recommendations [JSCE 2006] furthermore stipulated guidelines for mix proportion by limiting fiber quantity, aggregate size and water-cement ratio.

According to the proposed classification of fiber-reinforced concretes (FRC) [Naaman, Reinhardt 2006] and [Stang, Li 2004], UHP-FRC is different from other FRCs as a material that exhibits strain hardening in tension (Figure 2-2), where other FRCs can display a hardening behavior in bending, however are exhibit strain softening in tension.

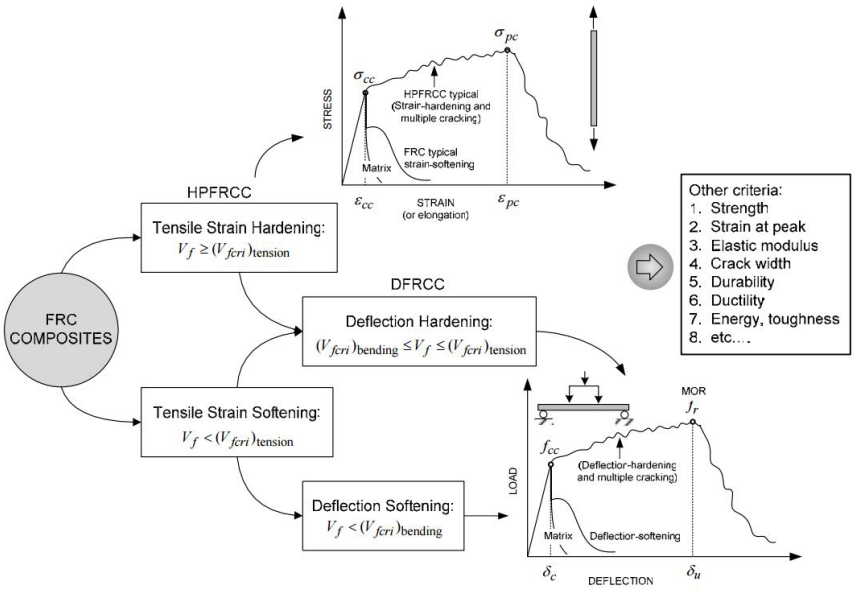

Figure 2-1 Classification of FRC [Naaman, 2006]

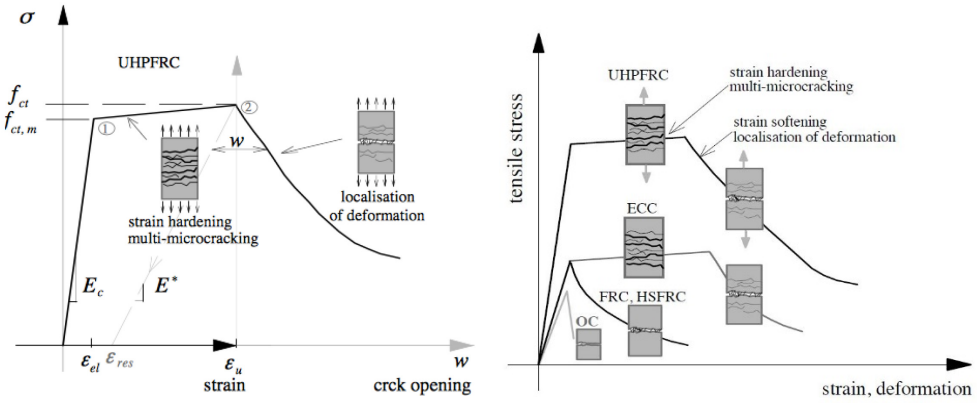

(a) (b)

Figure 2-2 (a) Typical uniaxial tensile response of UHP-FRC [Spasojevic, 2008]

(b) Comparison of tensile response of UHP-FRC with other concretes

[Li and Fischer, 2002 and Spasojevic, 2008]

UHP-FRC typically consists of cement, silica fume, fine quartz sand, fibers, high-range water-reducing admixtures and water-cementitious material ratios ranging between 0.15 and 0.25.

The key material characteristics of UHP-FRC are accomplished through the succeeding principles, [Richard and Cheyrezy 1995] greater density by optimized gradation and mix composition, improved homogeneousness by excluding coarse aggregates in the matrix and enrichment of ductility by addition of fibers. UHP-FRC can be considered as the latest innovation in concrete development, first invented by Bouygues SA, France, in 1995 [Richard, Cheyrezy 1995].

Since 1960 more intricate concrete mixes were obtained with the addition of filler materials and superplasticizers [Mielenz 1984]. Development of UHPC began through studies on high-strength cement pastes with low water-cementitious materials ratios (w/cm) of 0.20 to 0.30 [Yudenfreund et al. (1972a, b, c), Odler et al. (1972a, b), and Brunauer et al. (1973a, b)]. These pastes had low porosity resulting in compressive strengths up to 29 ksi (200 MPa). Hot pressing methods were first used by Roy and Gouda (1973) and Roy et al. (1972) which produced very high strength cement pastes with compressive strengths up to 95 ksi (655 MPa) and indirect tensile strengths up to 9 ksi (64 MPa). Advent of high-range water-reducing admixtures and pozzolanic materials such as silica fume, facilitated in invention of two new concrete materials, macro-detect-free (MDF) concrete [Kendall et al. 1983] and Densified systems containing homogeneously arranged ultrafine particles (DSP) [Bache 1981]. DSP comprises of densely packed particles ranging from 0.5 to 100 μ and homogeneously arranged, ultra-fine particles ranging in size 50 n to 0.5 μ, filling the spaces between larger particles. DSP was the basis for contemporary UHPC development. Optimal mix proportion for UHPC was studied by de Larrard and Sedran (1994) and produced a fluid mortar with a water/binder ratio of 0.14 reaching a compressive strength of 34 ksi (236 MPa). With the increase in density of concrete mixes strength increased and so the brittleness. Ductility is attained by addition of discontinuous fibers, which has been used since ancient times. Numerous combinations of steel and synthetic fibers were used to increase ductility of the matrix [Richard and Cheyrezy 1995; Bache 1987].

2.1.2 Mechanical Properties:

2.1.2.1 Uniaxial Compression:

UHPC without fibers: Mechanical properties of UHPC differ with mix composition, because unlike conventional concrete and high performance concrete, UHPC does not have a distinctive mix proportion. Typically, UHPC mix without fibers has a characteristic compressive strength of higher than 22 ksi (150 MPa), with a high modulus of elasticity in the range of 6,500 ksi to 8,000 ksi (45 GPa to 55 GPa) and exhibiting extremely brittle failure after peak strength. Figure 2-3 (b) shows the comparison of uniaxial compression behavior of conventional, high-strength concrete and UHPC without fibers [Tue et al. 2004, Fehling et al. 2004]. Descending curve cannot be recorded because of the explosive failure after peak compressive strength. Increase in brittleness with the increase in compressive strength is observed in UHPC which has already been seen in conventional and high-strength concretes. Higher modulus of elasticity of UHPC is due to increased density of the hardened cement paste. Elastic modulus of reactive powder concrete (RPC) can increase up to 11,000 ksi (75 GPa), whereas for conventional matrix is approximately 4,500 ksi (30 GPa) [Richard, Cheyrezy 1995].

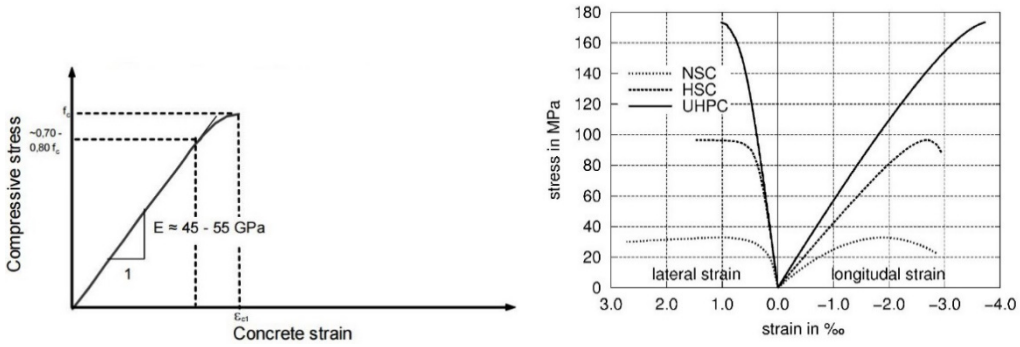

(a) (b)

Figure 2-3 (a) Fehling et al., 2004 (b) Uniaxial compressive behavior of normal strength concrete, high-strength concrete and UHPC without fibers [Tue et al., 2004]

UHPC with fibers: Addition of fibers to the matrix decreases the brittleness and increases the maximum useable compressive strain. Figures 2-4 (a), (b), (c) and (d) uniaxial compressive stress-strain behavior of different UHP-FRC mixes and mix developed at UTA which is also used in this research [Parham et al., 2016].

Addition of fibers slightly increases the compressive strength. With addition of fibers up to 4% by volume fraction compressive strength increased by 5 – 10% [Nielson, 1995 and Behloul, 1996]. Compared to UHPC without fibers, matrix with fibers have more noticeable non-linear behavior before the peak compressive strength. Compressive stress-strain relations presented by different researchers in figures 2-4 (a), (b) and (c) has shown that the compressive strength is attained at a compressive strain of 0.35 – 0.5%. Whereas mix presented by Parham et al., 2016 reached an ultimate compressive strength at a strain range of approximately 1.2 – 1.4%. Post peak behavior is affected by several reasons attributing to fiber content, fiber type and distribution and size of the specimen.

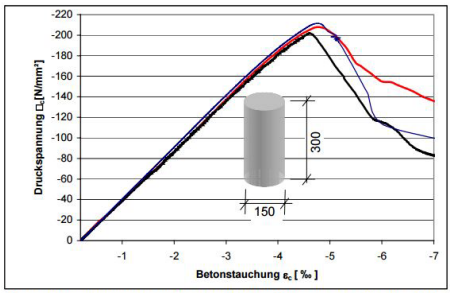

(a)

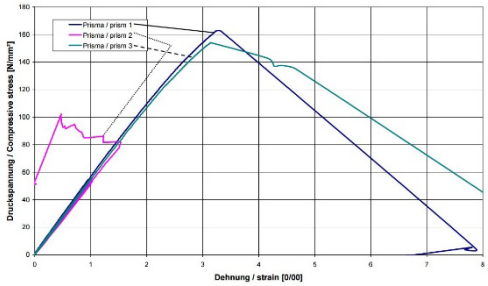

(b)

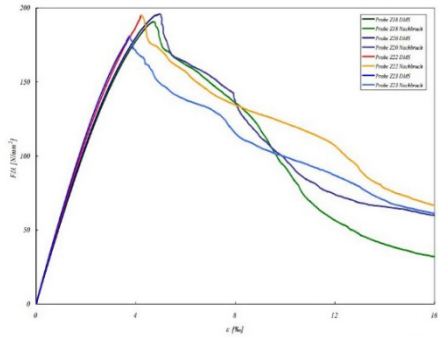

(c)

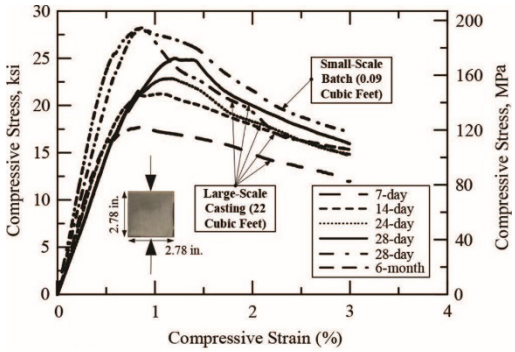

(d)

Figure 2-4 Compressive stress-strain relationship of UHP-FRC

(a) Fehling et al., 2005 (b) Reineck and Greiner, 2004

(c) Jungwirth and Muttoni, 2005 (d) Parham et al., 2016

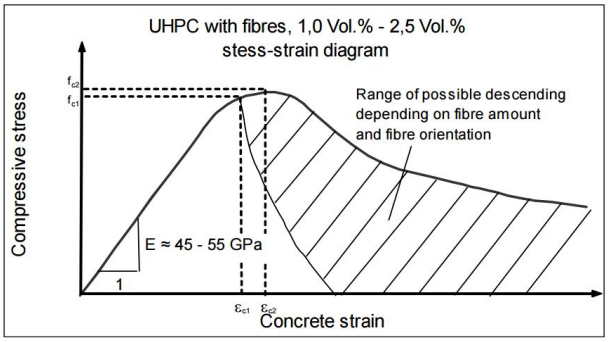

Figure 2-5 Range of possible descending portion of the compressive stress-strain relation of UHPC mix with fibers [Fehling et al., 2005]

2.1.3 Design recommendation for UHP-FRC:

Currently there are no commonly accepted design recommendations for UHP-FRC in US. However, there are design guidelines and recommendations for UHP-FRC in France, Japan and Australia, but are very conservative limiting the use of very high compressive ductility of UHP-FRC. Compressive stress-strain model for ultimate limit state and serviceability limit state design recommended by AFGC and JSCE uses a linear constitutive law with a yield plateau. Compressive stress-strain curve recommended by AFGC for design at ULS is shown in figure 2-6. AFGC codes were utilized for bridges all over the world. In United States only design recommendations proposed was by Professor Franz-Josef Ulm at MIT and the Cat Point Creek Bridge in Virginia was the first to use the MIT recommendations [Davila, 2007].

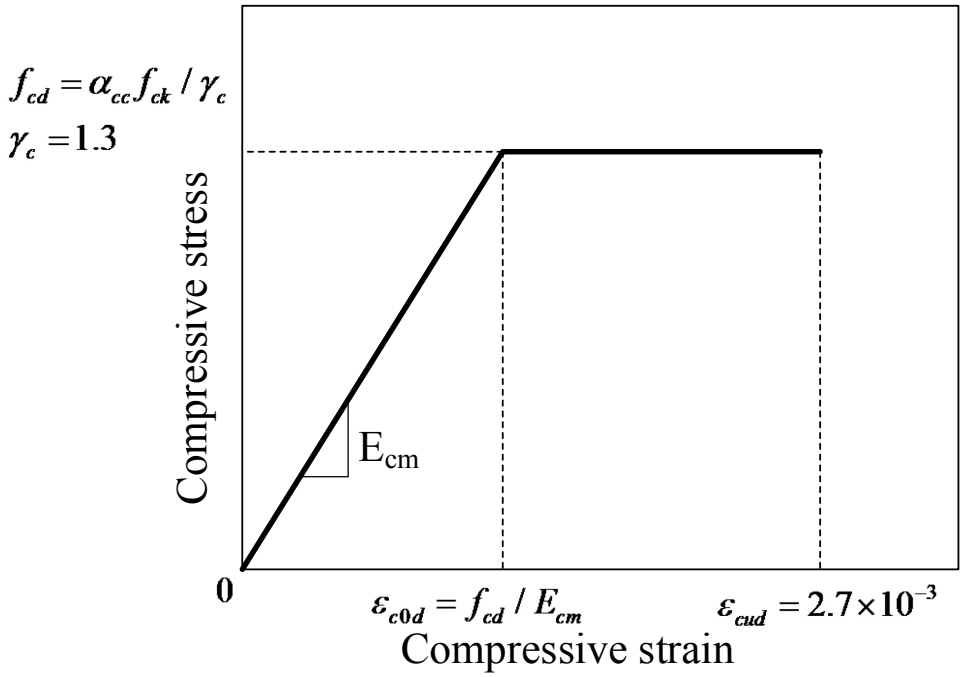

Figure 2-6 Compressive stress-strain

2.2 High Strength Steel Reinforcement

2.2.1 ASTM A1035 Reinforcement

Compared to ASTM A615/A615M steel, the ASTM A1035 reinforcement has low carbon content and high chromium content, resulting in high-strength and more corrosion resistant bars [ACI, 2010a]. It has been mainly used in bridge decks exposed to de-icing salts [Seliem et al., 2008; Shahrooz et al., 2011].

2.2.1.1 Tensile properties

For any reinforcement, knowledge of actual tensile properties is important for understanding the behavior of reinforced concrete structural members. The strength reduction factors used in reinforced concrete design are derived from probabilistic studies for which tensile properties are essential. Figure 2-7 shows actual stress-strain curves for samples of ASTM A1035/A1035M bars in Grades 100 (690) and 120 (830) to similar curves for samples of

ASTM A615/A615M bars in Grades 60 (420) and 75 (520), and ASTM A706/A706M bars. ASTM A1035/A1035M bars have a higher tensile strength but the yield point is not well defined. ASTM A1035/A1035M bars reach a proportionate limit at a stress from 60,000 to 80,000 psi (410 to 550 MPa), which is similar to the yield stress of ASTM A615/A615M Grade 60 (420) and ASTM A706/A706M bars [WJE 2008]. Strains at peak tensile stress for ASTM A615/ A615M Grade 60 (420) steel is within 0.07 to 0.10, and for ASTM A706/A706M steel is from 0.10 to 0.14. Ultimate strain at the time of fracture varies for different steel, the elongation in 8 in. (200mm) for ASTM A1035/A1035M steel, ranges from 0.08 to 0.13, whereas for ASTM A615/A615M Grade 60 (420) and ASTM A706/A706M steels range from 0.09 to 0.12 and 0.14 to 0.20 respectively. Modulus of elasticity of ASTM A1035/A1035M steel is observed to be same as other grade steel as 29,000 ksi (200,000 MPa) [WJE 2008]. Yield strength obtained by 0.2% offset method from actual testing of ASTM A1035/A1035M bars, is more than 115,000 psi (790 MPa) for Grade100 bar and 125,000 psi (860 MPa) for Grade 120 (830) bar.

The tensile strength for ASTM A1035/A1035M Grade 100 (690) bar exceeds 155,000 psi (1070 MPa) and for Grade 120 (830) bar exceeds 160,000 psi (1100 MPa). Following equations represent an approximate lower bound for the stress-strain curves of Grade 100 (690). The equations 2-1 to 2-3 are based on a proportional limit of 70,000 psi (480 MPa) and an assumed tensile strength of 150,000 psi (1030 MPa) at a strain of 0.02.

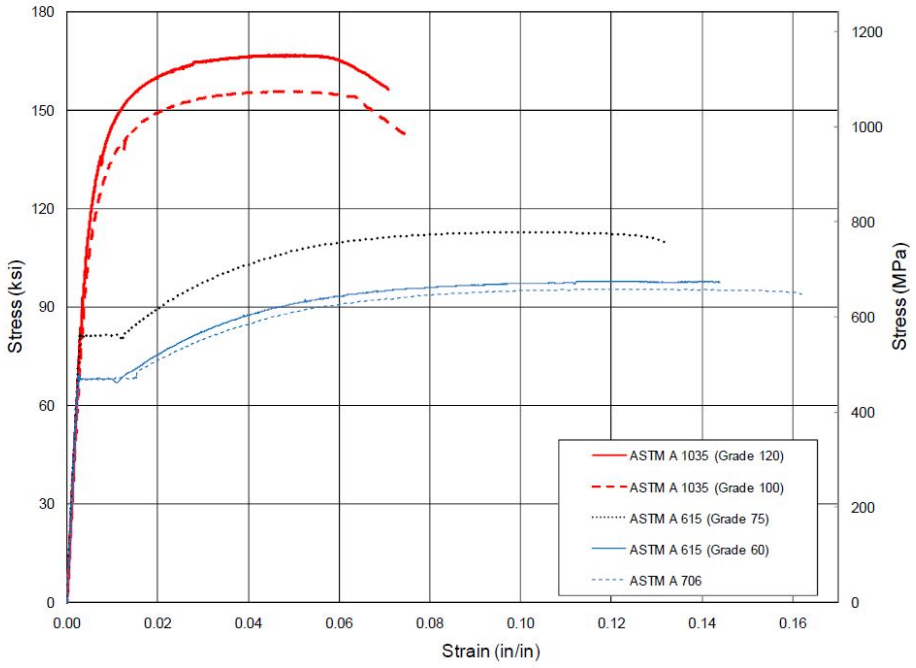

Figure 2-7 Stress Strain curves of various grades of steel reinforcing bars [WJE 2008]

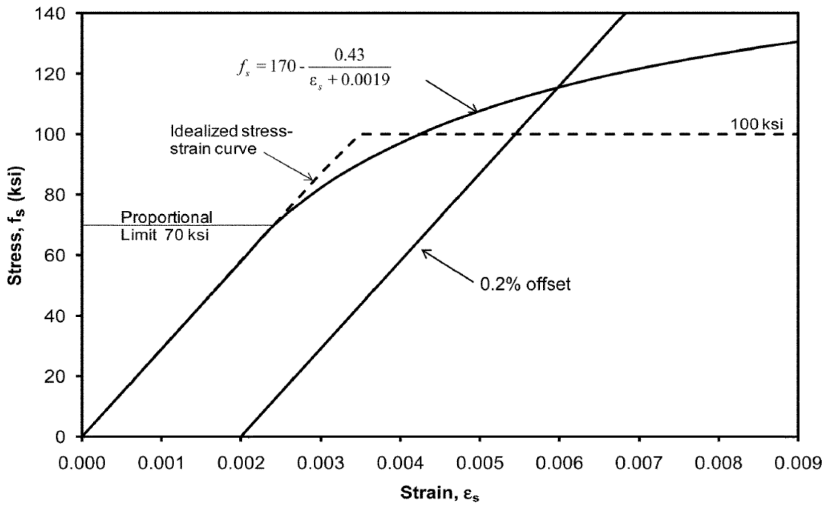

Figure 2-8 Approximated nonlinear stress-strain relationship of ASTM A1035/A1035M Grade 100 (690) steel and idealized bilinear elastic-plastic stress-strain relationship for simplified design [ACI ITG-6R-10]

Approximate lower bound of stress-strain curves of Grade 100 (690) are represented by following equations:

$f_s = 29,000\varepsilon_s$ (ksi) for $0 \le \varepsilon_s \le 0.0024$ Eq. (2-1)

$f_s = 170 - \dfrac{0.43}{\varepsilon_s + 0.0019}$ (ksi) for $0.0024 \le \varepsilon_s \le 0.02$ Eq. (2-2)

$f = 150$ (ksi) for $0.02 \le \varepsilon_s \le 0.06$ Eq. (2-3)

Aforementioned equations in SI units:

$f_s = 200,000\varepsilon_s$ (MPa) for $0 \le \varepsilon_s \le 0.0024$ Eq. (2-1M)

$f_s = 1170 - \dfrac{2.96}{\varepsilon_s + 0.0019}$ (MPa) for $0.0024 \le \varepsilon_s \le 0.02$ Eq. (2-2M)

$f = 1040$ (MPa) for $0.02 \le \varepsilon_s \le 0.06$ Eq. (2-3M)

Table 2-1 Specified tensile and yield strengths of different steel reinforcement

Bar type	Tensile strength, minimum, psi (MPa)	Yield strength[a]		Stress corresponding to prescribed strain	
		Minimum, psi (MPa)	Maximum, psi (MPa)	Minimum stress, psi (MPa)	Strain, %
ASTM A615/A615M Grade 60	90,000 (620)	60,000 (420)	—	60,000 (420)[b]	0.35[b]
ASTM A615/A615M Grade 75	100,000 (690)	75,000 (520)	—	75,000 (520)[b]	0.35[b]
ASTM A615/A615M Grade 80	105,000 (725)	80,000 (550)	—	80,000 (550)[b]	0.35[b]
ASTM A706/A706M Grade 60	80,000 (550)[c]	60,000 (420)	78,000 (540)	60,000 (420)[b]	0.35[b]
ASTM A706/A706M Grade 80	100,000 (690)[c]	80,000 (550)	98,000 (675)	80,000 (550)[b]	0.35[b]
ASTM A1035/A1035M Grade 100	150,000 (1030)	100,000 (690)	—	80,000 (550)	0.35
ASTM A1035/A1035M Grade 120	150,000 (1030)	120,000 (830)	—	90,000 (620)	0.35

[a] Observed yield point for ASTM A615/A615M and ASTM A706/A706M bars, and yield strength according to 0.2% offset method for ASTM A1035/A1035M bars.

[b] Applicable to ASTM A615/A615M and ASTM A706/706M bars only when steel bar tested does not exhibit a well-defined yield point.

[c] Tensile strength for ASTM A706/A706M bars should also be not less than 1.25 times actual yield strength.

Table 2-2 Typical chemical compositions of different grade steel

Element	Bar type		
	ASTM A1035/A 1035M	ASTM A615/A615M	ASTM A706/A706M
	Maximum content, %		
Carbon	0.15	b	0.30
Chromium	8.0 to 10.9[a]	—	— [c]
Manganese	1.50	b	1.50[c]
Nitrogen	0.05	—	—
Phosphorus	0.035	0.06	0.035
Sulphur	0.045	b	0.045
Silicon	0.50	—	0.50

2.2.1.2 Flexure design

ACI Innovation Task Group 6 (2010) well presented the relevant research and design guidelines for using ASTM A1035/A1035M bars. ACI-ITG 6 (2010) discussed material properties of both Grade 100 (690) and 120 (830) bars. Simplified strength design procedures are limited to Grade 100 (690) steel, whereas for Grade 120 (830) bars research data is insufficient for design recommendations. Strain developed in longitudinal reinforcement is limited to 0.015 in flexural design to avoid excessive cracking and deflection. Equations (2-1) and (2-2) need to be used with a limiting strain of 0.015 for a viable design. Nonlinear flexural analysis can be performed on a reinforced concrete section, reinforced with ASTM

A1035/A1035M Grade 100 (690) bars by using stress-strain relationship defined by equations (2-1) and (2-2).

A simplified method for flexural strength design with ASTM A1035/1035M was proposed by Mast et al. (2008). Simplified model comprises of a linear elastic portion with elastic modulus of 29,000 ksi (200,000 MPa) and a plastic yield plateau with yield strength of 100 ksi (690 MPa) (Figure 2-8).

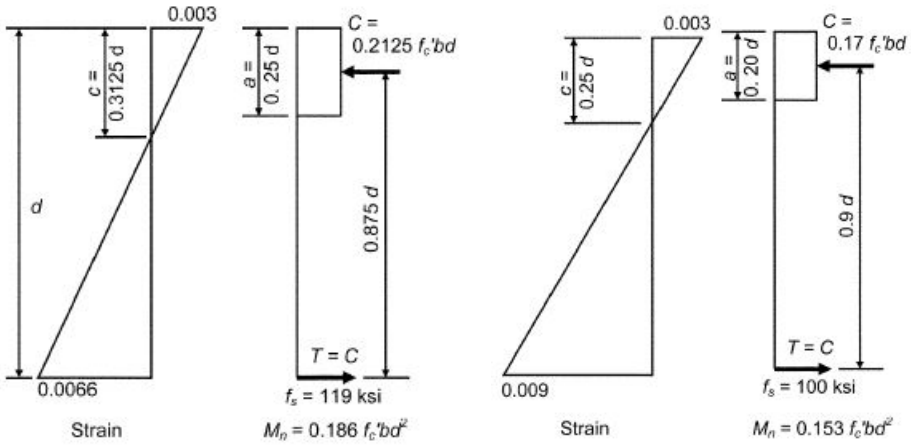

(a) (b)

Figure 2-9 (a) Behavior based on Eq. (2-2) (b) Behavior based on simplified method (Tension controlled strain limits with $f_c^{'}=5ksi$ and $\beta=0.8$)

Table 2-3 Comparison of design methods using ASTM A 1035/A1035M Grade 100 (690) steel (in.-lb units) [ACI ITG6R-10]

	Using Eq. 2-1 and 2-2	Simplified method
Tension-controlled strain limit	0.0066	0.009
Steel tensile stress f_s, ksi	119	100
Neutral axis depth c, in.	$0.3125d$	$0.25d$
Stress block depth $a=\beta_1 c$, in.	$0.3125\beta_1 d$	$0.25\beta_1 d$

Compression force C, kip	$0.85f_c^1ab$	$0.85f_c^1ab$
Steel area $A_s = C / f_s$, in.²	$0.85(f_c^1/119)(0.3125\beta_1 d)b$	$0.85(f_c^1/100)(0.25\beta_1 d)b$
Tension-controlled reinforcement ratio $\rho_t = A_s / bd$	$0.002232f_c^1\beta_1$	$0.002125f_c^1\beta_1$
$T = C = A_s f_s = \rho_t bdf_s$, kip	$0.2656f_c^1\beta_1 bd$	$0.2125f_c^1\beta_1 bd$
Lever arm = $d - a/2$, in.	$d(1-0.156\beta_1)$	$d(1-0.125\beta_1)$
M_n for $f_c^1 = 22$ ksi; $\beta_1 = 0.8$, kip-in.	$0.232f_c^1bd^2$	$0.191f_c^1bd^2$

Table 2-4 Comparison of design methods using ASTM A 1035/A1035M Grade 100 (690) steel (SI units) [ACI ITG6R-10]

	Using Eq. 2-1 and 2-2	Simplified method
Tension-controlled strain limit	0.0066	0.009
Steel tensile stress f_s, MPa	820	690
Neutral axis depth c, mm	$0.3125d$	$0.25d$
Stress block depth $a = \beta_1 c$, mm	$0.3125\beta_1 d$	$0.25\beta_1 d$
Compression force C, N	$0.85f_c^1ab$	$0.85f_c^1ab$
Steel area $A_s = C / f_s$, mm²	$0.85(f_c^1/820)(0.3125\beta_1 d)b$	$0.85(f_c^1/690)(0.25\beta_1 d)b$
Tension-controlled reinforcement ratio $\rho_t = A_s / bd$	$0.0003239f_c^1\beta_1$	$0.0003079f_c^1\beta_1$
$T = C = A_s f_s = \rho_t bdf_s$, N	$0.2656f_c^1\beta_1 bd$	$0.2125f_c^1\beta_1 bd$
Lever arm = $d - a/2$, mm	$d(1-0.156\beta_1)$	$d(1-0.125\beta_1)$
M_n for $f_c^1 =$ ksi; $\beta_1 = 0.8$, N-mm	$0.232f_c^1bd^2$	$0.191f_c^1bd^2$

2.2.1.3 Tension and Compression-Controlled Sections

Flexural members with a net tensile strain of 0.005 or greater in extreme tension reinforcement are defined as tension controlled section [ACI 318-14], which for Grade 60 steel is approximately 2.5 times the yield strain. This strain limit is used for all reinforcements allowed by ACI 318-14, which covers reinforcement with yield strengths up to 80 ksi. A tension

controlled strain limit of 0.0066 for Grade 100 for ASTM A1035/A1035M bars resulted in a performance like members designed with Grade 60 (420) and 75 (520) and a strain limit of 0.005 [Mast et al. 2008]. On the other hand, for simplified design method strain limit is 0.009 [Mast et al. 2008, ACI ITG-6R-10] for the case of tension controlled section to accommodate for the actual steel stress being higher than the assumed 100,000 psi (690 MPa).

Compression-controlled section is defined by ACI 318 as net tensile strain at balanced condition. Compression controlled strain limit is 0.00345 for yield strength of 100,000 psi (690 MPa) and E_s of 29,000 ksi (200,000 MPa). For a simpler purpose strain limit is rounded to 0.004. For simplified method, tension controlled limit happens at a c/d = 0.25 and the compression controlled limit at a c/d = 0.43.

2.3 FRP Reinforcement

Non-pre-stressed or pre-stressed steel used in reinforced concrete structures are susceptible to corrosion especially when subjected to aggressive environments [ACI 440.1R-15], predominantly where deicing salts are regularly used, such as concrete deck slabs and parking garages. Composite materials such as fiber reinforced polymer offers a replacement of steel reinforcement. Fiber reinforced polymers are made of polymer matrix reinforced with fibers. Fibers are typically aramid, basalt, carbon or glass and the polymer is usually an epoxy, phenol formaldehyde resin, polyester thermosetting plastic or vinyl ester. Since FRP is a combination of resin and fibers, the properties of resulting composites combine properties of individual material (Figure 2-10). The resin system bonds the fibers together and spreads the load applied to the composite between each of the individual fibers and also protects the fibers from abrasion and impact damage as well as severe environmental conditions [SP System]. FRP materials are anisotropic consequently tensile strength is high only in the direction of the reinforcing fibers and in transverse direction depends on resin matrix. Use of composites can be

dated back to early 1900's which was more prominently used in automotive and aerospace industry.

FRP bars for internal reinforcing of concrete have been under development since as early as 1960s in United States and 1970s in Europe and Japan [Bakis et al., 2002]. Carbon fiber reinforced polymer (CFRP), Aramid fiber reinforced polymer (AFRP) and Glass fiber reinforced polymer (GFRP) are the most commonly used FRP composites in infrastructure. Basalt fiber reinforced polymer (BFRP) relatively new in the United States with dearth of published research and guidelines. Many other applications of these composites are FRP sheets and plates for external strengthening using epoxy, internal FRP plates, non-prestressed and prestressed internal reinforcing bars, near surface mounted FRP reinforcement bars.

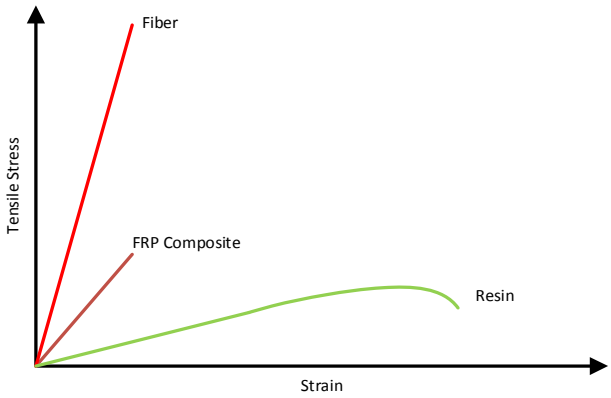

Figure 2-10 Composite properties

2.3.1 Tensile Behavior:

Tensile properties of FRP bars are typically governed by various factors such as fiber volume, fiber type, type of resin, fiber orientation and size of the rebar. All FRP bars are anisotropic in nature, implying strong in the direction of fiber orientation and weak in transverse direction. FRP bars are characterized by a linear elastic stress-strain relationship up to failure, where strength and stiffness varies depending on fiber type and volume. Typical tensile behavior of different FRP bars and steel bars are as presented in figure 2-11. In general FRP

bars are stronger than steel but does not display any ductility prior to failure. Stiffness of FRP bars can we very small, as small as 20% that of the steel [ACI.1R-15, 2015].

On the other hand FRP bars are very weak in compression compared to tension. Compressive strengths are 20, 55 and 78% of the tensile strength of AFRP, GFRP and CFRP [ACI.1R-15, 2015].

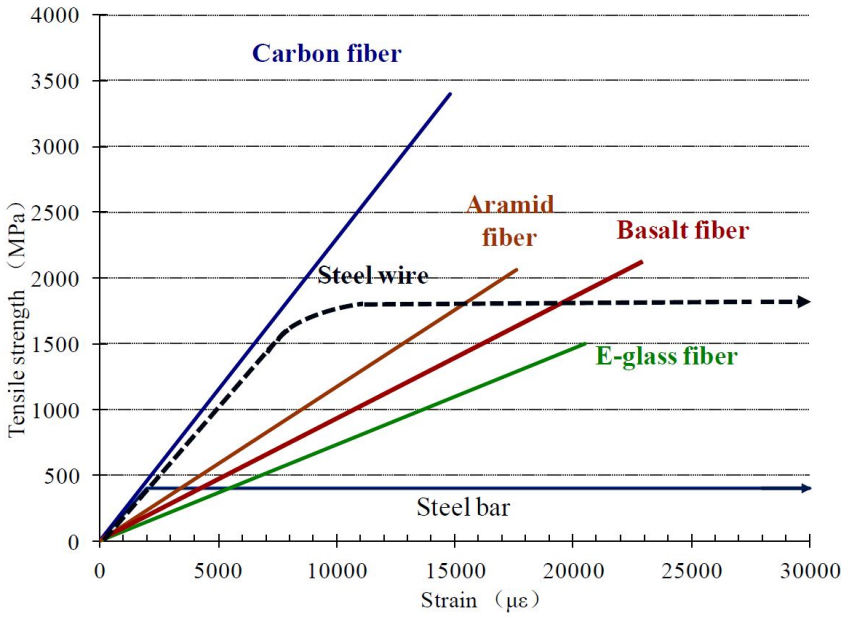

Figure 2-11 Tensile stress-strain relationship of various FRP bars [Wu et al., 2012]

2.3.2 Flexure Design:

Design of concrete members reinforced with FRP bars as flexural reinforcement is similar to steel-reinforced concrete members. Concrete members reinforced with steel bars are designed to behave in a tension-controlled manner showed by yielding of steel before the crushing of concrete. Yielding of the steel gives a warning of failure of the members and offers ductility unlike FRP bars which will not exhibit any ductility. Rupture of FRP bars prior to crushing of concrete is less desirable as the failure of members is abrupt and disastrous. Hence it is more desirable for concrete members in flexure reinforced with FRP bars to fail in crushing of concrete rather than rupture of FRP bars [Nanni, 1993]. Either of the two designs will not offer

a ductile behavior compared to members reinforced with steel bars. Hence, ACI 440.1R (2015) suggested a higher margin of safety for failure than that used for design in reinforced concrete members with steel bars. Use of high-strength concrete with FRP bars benefits in increasing the stiffness of the cracked section, but the deformability of the flexural member is reduced compared to normal strength concrete [ACI 440.1R-15, 2015].

Nominal flexural strength of concrete beams reinforced with FRP bars can be computed using strain compatibility and force equilibrium.

$$\rho_{fb} = 0.85\beta_1 \frac{f_c^{'}}{f_{fu}} \frac{E_f \varepsilon_{cu}}{E_f \varepsilon_{cu} + f_{fu}} \qquad \text{Eq. (2-4)}$$

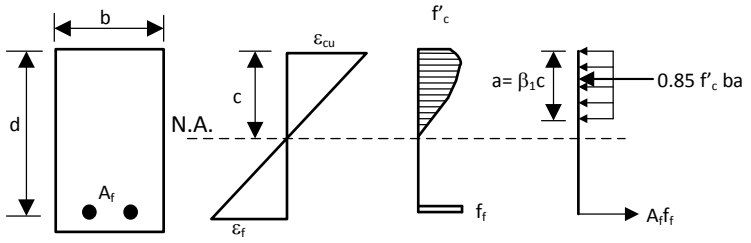

(a) Failure governed by concrete crushing

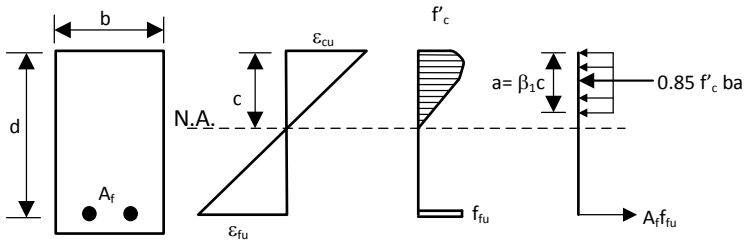

(b) Balanced failure condition

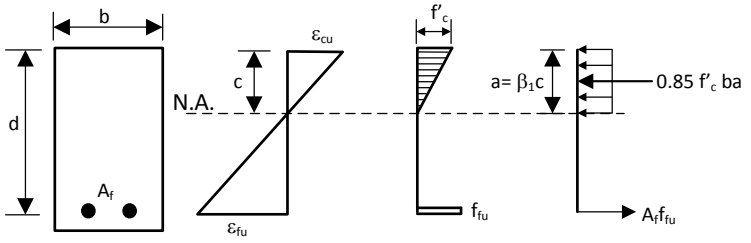

(c) Failure governed by FRP rupture (concrete stress maybe nonlinear)

Figure 2-12 Stress-strain distribution at ultimate conditions [ACI 440.1R-15, 2015]

2.3.3 Nominal Flexural Strength

2.3.3.1 Concrete crushing limit state: ($\rho_f > \rho_{fb}$)

Concrete crushing is the controlling limit state, and the stress block can be approximated with the ACI rectangular stress block. Following equations can be derived based on force equilibrium and strain compatibility [Figure 2-12]. The nominal flexural strengths can be calculated from the equations (2-5),(2-6) and (2-7)

$$M_n = A_f f_f \left(d - \frac{a}{2} \right) \quad \text{Eq. (2-5)}$$

$$a = \frac{A_f f_f}{0.85 f_c^{'} b} \quad \text{Eq. (2-6)}$$

$$f_f = E_f \varepsilon_{cu} \frac{\beta_1 d - a}{a} \quad \text{Eq. (2-7)}$$

Solving Equations (2-6) and (2-7) for f_f gives

$$f_f = \left(\sqrt{\frac{\left(E_f \varepsilon_{cu} \right)^2}{4} + \frac{0.85 \beta_1 f_c^{'}}{\rho_f} E_f \varepsilon_{cu}} - 0.5 E_f \varepsilon_{cu} \right) \leq f_{fu} \quad \text{Eq. (2-8)}$$

2.3.3.2 FRP Rupture limit state: ($\rho_f < \rho_{fb}$)

Rupture of FRP reinforcement is the controlling limit state and the nominal flexural strength can be calculated from equation

$$M_n = A_f f_{fu} \left(d - \frac{\beta_1 c}{2} \right) \quad \text{Eq. (2-9)}$$

At ultimate state, concrete compressive strain (ε_c) and depth of neutral axis c are unknown which makes the analysis intricate. As the maximum compressive strain of concrete may not be attained $(\varepsilon_c < \varepsilon_{cu})$, the ACI equivalent rectangular stress block parameters cannot be used. In this case ACI 440-1R (2015) has set a conservative lower bound limit in computing the depth of neutral axis c_b. Nominal flexural strength calculations for the limit state of FRP rupture are based on equations (2-10) and (2-11)

$$M_n = A_f f_{fu}\left(d - \frac{\beta_1 c_b}{2}\right) \quad \text{Eq. (2-10)}$$

$$c_b = \left(\frac{\varepsilon_{cu}}{\varepsilon_{cu} + \varepsilon_{fu}}\right) d \quad \text{Eq. (2-11)}$$

2.3.4 Strength reduction factor for flexure:

ACI recommended a conservative strength reduction factor to compensate the fact that FRP bars do not show ductile performance.

2.3.5 Shear Design:

Design of concrete members reinforced with FRP bars for shear is similar to steel-reinforced concrete members. However the affect of low modulus of elasticity, low transverse shear resistance and lack of ductility of FRP bars needs to be condered for shear design. Strength reduction factor (0.75) for shear proposed by ACI 318 steel-reinforced conrete members can be used for FRP-reinforced concrete members.

Depth of the compression zone is reduced in concrete members reinforced with FRP bars as flexural reinforcement because of deeper and wider cracks. Consequently, the contribution of aggregate interlock and compression zone in resisting shear is reduced significantly. Earlier research on shear capacity of flexural concrete members without shear reinforcement has shown that shear strength of concrete depends on stiffness of flexural reinforcement [Nagasaka et al., 1993; Sonobe et al., 1997; Michaluk et al., 1998; Tureyen and Frosch 2002]. Proportion of dowel action of longitudinal FRP reinforcement in resisting shear of concrete members has not yet been studied. Because of the lesser strength and stiffness in transverse direction of FRP bars, dowel action contribution is assumed to be less than comparable area of steel.

Shear capacity of flexural concrete members reinforced with FRP bars can be estimated using the equation (2-12). The parameter ‘k’ accounts for axial stiffness of FRP reinforcement.

$$V_c = 5\sqrt{f_c^{'}} b_w \left(kd\right) \quad \text{Eq. (2-12)}$$

Where, $k = \sqrt{2\rho_f n_f + \left(\rho_f n_f\right)^2} - \rho_f n_f$ Eq. (2-13)

2.3.6 Deflections

Most of the methods for calculating deflections involve the use of the term called the effective moment of Inertia, I_e. This concept of effective moment of Inertia was first introduced by Branson in 1965 which includes the effects of tension stiffening and variation in stiffness along the flexural member. Effective moment of Inertia proposed by Branson was adopted by ACI in 1971 and has since been used till the newest revision [ACI 318-14].

$$I_e = \left[\left(\frac{M_{cr}}{M_a}\right)^3\right] I_g + \left[1 - \left(\frac{M_{cr}}{M_a}\right)^3\right] I_{cr} \leq I_g \quad \text{Eq. (2-14)}$$

However, this equation is not applicable to flexural concrete members reinforced with FRP bars because of the difference in cracking and deflection behavior compared to steel-reinforced flexural members. One of the early studies on beams reinforced with FRP bars has shown that the mid span deflections are two to three times the deflections calculated using Branson's equation [Brown and Bartholomew, 1993].

Benmokrane et al., (1996) proposed a modified effective moment of inertia equation using correction factors to Branson's equation. Where the correction factors used for I_g and I_{cr} are $\alpha = 0.84$ and $\beta = 7$. These factors were to account for reduced compression zone depth after cracking of beams reinforced with FRP bars.

$$I_e = \left[\left(\frac{M_{cr}}{M_a}\right)^3\right] \frac{I_g}{\beta} + \left[1 - \left(\frac{M_{cr}}{M_a}\right)^3\right] \alpha I_{cr} \leq I_g \quad \text{Eq. (2-15)}$$

Further modification to Branson's equation was suggested by Theriault and Benmokrane (1998) which uses a correction factor $\beta_d = 0.6$. A total of twelve GFRP reinforced

concrete beams with $\rho = 0.0116$ and $\rho = 0.0215$ were tested underneath two concentrated load points.

$$I_e = I_{cr} + \left(\beta_d I_g - I_{cr}\right)\left(\frac{M_{cr}}{M_a}\right)^3 \leq I_g \qquad \text{Eq. (2-16)}$$

ACI.1R-01 and ACI.1R-03 adopted the equation (2-16) with $\beta_d = \alpha_b \left(E_f / E_s + 1\right)$, which accommodates for the difference in bond characteristics by including a bond dependent coefficient, α_b. Further studies have shown that the effective moment of inertia by Branson's equation overestimated the actual stiffness. Branson's equations are applicable to reinforcement ratios higher than 0.01 that corresponds to $I_g / I_{cr} < 3$. Whereas for FRP-reinforced concrete beams these ratios are beyond the calibrated range.

Each edition of ACI 440 committee reports stated that Branson's effective moment of inertia over estimates the stiffness, however gave a different reason for over estimation. Consequently, each of the committee reports adopted a different modified version of Branson's equation. ACI 440.1R-01 (2001) and ACI.1R-03 (2003) has accepted the same effective moment of inertia equation with correction considering the difference in bond behavior and elastic modulus. ACI 440.1R-06 (2006) has changed the reduction coefficient, $\beta_d = 1/5\left(\rho_f / \rho_{fb}\right)$ in view of decreased tension stiffening effect in FRP-reinforced concrete beams.

An alternative section-based expression was proposed for the effective moment of Inertia by Bischoff (2005) that is applicable both to steel and FRP reinforced concrete beams. Bischoff's expression for effective moment of Inertia was modified and adopted by ACI 440.1R-15 (2015) including a factor γ, that accounts for stiffness variation along the length of the member.

$$I_e = \frac{I_{cr}}{1-\gamma\left(\frac{M_{cr}}{M_a}\right)^2\left[1-\frac{I_{cr}}{I_g}\right]} \le I_g \text{ where } M_a \ge M_{cr} \quad \text{Eq. (2-17)}$$

$$\gamma = 1.72 - 0.72\left(M_{cr}/M_a\right) \quad \text{Eq. (2-18)}$$

Basalt-fiber-reinforced polymer (BFRP) is cost-effective compared to other fiber-reinforced polymers and provides numerous benefits that are superior to other types of FRP [Parnas et al., 2007; Wang et al., 2012; Lopresto et al., 2011].

2.3.7 High strength to weight ratio

Specific weight of FRP composite materials is less than 2 [SP Systems], whereas most steels is nearly 8. Due to their low specific gravity, the FRP composites have a significant high strength-to-weight ratio and high stiffness-to-weight ratios compared to metals. Because of this property FRP bars have a great potential for use in concrete structures [El-Sayed et al. 2006a, b; Mukherjee and Arwikar, 2005].

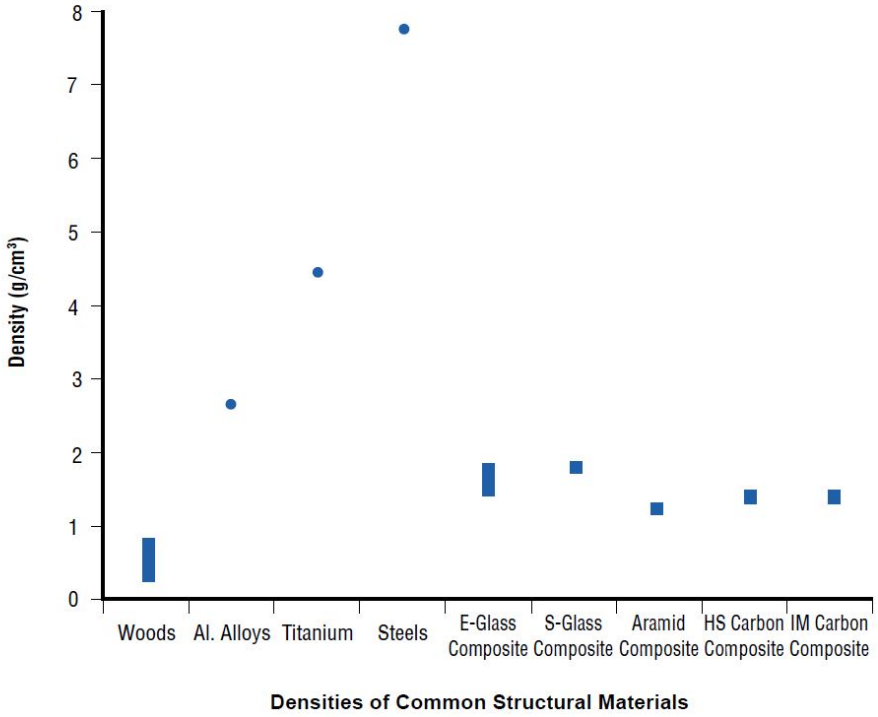

Figure 2-13 Densities of common structural materials [SP Systems]

Chapter 3

Part I: Experimental Program – Testing of flexural structural members

3.1 Design of specimens

A total of 9 simply supported RC, SFRC and UHPFRC beams were monotonically loaded up to failure. All beams had a same cross section of 9-inch width and 16-inch height, with two shear spans of 57 inches each and a constant moment region of 20 inches. Steel fibers used in SFRC specimens were hooked-end fibers (*l/d* =65, *l* = 2.36 in. (60 mm), *d* = 0.035 in. (0.9 mm), *ft* = 334 ksi (2300MPa)) and in UHP-FRC beams were micro short steel fibers (*l/d* = 62, *l* = 0.51 in. (13.0 mm), *d* = 0.0083 in. (0.21 mm), *ft* = 399 ksi (2750 MPa)) confirming to ASTM A820. The fiber content for SFRC and UHP-FRC beams was 0.75% and 3.0% by volume, where 0.75% for SFRC is the minimum amount as specified by the ACI 318 (2014). The design compressive strength of concrete was 6000 psi in compliance with the maximum allowable compressive strength for SFRC (ACI 318, 2014). Table 3.1 lists the design properties of beams used in this experimental program.

Table 3-1 Design summary of specimens

Specimen	Effective depth (d) in.	a/d	ρ (%)	V_f (%)	Targeted, f'c (psi)	Measured, f'c (psi)
RC1	12.0	4.75	2.58(S60)	0	5000	5000
RC2	14.5	3.93	1.38(BFRP)	0	5000	5100
SFRC1	14.5	3.93	3.16(S60)	0.75	5000	5439
SFRC2	14.5	3.93	1.53(MMFX)	0.75	5000	5439
UHP-FRC1	12.0	4.75	13.0(S60)	3.0	22000	21000
UHP-FRC2	14.5	3.93	3.59(MMFX)	3.0	22000	20800
UHP-FRC3	14.5	3.93	2.30(MMFX)	3.0	22000	20800
UHP-FRC4	13.25	4.3	3.02(BFRP)	3.0	22000	18500
UHP-FRC5	12.0	4.75	5.85(BFRP)	3.0	22000	18500

3.2 Fiber type and fiber volume fraction

Different types of fibers used in construction industries are made of different materials such as steel, polypropylene, GFRC glass, asbestos, carbon and organic. Two different types of steel fibers are primarily used in this research. Steel fibers are produced in two different forms, discrete and bundled. The steel fibers used in SFRC specimens were Dramix 5D fibers produced by Bekaert Corporation. The steel fibers are bent five times at each end and glued together in to bundles by a dissolvable glue to prevent the clumping of fibers, allowing the fibers to be uniformly distributed in the mixture. However, this is contradicted by the research carried out by Cho (2011), where the adhesion between the fibers was not properly dissolved and the steel fibers remained in bundles Figure 3-2. Bundled dramix 5-D fibers used in SFRC beams have mechanical properties of (l/d =65, l = 2.36 in. (60 mm), d = 0.035 in. (0.9 mm), ft = 334 ksi (2300MPa)). The fiber content of 0.75% by volume was used, which is the minimum amount as specified by the ACI 318 (2014). For UHP-FRC mix micro-short steel fibers of 3.0% by volume were used with following mechanical properties, (l/d = 62, l = 0.51 in. (13.0 mm), d = 0.0083 in. (0.21 mm), ft = 399 ksi (2750 MPa)).

(a) (b)

Figure 3-1 (a) Bundled hooked end steel fibers (Dramix-5D)

(b) Micro-short straight steel fibers (Dramix OL 13/0.20)

Figure 3-2 Lumpy distribution of fibers due to undissolved adhesion (Cho, 2011)

Table 3-2 Used fiber type and properties

Type of fiber	Length (L), in. (mm)	Diameter (D), in. (mm)	Aspect ratio (L/D)	Tensile strength (f_t), ksi (MPa)
Hooked-end	2.36 (60)	0.035 (0.90)	65	334 (2,300)
Micro short	0.51 (13)	0.008 (0.21)	62	399 (2,750)

3.3 Concrete mix design

3.3.1 RC and SFRC mix design

For both RC beams concrete with a target compressive strength of 5,000 psi (35 MPa) was ordered through a ready-mix truck. For SFRC beams, 0.75% measured by volume of hooked end high strength steel fibers (Dramix-5D) were added to the ready-mix truck at CELB.

3.3.2 UHP-FRC mix design

UHP-FRC used in this program was developed at University of Texas at Arlington with locally available materials in USA. UHP-FRC mix was nearly self-consolidating consists of mix components as tabulated (Table 3-4). Target compressive strength of the mix was 22,000 psi (150 MPa). However, the actual compressive strengths obtained were less than 22,000 psi because of the fact that mixing process of the dry materials was performed in outdoor conditions resulting in loss of large amount of cementitious materials and fly ash due to wind.

3.3.3 Mix proportions by weight

3.3.3.1 Typical mix proportions for SFRC:

Table 3-3 Typical Mix proportion for SFRC

Cement (Type 1)	Fly Ash (Class C)	Sand	Coarse aggregate3/8"	Water	Steel fiber	Total weight
1.0	0.5	1.7	1.0	0.45	0.117	4.77

3.3.3.2 Mix proportions for UHP-FRC (developed at UTA):

Table 3-4 Mix proportions for UHP-FRC (developed at UTA)

Mix component	Particle size	Proportions by weight
Silica sand 1 (US Silica)	0.02 in. (500 μm)	1.7
Silica sand 2 (US Silica)	0.0047 in. (120 μm)	0.37
Steel fiber (Maccaferri/BTM)	D = 0.0069 in. (0.175 mm); L = 0.49 in. (12.5 mm); f_t = 319 ksi (2200 MPa)	0.275
Cement (Portland type I)	0.00079 in. (20 μm)	1
Fly ash (Class F)	0.00079 in. (20 μm)	0.2
Glass powder (US Silica)	0.00067 in. (1.7 μm)	0.25
Silica Fume (Norchem/Elkem)	0.00047 in. (1.2 μm)	0.25
Superplasticizer (Cast 575/Melflux 4930F)	Polycarboxylate-based	0.01/0.021

3.4 Construction of specimens

Construction work of all the specimens except UHP-FRC1 was conducted at the UTA Civil Engineering Laboratory Building (CELB), by the author with help of Dr. Shih-Ho (Simon) Chao's research group. For specimen UHP-FRC1, form work and the rebar cage were prepared

at CELB and was shipped to Bailey Tools and Manufacturing for casting at their facility in Lancaster, TX.

3.5 Strain gauge installation

For each specimen with the exception of specimens UHP-FRC1 and RC1 strain gauges were mounted on the longitudinal bars in the constant moment region extending to one shear span. For the two specimens UHP-FRC1 and RC1 strain gauges were mounted only in the constant moment region spaced at 5 inches apart.

To install a strain gage, ribs on a rebar at the marked place were grinded and sanded with 400 grit sand paper for a flat, smooth surface. After scouring the surface, the strain gage was glued and protected by three different layers of coating namely, polyurethane, nitrile, rubber mastic electrical tape and electric liquid tape to seal the moisture (Figure 3-3).

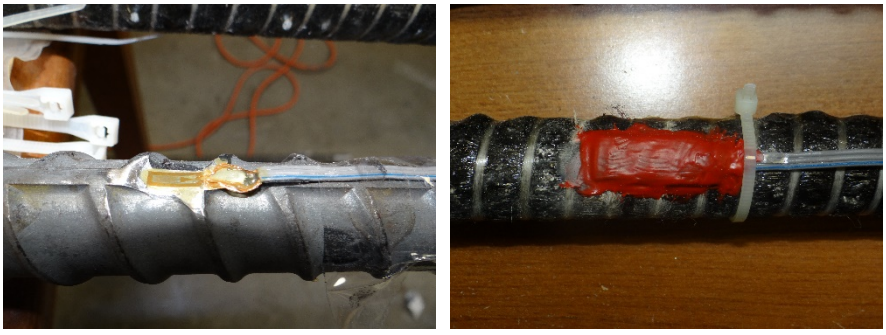

(a) (b)

Figure 3-3 Strain gauge installation (a) Glued strain gauge to cleaned rebar (MMFX) (b) Sealed strain gauge with liquid electrical tape (BFRP rebar)

Figures 3-4 through 3-12 shows the design drawings with location of strain gauges.

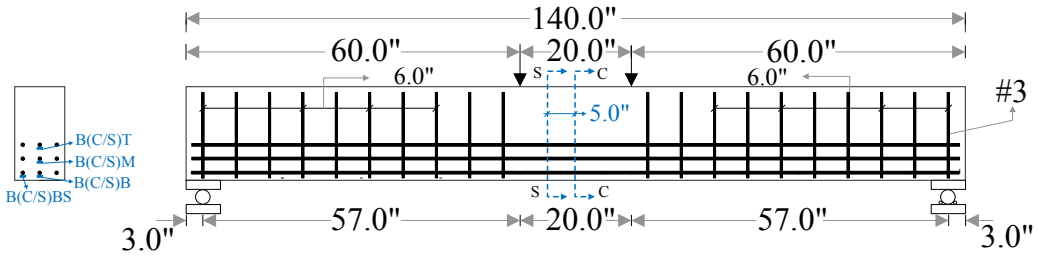

Figure 3-4 Location of strain gauges in RC #1 60S

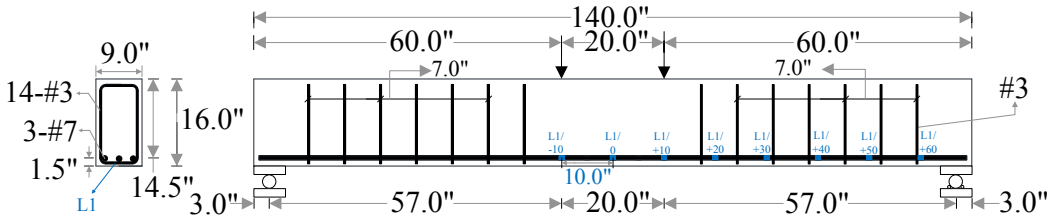

Figure 3-5 Location of strain gauges in RC #2 BFRP

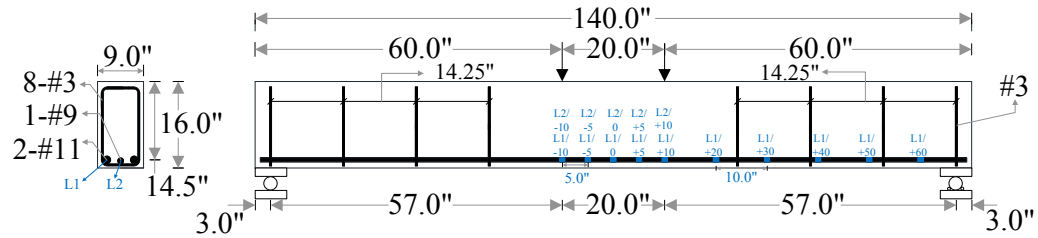

Figure 3-6 Location of strain gauges in SFRC #2 60S

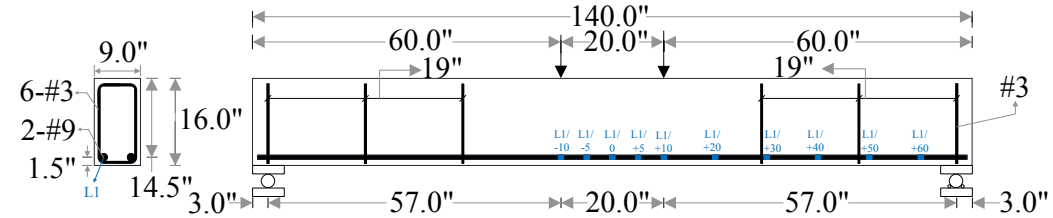

Figure 3-7 Location of strain gauges in SFRC #3 100S

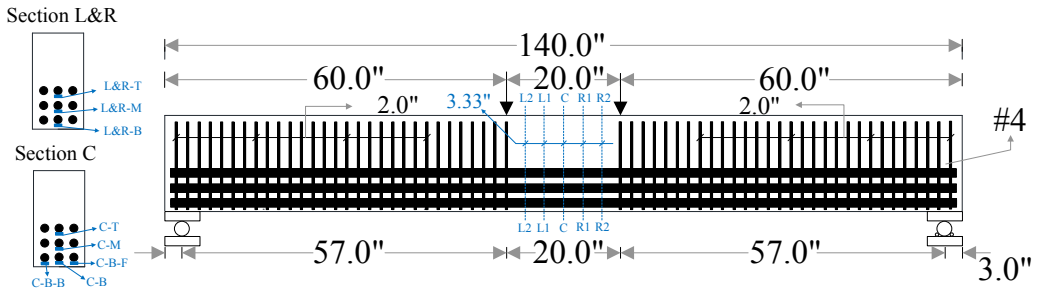

Figure 3-8 Location of strain gauges in UHP-FRC #1 60S

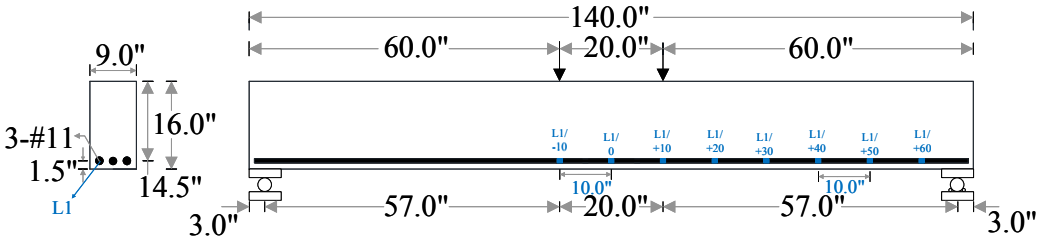

Figure 3-9 Location of strain gauges in UHP-FRC #2 100S

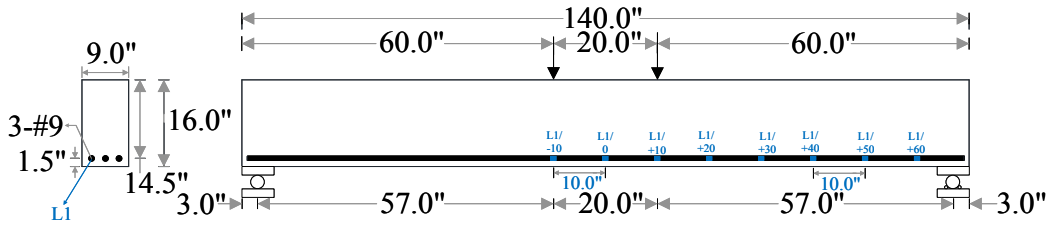

Figure 3-10 Location of strain gauges in UHP-FRC #3 100S

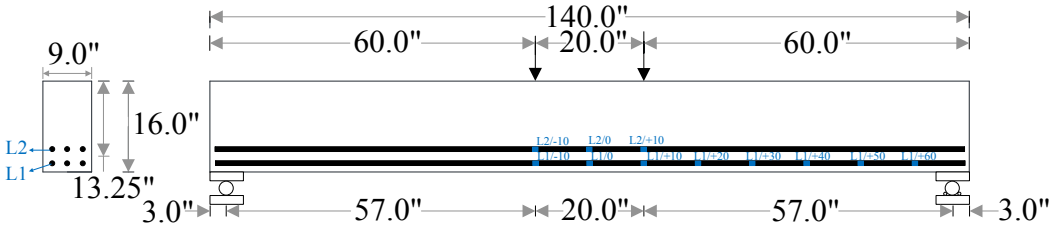

Figure 3-11 Location of strain gauges in UHP-FRC #4 BFRP

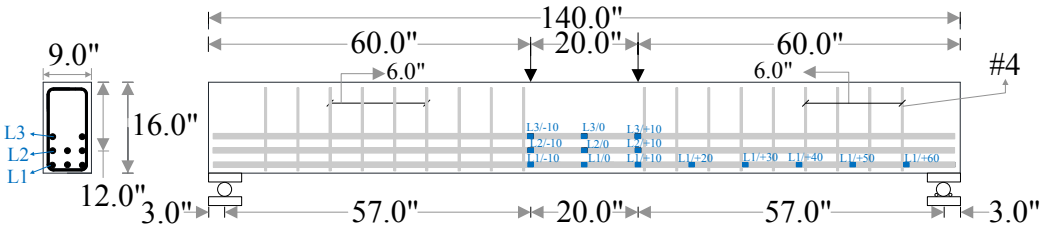

Figure 3-12 Location of strain gauges in UHP-FRC #5 BFRP

3.6 Caging and formwork fabrication

Reinforcing bar cage and formwork were fabricated at CELB by the author with help of graduate students at UTA. Longitudinal bars for all specimens were straight without any bends or mechanical terminators.

3.7 Mixing of concrete, casting and curing of the specimens

3.7.1 RC and SFRC beams

RC beams were cast using concrete of 5 ksi target compressive strength provided by a local ready mix truck (Figure 3-13 (a)) with a specified slump of 5 inches. For SFRC beams a volume fraction of 0.75% of steel fibers were measured and added in to the mixing drum of a similar ready mix truck. Drum was continued to rotate until a uniform mix of fibers with concrete is attained. A wheel barrel of concrete is taken from the ready mix truck prior to casting beams for slump and casting cylinders. Concrete was then poured in to formwork and vibrated with a needle vibrator to achieve compactness. Three large scale dog-bone shaped specimens used for direct tension test were casted for SFRC alongside nine 4x8 in. cylinders.

(a) (b)

Figure 3-13 (a) Ready mix truck (b) Concrete bucket used for casting beams

(a) (b)

Figure 3-14 (a) Pouring of concrete in formwork and compacting with needle vibrator

(b) Uniform distribution of fibers

(a) (b)

Figure 3-15 (a) Direct tensile test specimens (b) Final cast beams

3.7.2 UHP-FRC beams

Unlike the RC and SFRC castings, mixing of UHP-FRC requires a high shear mixer which poses a construction challenge in casting large scale structural elements. For a contemporary research project by Dr. Shih-Ho Chao, that involves a cubic yard of UHP-FRC casting, a special concrete mixer (Figure 3-16) was designed and fabricated with the help of Bailey Tool and Manufacturing Company. Working of the mixer resembles a twin shaft concrete mixer and operates on hydraulic power, which was also used for casting of the specimen UHP-FRC1.

Dry materials were measured in a big bucket and was transferred in to the mixer during the mixing process where the water combined with super-plasticizer was added simultaneously to the mixer. Micro-short steel fibers of 3% by volume were added to the mix in the end.

Figure 3-16 Special hydraulic concrete mixer used for casting of beam UHP-FRC #1

Figure 3-17 Cast beam UHP-FRC #1

Figure 3-18 Direct tensile test specimens for UHP-FRC

Employing this special mixer that works on hydraulic power for large scale castings is not a viable solution. Hence a mixer that is more feasible for large scale castings was considered for later castings. A rough terrain self-loading concrete mixer truck (Figure 3-19)

from Fiori group was used for casting the rest UHP-FRC specimens. Driver's cabin on the truck is equipped with an accurate dosing system, integrated to an onboard computer through which multiple mix proportions can be saved by storing different components for each of them. This system guides the operator during mix design preparation, assuring a high dosing precision, homogeneity in the mix and therefore an extremely strong concrete. All the dry materials were measured using loading arm of the mixer and transferred to the mixing drum where the water was added simultaneously.

Figure 3-19 Concrete mixer truck used for casting beams UHP-FRC #2, #3, #4 and #5

(a) (b)

Figure 3-20 (a) Measured dry materials in loading arm of truck

(b) Loading of steel fibers into wet UHPC mix using loading arm

Figure 3-21 Pouring of UHP-FRC using chute

3.8 Test setup and instrumentation

All the specimens were loaded to failure using 650 kips hydraulic cylinder attached to one of the steel frames erected at CELB. Beams were tested under simply supported conditions, where at one end of the beam, a 2 in. roller with two steel plates spread through the entire beam width were used. At the other end, same set of roller and plates were used by

welding on either sides of the roller with bars to the bottom plate which simulates a hinge support. Figure 3-22 (a) and (b) shows supports used for all the specimens. Plates used at the supports were 6 in. wide along length of the beam and 3 in. thick.

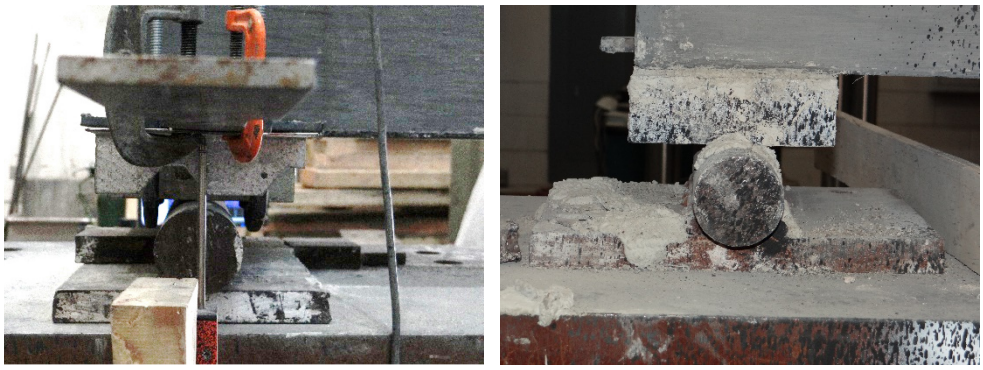

(a) (b)

Figure 3-22 (a) Roller support (b) Hinge support

Beams were loaded at two points 20 in. apart from the center of the beam, at each loading point two bearing plates of 6 in. wide along the length of the beam and 1 in. thick were used. These plates were spread along the entire width of the beam and load from hydraulic cylinder was transferred to these plates using a stiffened W12x87 steel beam (Figures 3-23 and 3-24). In order to ensure uniform interface contact between four bearing plates used at loading points and supports, a non-shrink grout was used between the plates and the beam.

Figure 3-23 A view of steel frame and hydraulic cylinder used for test setup

Figure 3-24 A view of test setup and CCD cameras mounted for DIC

For each specimen, strain gauges were placed on longitudinal rebar within the constant moment region 10 in. apart to obtain the stress distribution along the depth of the beam. Strain gauges were also extended into shear span on the bottom layer of steel. To measure the mid-span deflection and settlement of supports, three linear variable transformers (LVDTs) were used. Load applied was measured using a load cell, and all the sensors were connected to Vishay data acquisition (DAQ) system.

Full-field optical measuring technique was used to measure the strains on displacements on the specimen. The specimens under test were captured by a pair of high resolution CCD cameras, which measure the 3D coordinates and the 3D deformations during the test. Resolution of the cameras used for beams testing were 5 mega pixels with a focal length of 8 mm. A contrast pattern was prepared on the specimen by using two layers of flat white paint and black speckles, that deforms with the specimen. Flat paint was used for speckle pattern to prevent any glare.

Figure 3-25 Speckle pattern on beam (SFRC #2)

3.9 Material Testing

3.9.1 UHP-FRC flexural strength

The flexural behavior UHP-FRC mixes used in this research study was determined in accordance with ASTM C1609, Standard Test Method for Flexural Performance of Fiber-Reinforced Concrete. The specimens were 6x6x20 inches with a span length of 18 inches. The test was a displacement-controlled, loading head moving at a rate of 0.002 in./min. The mid-span deflection of the specimens was measured using a pair of LVDTs. The tests were continued until the mid-span deflection reached 1/150 of the span length (0.12 in.). Crack location is required to fall with in the 6 in. middle region, where the bending moment was invariable due to zero shear. This is because the results from the tests were to reflect the flexural behavior of UHP-FRC, failure was needed to be induced by pure flexure rather than any other forces. Third-point loading test setup is illustrated in Figure 3-26.

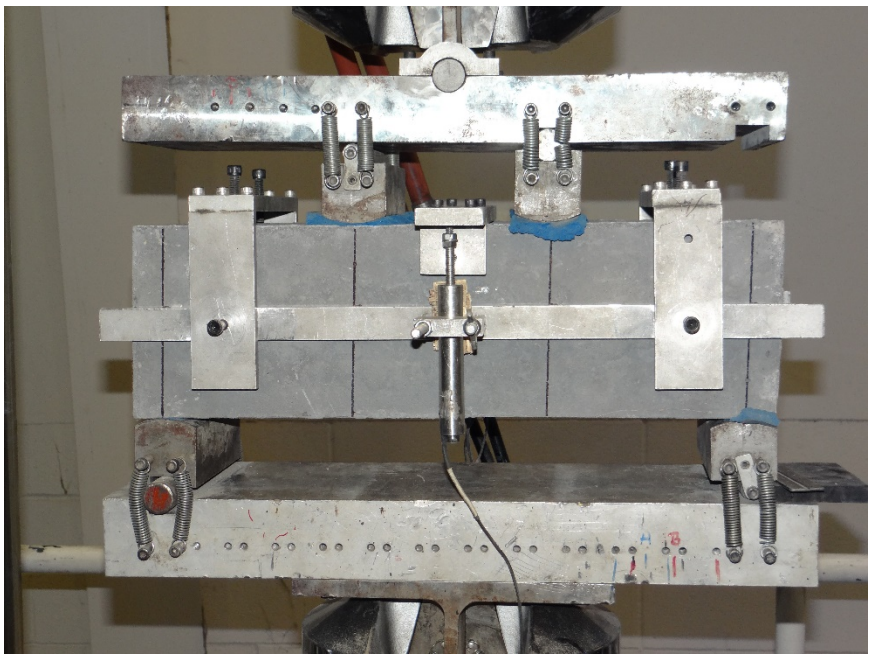

Figure 3-26 Third-point loading test setup [ASTM C1609]

Typical load versus mid-span deflection relationships for a simply supported fiber-reinforced concrete beam under third-point loading test are schematically presented in Figures

3-27 and 3-28. In both cases, the specimen shows a linear behavior up to the first flexural cracking which mostly causes a sudden drop in the applied load. After initial flexural cracking, the specimen may either display a deflection hardening before reaching the softening branch (Figure 3-28) or exhibit a softening after initial cracking (Figure 3-27). The first peak load (P_1) corresponds to the first point at which the load-deflection curve has a zero slope. Similarly, the peak load (P_p) is the largest load on the load-deflection curve. For the load-deflection curve shown in Figure 3-27, P_1 and P_p lies at the same point.

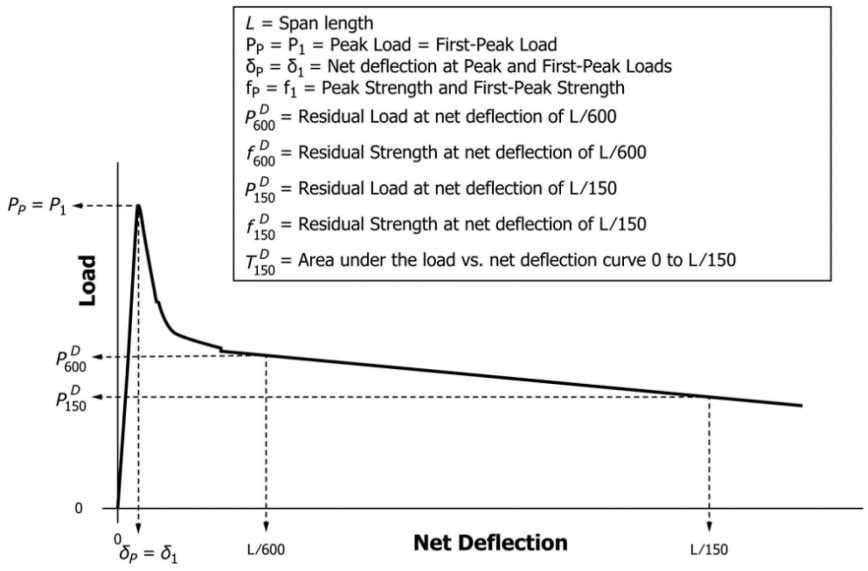

Figure 3-27 Typical load vs mid-span deflection relationships for a SFRC specimen under third-point loading test (first peak load matching the peak load)

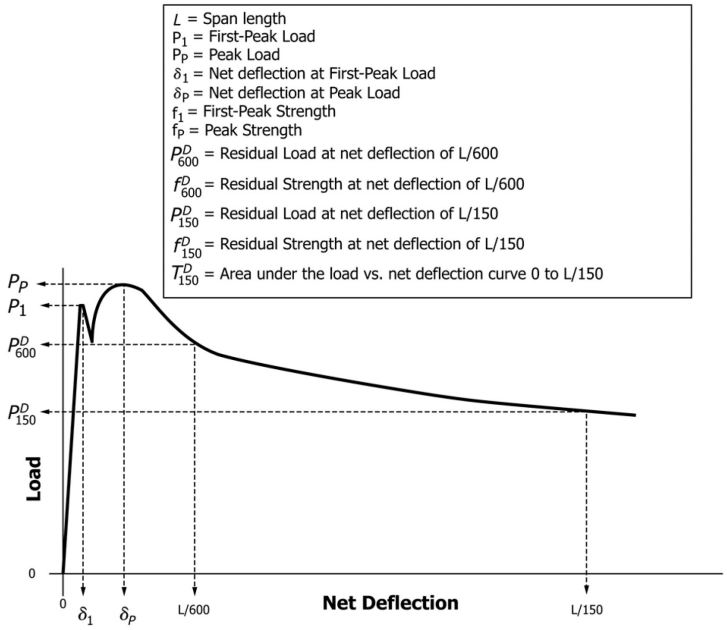

Figure 3-28 Typical load vs mid-span deflection relationships for a SFRC specimen under third-point loading test (first peak load lower than the peak load)

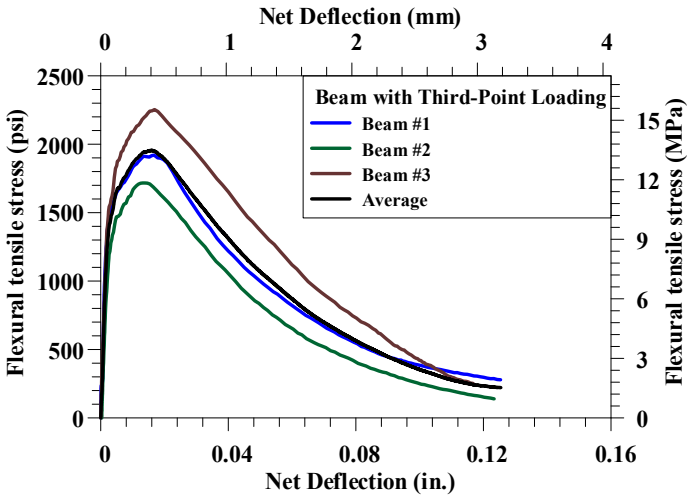

Figure 3-29 UHP-FRC flexural stress vs deflection

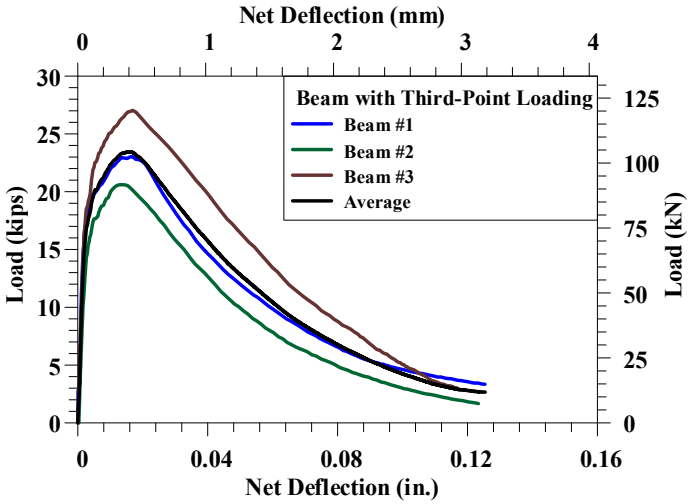

Figure 3-30 UHP-FRC flexural load vs deflection

Load-deflection curves shown in figure 3-30 were the typical results of ASTM beams casted with UHP-FRC during this research. Load values at critical deflections were tabulated as shown in Table 3-5.

Table 3-5 Summary of ASTM C1609 Test: Load at various deflection

Specimen	First-peak load, P_1 lb, (kN)	Peak load, P_p lb, (kN)	Load at 0.03 in. (L/600) deflection lb, (kN)	Load at 0.06 in. (L/300) deflection lb, (kN)	Load at 0.12 in. (L/150) deflection lb, (kN)
#1	23062 (103)	23062 (103)	18205 (81)	9825 (44)	3537 (16)
#2	20629 (92)	20629 (92)	15783 (70)	7780 (35)	1782 (8)
#3	27051 (120)	27051 (120)	23196 (103)	13524 (60)	2980 (13)
Mean	23581	23581	19061	10376	2766
Standard deviation	3242	3242	3780	2911	897
Coefficient of variation	13.7%	13.7%	19.8%	28.1%	32.4%

ACI 318-14, section 26.12.5.1 states that steel fiber reinforced concrete shall be considered acceptable for shear resistance if the following two criteria from ASTM C1609 are satisfied (Figure 3-31):

1. The residual strength obtained from flexural testing in accordance with ASTM C1609 at a mid-span deflection of 1/300 of the span length is greater than or equal to 90 percent of the measured first-peak strength obtained from a flexural test or 90 percent of the strength corresponding to f_r from Equation 3-1, whichever is larger:

$$f_r = 7.5\sqrt{f_c'} \qquad (Modulus\ of\ rupture) \qquad f_c'\ in\ psi \qquad \text{Eq. (3-1)}$$

2. The residual strength obtained from flexural testing in accordance with ASTM C1609 at a mid-span deflection of 1/150 of the span length is greater than or equal to 75 percent of the measured first-peak strength obtained from a flexural test or 75 percent of the strength corresponding to f_r from Equation 3-1, whichever is larger.

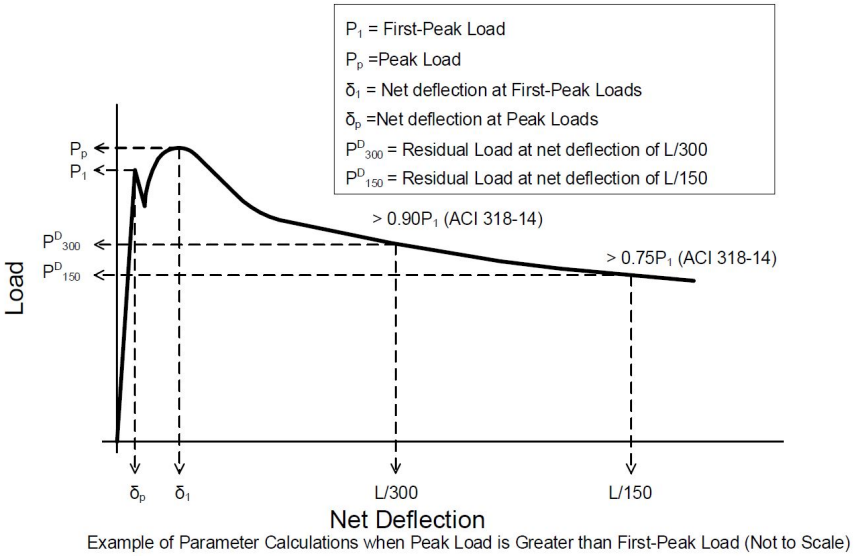

Figure 3-31 Shear performance criteria of SFRC under ASTM C1609 test required by ACI 318-14

ACI performance criteria were studied for the UHP-FRC specimens and shown in Table 3-6 and Table 3-7 respectively. The data clearly indicates that none of the specimens met the two ACI criteria, and therefore this UHP-FRC mix shall not be used to replace conventional shear reinforcement.

Table 3-6 Summary of ASTM C1609 Tests: ACI requirement comparison-I

Specimen	90% P_r lb (kN)	90% of first peak load lb (kN)	Maximum (90% P_r, 90% P_1) lb (kN)	Load at 0.06 in. (L/300) deflection lb (kN)	Difference
#1	11738 (52)	20,756 (92)	20,756 (92)	9825 (44) (47.3%)	-10931 Not pass
#2	11738 (52)	18,566 (83)	18,566 (83)	7780 (35) (41.9%)	-10786 Not pass
#3	11738 (52)	24,566 (109)	24,566 (109)	13524 (60) (55.05%)	-11042 Not pass

Table 3-7 Summary of ASTM C1609 Tests: ACI requirement comparison- II

Specimen	75% P_r lb (kN)	75% of first peak load lb (kN)	Maximum (75% P_r, 75% P_1) lb (kN)	Load at 0.12 in. (L/150) deflection lb (kN)	Difference
#1	9782 (43)	17,297 (92)	17,297 (92)	3537 (16) (20.7%)	-13,760 Not pass
#2	9782 (43)	15,472 (69)	15,472 (69)	1782 (8) (11.5%)	-13,690 Not pass
#3	9782 (43)	20,472 (90)	20,472 (90)	2980 (13) (14.5%)	-17,492 Not pass

3.9.2 UHP-FRC Compressive strength

Compression testing of cylinders is often used test method to check the quality of structural concrete, therefore, engineers frequently aim to connect other properties of concrete's performance to this parameter. However, determination of the compressive strength for very high strength concrete is difficult because of the need for the machines with higher capacity and

is required for cylinders to have ends prepared [Graybeal and Davis, 2008]. During this program 2.78 in. (70.7 mm) cubes that are acceptable alternative to standard 4 in. (102 mm) cylinders [Graybeal and Davis, 2008] are used to determine the compressive strength and its properties. This is to lessen the amount of labor work required for ends preparation of cylinders during the phase of material development. Main interest here for the compression test is to obtain relationship between compressive strength and the uniaxial strains when loaded under compression.

Uniaxial-compressive stress strain relationships for UHP-FRC were obtained for a total of three cubes from each beam casting. Cubes sampled from every casting were removed from molds after one day of casting and stored near the beams until. No end surface preparation is required for testing these cubes and compression test machine and setup are as shown in Figure 3-32 (a). Both ascending and softening braches of compressive stress-strain curve presented were obtained through a load controlled method with a loading rate of 400 lb/sec [ASTM C109/C109M].

(a) (b)

Figure 3-32 (a) Compression test machine and setup

(b) Typical crushing of cube at the end of testing (7% strain)

UHP-FRC offers a new way to design reinforced concrete flexural members due to its superior mechanical properties as compared to conventional concrete. Figure 3-33 shows

typical compressive and tensile stress-strain relations of one of the UHP-FRC materials developed at UT Arlington. The maximum usable compressive strain (at a post-peak stress of approximately 80% of the peak stress), ε_{cu}, is approximately 0.015. For plain concrete, the compressive strain at this level of stress is 0.003. ACI 318-14 and AASHTO LRFD (AASHTO, 2014) use 0.003 as the design maximum strain at crushing of concrete. Due to this small strain capacity of plain concrete, only a small amount of longitudinal reinforcement could be used in order to ensure that the flexural member is tension-controlled. For a tension-controlled beam section, the tensile strain in the extreme tension reinforcement (closest to the tension face) is sufficiently large (≥ 0.005); therefore, the beam shows a large deflection as a warning before failure occurs. If the concrete compressive strain can be 5 to 10 times greater, the beam could be more efficiently utilized by placing considerably higher amount of longitudinal reinforcement while still maintaining tension-controlled behavior.

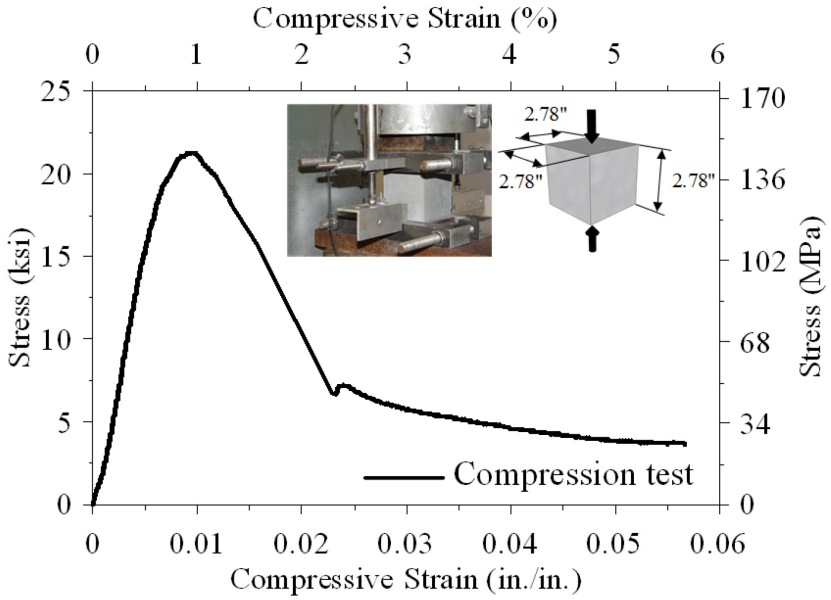

Figure 3-33 Average compressive stress-strain of UHP-FRC

3.9.3 UHP-FRC direct tension test

It is generally known that conventional concrete is weak in tension, and the tensile strength of conventional concrete is typically about $1/10 \sim 1/12$ of their compressive strength. Hence the tensile strength of conventional concrete is considerably influenced by the fracture strength of the matrix. Since the UHP-FRC mixes have very high compressive strengths compared to conventional concrete (nearly 5 times), the tensile strength of UHP-FRC matrix is also presumed to be higher. Addition of fibers in UHP-FRC mix helps in redistribution of tensile stresses after the initial cracking, resulting in strain hardening after the first cracking.

Tensile behavior of UHP-FRC investigated by other researchers were based on small-scale specimens with cross sectional area of 2.0 in.2 (1,290 mm2) [Wille et al., 2011, 2012], 0.59 in.2 (381 mm2) [Ranade et al., 2013] and 16.0 in.^{2} (10,323 mm^2) [Parham et al., 2016]. Wille et al. (2011) reported a tensile strength of 2.9 ksi (20 MPa) at a strain value at peak tensile stress of 0.6% with a 3% volume fraction of straight steel fibers. Whereas, Ranade et al. (2013) reported a tensile strength of 2.1 ksi (14.5 MPa) at a strain value at peak tensile stress of 3.4% with a 2% volume fraction of ultra-high-molecular-weight poly-ethylene fibers. Furthermore, Parham et al. (2016) reported a tensile strength of 1.21 ksi (8.3 MPa) at a strain value with a peak stress of 0.17% with a 3% volume fraction of micro-short steel fibers. Hence the direct tensile behavior of UHP-FRC needs to be studied using large scale tensile specimens to better represent the direct the tensile strength of UHP-FRC.

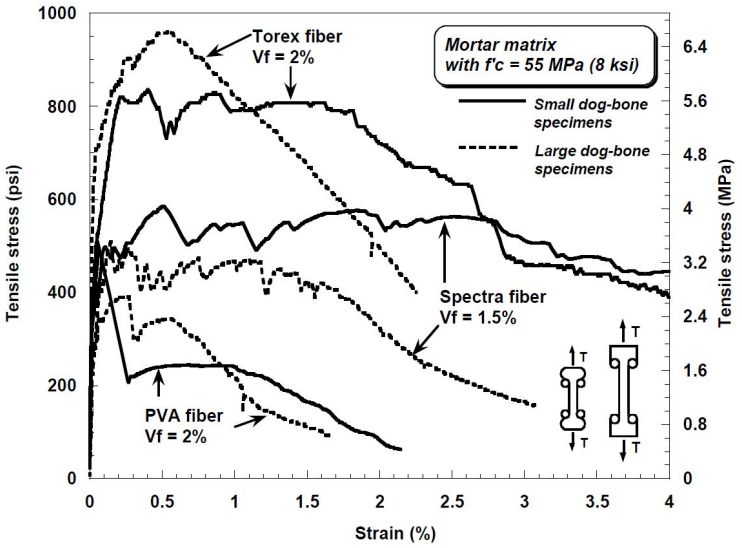

Figure 3-34 Size effect of FRC in direct tension [Naaman, 2006]

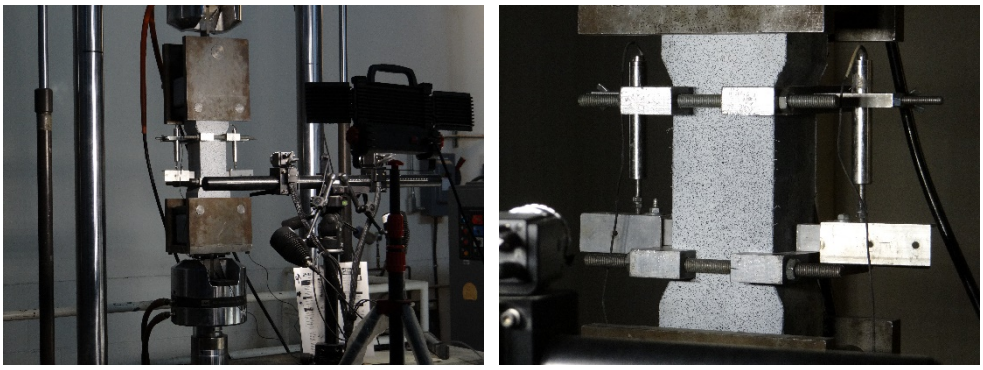

(a) (b)

Figure 3-35 (a) DIC system used to measure strain and crack width

(b) Large-scale dogbone specimen

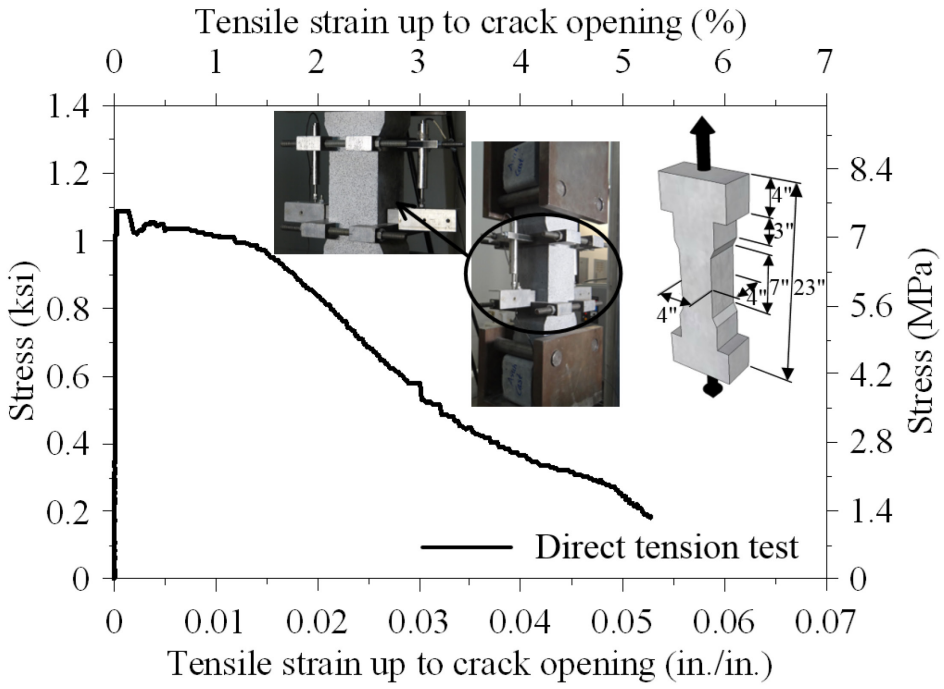

Figure 3-36 Direct tension test response for UHP-FRC

Chapter 4

Part I: Experimental Results – Flexural Structural members

4.1 Beam UHP-FRC #1 60S:

Load mid-span deflection relationship of beam UHP-FRC #1 showed as tri-linear behavior up to peak. Initial segment representing un-cracked response of the beam. Since the cracks did not appear on the beam until very high loads, load for the first flexural crack was approximated from a negligible change in stiffness of load deflection curve. Second segment of the load-deflection curve is representing cracked section with an unnoticeable decrease in stiffness after the first crack. First visible flexural and shear cracks appeared in the shear span at a very high external load of 180 kips. Third non-linear segment began after the yielding of bottom steel layer at 165 kips, followed by concrete crushing under the loading point when the external applied load reached 250 kips. Crushing of the concrete in compression zone extended to nearly entire length of the compression strut in the constant moment region. Load started to drop after attaining a peak load of 318 kips.

Figure 4-1 Compression zone damage of beam UHP-FRC #1 at 318 kips (peak load)

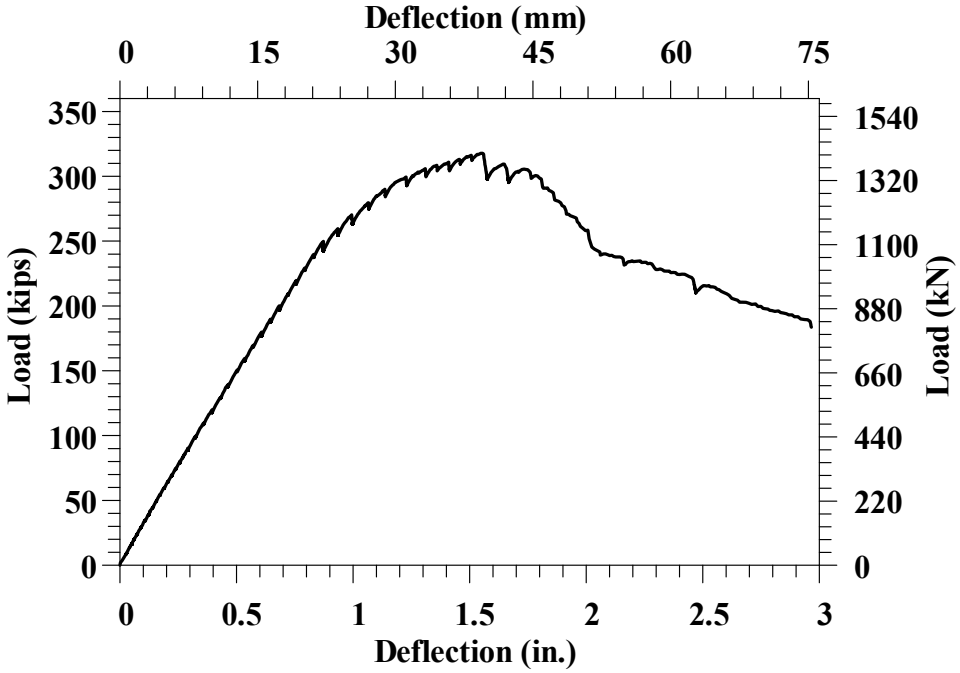

Figure 4-2 Load versus net deflection for beam UHP-FRC #1

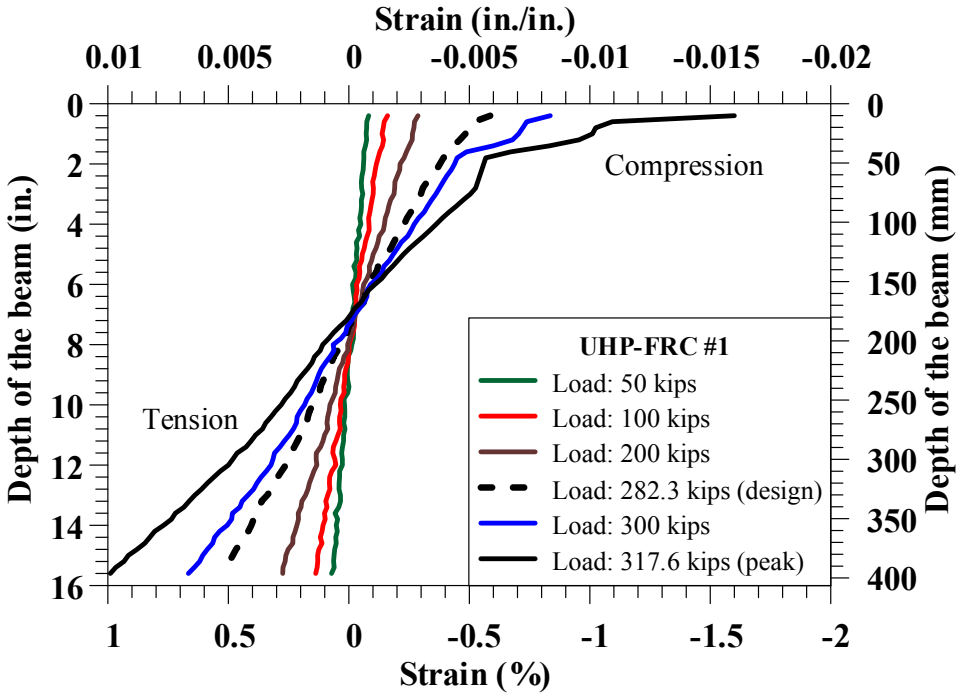

Figure 4-3 Strain variation in beam UHP-FRC #1

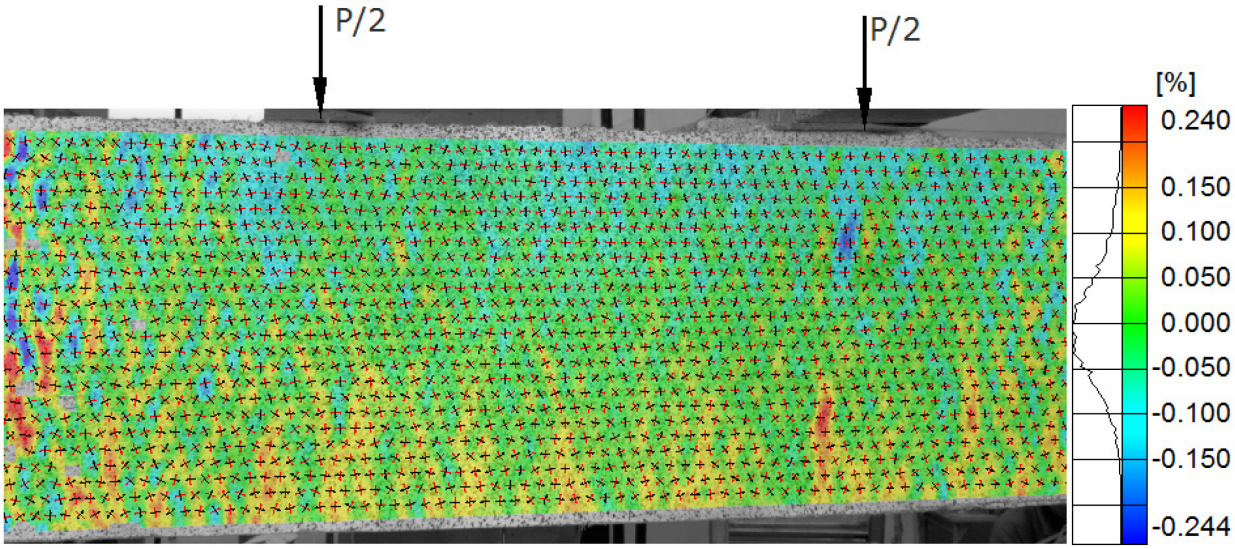

Figure 4-4 Full-field concrete longitudinal strain (ε_x) along moment region for UHP-FRC#1 at an applied load of 50 kips

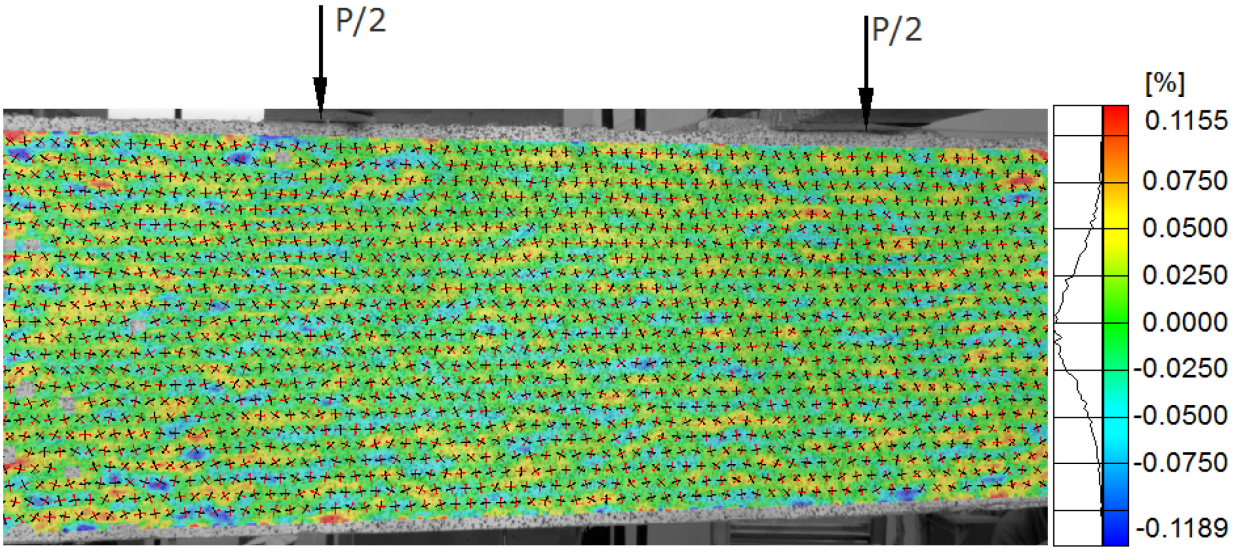

Figure 4-5 Full-field concrete transverse strain (ε_y) along moment region for UHP-FRC#1 at an applied load of 50 kips

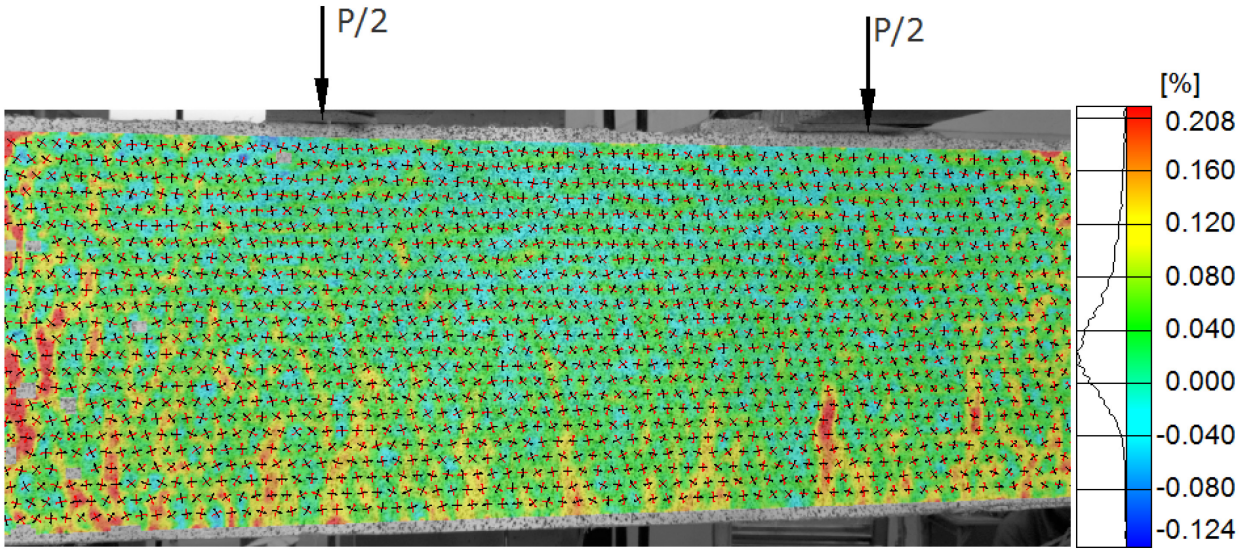

Figure 4-6 Full-field concrete maximum principal strain (σ_1) along moment region for UHP-FRC#1 at an applied load 50 kips

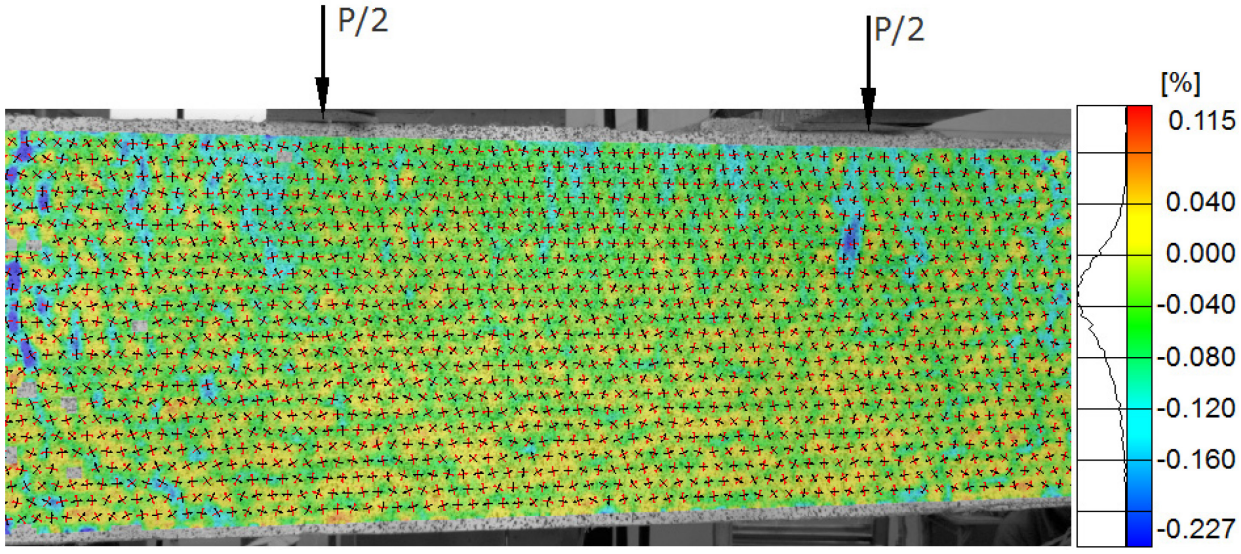

Figure 4-7 Full-field concrete minimum principal strain (σ_2) along moment region for UHP-FRC#1 at an applied load 50 kips

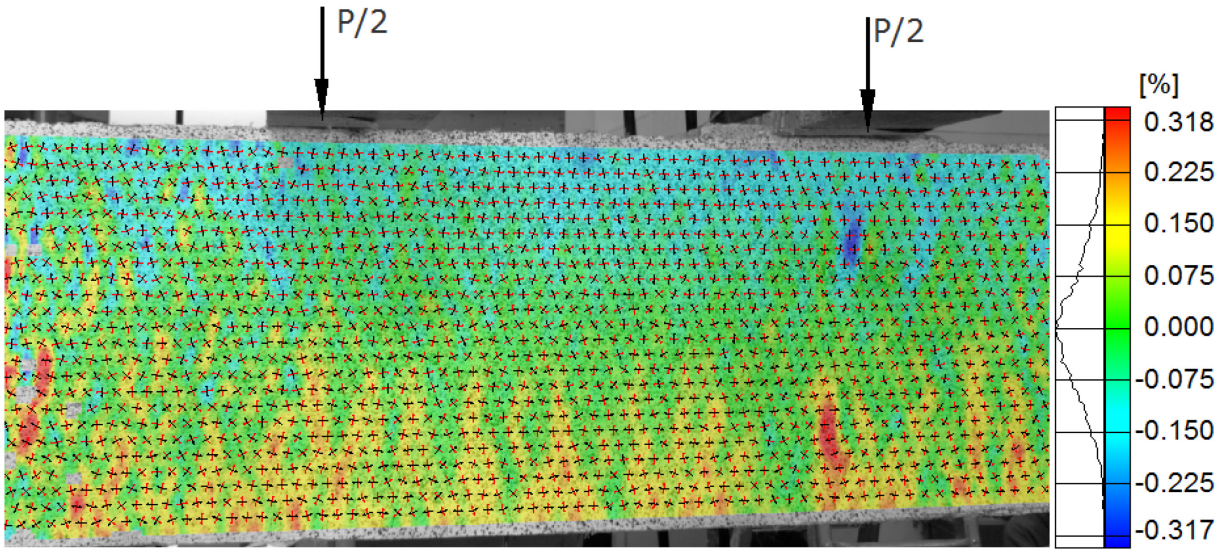

Figure 4-8 Full-field concrete longitudinal strain (ε_x) along moment region for UHP-FRC#1 at an applied load of 100 kips

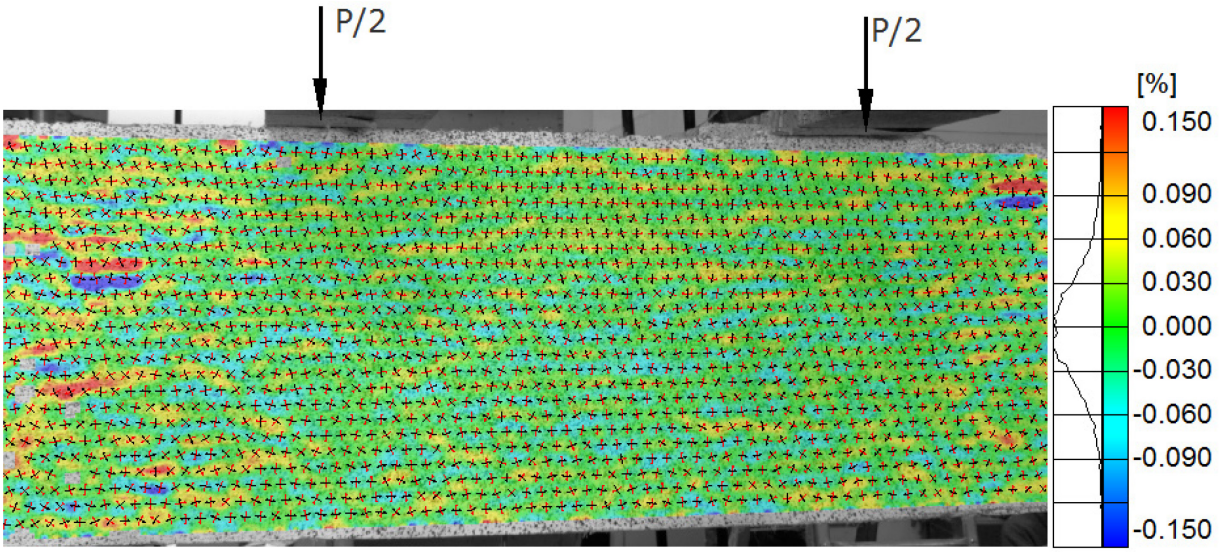

Figure 4-9 Full-field concrete transverse strain (ε_y) along moment region for UHP-FRC#1 at an applied load of 100 kips

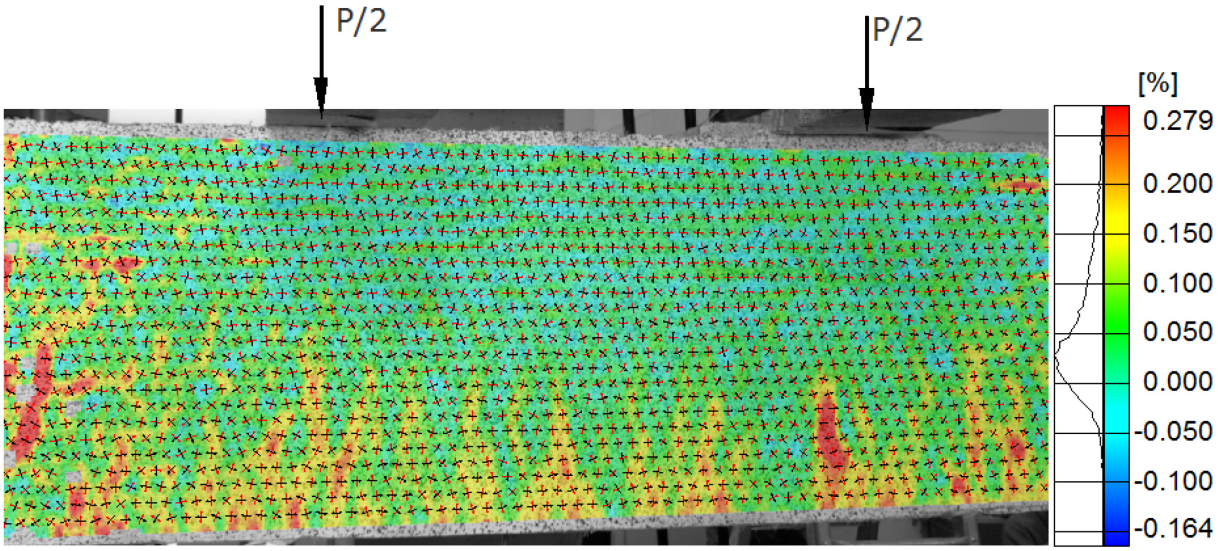

Figure 4-10 Full-field concrete maximum principal strain (σ_1) along moment region for UHP-FRC#1 at an applied load 100 kips

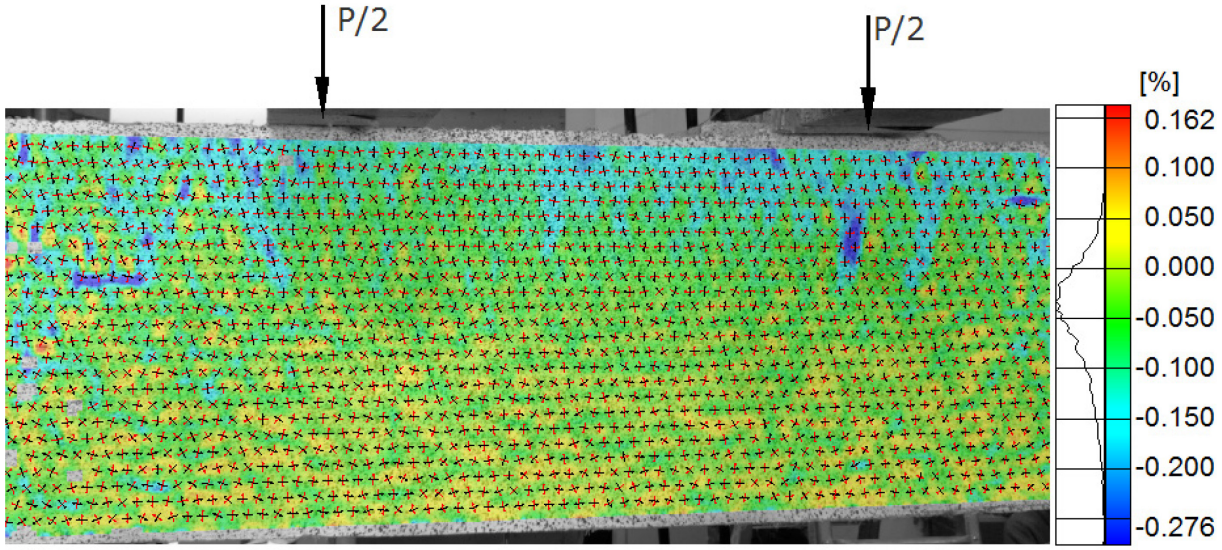

Figure 4-11 Full-field concrete minimum principal strain (σ_2) along moment region for UHP-FRC#1 at an applied load 100 kips

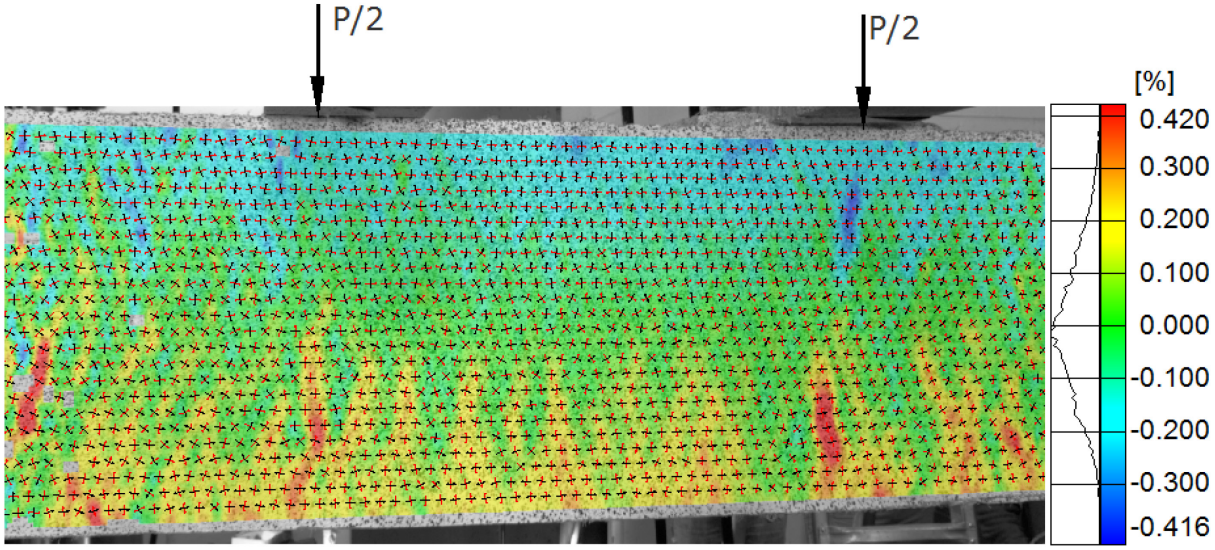

Figure 4-12 Full-field concrete longitudinal strain (ε_x) along moment region for UHP-FRC#1 at an applied load of 150 kips

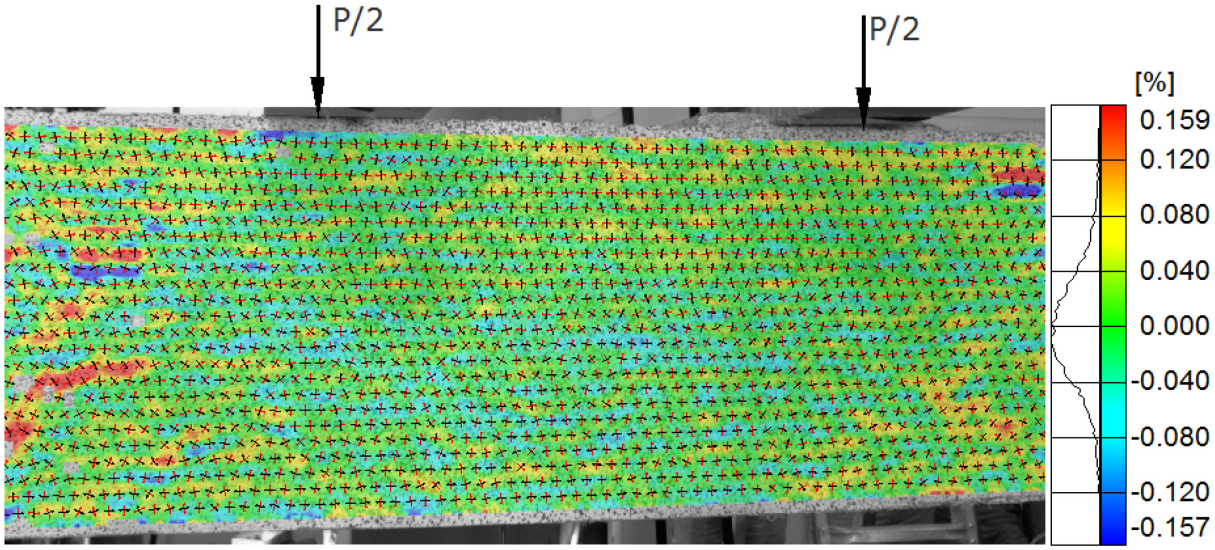

Figure 4-13 Full-field concrete transverse strain (ε_y) along moment region for UHP-FRC#1 at an applied load of 150 kips

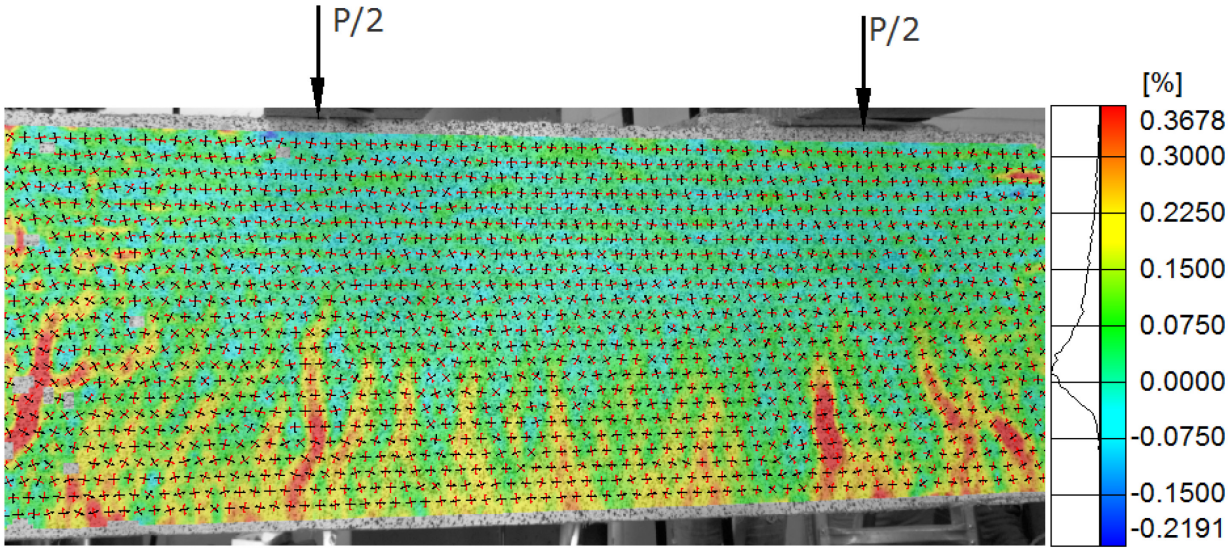

Figure 4-14 Full-field concrete maximum principal strain (σ_1) along moment region for UHP-FRC#1 at an applied load 150 kips

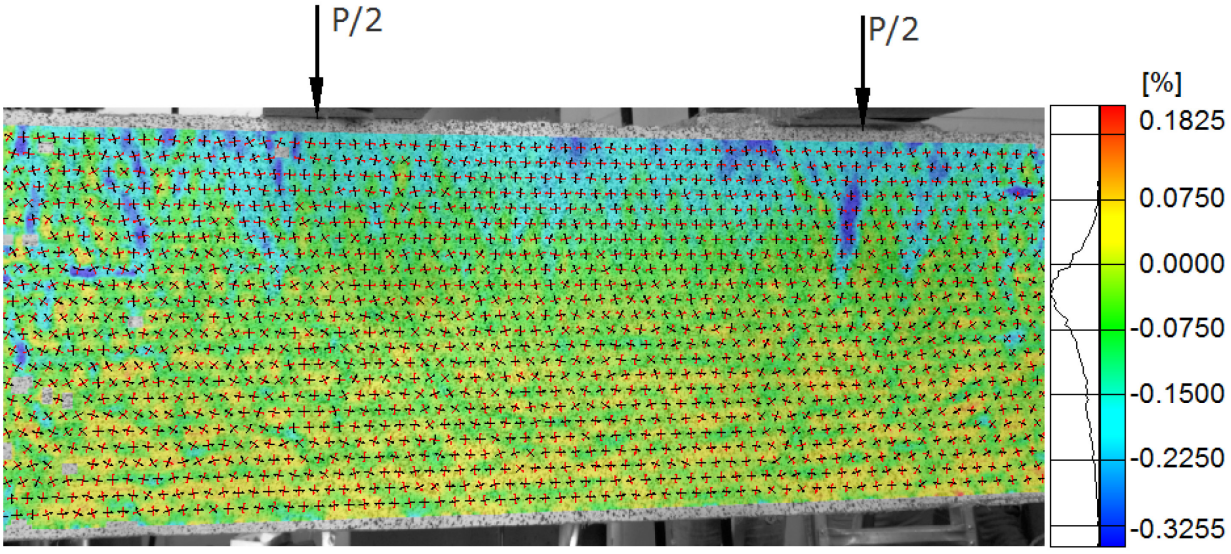

Figure 4-15 Full-field concrete minimum principal strain (σ_2) along moment region for UHP-FRC#1 at an applied load 150 kips

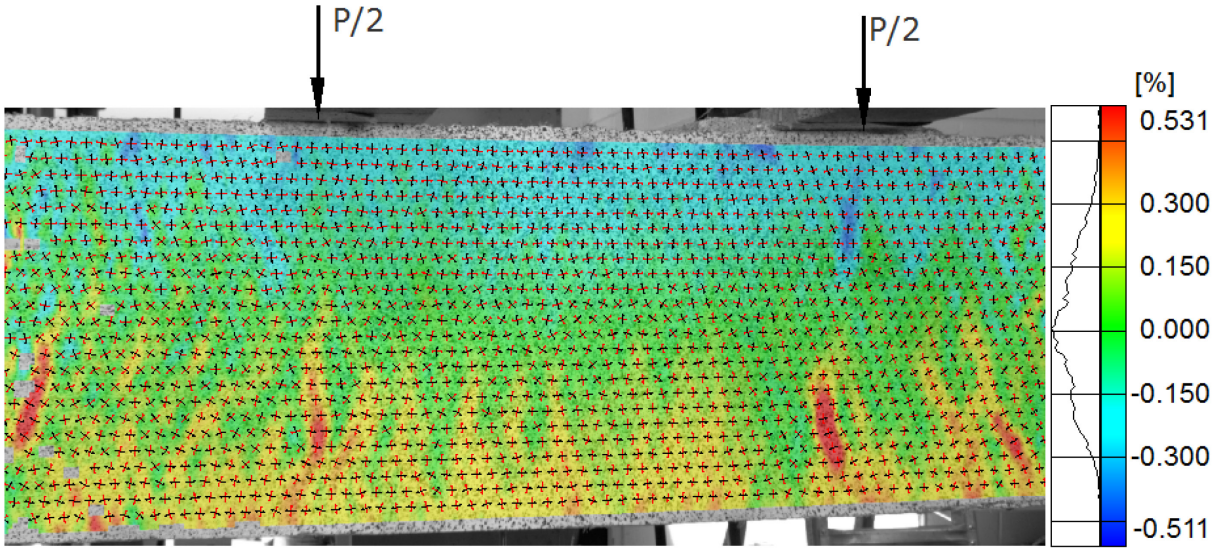

Figure 4-16 Full-field concrete longitudinal strain (ε_x) along moment region for UHP-FRC#1 at an applied load of 200 kips

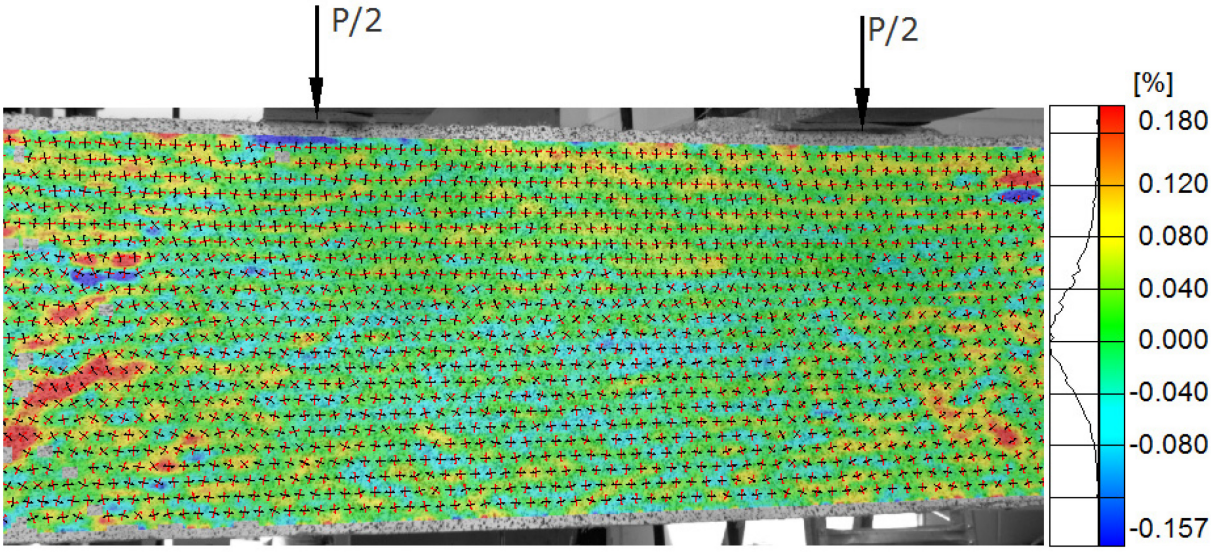

Figure 4-17 Full-field concrete transverse strain (ε_y) along moment region for UHP-FRC#1 at an applied load of 200 kips

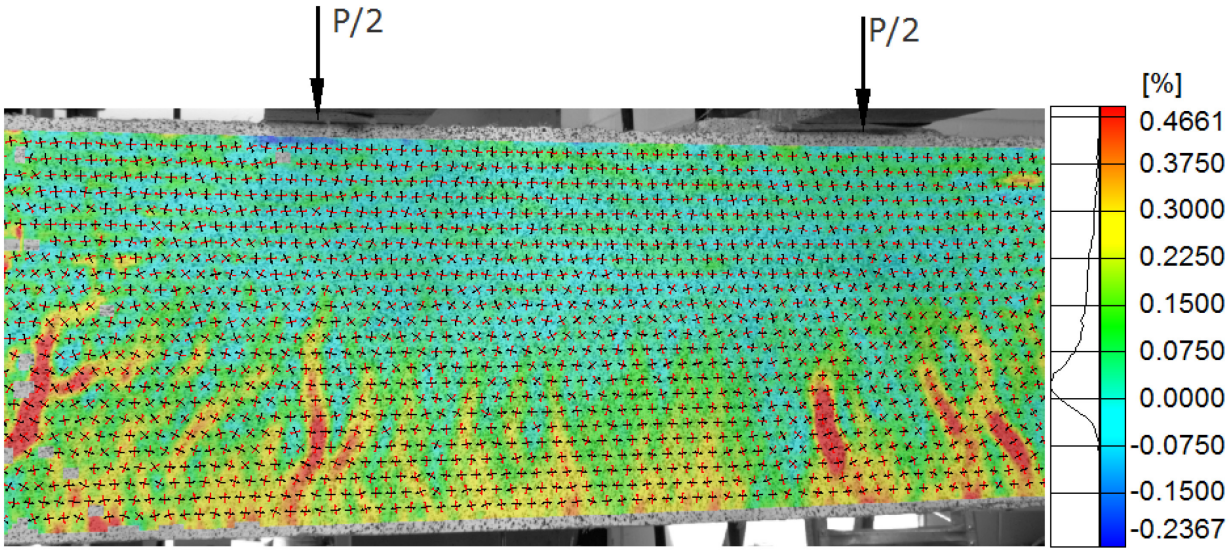

Figure 4-18 Full-field concrete maximum principal strain (σ_1) along moment region for UHP-FRC#1 at an applied load 200 kips

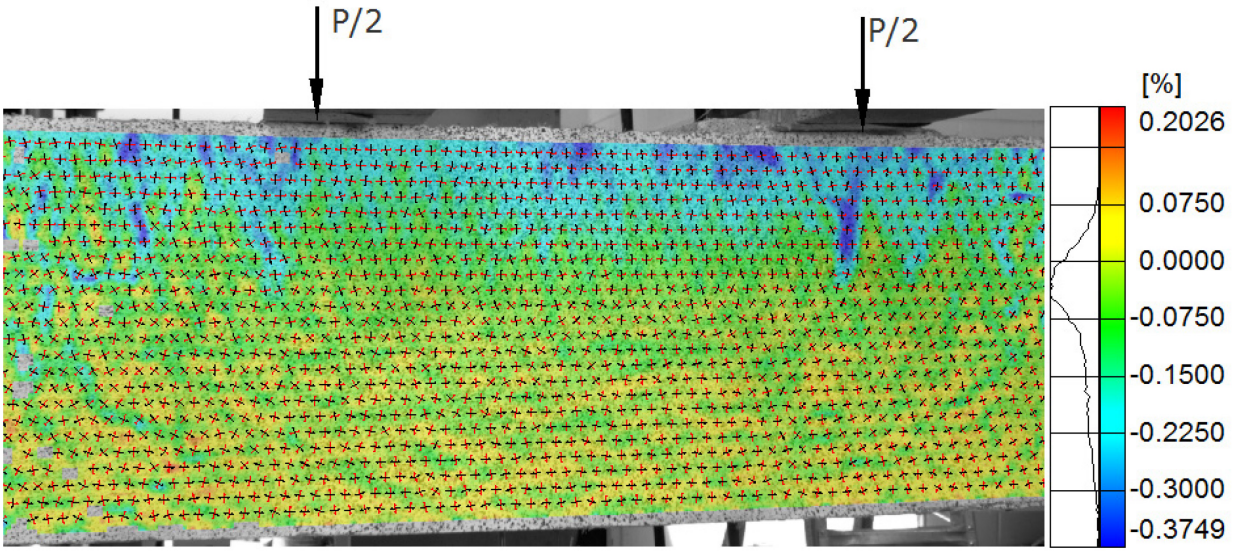

Figure 4-19 Full-field concrete minimum principal strain (σ_2) along moment region for UHP-FRC#1 at an applied load 200 kips

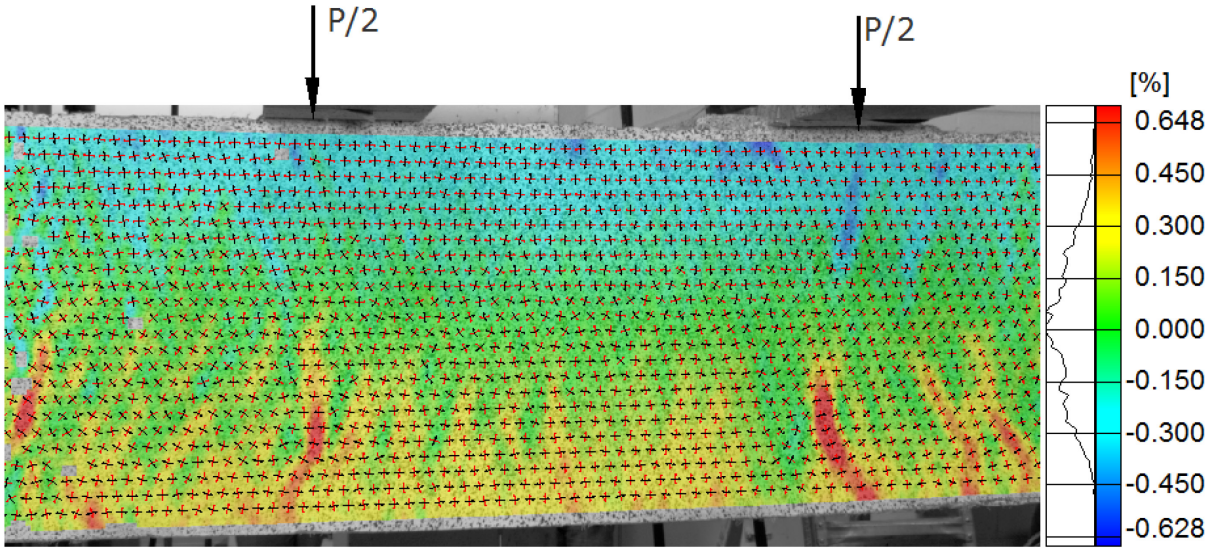

Figure 4-20 Full-field concrete longitudinal strain (ε_x) along moment region for UHP-FRC#1 at an applied load of 250 kips

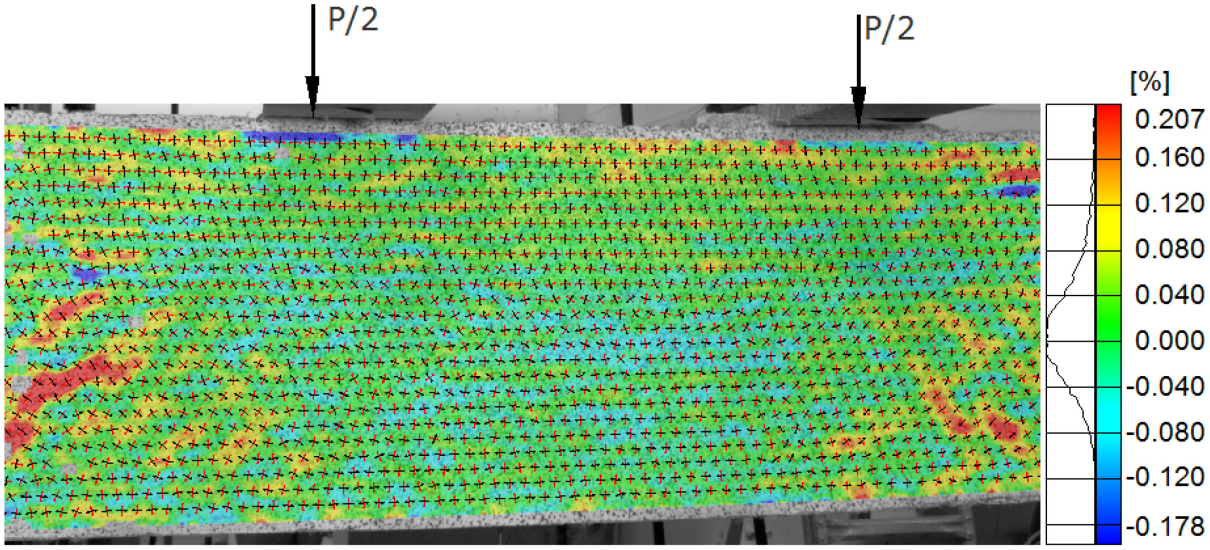

Figure 4-21 Full-field concrete transverse strain (ε_y) along moment region for UHP-FRC#1 at an applied load of 250 kips

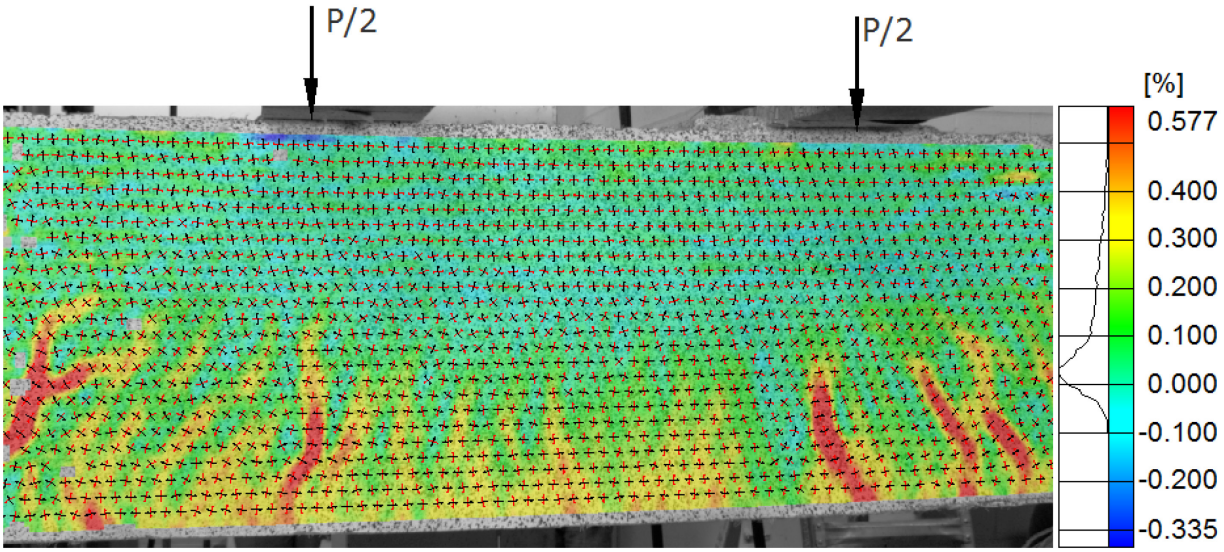

Figure 4-22 Full-field concrete maximum principal strain (σ_1) along moment region for UHP-FRC#1 at an applied load 250 kips

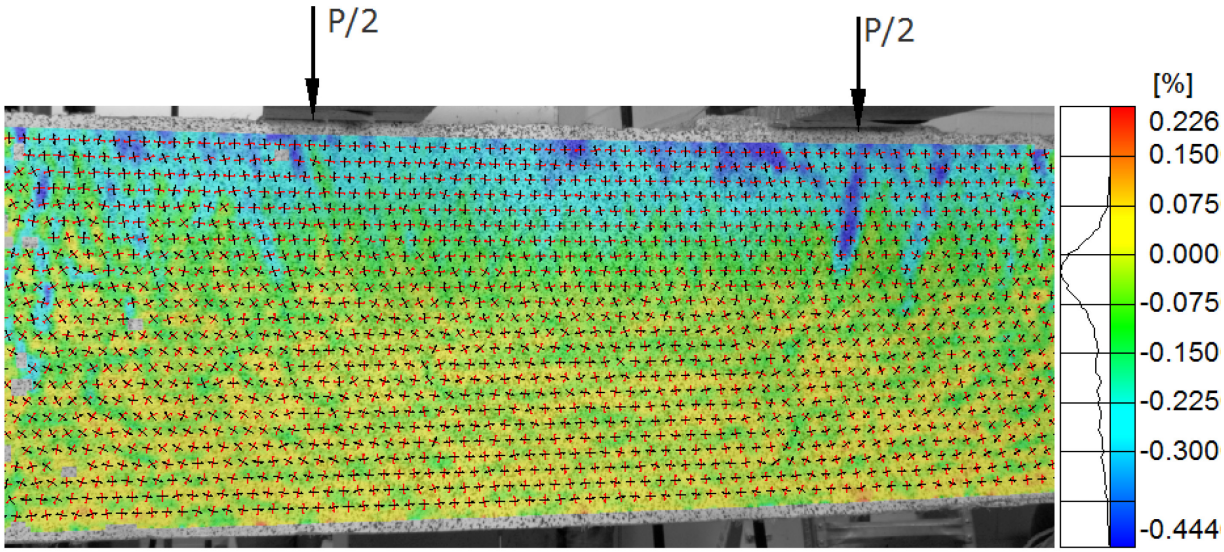

Figure 4-23 Full-field concrete minimum principal strain (σ_2) along moment region for UHP-FRC#1 at an applied load 250 kips

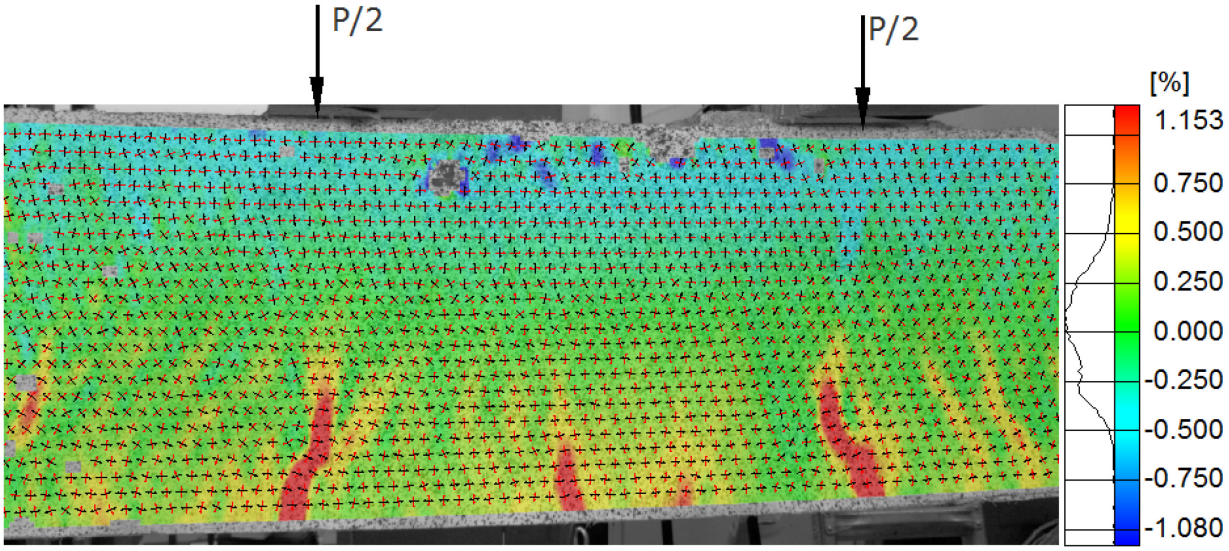

Figure 4-24 Full-field concrete longitudinal strain (ε_x) along moment region for UHP-FRC#1 at an applied load of 300 kips

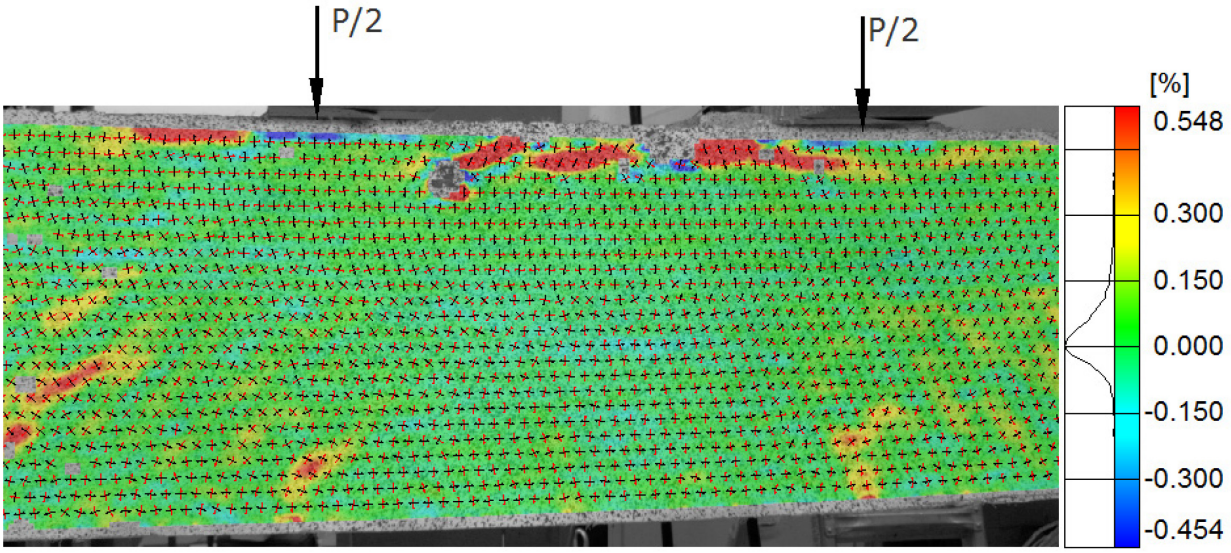

Figure 4-25 Full-field concrete transverse strain (ε_y) along moment region for UHP-FRC#1 at an applied load of 300 kips

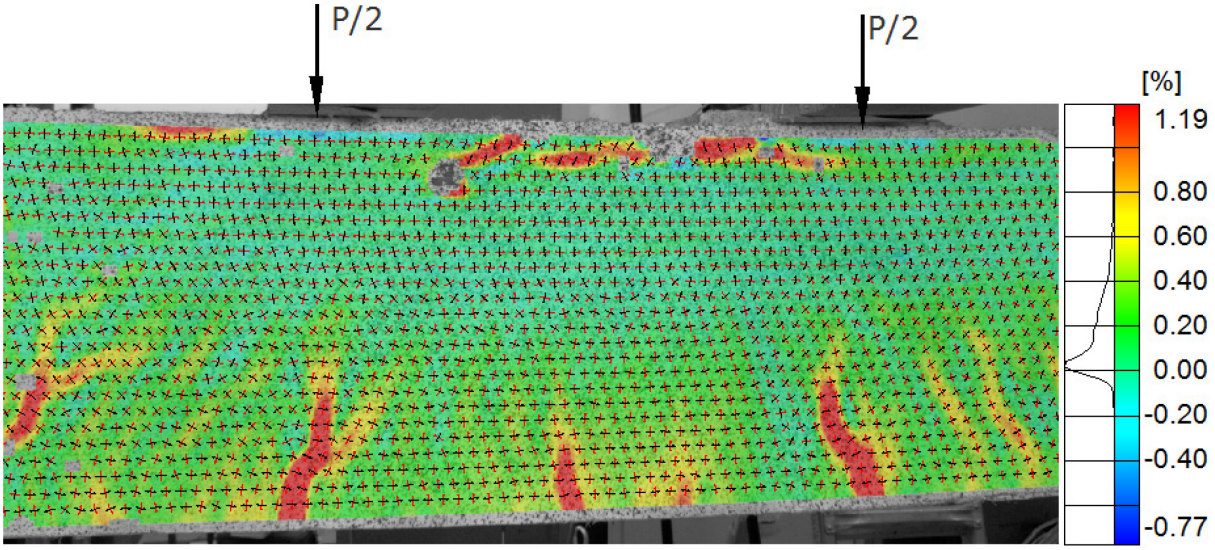

Figure 4-26 Full-field concrete maximum principal strain (σ_1) along moment region for UHP-FRC#1 at an applied load 300 kips

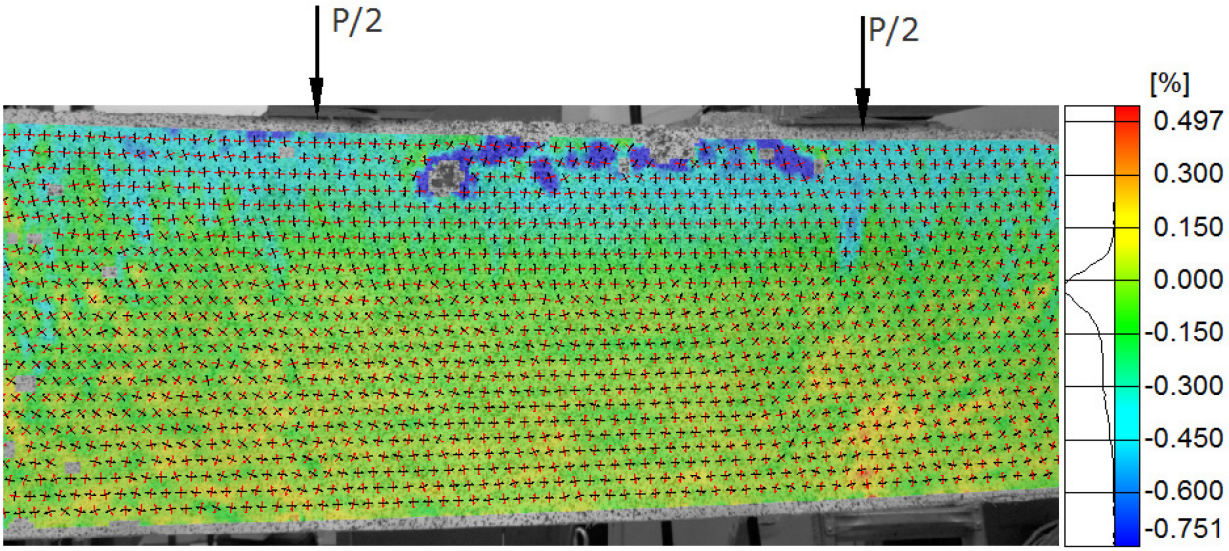

Figure 4-27 Full-field concrete minimum principal strain (σ_2) along moment region for UHP-FRC#1 at an applied load 300 kips

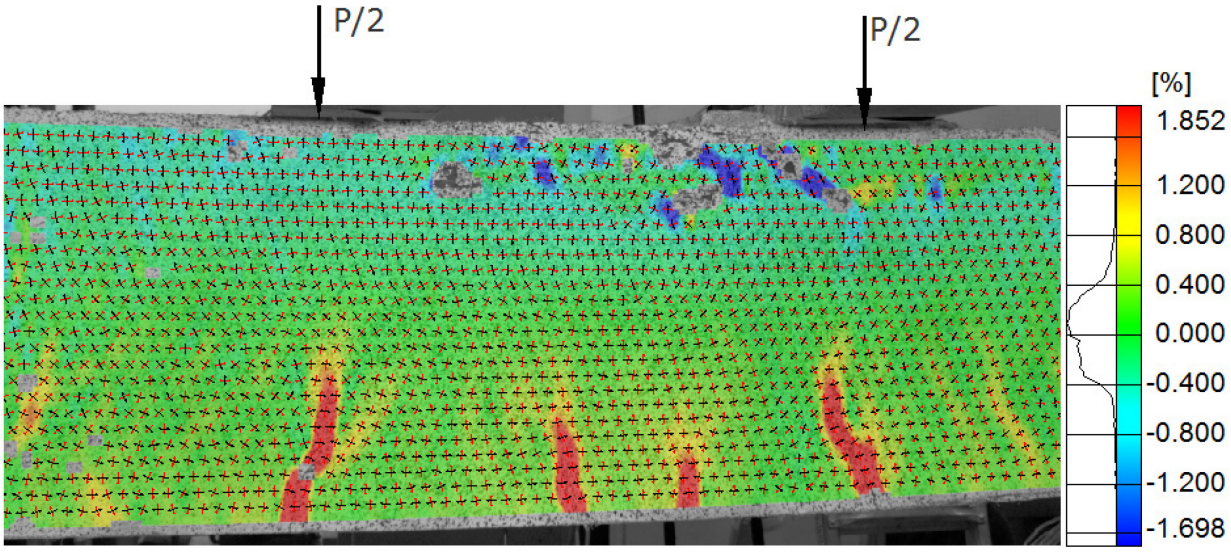

Figure 4-28 Full-field concrete longitudinal strain (ε_x) along moment region for UHP-FRC#1 at an applied load of 317.7 kips (peak load)

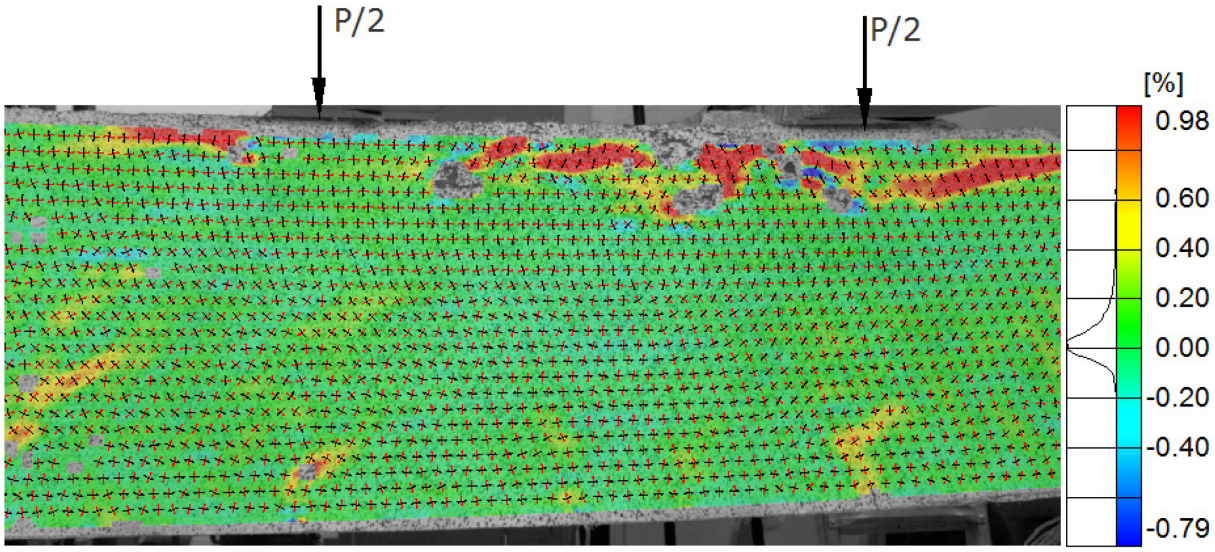

Figure 4-29 Full-field concrete transverse strain (ε_y) along moment region for UHP-FRC#1 at an applied load of 317.7 kips (peak load)

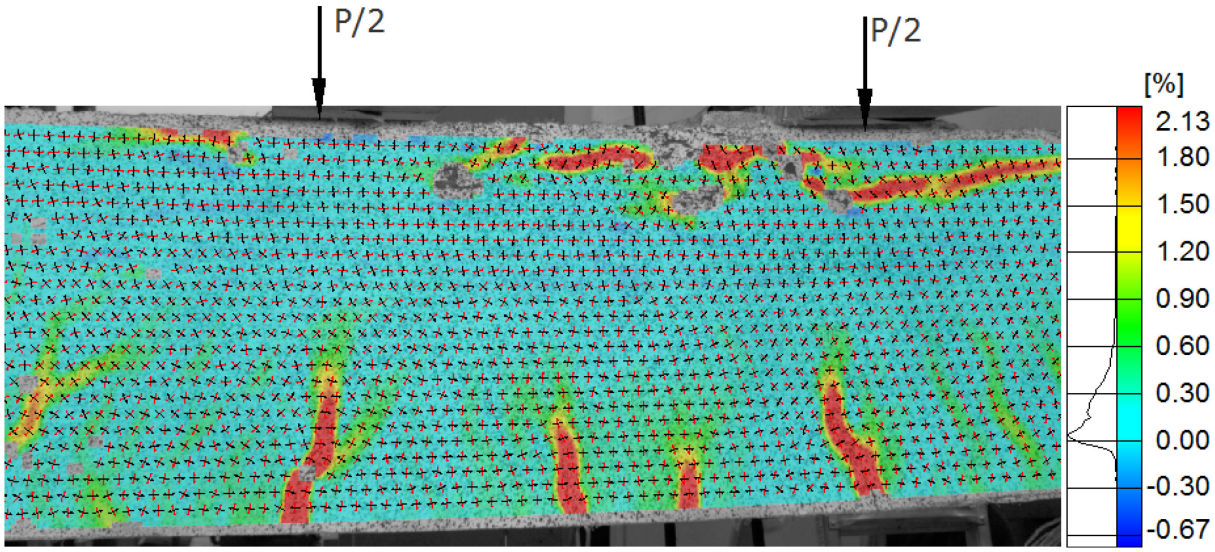

Figure 4-30 Full-field concrete maximum principal strain (σ_1) along moment region for UHP-FRC#1 at an applied load 317.7 kips (peak load)

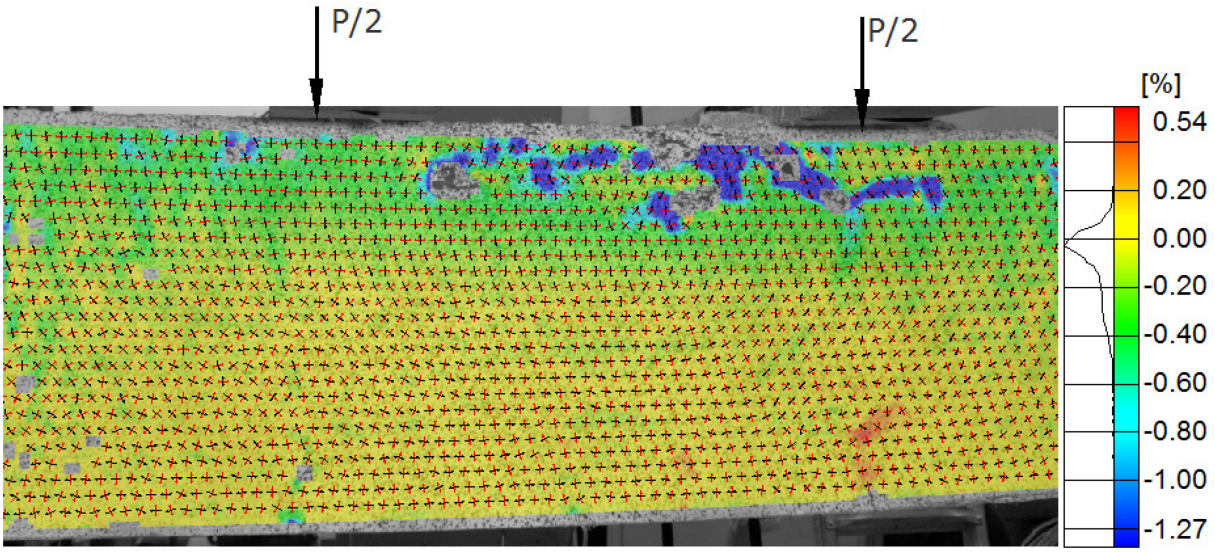

Figure 4-31 Full-field concrete minimum principal strain (σ_2) along moment region for UHP-FRC#1 at an applied load 317.7 kips (peak load)

4.2 Beam UHP-FRC #2 100S:

Load deflection behavior for UHP-FRC #2 is shown in figure 4-32. First visible flexural crack was on the soffit of the beam at 60 kips. Vertical cracks formed at latter load stages were very shallow with crack widths less than 0.3 mm. A critical diagonal crack independent of flexural cracks characterized as web shear crack was developed at 150 kips (shear stress: $4.0\sqrt{f_c^{'}} = 577\ psi$) and failed by shear and dowel at an ultimate load of 163 kips (shear stress: $4.5\sqrt{f_c^{'}} = 649\ psi$) . Existing web shear crack quickly continued to propagate in the direction of loading point and to support, eventually causing dowel cracking along the bars.

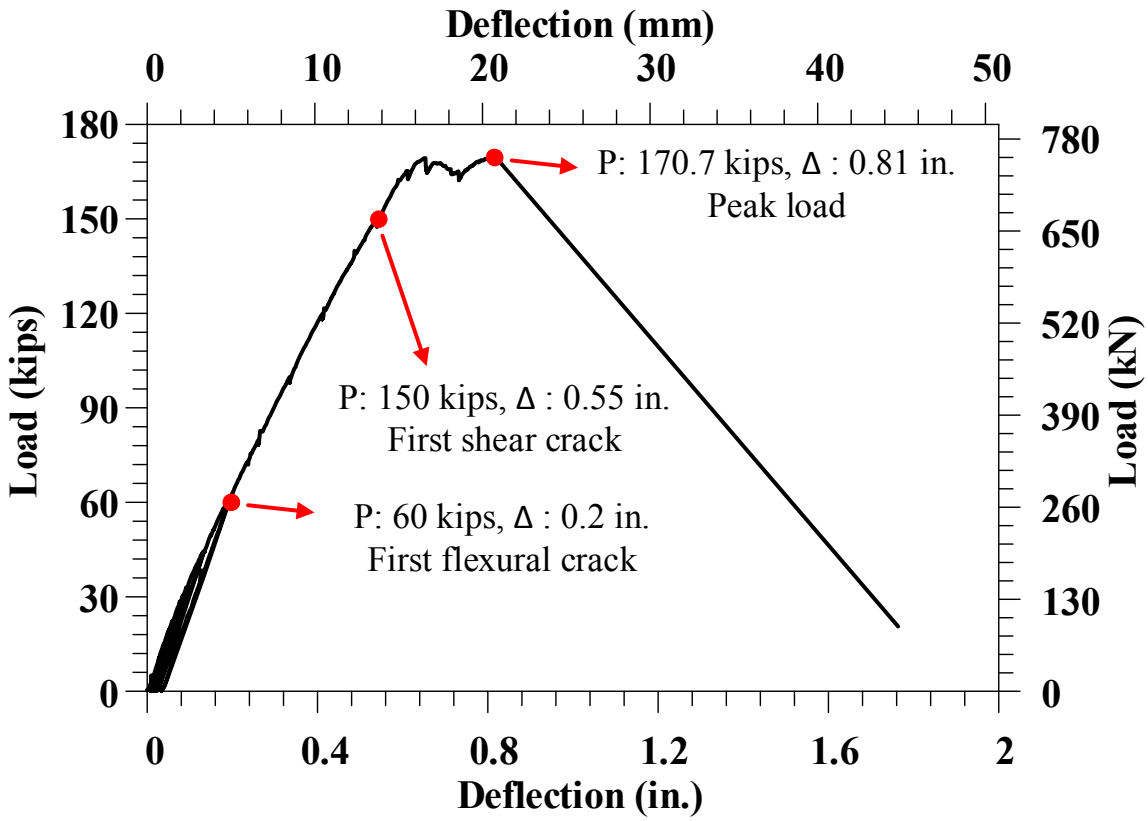

Figure 4-32 Load deflection behavior of UHP-FRC beam #2

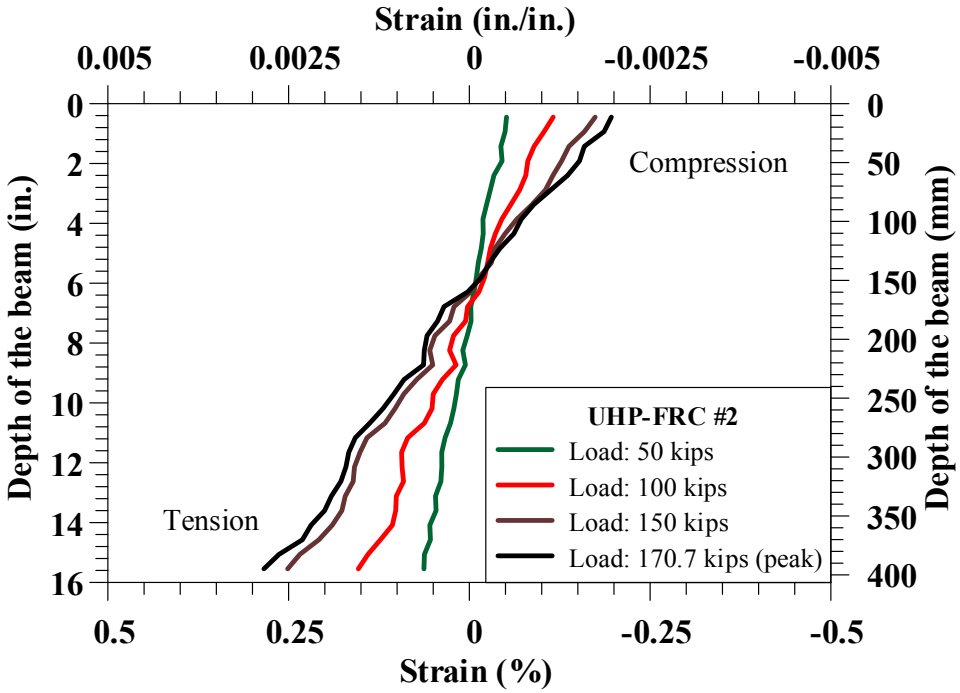

Figure 4-33 Strain variation in beam UHP-FRC #2

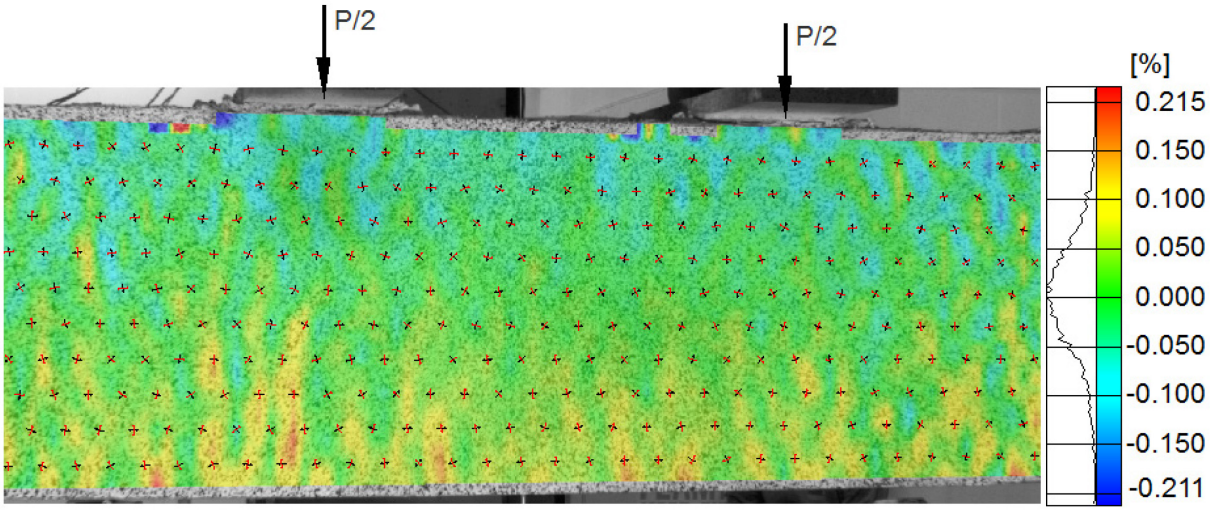

Figure 4-34 Full-field concrete longitudinal strain (ε_x) along moment region for UHP-FRC#2 at an applied load of 50 kips

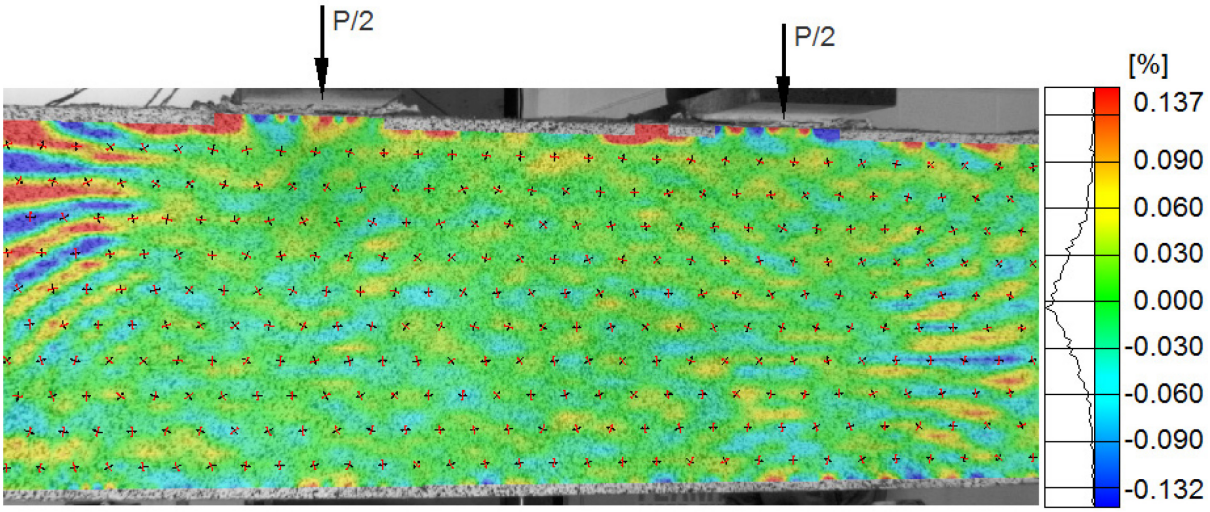

Figure 4-35 Full-field concrete transverse strain (ε_y) along moment region for UHP-FRC#2 at an applied load of 50 kips

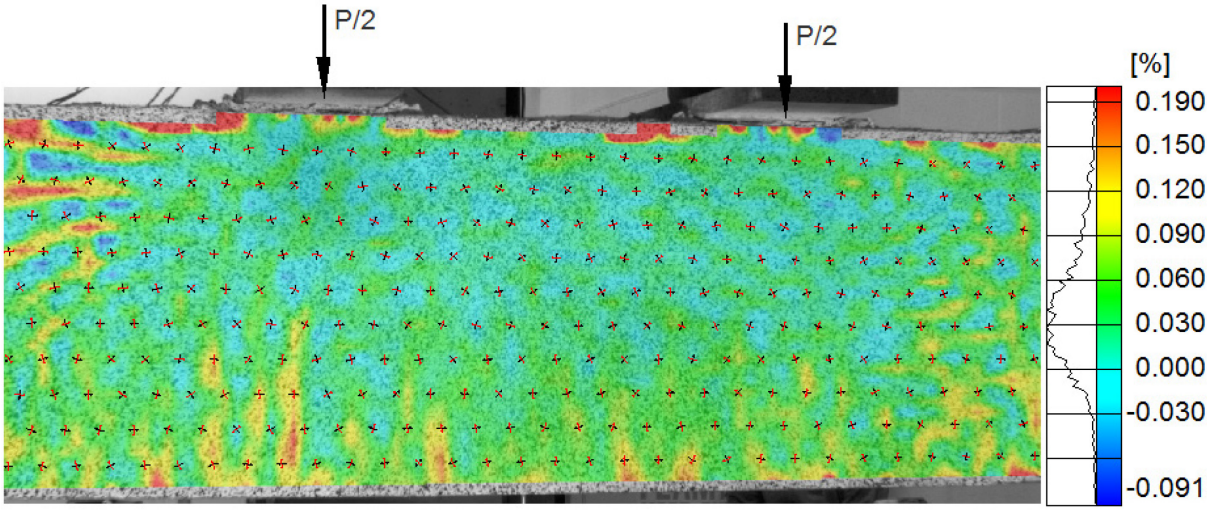

Figure 4-36 Full-field concrete maximum principal strain (σ_1) along moment region for UHP-FRC#2 at an applied load 50 kips

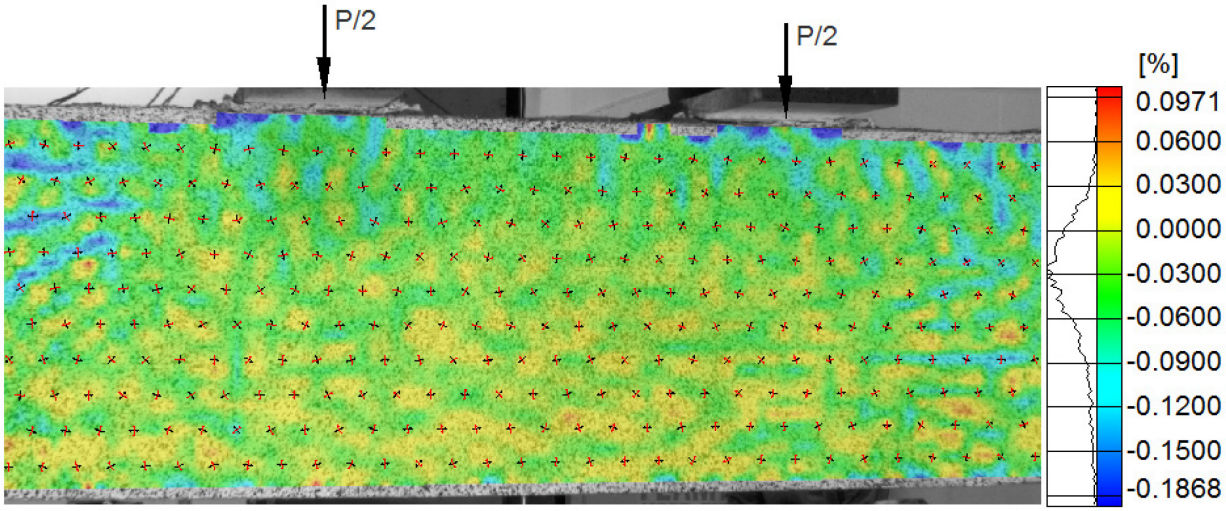

Figure 4-37 Full-field concrete minimum principal strain (σ_2) along moment region for UHP-FRC#2 at an applied load 50 kips

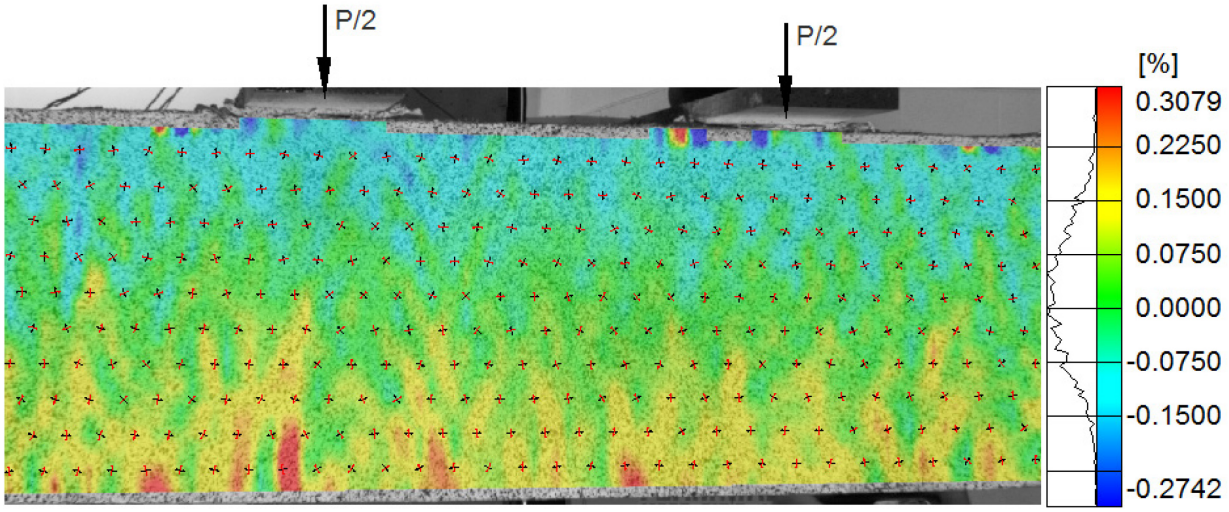

Figure 4-38 Full-field concrete longitudinal strain (ε_x) along moment region for UHP-FRC#2 at an applied load of 100 kips

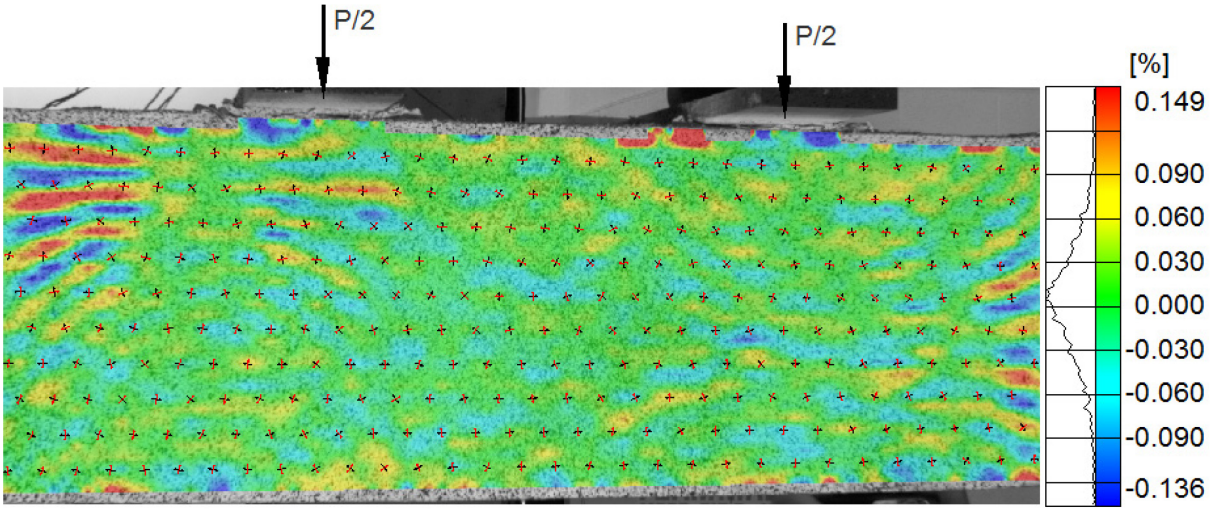

Figure 4-39 Full-field concrete transverse strain (ε_y) along moment region for UHP-FRC#2 at an applied load of 100 kips

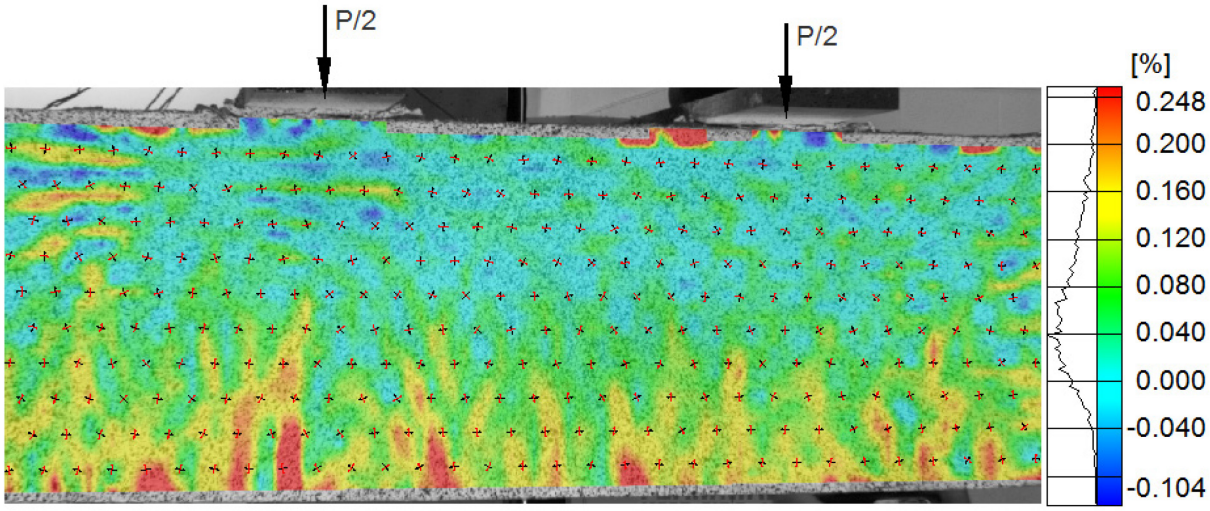

Figure 4-40 Full-field concrete maximum principal strain (σ_1) along moment region for UHP-FRC#2 at an applied load 100 kips

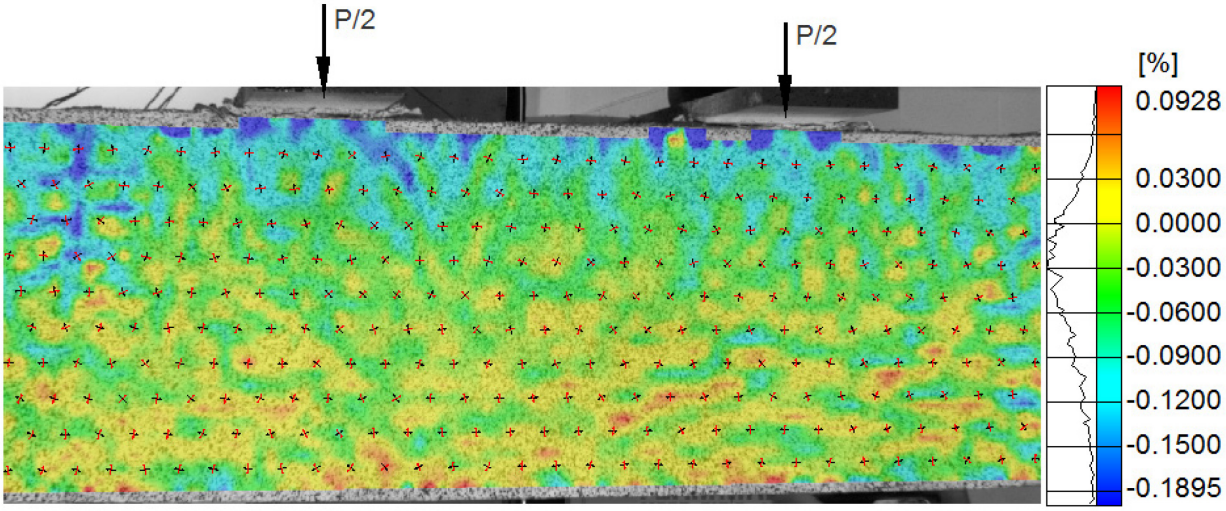

Figure 4-41 Full-field concrete minimum principal strain (σ_2) along moment region for UHP-FRC#2 at an applied load 100 kips

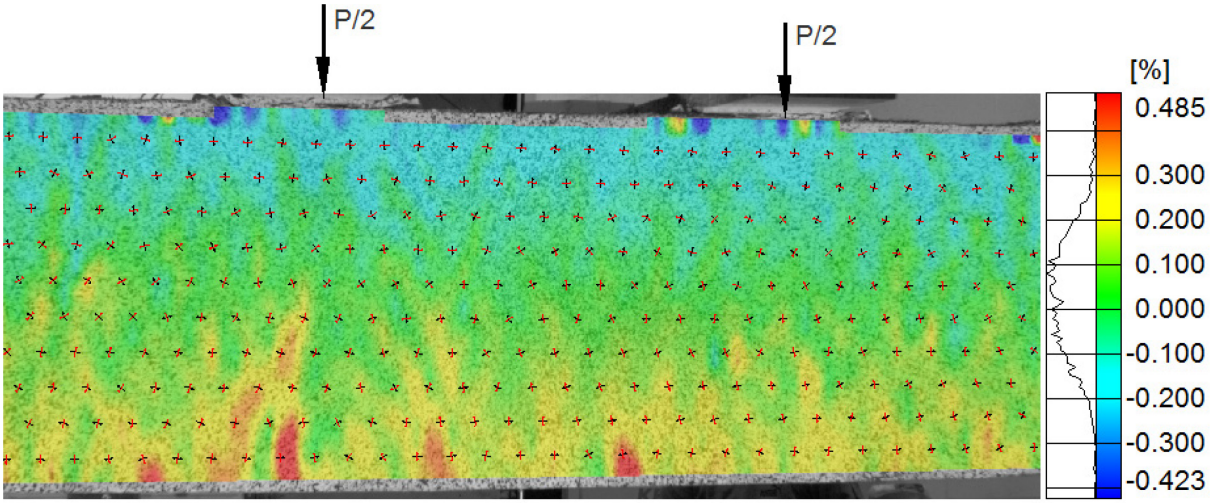

Figure 4-42 Full-field concrete longitudinal strain (ε_x) along moment region for UHP-FRC#2 at an applied load of 150 kips

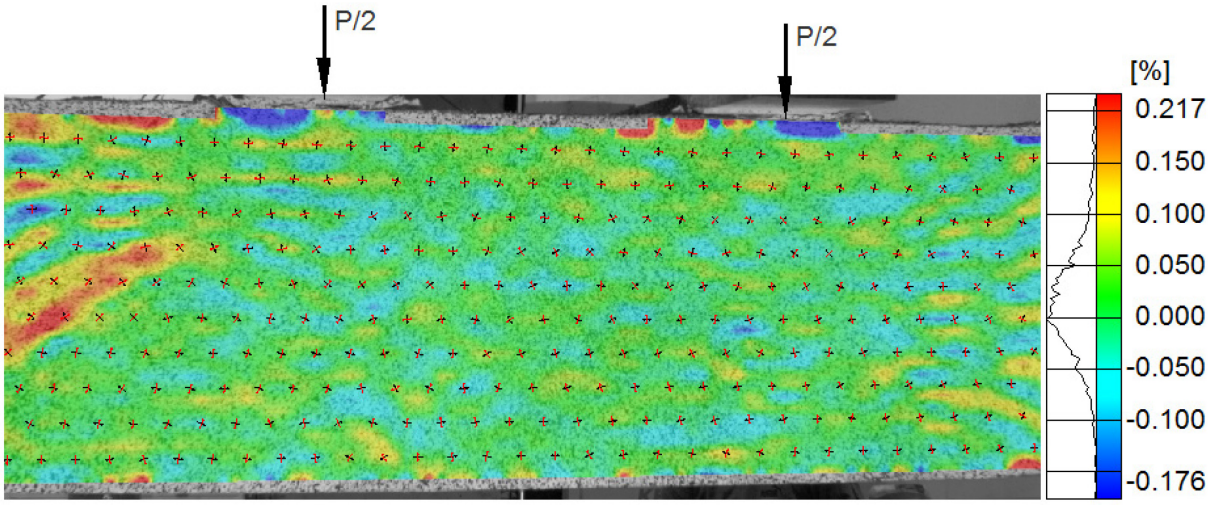

Figure 4-43 Full-field concrete transverse strain (ε_y) along moment region for UHP-FRC#2 at an applied load of 150 kips

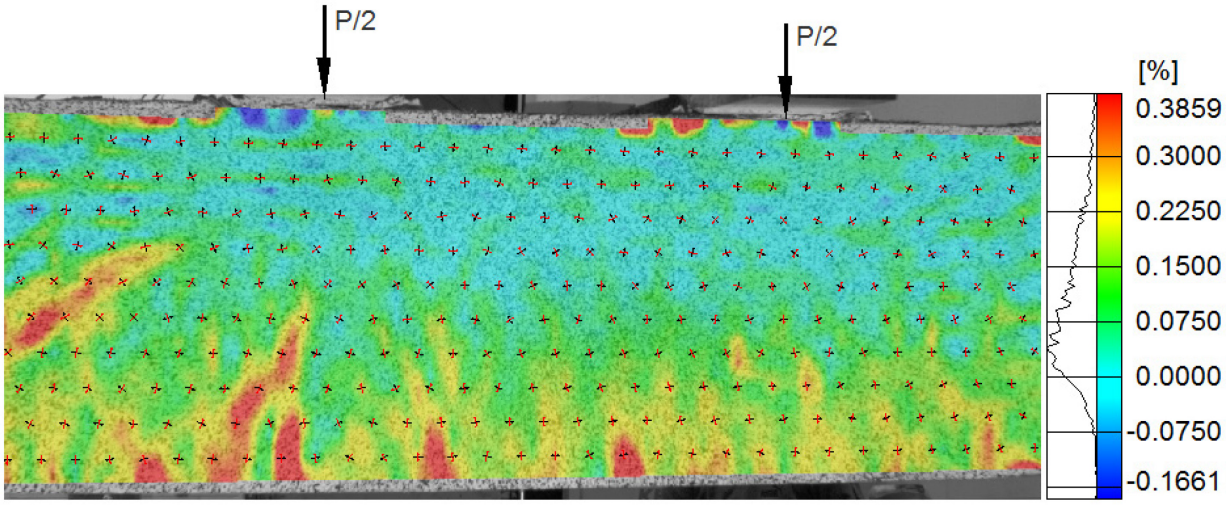

Figure 4-44 Full-field concrete maximum principal strain (σ_1) along moment region for UHP-FRC#2 at an applied load 150 kips

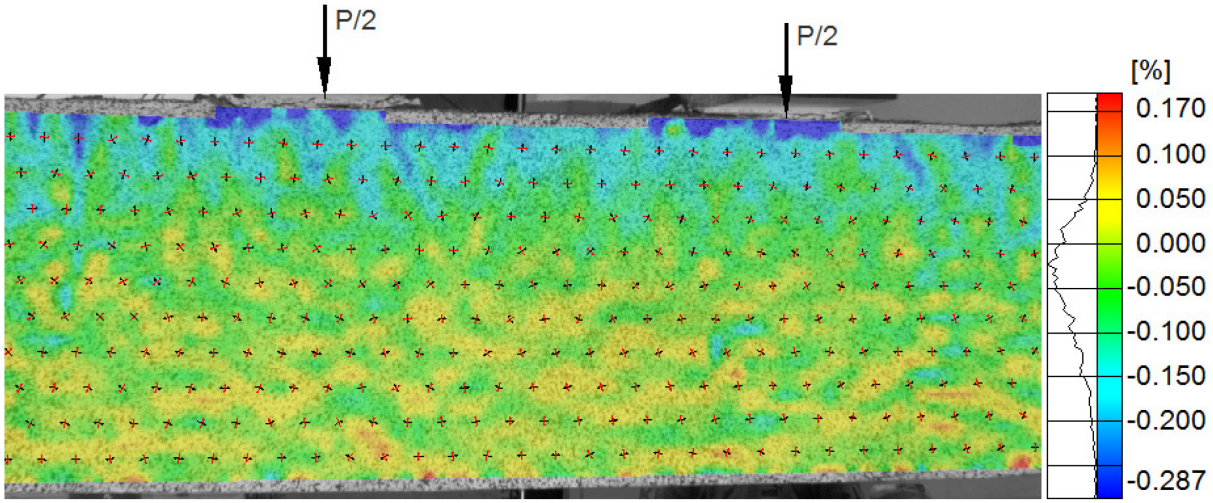

Figure 4-45 Full-field concrete minimum principal strain (σ_2) along moment region for UHP-FRC#2 at an applied load 150 kips

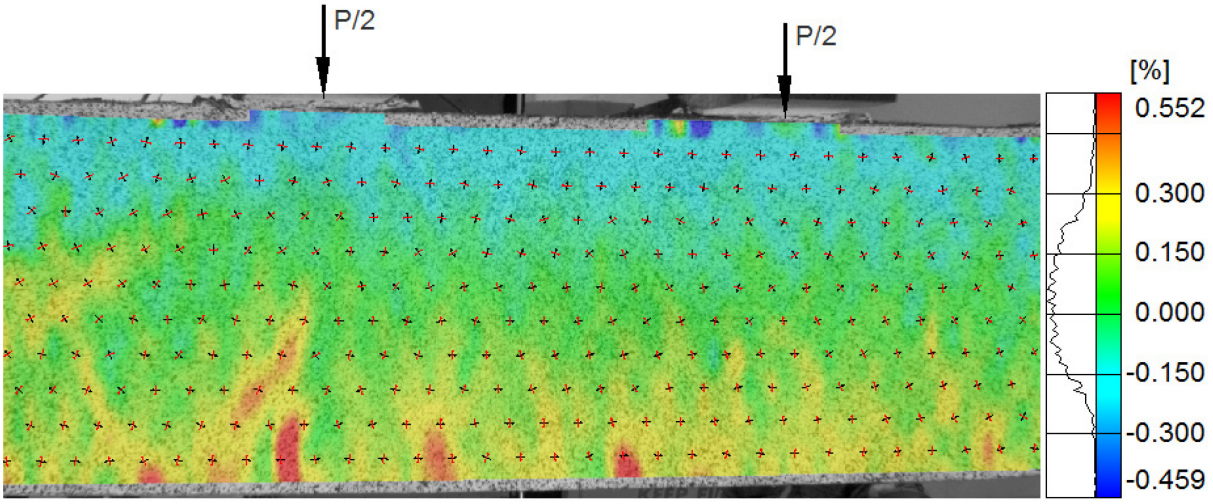

Figure 4-46 Full-field concrete longitudinal strain (ε_x) along moment region for UHP-FRC#2 at an applied load of 170.7 kips (peak load)

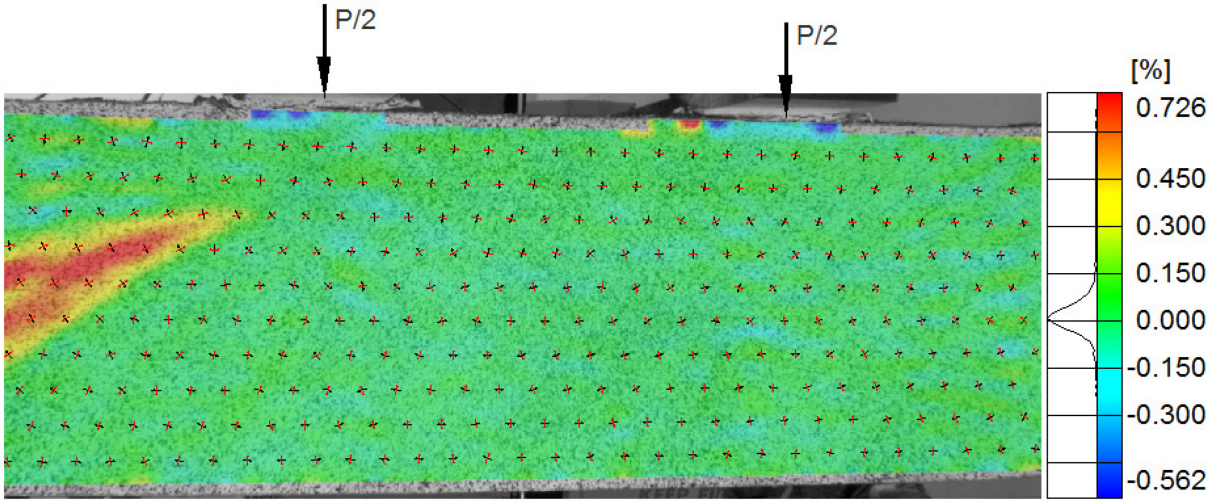

Figure 4-47 Full-field concrete transverse strain (ε_y) along moment region for UHP-FRC#2 at an applied load of 170.7 kips (peak load)

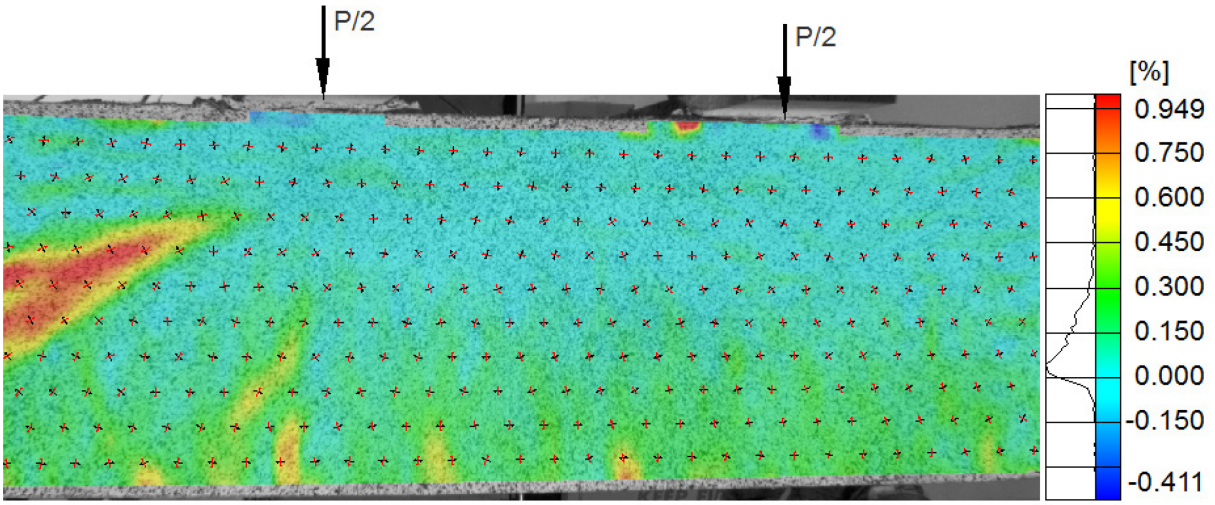

Figure 4-48 Full-field concrete maximum principal strain (σ_1) along moment region for UHP-FRC#2 at an applied load 170.7 kips (peak load)

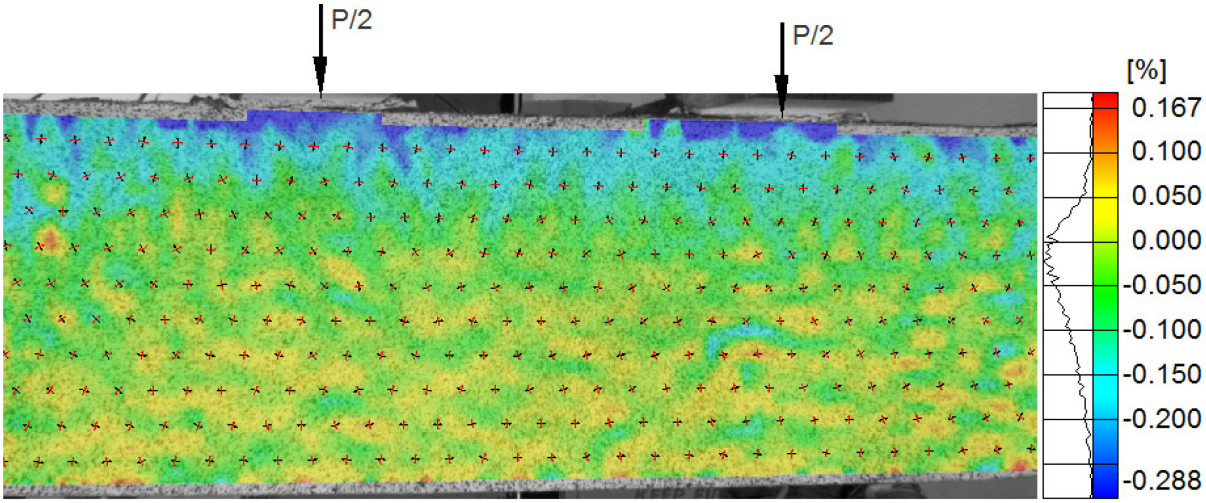

Figure 4-49 Full-field concrete minimum principal strain (σ_2) along moment region for UHP-FRC#2 at an applied load 170.7 kips (peak load)

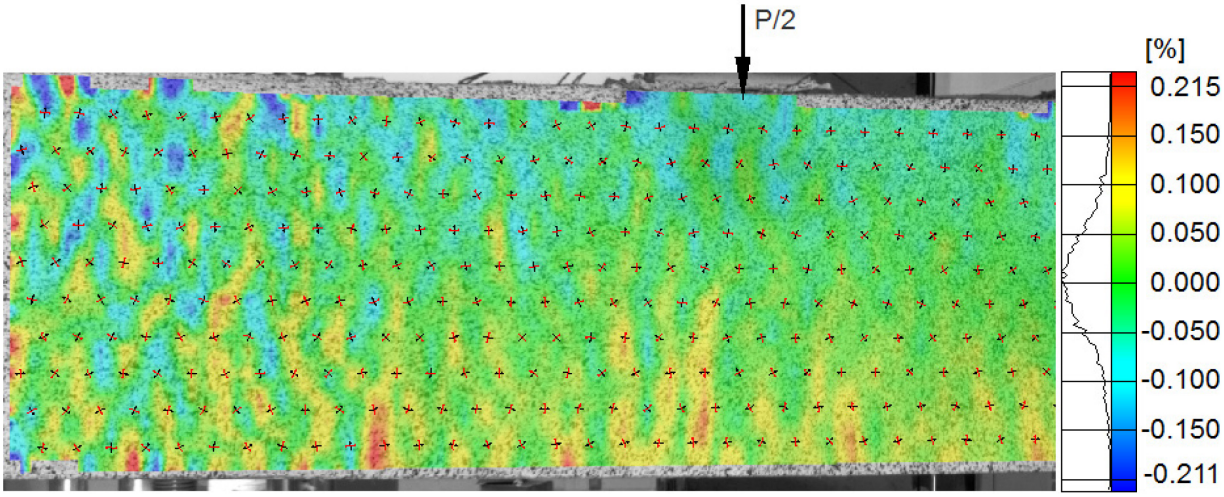

Figure 4-50 Full-field concrete longitudinal strain (ε_x) in a critical shear span for UHP-FRC#2 at an applied load of 50 kips

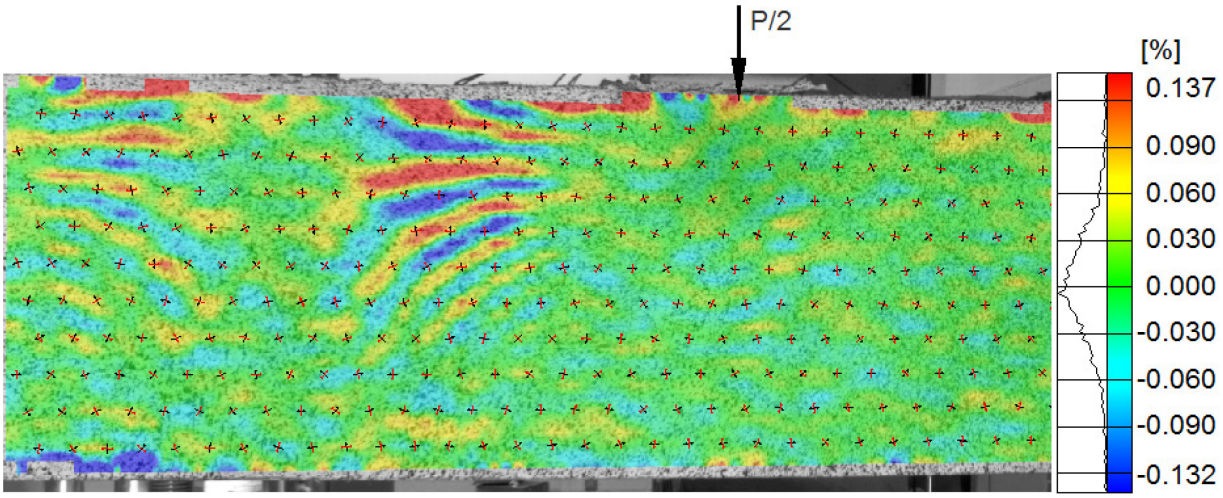

Figure 4-51 Full-field concrete transverse strain (ε_y) in a critical shear span for UHP-FRC#2 at an applied load of 50 kips

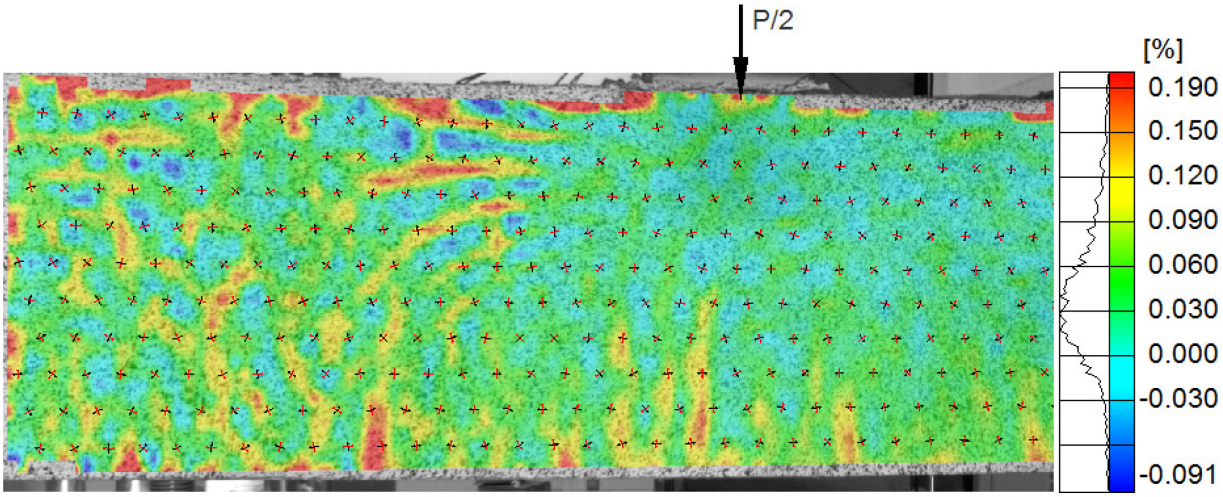

Figure 4-52 Full-field concrete maximum principal strain (σ_1) in a critical shear span for UHP-FRC#2 at an applied load 50 kips

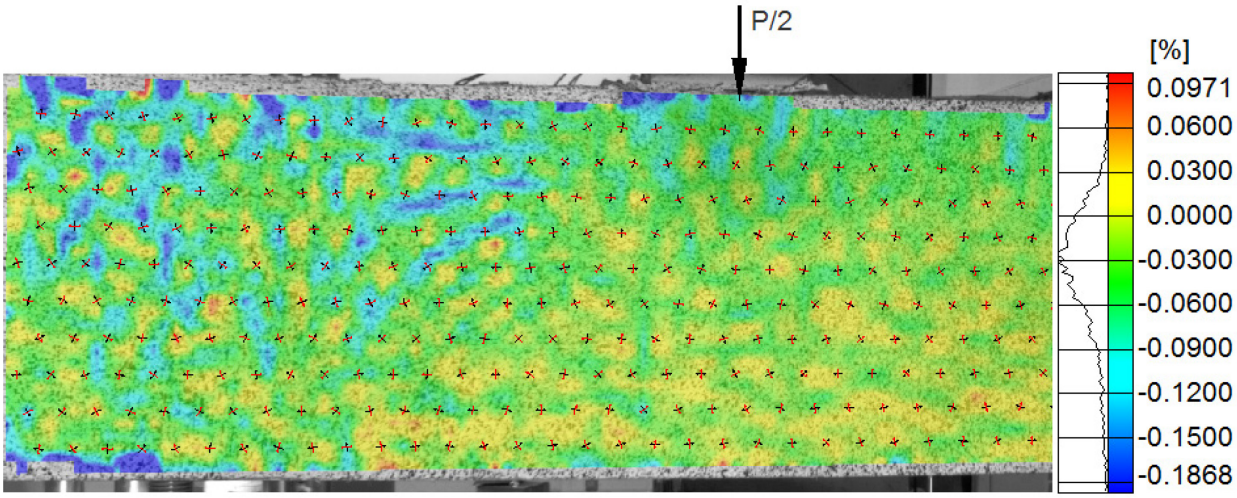

Figure 4-53 Full-field concrete minimum principal strain (σ_2) in a critical shear span for UHP-FRC#2 at an applied load 50 kips

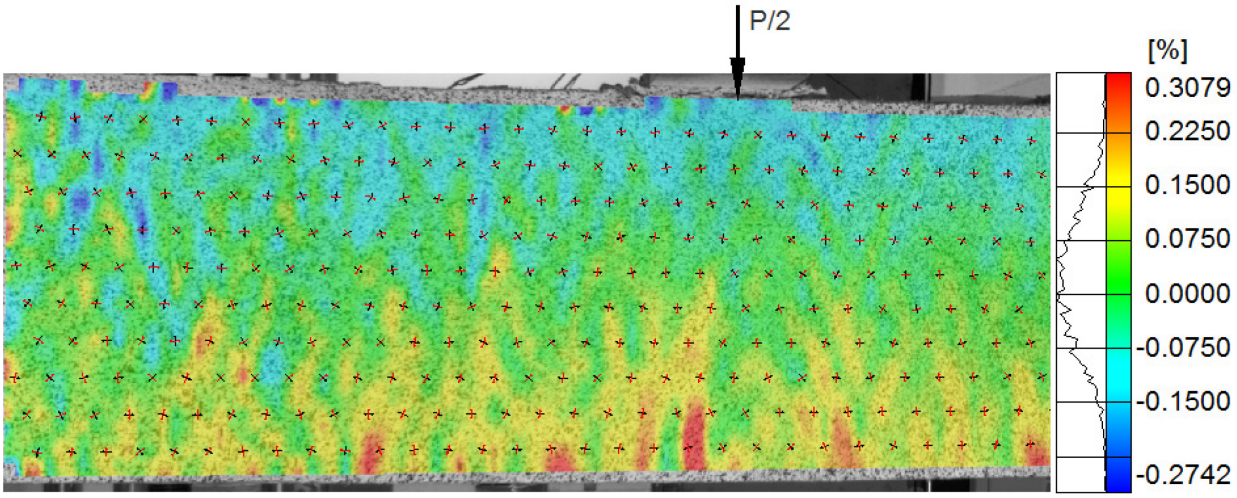

Figure 4-54 Full-field concrete longitudinal strain (ε_x) in a critical shear span for UHP-FRC#2 at an applied load of 100 kips

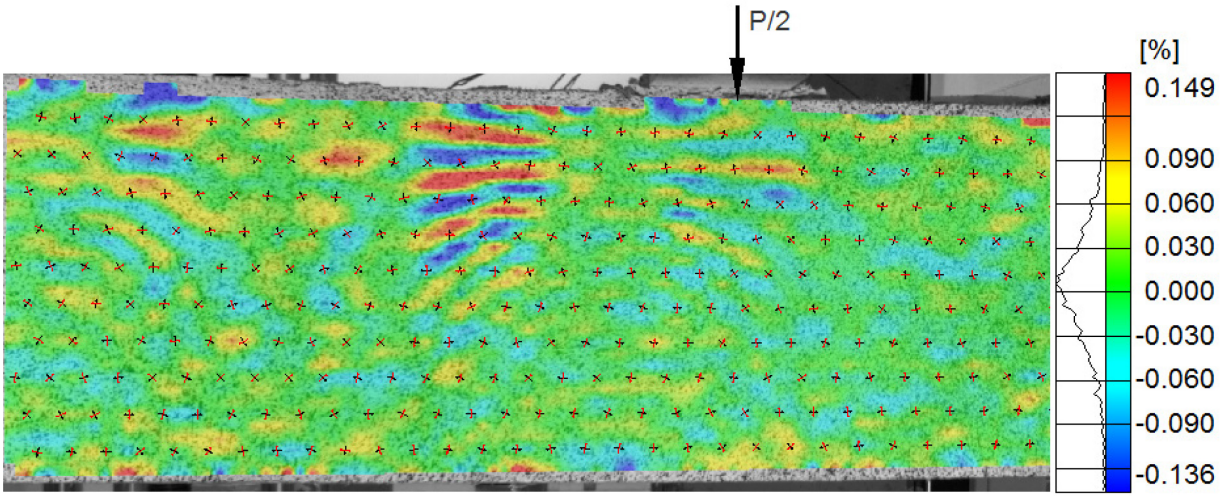

Figure 4-55 Full-field concrete transverse strain (ε_y) in a critical shear span for UHP-FRC#2 at an applied load of 100 kips

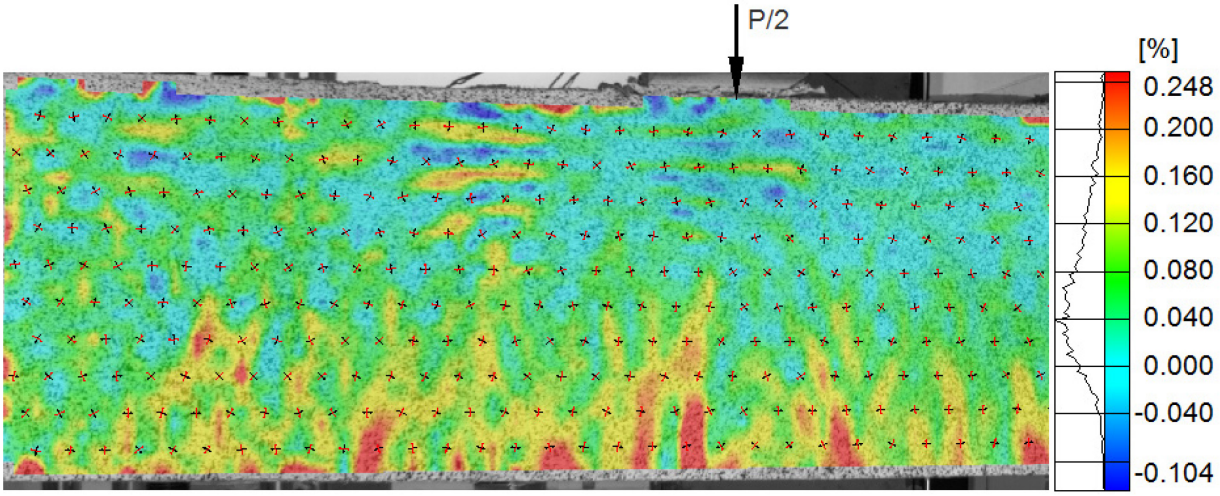

Figure 4-56 Full-field concrete maximum principal strain (σ_1) in a critical shear span for UHP-FRC#2 at an applied load 100 kips

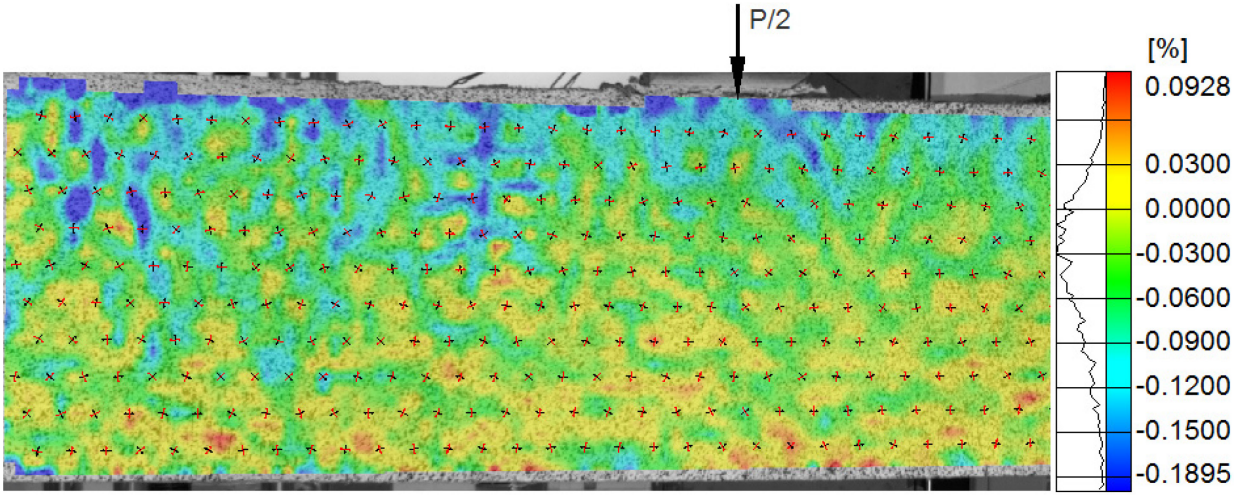

Figure 4-57 Full-field concrete minimum principal strain (σ_2) in a critical shear span for UHP-FRC#2 at an applied load 100 kips

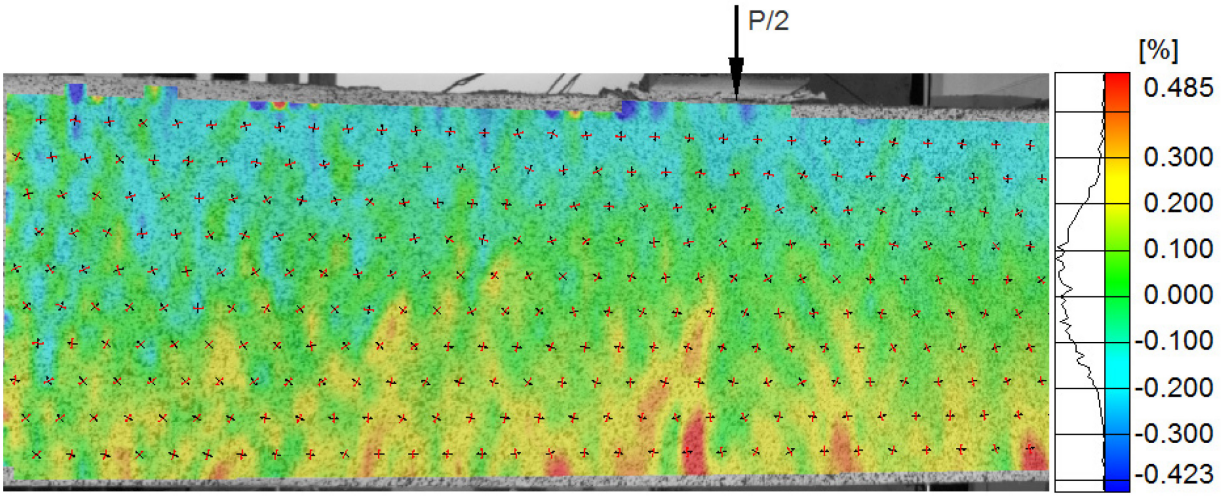

Figure 4-58 Full-field concrete longitudinal strain (ε_x) in a critical shear span for UHP-FRC#2 at an applied load of 150 kips

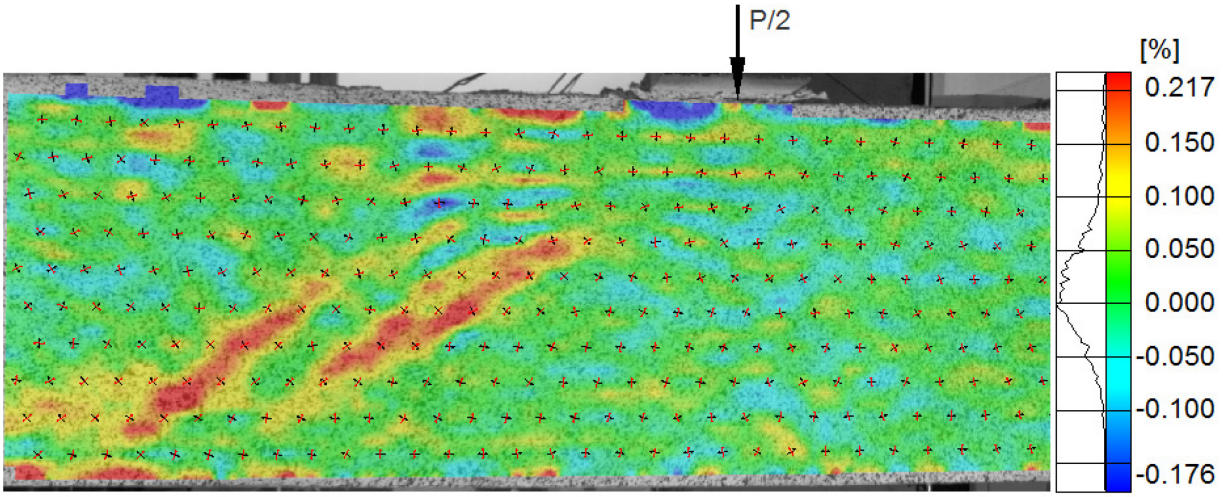

Figure 4-59 Full-field concrete transverse strain (ε_y) in a critical shear span for UHP-FRC#2 at an applied load of 150 kips

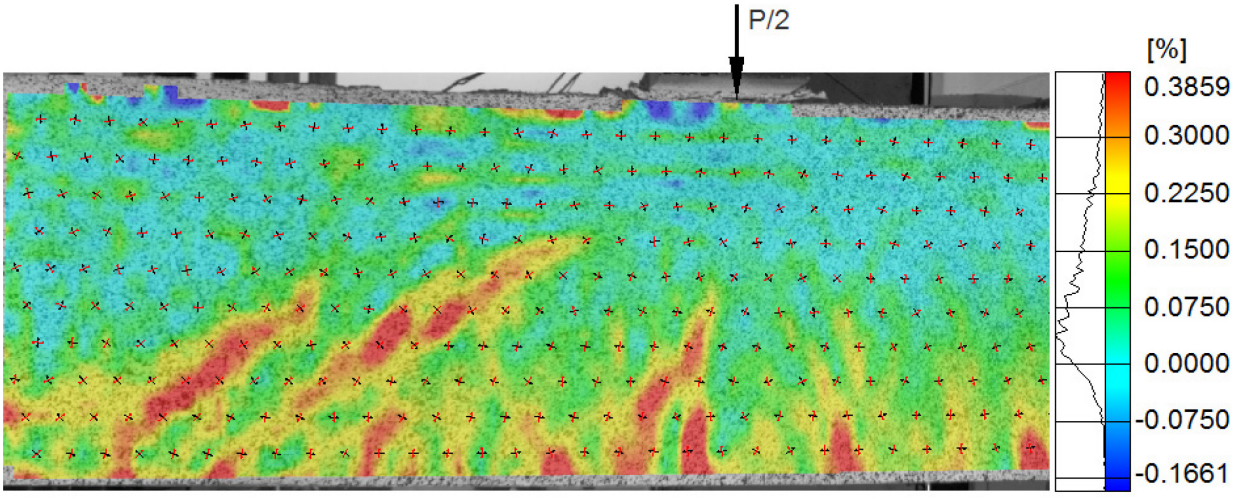

Figure 4-60 Full-field concrete maximum principal strain (σ_1) in a critical shear span for UHP-FRC#2 at an applied load 150 kips

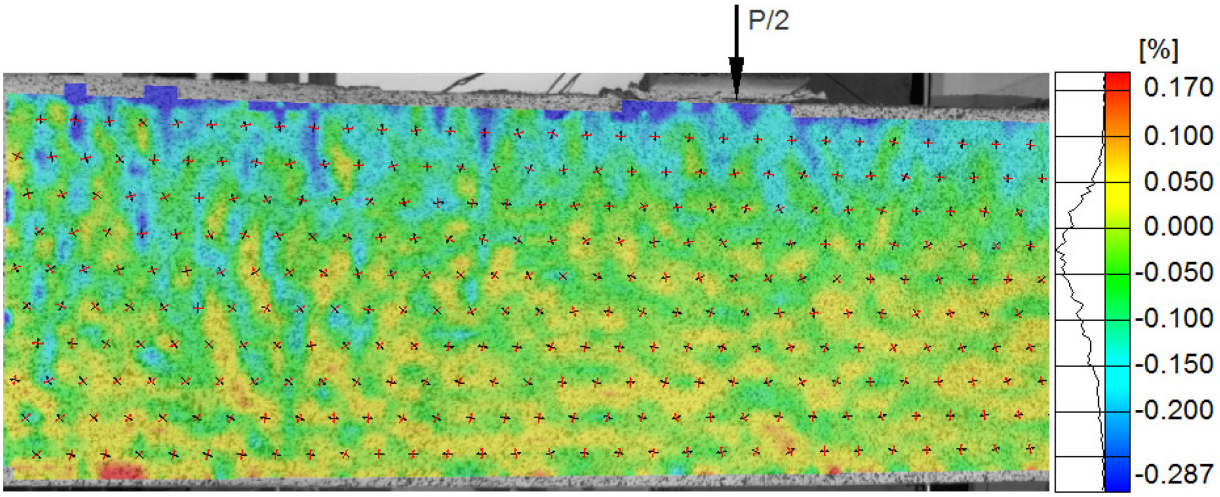

Figure 4-61 Full-field concrete minimum principal strain (σ_2) in a critical shear span for UHP-FRC#2 at an applied load 150 kips

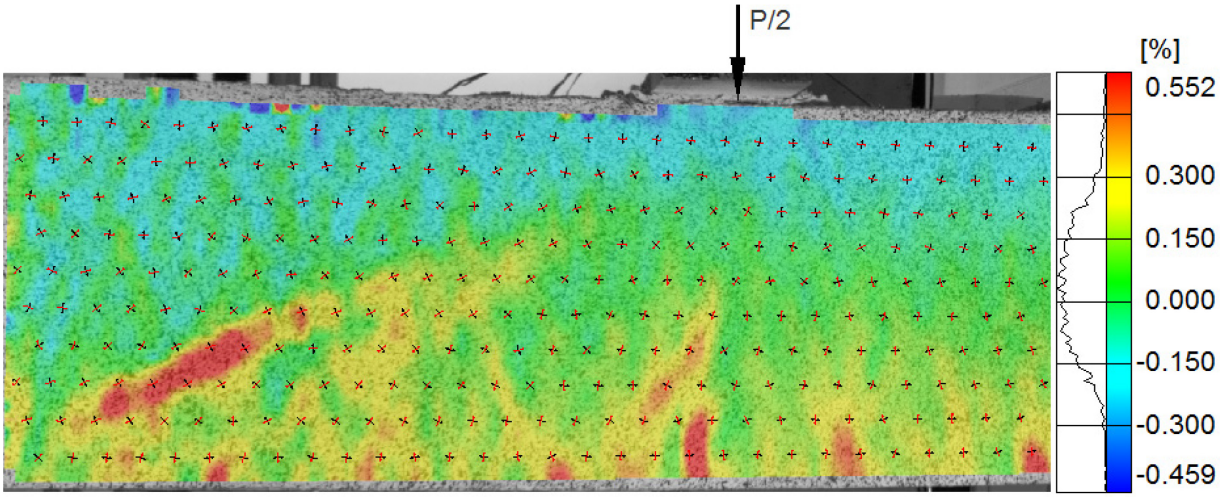

Figure 4-62 Full-field concrete longitudinal strain (ε_x) in a critical shear span for UHP-FRC#2 at an applied load of 169.5 kips (peak load)

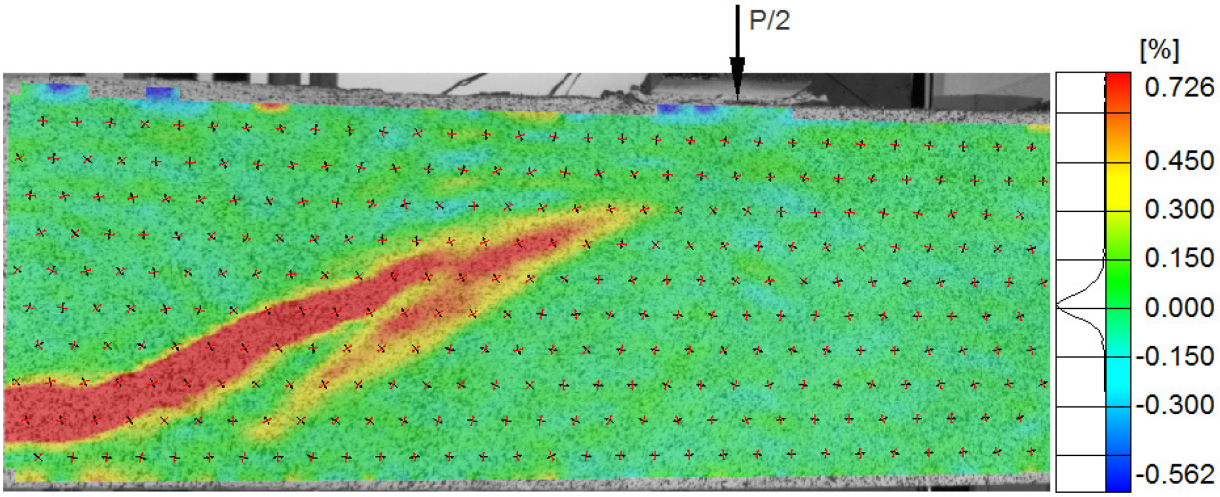

Figure 4-63 Full-field concrete transverse strain (ε_y) in a critical shear span for UHP-FRC#2 at an applied load of 169.5 kips (peak load)

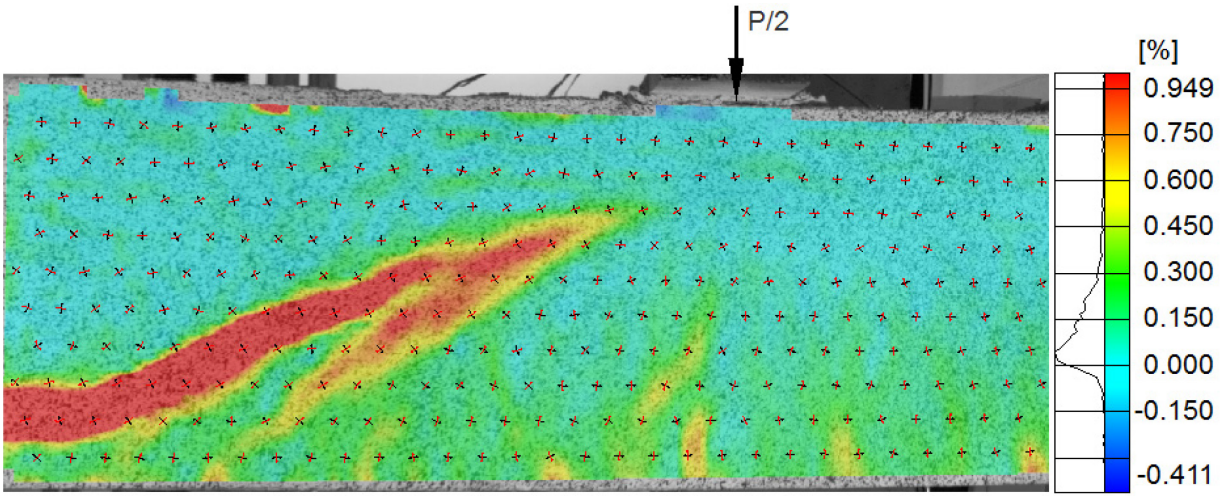

Figure 4-64 Full-field concrete maximum principal strain (σ_1) in a critical shear span for UHP-FRC#2 at an applied load 169.5 kips (peak load)

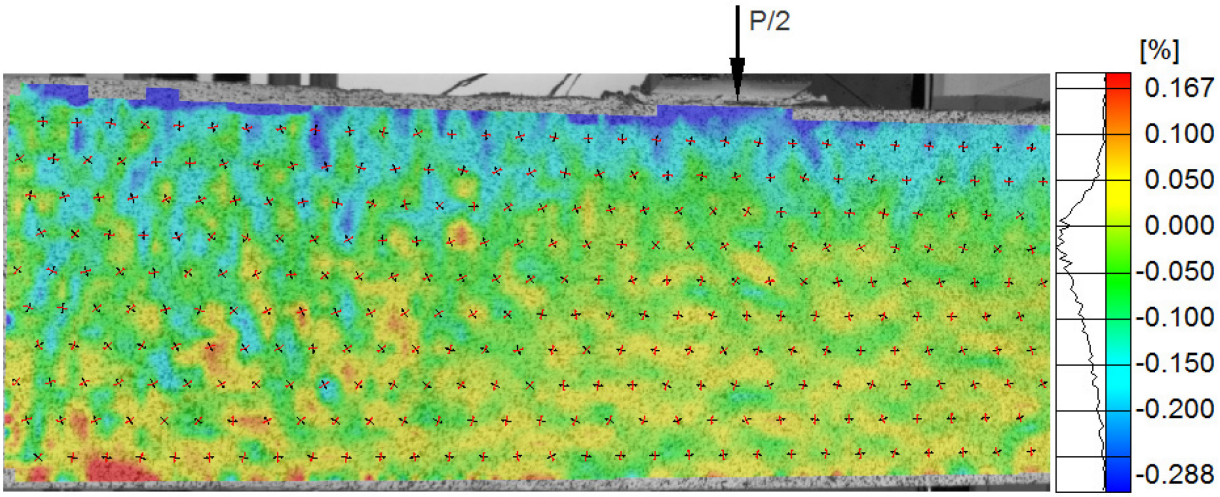

Figure 4-65 Full-field concrete minimum principal strain (σ_2) in a critical shear span for UHP-FRC#2 at an applied load 169.5 kips (peak load)

4.3 Beam UHP-FRC #3 100S:

Load deflection behavior for UHP-FRC #3 is shown in figure 4-66. First visible flexural crack was on the soffit of the beam at 50 kips. A critical diagonal crack independent of flexural cracks characterized as web shear crack was developed at 150 kips (shear stress: $4.0\sqrt{f_c^{'}} = 577\ psi$), reaching an ultimate failure load of 179 kips (shear stress: $4.9\sqrt{f_c^{'}} = 709 psi$). Existing web shear crack quickly continued to propagate towards loading point and to support, ultimately triggering dowel cracking along the bars. Load deflection and cracking behavior or UHP-FRC #3 is very similar to UHP-FRC #2 except the fact that UHP-FRC #3 has slightly better contribution in dowel contribution, attributing to the smaller diameter of the bars. Hence which has a larger area of concrete surrounding the rebar that improved the bond strength.

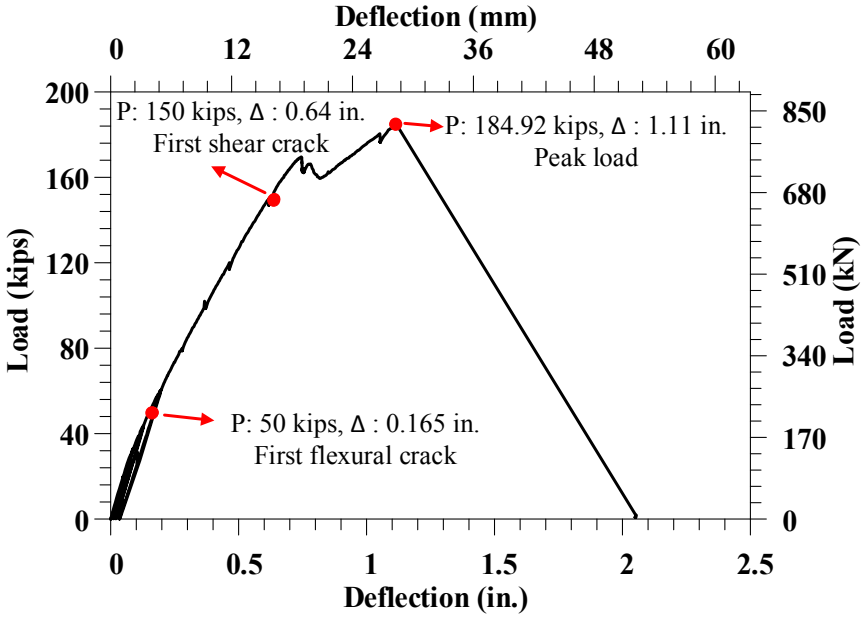

Figure 4-66 Load deflection behavior of beam UHP-FRC #3

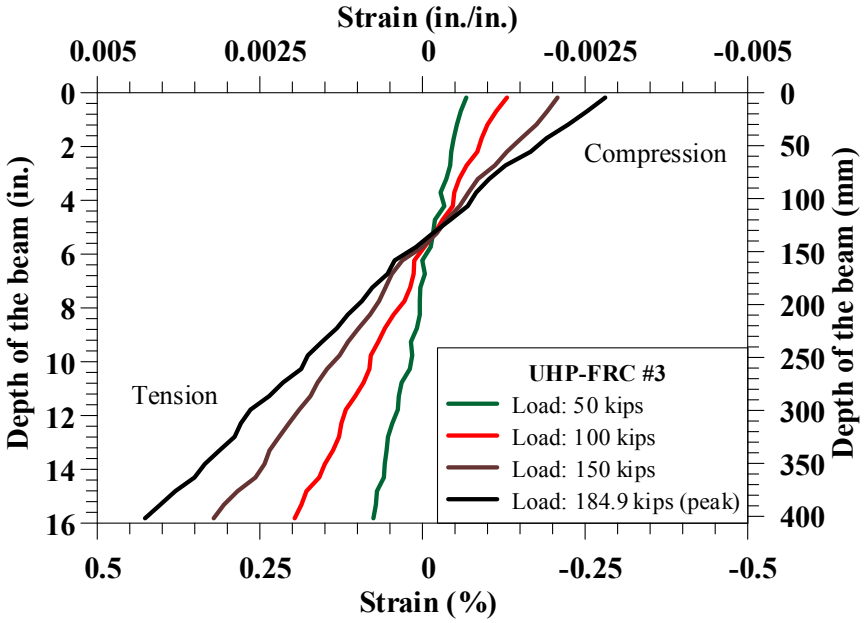

Figure 4-67 Strain variation in beam UHP-FRC #3

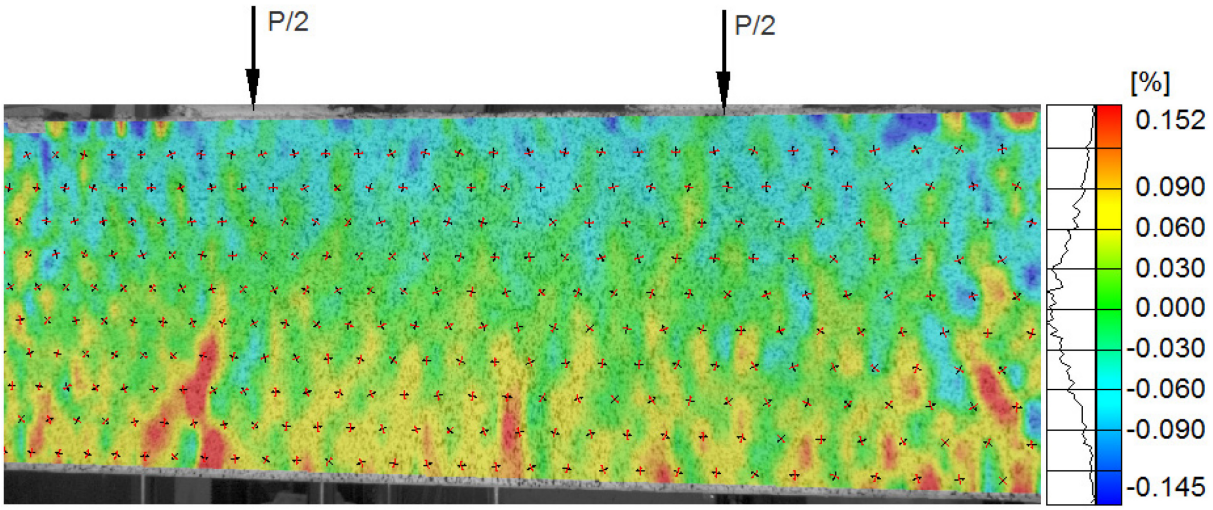

Figure 4-68 Full-field concrete longitudinal strain (ε_x) in moment region for UHP-FRC#3 at an applied load of 50 kips

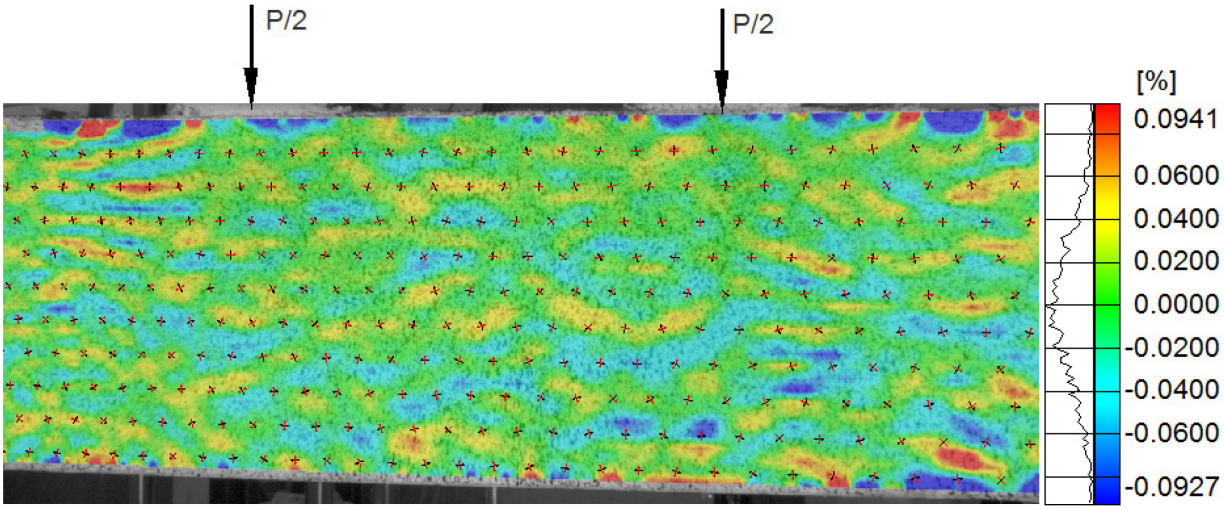

Figure 4-69 Full-field concrete transverse strain (ε_y) in moment region for UHP-FRC#3 at an applied load of 50 kips

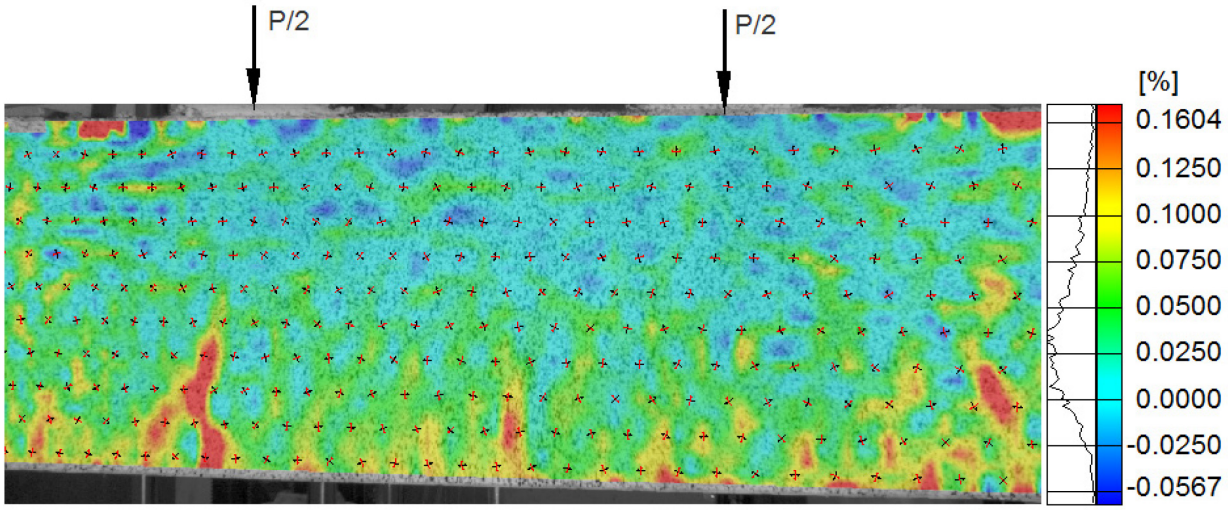

Figure 4-70 Full-field concrete maximum principal strain (σ_1) in moment region for UHP-FRC#3 at an applied load 50 kips

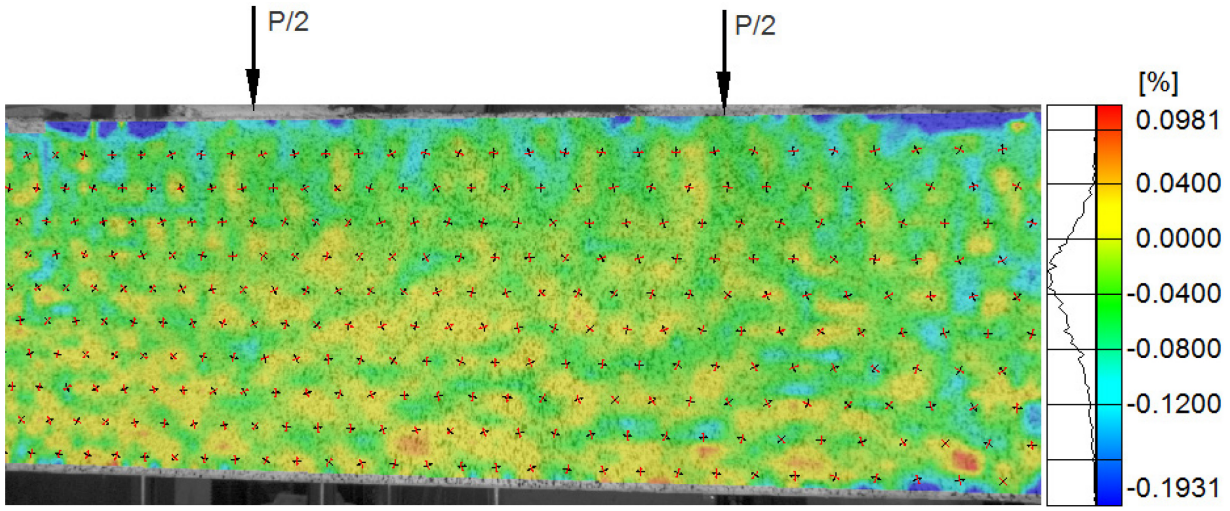

Figure 4-71 Full-field concrete minimum principal strain (σ_2) in moment region for UHP-FRC#3 at an applied load 50 kips

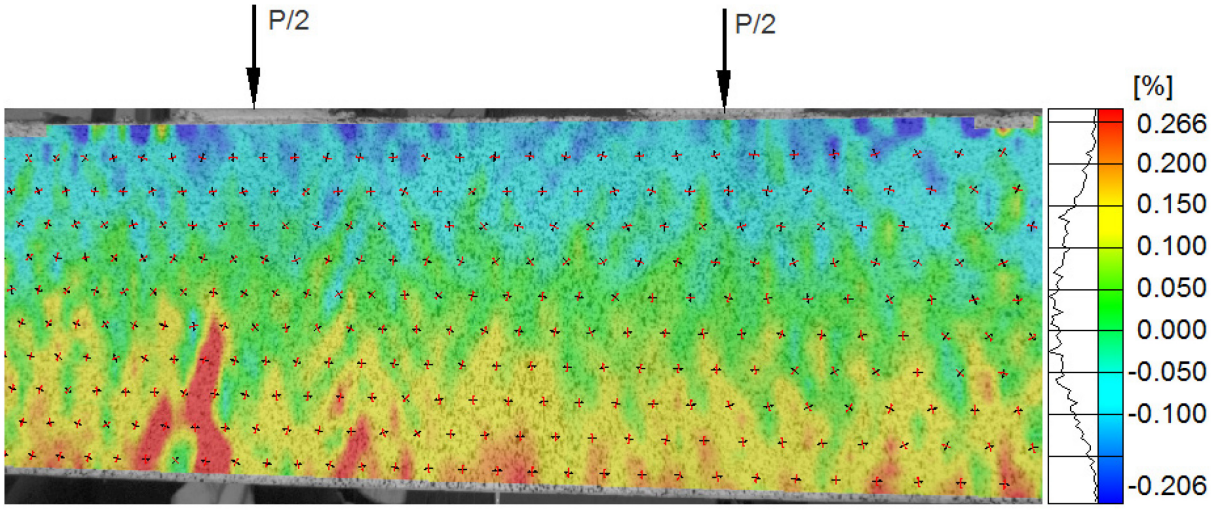

Figure 4-72 Full-field concrete longitudinal strain (ε_x) in moment region for UHP-FRC#3 at an applied load of 100 kips

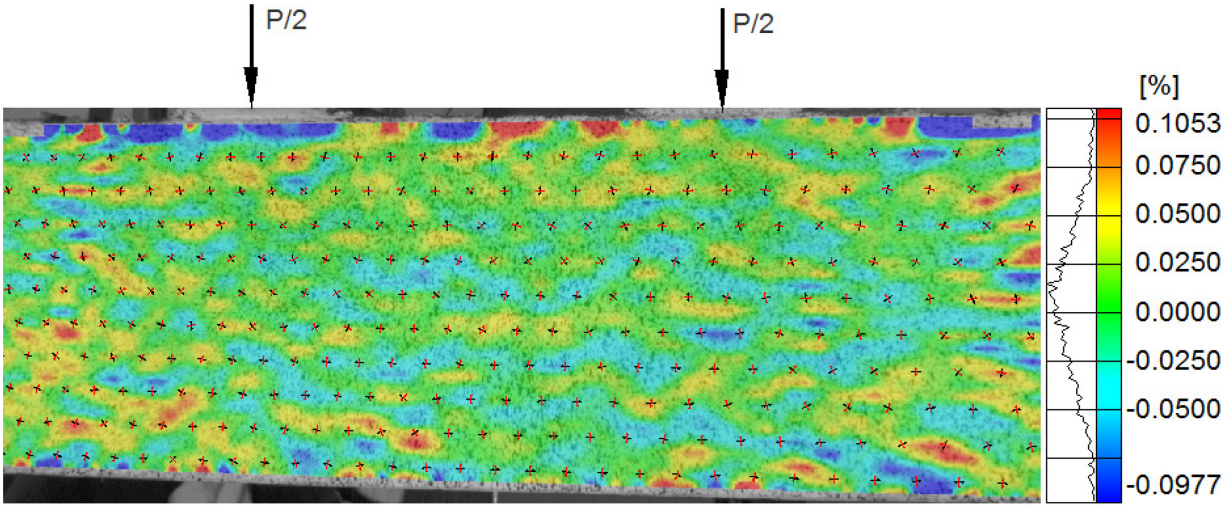

Figure 4-73 Full-field concrete transverse strain (ε_y) in moment region for UHP-FRC#3 at an applied load of 100 kips

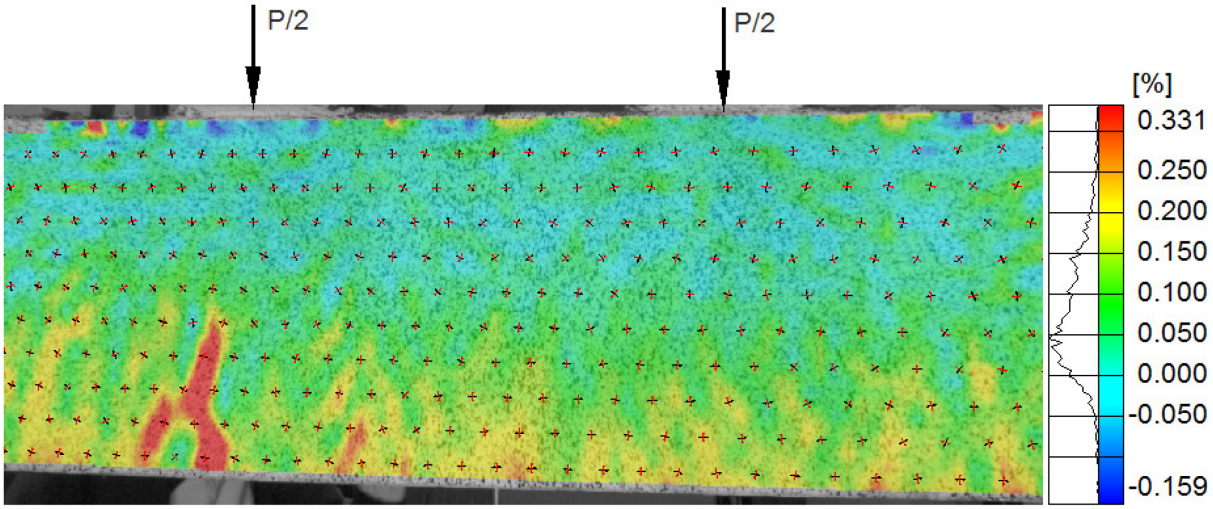

Figure 4-74 Full-field concrete maximum principal strain (σ_1) in moment region for UHP-FRC#3 at an applied load 100 kips

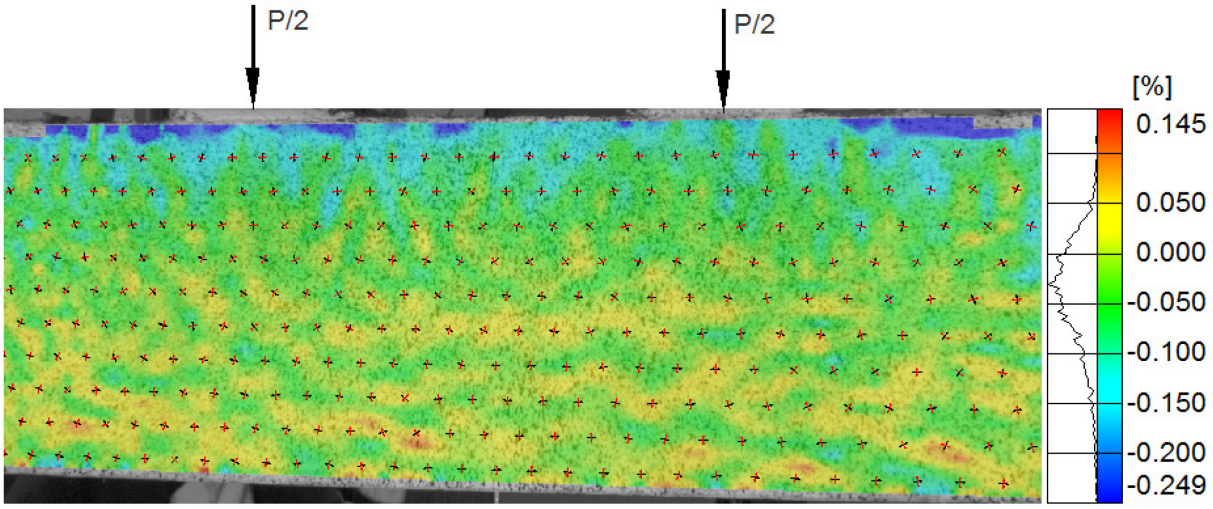

Figure 4-75 Full-field concrete minimum principal strain (σ_2) in moment region for UHP-FRC#3 at an applied load 100 kips

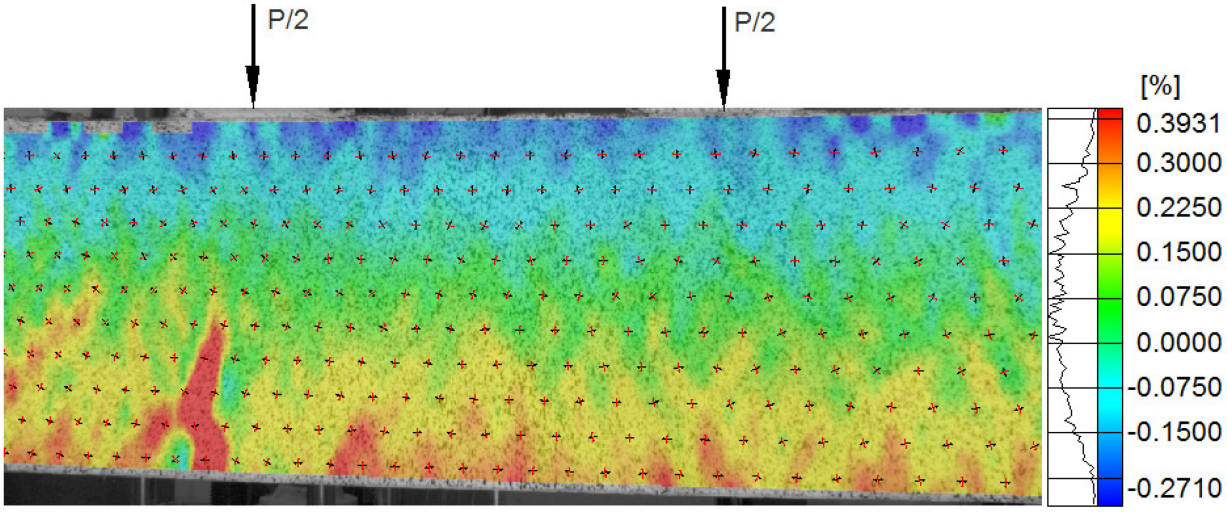

Figure 4-76 Full-field concrete longitudinal strain (ε_x) in moment region for UHP-FRC#3 at an applied load of 150 kips

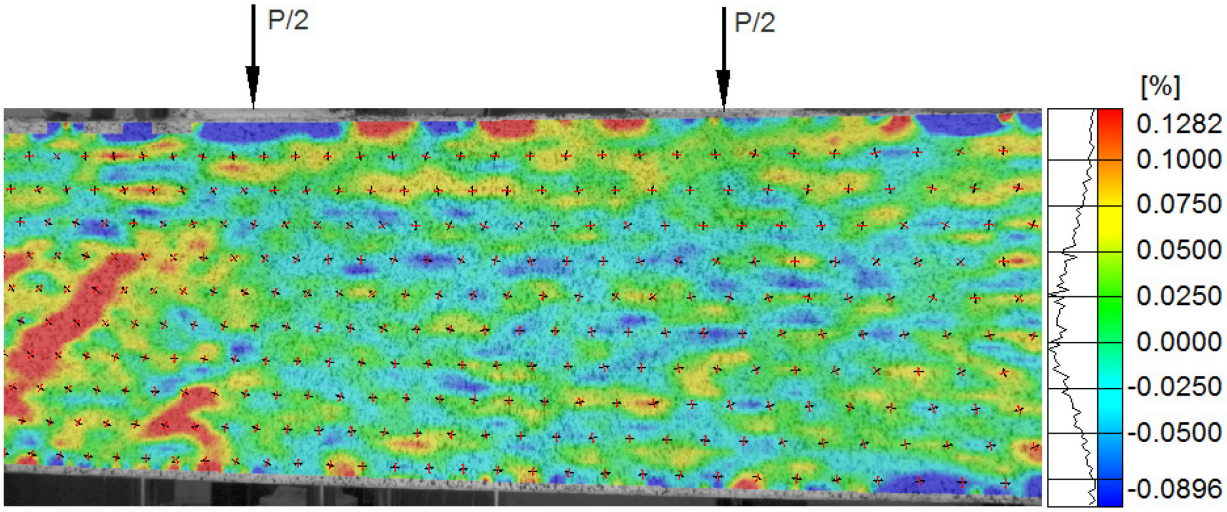

Figure 4-77 Full-field concrete transverse strain (ε_y) in moment region for UHP-FRC#3 at an applied load of 150 kips

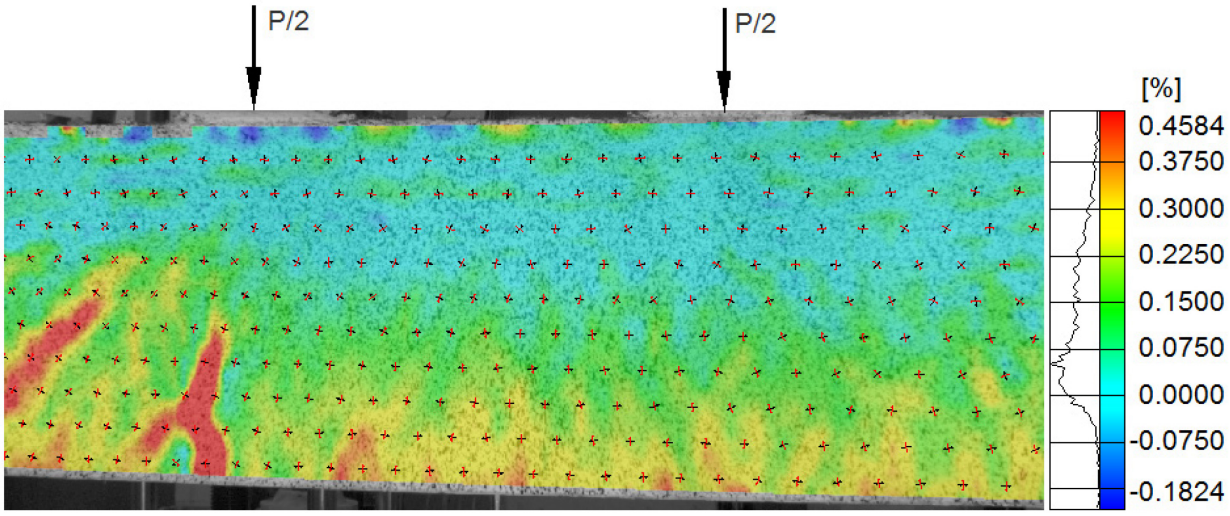

Figure 4-78 Full-field concrete maximum principal strain (σ_1) in moment region for UHP-FRC#3 at an applied load 150 kips

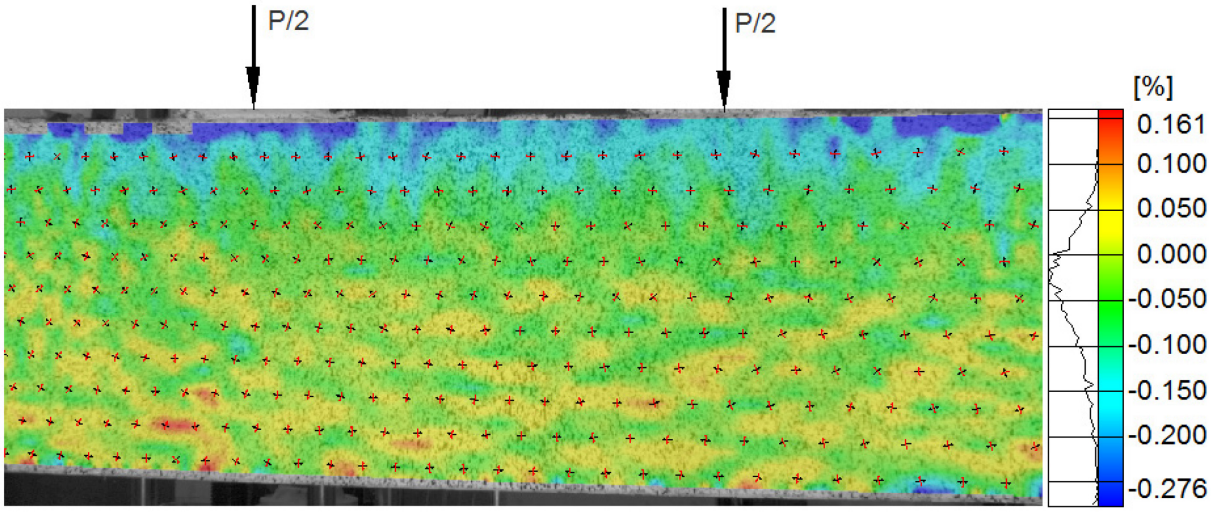

Figure 4-79 Full-field concrete minimum principal strain (σ_2) in moment region for UHP-FRC#3 at an applied load 150 kips

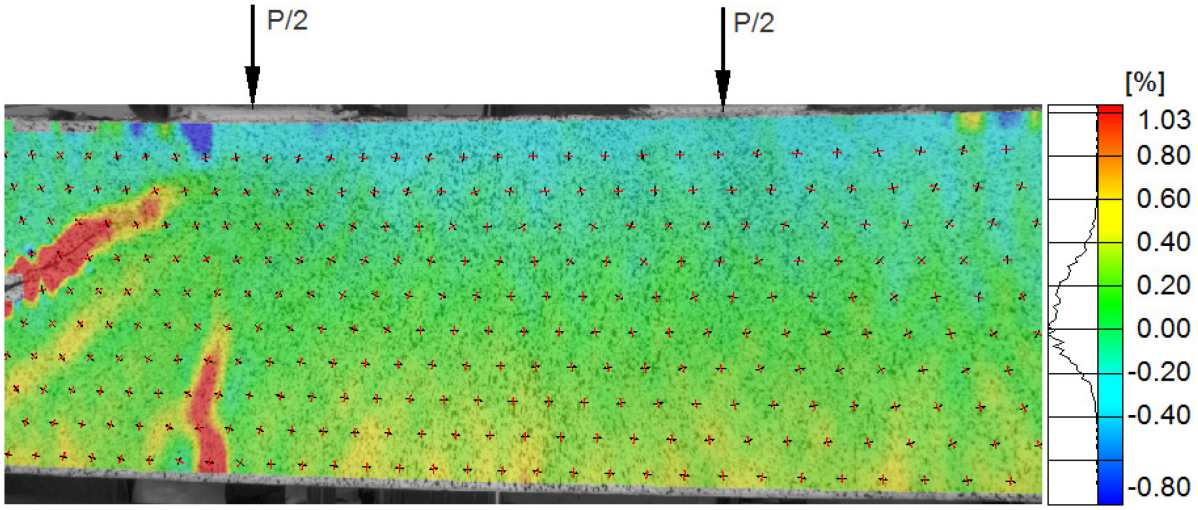

Figure 4-80 Full-field concrete longitudinal strain (ε_x) in moment region for UHP-FRC#3 at an applied load of 184.92 kips (peak load)

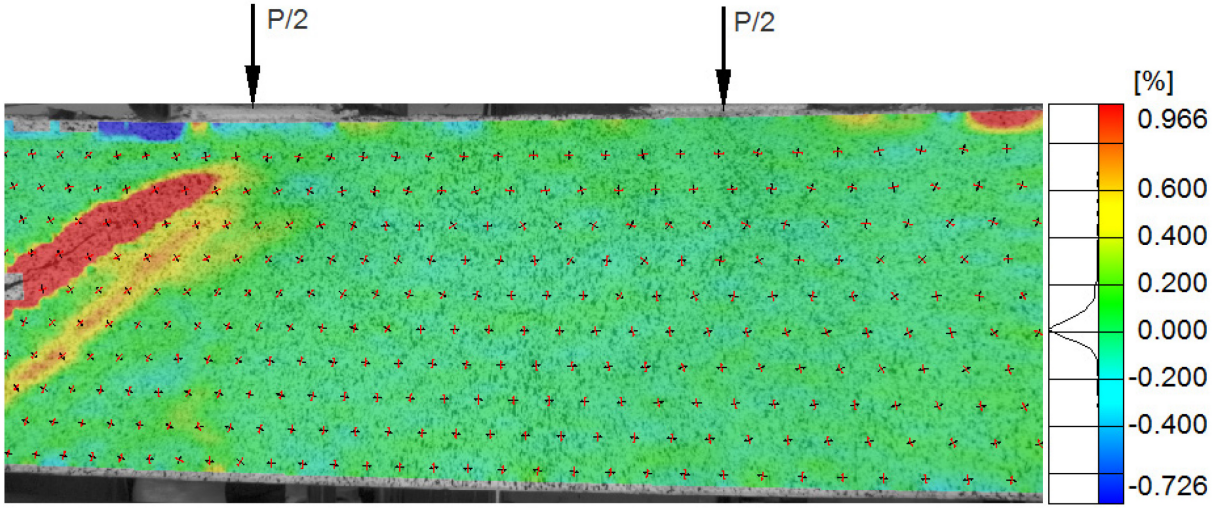

Figure 4-81 Full-field concrete transverse strain (ε_y) in moment region for UHP-FRC#3 at an applied load of 184.92 kips (peak load)

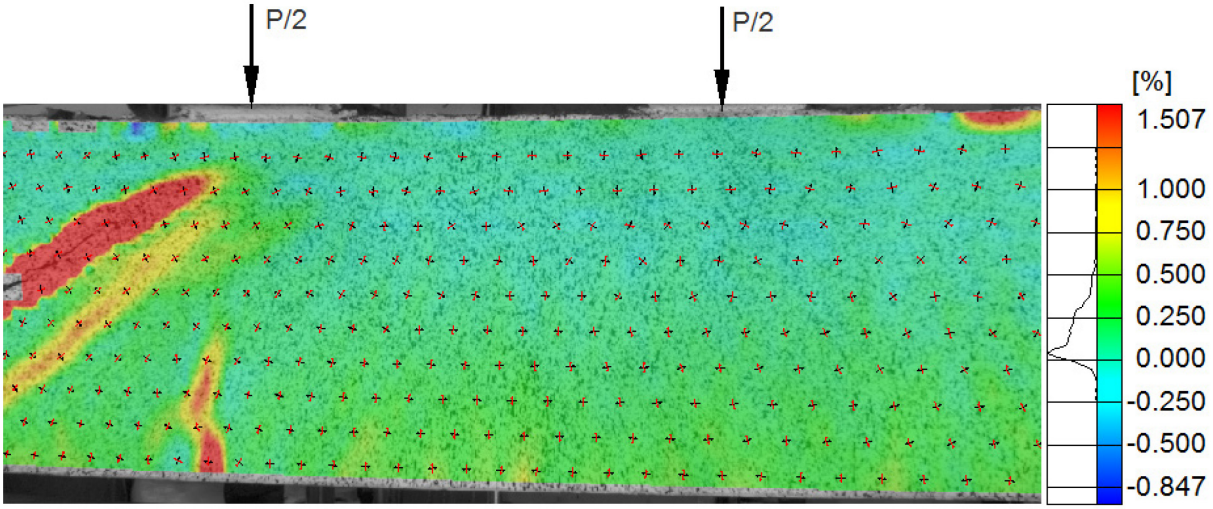

Figure 4-82 Full-field concrete maximum principal strain (σ_1) in moment region for UHP-FRC#3 at an applied load 184.92 kips (peak load)

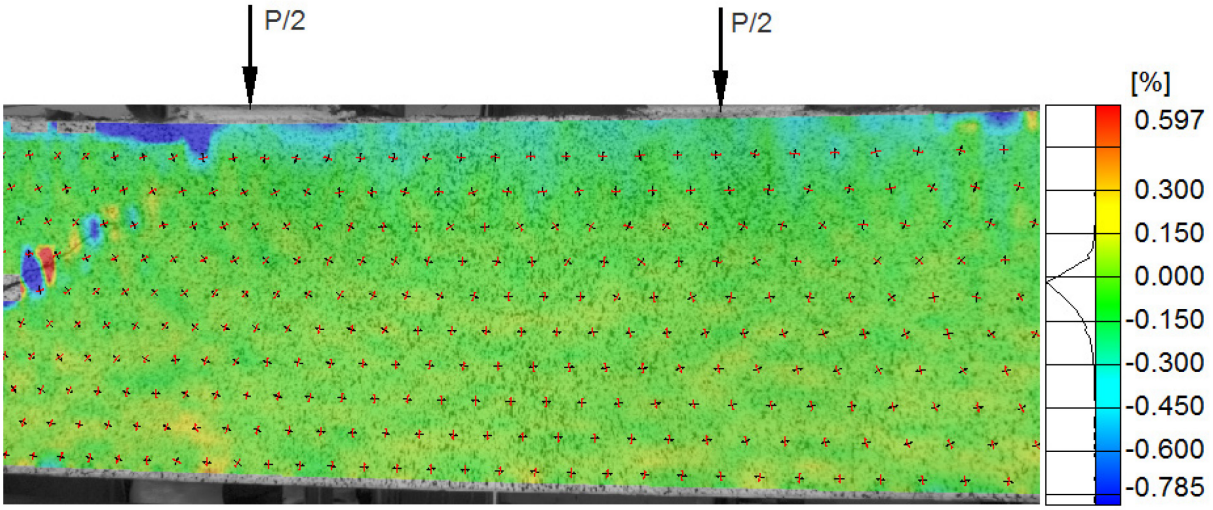

Figure 4-83 Full-field concrete minimum principal strain (σ_2) in moment region for UHP-FRC#3 at an applied load 184.92 kips (peak load)

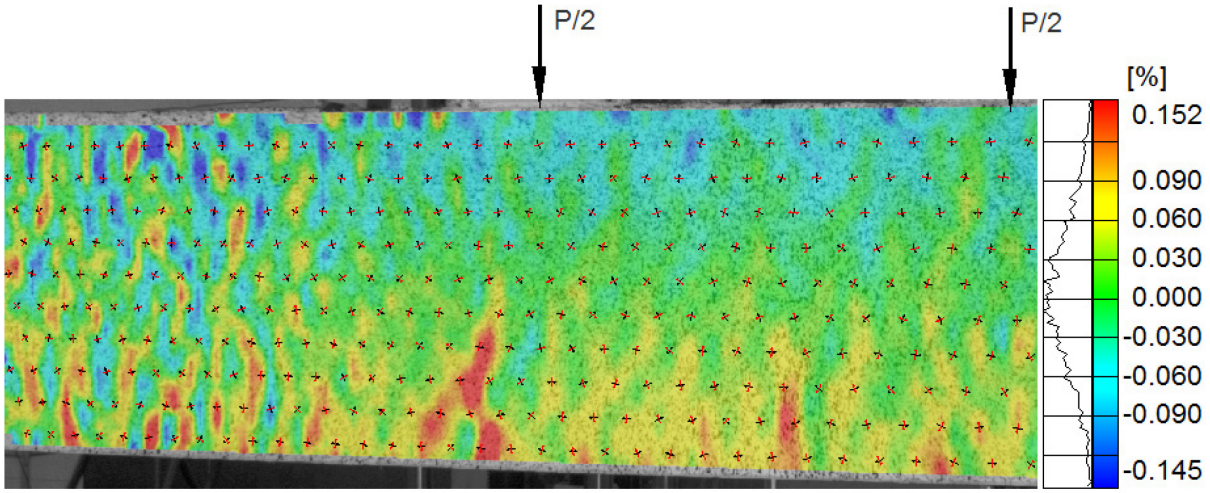

Figure 4-84 Full-field concrete longitudinal strain (ε_x) in a critical shear span for UHP-FRC#3 at an applied load of 50 kips

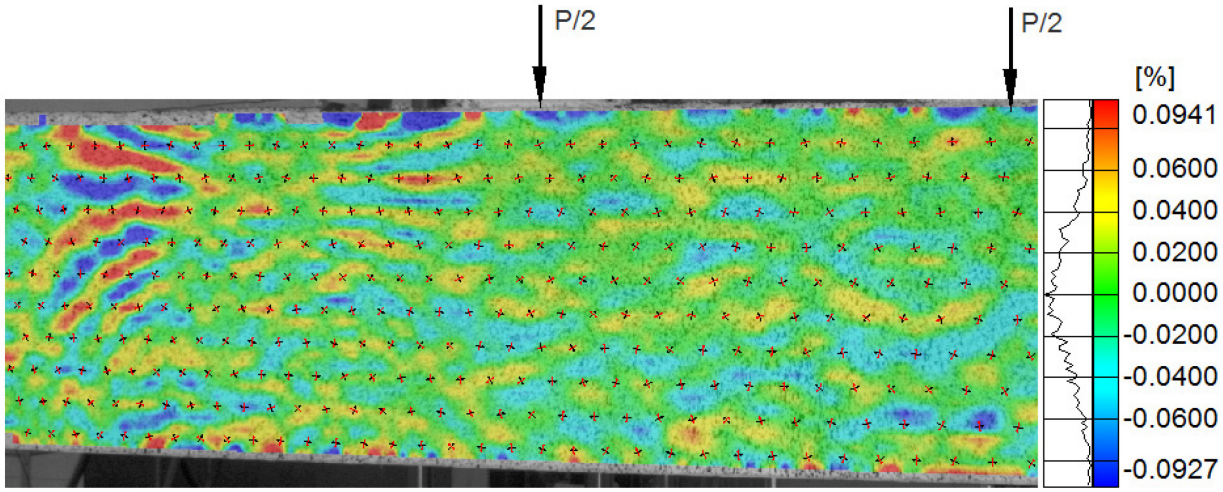

Figure 4-85 Full-field concrete transverse strain (ε_y) in a critical shear span for UHP-FRC#3 at an applied load of 50 kips

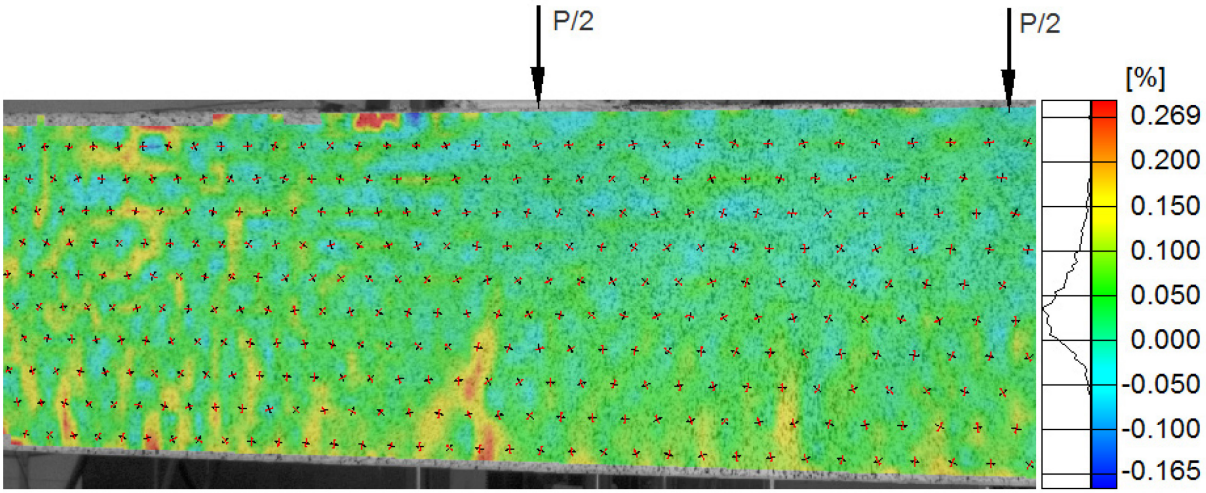

Figure 4-86 Full-field concrete maximum principal strain (σ_1) in a critical shear for UHP-FRC#3 at an applied load 50 kips

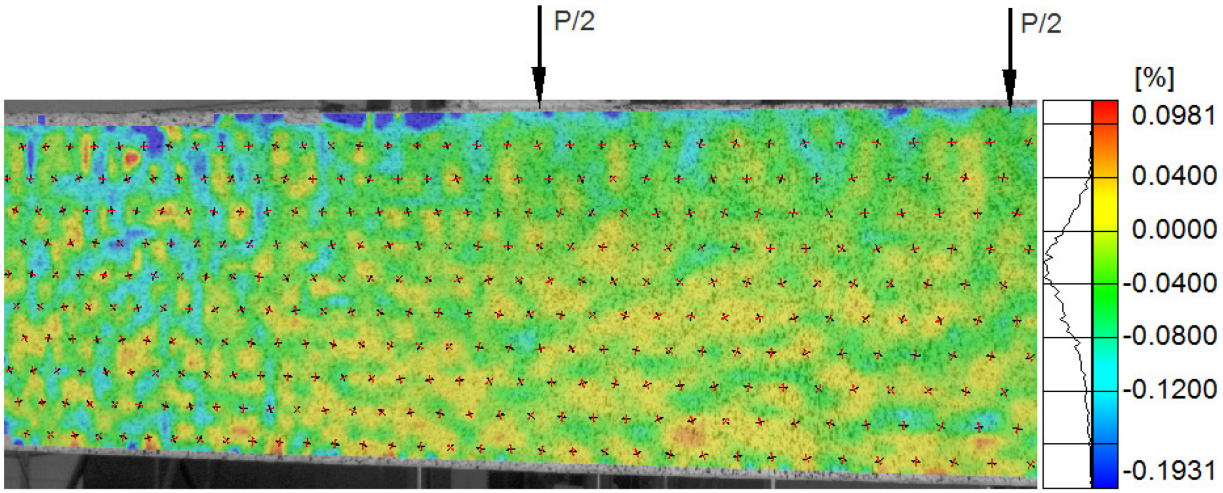

Figure 4-87 Full-field concrete minimum principal strain (σ_2) in a critical shear span for UHP-FRC#3 at an applied load 50 kips

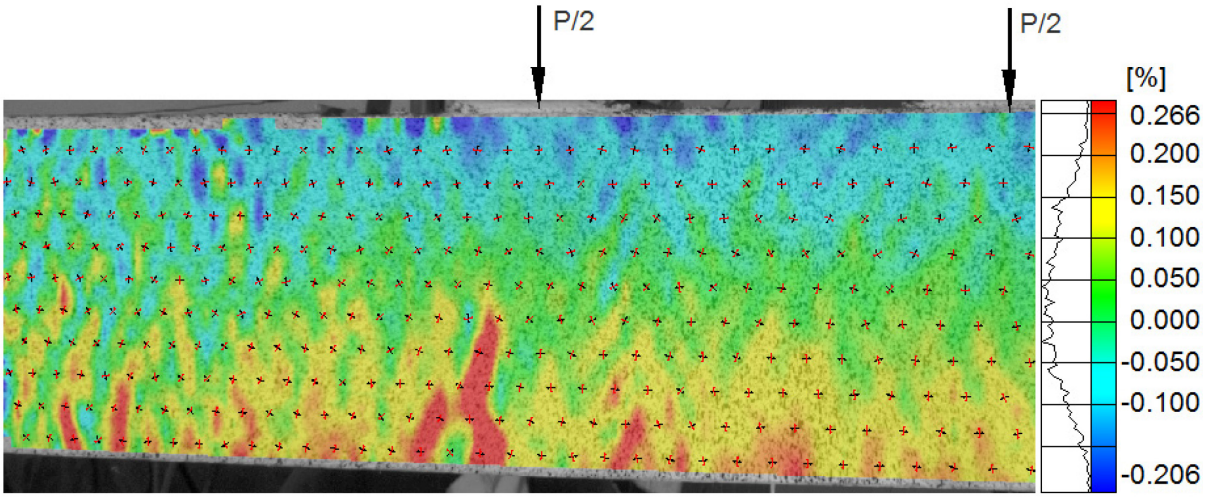

Figure 4-88 Full-field concrete longitudinal strain (ε_x) in a critical shear span for UHP-FRC#3 at an applied load of 100 kips

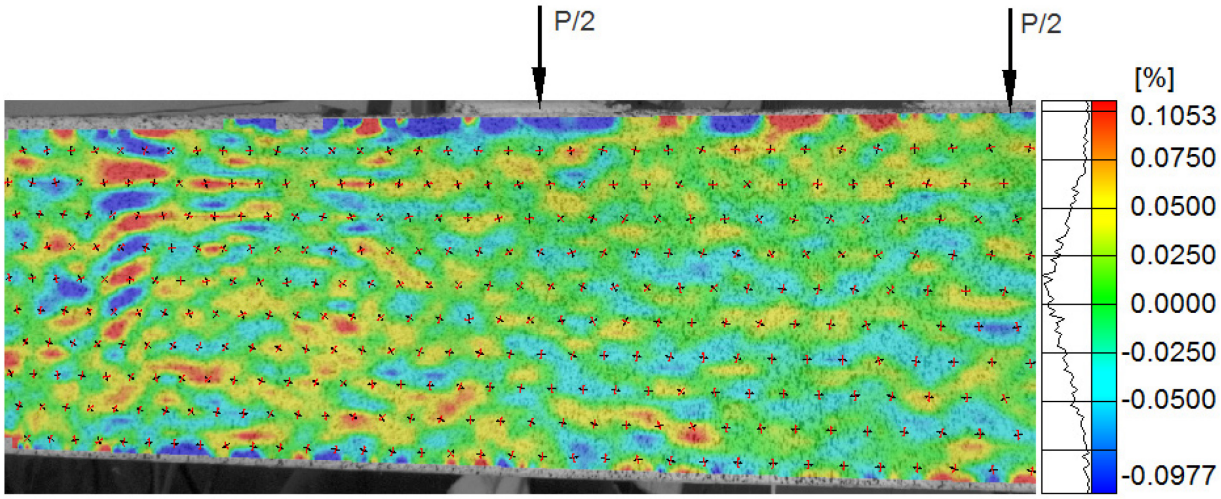

Figure 4-89 Full-field concrete transverse strain (ε_y) in a critical shear span for UHP-FRC#3 at an applied load of 100 kips

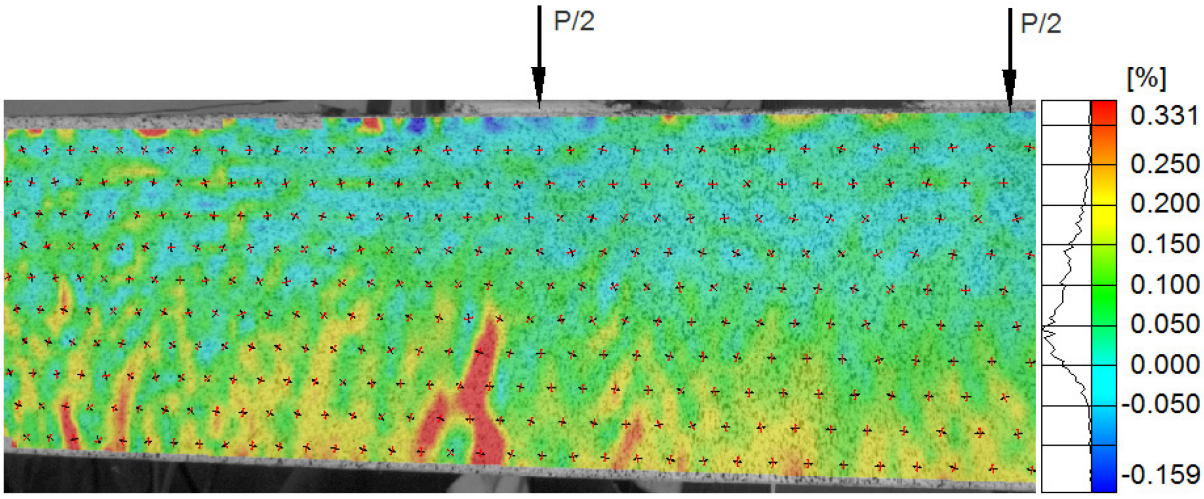

Figure 4-90 Full-field concrete maximum principal strain (σ_1) in a critical shear for UHP-FRC#3 at an applied load 100 kips

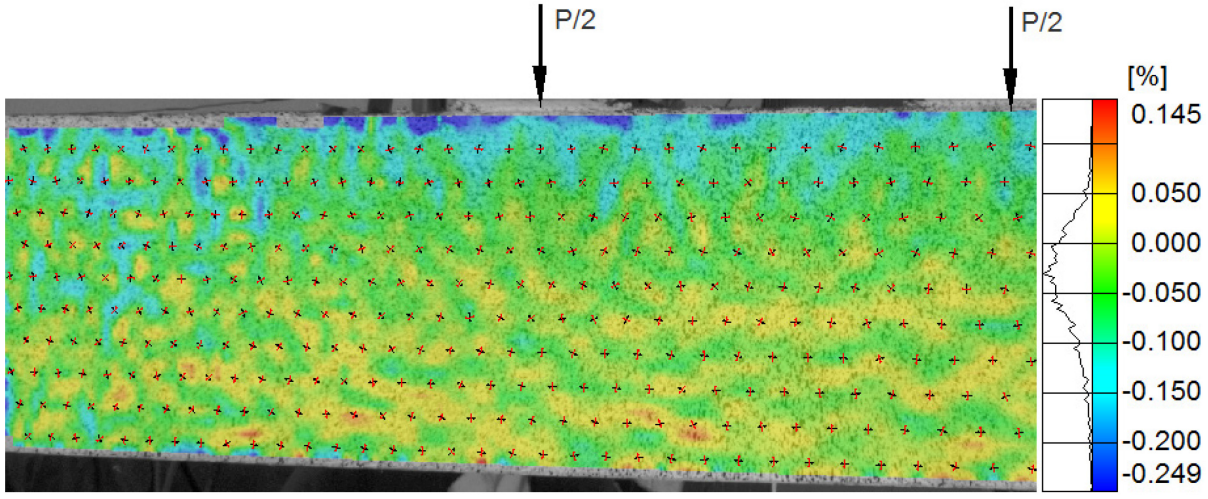

Figure 4-91 Full-field concrete minimum principal strain (σ_2) in a critical shear span for UHP-FRC#3 at an applied load 100 kips

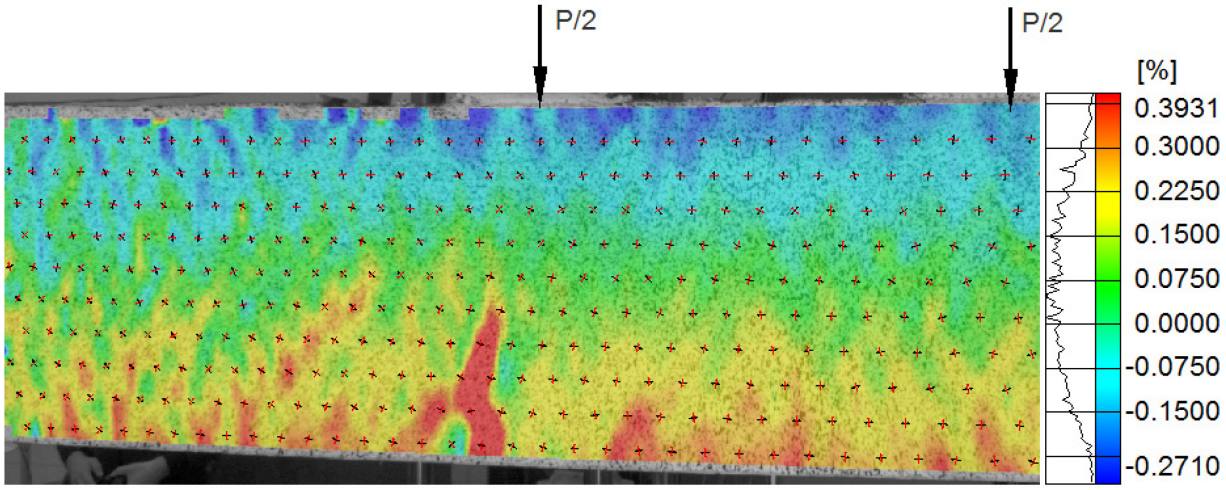

Figure 4-92 Full-field concrete longitudinal strain (ε_x) in a critical shear span for UHP-FRC#3 at an applied load of 150 kips

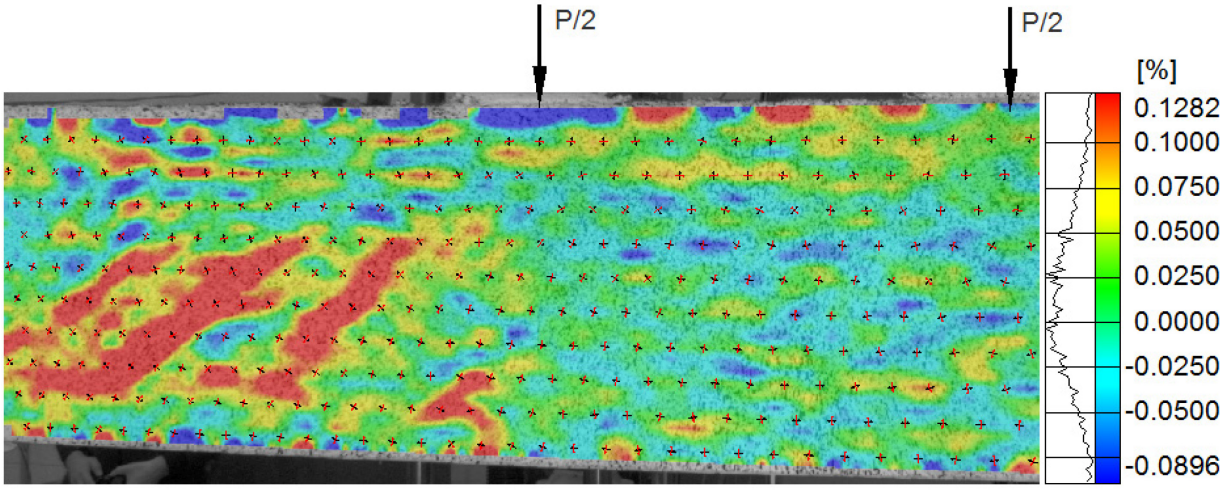

Figure 4-93 Full-field concrete transverse strain (ε_y) in a critical shear span for UHP-FRC#3 at an applied load of 150 kips

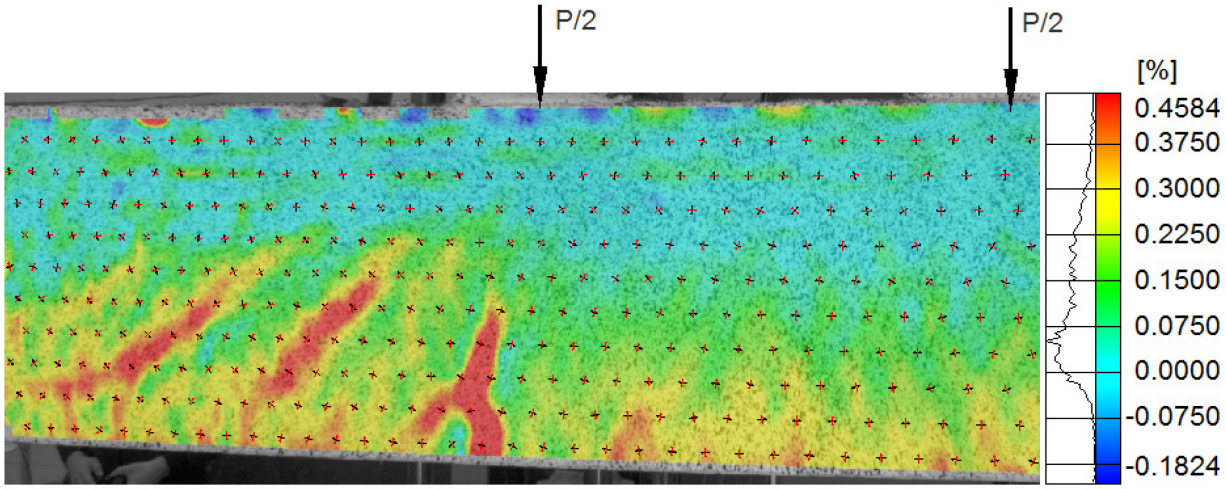

Figure 4-94 Full-field concrete maximum principal strain (σ_1) in a critical shear for UHP-FRC#3 at an applied load 150 kips

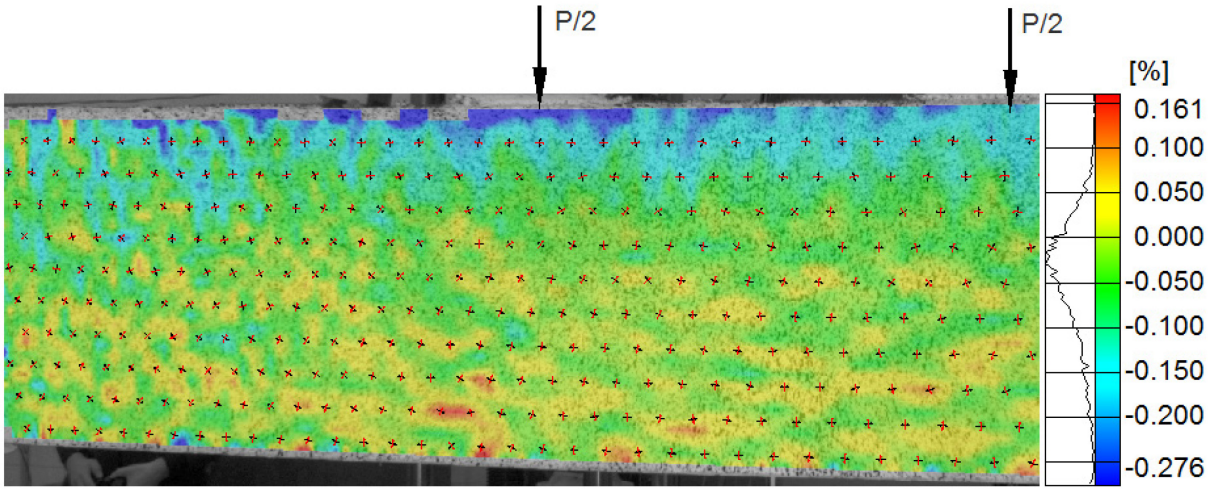

Figure 4-95 Full-field concrete minimum principal strain (σ_2) in a critical shear span for UHP-FRC#3 at an applied load 150 kips

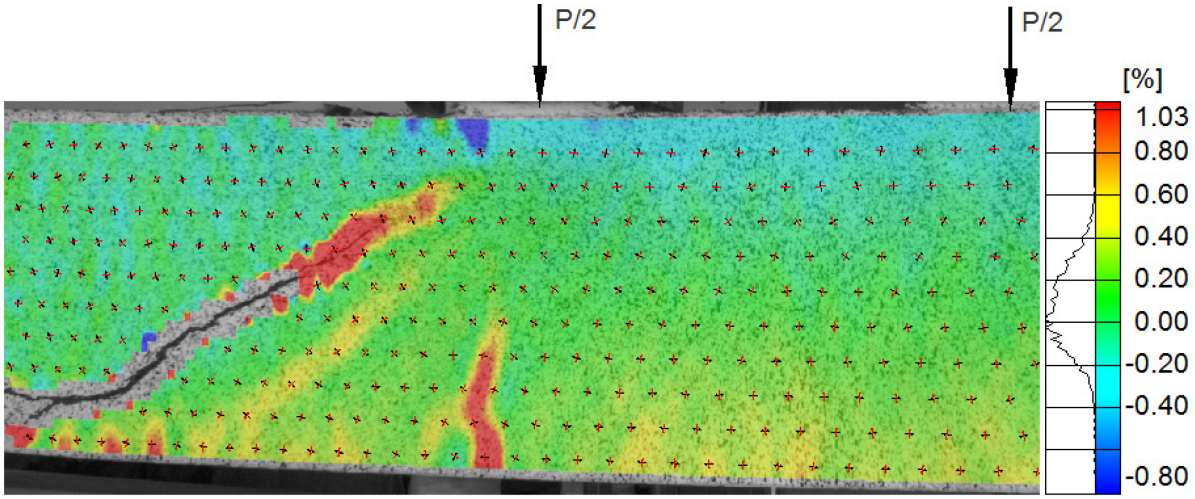

Figure 4-96 Full-field concrete longitudinal strain (ε_x) in a critical shear span for UHP-FRC#3 at an applied load of 184.92 kips (peak load)

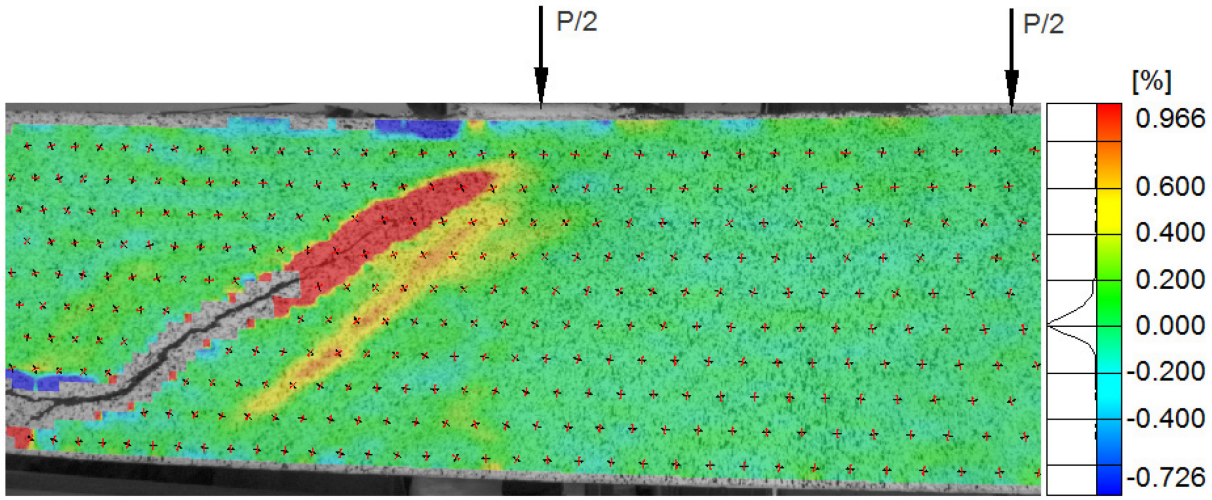

Figure 4-97 Full-field concrete transverse strain (ε_y) in a critical shear span for UHP-FRC#3 at an applied load of 184.92 kips (peak load)

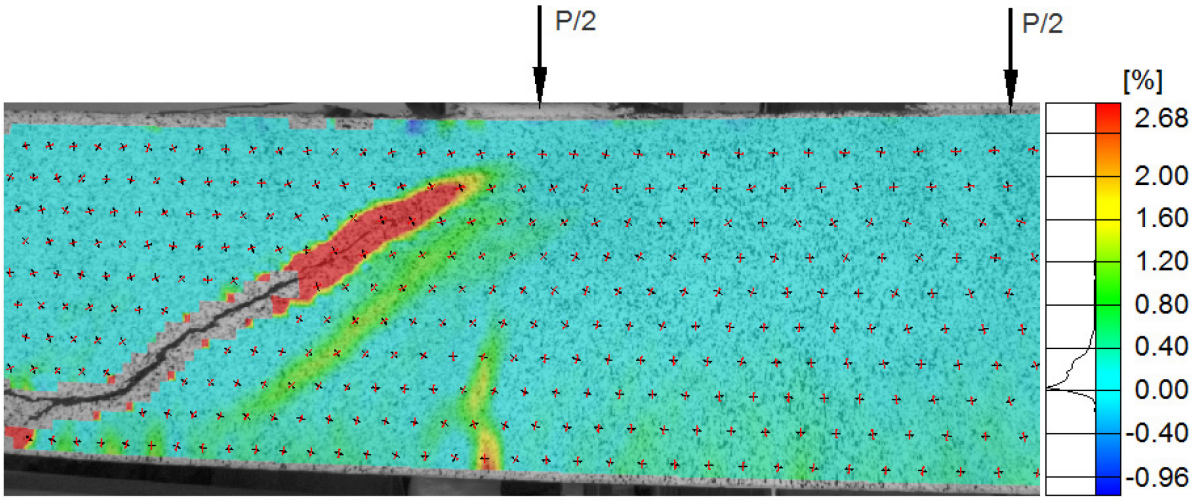

Figure 4-98 Full-field concrete maximum principal strain (σ_1) in a critical shear for UHP-FRC#3 at an applied load 184.92 kips (peak load)

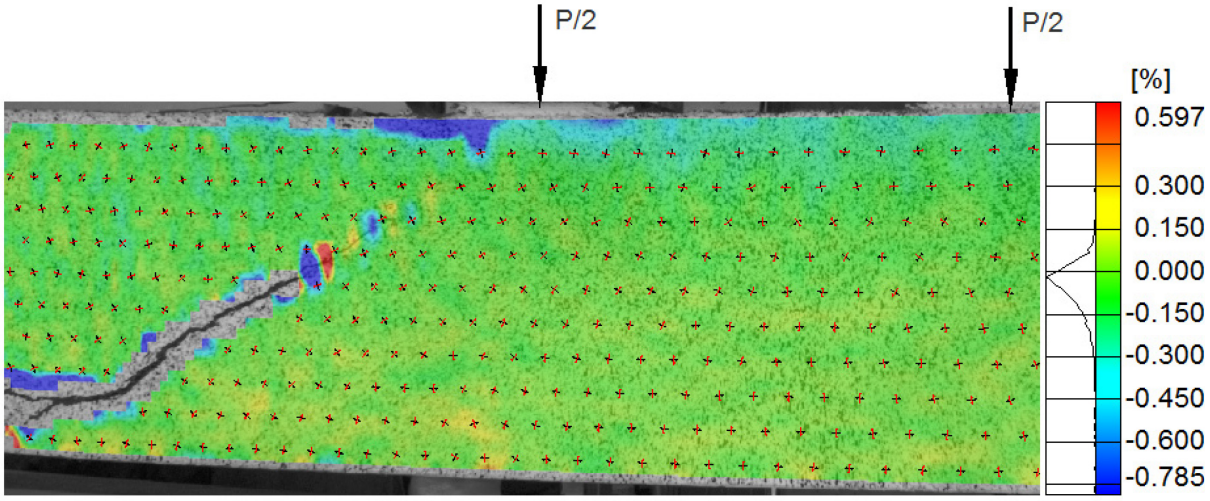

Figure 4-99 Full-field concrete minimum principal strain (σ_2) in a critical shear span for UHP-FRC#3 at an applied load 184.92 kips (peak load)

4.4 Beam UHP-FRC #4 BFRP:

Figure 4-100 shows load deflection behavior of the beam UHP-FRC #4 BFRP. Load deflection showed bilinear behavior up to peak, with a noticeable non-linearity before the peak load. Non-linear behavior observed near the peak is because of the gradual opening of shear

cracks. First linear segment corresponding to un-cracked response of the beam and the latter segment with a reduced stiffness corresponds to cracked response of the beam. First flexural crack was observed at the soffit of the beam near loading point at a load of 22 kips. With further increase in load more vertical cracks were seen in the constant moment extending to shear span attributing to a very low modulus of elasticity of Basalt FRP bars. Flexural crack formation was more significant after a load of 80 kips with a numerous hairline cracks between the major marked cracks pertaining to a very good tension stiffening effect. Initial visible shear crack was originated in the shear span as the flexural crack is inclined in diagonal direction at a load of 120 kips. A critical flexural shear crack formed in the shear span near the loading point extended towards the loading point and began to widen after a load of 140 kips. Which eventually led to the load drop after attaining a peak of 163.74 kips. This flexural shear crack is accompanied by a bond failure at the bottom layer of BFRP bars which was depicted by a wide-open crack along the longitudinal bars at the beam soffit.

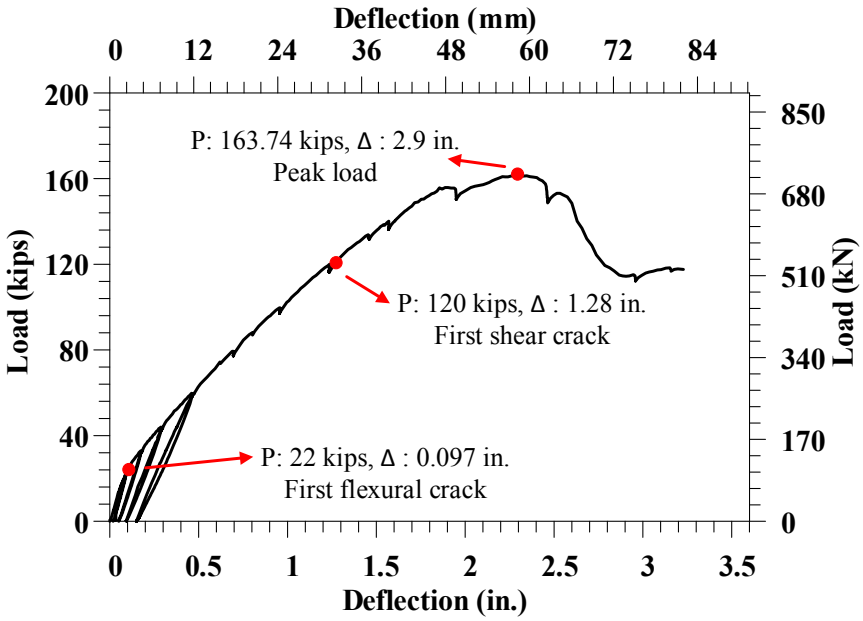

Figure 4-100 Load deflection behavior of beam UHP-FRC #4

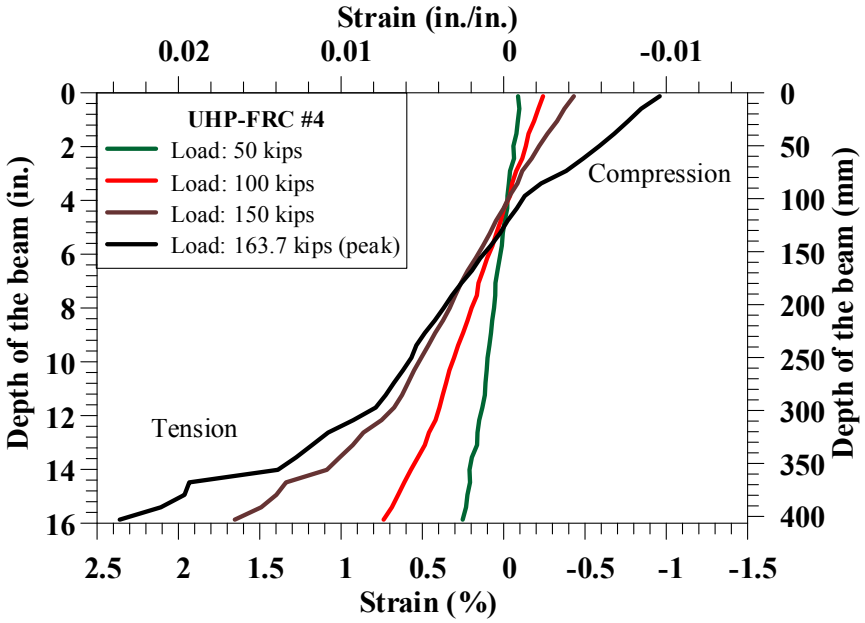

Figure 4-101 Strain variation in beam UHP-FRC #4

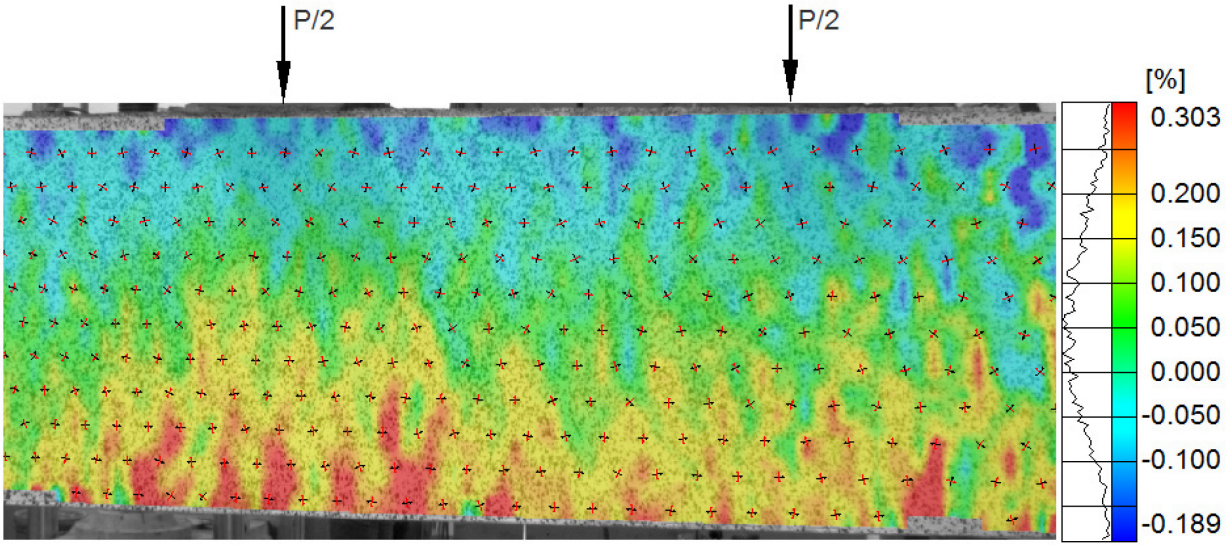

Figure 4-102 Full-field concrete longitudinal strain (ε_x) in moment region for UHP-FRC#4 at an applied load of 50 kips

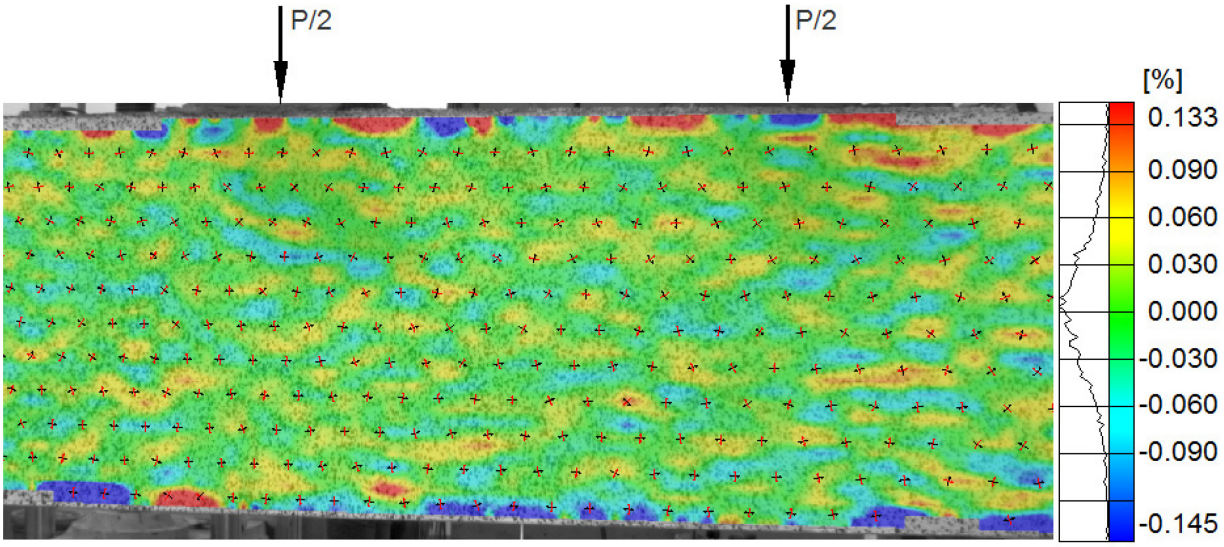

Figure 4-103 Full-field concrete transverse strain (ε_y) in moment region for UHP-FRC#4 at an applied load of 50 kips

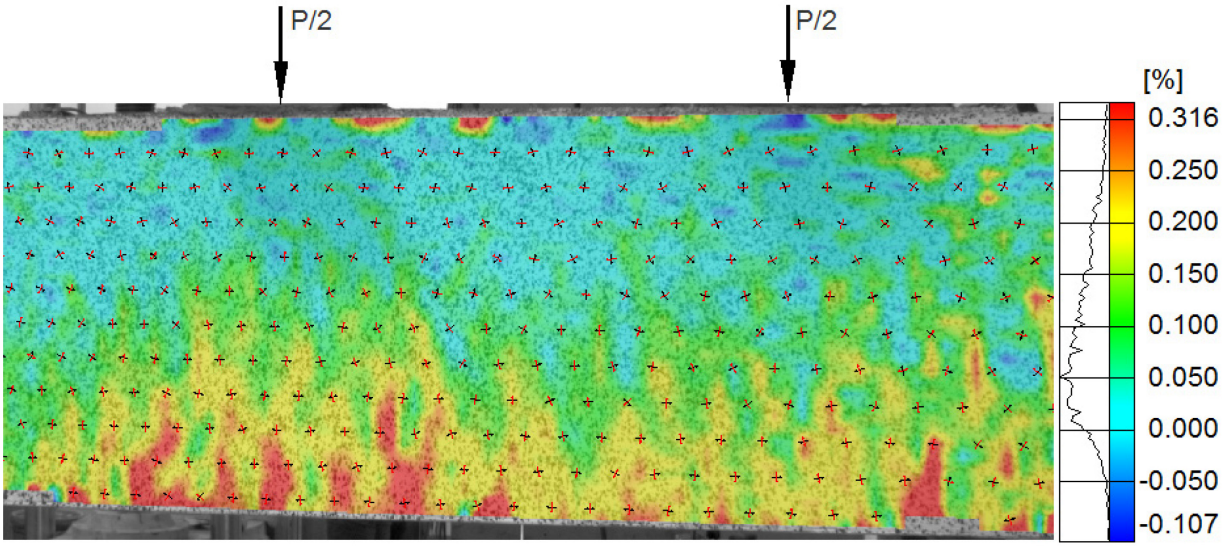

Figure 4-104 Full-field concrete maximum principal strain (σ_1) in moment region for UHP-FRC#4 at an applied load 50 kips

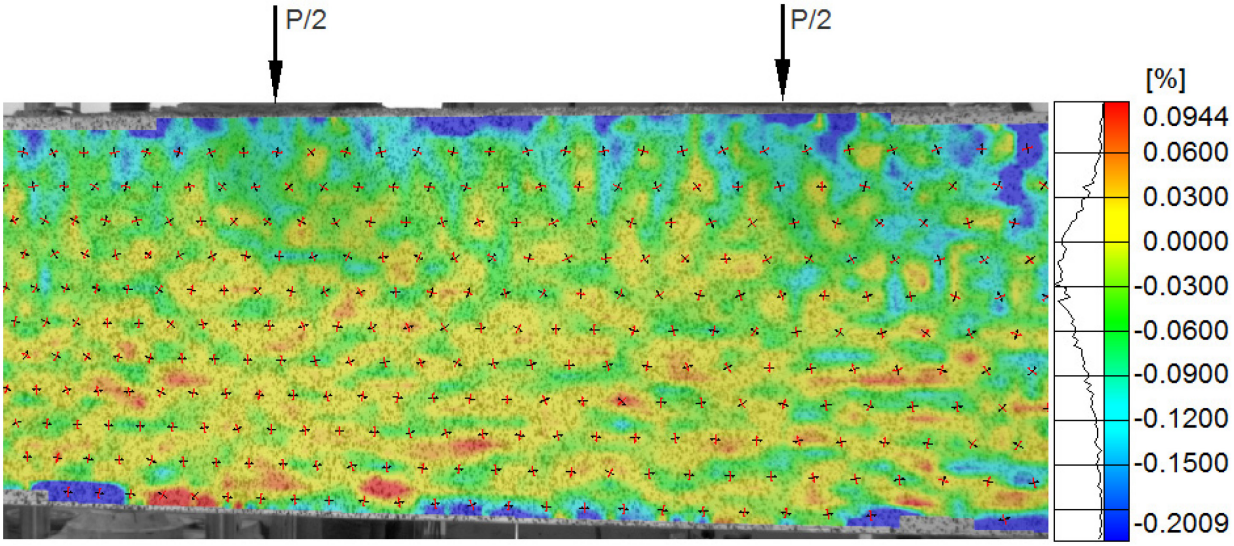

Figure 4-105 Full-field concrete minimum principal strain (σ_2) in moment region for UHP-FRC#4 at an applied load 50 kips

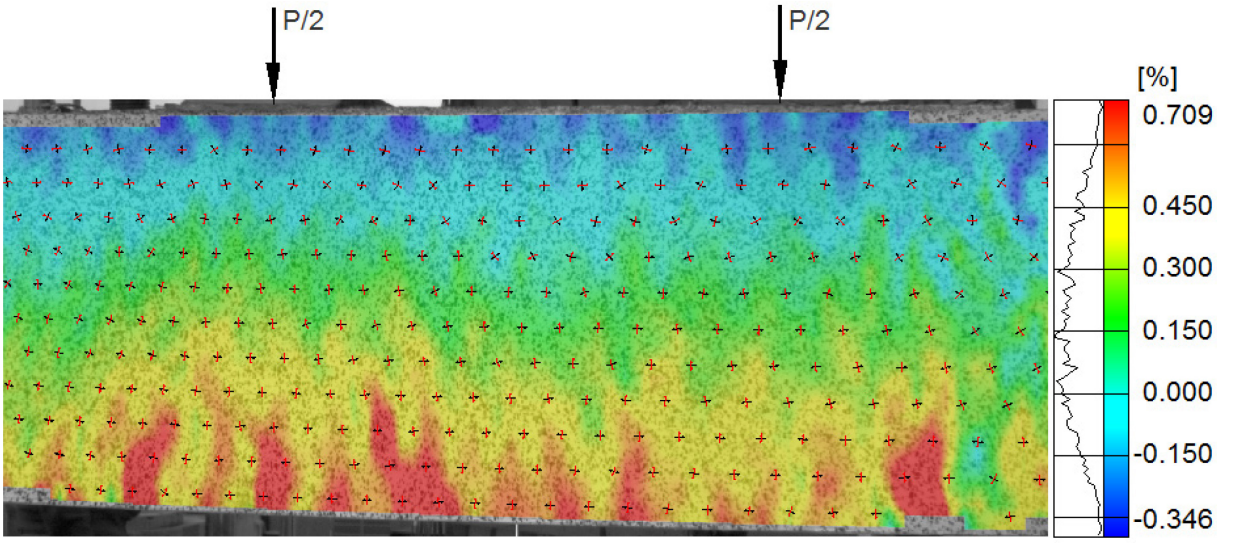

Figure 4-106 Full-field concrete longitudinal strain (ε_x) in moment region for UHP-FRC#4 at an applied load of 100 kips

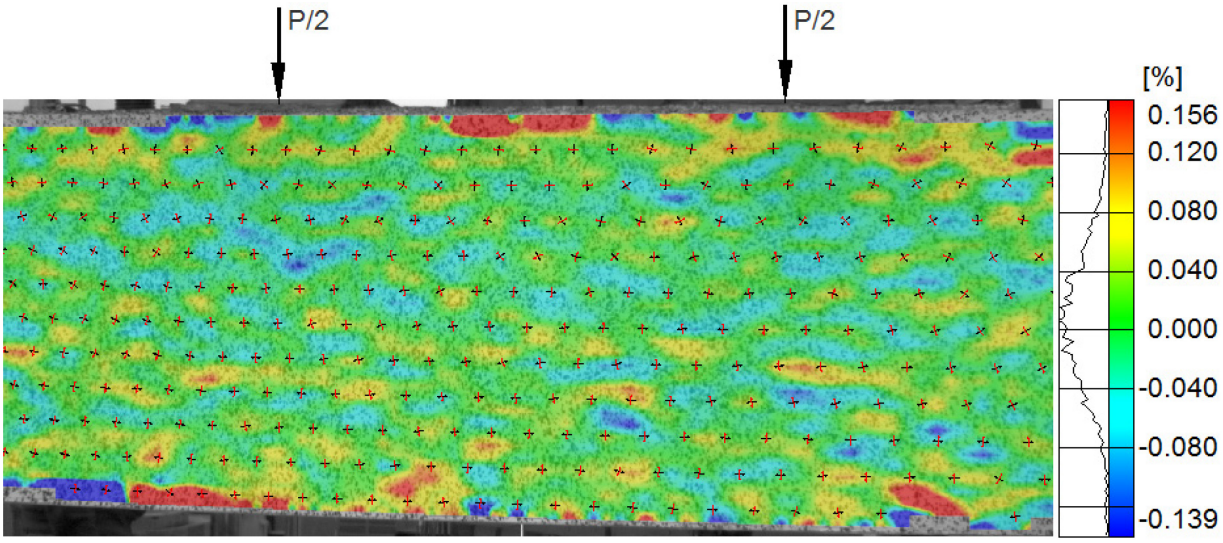

Figure 4-107 Full-field concrete transverse strain (ε_y) in moment region for UHP-FRC#4 at an applied load of 100 kips

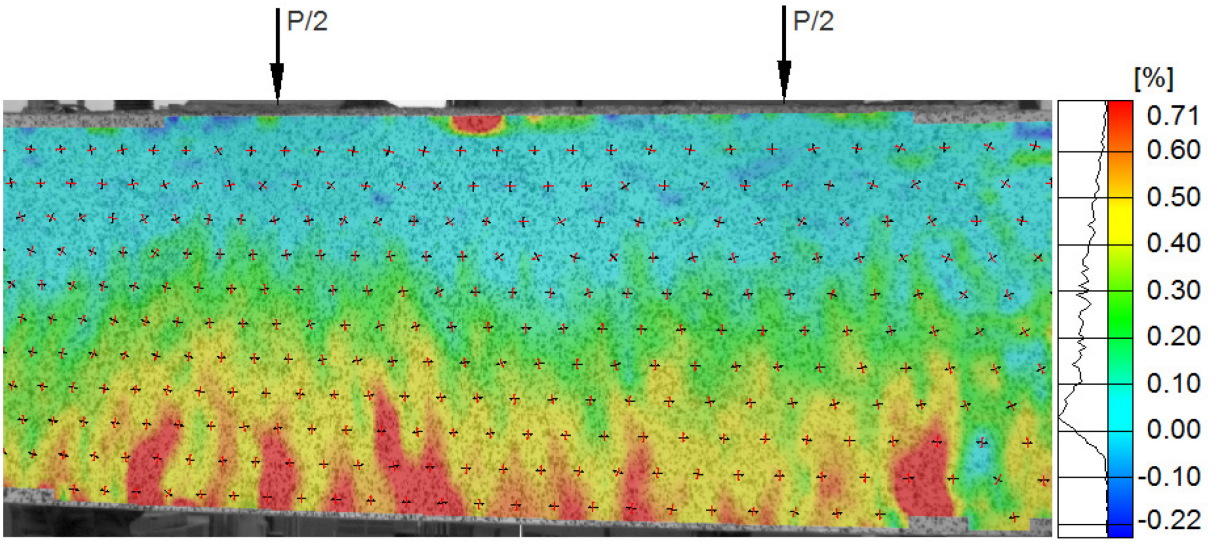

Figure 4-108 Full-field concrete maximum principal strain (σ_1) in moment region for UHP-FRC#4 at an applied load 100 kips

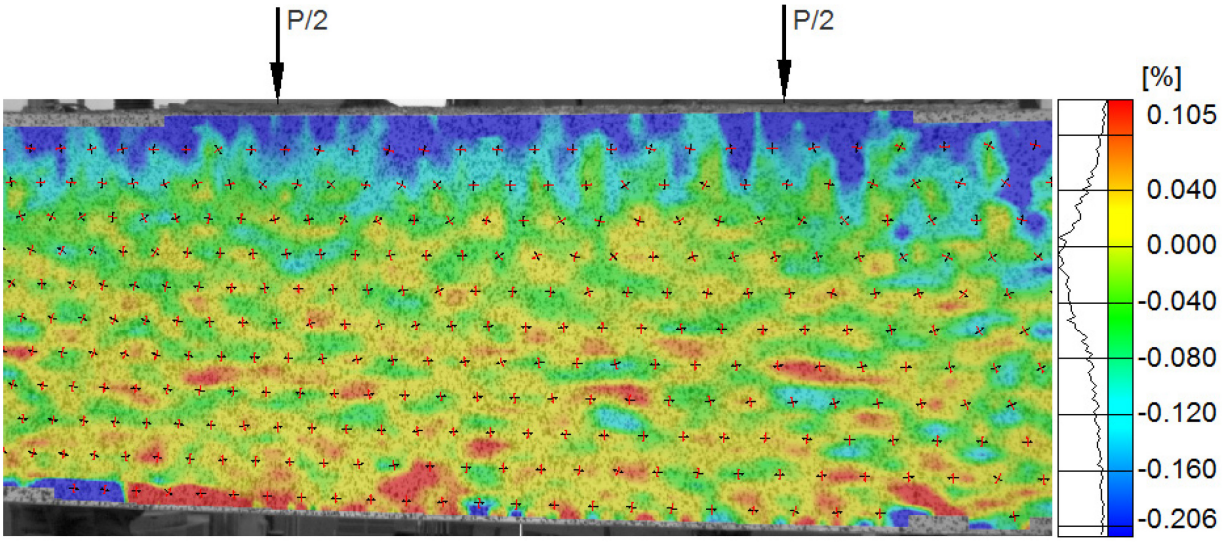

Figure 4-109 Full-field concrete minimum principal strain (σ_2) in moment region for UHP-FRC#4 at an applied load 100 kips

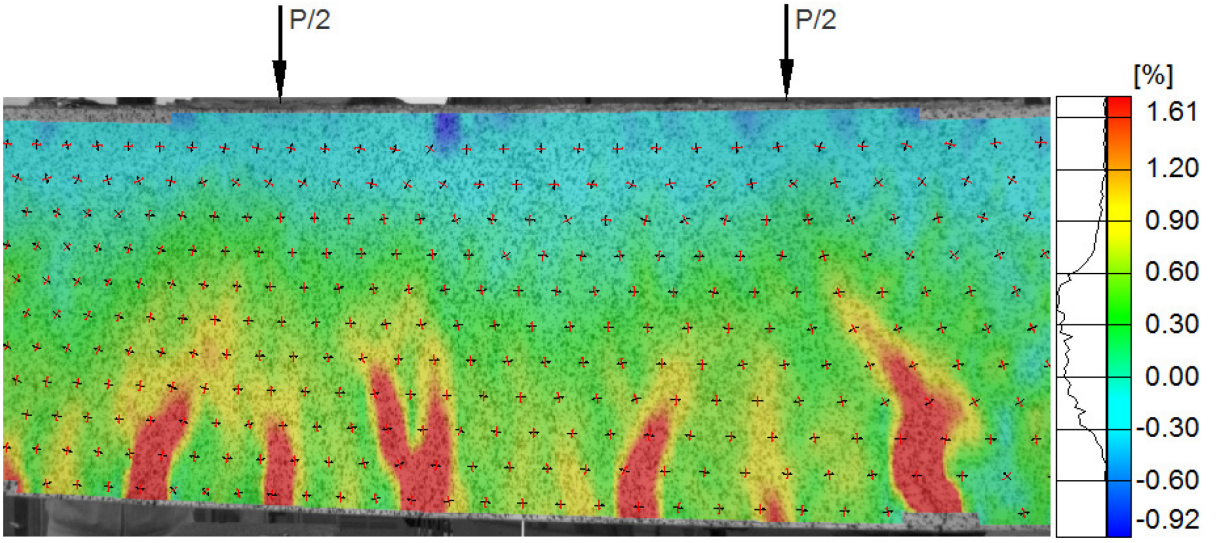

Figure 4-110 Full-field concrete longitudinal strain (ε_x) in moment region for UHP-FRC#4 at an applied load of 150 kips

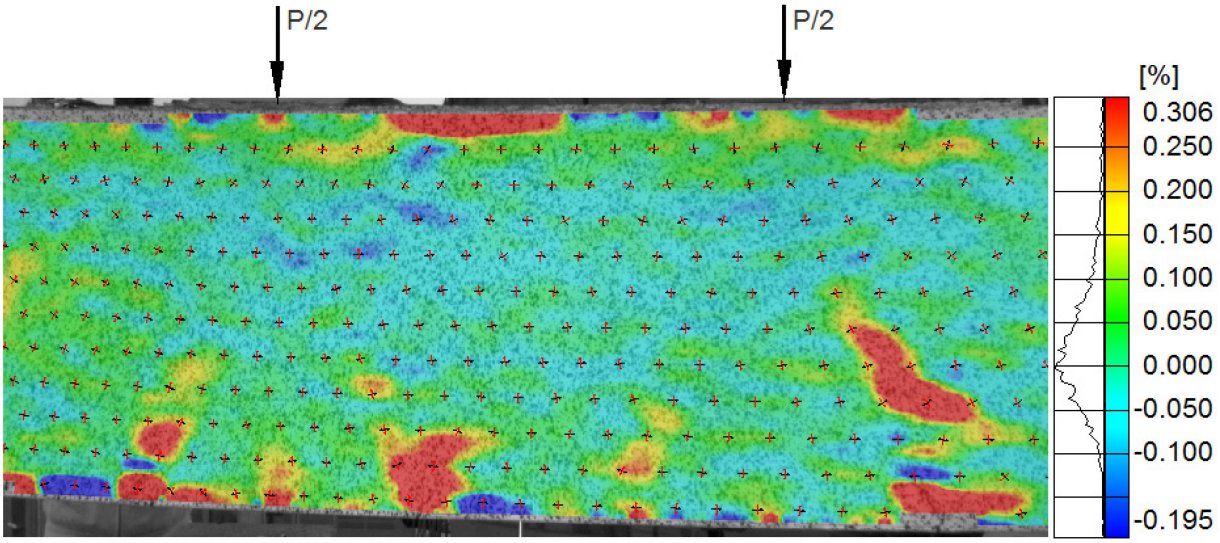

Figure 4-111 Full-field concrete transverse strain (ε_y) in moment region for UHP-FRC#4 at an applied load of 150 kips

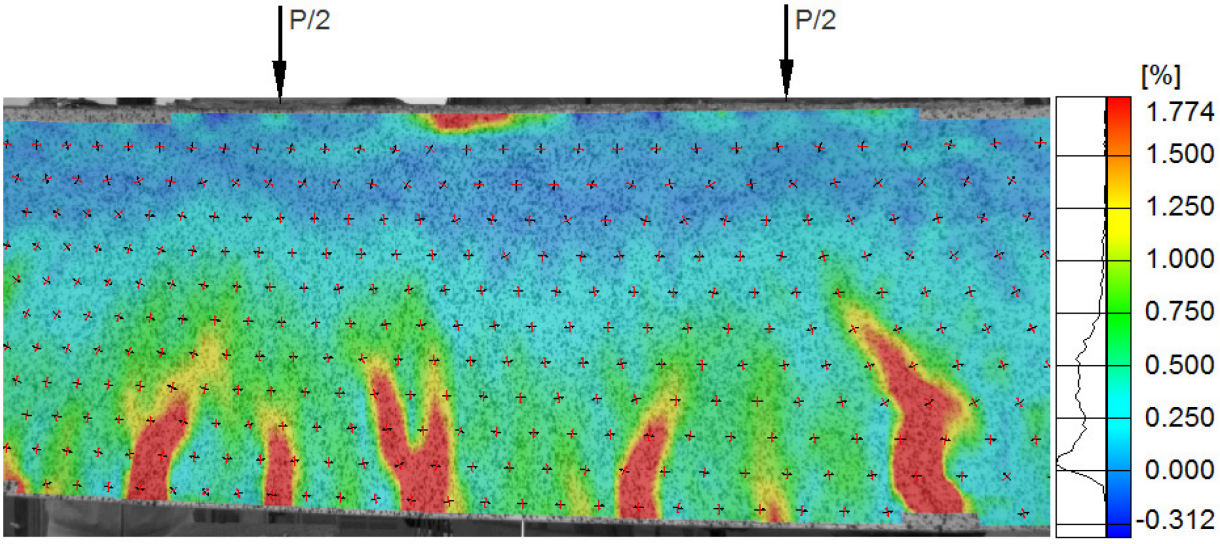

Figure 4-112 Full-field concrete maximum principal strain (σ_1) in moment region for UHP-FRC#4 at an applied load 150 kips

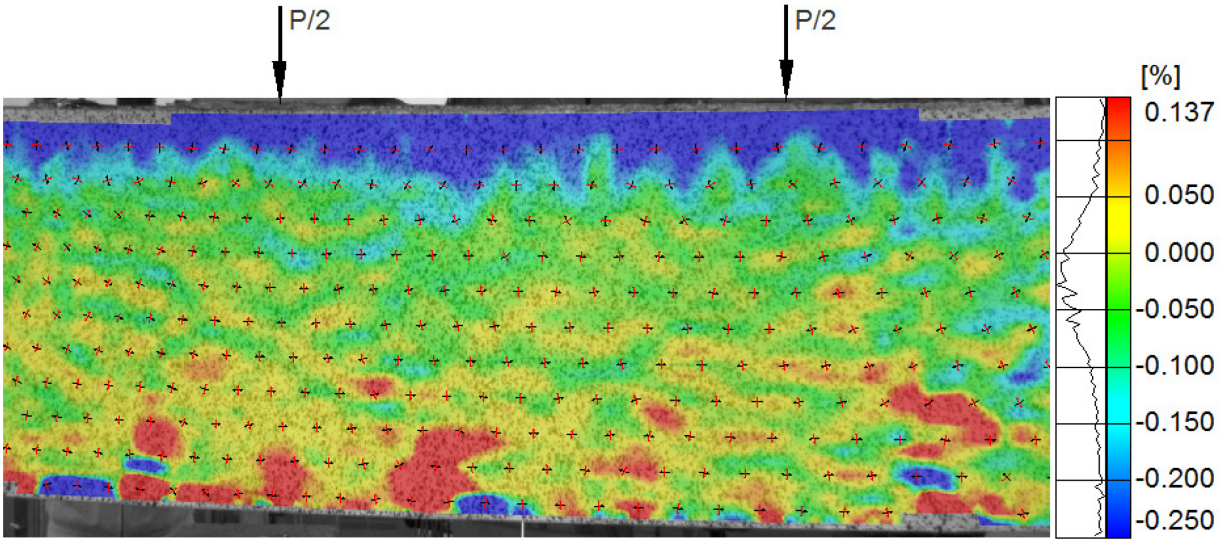

Figure 4-113 Full-field concrete minimum principal strain (σ_2) in moment region for UHP-FRC#4 at an applied load 150 kips

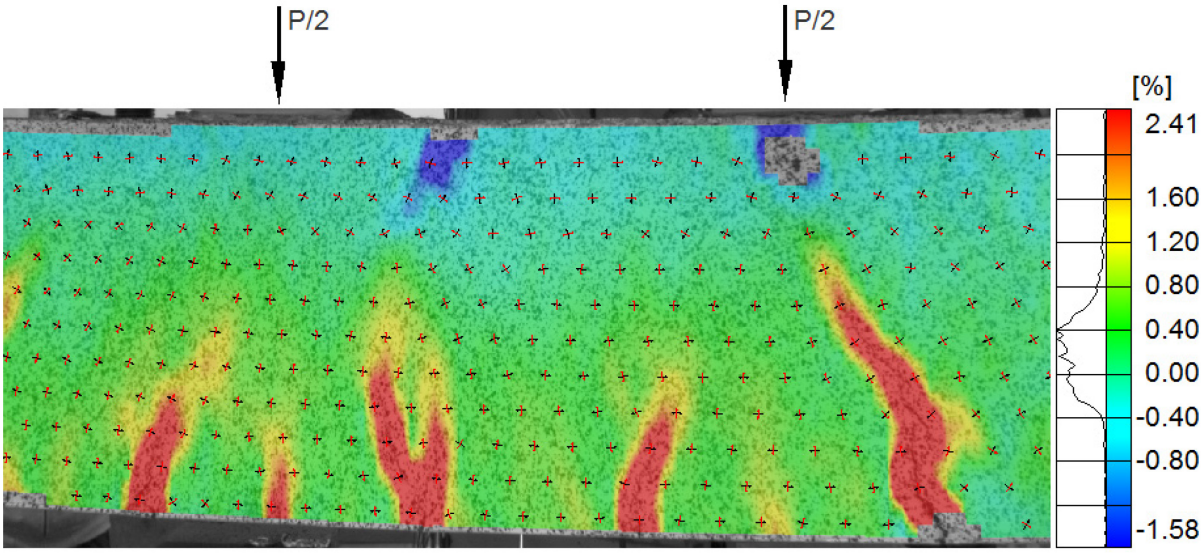

Figure 4-114 Full-field concrete longitudinal strain (ε_x) in moment region for UHP-FRC#4 at an applied load of 163.74 kips (peak load)

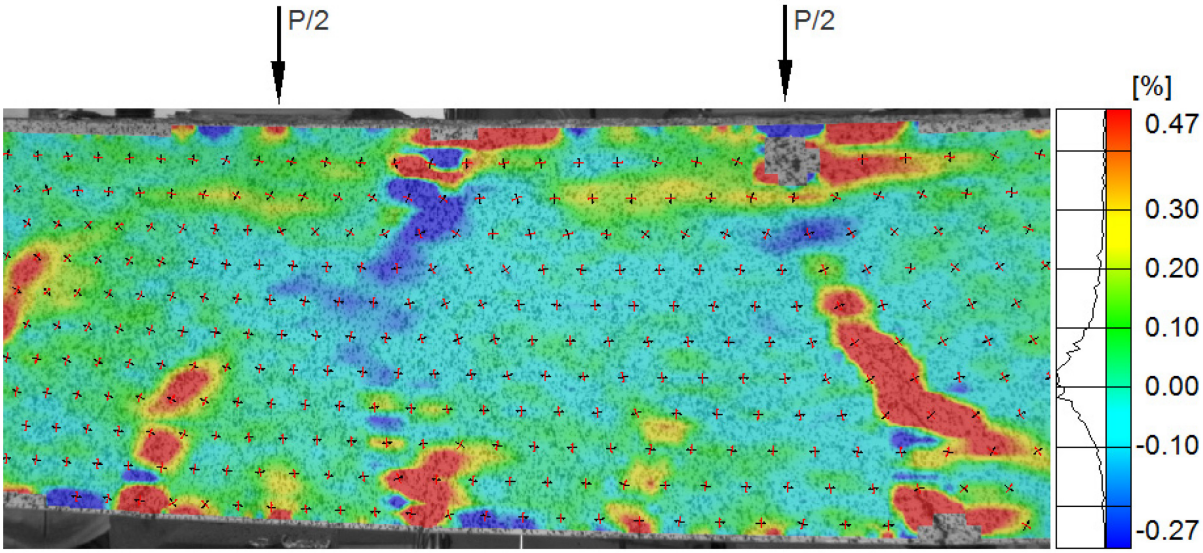

Figure 4-115 Full-field concrete transverse strain (ε_y) in moment region for UHP-FRC#4 at an applied load of 163.74 kips (peak load)

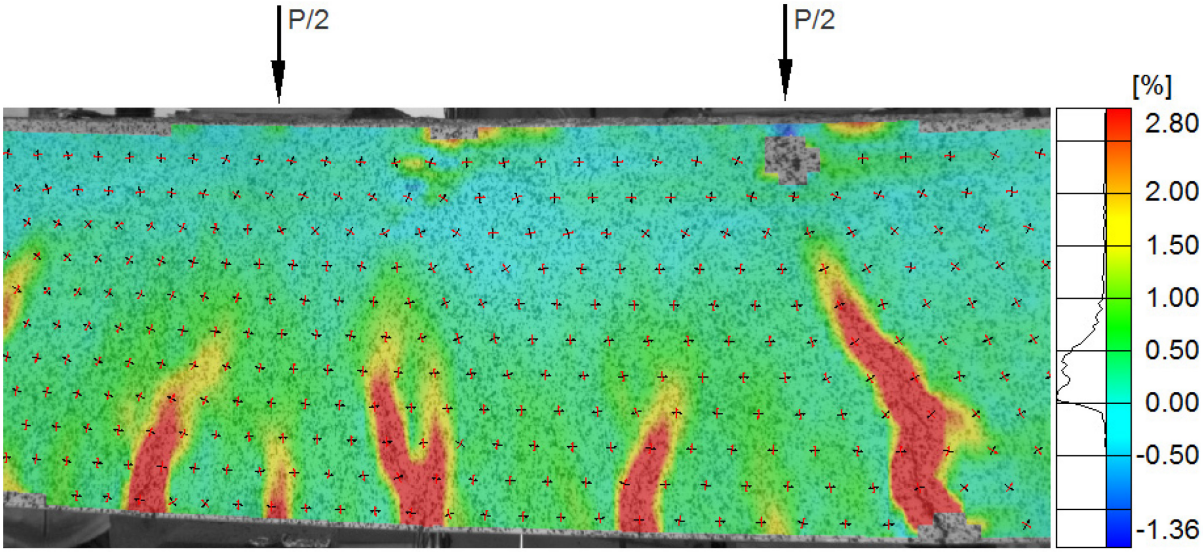

Figure 4-116 Full-field concrete maximum principal strain (σ_1) in moment region for UHP-FRC#4 at an applied load 163.74 kips (peak load)

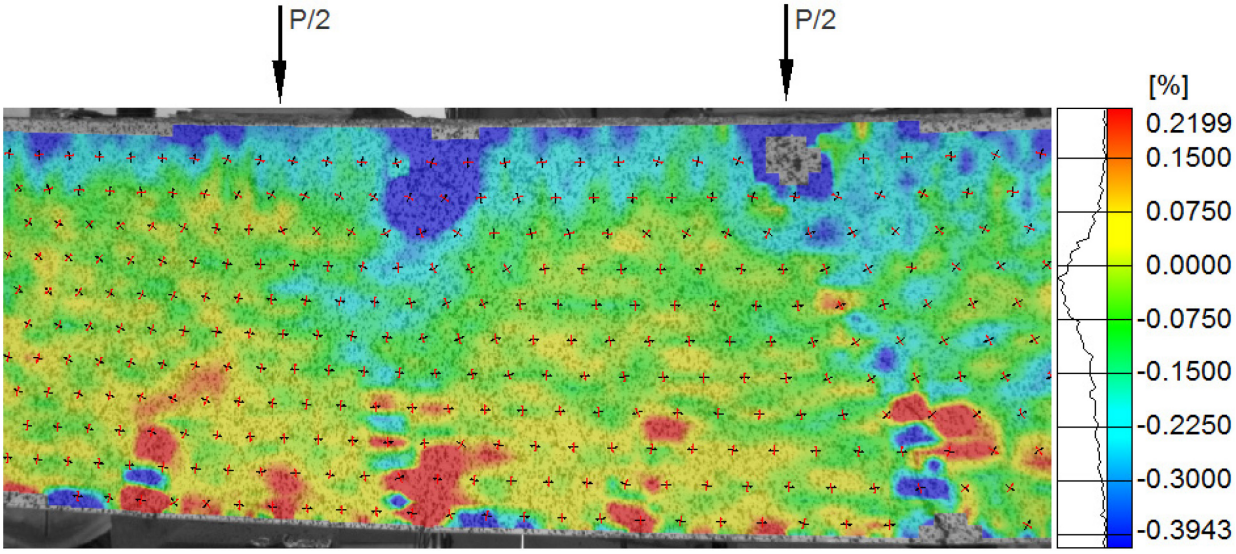

Figure 4-117 Full-field concrete minimum principal strain (σ_2) in moment region for UHP-FRC#4 at an applied load 163.74 kips (peak load)

4.5 Beam UHP-FRC #5:

BFRP Load deflection behavior of UHP-FRC #5 BFRP is shown in figure 4-118. First flexural crack was observed in shear span at a load of 22 kips. Vertical cracks continued to form within the constant moment region and shear spans with additional increase in load. Analogous to UHP-FRC #4 BFRP beam, closely spaced vertical cracks were formed at an applied load of 80 kips that includes several micro cracks. Primary visible shear crack was initiated in the shear span as the flexural crack is inclined in diagonal at 120 kips of external load. After 160 kips of external load, crushing of concrete in compression was observed in the shear span near to loading point, followed by crushing in the constant moment region. Crushing of concrete in the compression zone extended to a greater length of constant moment region. Non-linear behavior before the peak load seen from the load-deflection curve is substantial due to very high ductile response of UHP-FRC in compression. Eventually reached a peak load of 211.33 kips after which load gradual drop in load was seen.

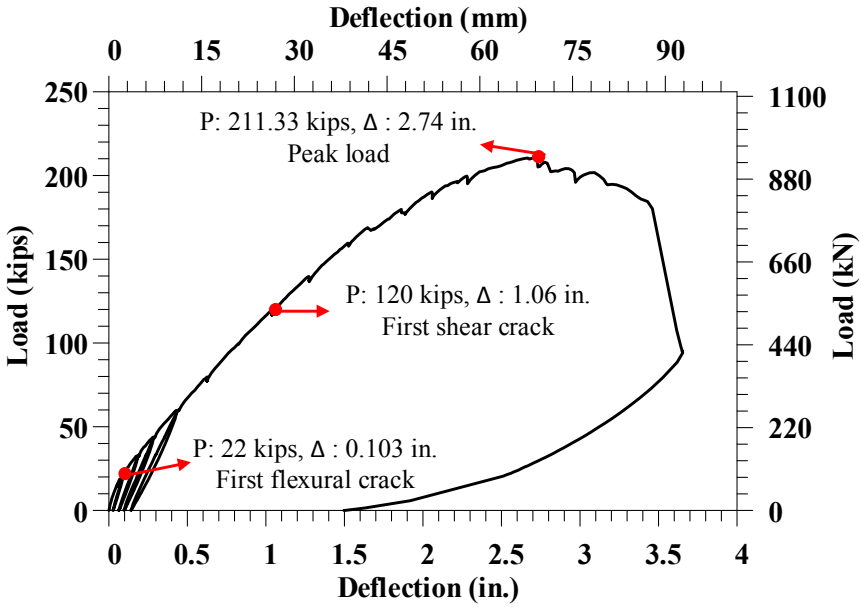

Figure 4-118 Load deflection behavior for beam UHP-FRC #5

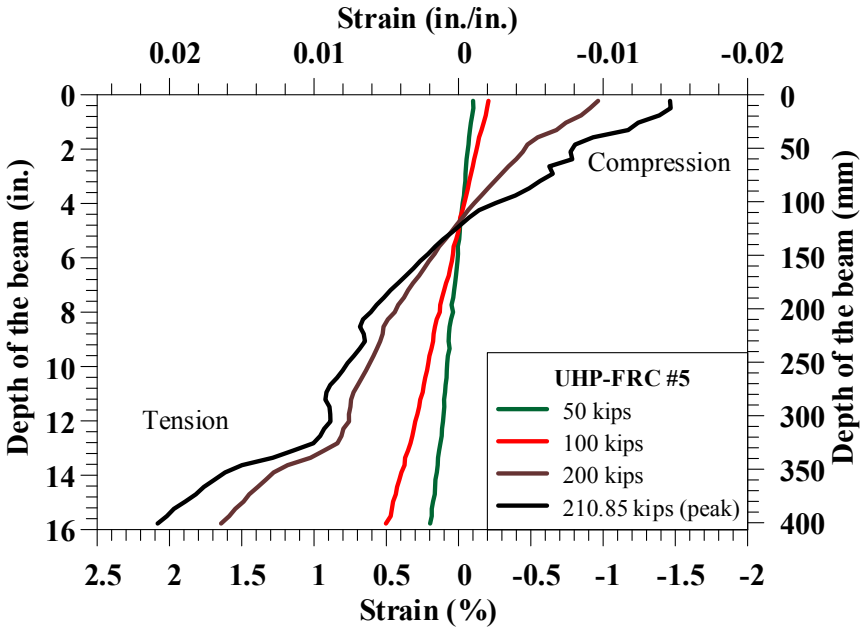

Figure 4-119 Strain variation in beam UHP-FRC #5

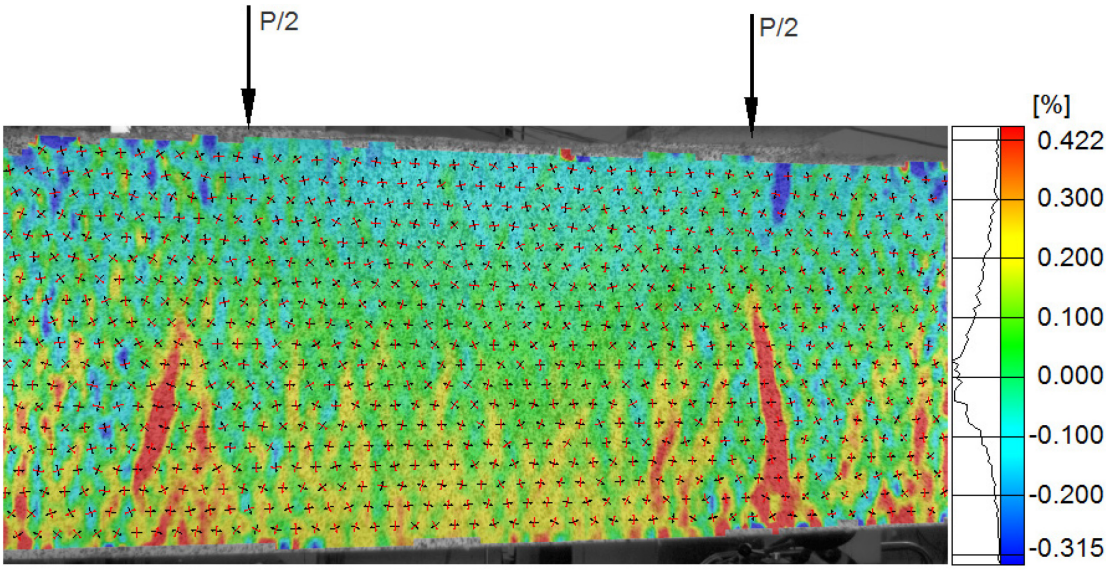

Figure 4-120 Full-field concrete longitudinal strain (ε_x) in moment region for UHP-FRC#5 at an applied load of 50 kips

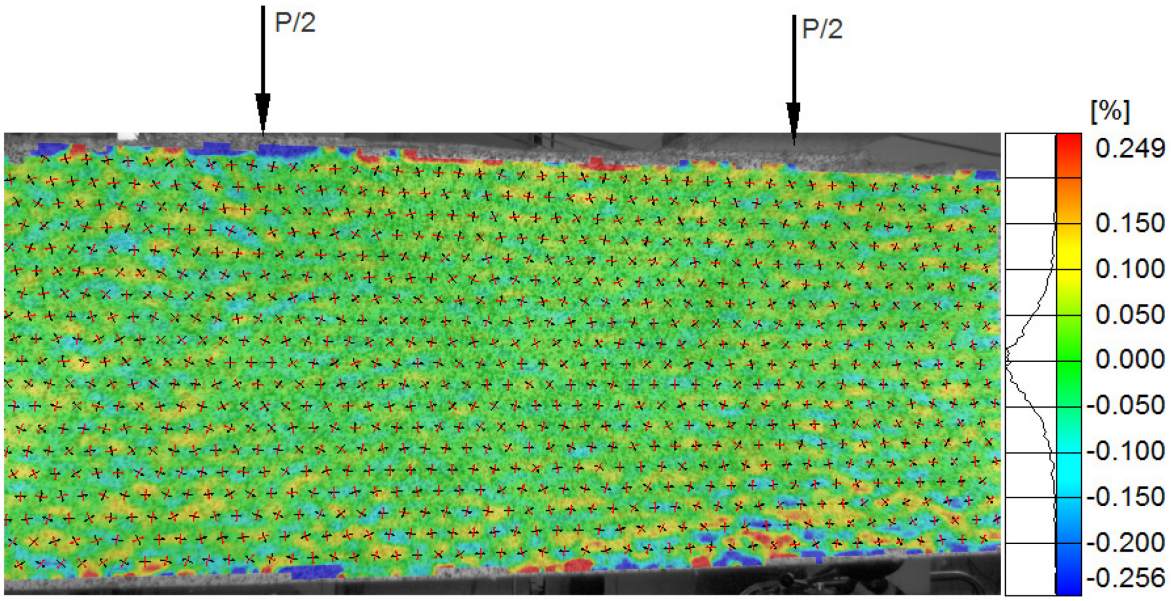

Figure 4-121 Full-field concrete transverse strain (ε_y) in moment region for UHP-FRC#5 at an applied load of 50 kips

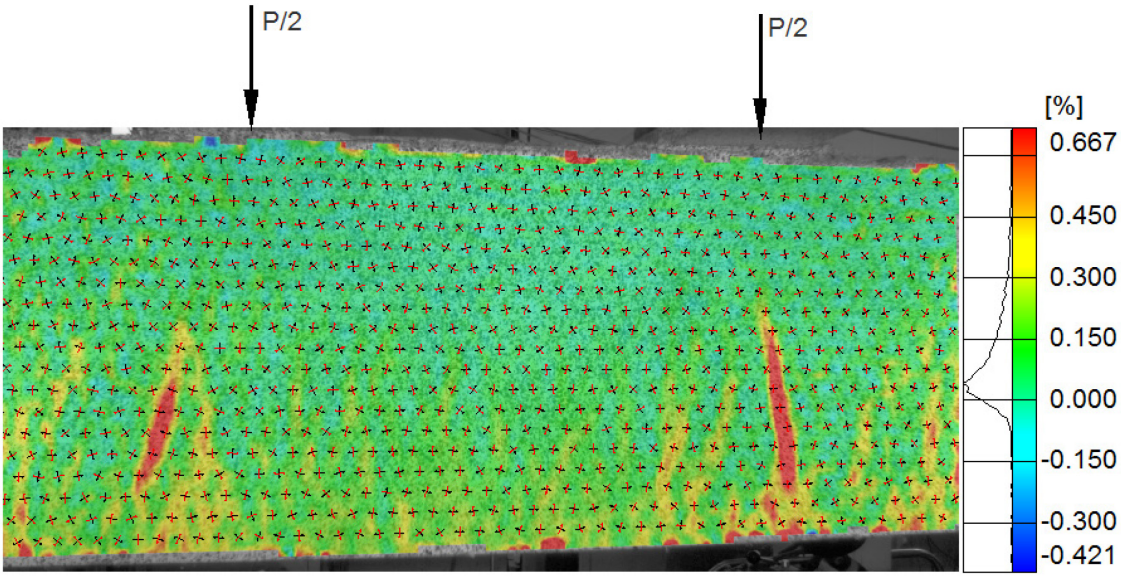

Figure 4-122 Full-field concrete maximum principal strain (σ_1) in moment region for UHP-FRC#5 at an applied load 50 kips

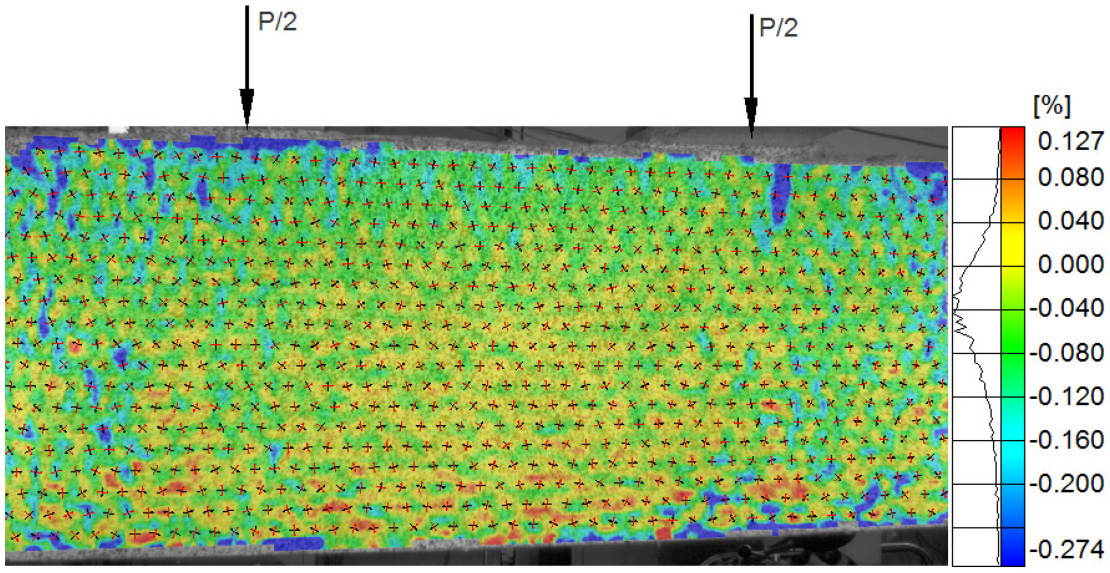

Figure 4-123 Full-field concrete minimum principal strain (σ_2) in moment region for UHP-FRC#5 at an applied load 50 kips

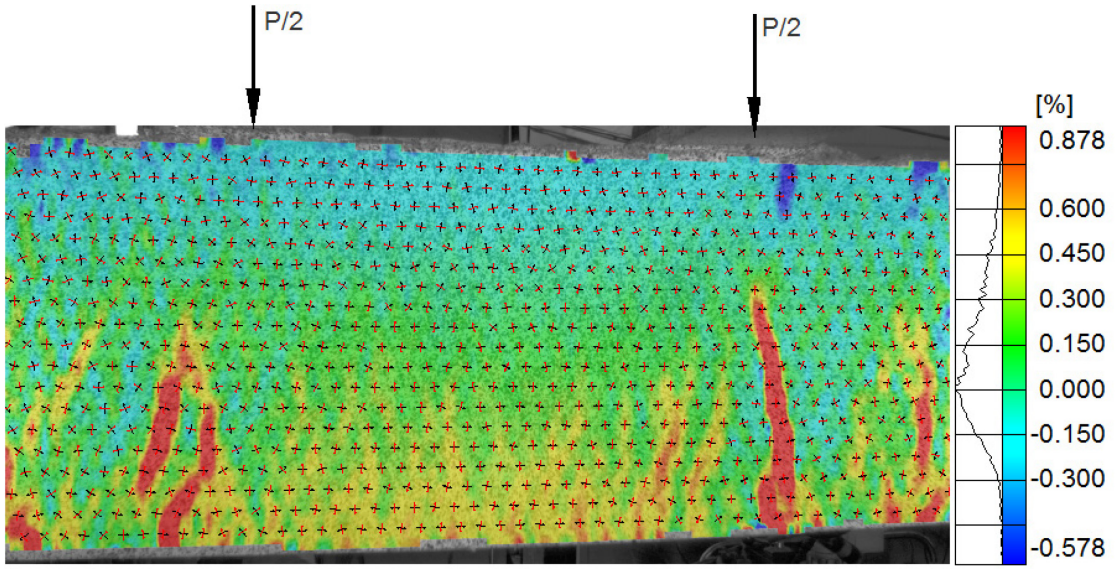

Figure 4-124 Full-field concrete longitudinal strain (ε_x) in moment region for UHP-FRC#5 at an applied load of 100 kips

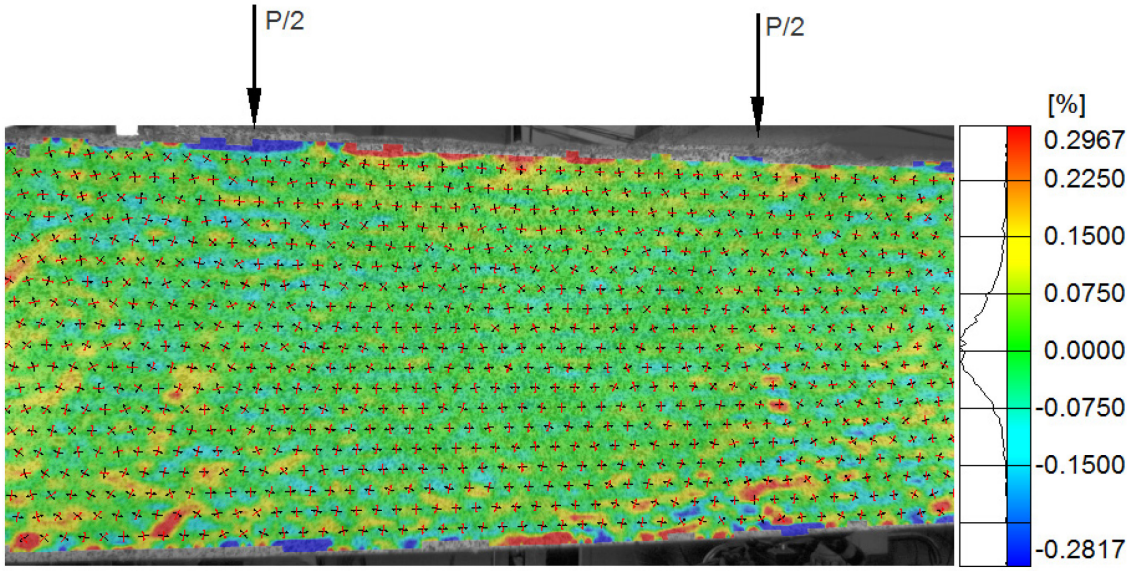

Figure 4-125 Full-field concrete transverse strain (ε_y) in moment region for UHP-FRC#5 at an applied load of 100 kips

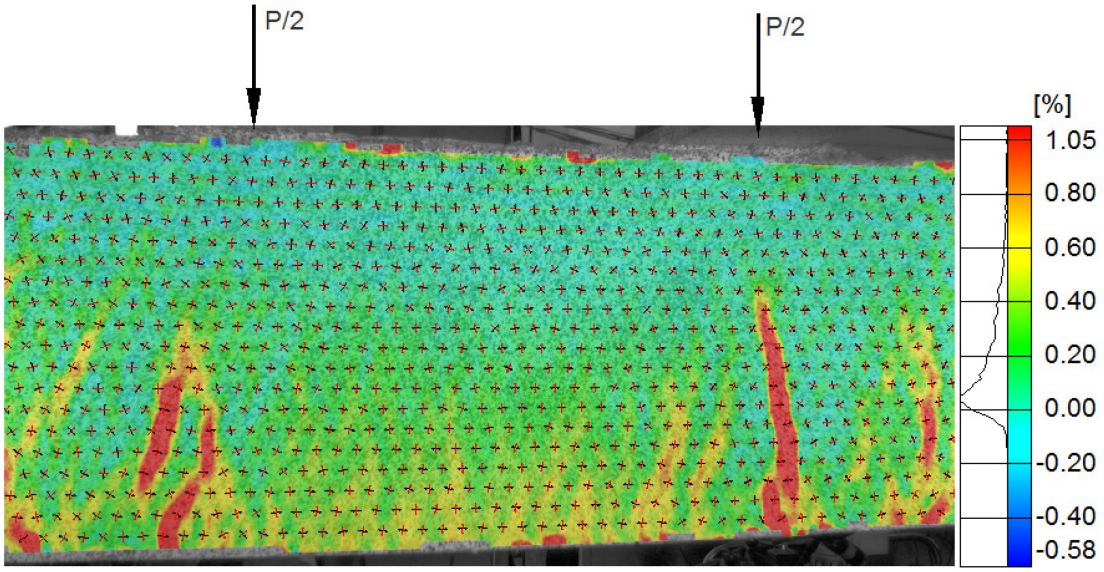

Figure 4-126 Full-field concrete maximum principal strain (σ_1) in moment region for UHP-FRC#5 at an applied load 100 kips

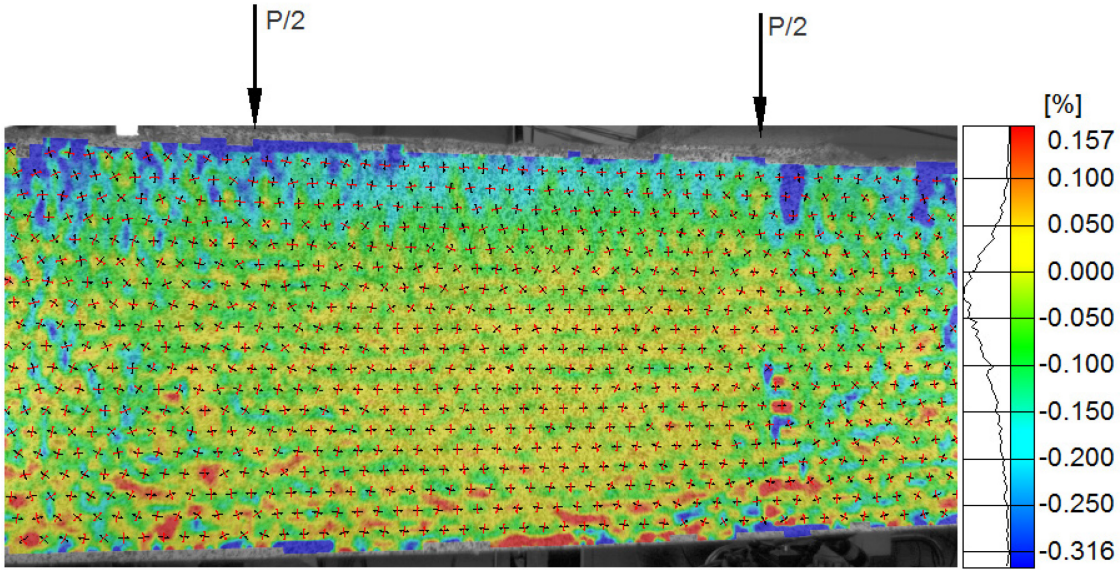

Figure 4-127 Full-field concrete minimum principal strain (σ_2) in moment region for UHP-FRC#5 at an applied load 100 kips

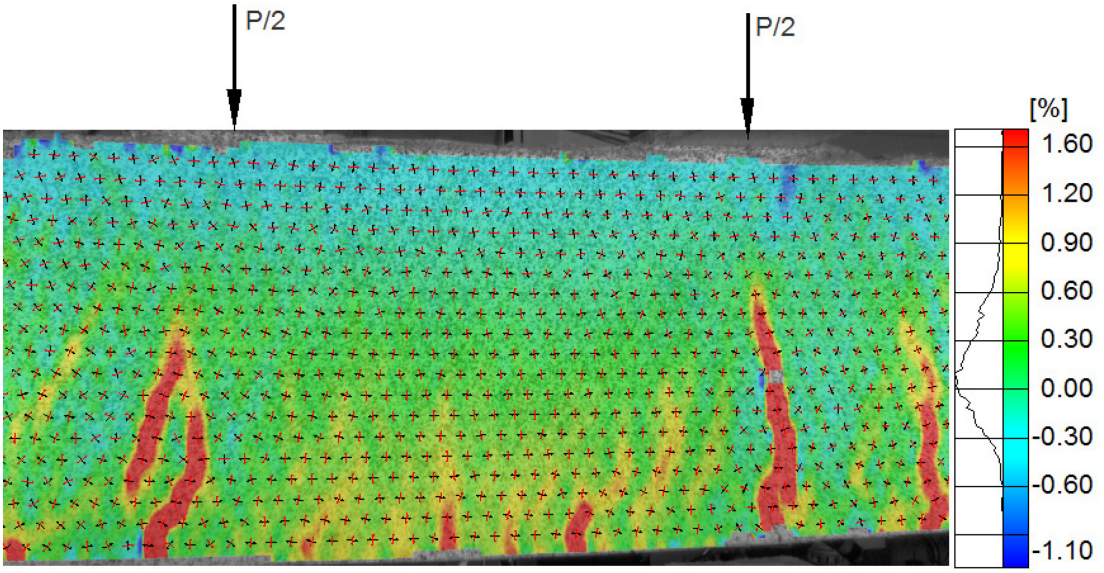

Figure 4-128 Full-field concrete longitudinal strain (ε_x) in moment region for UHP-FRC#5 at an applied load of 150 kips

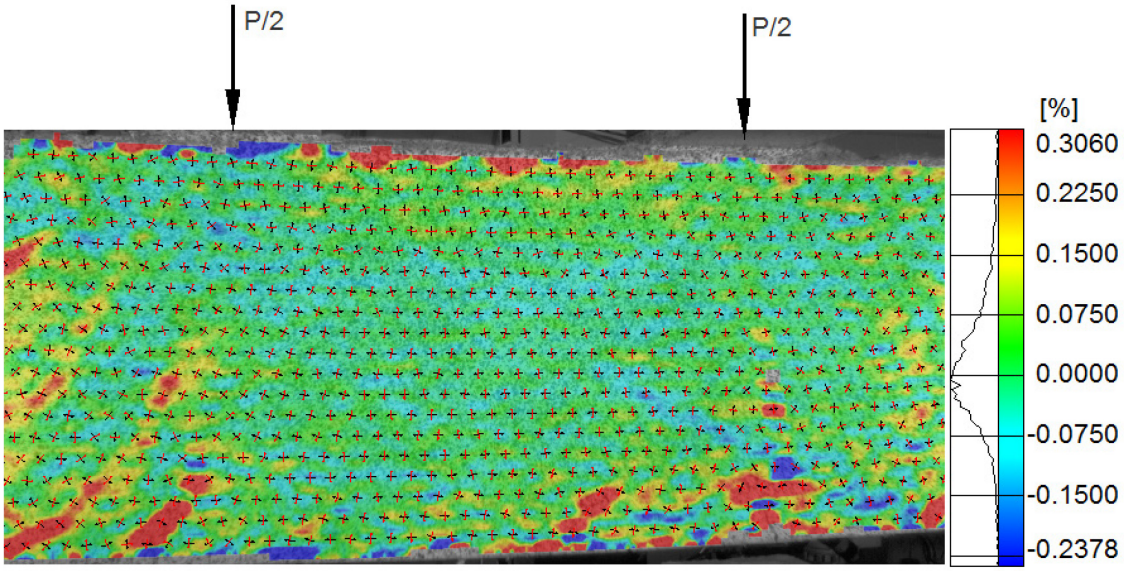

Figure 4-129 Full-field concrete transverse strain (ε_y) in moment region for UHP-FRC#5 at an applied load of 150 kips

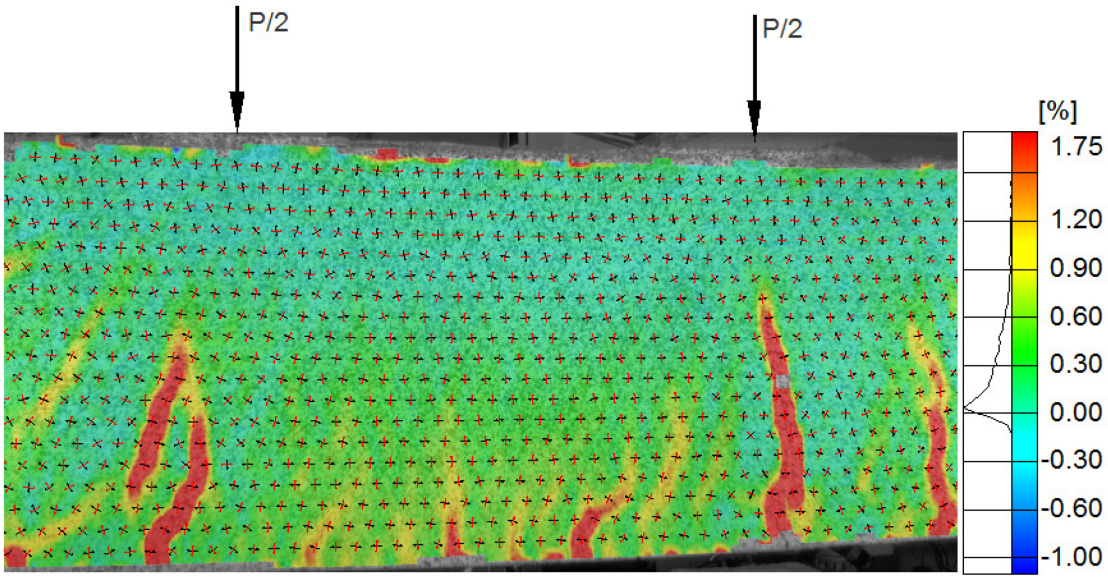

Figure 4-130 Full-field concrete maximum principal strain (σ_1) in moment region for UHP-FRC#5 at an applied load 150 kips

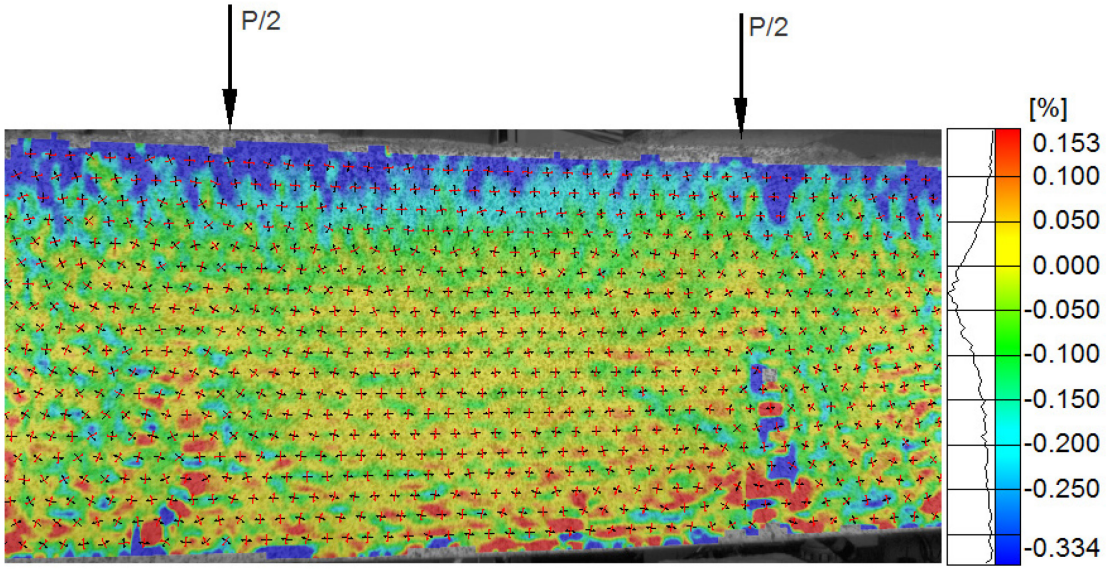

Figure 4-131 Full-field concrete minimum principal strain (σ_2) in moment region for UHP-FRC#5 at an applied load 150 kips

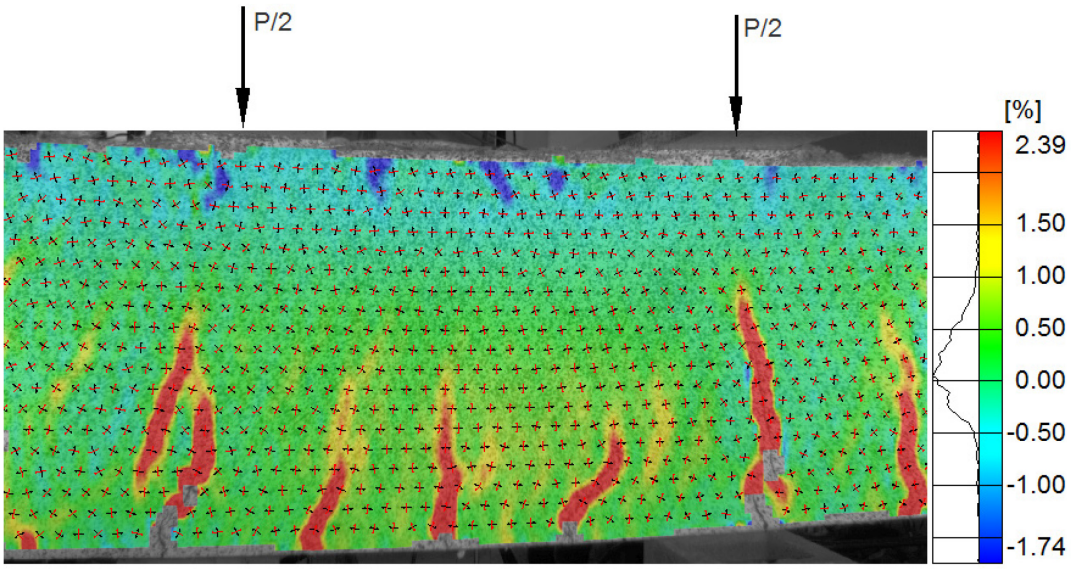

Figure 4-132 Full-field concrete longitudinal strain (ε_x) in moment region for UHP-FRC#5 at an applied load of 200 kips

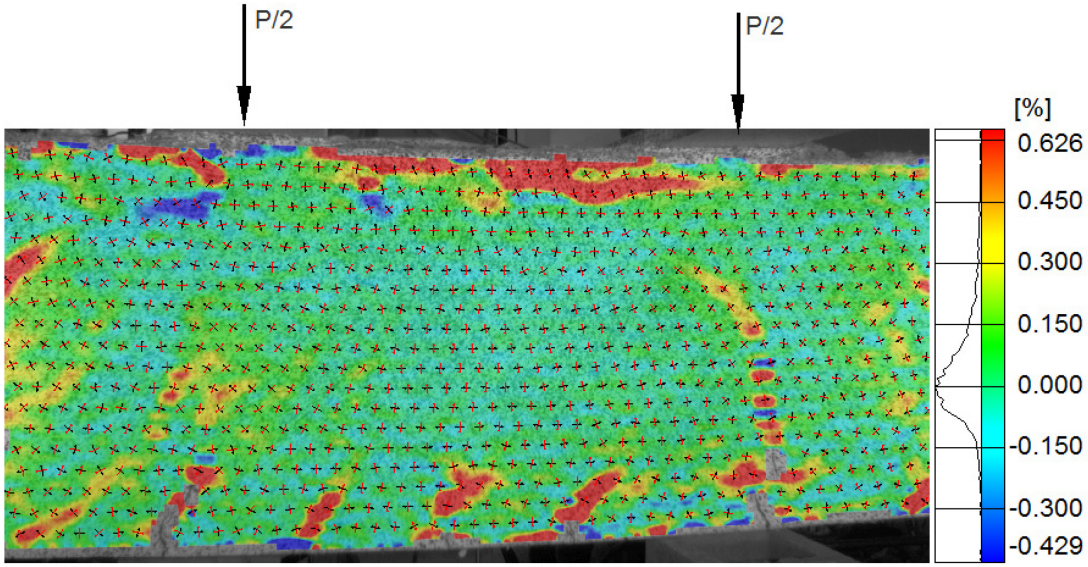

Figure 4-133 Full-field concrete transverse strain (ε_y) in moment region for UHP-FRC#5 at an applied load of 200 kips

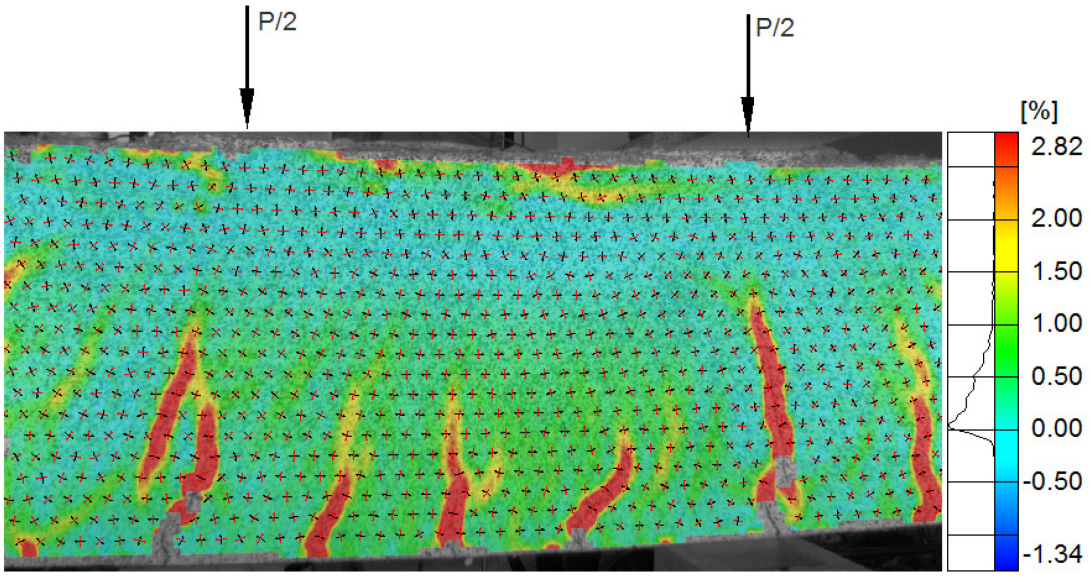

Figure 4-134 Full-field concrete maximum principal strain (σ_1) in moment region for UHP-FRC#5 at an applied load 200 kips

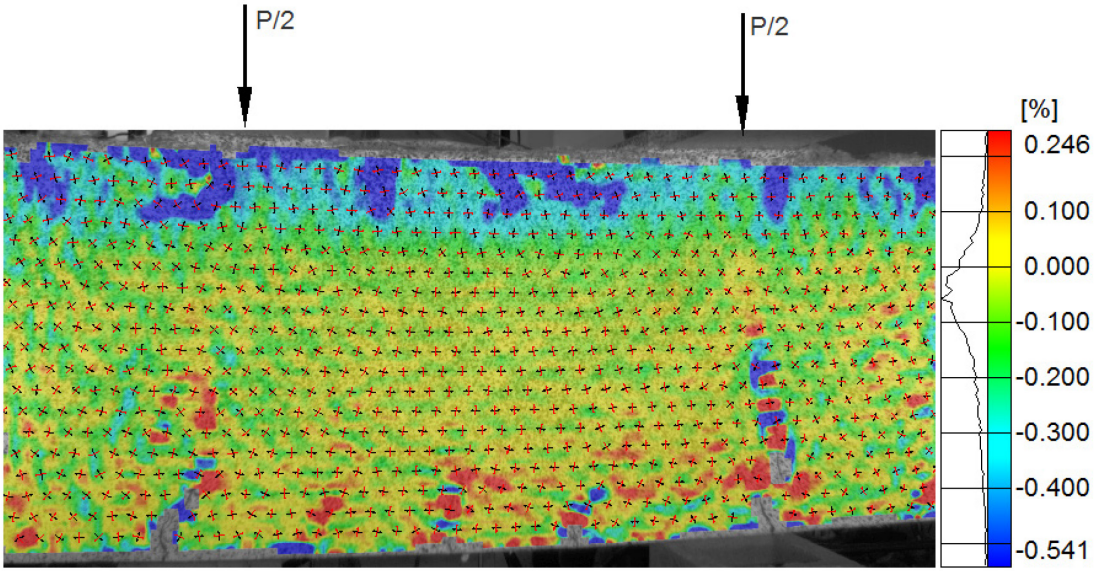

Figure 4-135 Full-field concrete minimum principal strain (σ_2) in moment region for UHP-FRC#5 at an applied load 200 kips

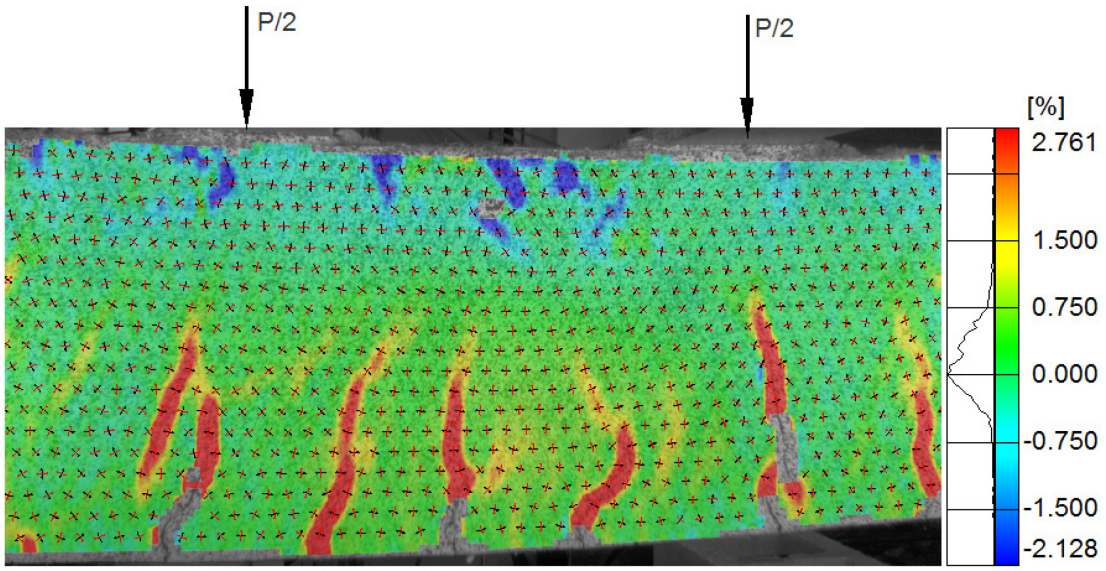

Figure 4-136 Full-field concrete longitudinal strain (ε_x) in moment region for UHP-FRC#5 at an applied load of 210.8 kips (peak load)

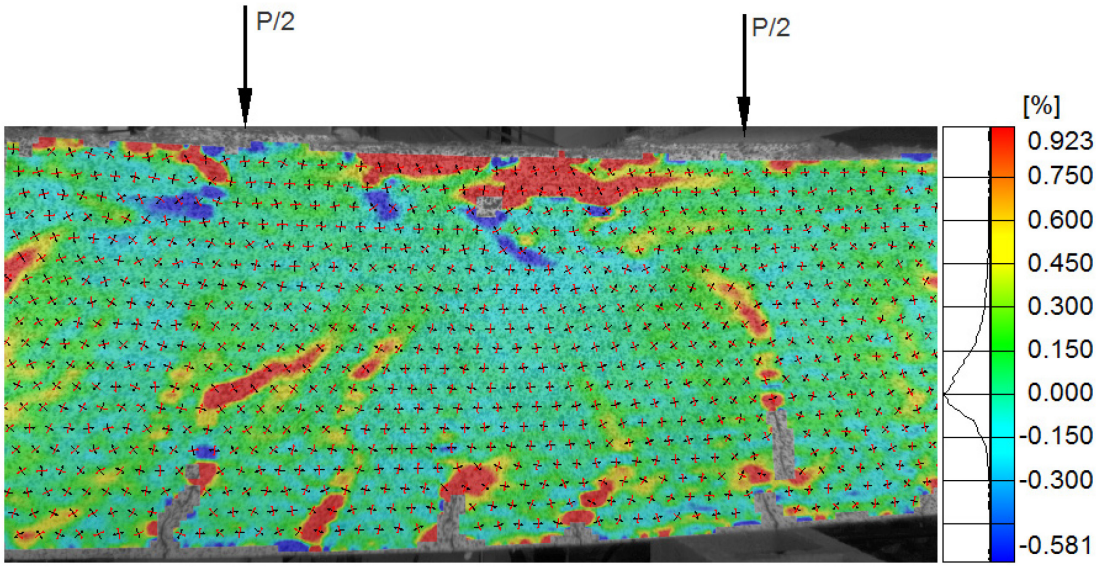

Figure 4-137 Full-field concrete transverse strain (ε_y) in moment region for UHP-FRC#5 at an applied load of 210.8 kips (peak load)

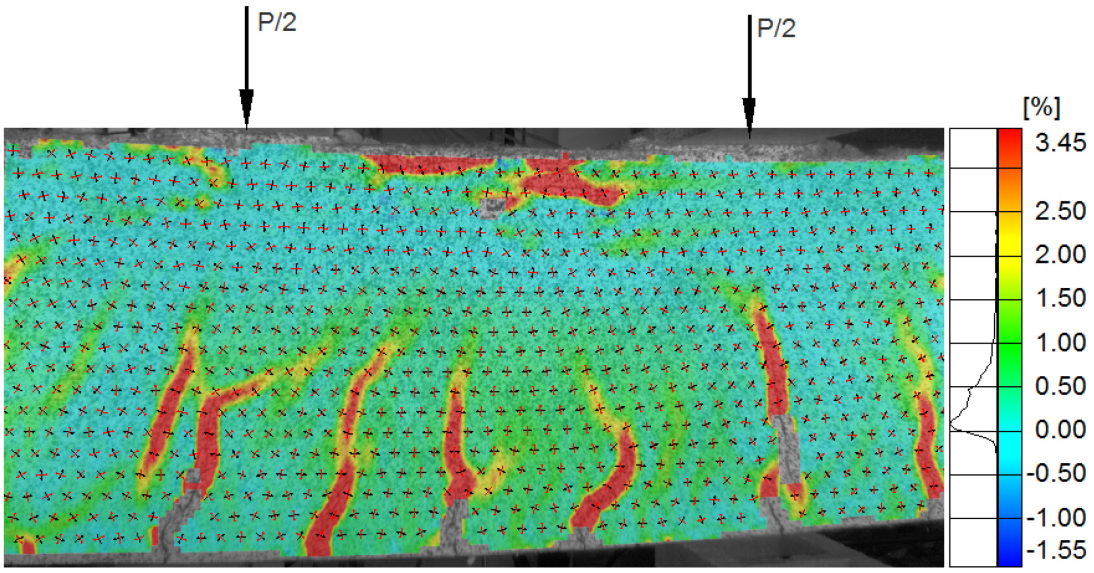

Figure 4-138 Full-field concrete maximum principal strain (σ_1) in moment region for UHP-FRC#5 at an applied load 210.8 kips (peak load)

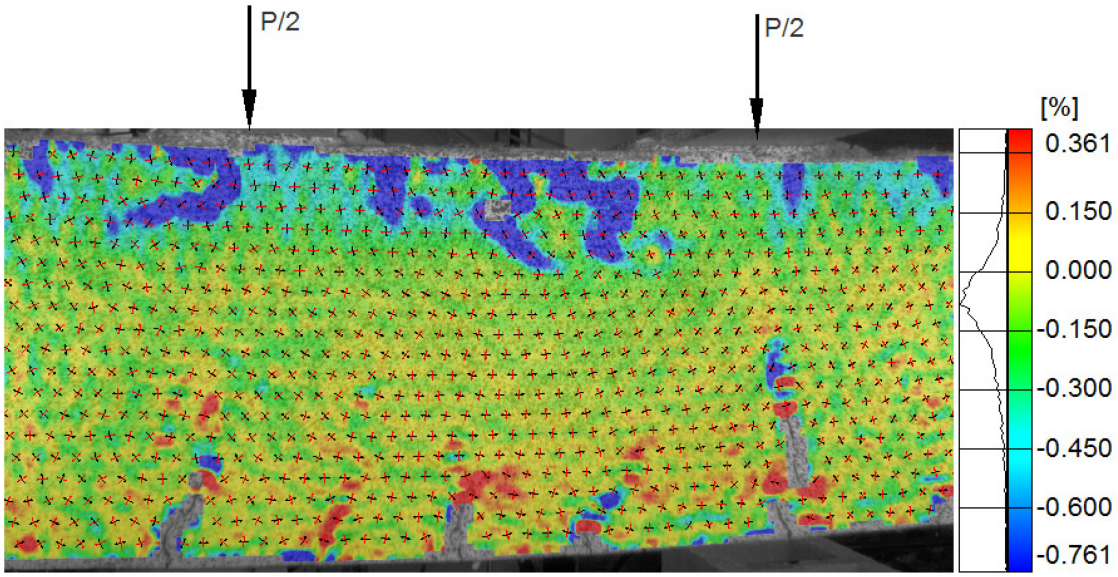

Figure 4-139 Full-field concrete minimum principal strain (σ_2) in moment region for UHP-FRC#5 at an applied load 210.8 kips (peak load)

4.6 Beam RC #1 60S:

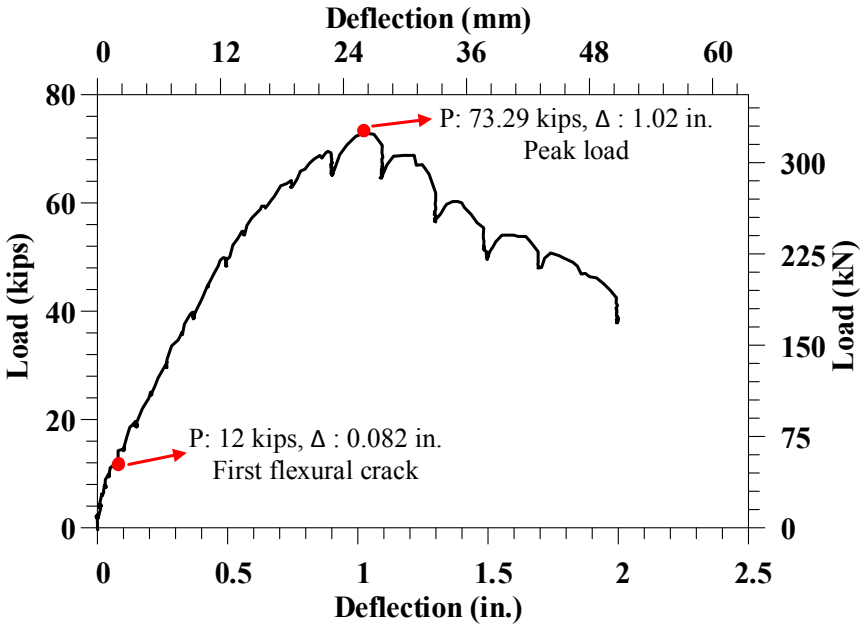

Figure 4-140 Load deflection behavior in RC #1

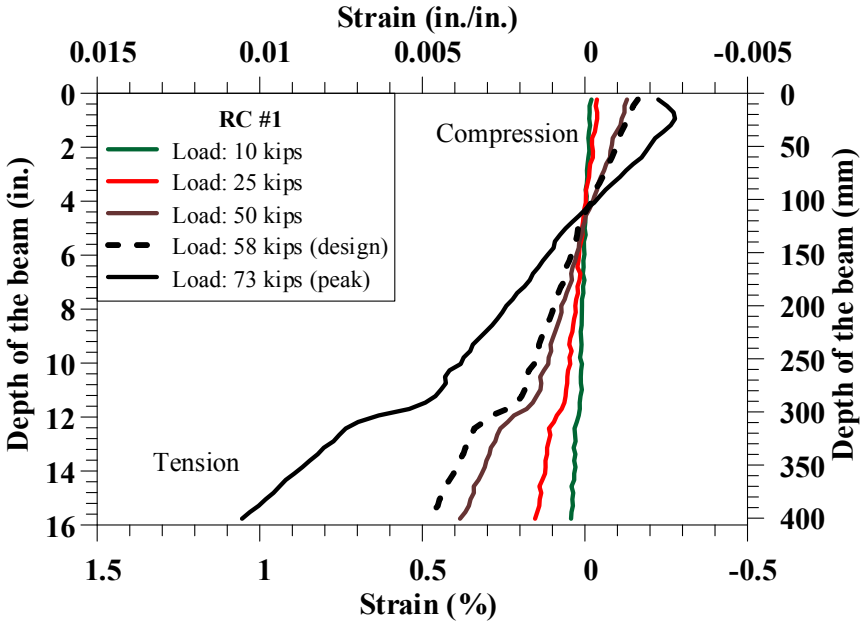

Figure 4-141 Strain variation in beam RC #1

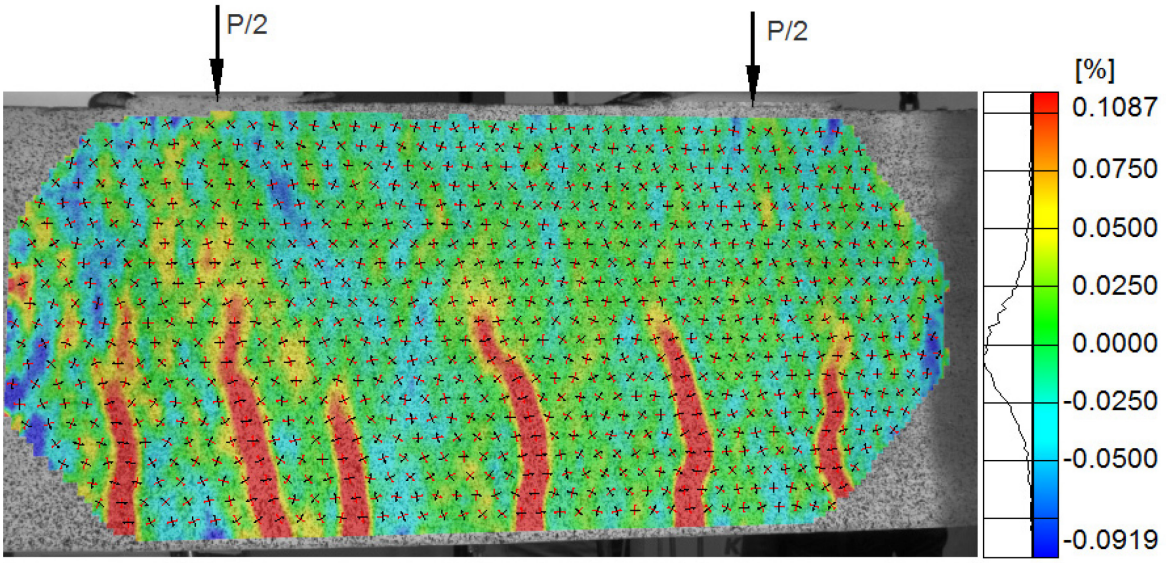

Figure 4-142 Full-field concrete longitudinal strain (ε_x) along moment region for RC#1 at an applied load of 10 kips

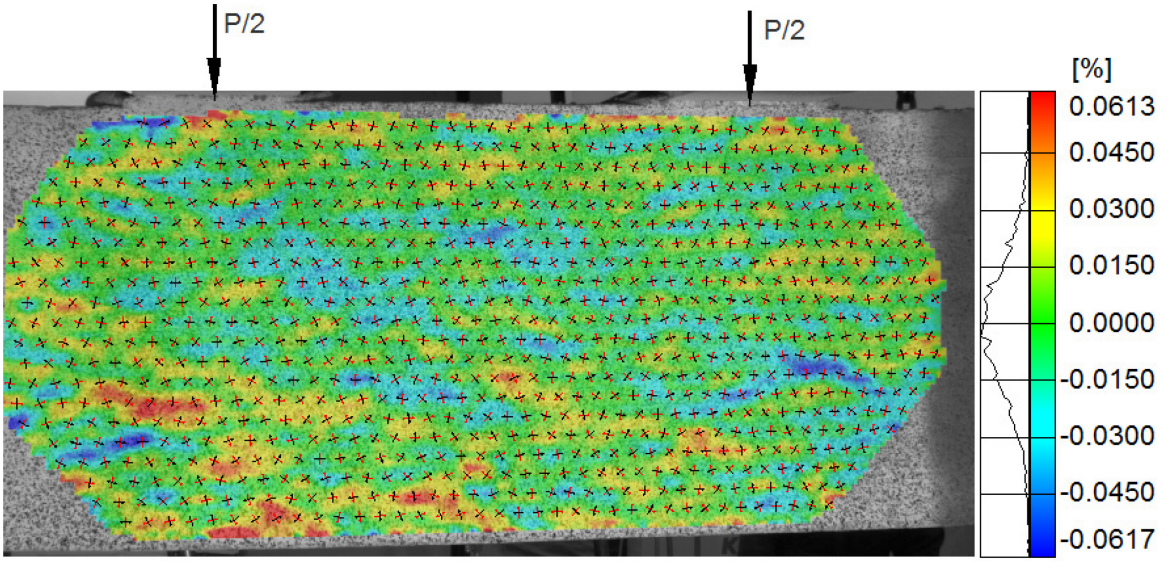

Figure 4-143 Full-field concrete transverse strain (ε_y) along moment region for RC#1 at an applied load of 10 kips

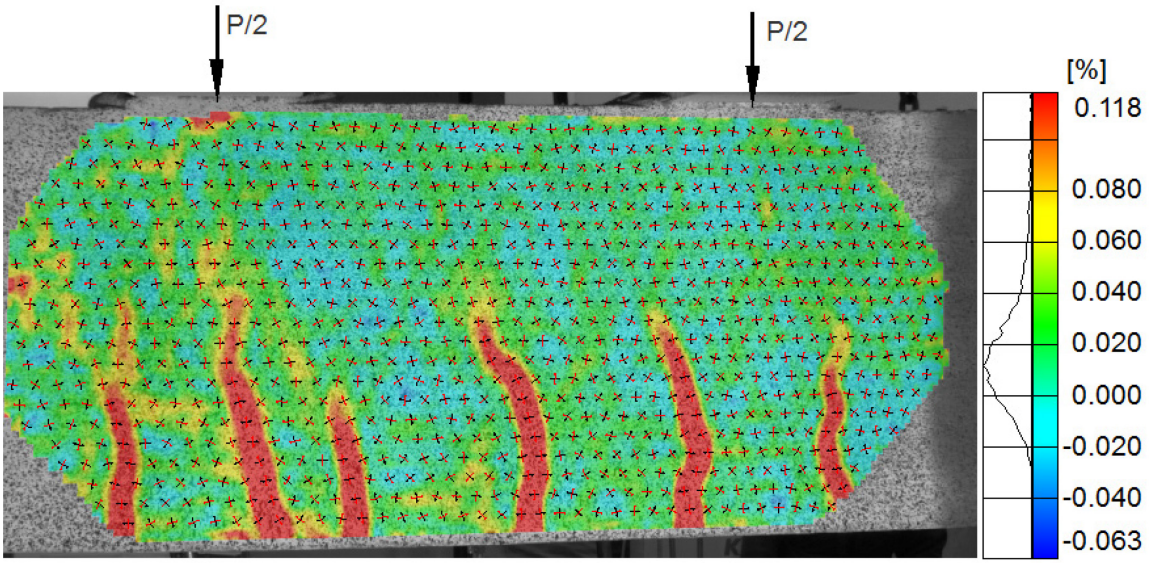

Figure 4-144 Full-field concrete maximum principal strain (σ_1) along moment region for RC#1 at an applied load 10 kips

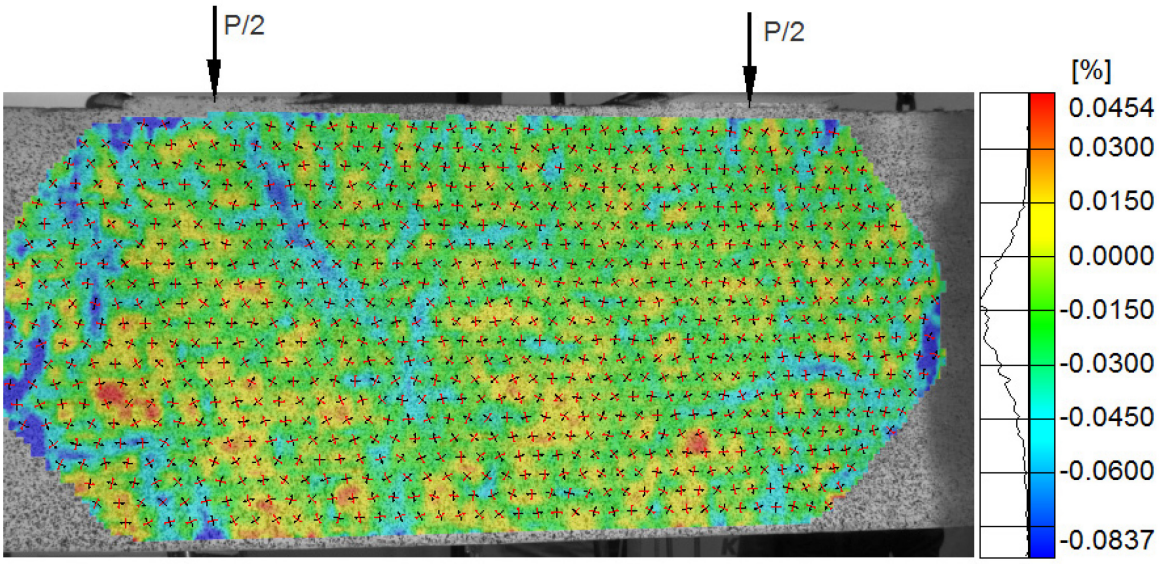

Figure 4-145 Full-field concrete minimum principal strain (σ_2) along moment region for RC#1 at an applied load 10 kips

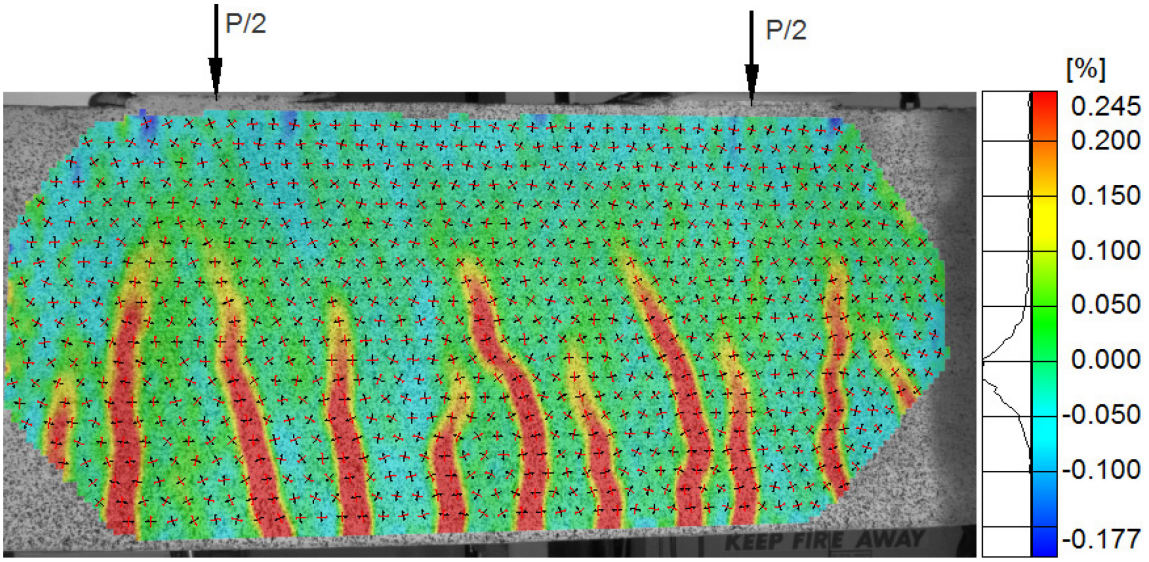

Figure 4-146 Full-field concrete longitudinal strain (ε_x) along moment region for RC#1 at an applied load of 25 kips

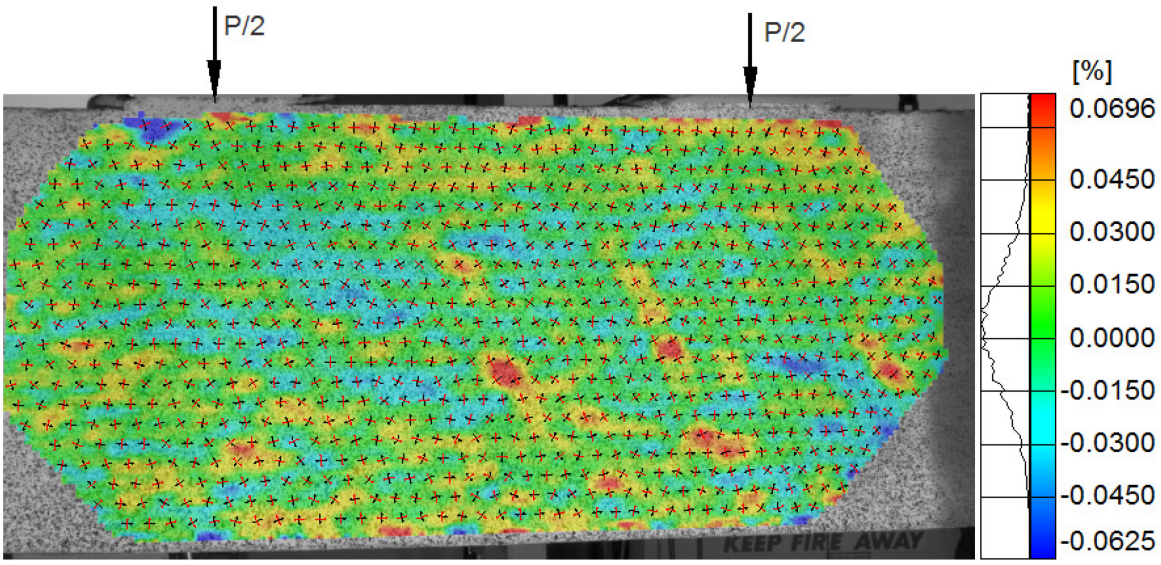

Figure 4-147 Full-field concrete transverse strain (ε_y) along moment region for RC#1 at an applied load of 25 kips

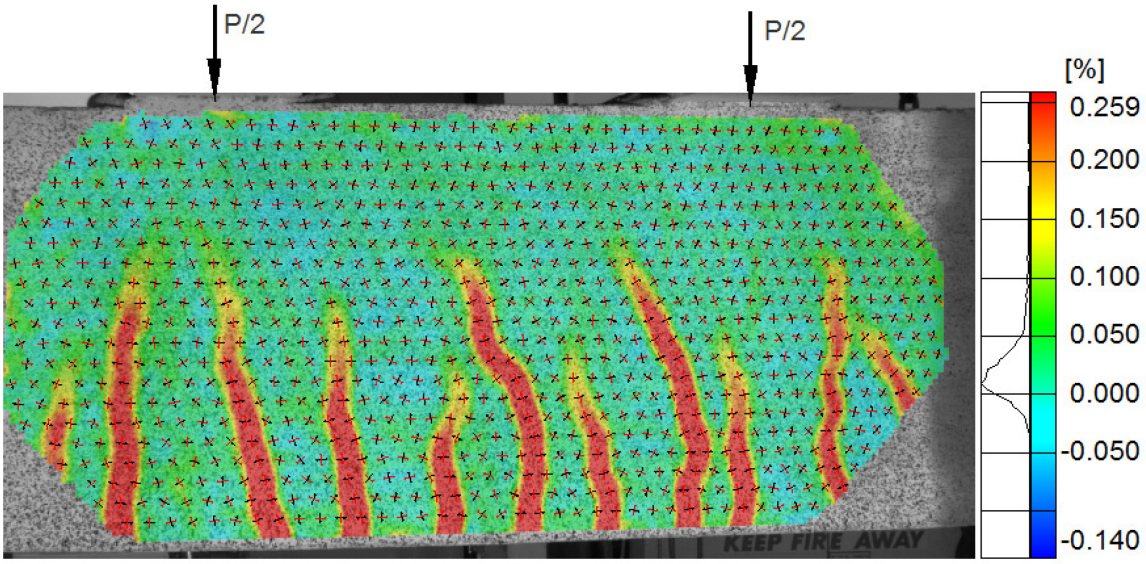

Figure 4-148 Full-field concrete maximum principal strain (σ_1) along moment region for RC#1 at an applied load 25 kips

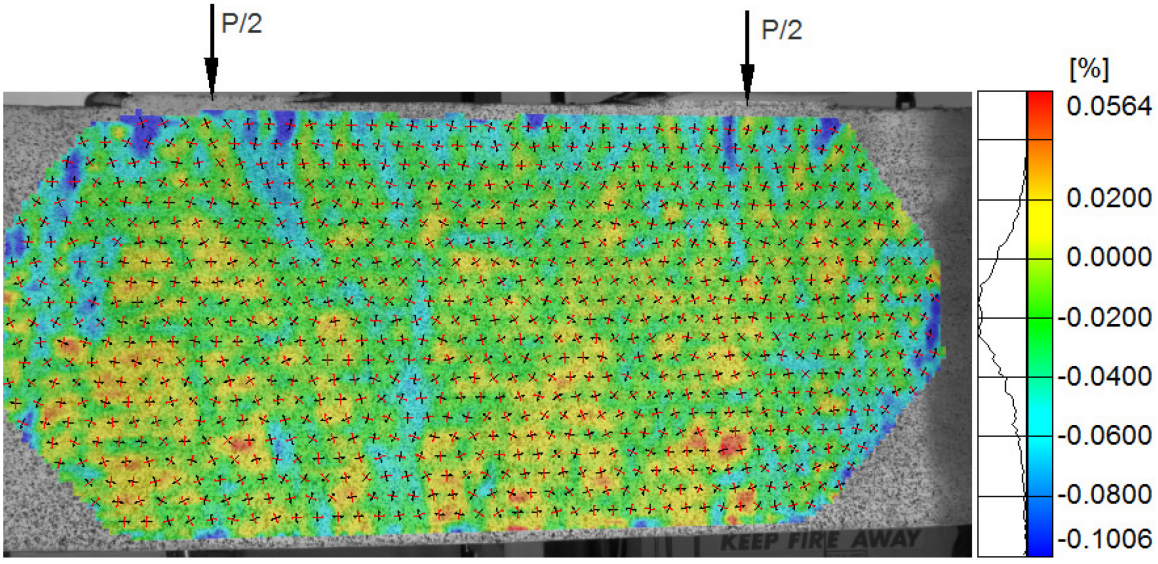

Figure 4-149 Full-field concrete minimum principal strain (σ_2) along moment region for RC#1 at an applied load 25 kips

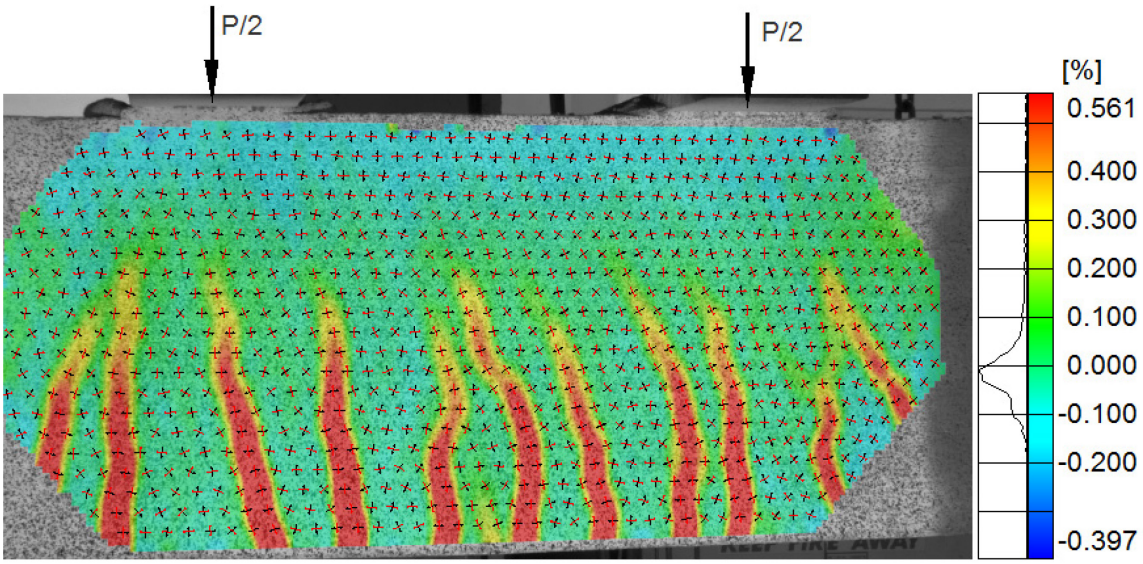

Figure 4-150 Full-field concrete longitudinal strain (ε_x) along moment region for RC#1 at an applied load of 50 kips

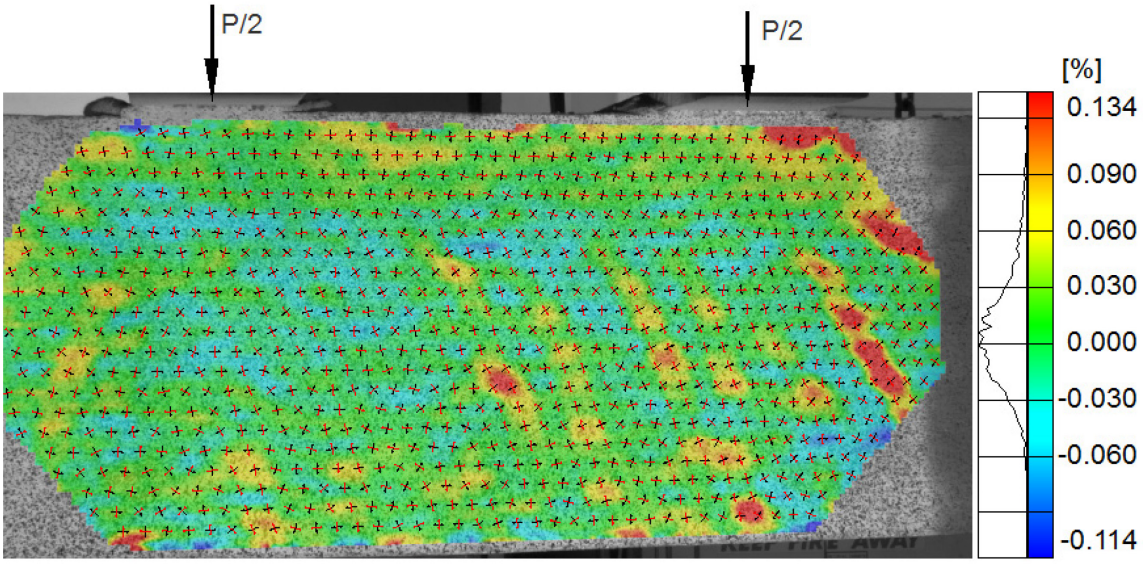

Figure 4-151 Full-field concrete transverse strain (ε_y) along moment region for RC#1 at an applied load of 50 kips

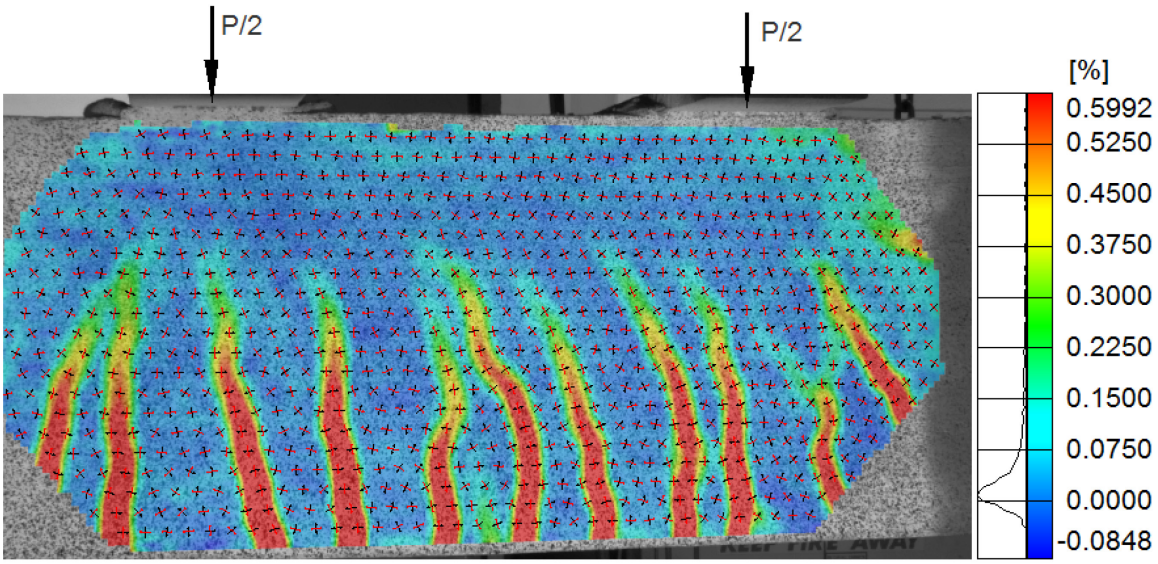

Figure 4-152 Full-field concrete maximum principal strain (σ_1) along moment region for RC#1 at an applied load 50 kips

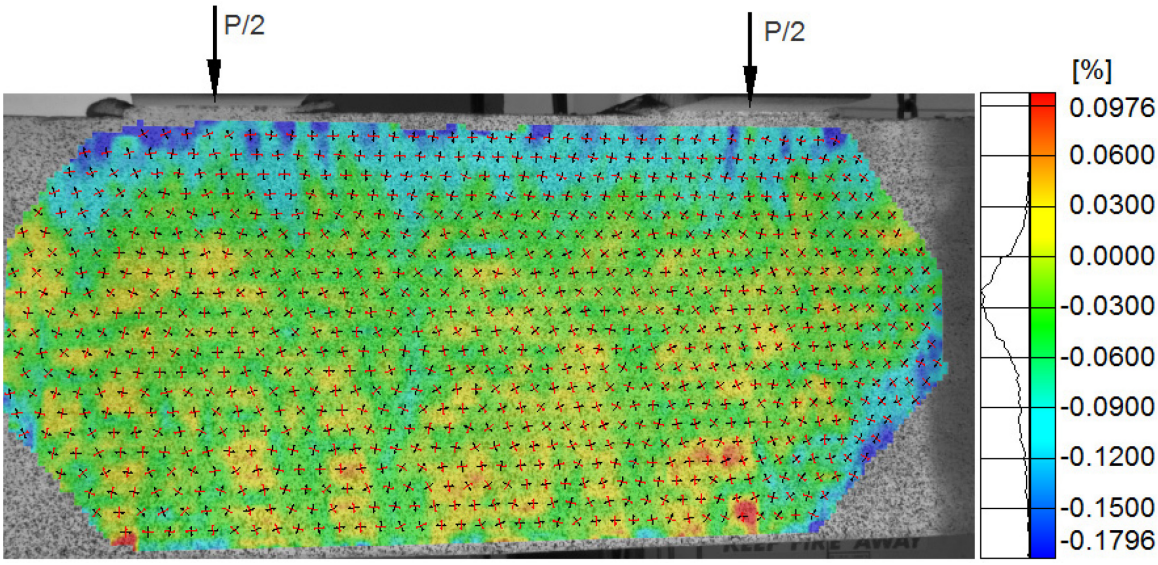

Figure 4-153 Full-field concrete minimum principal strain (σ_2) along moment region for RC#1 at an applied load 50 kips

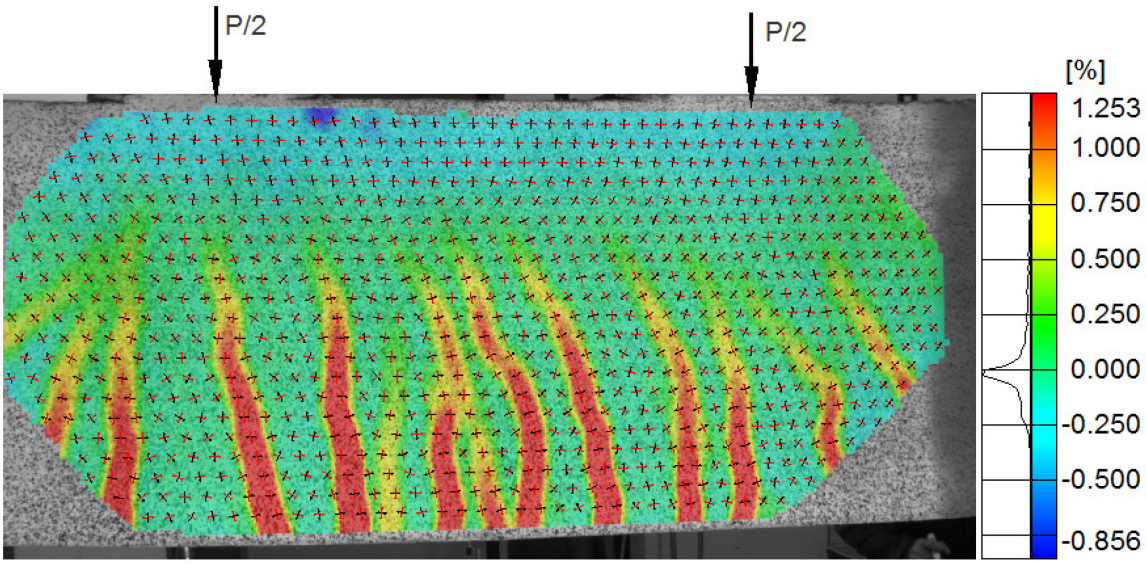

Figure 4-154 Full-field concrete longitudinal strain (ε_x) along moment region for RC#1 at an applied load of 72 kips (peak load)

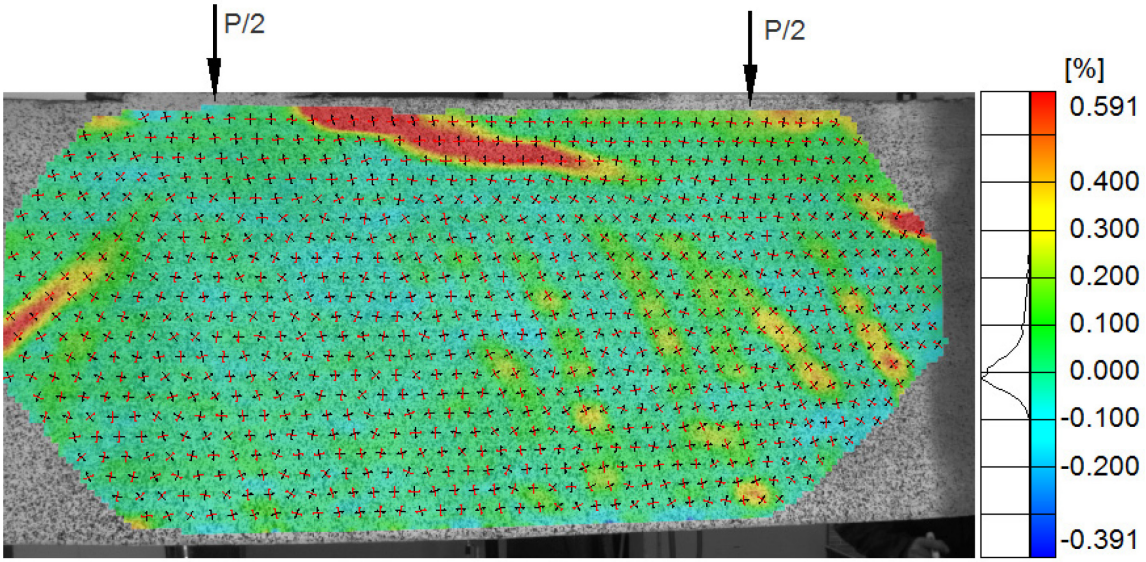

Figure 4-155 Full-field concrete transverse strain (ε_y) along moment region for RC#1 at an applied load of 72 kips (peak load)

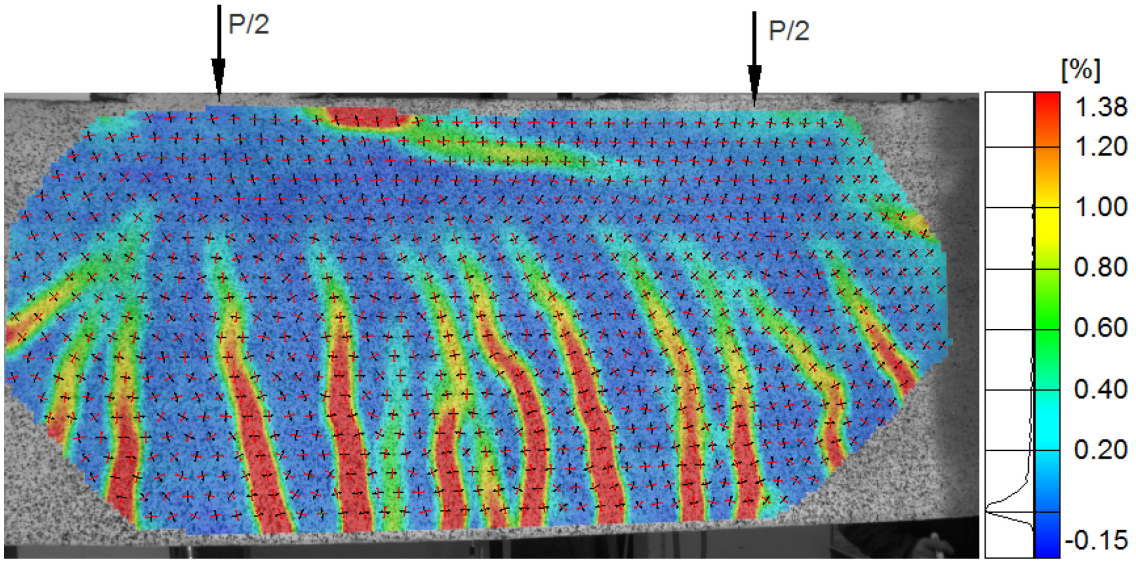

Figure 4-156 Full-field concrete maximum principal strain (σ_1) along moment region for RC#1 at an applied load 72 kips (peak load)

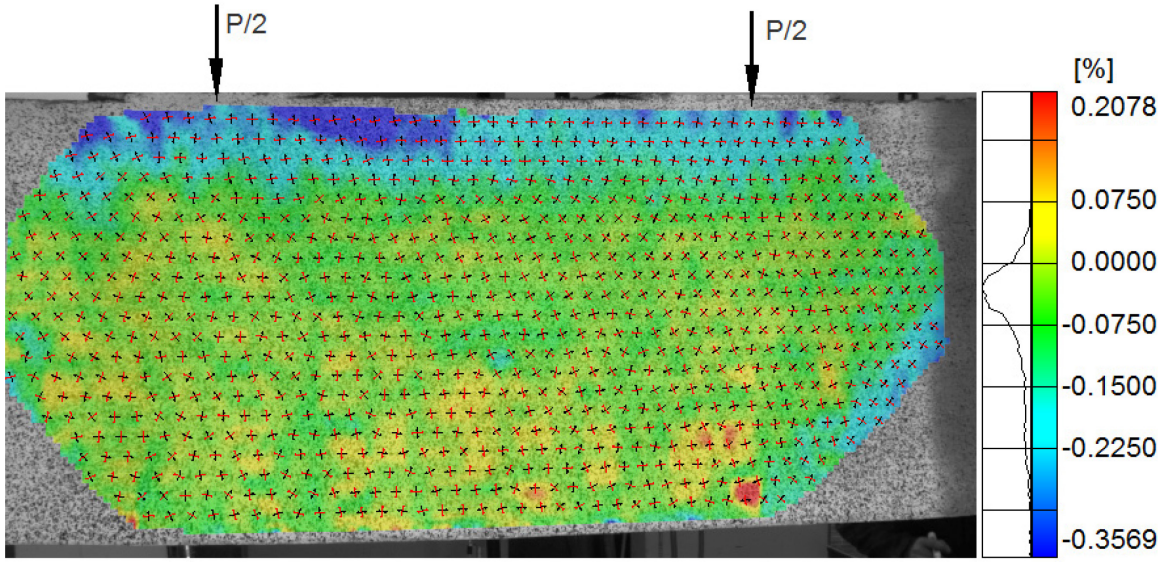

Figure 4-157 Full-field concrete minimum principal strain (σ_2) along moment region for RC#1 at an applied load 72 kips (peak load)

4.7 Beam RC #2 BFRP:

Figure 4-158 shows load deflection behavior of the beam RC #2 BFRP. Load deflection curve of RC #2 BFRP showed nearly bilinear behavior up to peak. First linear segment corresponding to un-cracked response of the beam and the latter segment with a reduced stiffness corresponds to cracked response of the beam. Initial flexural cracks were observed in a both constant moment region and shear spans at a load of 6 kips. Decrease in stiffness can be ascribed to the decrease in moment of Inertia due to sequential cracking in the cross-section. First shear crack was witnessed as a flexural-shear crack in the shear span close to the loading point at a load of 22 kips. Inclined cracks (flexure-shear cracks) were developed with further loading. A critical flexural shear crack was observed in the constant moment region along with the initiation of splitting cracks at the level of rebar. Minimal non-linear behavior can be observed prior to peak load due to the widening of shear cracks and crushing of concrete.

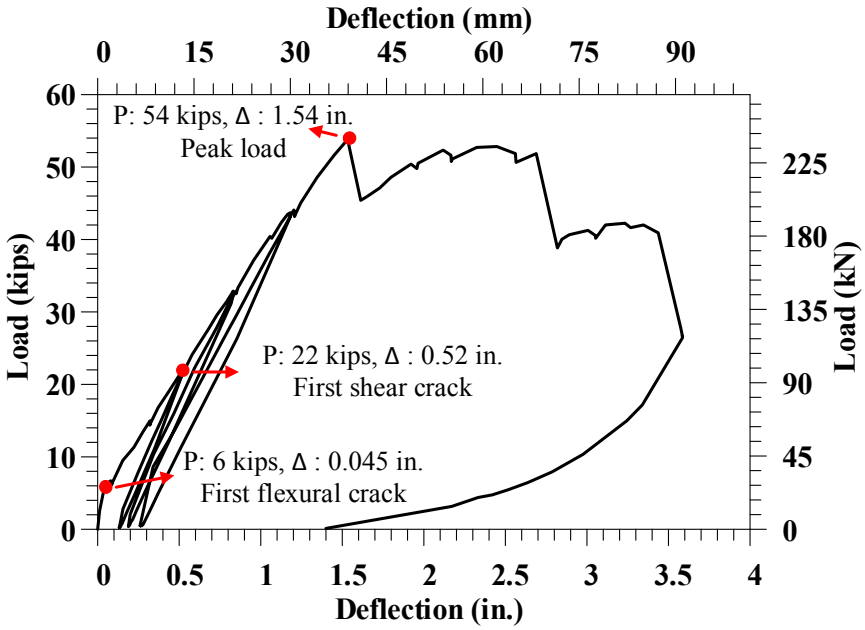

Figure 4-158 Load deflection behavior of beam RC #2

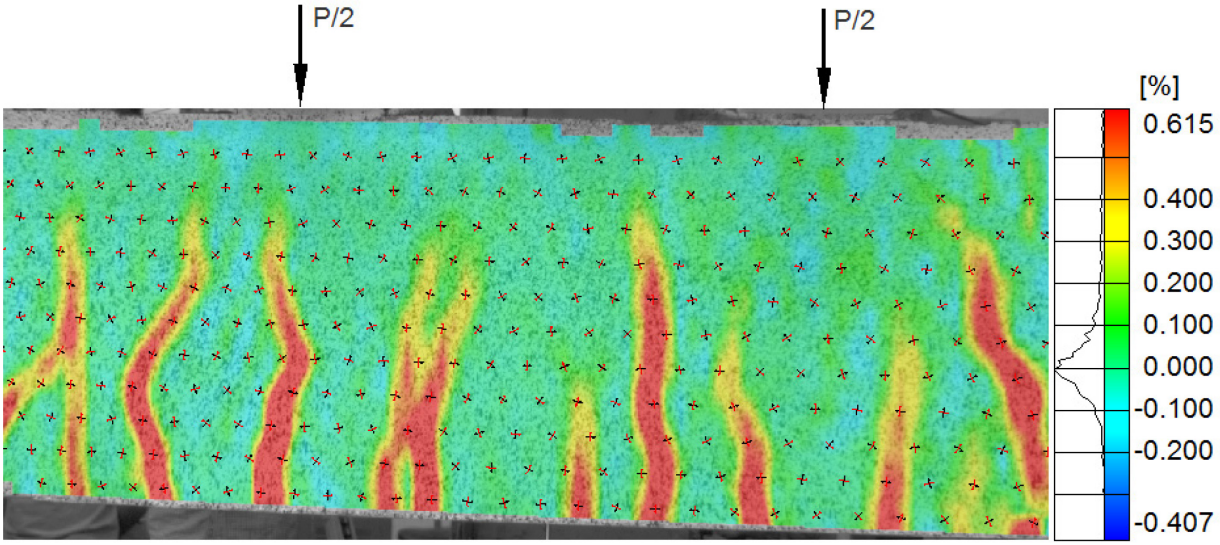

Figure 4-159 Full-field concrete longitudinal strain (ε_x) along moment region for RC#2 at an applied load of 20 kips

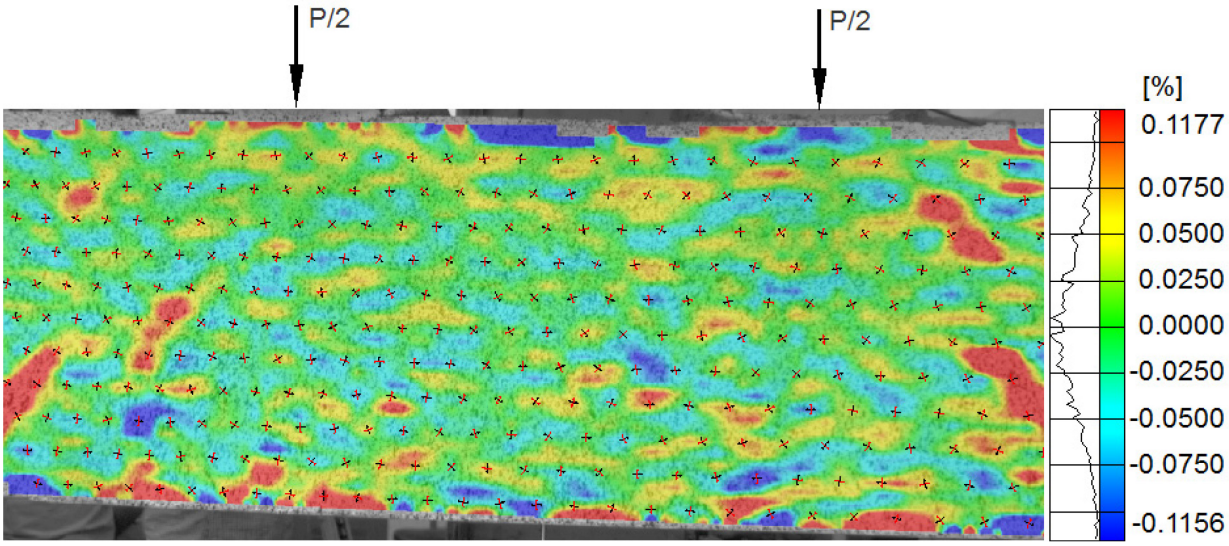

Figure 4-160 Full-field concrete transverse strain (ε_y) along moment region for RC#2 at an applied load of 20 kips

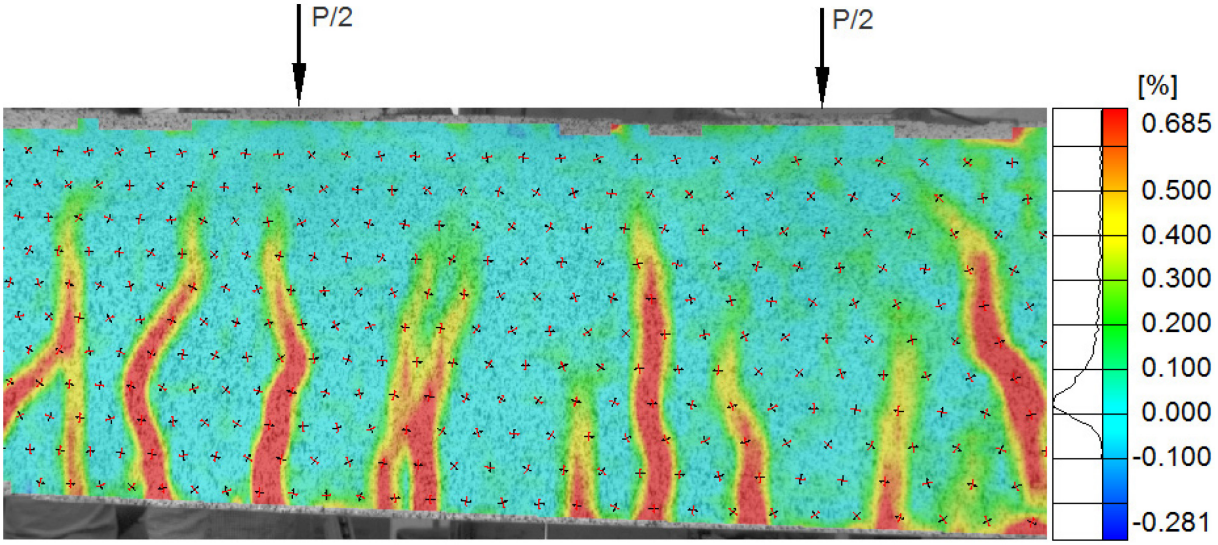

Figure 4-161 Full-field concrete maximum principal strain (σ_1) along moment region for RC#2 at an applied load 20 kips

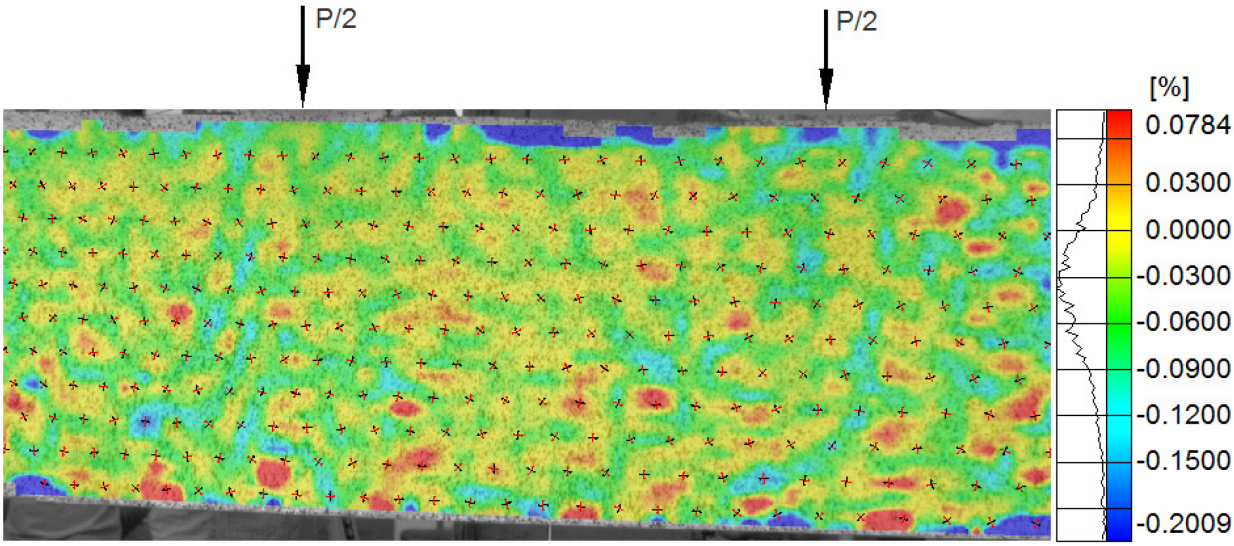

Figure 4-162 Full-field concrete minimum principal strain (σ_2) along moment region for RC#2 at an applied load 20 kips

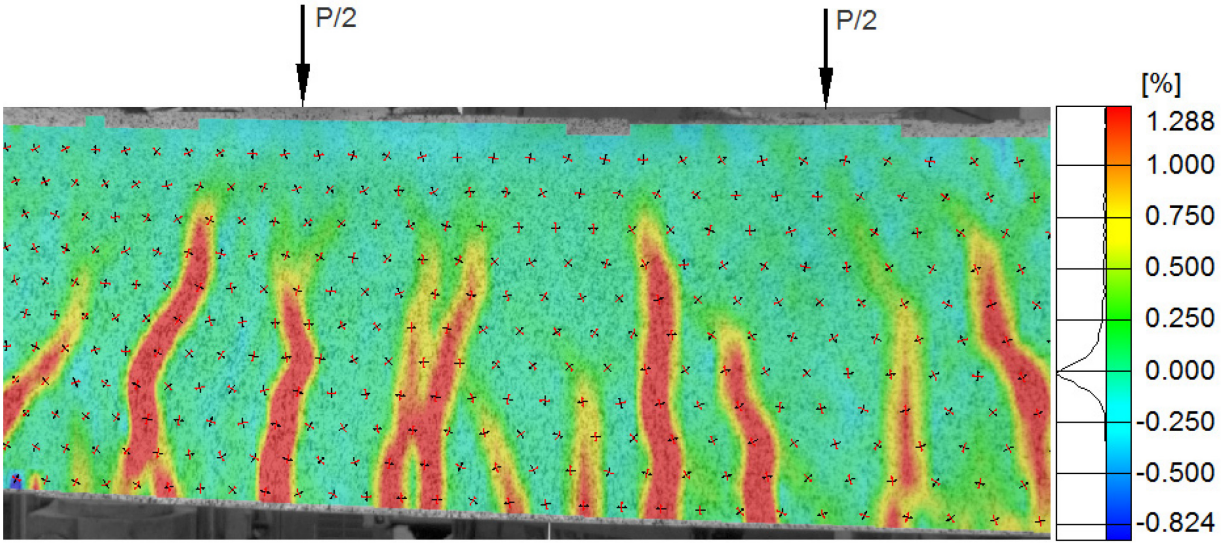

Figure 4-163 Full-field concrete longitudinal strain (ε_x) along moment region for RC#2 at an applied load of 40 kips

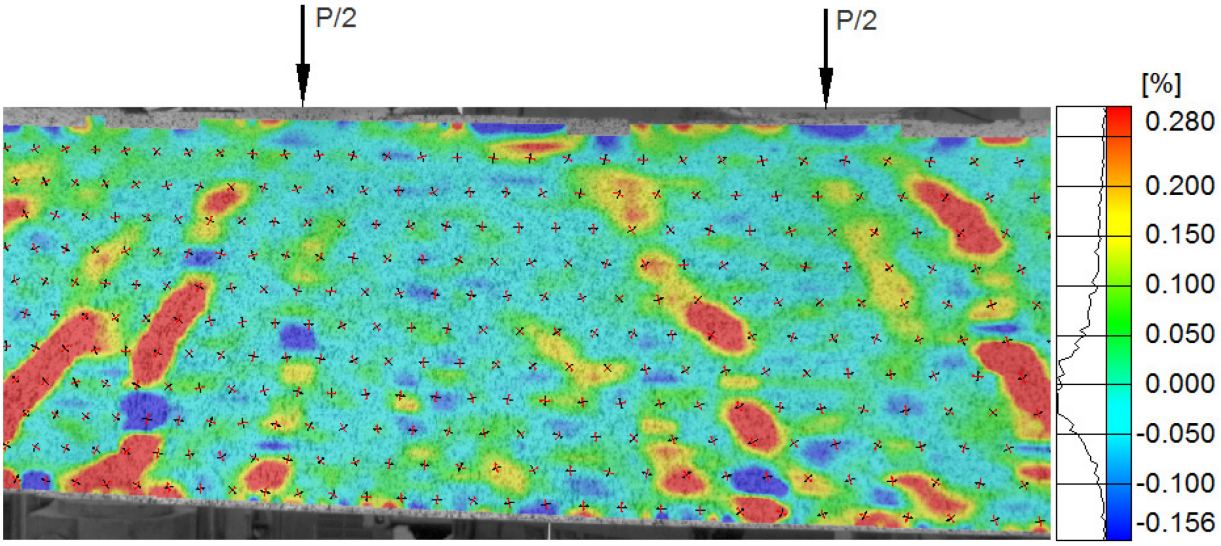

Figure 4-164 Full-field concrete transverse strain (ε_y) along moment region for RC#2 at an applied load of 40 kips

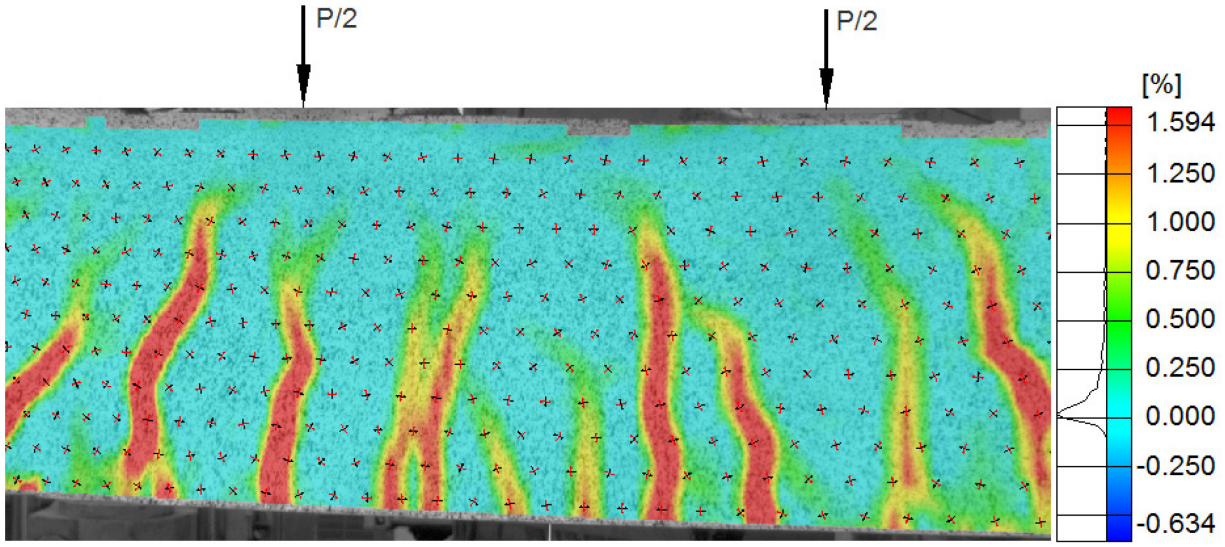

Figure 4-165 Full-field concrete maximum principal strain (σ_1) along moment region for RC#2 at an applied load 40 kips

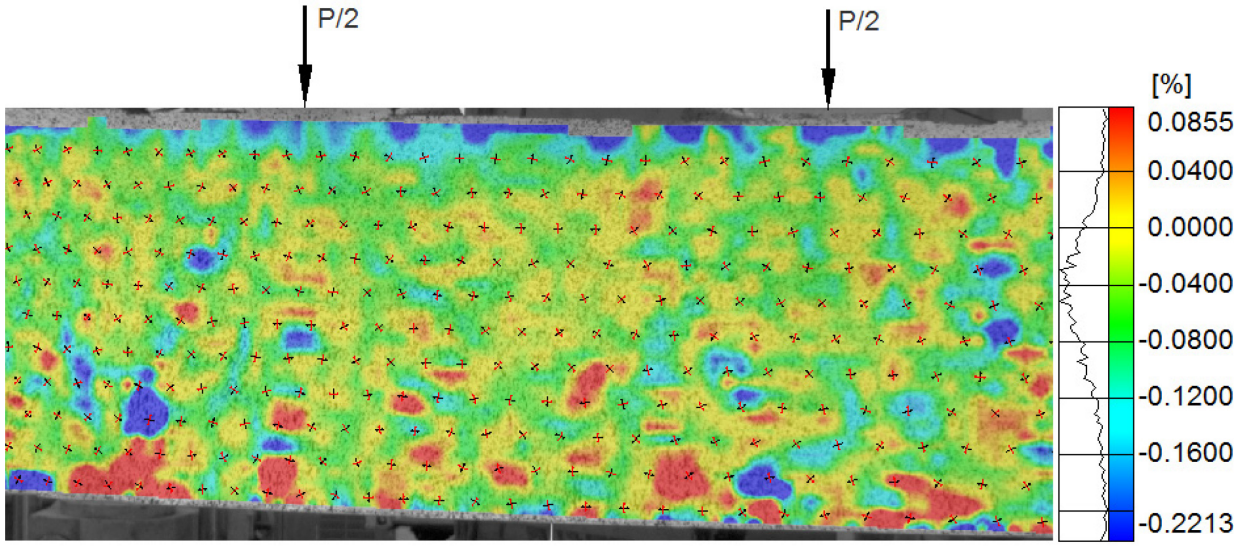

Figure 4-166 Full-field concrete minimum principal strain (σ_2) along moment region for RC#2 at an applied load 40 kips

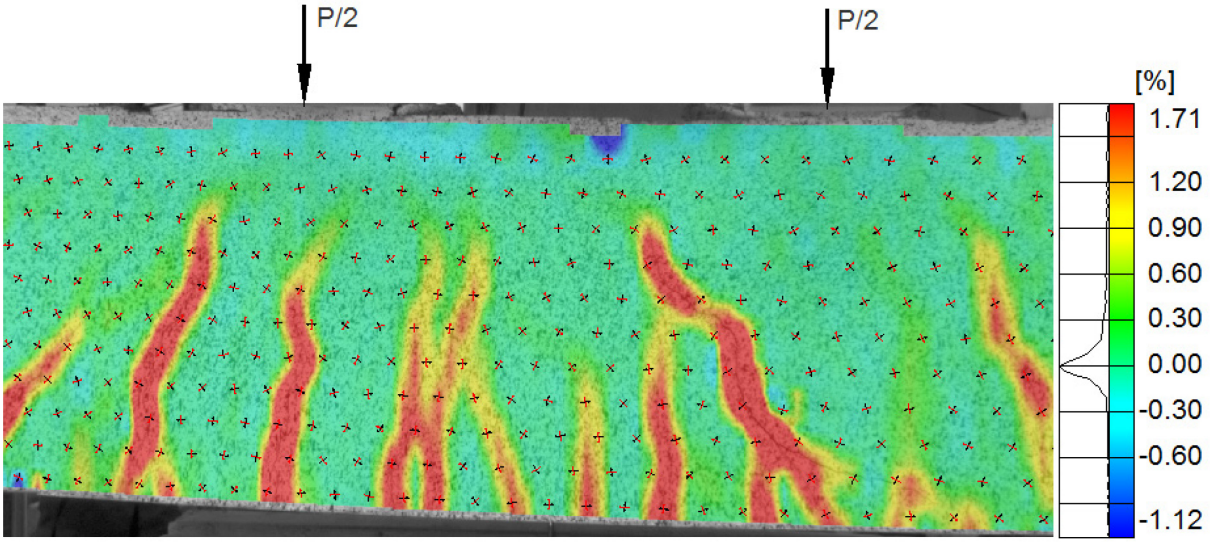

Figure 4-167 Full-field concrete longitudinal strain (ε_x) along moment region for RC#2 at an applied load of 50 kips

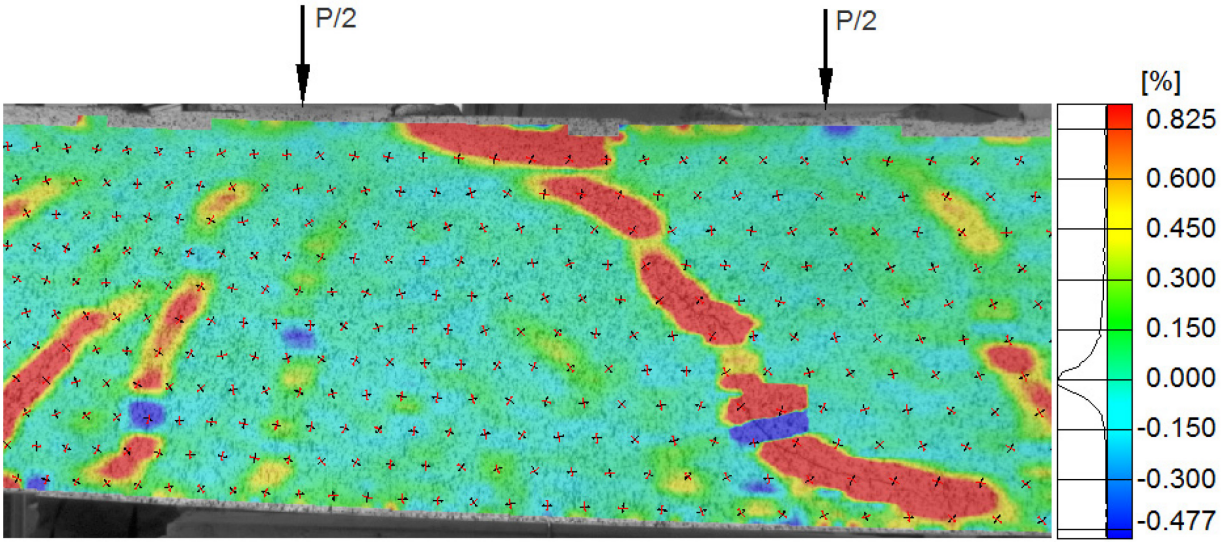

Figure 4-168 Full-field concrete transverse strain (ε_y) along moment region for RC#2 at an applied load of 50 kips

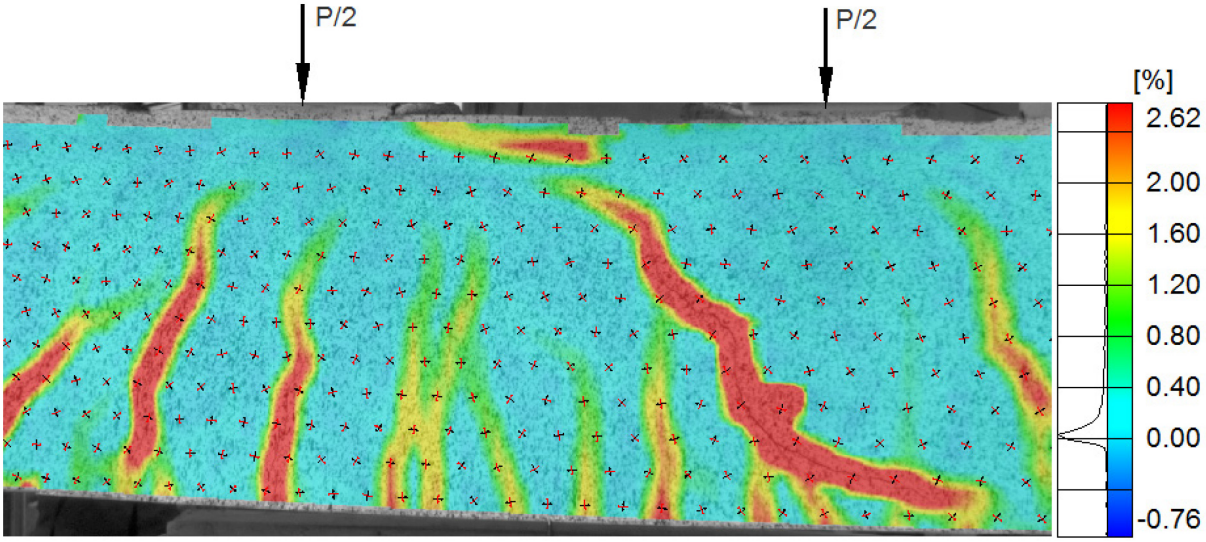

Figure 4-169 Full-field concrete maximum principal strain (σ_1) along moment region for RC#2 at an applied load 50 kips

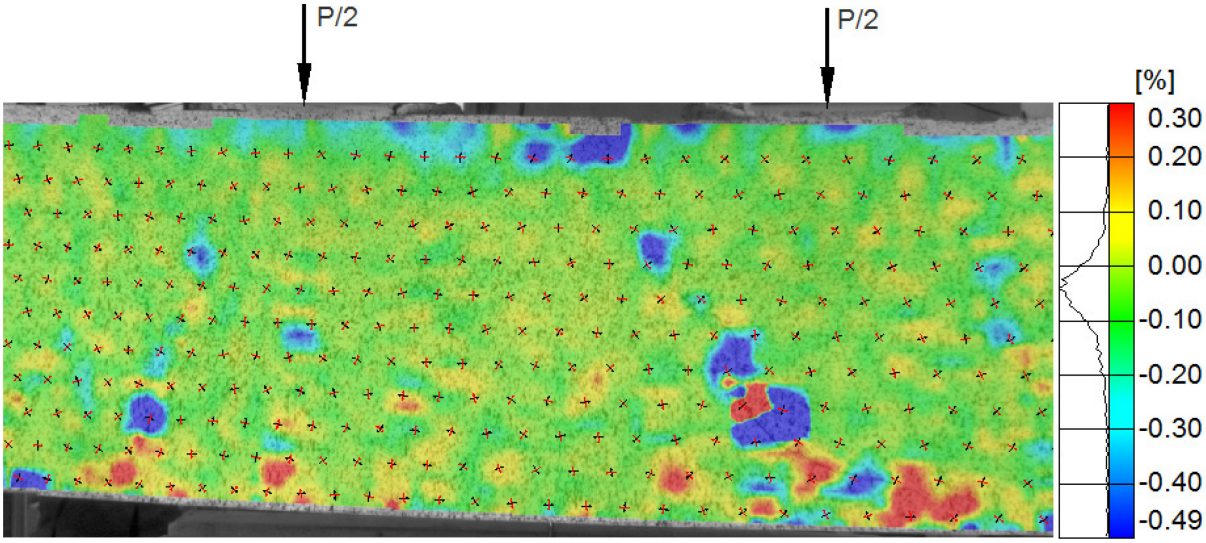

Figure 4-170 Full-field concrete minimum principal strain (σ_2) along moment region for RC#2 at an applied load 50 kips

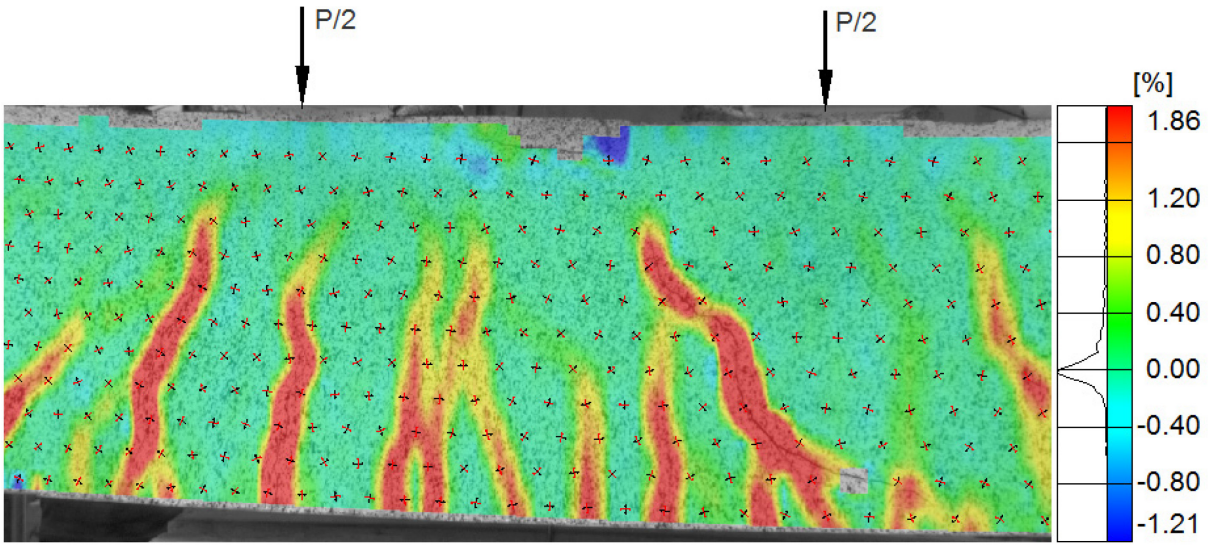

Figure 4-171 Full-field concrete longitudinal strain (ε_x) along moment region for RC#2 at an applied load of 54.7 kips (peak load)

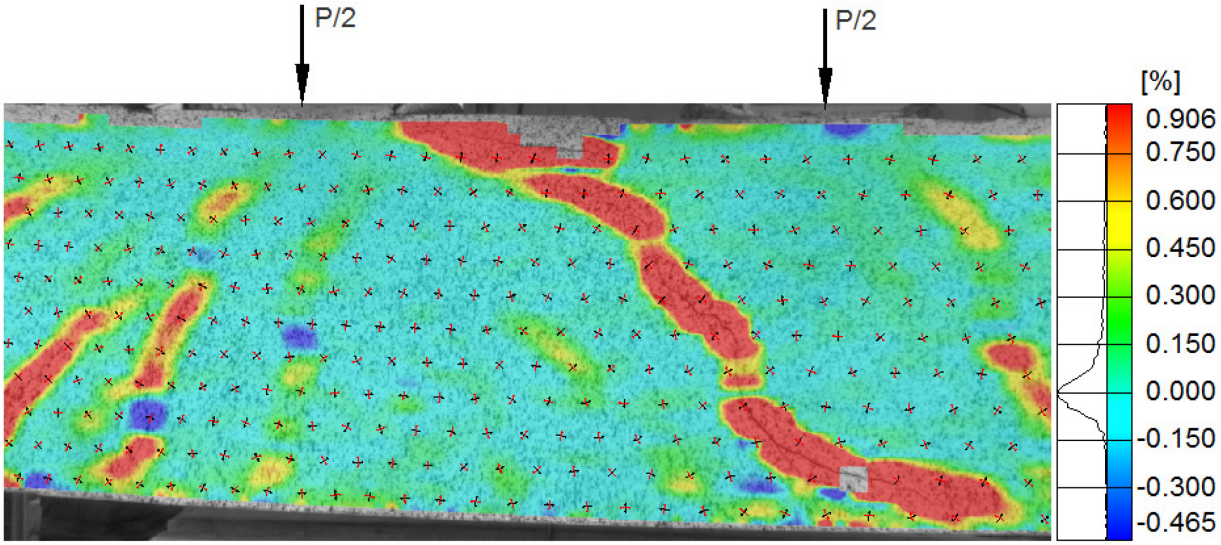

Figure 4-172 Full-field concrete transverse strain (ε_y) along moment region for RC#2 at an applied load of 54.7 kips (peak load)

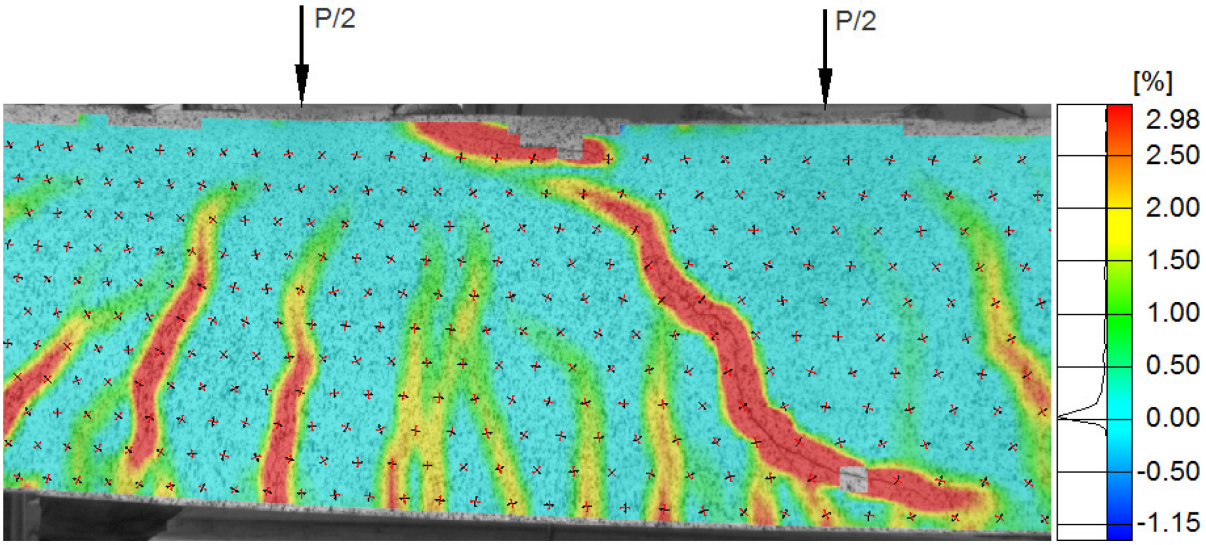

Figure 4-173 Full-field concrete maximum principal strain (σ_1) along moment region for RC#2 at an applied load 54.7 kips (peak load)

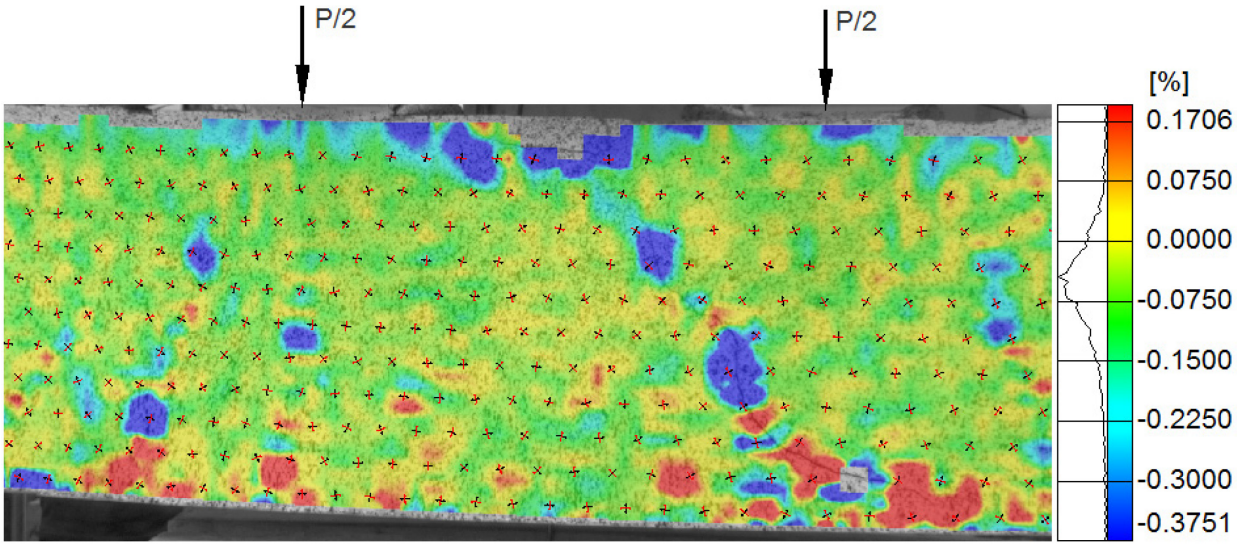

Figure 4-174 Full-field concrete minimum principal strain (σ_2) along moment region for RC#2 at an applied load 54.7 kips (peak load)

4.8. Beam SFRC #2 60S:

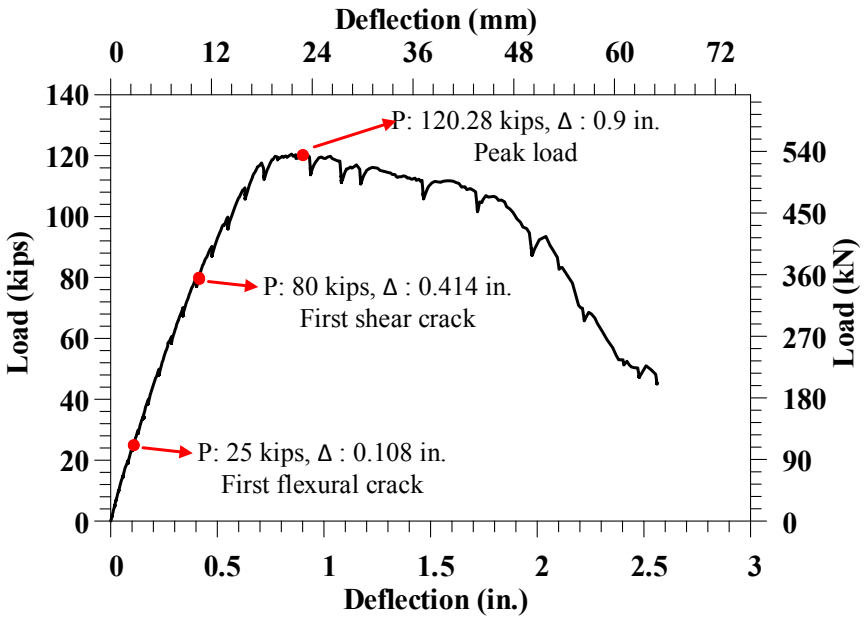

Figure 4-175 Load deflection behavior of beam SFRC #2

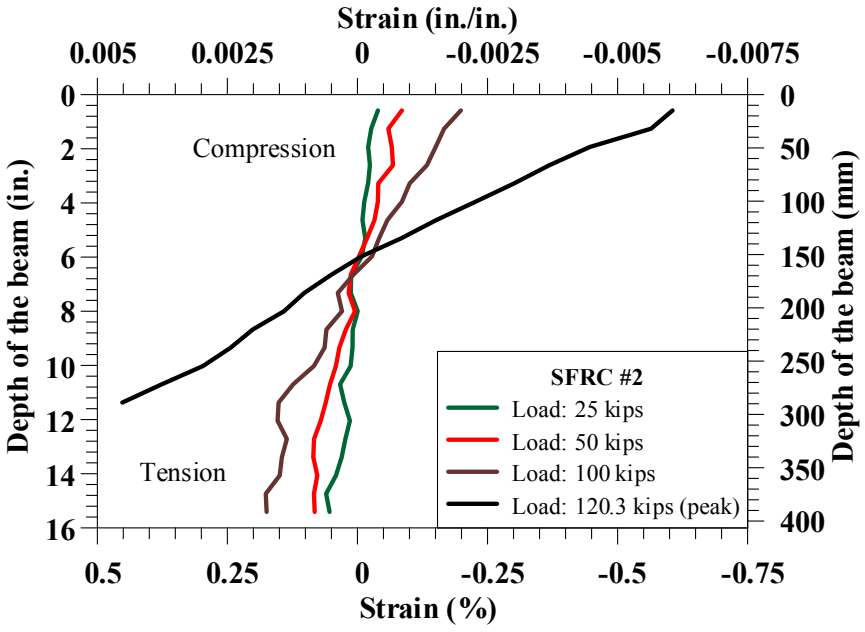

Figure 4-176 Strain variation in beam SFRC #2

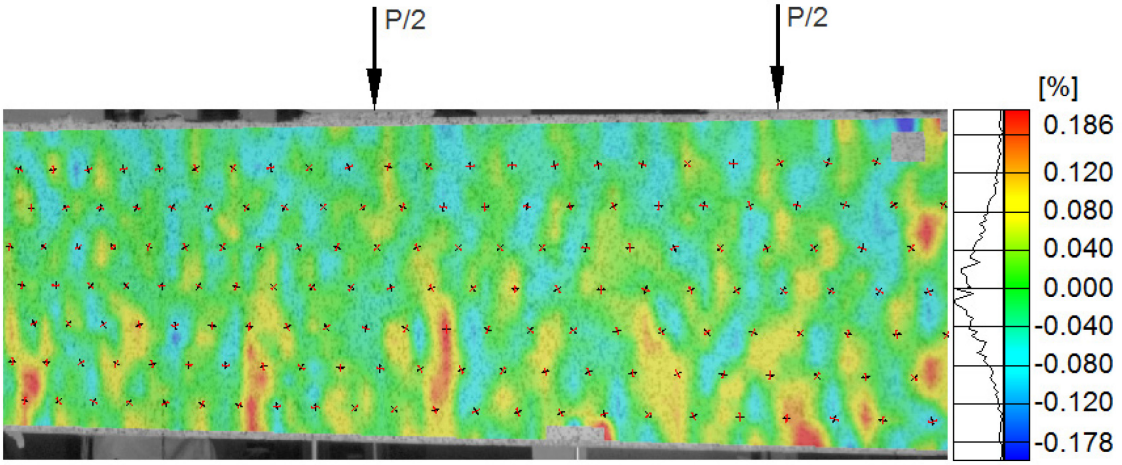

Figure 4-177 Full-field concrete longitudinal strain (ε_x) along moment region for SFRC#2 at an applied load of 20 kips

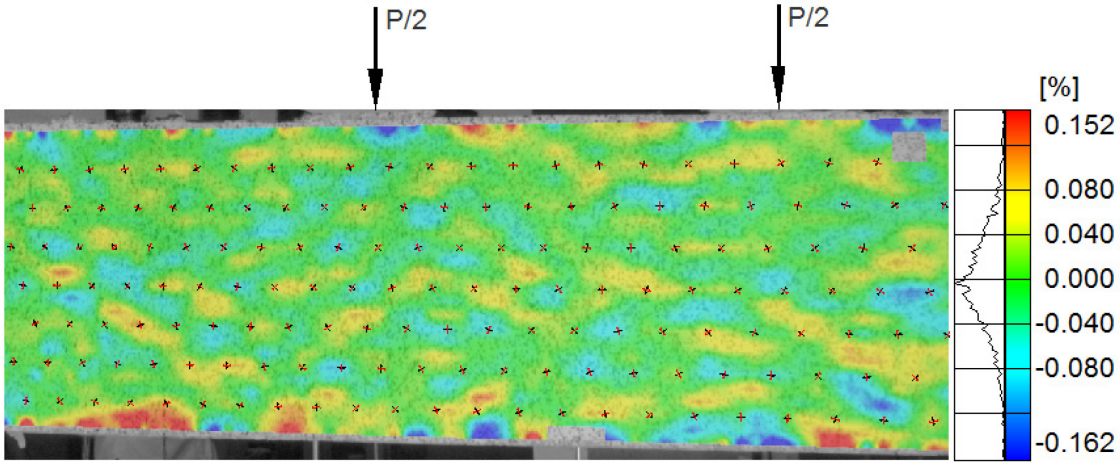

Figure 4-178 Full-field concrete transverse strain (ε_y) along moment region for SFRC#2 at an applied load of 20 kips

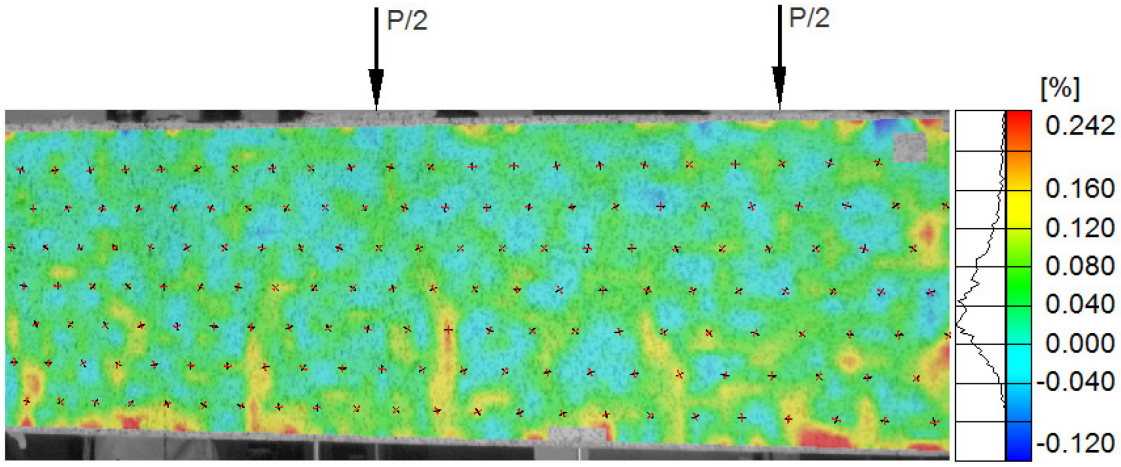

Figure 4-179 Full-field concrete maximum principal strain (σ_1) along moment region for SFRC#2 at an applied load 20 kips

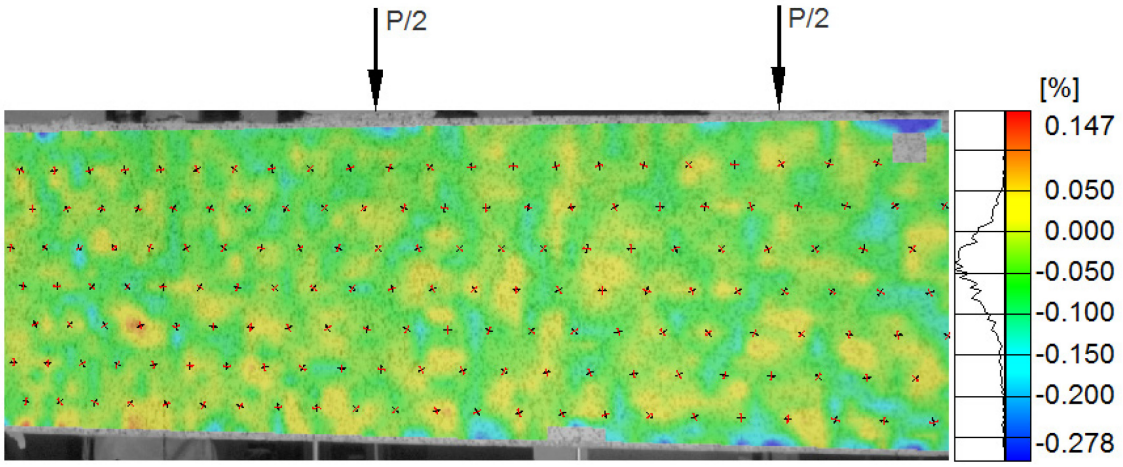

Figure 4-180 Full-field concrete minimum principal strain (σ_2) along moment region for SFRC#2 at an applied load 20 kips

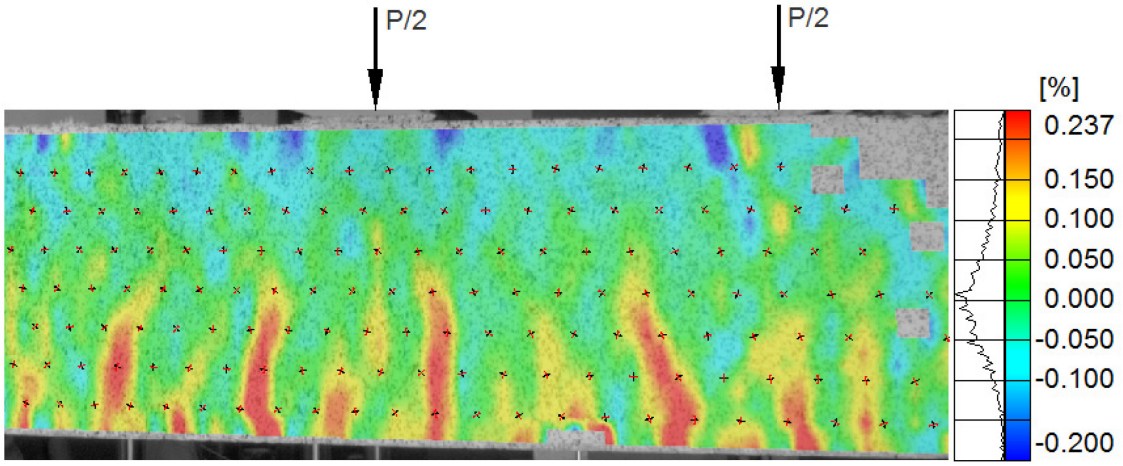

Figure 4-181 Full-field concrete longitudinal strain (ε_x) along moment region for SFRC#2 at an applied load of 50 kips

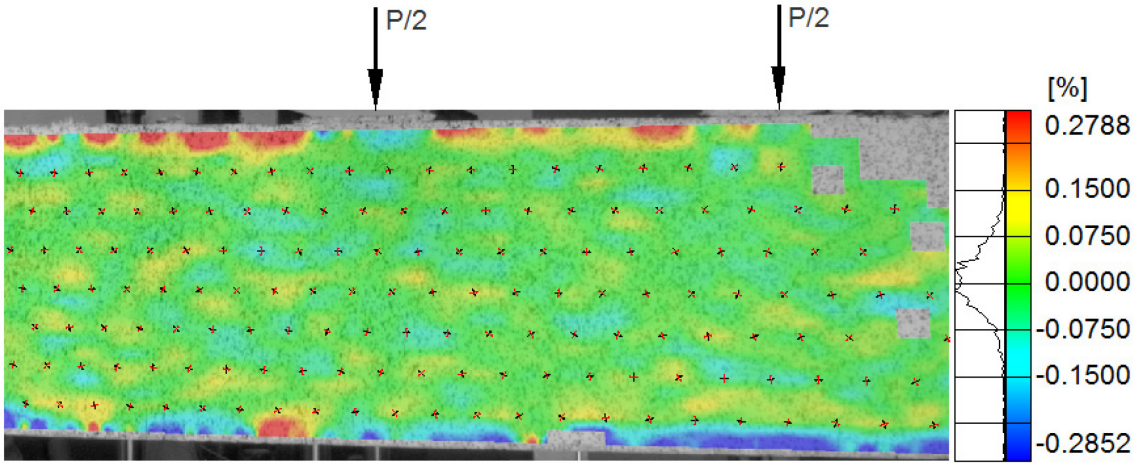

Figure 4-182 Full-field concrete transverse strain (ε_y) along moment region for SFRC#2 at an applied load of 50 kips

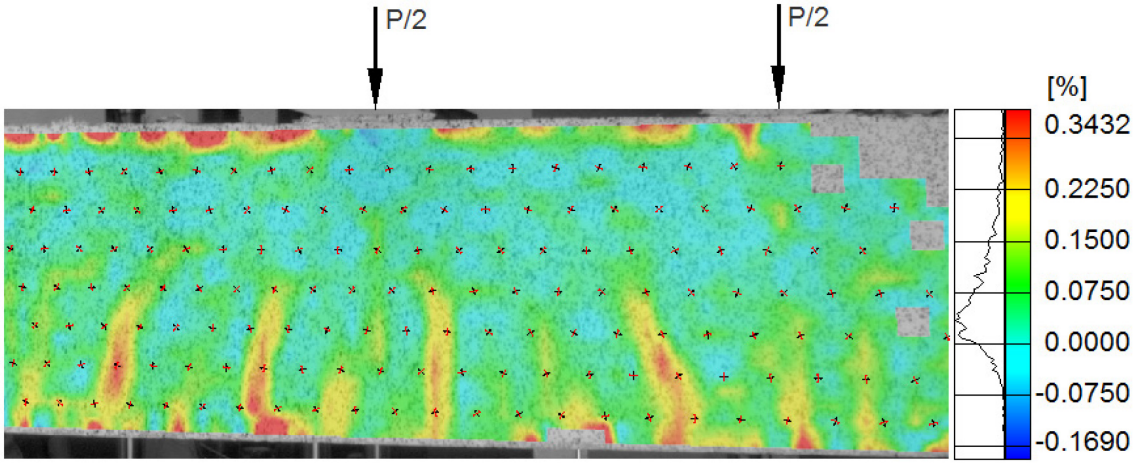

Figure 4-183 Full-field concrete maximum principal strain (σ_1) along moment region for SFRC#2 at an applied load 50 kips

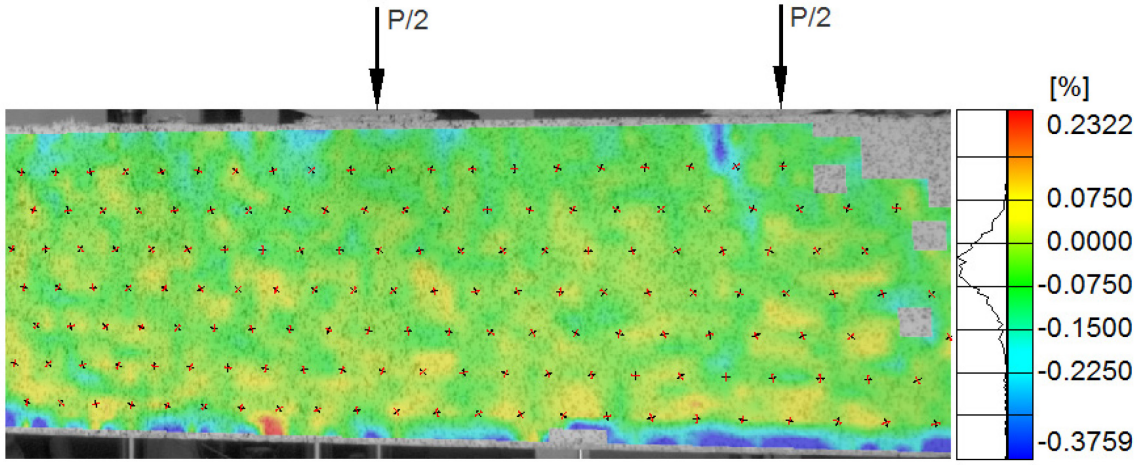

Figure 4-184 Full-field concrete minimum principal strain (σ_2) along moment region for SFRC#2 at an applied load 50 kips

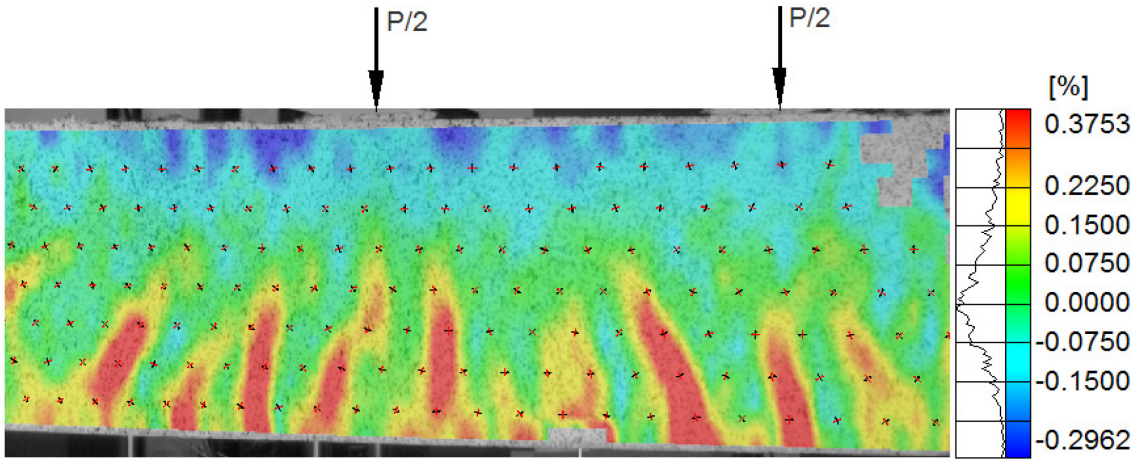

Figure 4-185 Full-field concrete longitudinal strain (ε_x) along moment region for SFRC#2 at an applied load of 100 kips

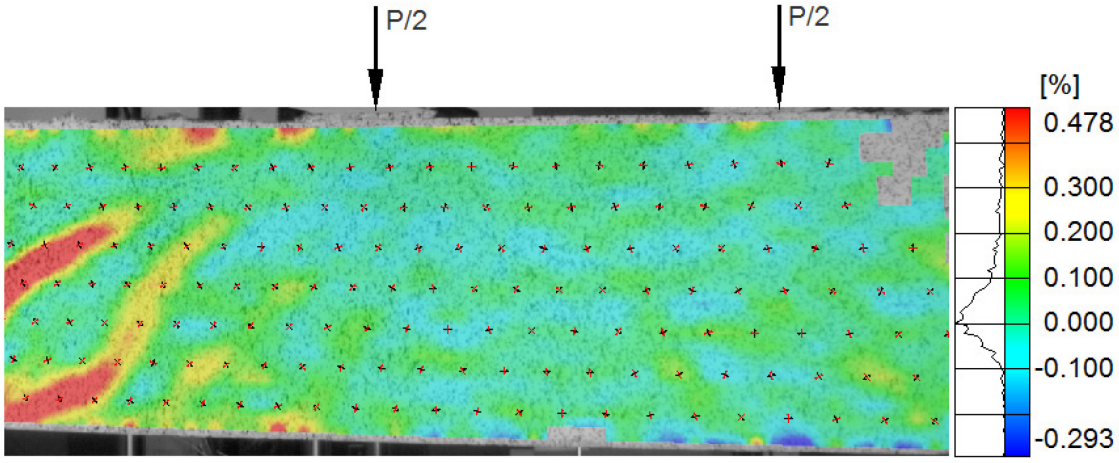

Figure 4-186 Full-field concrete transverse strain (ε_y) along moment region for SFRC#2 at an applied load of 100 kips

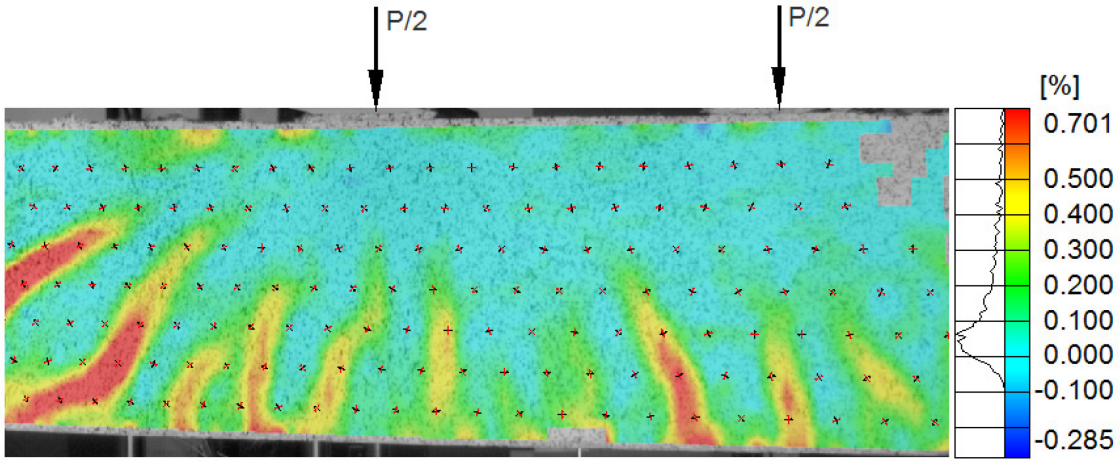

Figure 4-187 Full-field concrete maximum principal strain (σ_1) along moment region for SFRC#2 at an applied load 100 kips

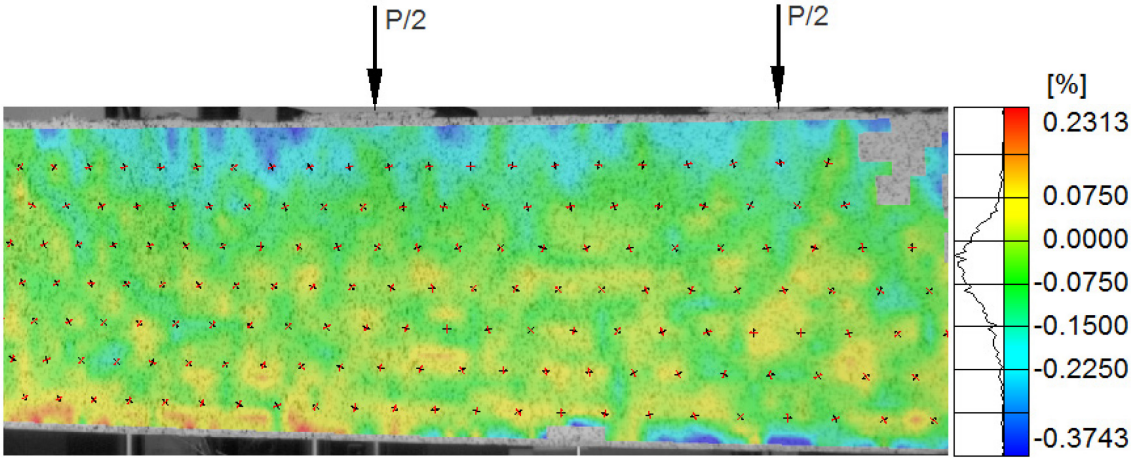

Figure 4-188 Full-field concrete minimum principal strain (σ_2) along moment region for SFRC#2 at an applied load 100 kips

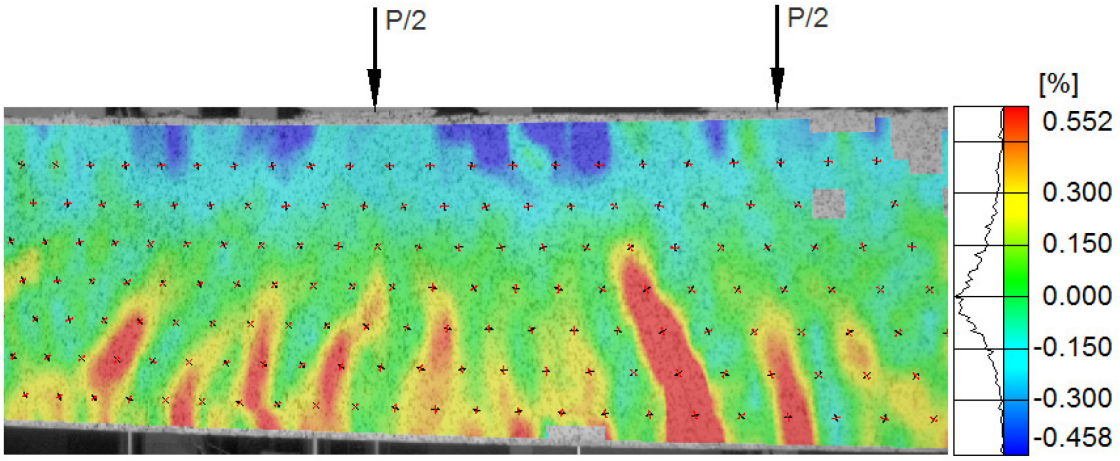

Figure 4-189 Full-field concrete longitudinal strain (ε_x) along moment region for SFRC#2 at an applied load of 120.28 kips (peak load)

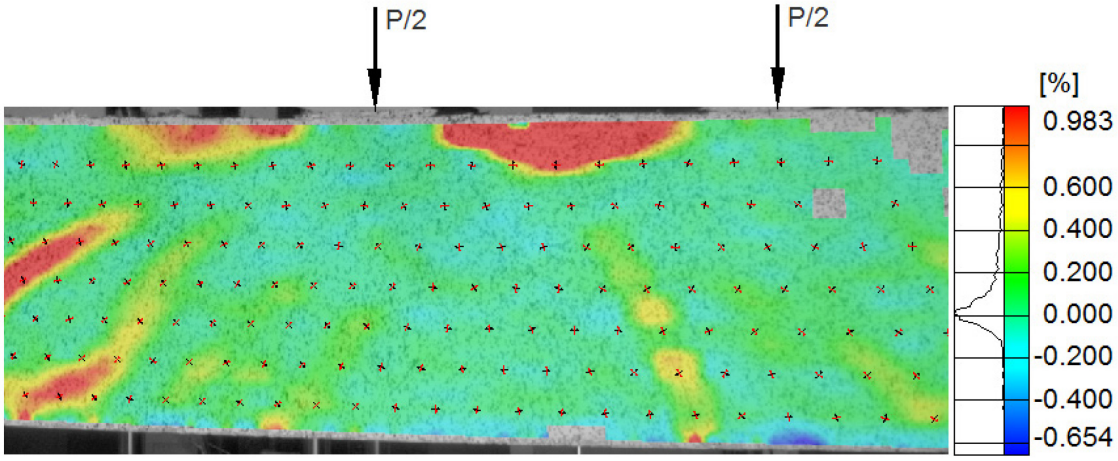

Figure 4-190 Full-field concrete transverse strain (ε_y) along moment region for SFRC#2 at an applied load of 120.28 kips (peak load)

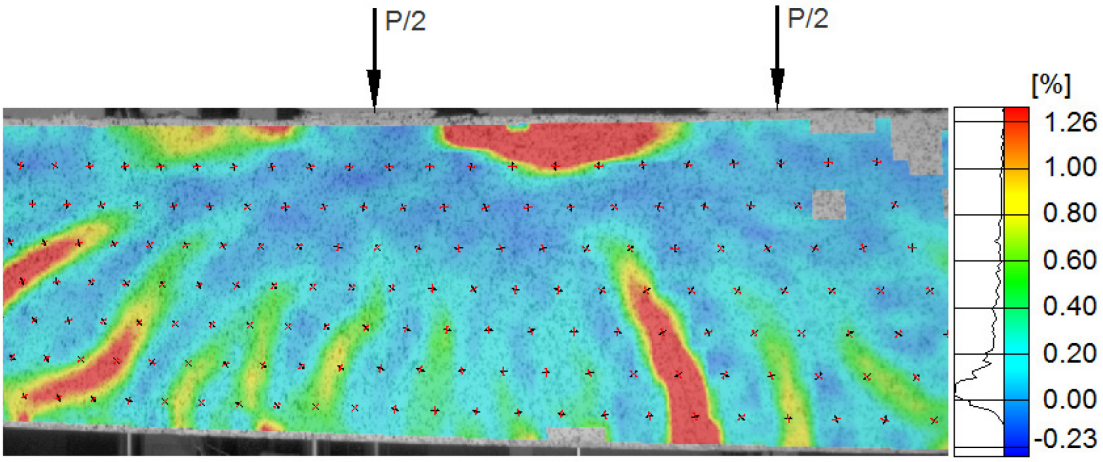

Figure 4-191 Full-field concrete maximum principal strain (σ_1) along moment region for SFRC#2 at an applied load 120.28 kips (peak load)

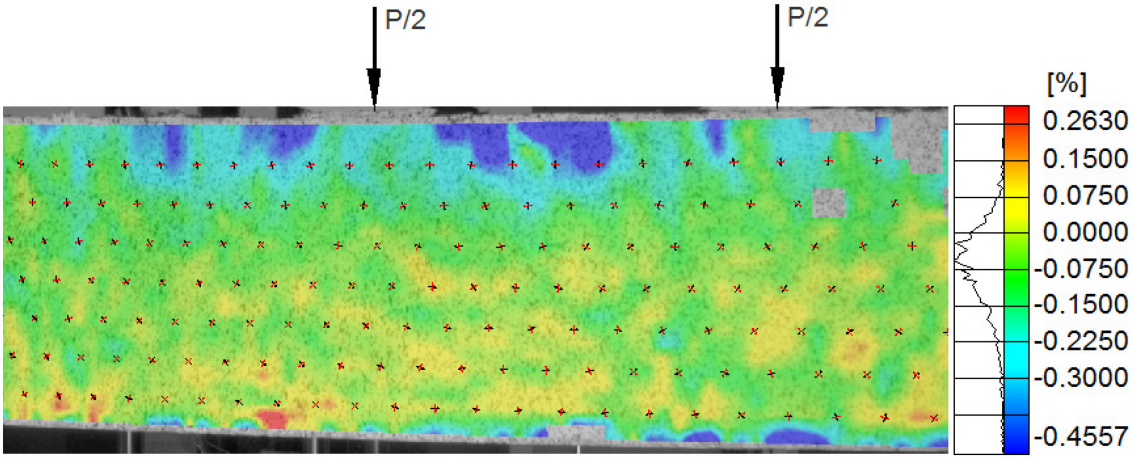

Figure 4-192 Full-field concrete minimum principal strain (σ_2) along moment region for SFRC#2 at an applied load 120.28 kips (peak load)

4.9 Beam SFRC #3 100S:

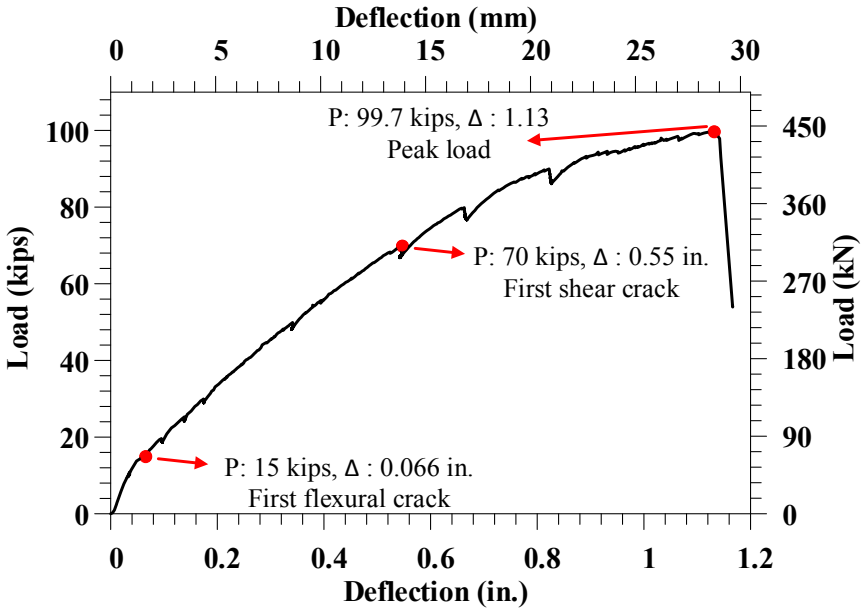

Figure 4-193

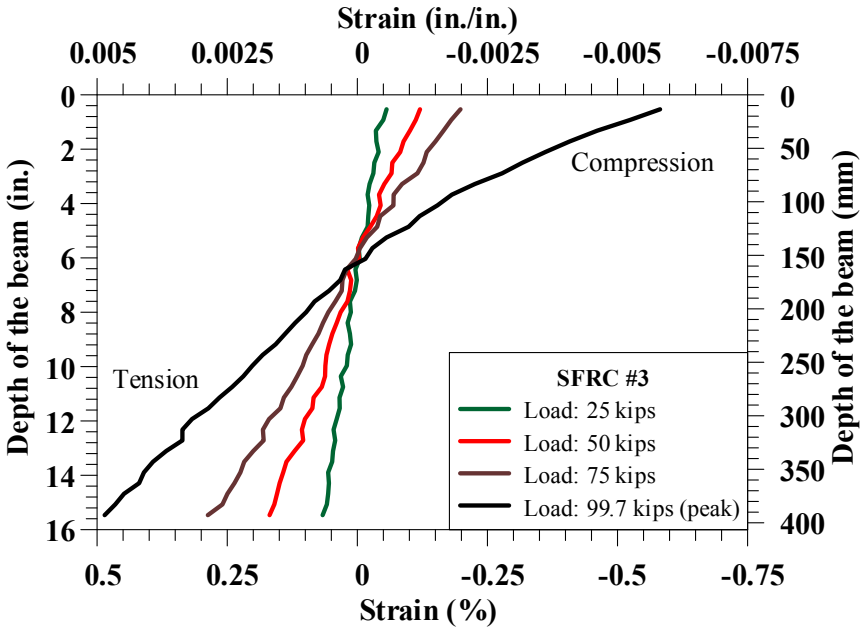

Figure 4-194 Strain variation in beam SFRC #3

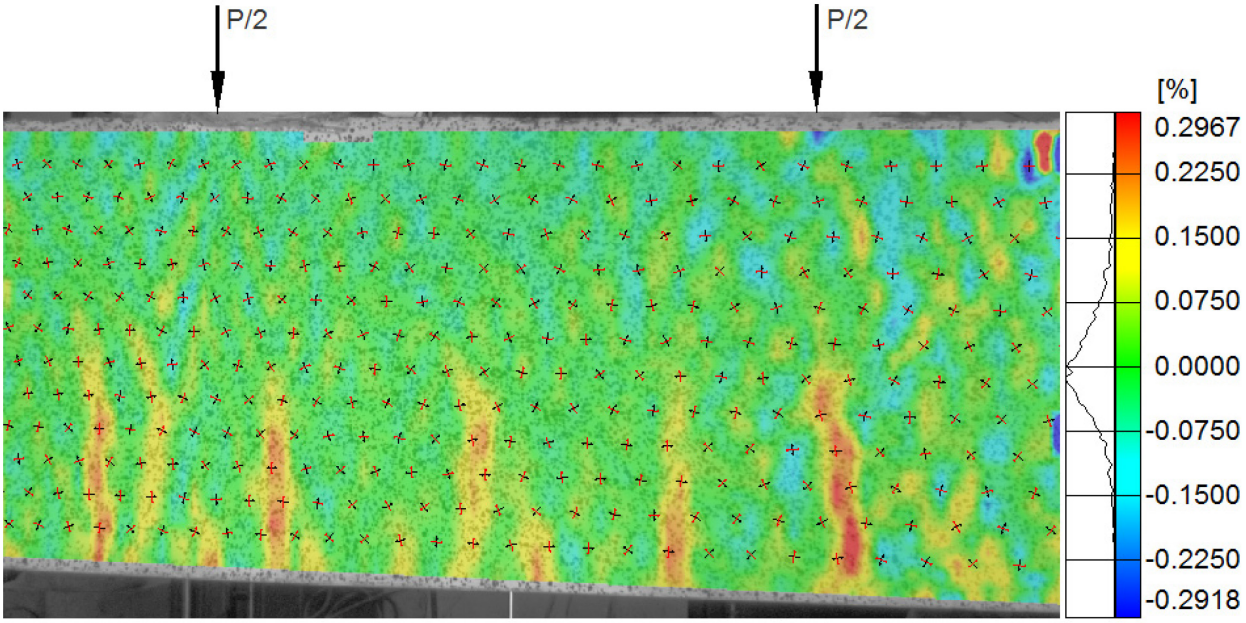

Figure 4-195 Full-field concrete longitudinal strain (ε_x) along moment region for SFRC#3 at an applied load of 20 kips

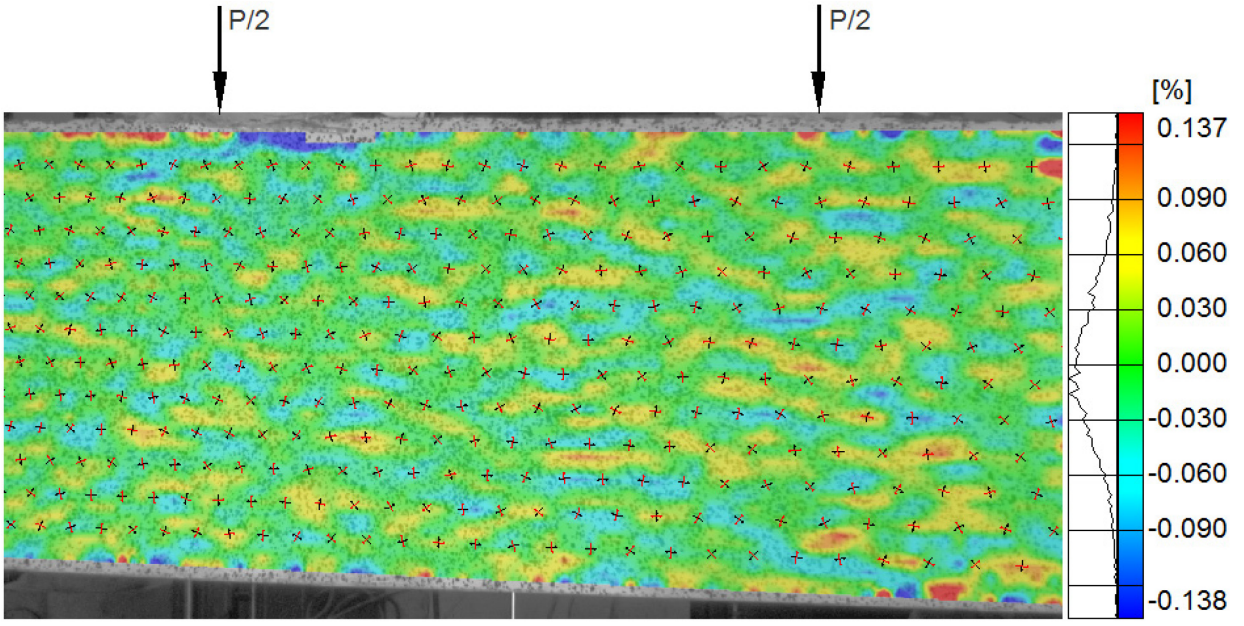

Figure 4-196 Full-field concrete transverse strain (ε_y) along moment region for SFRC#3 at an applied load of 20 kips

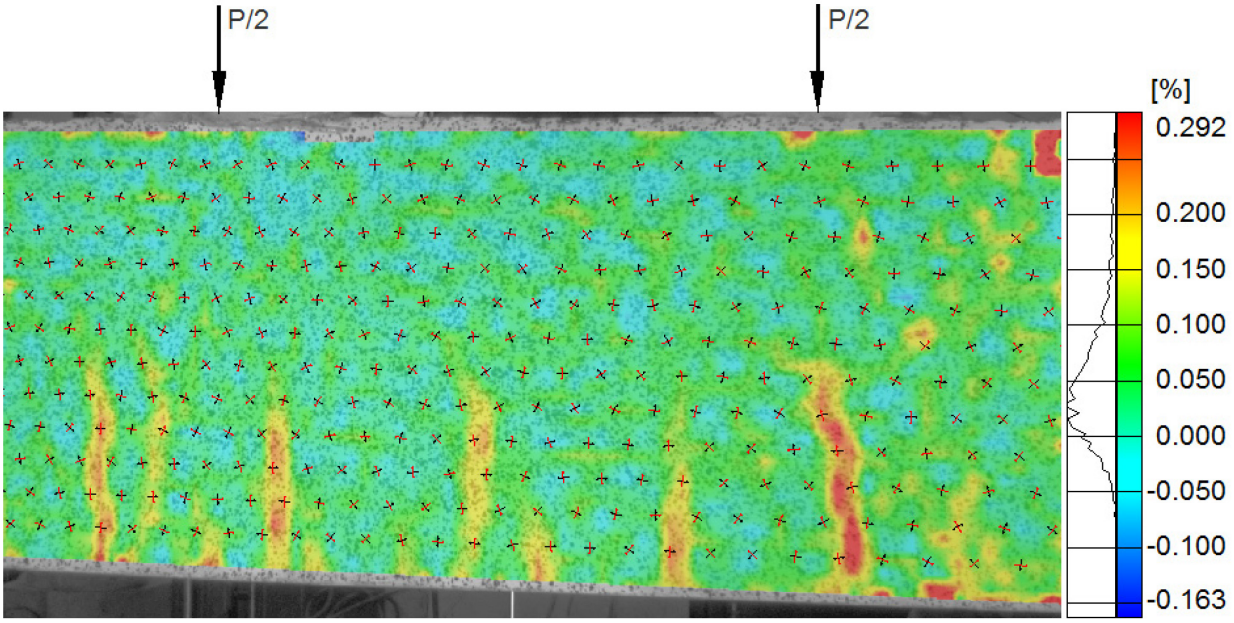

Figure 4-197 Full-field concrete maximum principal strain (σ_1) along moment region for SFRC#3 at an applied load 20 kips

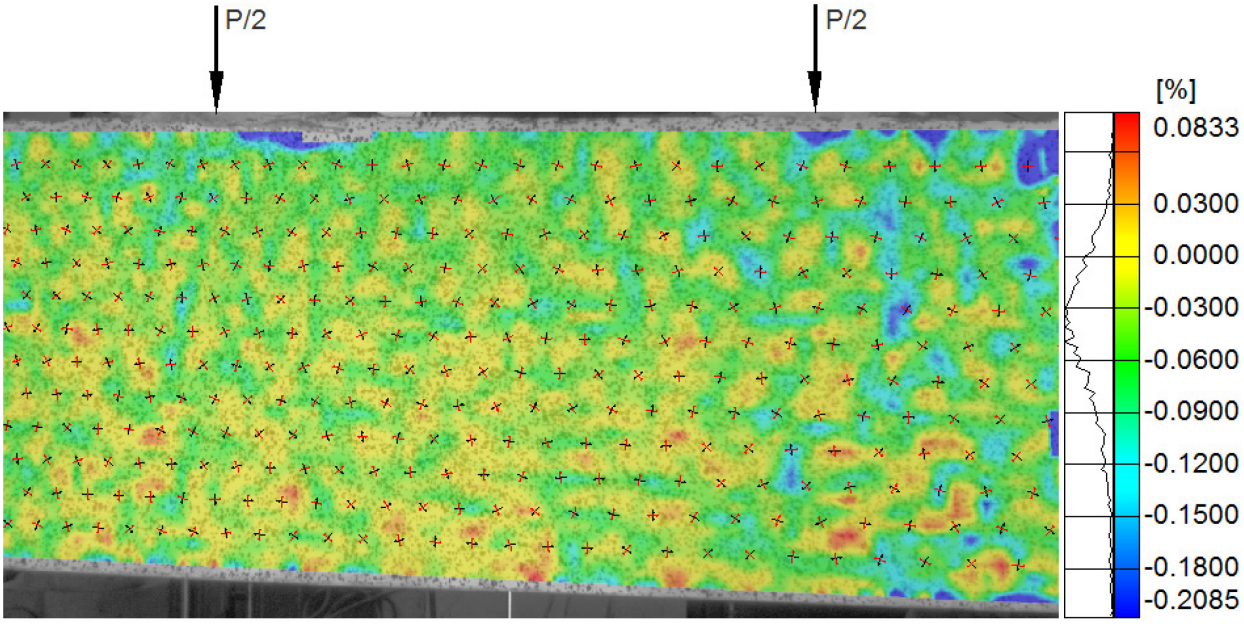

Figure 4-198 Full-field concrete minimum principal strain (σ_2) along moment region for SFRC#3 at an applied load 20 kips

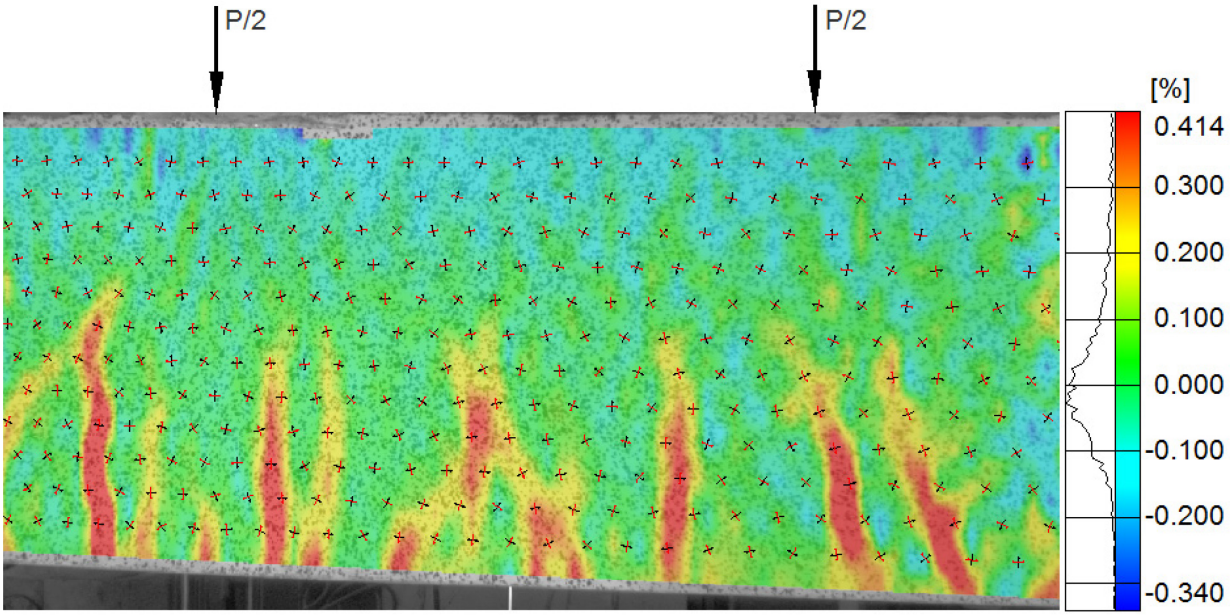

Figure 4-199 Full-field concrete longitudinal strain (ε_x) along moment region for SFRC#3 at an applied load of 50 kips

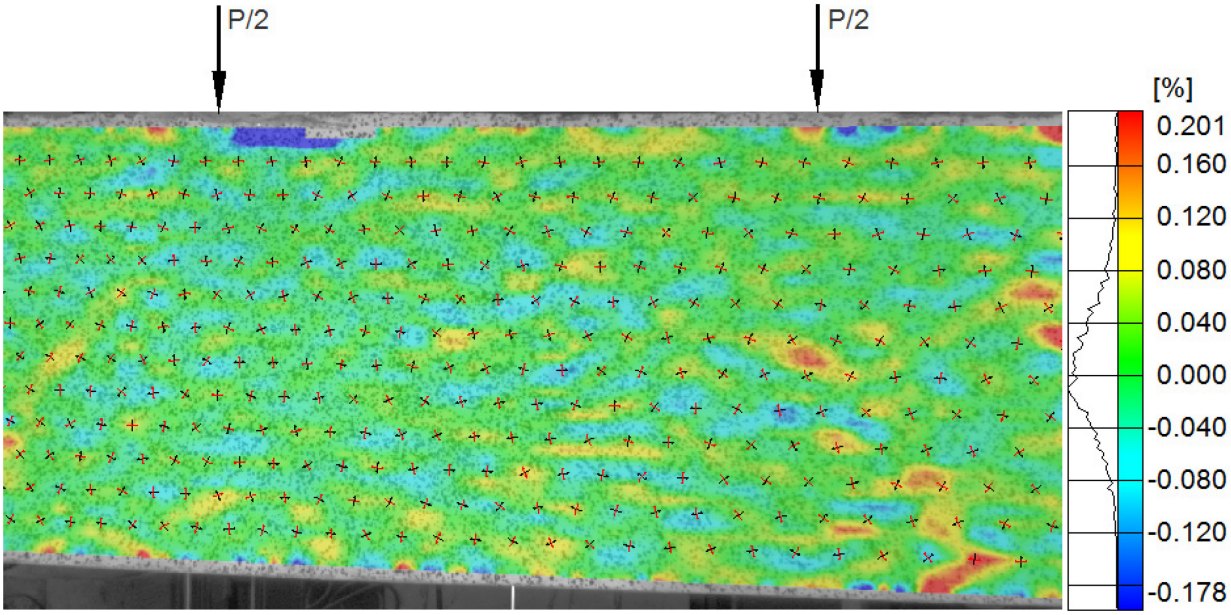

Figure 4-200 Full-field concrete transverse strain (ε_y) along moment region for SFRC#3 at an applied load of 50 kips

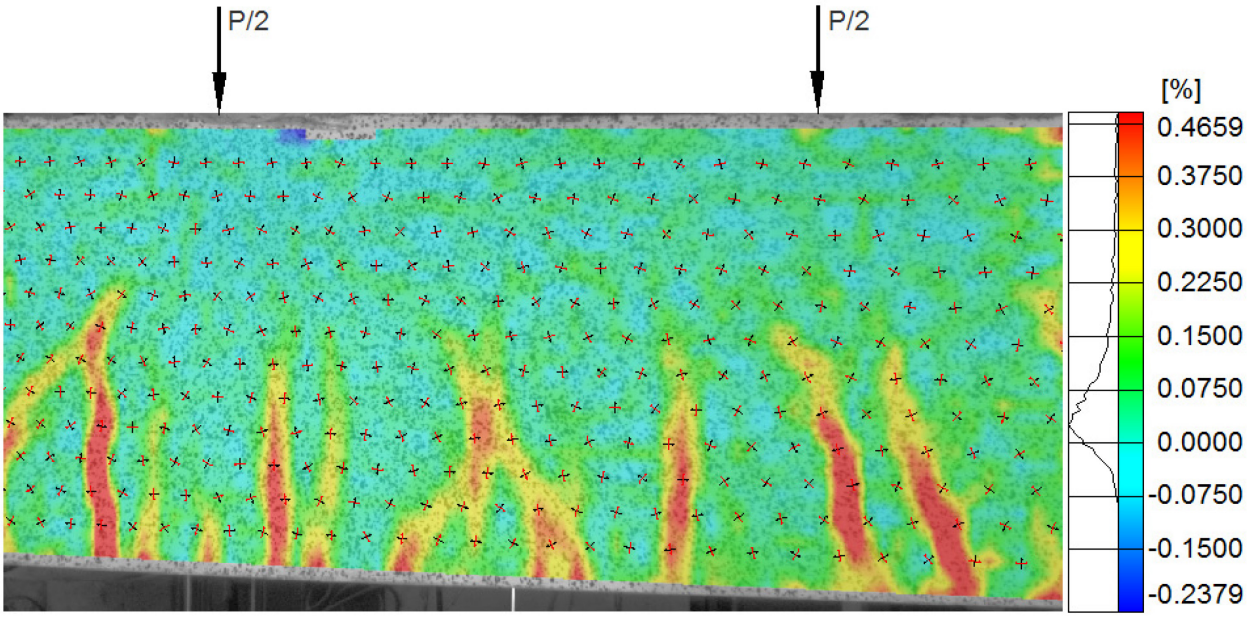

Figure 4-201 Full-field concrete maximum principal strain (σ_1) along moment region for SFRC#3 at an applied load 50 kips

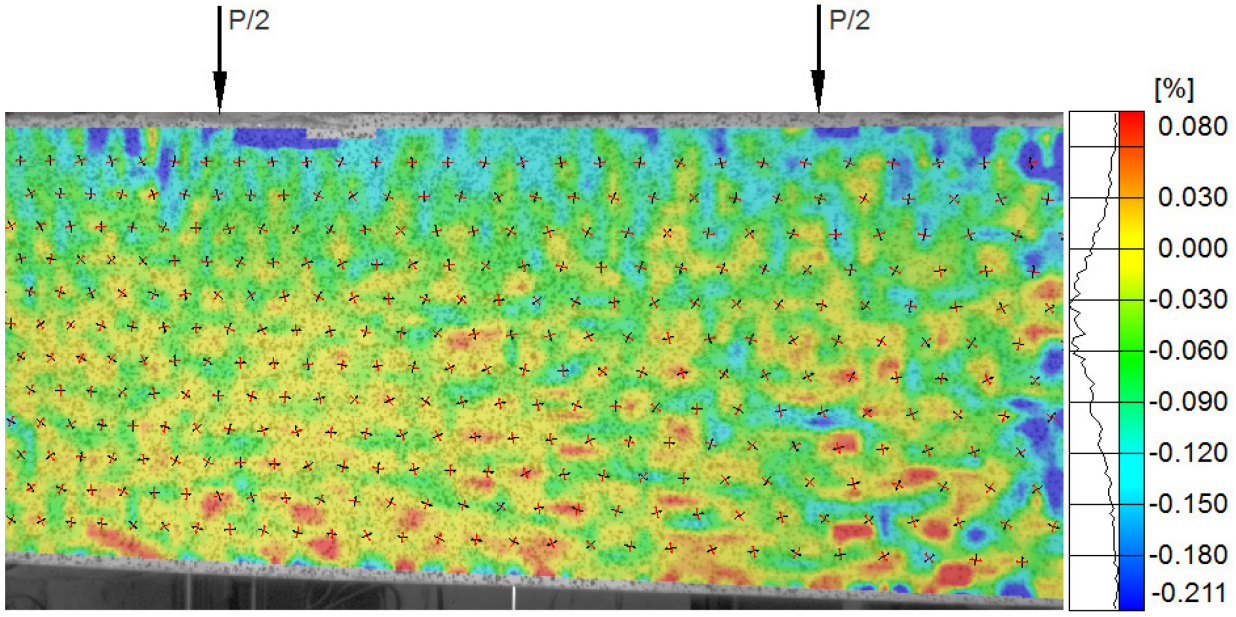

Figure 4-202 Full-field concrete minimum principal strain (σ_2) along moment region for SFRC#3 at an applied load 50 kips

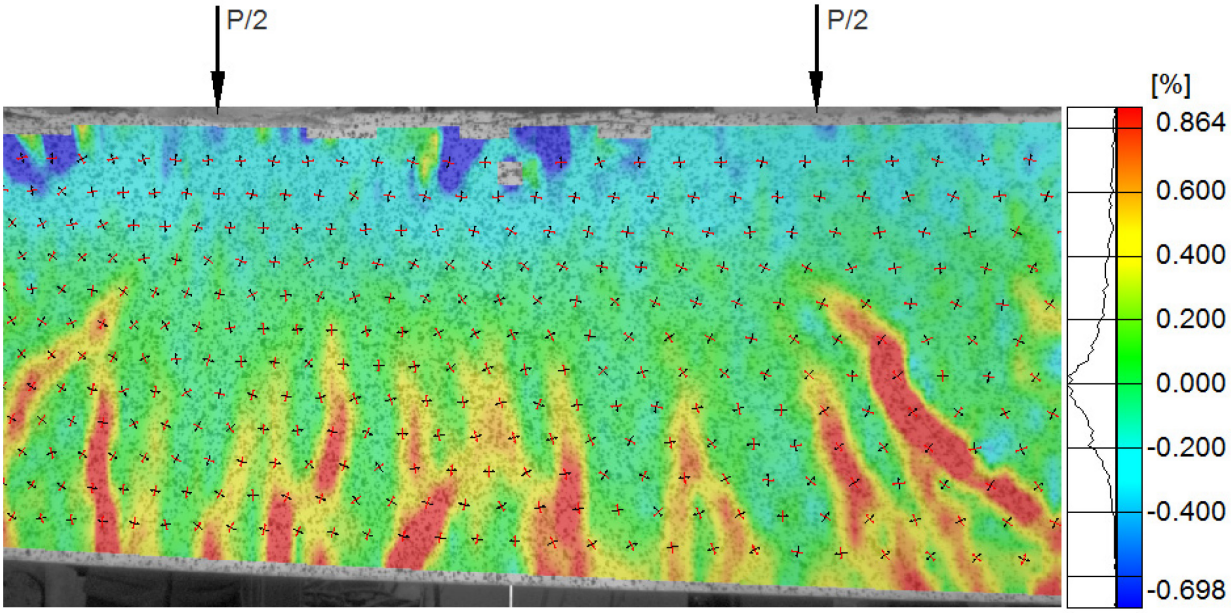

Figure 4-203 Full-field concrete longitudinal strain (ε_x) along moment region for SFRC#3 at an applied load of 99.7 kips (peak load)

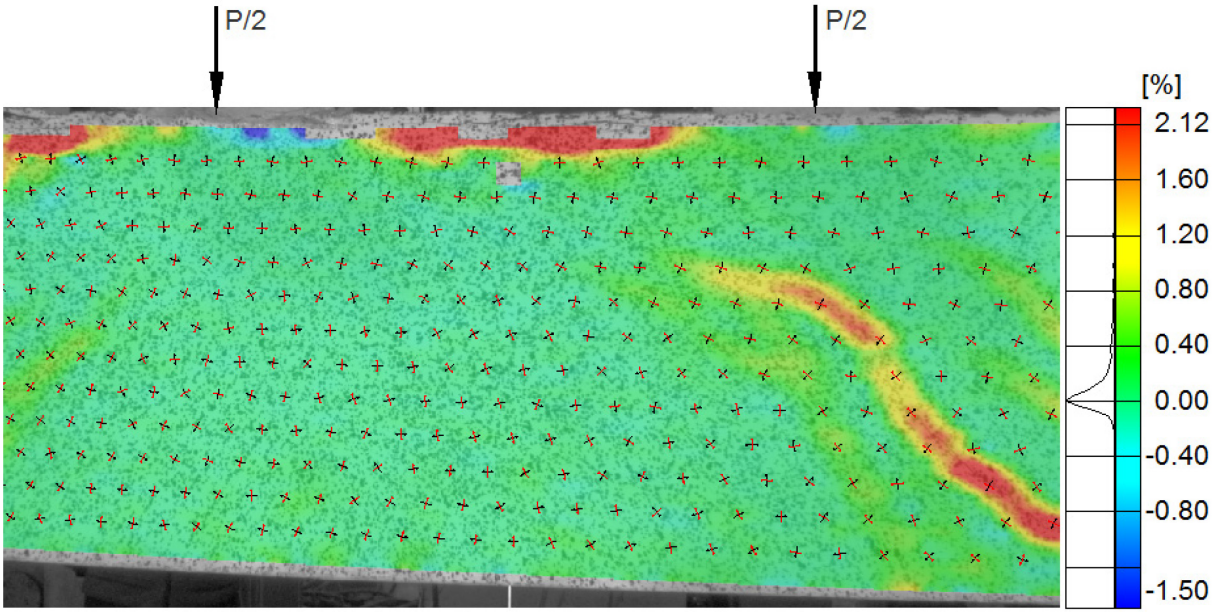

Figure 4-204 Full-field concrete transverse strain (ε_y) along moment region for SFRC#3 at an applied load of 99.7 kips (peak load)

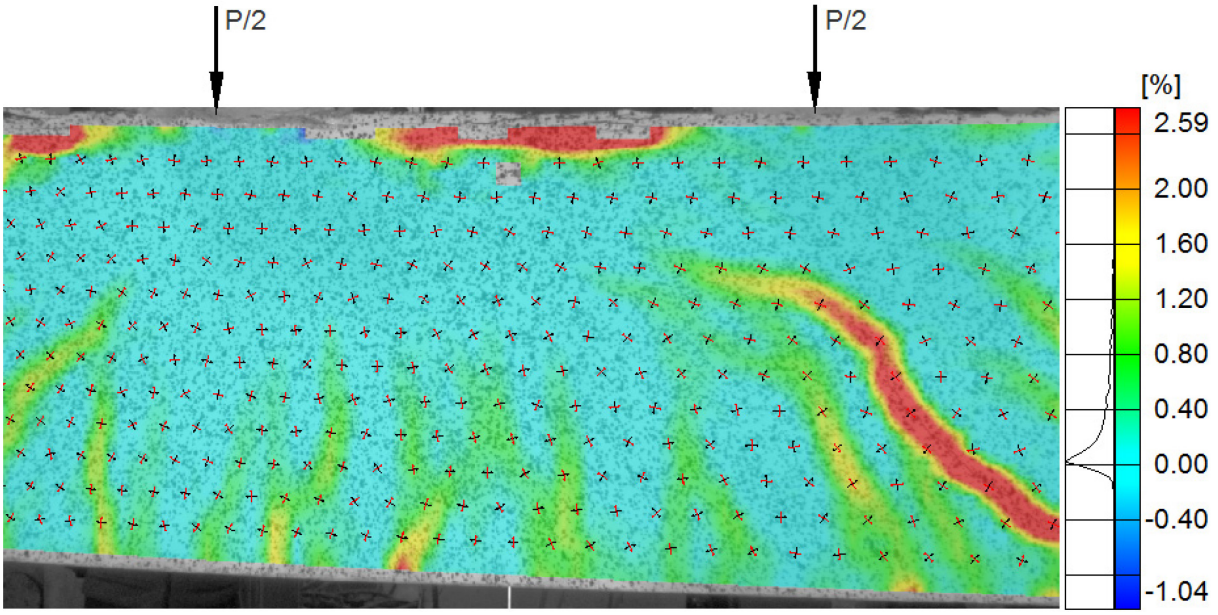

Figure 4-205 Full-field concrete maximum principal strain (σ_1) along moment region for SFRC#3 at an applied load 99.7 kips (peak load)

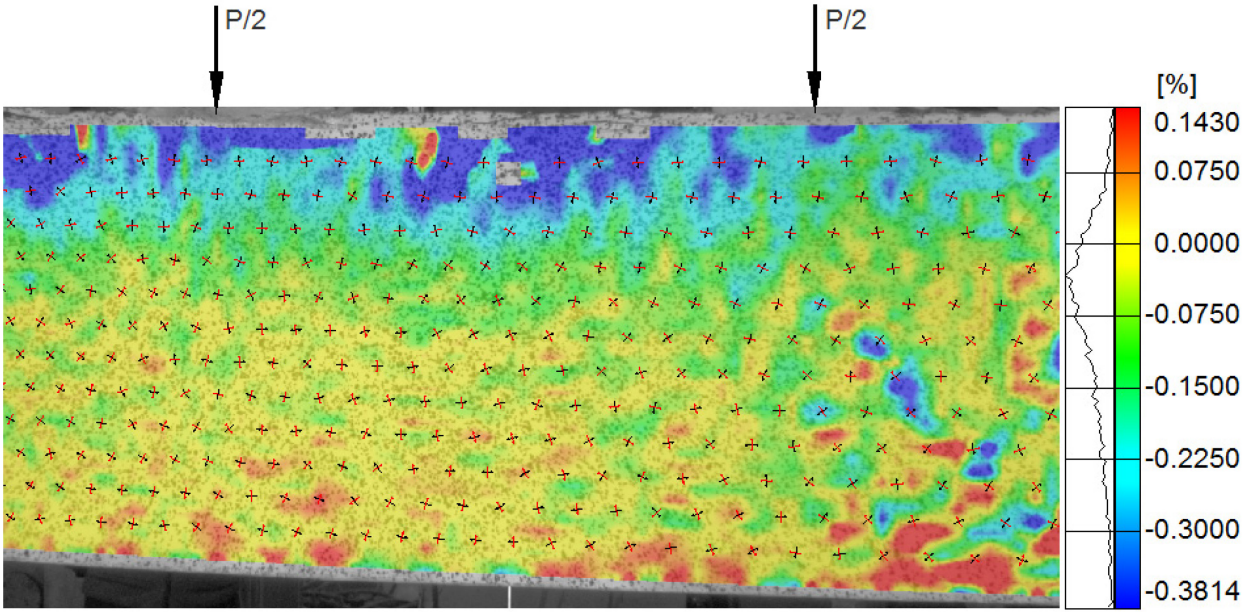

Figure 4-206 Full-field concrete minimum principal strain (σ_2) along moment region for SFRC#3 at an applied load 99.7 kips (peak load)

Comparison of load-deflection behaviors of different beams:

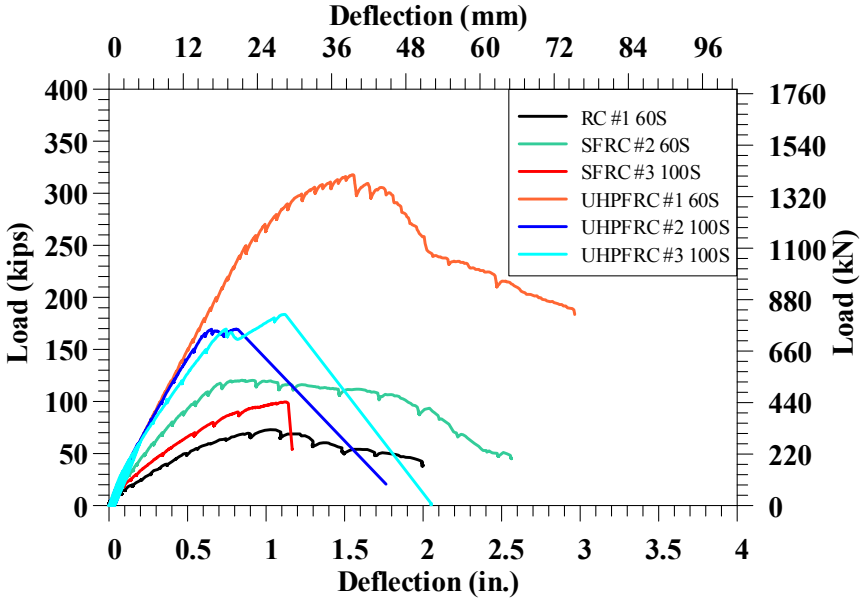

Figure 4-207 Load deflection behaviors of beams with steel reinforcement

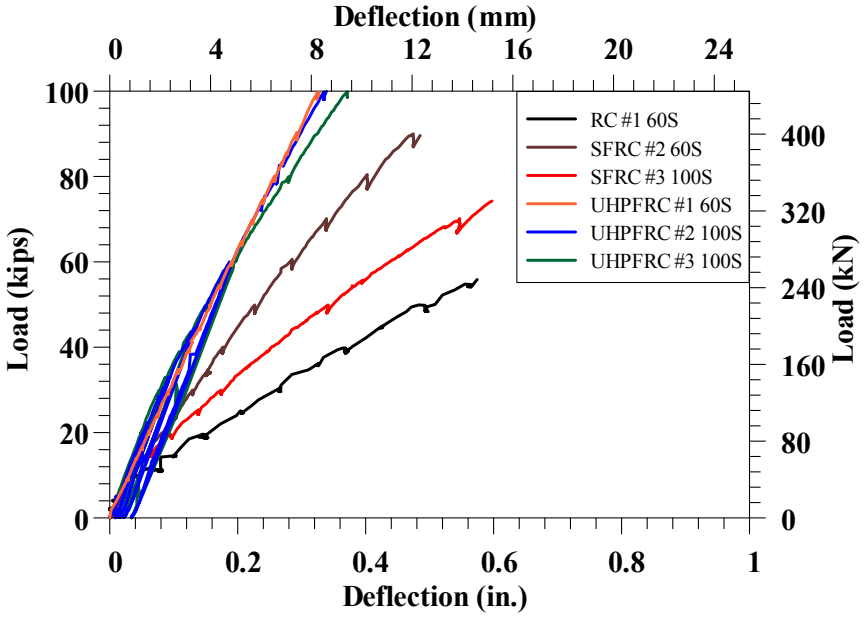

Figure 4-208 Comparison of stiffness of load deflection plots of beams with steel reinforcement

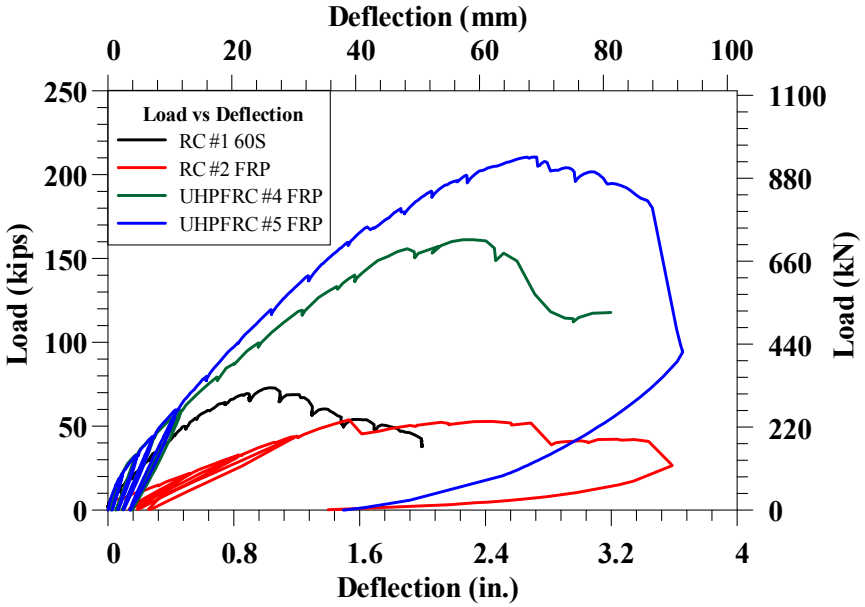

Figure 4-209 Load deflection behavior of beams with BFRP reinforcement

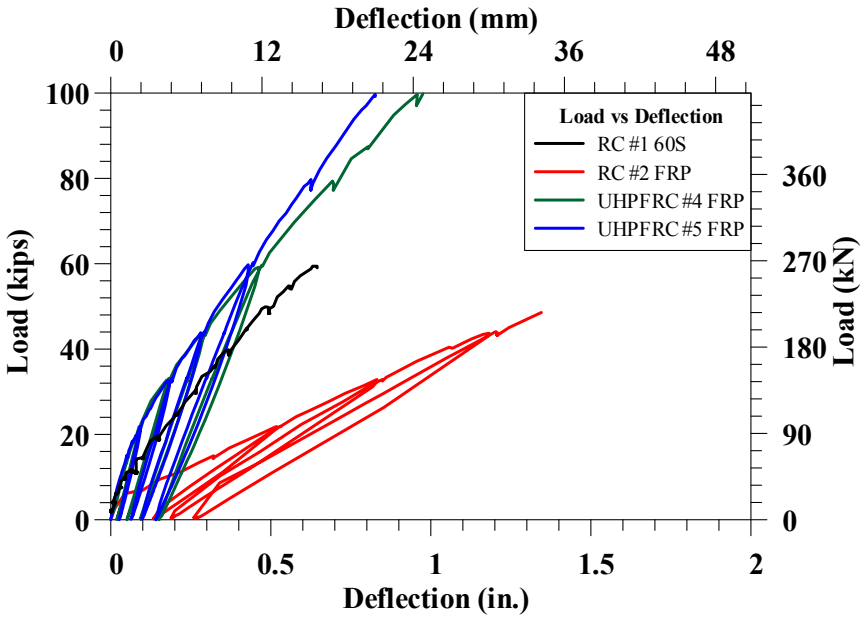

Figure 4-210 Stiffness of beams with BFRP reinforcement

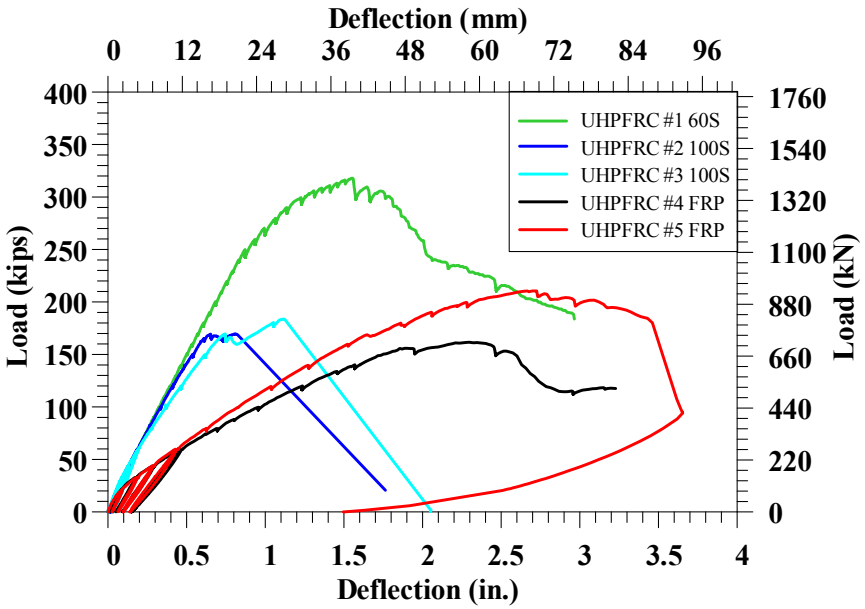

Figure 4-211 Load deflection behavior of all UHP-FRC beams

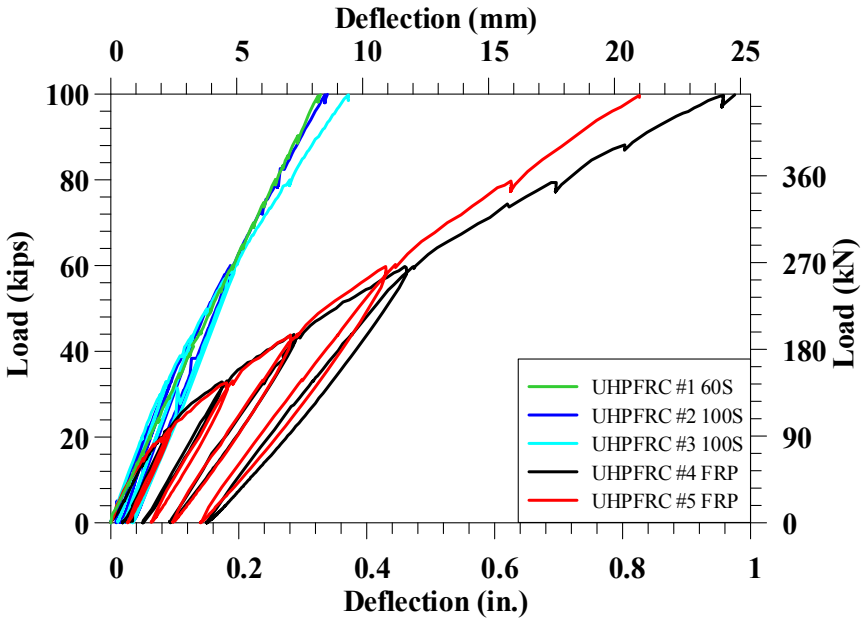

Figure 4-212 Initial stiffness of all load deflection plots

Figures 4-213 through 4-234 presents the tensile strains in flexural bars in constant moment region and shear span. The load vs strain relationships in constant moment region depicted a typical bilinear behavior up to peak load with a different degree of increase in reinforcement strains after initiation of cracking. RC beam reinforced with BFRP bars (RC #2 BFRP) has shown a sudden increase in reinforcement strains after cracking, conversely UHP-FRC beams has shown a steadier rise of strains in post cracking stage.

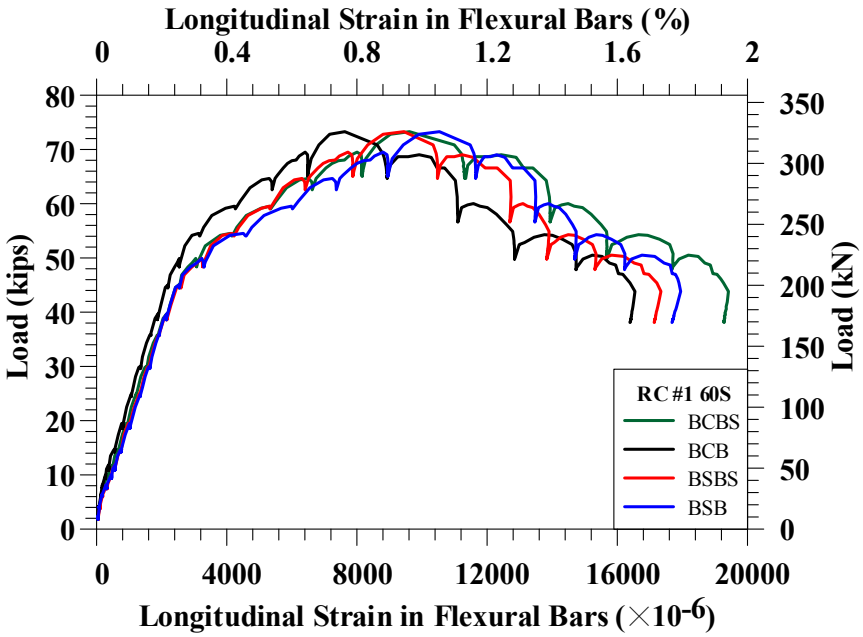

Figure 4-213 Load versus longitudinal reinforcement strains for beam RC #1

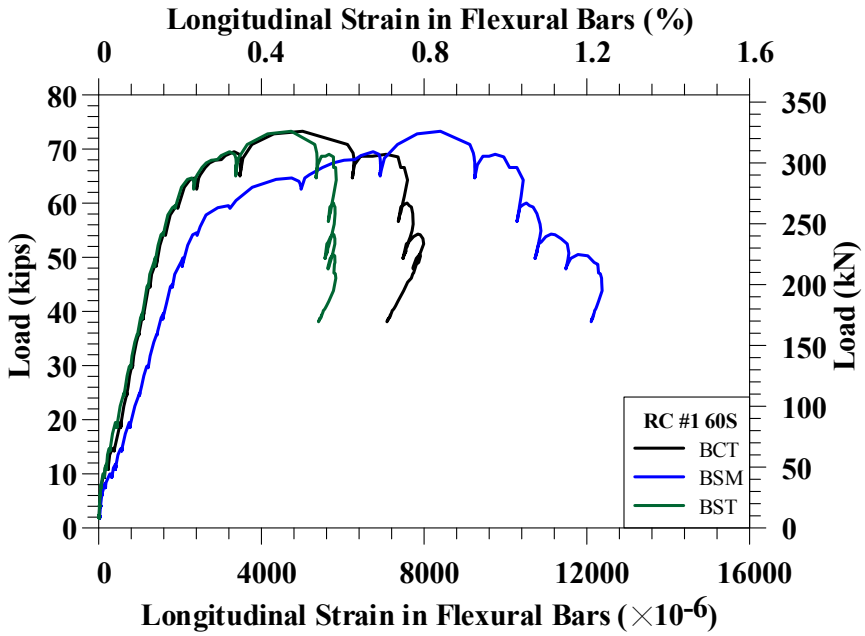

Figure 4-214 Load versus longitudinal reinforcement strains for beam RC #1

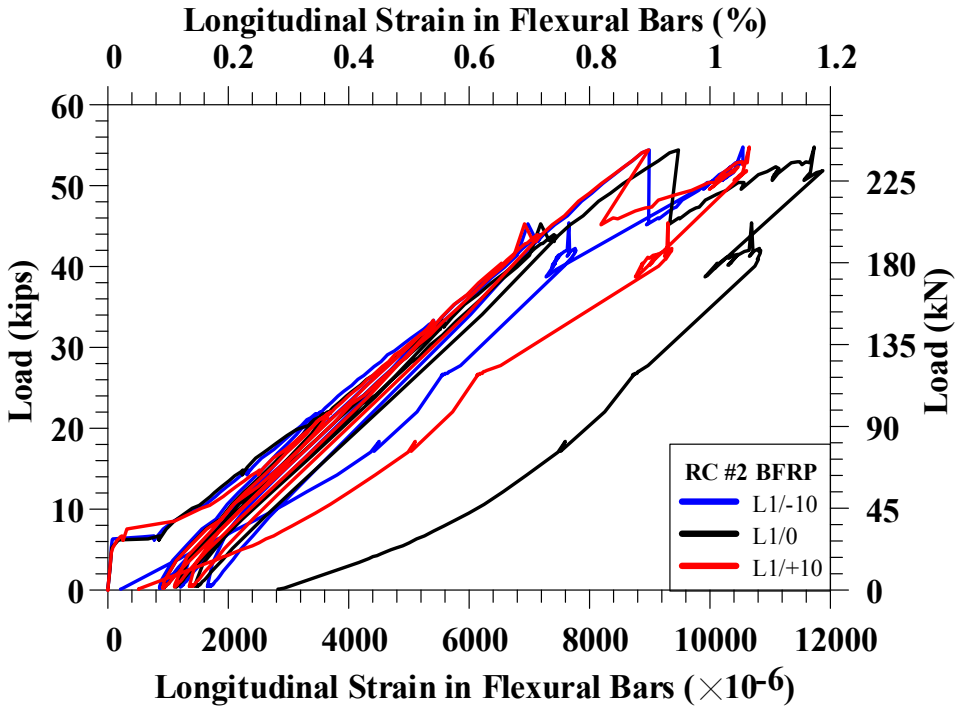

Figure 4-215 Load versus longitudinal reinforcement strains for beam RC #2

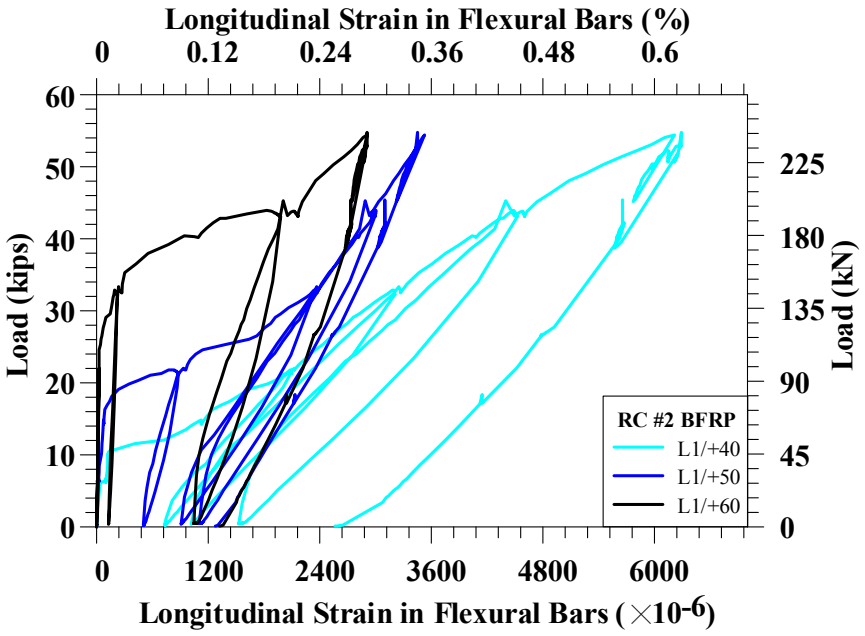

Figure 4-216 Load versus longitudinal reinforcement strains for beam RC #2

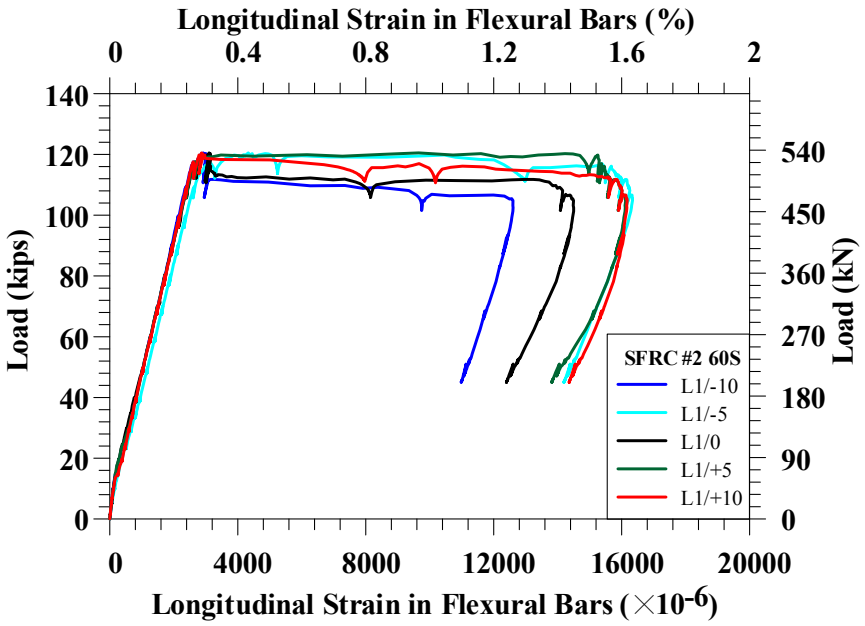

Figure 4-217 Load versus longitudinal reinforcement strains for beam SFRC #2

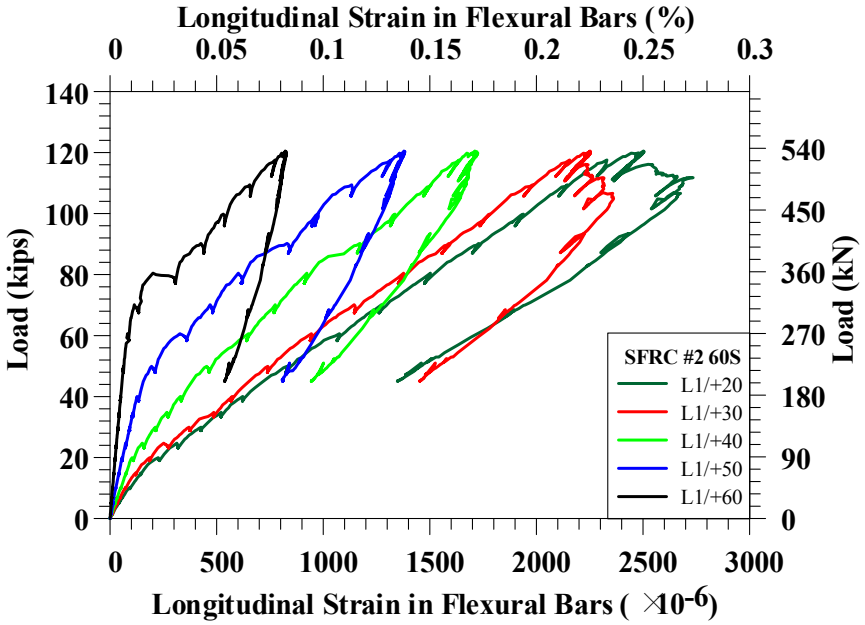

Figure 4-218 Load versus longitudinal reinforcement strains for beam SFRC #2

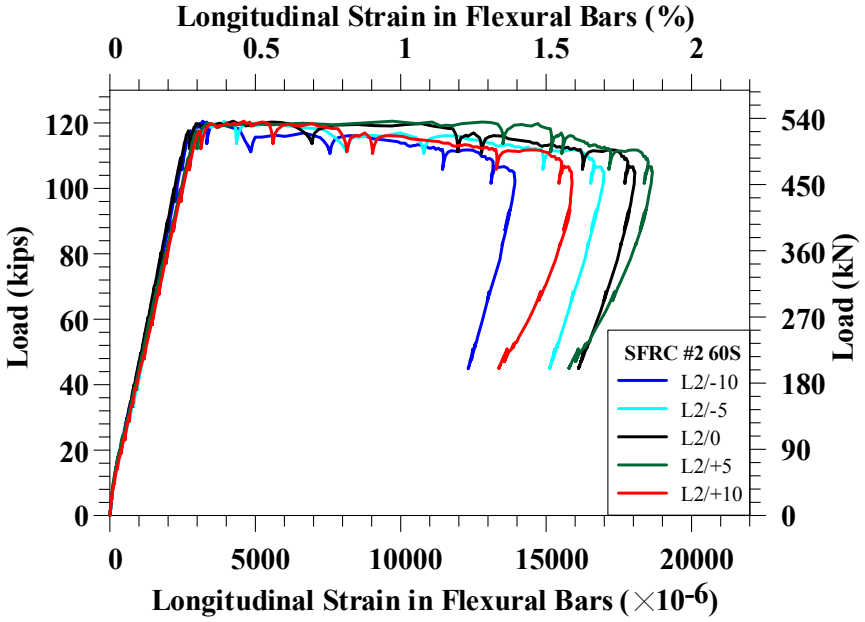

Figure 4-219 Load versus longitudinal reinforcement strains for beam SFRC # 2

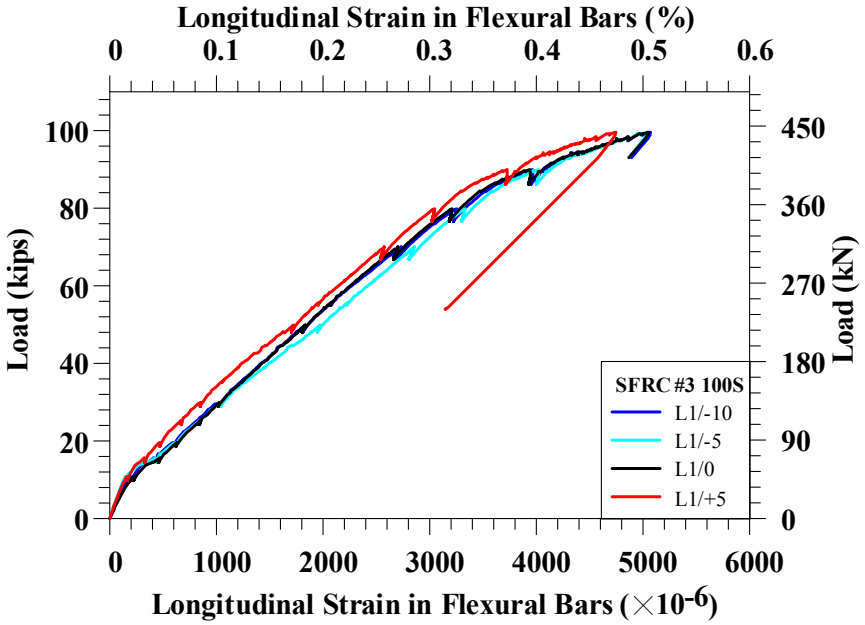

Figure 4-220 Load versus longitudinal reinforcement strains for beam SFRC # 3

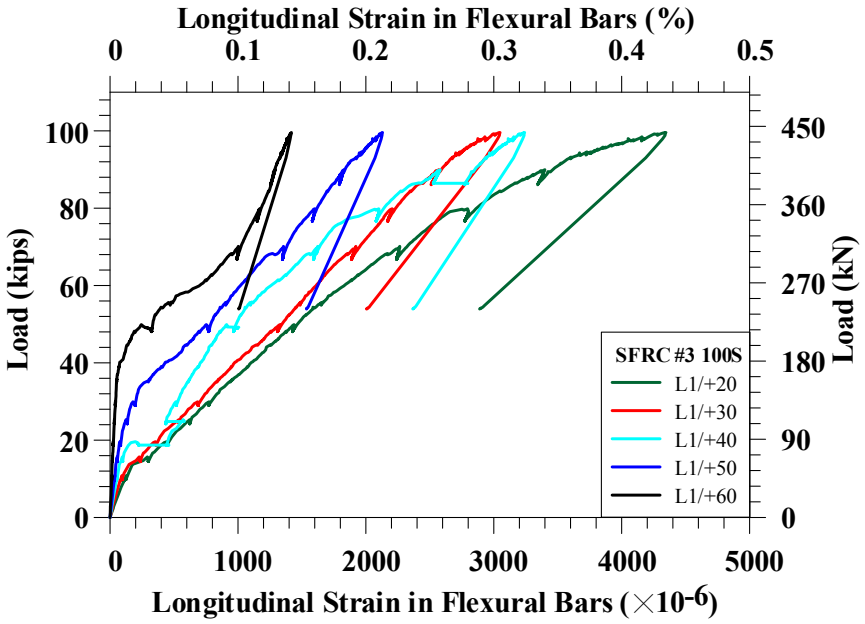

Figure 4-221 Load versus longitudinal reinforcement strains for beam SFRC # 3

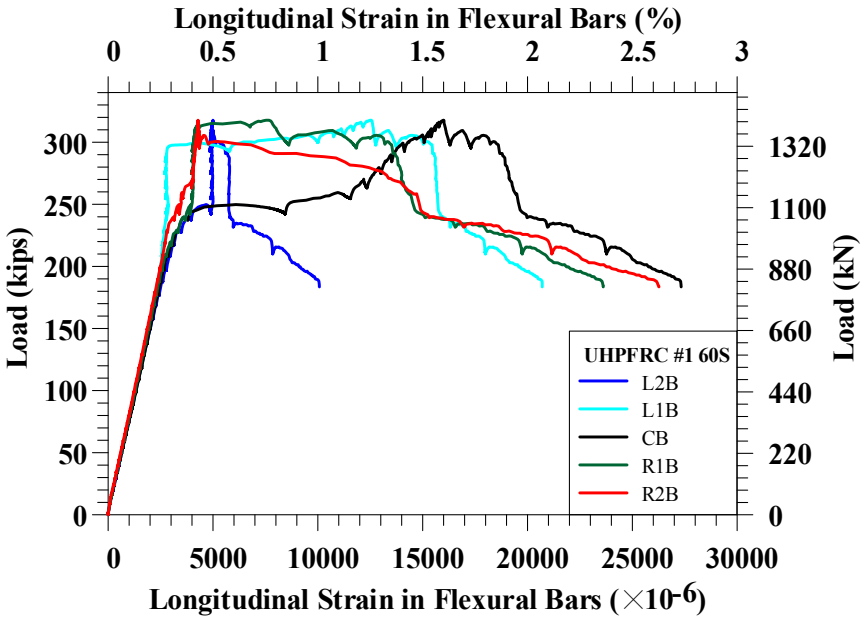

Figure 4-222 Load versus longitudinal reinforcement strains for beam UHP-FRC # 1

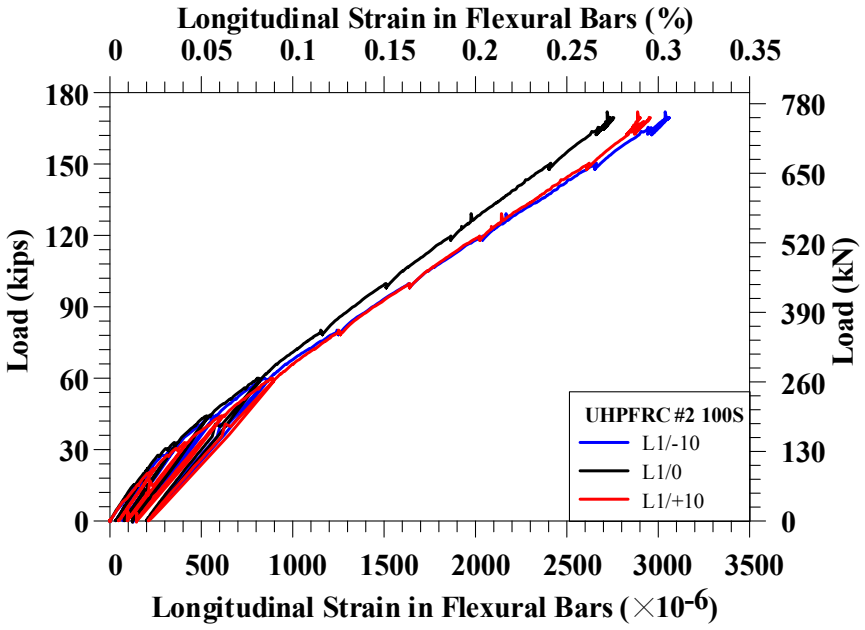

Figure 4-223 Load versus longitudinal reinforcement strains for beam UHP-FRC #2

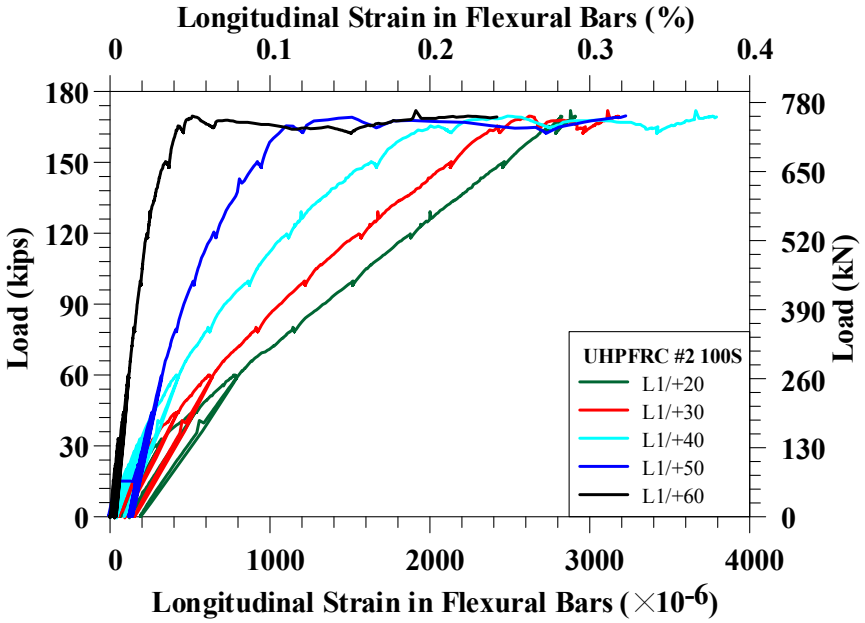

Figure 4-224 Load versus longitudinal reinforcement strains for beam UHP-FRC # 2

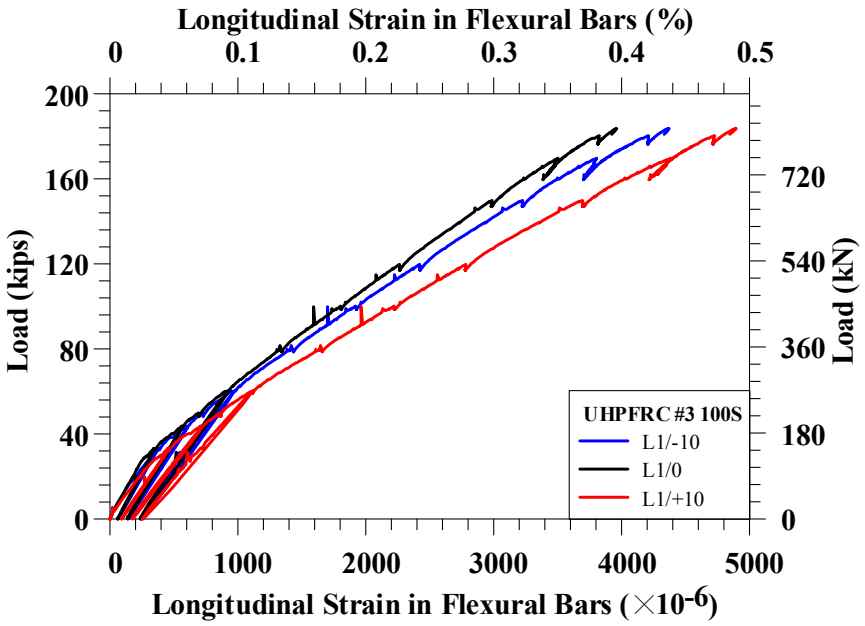

Figure 4-225 Load versus longitudinal reinforcement strains for beam UHP-FRC # 3

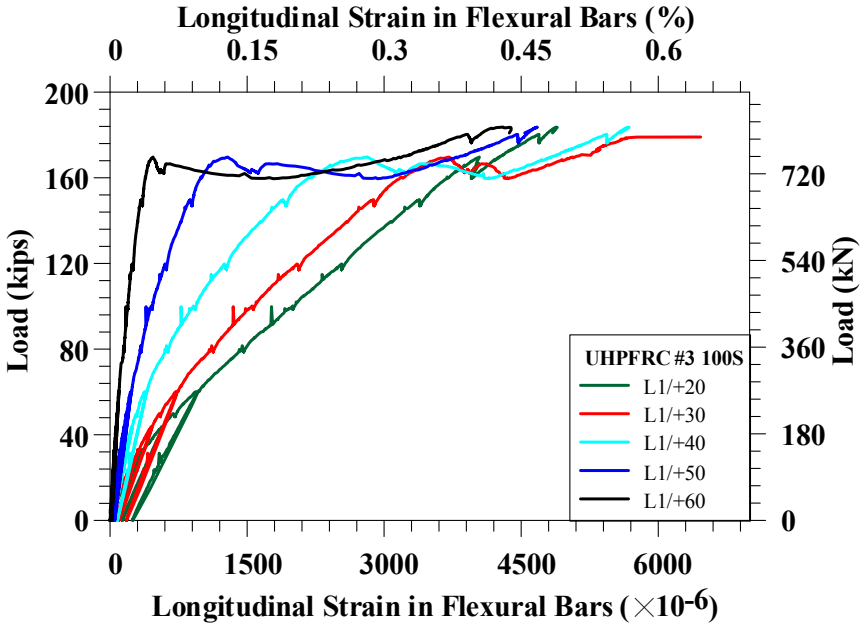

Figure 4-226 Load versus longitudinal reinforcement strains for beam UHP-FRC #3

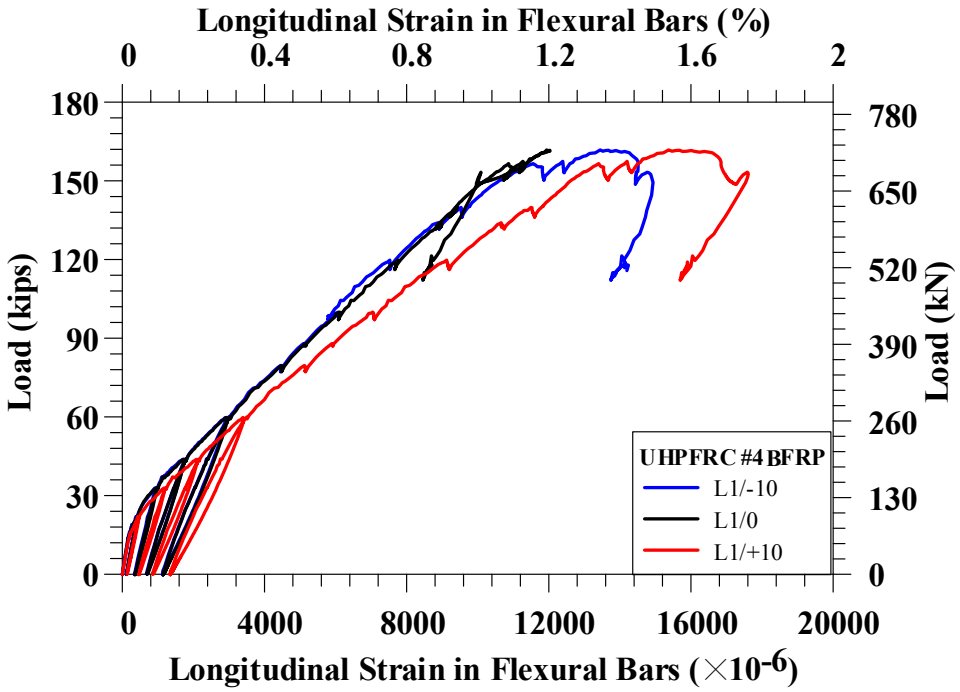

Figure 4-227 Load versus longitudinal reinforcement strains for beam UHP-FRC # 4

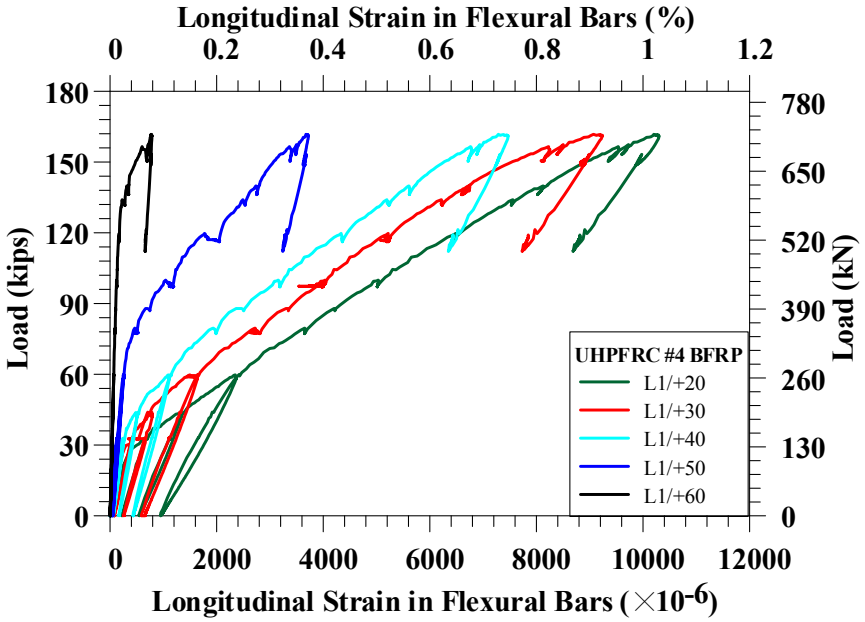

Figure 4-228 Load versus longitudinal reinforcement strains for beam UHP-FRC # 4

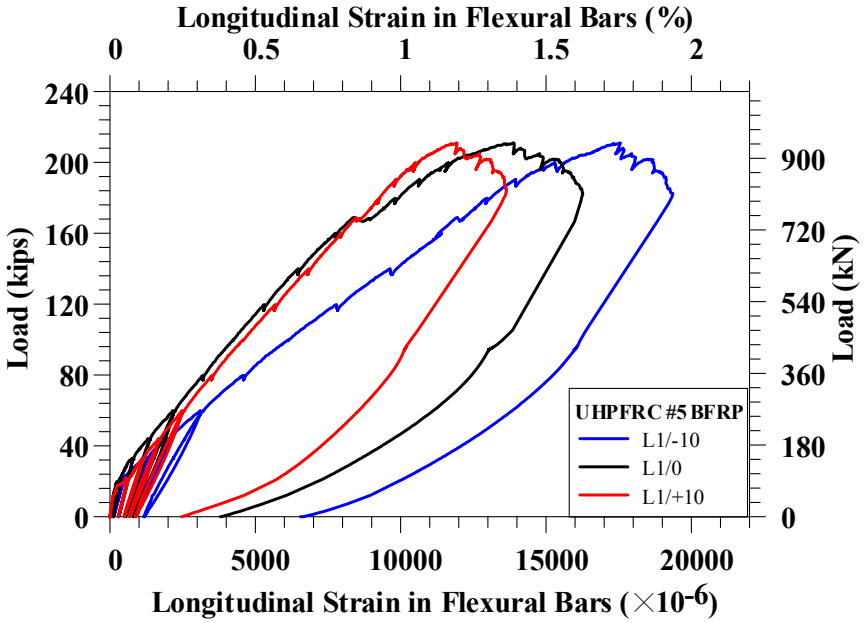

Figure 4-229 Load versus longitudinal reinforcement strains for beam UHP-FRC # 5

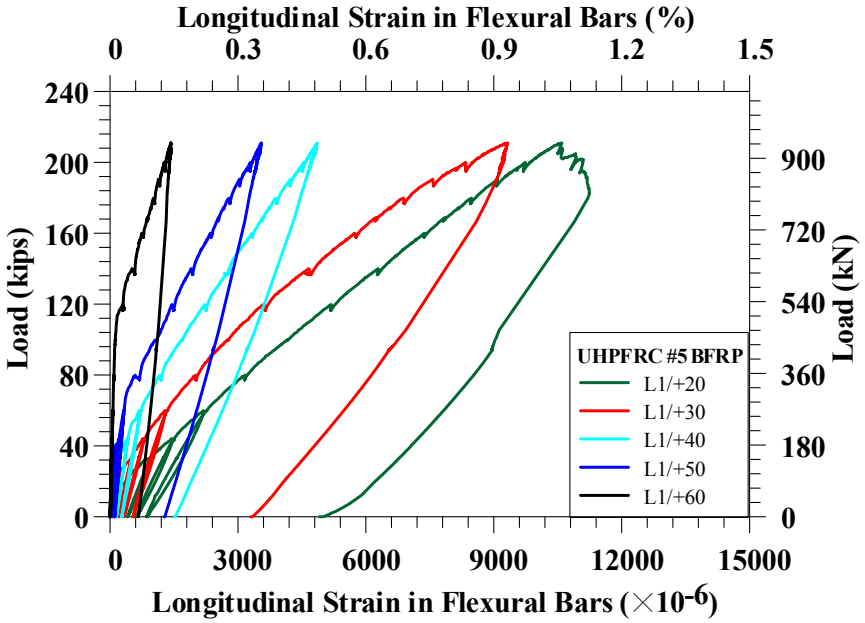

Figure 4-230 Load versus longitudinal reinforcement strains for beam UHP-FRC # 5

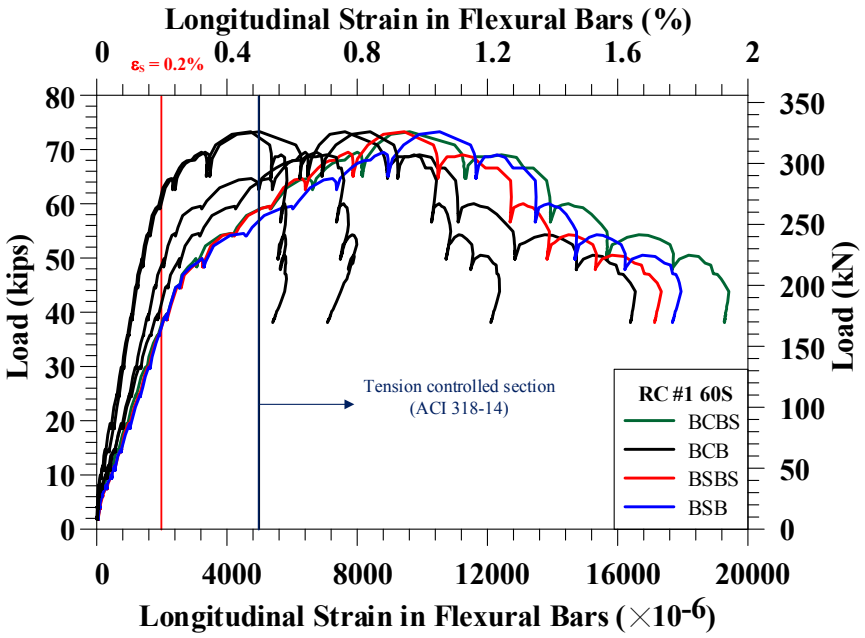

Figure 4-231 Load versus longitudinal reinforcement strains for beam RC # 1

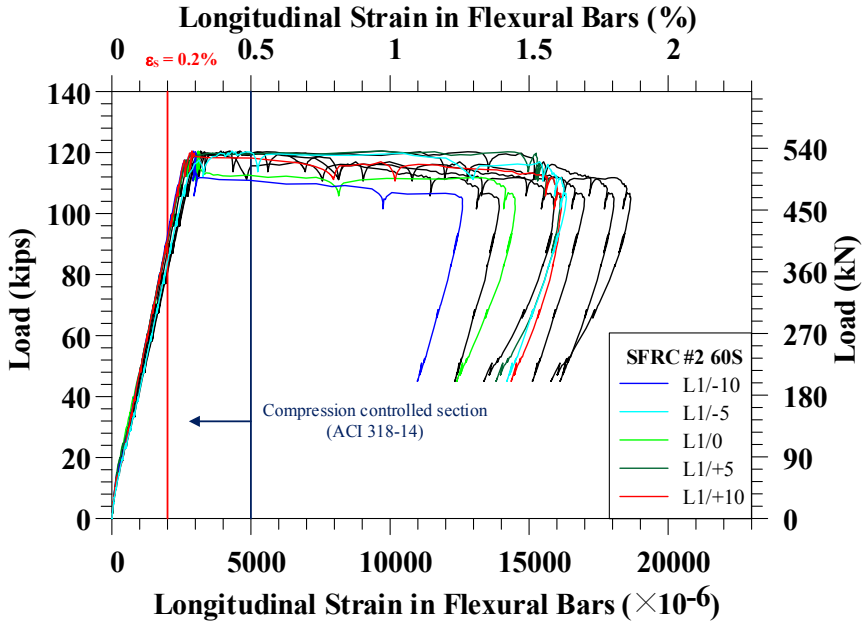

Figure 4-232 Load versus longitudinal reinforcement strains for beam SFRC # 2

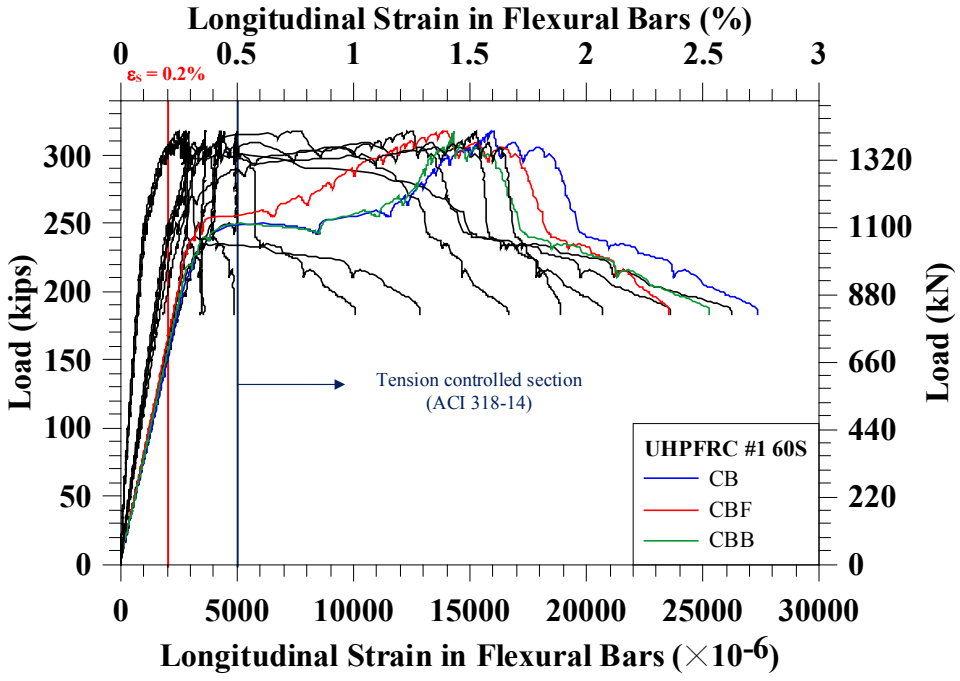

Figure 4-233 Load versus longitudinal reinforcement strains for beam UHP-FRC # 1

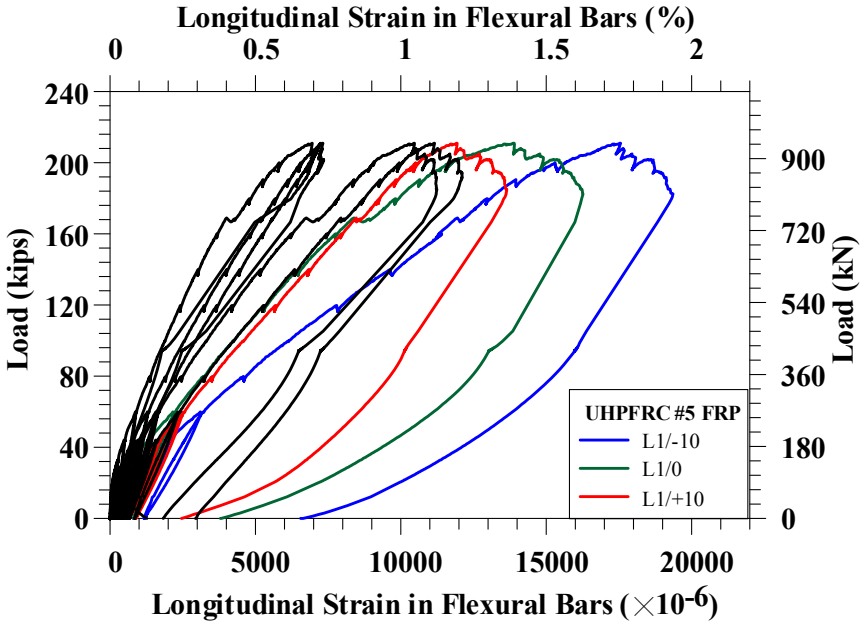

Figure 4-234 Load versus longitudinal reinforcement strains for beam UHP-FRC # 5

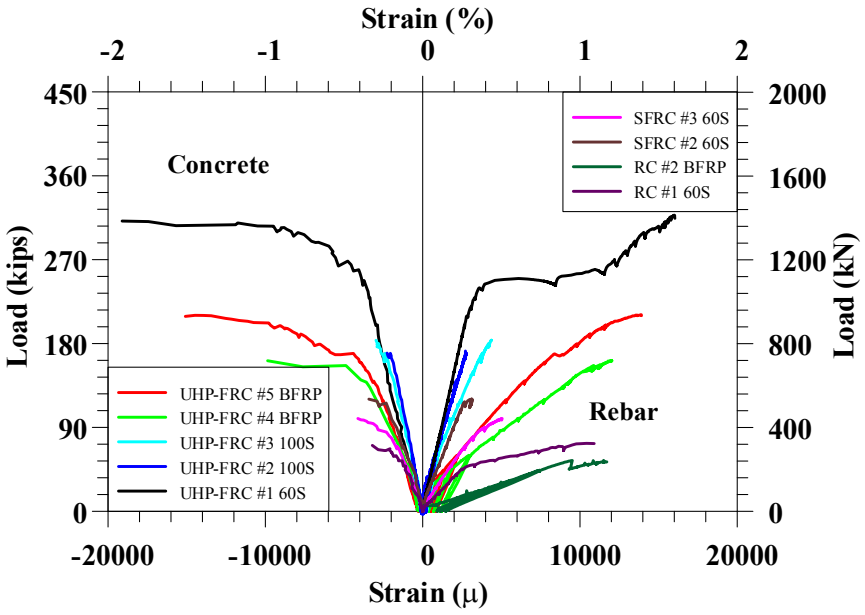

Figure 4-235 Load versus concrete and longitudinal reinforcement strains for all tested beams

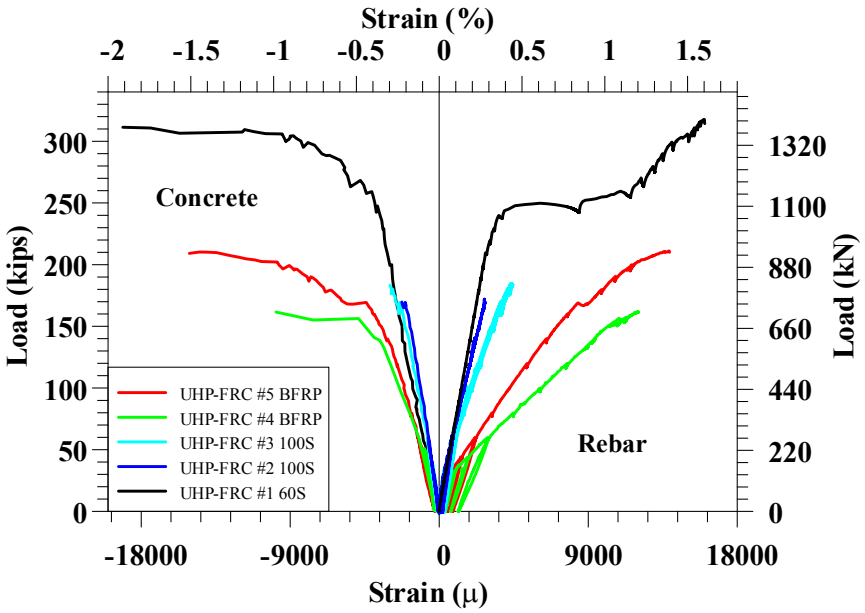

Figure 4-236 Load versus concrete and longitudinal reinforcement strains for UHP-FRC beams

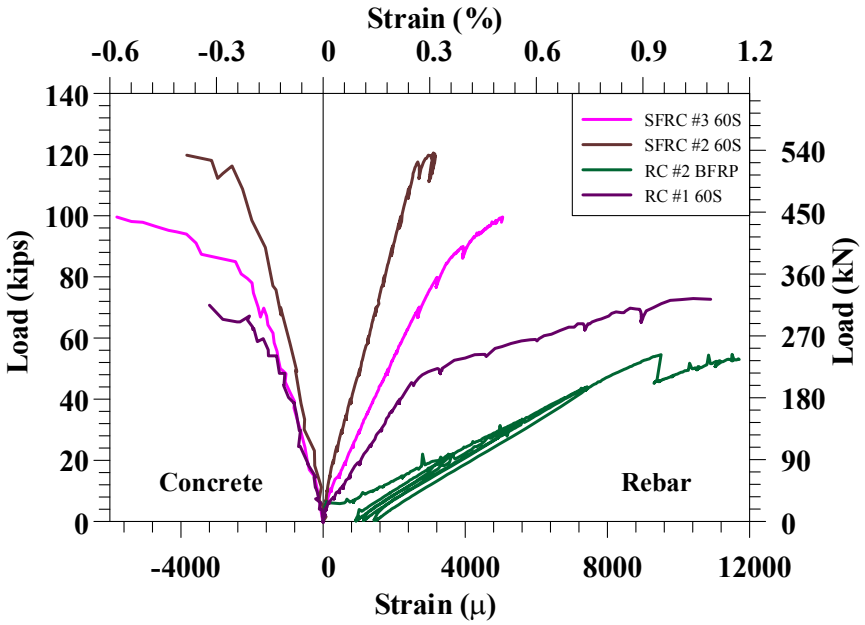

Figure 4-237 Load versus concrete and longitudinal reinforcement strains for RC and SFRC beams

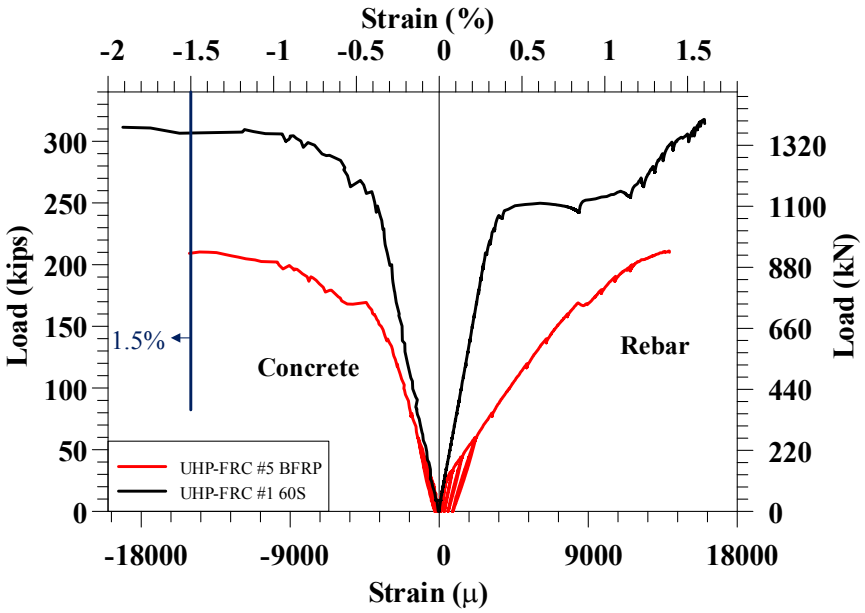

Figure 4-238 Measured concrete strain of 1.5% in UHP-FRC beams

Chapter 5

Part I: Summary and Conclusions

5.1 Summary

In this thesis, the author has presented a new class of concrete material, Ultra-High-Performance Fiber-reinforced concrete (UHP-FRC). Because of its increased strength, stiffness, ductility and durability UHP-FRC has become an attractive choice of material in structural design. Furthermore, its ability to lend itself into complex geometries and into very thin elements makes it suitable for Architectural applications. Both the structural and architectural applications are verified experimentally during this research program.

A total of nine beams were tested amongst which five were casted with UHP-FRC with the following objectives:

1. To determine if the full compressive stress-strain curve can be used to design or predict the flexural capacity of structural members.
2. To determine the shear strength and behavior of UHP-FRC beams.
3. To investigate the flexural behavior and serviceability performance of UHP-FRC beams reinforced with BFRP bars.

Table 5-1 Summary of cracking moments and modulus of rupture observed from beam testing

Specimen	Cracking load, kips (kN)	Cracking Moment, kip-inch (kN-m)	Modulus of rupture, ksi (MPa)
RC #1	12 (53)	342 (39)	0.76 (5.24)
RC #2	6 (27)	171 (19)	0.42 (2.90)
SFRC #2	25 (111)	713 (81)	1.25 (8.61)
SFRC #3	15 (67)	428 (48)	0.90 (6.21)
UHP-FRC #1	60 (267)	1,710 (193)	3.18 (21.92)
UHP-FRC #2	60 (267)	1,710 (193)	2.78 (19.17)
UHP-FRC #3	50 (222)	1,425 (161)	2.67 (18.41)
UHP-FRC #4	22 (98)	627 (71)	1.47 (10.14)
UHP-FRC #5	22 (98)	627 (71)	1.42 (9.79)

Note: Modulus of rupture calculated using un-cracked transformed section properties

5.1.1 Moment versus curvature behavior of UHP-FRC beams:

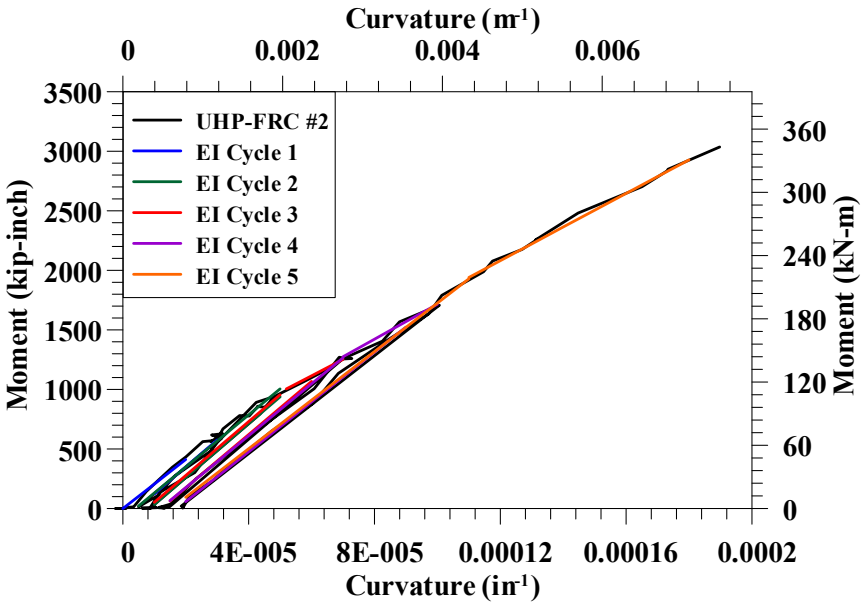

Figure 5-1 Moment versus curvature behavior showing initial stiffness of beam UHP-FRC #2

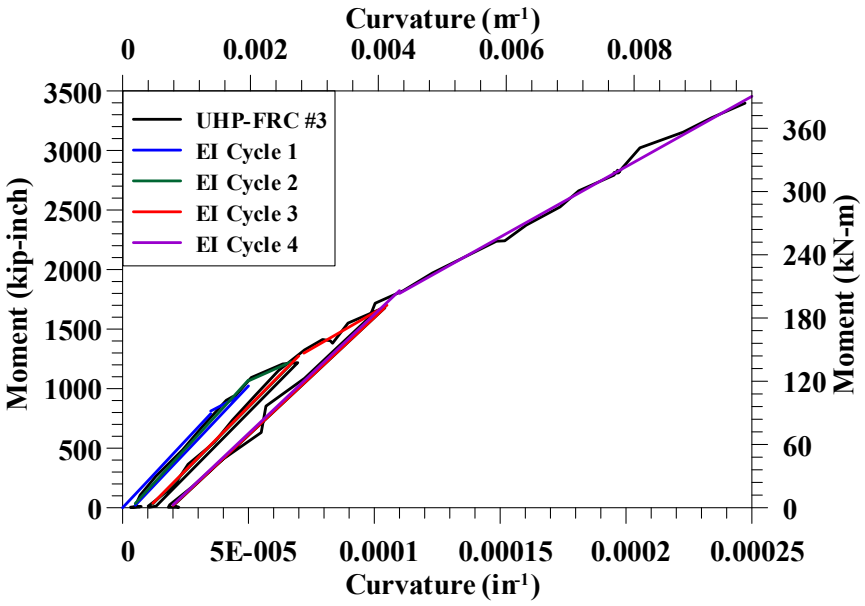

Figure 5-2 Moment versus curvature behavior showing initial stiffness of beam UHP-FRC #3

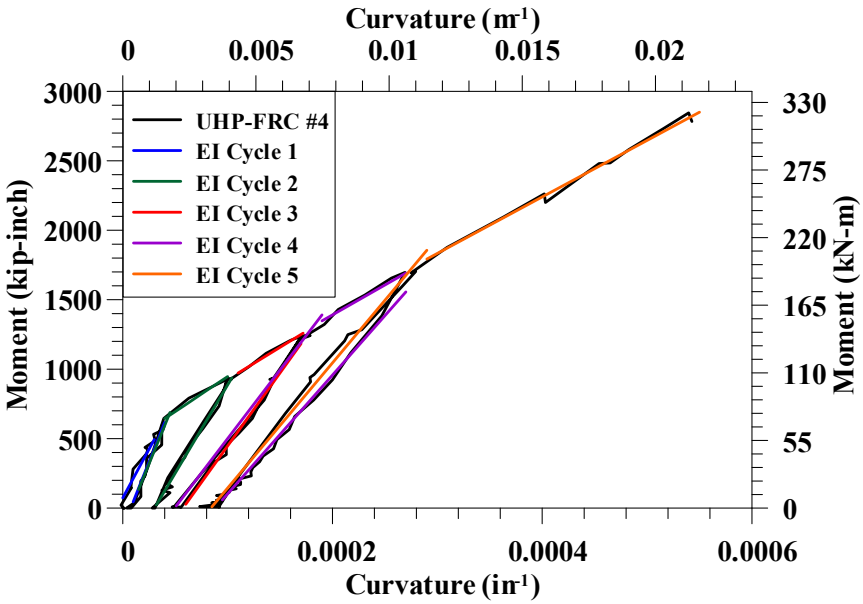

Figure 5-3 Moment versus curvature behavior showing initial stiffness of beam UHP-FRC #4

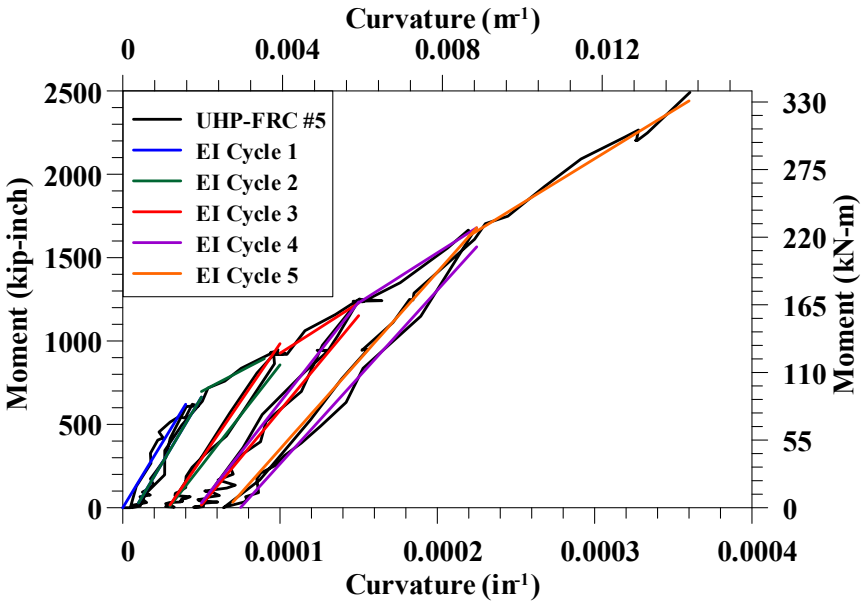

Figure 5-4 Moment versus curvature behavior showing initial stiffness of beam UHP-FRC #5

Table 5-2 Summary of stiffness of beam UHP-FRC #2

with loading and unloading cycles

UHP-FRC #2		**EI (kip-in^2)**
Cycle 1 loading		20.6×10^6
Cycle 1 unloading		22.7×10^6
Cycle 2 loading		21.9×10^6
Cycle 2 unloading		22.6×10^6
Cycle 3 loading	Segment 1	22.6×10^6
	Segment 2	13.7×10^6
Cycle 3 unloading		22.3×10^6
Cycle 4 loading	Segment 1	21.8×10^6
	Segment 2	14.7×10^6
Cycle 4 unloading		20.9×10^6
Cycle 5 loading	Segment 1	20.4×10^6
	Segment 2	14.1×10^6

Table 5-3 Summary of stiffness of beam UHP-FRC #3

with loading and unloading cycles

UHP-FRC #3		**EI (kip-in^2)**
Cycle 1 loading	Segment 1	22.6×10^6
	Segment 2	11.2×10^6
Cycle 1 unloading		22.3×10^6
Cycle 2 loading	Segment 1	23.0×10^6
	Segment 2	9.4×10^6
Cycle 2 unloading		21.3×10^6
Cycle 3 loading	Segment 1	21.3×10^6
	Segment 2	12.2×10^6
Cycle 3 unloading		19.7×10^6
Cycle 4 loading	Segment 1	20.0×10^6
	Segment 2	11.8×10^6

Table 5-4 Summary of stiffness of beam UHP-FRC #4

with loading and unloading cycles

UHP-FRC #4		**EI (kip-in^2)**
Cycle 1 loading		14.0×10^6
Cycle 1 unloading		19.0×10^6
Cycle 2 loading	Segment 1	18.5×10^6
	Segment 2	5.0×10^6
Cycle 2 unloading		12.7×10^6
Cycle 3 loading	Segment 1	11.8×10^6
	Segment 2	4.6×10^6
Cycle 3 unloading		10.5×10^6
Cycle 4 loading	Segment 1	9.9×10^6
	Segment 2	4.3×10^6
Cycle 4 unloading		8.6×10^6
Cycle 5 loading	Segment 1	9.0×10^6
	Segment 2	4.1×10^6

Table 5-5 Summary of stiffness of beam UHP-FRC #5

with loading and unloading cycles

UHP-FRC #5		**EI (kip-in^2)**
Cycle 1 loading		15.5×10^6
Cycle 1 unloading		15.9×10^6
Cycle 2 loading	Segment 1	15.9×10^6
	Segment 2	4.9×10^6
Cycle 2 unloading		12.1×10^6
Cycle 3 loading	Segment 1	13.8×10^6
	Segment 2	6.0×10^6
Cycle 3 unloading		11.4×10^6
Cycle 4 loading	Segment 1	12.0×10^6
	Segment 2	6.0×10^6
Cycle 4 unloading		10.4×10^6
Cycle 5 loading	Segment 1	10.6×10^6
	Segment 2	5.8×10^6

5.1.2 Summary of crack widths from beam test

Table 5-6 Summary of crack widths of beam RC #2

Load (kips)	Crack width (mm)
6	< 0.1
15	0.25
22	0.4
33	0.6
44	0.8

Table 5-7 Summary of crack widths of beam SFRC #2

Load (kips)	Crack width (mm)
35	0.1
40	0.1
50	0.1
60	0.1
70	0.1
80	0.15
90	0.15
100	0.2
110	0.2
120	1.5

Table 5-8 Summary of crack widths of beam SFRC #3

Load (kips)	Crack width (mm)
30	0.1
50	0.15
70	0.15
80	0.3
90	0.3

Table 5-9 Summary of crack widths of beam UHP-FRC #1

Load (kips)	Crack width (mm)
250	< 0.1
290	0.15
300	0.25
310	0.5
317	0.7

Table 5-10 Summary of crack widths of

beam UHP-FRC #2

	Load (kips)	Crack width (mm)
Cycle 1	22	No crack
	0	No crack
Cycle 2	33	No crack
	0	No crack
Cycle 3	44	No crack
	0	No crack
Cycle 4	60	< 0.1
	0	Closed completely
Cycle 5	60	< 0.1
	100	0.1
	150	0.2

Table 5-11 Summary of crack widths of

beam UHP-FRC #3

	Load (kips)	Crack width (mm)
Cycle 1	33	No crack
	0	No crack
Cycle 2	44	No crack
	0	No crack
Cycle 3	50	< 0.1
	60	0.1
	0	Closed completely
Cycle 4	50	< 0.1
	60	0.1
	80	0.1
	100	0.25
	120	0.3
	150	0.3

Table 5-12 Summary of crack widths of

beam UHP-FRC #4

	Load (kips)	Crack width (mm)
Cycle1	22	< 0.1
	0	< 0.1
Cycle2	33	0.1
	0	< 0.1
Cycle3	33	0.1
	44	0.25
	0	0.1
Cycle4	33	0.2
	44	0.3
	60	0.3
	0	0.15
Cycle5	33	0.3
	44	0.3
	60	0.35
	80	0.6
	100	0.8
	120	1.5
	140	2.5

Table 5-13 Summary of crack widths of

beam UHP-FRC #5

	Load (kips)	Crack width (mm)
Cycle1	22	< 0.1
	0	< 0.1
Cycle2	33	0.1
	0	< 0.1
Cycle3	33	0.1
	44	0.15
	0	<0.1
Cycle4	33	0.15
	44	0.15
	60	0.2
	0	0.1
Cycle5	33	0.15
	44	0.15
	60	0.2
	80	0.3
	120	0.8
	140	1.5
	160	1.5
	180	2.0

Table 5-14 Drop in the depth of compression zone after initial crack

Specimen	Un-cracked transformed N.A (in.)	N.A position after initial crack (in.)
RC #1	8.4	4.5 (53.6%)
RC #2	8.2	2.8 (34.1%)
UHP-FRC #1	8.9	8.4 (94.4%)
UHP-FRC #2	9.1	6.6 (72.5%)
UHP-FRC #3	8.8	6.5 (73.8%)
UHP-FRC #4	8.3	4.7 (56.6%)
UHP-FRC #5	8.4	5.4 (64.3%)

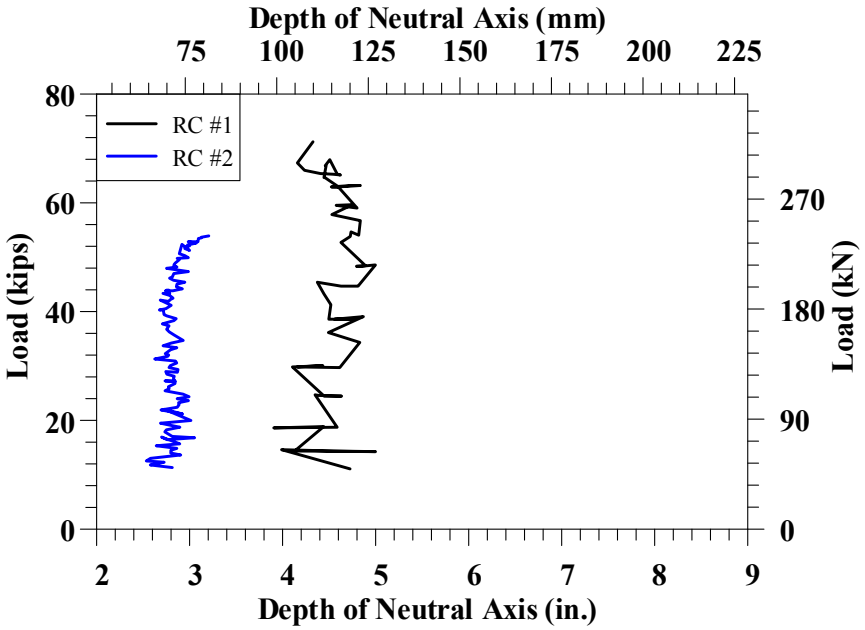

Figure 5-5 Load versus depth of compression zone for RC beams

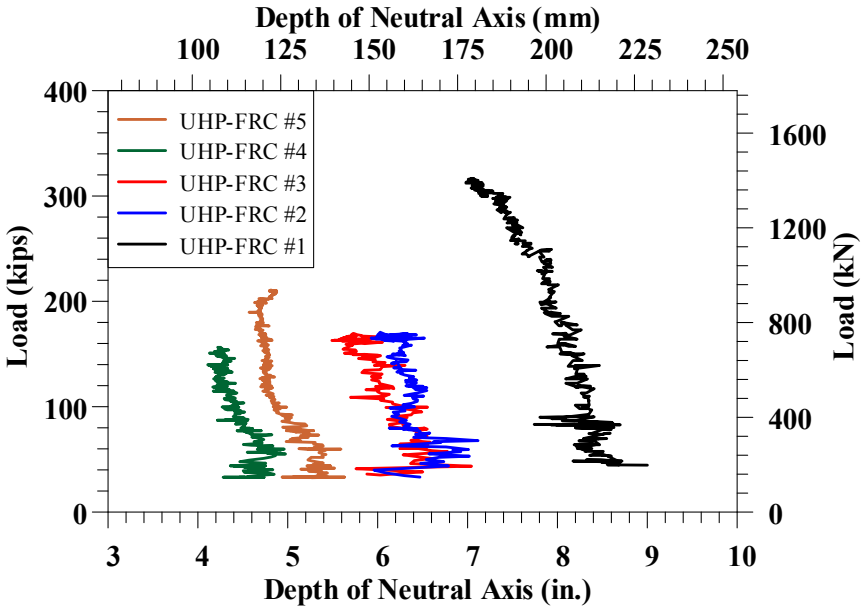

Figure 5-6 Load versus depth of compression zone for UHP-FRC beams

5.1.3 Concept of replacing prestressed concrete flexural structural members with un-prestressed UHP-FRC members

Experimental results have shown that UHP-FRC flexural members had very high strength and stiffness compared to counterpart RC and SFRC beams. UHP-FRC beams maintained high stiffness until very higher loads and had significantly higher cracking loads. These properties of utilizing the entire/maximum cross-section in resisting the external moments are comparable with prestressed concrete structural members. Hence the experimental results observed from beam testing were extended to design standard precast/prestress flexural structural members with UHP-FRC without prestressing subsequently cracking and deflection behavior were compared at service level loads. Cracking load is a main controlling parameter in design of flexural concrete members with UHP-FRC, as the cracking load in prestressed members is controlled by amount of prestress. However, for UHP-FRC elements cracking loads merely depends on the section modulus, hence the reader is advised to modify standard cross-sections with lower section modulus to replace prestressed concrete members with un-

prestressed UHP-FRC members. Several most commonly used standard precast elements were designed with both maximum allowable prestress and un-prestressed UHP-FRC. Designed elements include a rectangular beam, Tx 54 girder, Decked Bulb-Tee girder, precast framing elements including Double Tee and Inverted Tee.

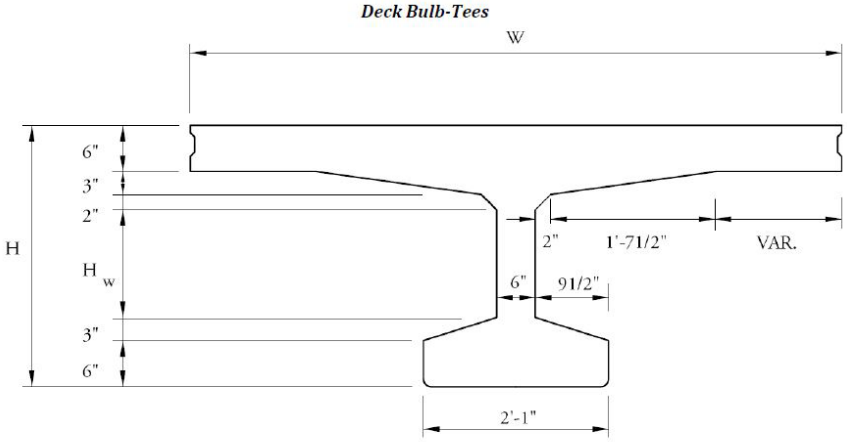

Figure 5-7 Standard decked bulb Tee – 65 [PCI Bridge design manual]

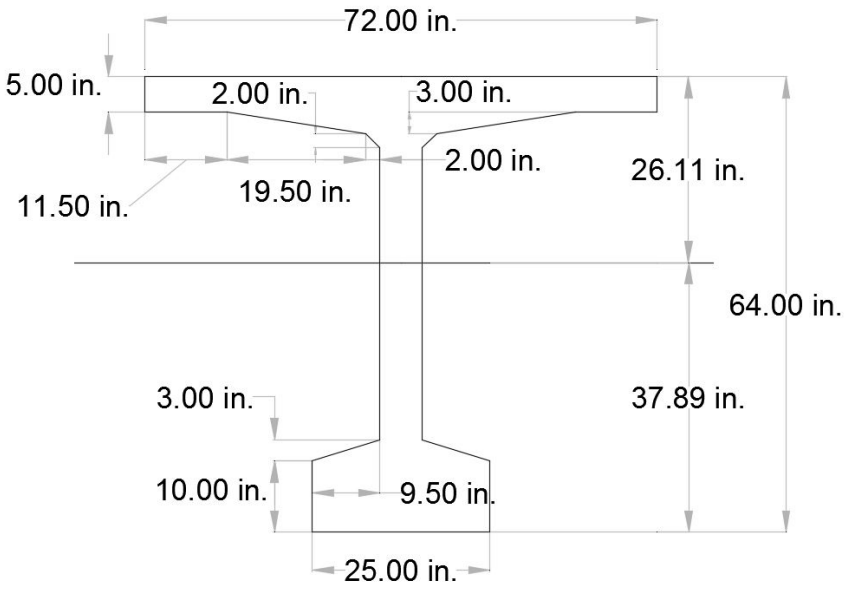

Figure 5-8 Modified/proposed decked bulb Tee – 64 for UHP-FRC

5.2 Conclusions

1. Considering the high compressive ductility of UHP-FRC, a maximum useable compressive strain ε_{cu} = 0.015 can be used for design of flexural members. This leads to a higher load-carrying capacity, which is 4.5 to 5 times greater than that of its counterpart RC beam, designed with tension-controlled behavior as recommended by ACI 318 and AASHTO LRFD Specifications. To simplify the design, other stress block design parameters such as the β1 factor could be the same for plain concrete. Experimental results indicated that longitudinal reinforcing bars in the beam UHP-FRC #1 reached a strain of 0.013 and higher, well beyond the 0.005 threshold for a tension-controlled section.
2. The UHP-FRC beam remained un-cracked in the constant moment region up to nearly 90% of the peak load. The beam showed very large deflection even with a few small flexural cracks. This is very different behavior as compared to conventional RC beams, and indicates a significant synergetic action and tension-stiffening effect between the reinforcing bars and UHP-FRC to carry the tensile stresses. The contribution of the tensile stress from UHP-FRC to the moment capacity warrants further study.
3. Average lower bound shear strength observed from two beams reinforced with high strength steel is $4.7\sqrt{f_c'} = 697\ psi$ which is five times higher than conventional concrete ($2\sqrt{f_c'} = 141\ psi$).
4. The UHP-FRC beams with Grade 100 steel and BFRP reinforcement showed typical bilinear behavior for strain and deflection until failure. Stiffness of the beams before initial cracking and cracking loads was nearly the same for UHP-FRC beams because they are governed by gross concrete section. However the behavior of beams after initial cracking is effected by the reinforcement ratio.

5. UHP-FRC beams reinforced with BFRP bars failed due to concrete crushing as they were designed as compression controlled sections. The beams showed distributed flexural cracks with no signs of slippage of the tensile reinforcement.
6. After initial cracking the UHP-FRC beams with BFRP reinforcement showed sharp increase in strains and deflection after initial cracking compared to UHP-FRC beams with steel reinforcing bars. The sudden increase in strains resulted in wider and deeper cracks, which is reflected on the stiffness and the location of the neutral axis of the cracked section. Increasing the reinforcement ratio, however, increased the amount of absorbed energy at the first crack, which enhanced the behavior, as it controls the immediate increase in strain and initial crack width.
7. UHP-FRC beams with steel reinforcement sustained higher stiffness until very high loads and are subjected to very little drop in depth of the compression zone after initial cracking utilizing the maximum cross-section in resisting external applied moments. This property of exploiting entire section in resisting external loads is attributed to prestressed concrete, hence it is viable to replace prestressed concrete members with Un-prestressed UHP-FRC members.
8. The concept of replacing prestressed concrete members with un-prestressed UHP-FRC members is practical for cross-sections with higher section modulus. Whereas for the members with lower section modulus, the concept is feasible with slight modification of standard existing sections to increase the section modulus.
9. A modified section for most commonly used Decked Bulb-Tee girder has been proposed for replacing prestressed bridge girders with UHP-FRC girders without prestressing. A modulus of rupture of 3.0 ksi (observed from large scale beam tests in this research) for UHP-FRC has been used in modifying the standard section properties.

Chapter 6

Part II a: UHP-FRC for architectural structural columns with non-Euclidean geometries

6.1 Introduction

6.1.1 Biomimicry

Biomimicry or Biomimetics is an act of imitating models and elements of nature to solve intricate engineering problems. Biomimicry has been applied in multi-disciplinary subjects like architecture, electronics, medicines, biology, chemistry, mathematics etc. The term biomimetics was coined by American biophysist and polymath Otto Schmitt during the 1950s. From Velcro (inspired from dog fur, 1941) to Bullet train (inspired from kingfisher bird, 1990), nature has inspired the most impressive innovations of humans. Hull of sailboat of NASA manufactured in collaboration with 3M is yet another example of innovation inspired by nature. Sharks have a unique skin, layered with microscopic patterns called dentricles, which help reduce drag and keep them exceptionally clear from algae and fellow travelers. NASA scientists copied the patterns to create drag-reducing patterns they call riblets.

(a) (b)

Figure 6-1-1 (a) Patterns on skin of shark (b) NASA's sailing boat

6.1.2 Biomimetic Architecture

Biomimicry is one of the best sources of new ideas that allows us to go beyond standard approaches to sustainable design and achieve restorative solutions. Nature has been a source of inspiration for Architecture for a long time. Tree-inspired columns were designed by ancient Greeks and Romans by integrating natural motifs. Biomimetic architecture also attempts to use nature to solve problems of the building's functioning besides using nature as inspiration for the aesthetic components of built structure. One of the well-known example of using nature's functional forms to answer a structural problem is Sagrada Familia church by Antonio Gaudi. He modeled columns based on branching canopies of trees to solve statics problems in supporting the vault. Gaudi strived to create a state-of-the-art architecture with balanced and self-supporting Structure, in order to do so he spent 10 years constructing a 1:10 scaled upside-down hanging chain model consisting of weights on strings that would serve as an upside down model of the arched forms he looked for. Gaudi designed all the branching columns as double twisted columns formed by two helicoidal columns. The base of each column has a cross section that is a polygon or star which twists up and the right and the left branches transform into a circular cross-section higher up. Construction of Sagrada Familia commenced in 1882, Gaudi was involved in the project since 1883 and this Architectural marvel is anticipated to be completed by 2026.

(a)

(b)

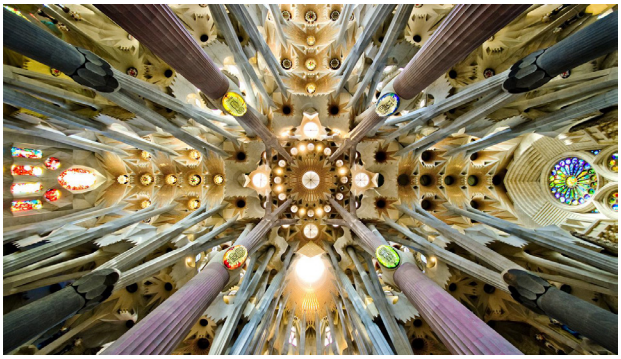

(c)

Figure 6-2 (a) Gaudi's hanging chain model, (b) Weight on strings and (c) Sagrada Familia roof and column detailing

One of the biggest influence of this research would be Antoni Gaudi's Sagrada Familia church. Gaudi's hanging chain model helped to predict the eccentric loading outcomes of non-Euclidean geometries. This approach allowed for 3D analysis to lead to maquettes (models built to scale) used to illustrate design intention to masons and fabricators. With the more recent introduction of computational toolsets, the increased capacity to quantitatively control and precisely optimize the performance of structural systems is now providing a very important area of research and exploration. As this relates to non-Euclidean geometry, there is an interest in exploring forms that may have a greater capacity of strength and efficiency as a result of modeling from biological references. Architects, engineers, and designers recognize the potential of the natural systems at work around them and have implemented design strategies to pursue performance driven outcomes that lead to new geometric possibilities.

Specifically, branching concrete columnar structures offer a unique opportunity to merge biomimetic form with structural geometry by implementing computationally controlled performance criteria. Because of advancements in the software used in the design and development process, precision of geometry or the ability to understand forces associated with asymmetrical loading, are no longer limited. Architects and engineers are now able to create digital models that will simulate loading patterns, material properties, and apply a physics engine calculation in order to derive optimized structural performance. In the case of columnar design, the geometric outcomes are now a byproduct of a range of parametric factors. What continues to make construction and fabrication challenging is not the formal generation or the analytical calculation, but rather the reinforcement fabrication when pursuing a standardized construction process.

6.2 Background:

A prototypical free form columnar branched structure, Cast Thicket was developed by collaboration of Yogiaman Tracy design (Yo-Cy), TEX-FAB fabrication network, the TOPOCAST lab and Buro Happold Engineering. Cast thicket uses tensile concrete moulds through the use of plastic formwork leveraging the fluid materiality of concrete and machinability of propylene. Form-exploration of long existed complex geometries has become effortless in contemporary Architecture with the advent of digital technology. Hence precise form-generation is possible with the ability to codify a design as an algorithmic expression of geometric and mathematical constructs. The initial modelling was all performed in Rhino 5, with scripting done is a plug-in called Grasshopper. Computational approach used by yo-cy in the development of form allowed a fluid exchange between design and analysis models. The 12’x8’x8’ white concrete structure provides a proof-of-concept model testing the software workflow, logistics, materiality and details of the system.

6.2.1 Steel Reinforcement:

Initial designs incorporated concrete which required steel reinforcement. Use of standard structural reinforcing bars will not be possible because of the complex geometry. Hence custom flat steel cut to specific lengths as well as to match the geometry of formwork. These custom cut pieces of steel were assembled in framework by either radially notched steel pipes or 3-D printed nodes. Each node accepting the corresponding reinforcing pieces. For the Cast thicket radially notched steel pipes were used at nodal joints which needs a precise configuration of each node and corresponding reinforcement.

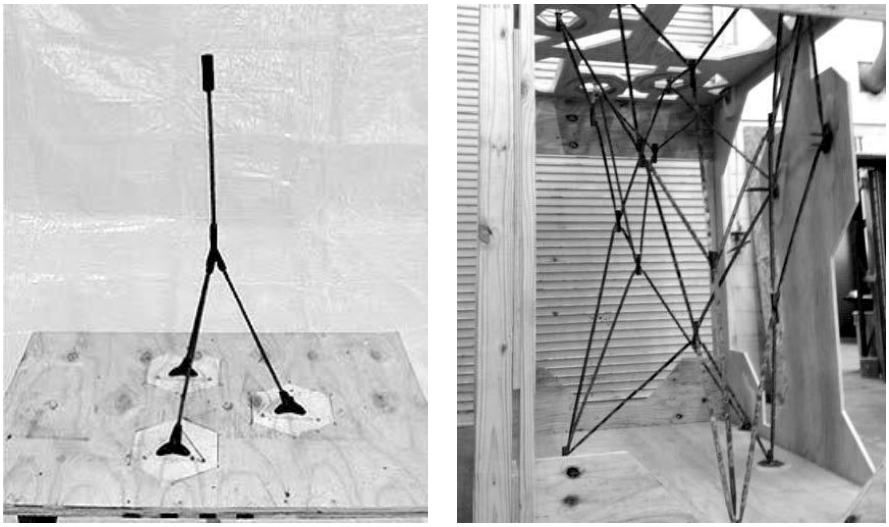

(a) (b)

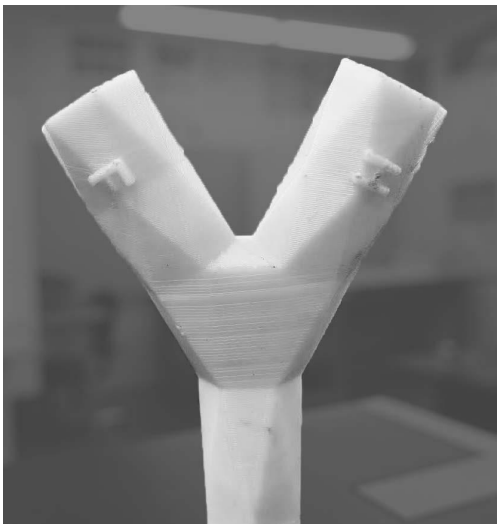

(c)

Figure 6-3 (a) Reinforcing elements and 3-D printed nodes (b) Steel framework for Cast thicket (c) 3-D printed nodes

6.2.2 Fabrication of formwork:

Formwork of polypropylene replaced the conventional rigid wooden or steel in order to mold in to the complex non-Euclidean geometries counting smooth seams. Parametric tabs were fabricated integrally that are used to tie the CNC machine cut pieces together.

Concrete mix composition: Concrete used for cast thicket is a low viscous white concrete made with Poraver expanded glass replacing sand as fine aggregate which reduces the overall weight of mix by 22%. Once the steel reinforcement is assembled in space, individual pieces of polypropylene is interlocked for final casting. This final cast product is a proof-of-concept prototype that presents formal qualities, structural configurations and spacial effects new to free form mold type. This casting has proved that the computational design predicted in simulations and small tests are achievable at this scale.

Figure 6-4 Form for Cast Thicket

Figure 6-5 Final Cast thicket

6.3 Research objective

Assembling nodes and reinforcing frame into larger scale complex non-Euclidean geometries is difficult to be practically implemented. UHP-FRC provides very high compressive and tensile strengths and ductility; moreover, with these mechanical properties, conventional reinforcement can be nearly eliminated. In addition, UHP-FRC's high flow ability allows it to easily satisfy the challenging geometry requirements.

As a means to examine the potential of implementing UHP-FRC into the formwork methodology and thereby eliminating the need for the internal reinforcement, a series of cross sectional profiles were produced to so that a testing and production sequence could be evaluated. The five casts have different configurations; yet, all employed the same hexagonal branching cross section and all maintained a height of three feet four inches. The casts simplify the bifurcation and twisting that were found in the larger piece. The cast also allowed structural testing of the material strengths relative to the geometry to be more precisely isolated. The columns were made at a scale of approximately 1/4~1/5 the size of the actual columns.

6.4 Experimental program

6.4.1 Phase 1:

Specimens numbered as 0, 2, 7, 10 and 11 were cast with UHP-FRC and tested to examine the structural behavior besides column #7 was used for presentation.

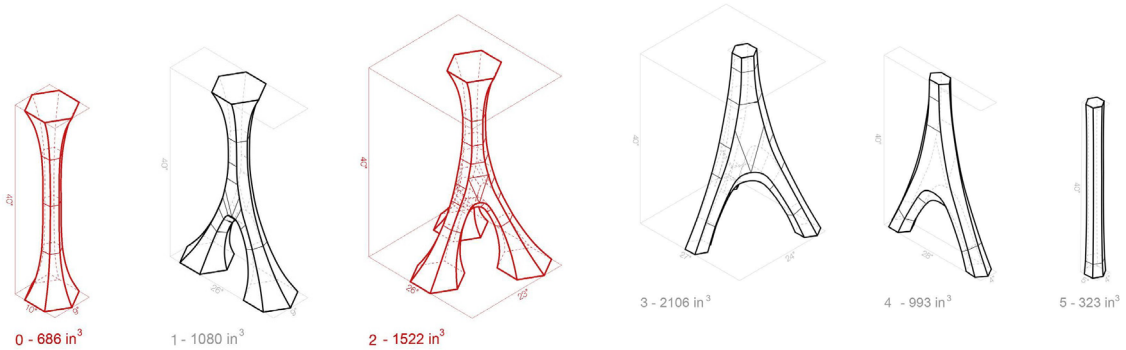

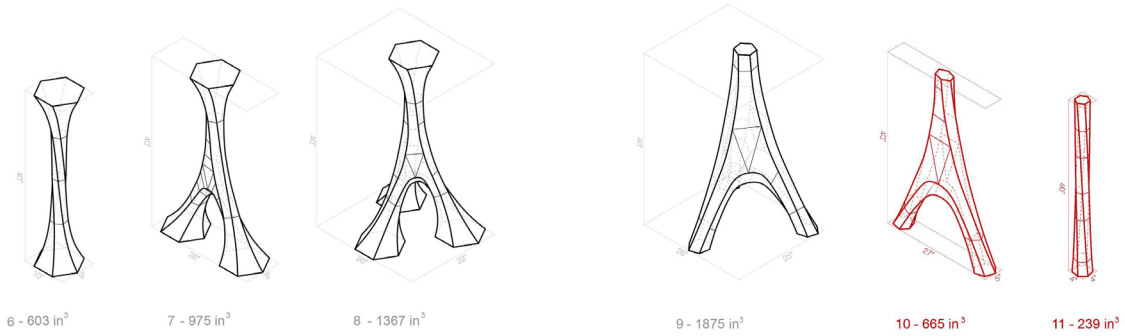

Figure 6-6 Specimens cast with UHP-FRC in phase 1

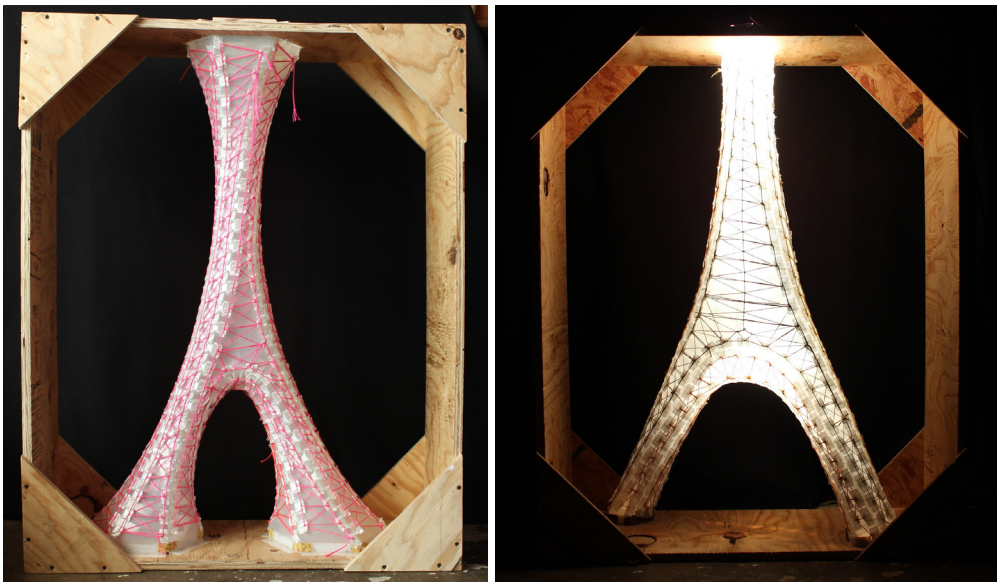

Figure 6-7 Semi rigid form with wooden scaffolding

6.4.1.1 Form preparation:

Once individual polypropylene sheets are interlocked in place; in-built tabs serves as an anchoring device for seam reinforcement. Nylon strings are laced through the tabs and reinforce the mold throughout along the seam. Semi-rigid plastic formwork is supported by a wooden box scaffolding which serves as a temporary exoskeleton; this scaffolding can be removed in first 20 hours of casting.

Figure 6-8 Seam lacing with Nylon string

6.4.1.2 Mixture Composition:

Casting of above mentioned forms was carried out in the Civil Engineering Laboratory building at University of Texas at Arlington. The UHP-FRC used in this research was developed based on the dense particle packing concept at the University of Texas at Arlington. It had 3% by volume straight steel fibers (12.5 mm long and 0.175 mm dia.) and a tensile strength of 2200 MPa). The UHP-FRC also had a compressive strength of about 22 ksi (150MPa) with excellent flow ability.

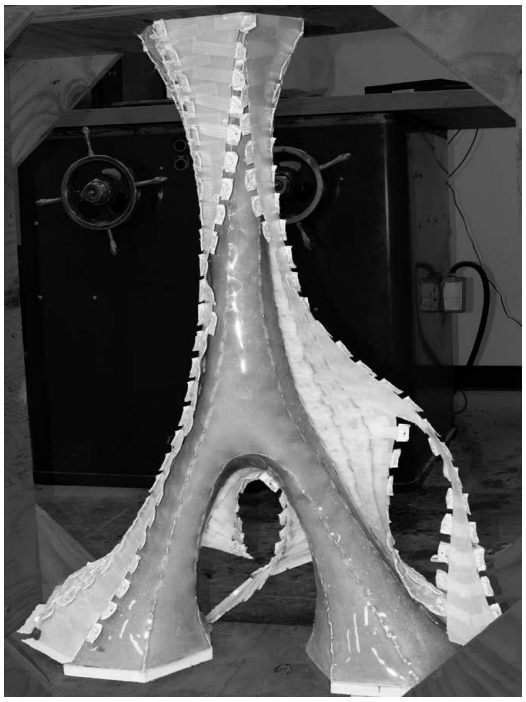

Figure 6-9 Unmolding of Semi-rigid formwork (UHP-FRC #7)

Figure 6-10 Final cast columnar specimens

6.3.1.3 Casting of RC column

Formwork used for RC column is digitally sculpted from an extruded polystyrene (XPS) foam. Formwork design was complex multi-step process that has issues such as sealing the central joint, dislocation at joints, time required for setup, alignment of rebar within the foam, and surface quality inconsistencies. Given trifurcated geometry was developed using grasshopper and detailed formwork was created through CNC milling. CNC milled XPS foam was supported by plywood that works as scaffolding for the assembled formwork parts (Figure 6-12 (a)). The forms were designed to be poured in two stretches, also allowing the nodes of reinforcing elements to be accurately aligned in the formwork.

Reinforcing element consist of four cut pieces of rebar each extending into main branch and trifurcated legs. All the four pieces were precisely connected using custom 3D printed nodes made of nylon.

(a) (b)

Figure 6-11 (a) Rebar placed in formwork (b) First pour

(a) (b)

Figure 6-12 (a) Assembled form and cast (b) RC column

6.3.1.4 Test setup and instrumentation

Four columns numbered 0, 2, 10 and 11 are loaded under uniaxial compression through a 650 kips (2891 kN) hydraulic cylinder. In each test, the column was initially loaded until the first visible crushing or flexural crack in case of branched columns. Then, loads were monotonically increased and paused at a few loadings to trace the cracks and take photos. The process continued until failure. For each test, a total of two bearing plates were used at the bottom of column and loading point. To provide a uniform interface contact, a layer of non-shrink grout was used between the concrete and bearing plate at the loading point. During the tests, the applied load was measured by a load cell. A DIC non-contact deformation measurement system with a measuring strain accuracy of 0.01% (in./in.) was used to view the full field of strains and displacements as they developed on the surface. One side of each specimen facing toward the cameras was regarded as a region of interest (ROI) and speckled by black paint dots on a white base.

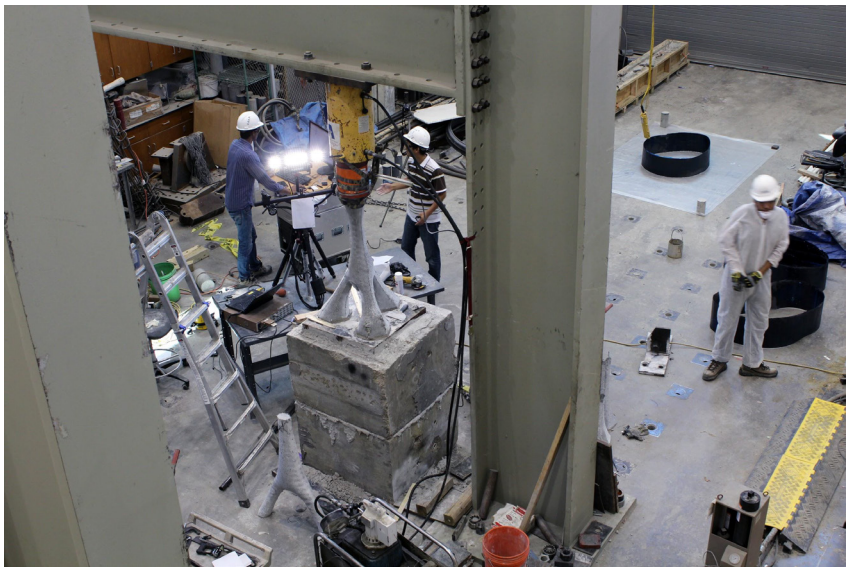

Figure 6-13 Experimental test setup with UHP-FRC column #2 in place

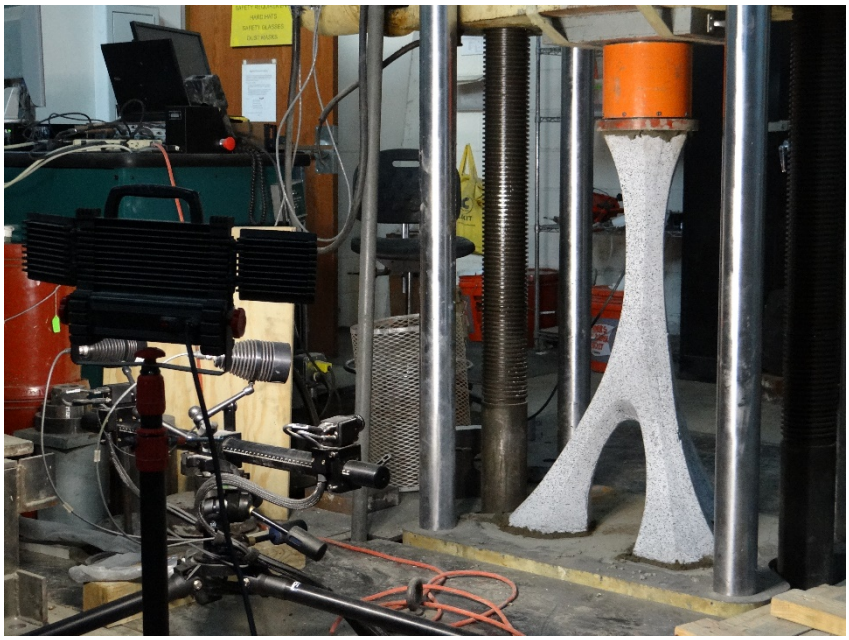

Figure 6-14 Test setup for RC columnar structure

6.3.1.5 Experimental results of phase 1

Column #0 has a varying cross section with the narrowest section near the mid-height of the column. This column was able to carry an ultimate load of 162 kips (720 kN). This load is corresponding to a compressive stress of about 22 ksi (150 MPa). Failure was due to the concrete crushing at the mid-height where had the maximum compressive strains were measured by the DIC.

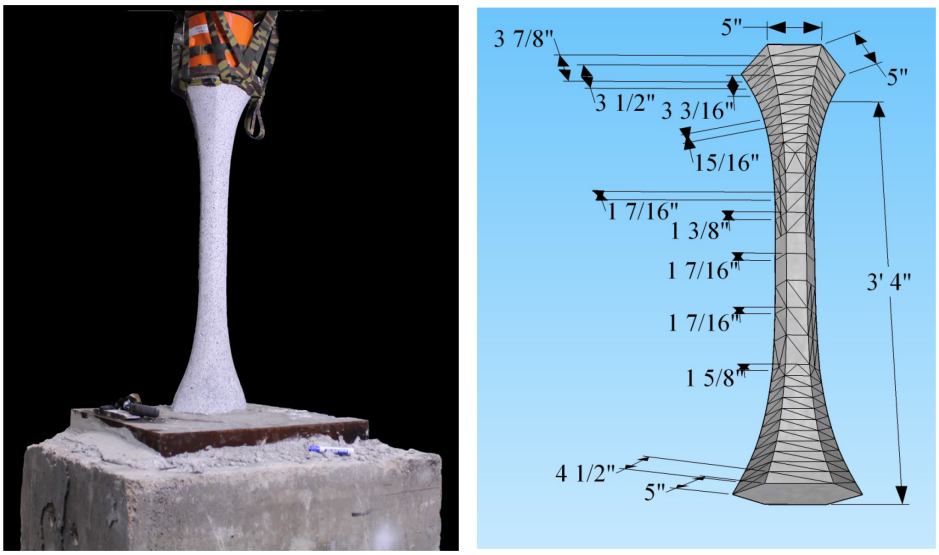

(a) (b)

Figure 6-15 (a) Column #0 test setup (b) Dimensions of column #0

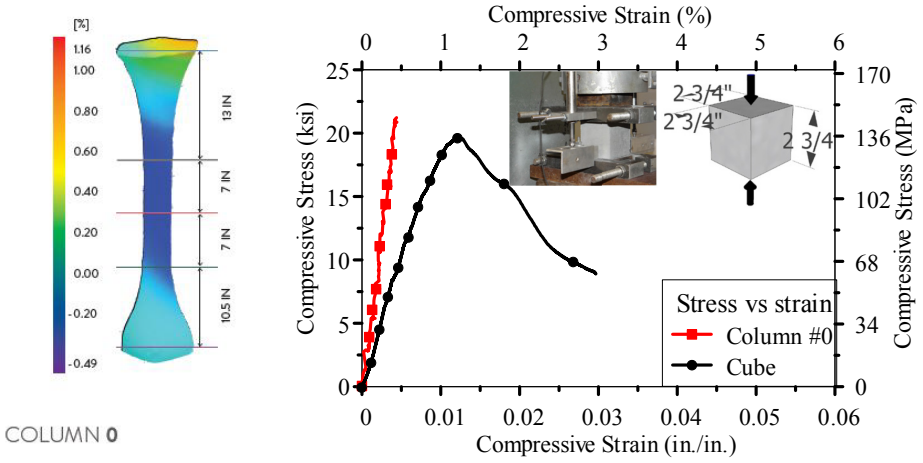

(a) (b)

Figure 6-16 (a) Column #0 compressive strain profile

(b) Compressive stress-strain curve from column #0 and cube

Column #2 has a varying cross section at the top portion, with the narrowest section measured at about 20-in. (508 mm) from the top surface. The lower part of the column consisted of three inclined legs having varying cross sections. This column carried an ultimate load of 267.7 kips (1191 kN). This load corresponds to a compressive stress of about 23.7 ksi (163.4 MPa). This column had a greater stiffness than that measured from cubes. Column #2 failed due to the crushing of concrete at the narrowest portion of the top branch of the column. The steel fibers proved capable of keeping the fractured pieces together thereby preventing any possibility of a catastrophic failure.

RC column has same cross-section and dimensions as column #2. RC column casted and tested with conventional concrete and reinforced with steel reinforcing elements failed by crushing of concrete at an applied external load of 33kips (147 kN) at the thinnest cross-section. This load corresponds to a compressive stress of about 2.8 ksi (19.3 MPa). Two fractured pieces of RC column were held together by the rebar alone.

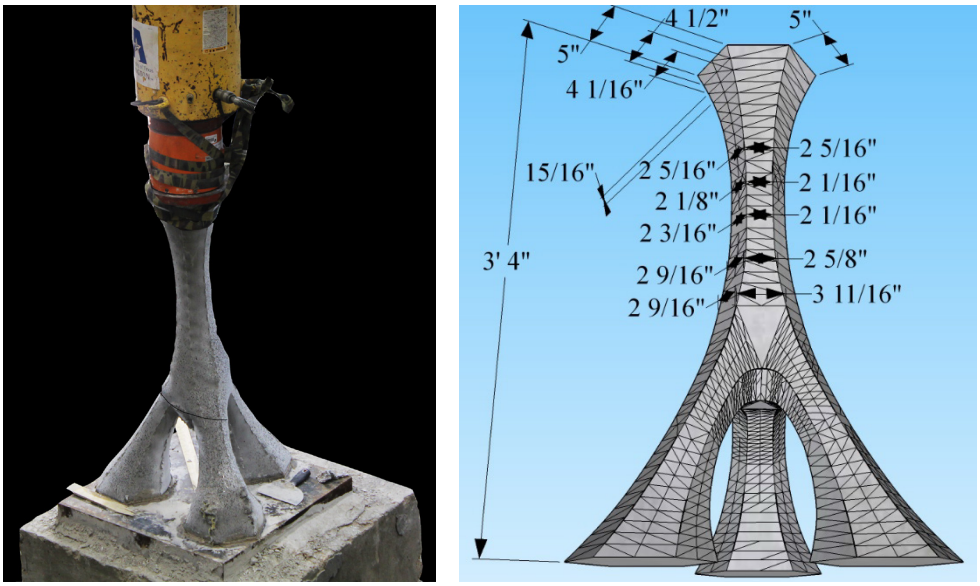

(a) (b)

Figure 6-17 (a) Column #2 test setup (b) Dimensions of column #2

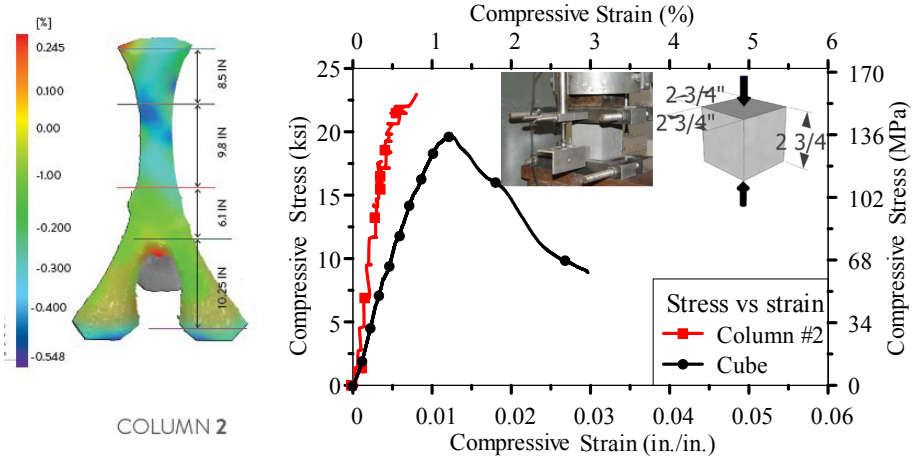

(a) (b)

Figure 6-18 (a) Column #2 compressive strain profile

(b) Compressive stress-strain curve from column #2 and cube

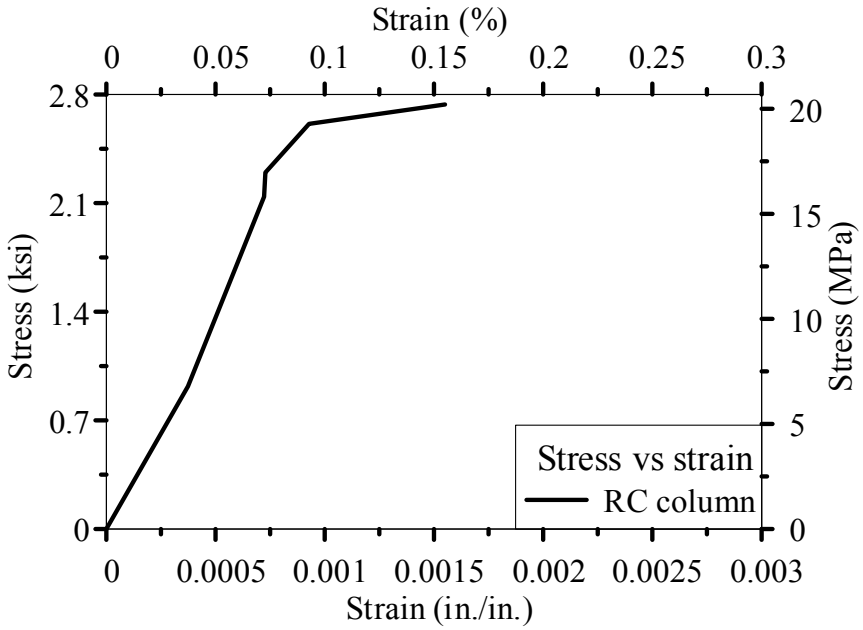

Figure 6-19 Compressive stress-strain curve from RC column

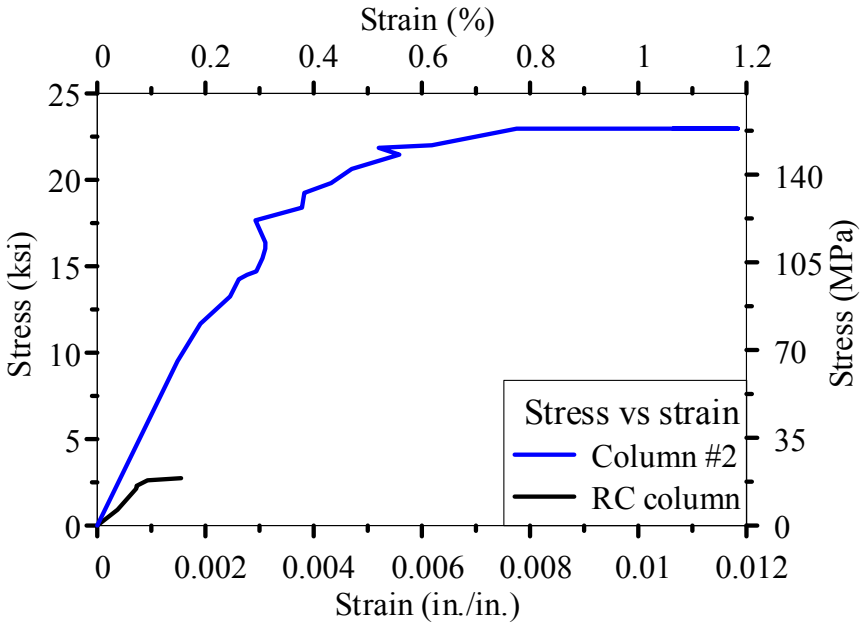

Figure 6-20 Compressive stress-strain curves of RC column and column #2

(a) (b)

(c)

Figure 6-21 Comparison of compression failure pattern

(a) UHP-FRC column #2 at the end of the test (b) and (c) RC column at the end of test

Columns #10 and #11 crushed at loads of 160 kips and 85.6 kips respectively at the tip of the column where the cross-section is thinnest.

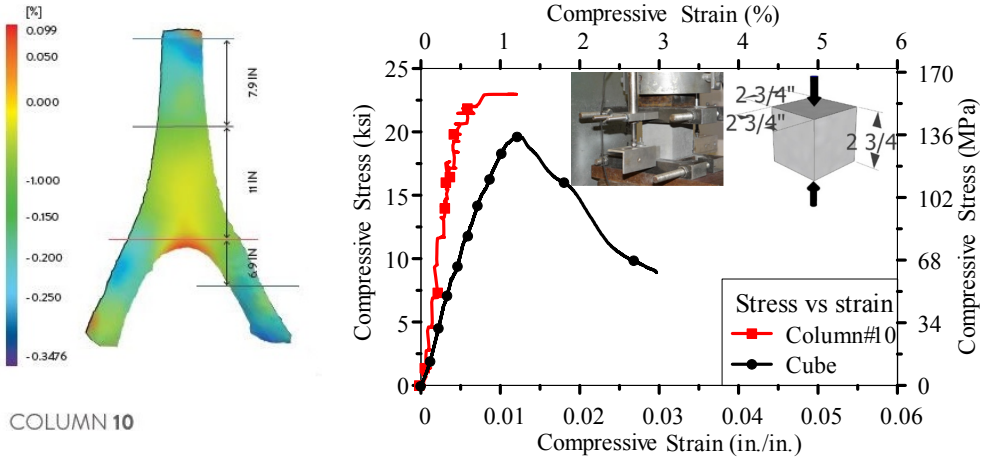

(a) (b)

Figure 6-22 (a) Compressive strain profile of column #10

(b) Compressive stress-strain from column #10 and cube

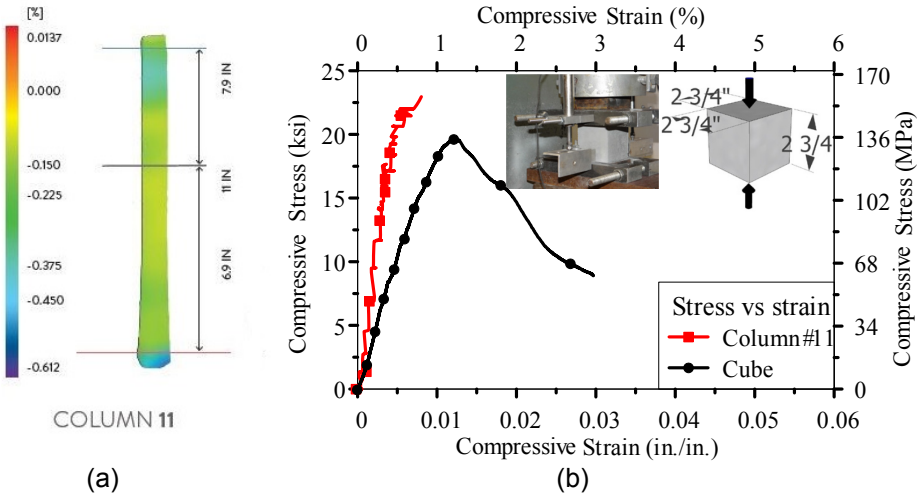

(a) (b)

Figure 6-23 Compressive strain profile of column #11

(b) Compressive stress-strain from column #11 and cube

6.3.2 Phase 2: Cast columnar branching with UHP-FRC

Extracting the results from phase one castings and testing results it was proven that use of UHP-FRC in non-Euclidean geometries is very viable. Hence motivated to cast a larger scale asymmetrical columnar branching structure. Considering the high density of UHP-FRC imposing excessive hydrostatic pressure at maximum curvature and lower parts of the column, previously used polypropylene is replaced with a much stronger material called MYLAR. Mylar is a polyester film made from stretched polyethylene terephthalate that was developed in the mid-1950s, originally by DuPont Imperial Chemical Industries. With a tensile strength of 30-35 ksi it is very strong. Polypropylene used previously was thicker and became very brittle once any cutting was done to the material.

Further tab iterations were done by Digital Architecture Research Consortium (DARC) at UT Arlington to improve the seam and connections. Iterations were made on tabs to minimize the amount of labor required to lace the seams together and create a self-supporting structure; similar to how a buckle works. Further tests were done on modified forms by casting with both highly flow able hydrostone and foam to check the leak at seams and also opening of form due to high pressure.

Figure 6-24 Form and scaffolding for 38” x 33” x 68”

columnar branched structure

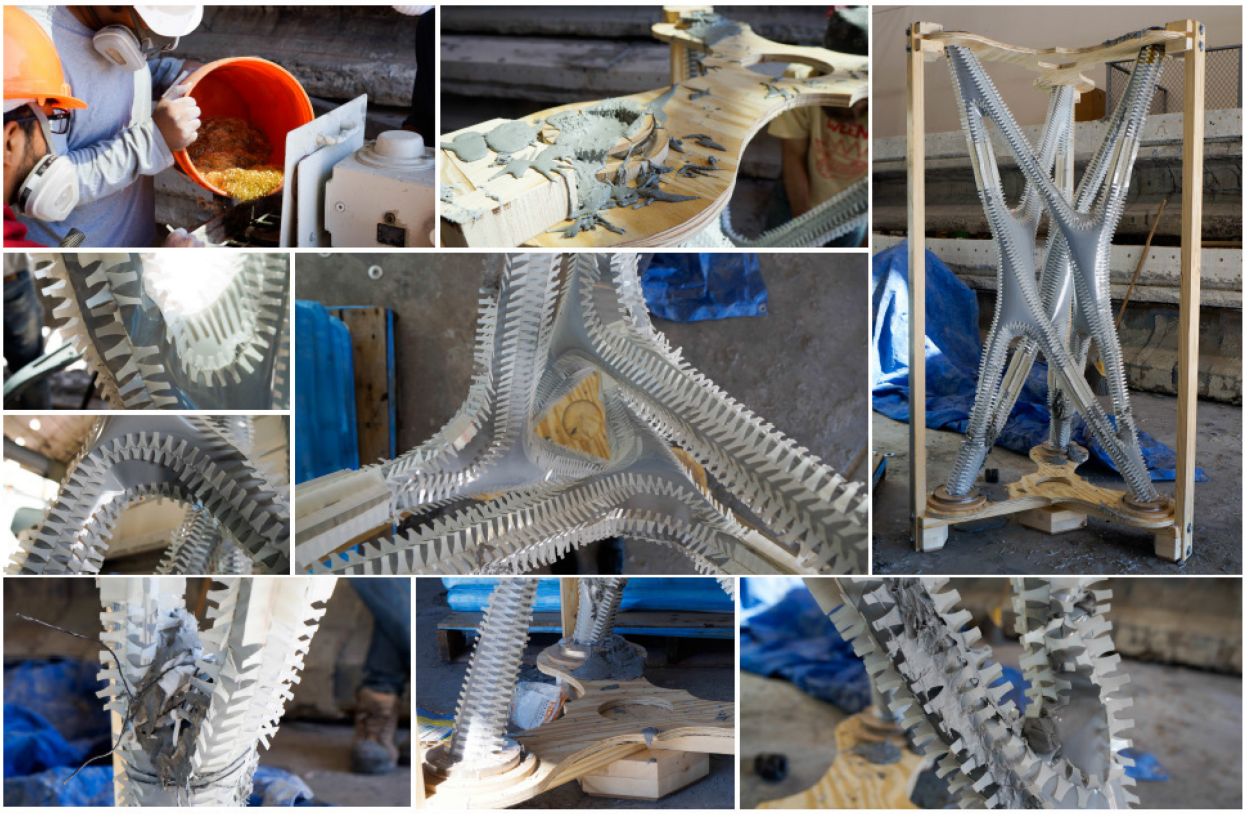

Figure 6-25 Final casting of 38” x 33” x 68” columnar branch

6.4 Results and discussion

Columns articulated by non-Euclidean geometries offer a new type of formal and structural possibilities. Specifically, branching concrete columnar structures offer a unique opportunity to merge biomimetic structural geometry with new computationally controlled performance criteria. Typical plain concrete does not willingly lend itself to these types of geometries due to its brittle nature and sensitivity to stress concentration. The non-Euclidean geometries also make the conventional reinforcing methodology difficult to be practically implemented. In the work shown in this research, the introduction of ultra-high-performance fiber reinforced concrete (UHP-FRC) allows for a new way of advancing beyond some of the limitations of conventional construction methods of reinforced concrete. UHP-FRC provides very

high compressive and tensile strengths and ductility against compressive forces. With these mechanical properties, conventional reinforcement can be nearly eliminated. In addition, UHP-FRC's high flow ability allows it to easily satisfy the challenging geometry requirements. This research tested five columns with various non-Euclidean geometries. No conventional reinforcement was used in these columns except UHP-FRC. The formwork used for these columns was done by a unique solution for assembling 2D materials in complex 3D forms. Compression type of failure observed would fully utilize the ultra-high strength of the UHP-FRC, and thereby considerably increase the load-carrying capacity to five-fold or more compared to columns made of plain concrete. The steel fibers proved capable of keeping the fractured pieces together thereby preventing any possibility of a catastrophic failure. This preliminary research demonstrated the feasibility of using UHP-FRC in geometrically complex structures, and provides valuable information showing a new proximity toward the realization of biomimetic structural geometry used in actual applications.

Chapter 7

Part IIb: UHP-FRC for Precast Facade Sandwich Panels

7.1 Introduction

The precast concrete sandwich panels are used as an effective building envelope and also for transferring the loads. The capacity to develop a thinner, lighter, more durable panel provides a compelling set of construction and design possibilities including the structural and thermal performance. This marks a significant advancement in the current methods being practiced in the industry. There are three different types of panels in use.

7.1.1 Non-composite:

A non-composite sandwich panel consists of two concrete wythes acting independently. It is made up of a structural wythe and a nonstructural wythe, with the structural wythe being the thicker of the two.

7.1.2 Composite:

A composite sandwich panel consist of two concrete wythes act together to resist applied loads. The entire panel acts as a single unit in bending. This is accomplished by providing full shear transfer between the wythes.

7.1.3 Partially Composite:

Partially composite sandwich panels have shear ties connecting the wythes, but the connectors do not provide full composite action. The bending stiffness and strength of these panel types fall between the stiffness and strengths of fully composite and non-composite sandwich panels.

The conventional sandwich panel consists of three primary layers; an insulation layer is provided in between the outer facing concrete wythe and inner facing concrete wythe. The

concrete sandwich panel in a building provides inherent weather barrier, wind and impact resistance and makes structure aesthetically appealing. However, three wythe sandwich panels made up of normal reinforced concrete are thick and heavy. Moreover, the amount of material required for structural rigidity is very large.

Through the introduction of Ultra-High-Performance Fiber-Reinforced Concrete (UHP-FRC), the sandwich panel façade typology can now be exploited to achieve a more optimized panel on many levels. Standard sandwich panels range from 8” to 14” in thickness with an R-Value typically ranging from 12-20 for most regions. Because UHP-FRC does not require rebar reinforcement and has a much greater compressive strength, the ability to cast thinner wythes provides an opportunity for a new approach to the insulated precast panel. The use of UHP-FRC in a precast application provides a new opportunity to develop high performance sandwich panels for building facades

7.1.4 UHP-FRC Material

The UHP-FRC mixture design used is a proprietary product developed at the University of Texas at Arlington [Aghdasi et al., 2015]. All the materials used are locally available in the U.S. market. The UHP-FRC mix design was developed using a dense particle-packing concept which aids in achieving a compressive strength of 25-30 ksi (207 MPa). The research has proven a much higher strength and ductility than conventional concrete or ultra-high performance concrete.

7.1.5 Building Envelope and Heat Transfer

Heat flows through the building envelope by two means of heat transfer; conduction and radiation. As a barrier separating two spaces typically of different temperatures understanding the thermal properties of the building envelope depends on three factors:

a. The surface area of the building envelope. The greater the surface area, the greater the flow (directly proportional).

b. The temperature difference on either side of the envelope. The greater the temperature difference, the greater the flow (directly proportional).

c. Heat conduction properties of the envelope assembly or the Resistance (R) to heat flow offered by the envelope material(s). The greater the resistance, the less the heat flow (inversely proportional).

CONDUCTION is the flow of heat through the substance due to a difference in temperature on two sides of the substance. Conduction is typically associated with the flow of heat through solids, but it can also happen through liquids and gases.

RADIATION is the heat transfer by electromagnetic radiant heat energy through space from one body to another without affecting the space in between. Radiant heat transfers to a body and its surrounding temperature depends on the absorptivity (A), transmissivity (T), and reflectivity (R).

$$A + T + R = 1$$

HEAT TRANSFER (Transmission) through a solid building envelope is due to the difference in temperature on either side of the building envelope. It can be determined by

$$Q_T = A_S * U * (T_O - T_I)$$

where,

Q_T = conduction heat transfers through the envelope

A_S = surface area of building envelope

U = conduction property of building envelope material

T_O = Temperature Outside (^oF)

T_I = Temperature Inside (^oF)

Heat Transmission (Q) occurs down the gradient of temperature (from higher temperature to lower temperature). It is directly proportional to the temperature difference. The greater the temperature difference the greater in the heat flow.

HEAT GAIN by the air in the enclosed space is because heat is being added to it through the building envelope. This heat is absorbed by the mass of air in the space increasing its temperature.

7.2 Objective

The UHP-FRC have greater strength, more flow ability and is more ductile than normal reinforced concrete. These physical properties give significant advantages to design and develop structurally and thermally optimized precast cladding system. The main research is focused on the use of UHP-FRC for stronger, thinner and more durable concrete sandwich panels. The other research objectives are: (i) to fabricate more detailed geometry that can create self-shading surface using UHP-FRC, (ii) to find out the thickness of UHP-FRC for minimum thermal heat transfer though the building envelope.

7.3 Panel design

The industry standard precast panel was used as prototype for this research in collaboration with Gate Precast and Thermomass.

The three different panels were designed and casted for the investigation.

7.3.1 Panel 1:

The typical non-composite assembly was chosen with size of 3 ft. by 3 ft. consisting of 3” facing wythe, 2” EPS rigid insulation, and a 3” structural backing wythe. Using Gate Precast standard, the front facing has a compression strength of 5 Ksi and the back facing has a compression strength of 7 Ksi. The 6”x6” wire mesh has been used in each wythe for cracking resistance attached to #4 (1/2”) rebar around the perimeter and through the ferrule loop inserts for tensile reinforcement. In order to tie the two wythes together with styrofoam as an insulation layer in between, the Thermomass MS-T are used. The ties are arranged in a grid of 4 X 4 inches equally spaced at 7.25 inches. This prototype is taken as an industry baseline for

comparing bending and compressive strengths, thickness of panel, weight, thermal conductivity and radiant properties of the panel.

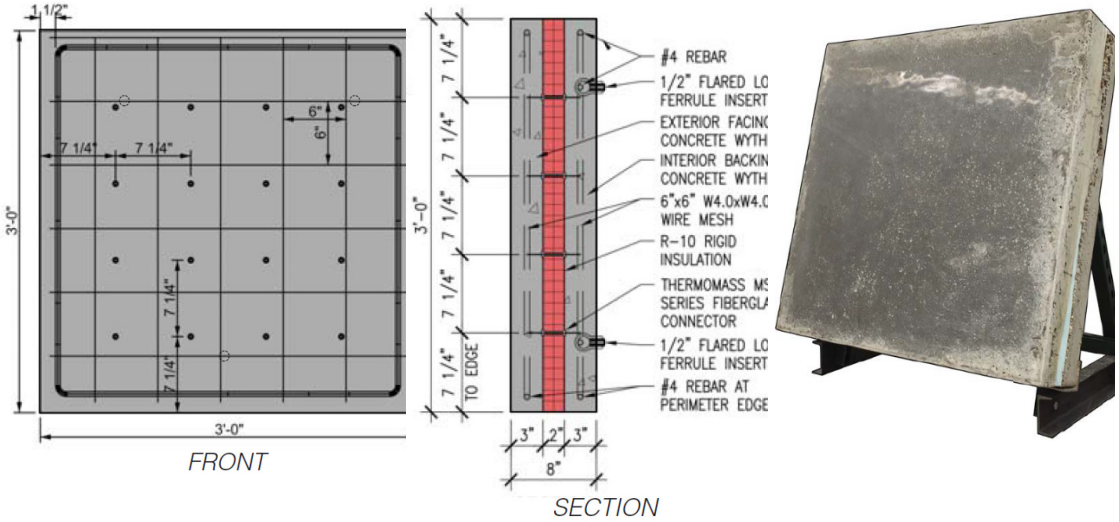

Figure 7-1: Reinforced Concrete Panel (Panel 1)

7.3.2 Panel 2:

A comparable non-composite assembly 3'x3' panel is made with similar compressive properties for UHP-FRC. This prototype consists of a 1-1/2" facing wythe, 2" extruded polystyrene rigid insulation, and a 1-1/2" structural backing wythe. ThermoMass CC-130 ties are used to connect the two wythes together through the Styrofoam. The ties extend 1-1/2" from the insulating foam are trimmed on each end to avoid extending through face on both sides. The spacing of the ties is same as in the standard industry panel.

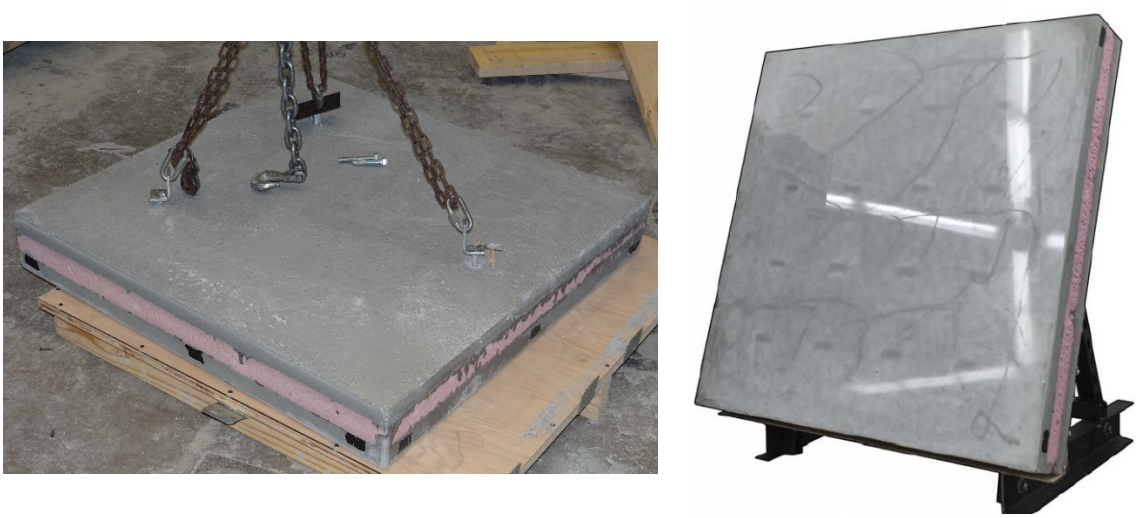

Figure 7-2: UHP-FRC panel (Panel 2)

7.3.2 Panel 3:

This prototype combines the standard baseline casting methods with a self-shading geometry in the outer facade for the thermal optimization in the panel. The thermal performative qualities have been improved with thinner layers from UHP-FRC. The outer architectural surface is defined by a series of faceted geometries that initiated a preliminary investigation into self-shading. While this aspect of the research is more thoroughly investigated in Phase II, the initial examination adequately determines that a non-uniform outer architectural geometry can be cast as a counterpoint to a very thin internal structural wythe. The architectural wythe ranges in thickness of 2.5” at the peak of the facet to 1” at the thinnest point.

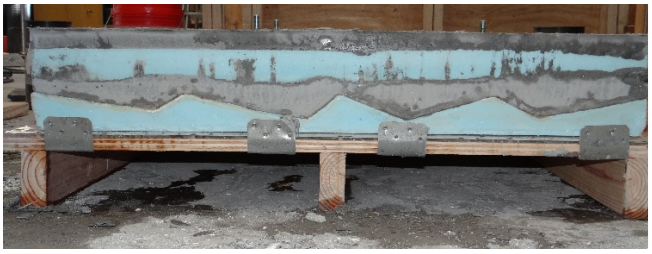

Figure 7-3: UHP-FRC Waffle Panel (Panel 3)

Table 7-1: showing panel properties

Particulars	Panel 1	Panel 2	Panel 3
Width	36 inches	36 inches	36 inches
Height	36 inches	36 inches	36 inches
Total Thickness	6 inches	5 inches	4 inches
Weight	650 lbs.	325 lbs.	250 lbs.
Compressive Strength	5 Ksi.	25 Ksi	25 Ksi
R- Value	10	10	13
Conduction heat transfer through the panel	15.26 Btu/hr	20.47 Btu/hr	18.84 Btu/hr 22.77 Btu/hr

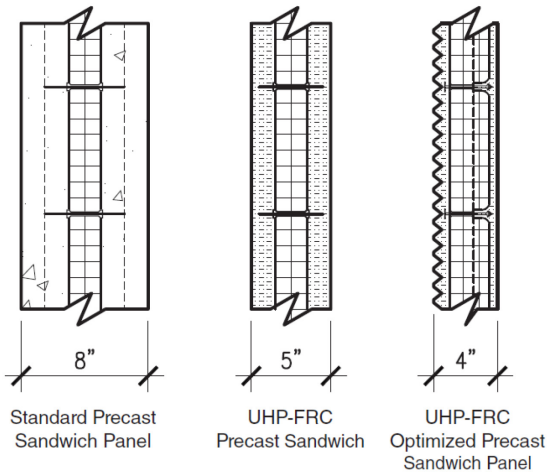

Figure 7-4: showing total thickness of panels

7.4 Structural Wythe & Connector Design

The investigation of the relationship of material properties, geometric arrangement, and nodal connections are carried to discover the full potential of using UHP-FRC for sandwich panels in a facade application maintaining structural rigidity. The backing wythe is need to be infused with the insulation considering structural rigidity and thermal performance. The two options are opted for this hybrid backing wythe as a Waffle and a Hollow Core. The thinness of the backing wythe are analyzed by a series of square grid, diagonal grid, and hexagonal grid for reinforcing to a good geometry. The grid study is to find the arrangement that minimizes the number of nodal connections, maintains an acceptable max length distance between nodal connections, and minimizes material. The hexagonal grid satisfied these requirements and further analysis was made for the hollow core option. The strengthening of the wythe was possible with simple misalignments of the grid and the effect of a hyperboloid connection between the two grid layers. The hollow core requires an injection casting process which does not integrate directly to industry standards and the waffle backing wythe was chosen for this research.

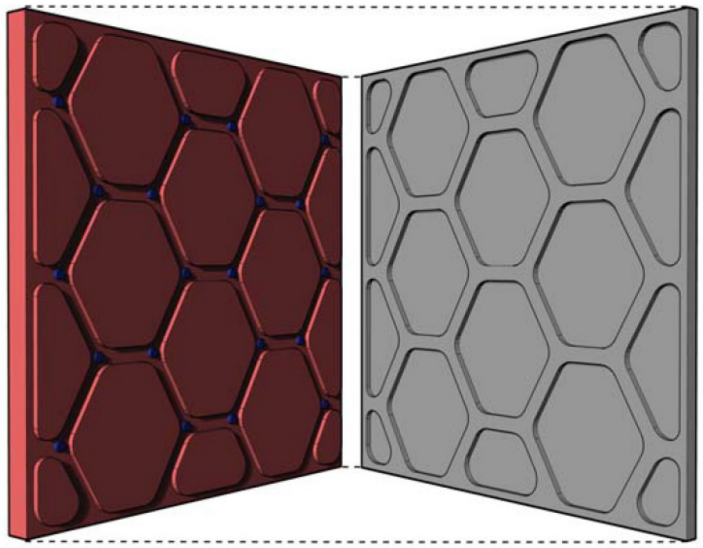

Figure 7-5: Hexagonal backing wythe

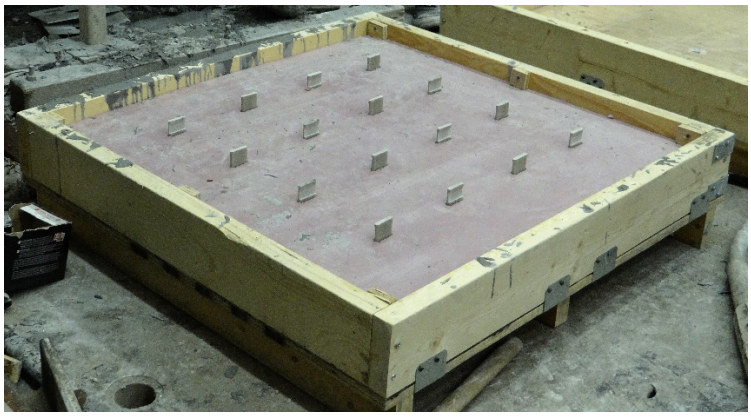

Figure 7-6: Connector ties (tying both front and back wythes)

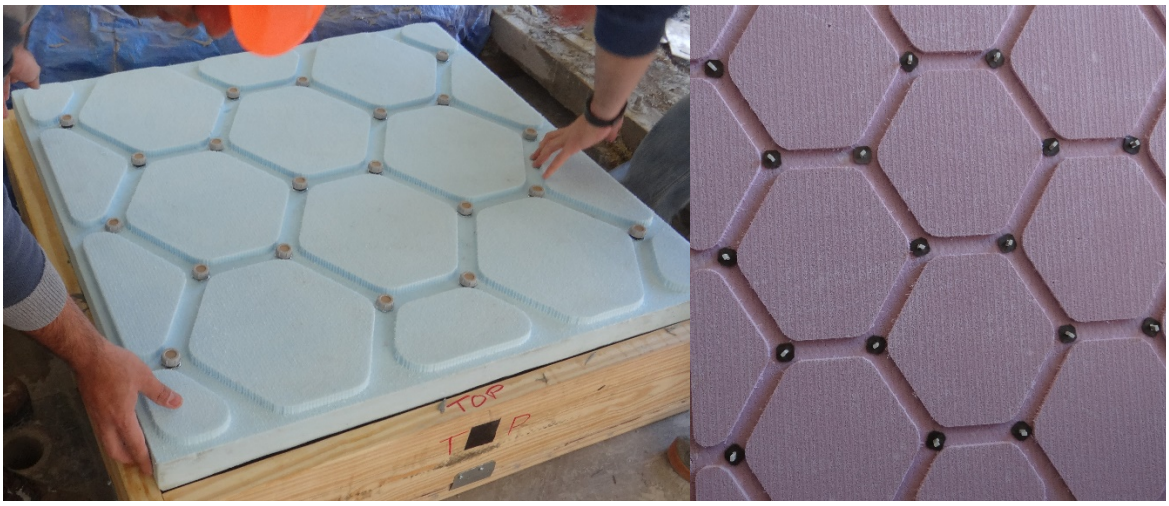

Figure 7-7: Rigid Insulation in Place

7.4.1 Self-Shading Surface

Self-shading surfaces are an attempt to reduce solar heat gain resulting in reduction of heat transfer. This system is investigated to determine its effectiveness on an insulated UHP-FRC concrete panel. Compared to a typical flat panel self-shading may provide thermal performance able to further assist sustainable building strategies.

There are two primary factors related to geometry: Micro articulation and Macro articulation. Macro articulation uses the asymmetrical Perlin sine wave provides the best thermal optimization and also the greatest level of design variation. The latter point desirable so that surface texture can be controllable - more like camouflage and less like static on an old tv screen - when viewed from different distances. Micro articulation is a relatively new part of our theory on heatsink used in some experimental forms of ceramics and possibly providing opportunities for 1-2 degrees change depending on the max/min solstice. This system on the surface can be accomplished with traditional concrete. However, the architectural wythe would need to be substantially thicker to accommodate the rebar.

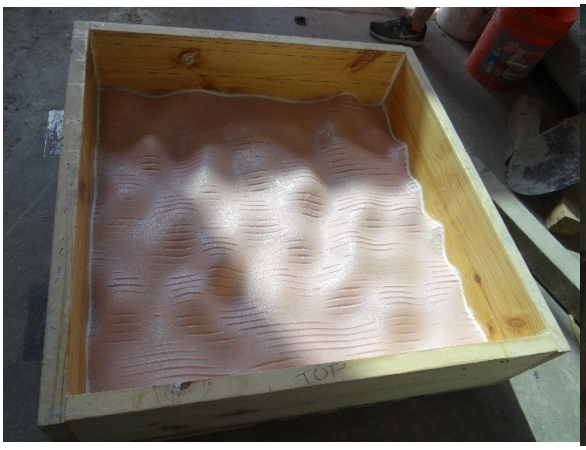

Figure 7-8: Optimized Self -Shading (Surface Articulated Mold)

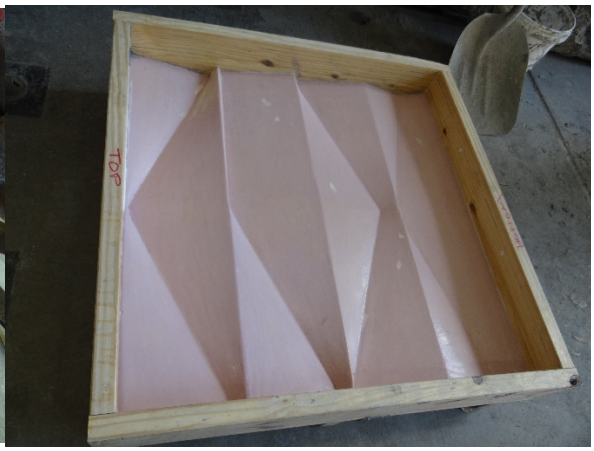

Figure 7-9: Waffled backing wythe (Surface Articulated Mold)

Figure 7-10: Self shading surfaces

An inventory of macro surface articulations is made to investigate the performative self-shading result for a different sinuous surface. Grasshopper and Rhino are used to generate the geometries and analysis. Designed on the premise of uniform to irregular, each surface is created from a manipulation of a point grid with attractor points. The distance is fed through calculations measuring the distance between the grid which makes the surface and the attractor

points. These values are then fed through each of the graph types of a Sine Wave, Sink Wave, Sine Sim, and Perlin wave. Each graph type creates a different surface type.

Each surface type is then analyzed for radiance in a given location for a set period of time. Each season is analyzed separately to determine its effectiveness year round and given an average total radiance. These results help to determine which sinuous surface provides the most shading. To fine tune the surface and in addition to providing self-shading performance the method for generating the final result must fulfill three primary functions: 1) The design method must be repeatable. 2) The final surface must have an anticipated result, not a random result. 3) The generating script must provide a level of variability to create different results.

7.5 Panel Thermal Analysis

Self-shading changes the surface temperature at any given point on the surface. Therefore, to study the effectiveness of self-shading on heat transfer individual sections need to be analyzed with the appropriate surface temperatures. The thermal heat through the building envelope depends upon the R-Value. This research is also about improving the thermal performance of the panel as a non-composite panel has minimum thermal bridging.

Our goal is to further enhance the R-value of the insulation layer and also consider the U-value of the entire panel through the introduction of self-shading geometry on the exposed architectural surface in combination with different approaches to the insulation layer. In order to thermally optimize the facing wythe, it had to run through a digital simulation which would result in a radiation analysis utilizing rhino and grasshopper. In addition, the ladybug + honeybee plug in was used to obtain a radiation analysis based on geodata to provide corresponding information according to a given date and time. The intent of the simulation is to provide greater surface area of a cooled surface to decrease thermal transfer.

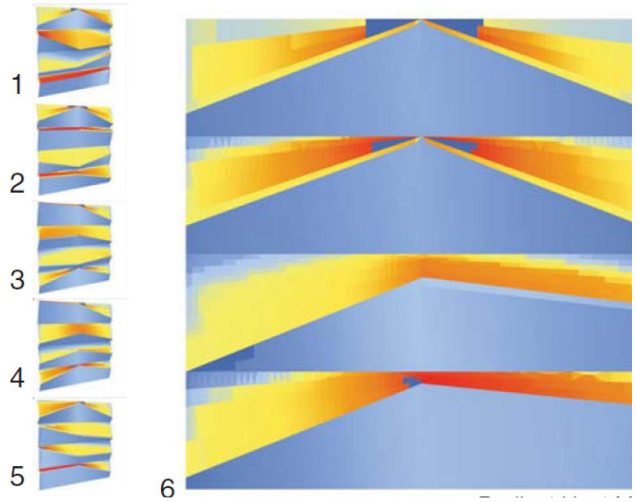

Figure 7-11: Heat radiant Map Optimized for Panel 3

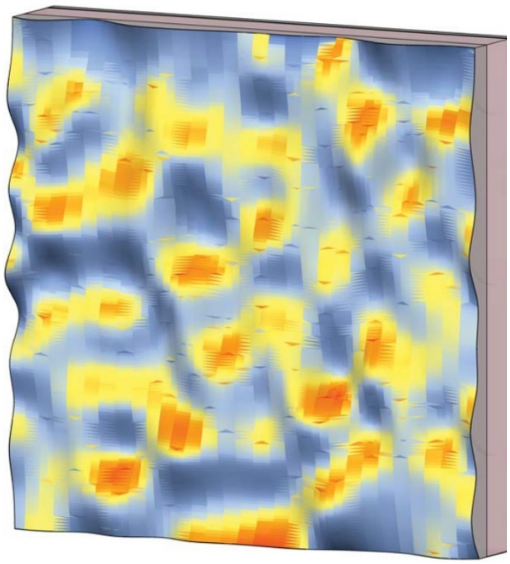

Figure 7-12: Thermally Optimized Self shading surface

7.6 Experimental Program

The panels were loaded by a concentrated force at mid-span through 300 Kips actuator. In each test, the panel was initially loaded until the first visible flexural crack at the surface. Then, loads were monotonically increased and paused at a few loadings to trace the cracks and take photos. The process continued until failure.

For each test, the width of the support was 3 in. with pin and roller support on either side. To provide a uniform interface contact, a layer of non-shrink grout was used between the concrete and bearing plate at the loading point. A schematic view of the test setup, instrumentations, and loading configuration is depicted in Fig.11. Four number of linear variable differential transformers (LVDTs) were mounted at the end of support in North and South direction for each specimen. An LVDT was place to measure the deflections under the loading point.

Figure 7-13: 3 point bending test

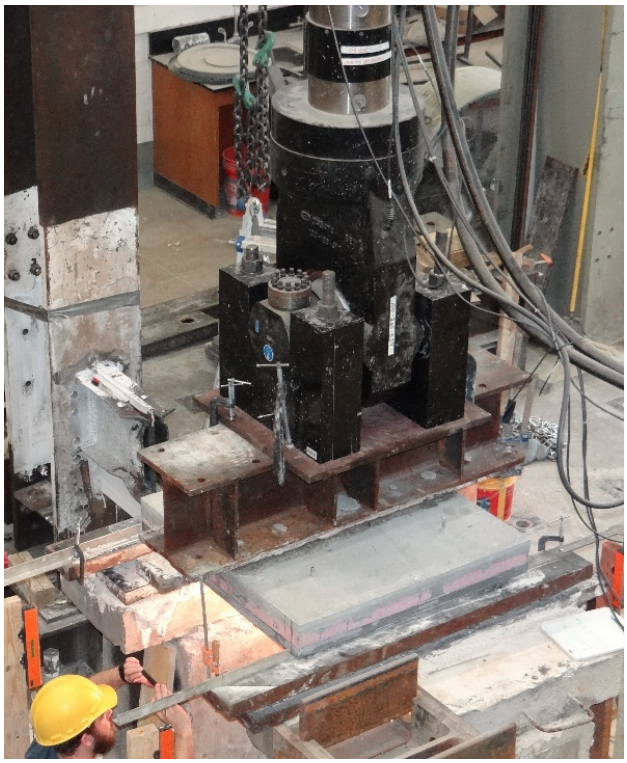

Figure 7-14: Experimental Setup

7.7 Experimental Results and Conclusion

A 3-point flexure test was performed on each panel to determine their bending strength for comparison. The results show that the industry standard panel initially cracked at a lower load compared to both panels 2 and 3 despites both of the Ultra High Performance panels being much thinner. Both the standard panel and the initial Ultra High Performance panel were able to take more load than the final Ultra High Performance panel. However, it is important to note that this 3rd panel was only slightly weaker than the other two despites being quite a bit thinner. This can likely be attributed to the waffle pattern of the structural backing wythe which was able to more evenly distribute the load throughout the panel despite being only an inch thick.

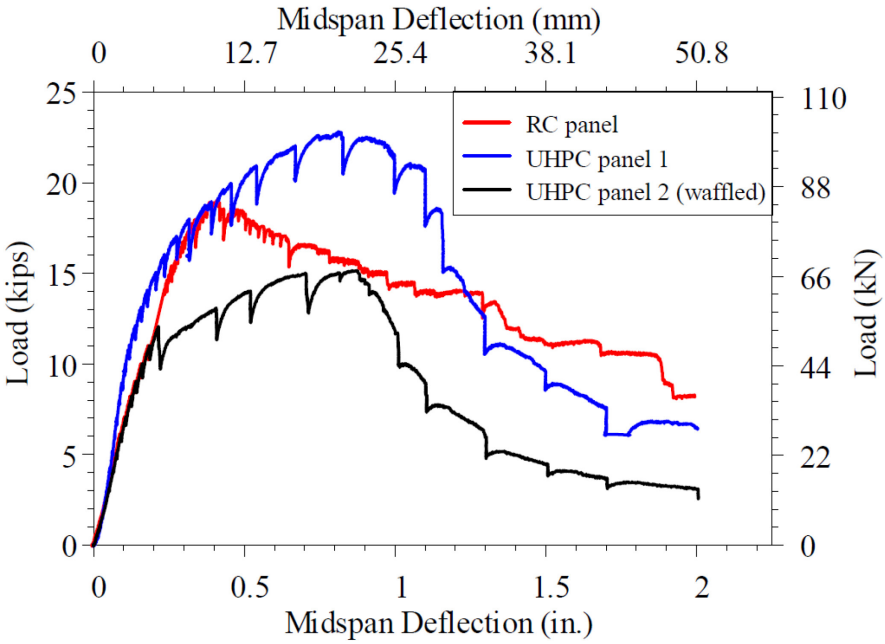

Figure 7-15: Load- Deflection curve

Test results for Panel 1, establishing a baseline using industry standard fabrication methods, reveal initial cracking at 5.8 kps with a peak load of 19kps. The panel has a structural wythe width of 3” (8” overall) and weighs 676 lbs. Test results for Panel 2, establishing a baseline using the UHP-FRC, reveals initial cracking at 19kps with a peak load at 22.8 kps. The panel has a structural thickness of 1.5” (5” overall) and weighs 338 lbs. Test results for Panel 3

reveals an initial cracking of 12.8 kps and a peak loading of 15.15 kps. The panel has a structural thickness of 1” (4” overall) and weighs 233 lbs.

Figure 7-16: Cracking at peak load

Figure 7-17: Panels after testing

Figure 7-18: Deflection of panel

It is possible to fabricate a stronger, lighter, and more thermally superior panel than current industry standards for the UHP-FRC insulated precast panel with structural and thermal performance optimized. With the greater flow ability properties of UHP-FRC, it has been possible to fabricate the more detailed geometry that can create self-shading surface. The panels are designed to be most efficient in terms of time, materials and cost using UHP-FRC.

Appendix A

Deck bulb Tee

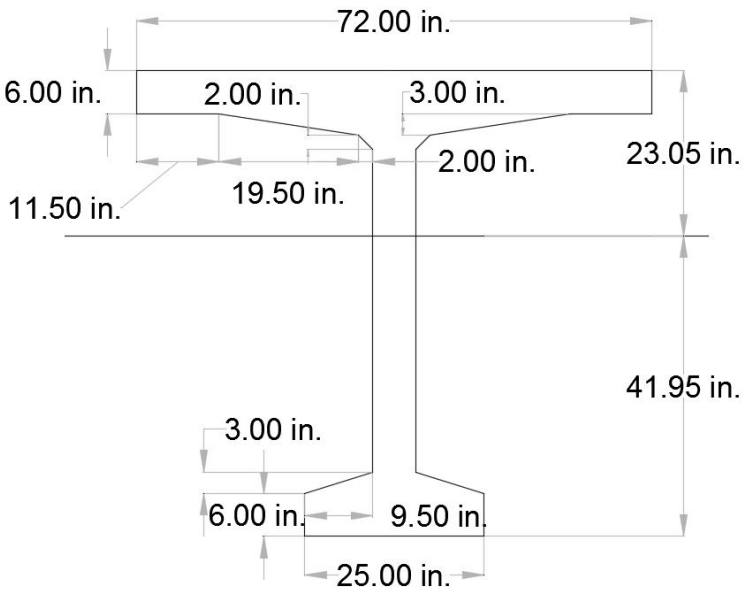

Deck BT 65

Area, A	1,003 $in.^2$
Moment of Inertia, I	559,367 $in.^4$
Y_t	23.05 in.
Y_b	41.95 in.
S_t	24,268 $in.^3$
S_b	13,334 $in.^3$
wt	1,045 lb/ft
M_{cr}	26,668 kip-inch (f_r = 2 ksi)
	40,002 kip-inch (f_r = 3 ksi)
	53,336 kip-inch (f_r = 4 ksi)

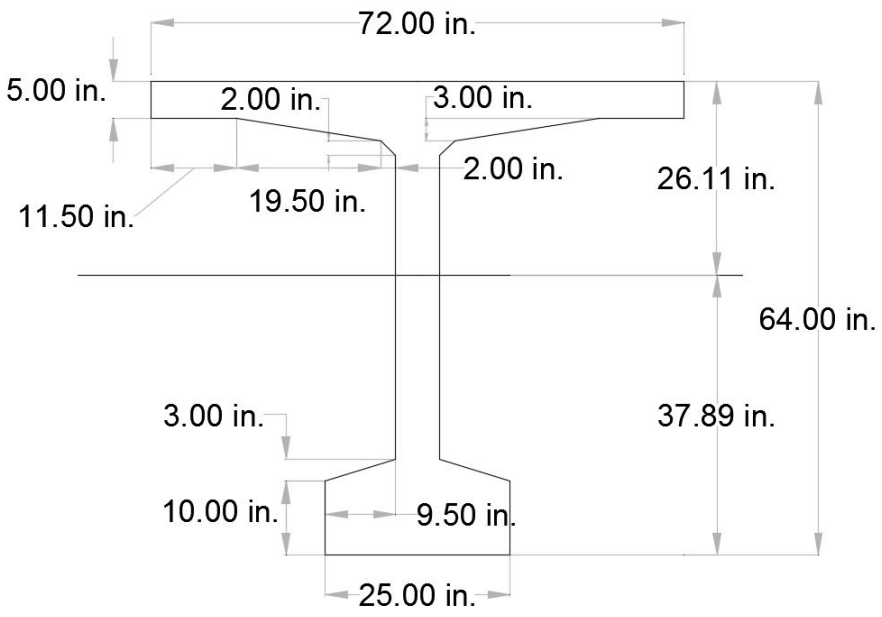

Deck BT 64 M4

Area, A	1,007 $in.^2$
Moment of Inertia, I	586,301 $in.^4$
Y_t	26.11 in.
Y_b	37.89 in.
S_t	22,455 $in.^3$
S_b	15,474 $in.^3$
wt	1,049 lb/ft
M_{cr}	30,948 kip-inch (f_r = 2 ksi)
	46,422 kip-inch (f_r = 3 ksi)
	61,896 kip-inch (f_r = 4 ksi)

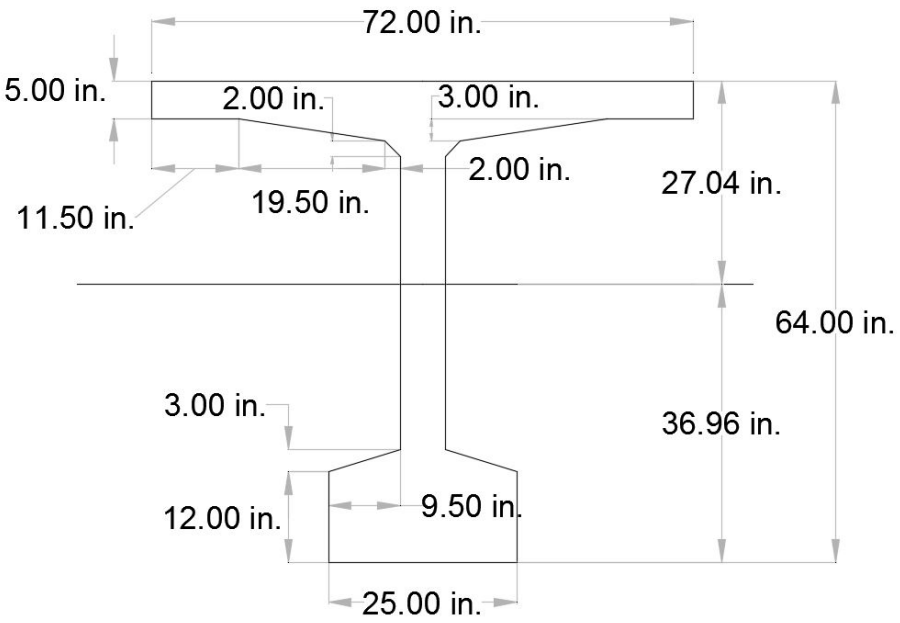

Deck BT 64 M5

Area, A	1,045 $in.^2$
Moment of Inertia, I	609,940 $in.^4$
Y_t	27.04 in.
Y_b	36.96 in.
S_t	22,557 $in.^3$
S_b	16,503 $in.^3$
wt	1,089 lb/ft
M_{cr}	33,005 kip-inch (f_r = 2 ksi)
	49,509 kip-inch (f_r = 3 ksi)
	66,012 kip-inch (f_r = 4 ksi)

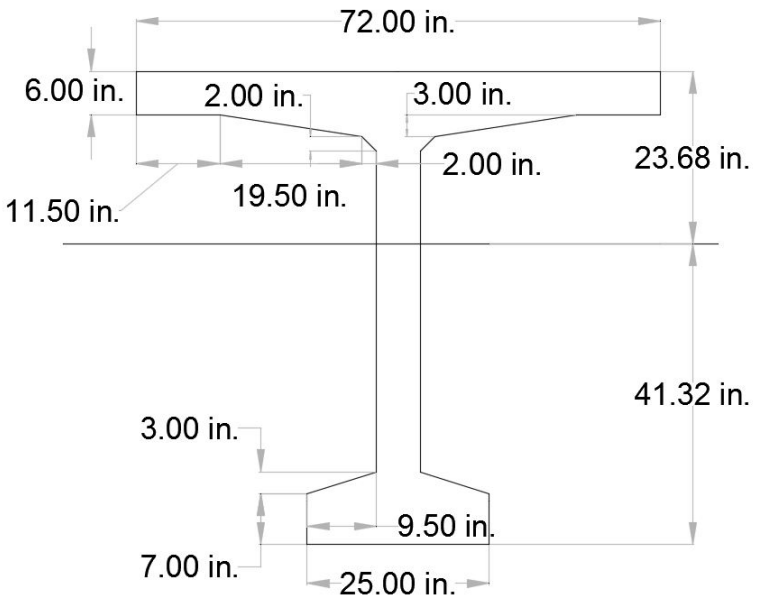

Deck BT 65 M1

Area, A	1,022 $in.^2$
Moment of Inertia, I	580,872 $in.^4$
Y_t	23.68 in.
Y_b	41.32 in.
S_t	24,530 $in.^3$
S_b	14,058 $in.^3$
wt	1,065 lb/ft
M_{cr}	28,116 kip-inch (f_r = 2 ksi)
	42,174 kip-inch (f_r = 3 ksi)
	56,232 kip-inch (f_r = 4 ksi)

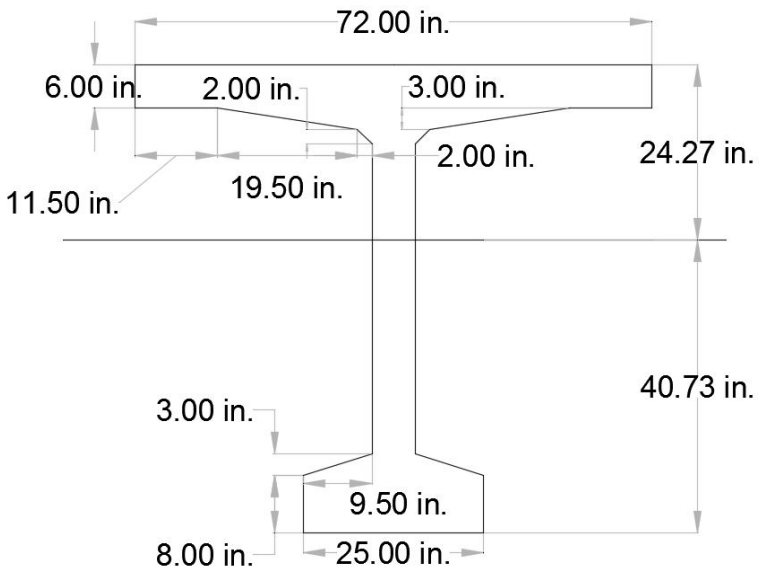

Deck BT 65 M2

Area, A	1,041 $in.^2$
Moment of Inertia, I	600,367 $in.^4$
Y_t	24.27 in.
Y_b	40.73 in.
S_t	24,737 $in.^3$
S_b	14,740 $in.^3$
wt	1,084 lb/ft
M_{cr}	29,480 kip-inch (f_r = 2 ksi)
	44,220 kip-inch (f_r = 3 ksi)
	58,960 kip-inch (f_r = 4 ksi)

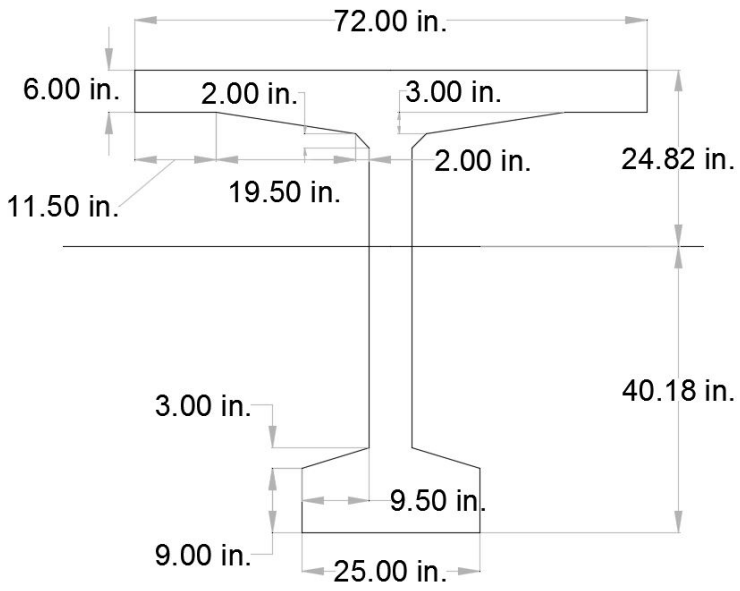

Deck BT 65 M3

Area, A	1,060 in.^{2}
Moment of Inertia, I	617,999 in.^{4}
Y_t	24.82 in.
Y_b	40.18 in.
S_t	24,899 in.^{3}
S_b	15,381 in.^{3}
wt	1,104 lb/ft
M_{cr}	30,762 kip-inch (f_r = 2 ksi)
	46,143 kip-inch (f_r = 3 ksi)
	61,524 kip-inch (f_r = 4 ksi)

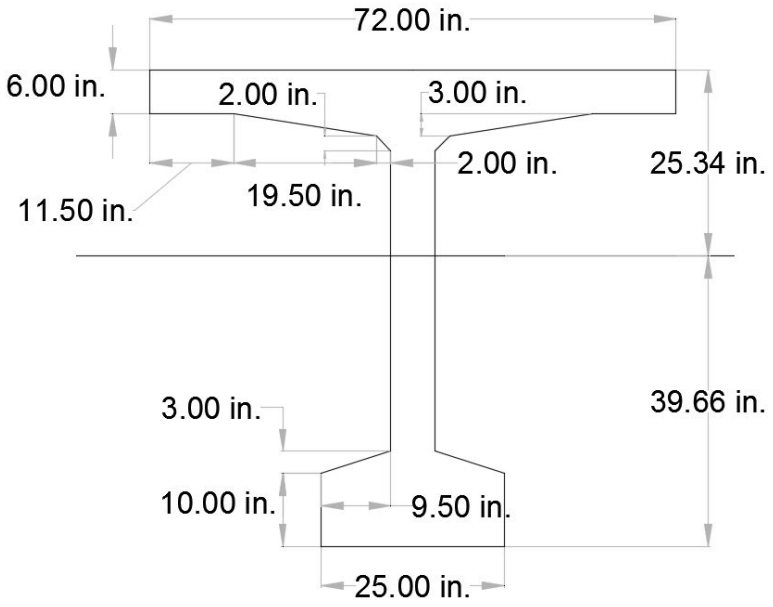

Deck BT 65 M4

Area, A	1,079 $in.^2$
Moment of Inertia, I	633,903 $in.^4$
Y_t	25.34 in.
Y_b	39.66 in.
S_t	25,016 $in.^3$
S_b	15,983 $in.^3$
wt	1,124 lb/ft
M_{cr}	31,966 kip-inch (f_r = 2 ksi)
	47,949 kip-inch (f_r = 3 ksi)
	63,932 kip-inch (f_r = 4 ksi)

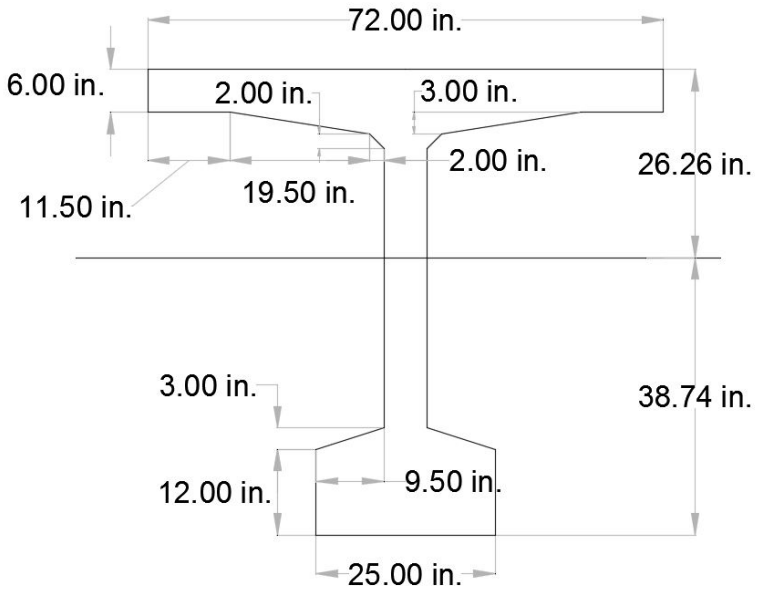

Deck BT 65 M5

Area, A	1,117 in.^{2}
Moment of Inertia, I	661,025 in.^{4}
Y_t	26.26 in.
Y_b	38.74 in.
S_t	25,172 in.^{3}
S_b	17,063 in.^{3}
wt	1,164 lb/ft
M_{cr}	34,126 kip-inch (f_r = 2 ksi)
	51,189 kip-inch (f_r = 3 ksi)
	68,252 kip-inch (f_r = 4 ksi)

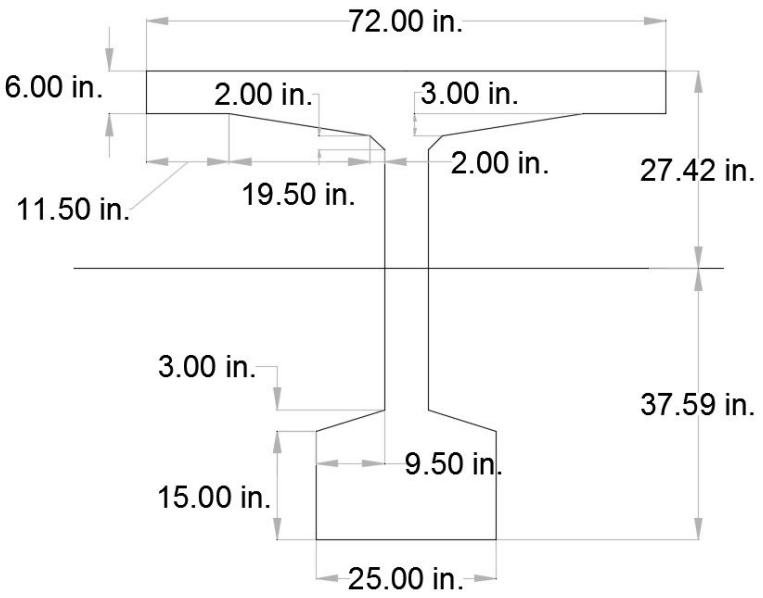

Deck BT 65 M6

Area, A	1,174 in.^{2}
Moment of Inertia, I	691,669 in.^{4}
Y_t	27.42 in.
Y_b	37.59 in.
S_t	25,225 in.^{3}
S_b	18,400 in.^{3}
wt	1,223 lb/ft
M_{cr}	36,800 kip-inch (f_r = 2 ksi)
	55,200 kip-inch (f_r = 3 ksi)
	73,600 kip-inch (f_r = 4 ksi)

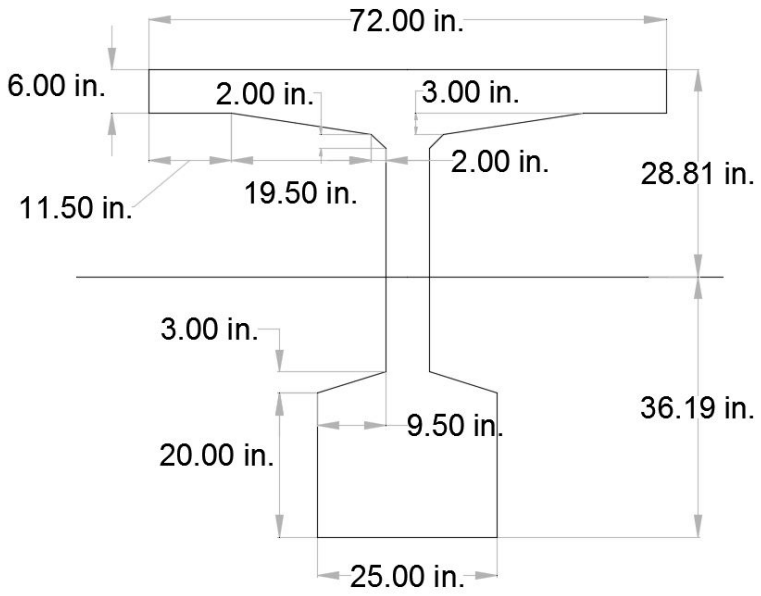

Deck BT 65 M7

Area, A	1,269 in.^{2}
Moment of Inertia, I	722,295 in.^{4}
Y_t	28.81 in.
Y_b	36.19 in.
S_t	25,071 in.^{3}
S_b	19,958 in.^{3}
wt	1,322 lb/ft
M_{cr}	39,916 kip-inch (f_r = 2 ksi)
	59,874 kip-inch (f_r = 3 ksi)
	79,832 kip-inch (f_r = 4 ksi)

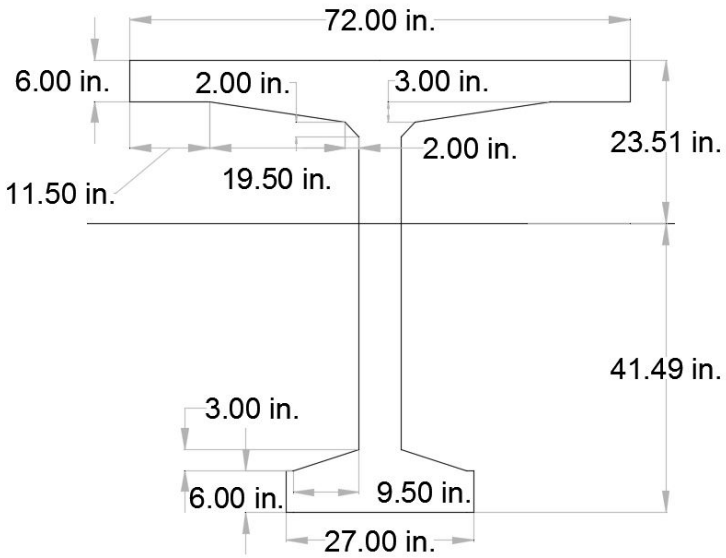

Deck BT 65 M8

Area, A	1,015 $in.^2$
Moment of Inertia, I	577,390 $in.^4$
Y_t	23.51 in.
Y_b	41.49 in.
S_t	24,559 $in.^3$
S_b	13,916 $in.^3$
wt	1,057 lb/ft
M_{cr}	27,832 kip-inch (f_r = 2 ksi)
	41,748 kip-inch (f_r = 3 ksi)
	55,664 kip-inch (f_r = 4 ksi)

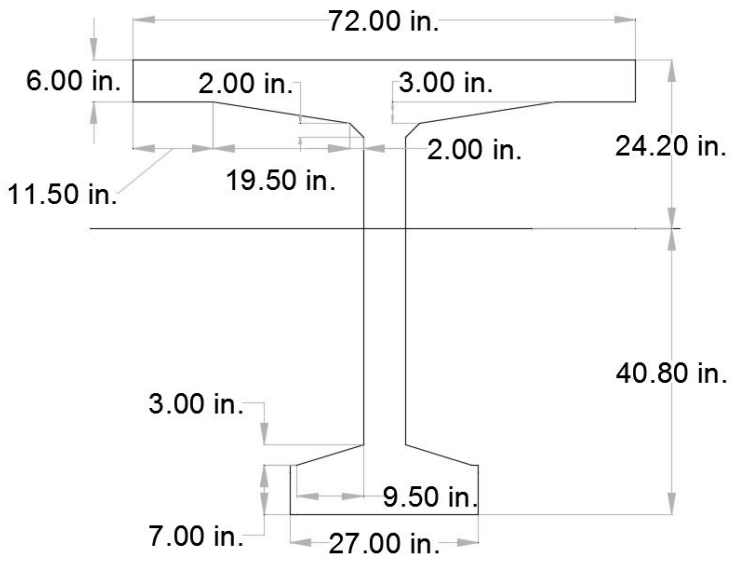

Deck BT 65 M9

Area, A	1,036 in.^{2}
Moment of Inertia, I	600,679 in.^{4}
Y_t	24.20 in.
Y_b	40.80 in.
S_t	24,821 in.^{3}
S_b	14,723 in.^{3}
wt	1,079 lb/ft
M_{cr}	29,446 kip-inch (f_r = 2 ksi)
	44,169 kip-inch (f_r = 3 ksi)
	58,892 kip-inch (f_r = 4 ksi)

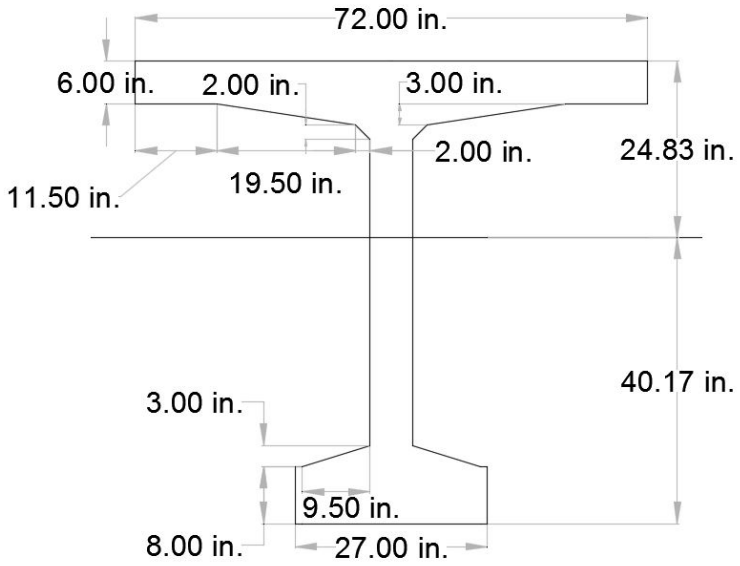

Deck BT 65 M10

Area, A	1,057 $in.^2$
Moment of Inertia, I	621,707 $in.^4$
Y_t	24.83 in.
Y_b	40.17 in.
S_t	25,039 $in.^3$
S_b	15,477 $in.^3$
wt	1,101 lb/ft
M_{cr}	30,954 kip-inch (f_r = 2 ksi)
	46,431 kip-inch (f_r = 3 ksi)
	61,908 kip-inch (f_r = 4 ksi)

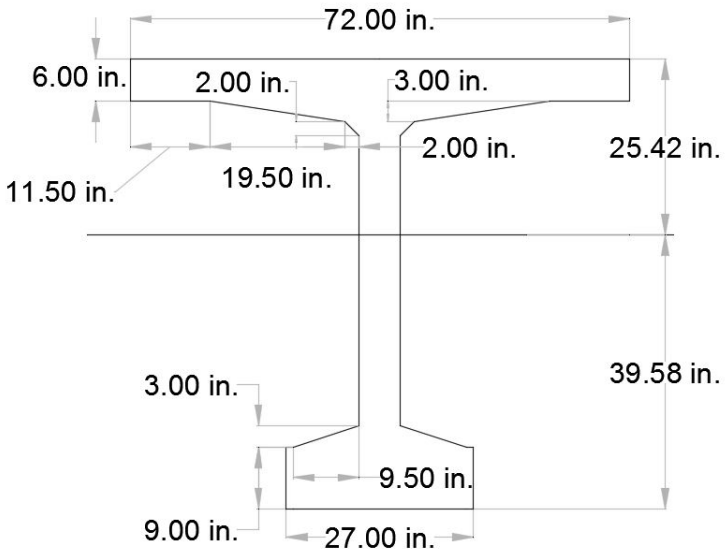

Deck BT 65 M11

Area, A	1,078 $in.^2$
Moment of Inertia, I	640,647 $in.^4$
Y_t	25.42 in.
Y_b	39.58 in.
S_t	25,202 $in.^3$
S_b	16,186 $in.^3$
wt	1,123 lb/ft
M_{cr}	32,372 kip-inch (f_r = 2 ksi)
	48,558 kip-inch (f_r = 3 ksi)
	64,744 kip-inch (f_r = 4 ksi)

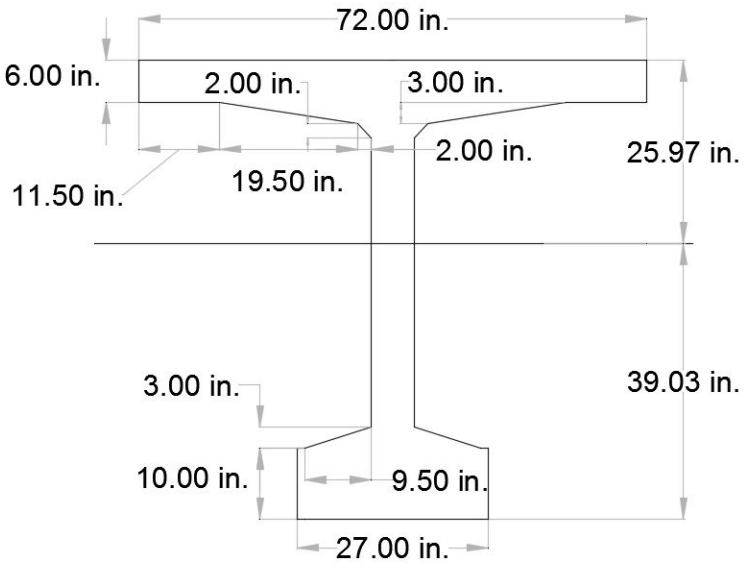

Deck BT 65 M12

Area, A	1,099 $in.^2$
Moment of Inertia, I	657,661 $in.^4$
Y_t	25.97 in.
Y_b	39.03 in.
S_t	25,324 $in.^3$
S_b	16,850 $in.^3$
wt	1,145 lb/ft
M_{cr}	33,700 kip-inch (f_r = 2 ksi)
	50,550 kip-inch (f_r = 3 ksi)
	67,400 kip-inch (f_r = 4 ksi)

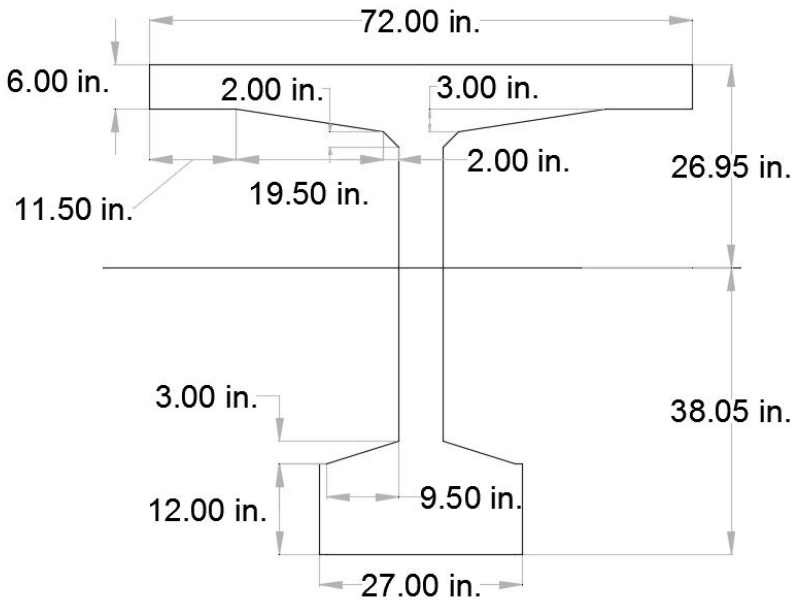

Deck BT 65 M13

Area, A	1,141 in.^{2}
Moment of Inertia, I	686,494 in.^{4}
Y_t	26.95 in.
Y_b	38.05 in.
S_t	25,473 in.^{3}
S_b	18,042 in.^{3}
wt	1,189 lb/ft
M_{cr}	36,084 kip-inch (f_r = 2 ksi)

	54,126 kip-inch (f_r = 3 ksi)
	72,168 kip-inch (f_r = 4 ksi)

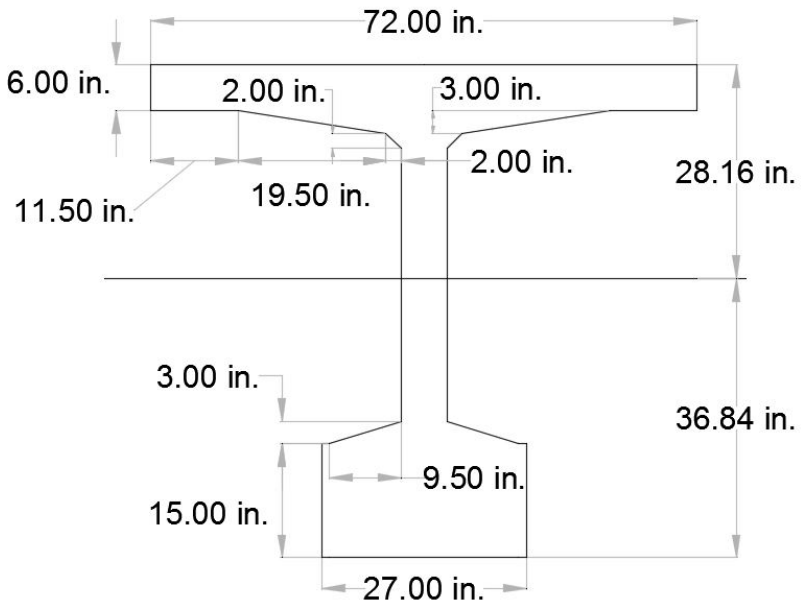

Deck BT 65 M14

Area, A	1,204 in.^{2}
Moment of Inertia, I	718,708 in.^{4}
Y_t	28.16 in.
Y_b	36.84 in.
S_t	25,522 in.^{3}
S_b	19,509 in.^{3}

wt	1,254 lb/ft
M_{cr}	39,018 kip-inch (f_r = 2 ksi)
	58,527 kip-inch (f_r = 3 ksi)
	78,036 kip-inch (f_r = 4 ksi)

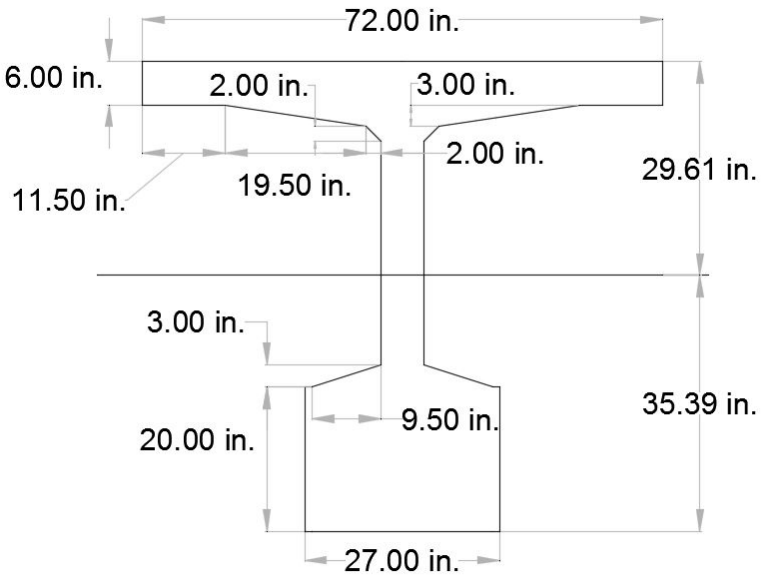

Deck BT 65 M15

Area, A	1,309 in.^{2}
Moment of Inertia, I	750,234 in.^{4}
Y_t	29.61 in.
Y_b	35.39 in.

S_t	25,337 in.^{3}
S_b	21,199 in.^{3}
wt	1,364 lb/ft
M_{cr}	42,398 kip-inch (f_r = 2 ksi)
	63,597 kip-inch (f_r = 3 ksi)
	84,796 kip-inch (f_r = 4 ksi)

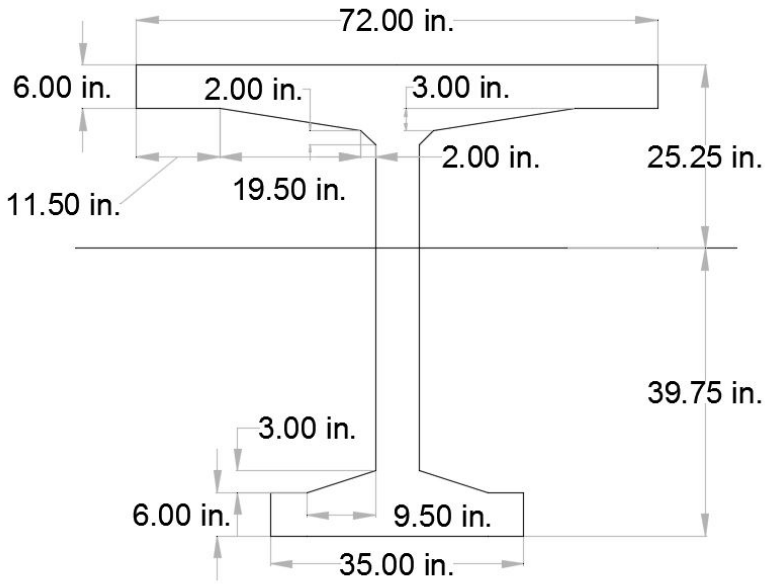

Deck BT 65 M16

Area, A	1,063 in.^{2}
Moment of Inertia, I	645,422 in.^{4}

Y_t	25.25 in.
Y_b	39.75 in.
S_t	25,561 in.^{3}
S_b	16,237 in.^{3}
wt	1,107 lb/ft
M_{cr}	32,474 kip-inch (f_r = 2 ksi)
	48,711 kip-inch (f_r = 3 ksi)
	64,948 kip-inch (f_r = 4 ksi)

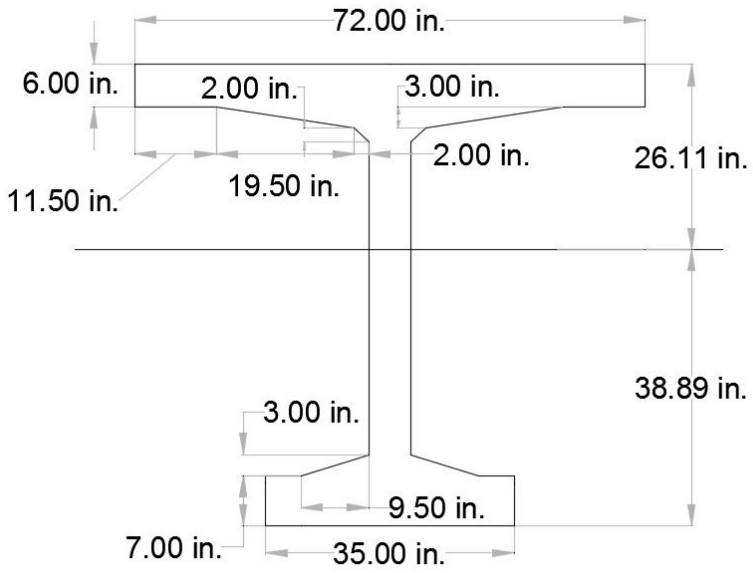

Deck BT 65 M17

Area, A	1,092 $in.^2$
Moment of Inertia, I	674,843 $in.^4$
Y_t	26.11 in.
Y_b	38.89 in.
S_t	25,846 $in.^3$
S_b	17,353 $in.^3$
wt	1,138 lb/ft
M_{cr}	34,706 kip-inch (f_r = 2 ksi)
	52,059 kip-inch (f_r = 3 ksi)
	69,412 kip-inch (f_r = 4 ksi)

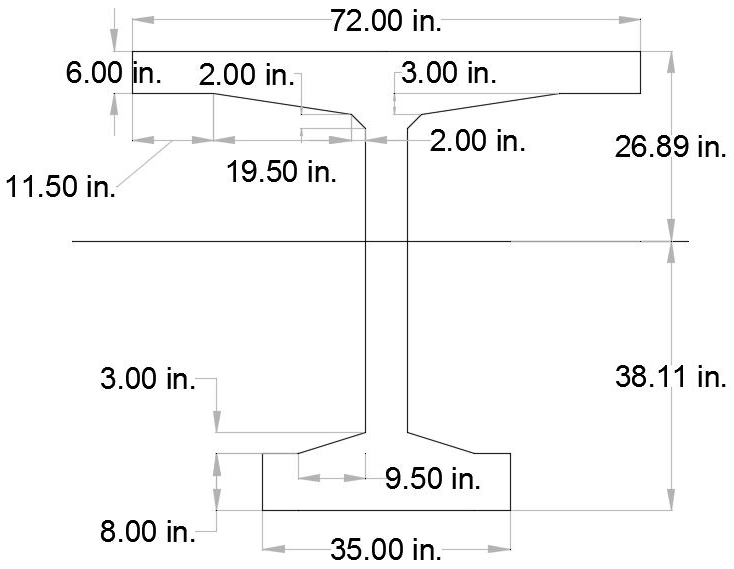

Deck BT 65 M18

Area, A	1,121 $in.^2$
Moment of Inertia, I	700,998 $in.^4$
Y_t	26.89 in.
Y_b	38.11 in.
S_t	26,069 $in.^3$
S_b	18,394 $in.^3$
wt	1,168 lb/ft
M_{cr}	36,788 kip-inch (f_r = 2 ksi)
	55,182 kip-inch (f_r = 3 ksi)
	73,476 kip-inch (f_r = 4 ksi)

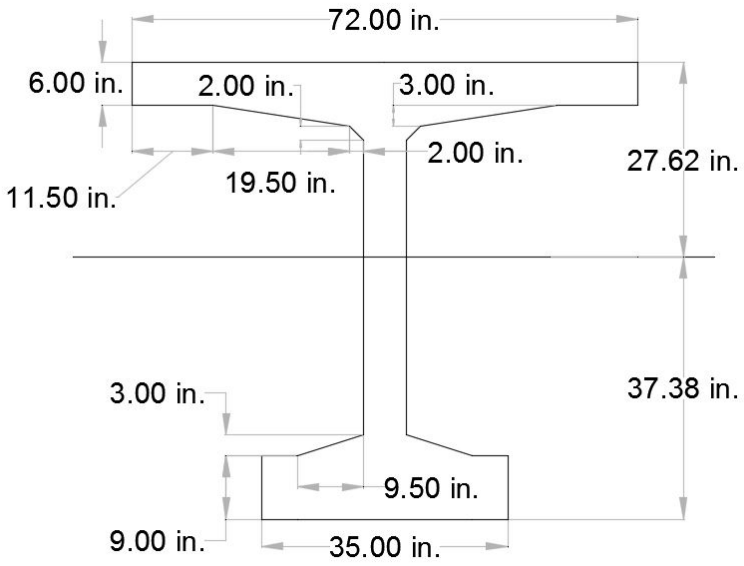

Deck BT 65 M19

Area, A	1,150 in.^{2}
Moment of Inertia, I	724,188 in.^{4}
Y_t	27.62 in.
Y_b	37.38 in.
S_t	26,220 in.^{3}
S_b	19,374 in.^{3}
wt	1,198 lb/ft
M_{cr}	38,748 kip-inch (f_r = 2 ksi)
	58,122 kip-inch (f_r = 3 ksi)

	77,496 kip-inch (f_r = 4 ksi)

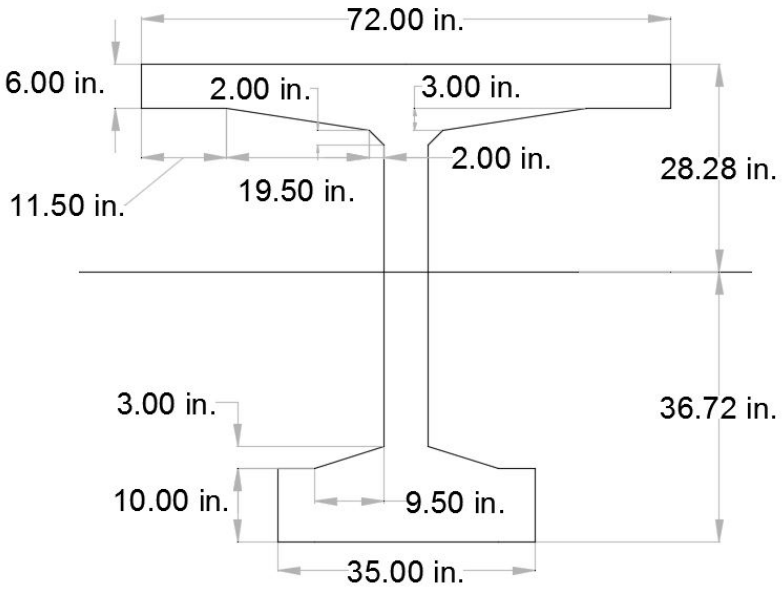

Deck BT 65 M20

Area, A	1,179 in.^{2}
Moment of Inertia, I	744,689 in.^{4}
Y_t	28.28 in.
Y_b	36.72 in.
S_t	26,333 in.^{3}
S_b	20,280 in.^{3}
wt	1,228 lb/ft

M_{cr}	40,564 kip-inch (f_r = 2 ksi)
	60,840 kip-inch (f_r = 3 ksi)
	81,120 kip-inch (f_r = 4 ksi)

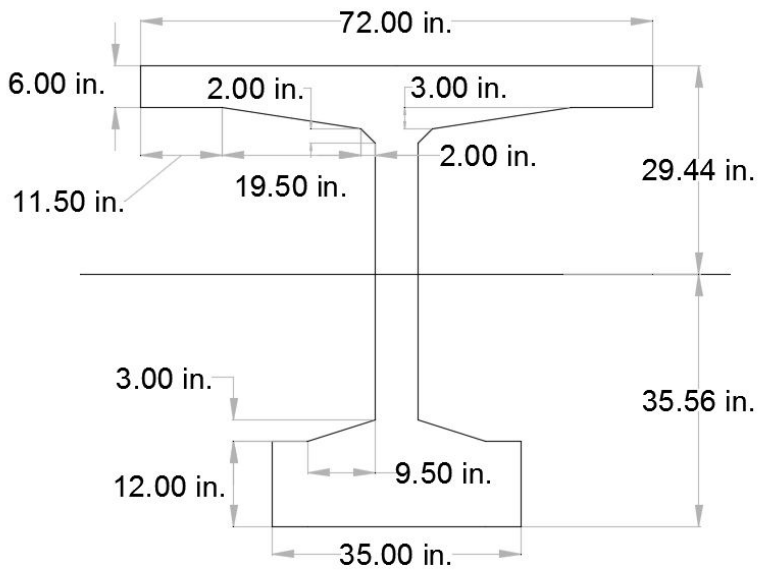

Deck BT 65 M21

Area, A	1,237 in.^{2}
Moment of Inertia, I	778,598 in.^{4}
Y_t	29.44 in.
Y_b	35.56 in.
S_t	26,447 in.^{3}

S_b	21,895 in.^{3}
wt	1,289 lb/ft
M_{cr}	43,790 kip-inch (f_r = 2 ksi)
	65,685 kip-inch (f_r = 3 ksi)
	87,580 kip-inch (f_r = 4 ksi)

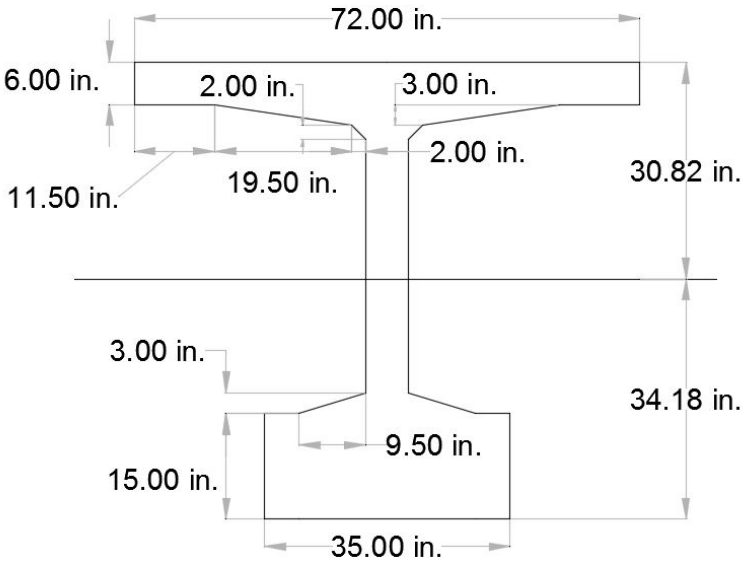

Deck BT 65 M22

Area, A	1,324 in.^{2}
Moment of Inertia, I	814,867 in.^{4}
Y_t	30.82 in.

Y_b	34.18 in.
S_t	26,440 in.^{3}
S_b	23,840 in.^{3}
wt	1,379 lb/ft
M_{cr}	47,680 kip-inch (f_r = 2 ksi)
	71,520 kip-inch (f_r = 3 ksi)
	95,360 kip-inch (f_r = 4 ksi)

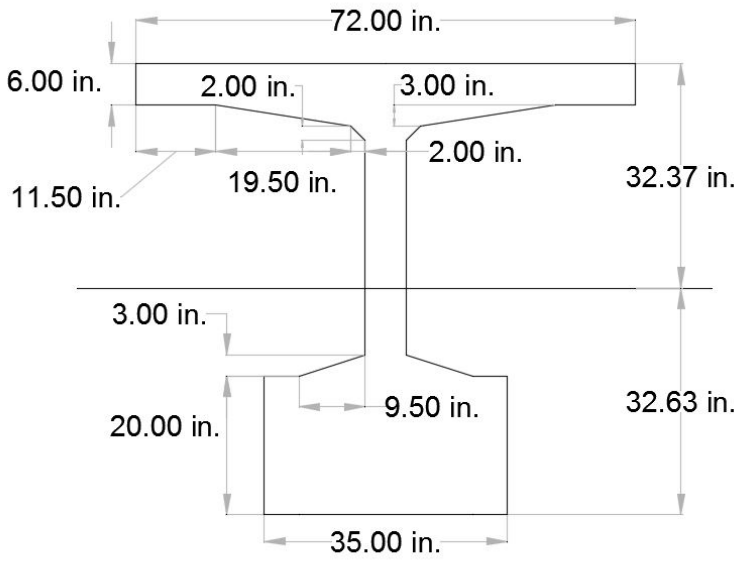

Deck BT 65 M23

Area, A	1,469 in.^{2}

Moment of Inertia, I	847,502 in.^{4}
Y_t	32.37 in.
Y_b	32.63 in.
S_t	26,182 in.^{3}
S_b	25,973 in.^{3}
wt	1,530 lb/ft
M_{cr}	51,946 kip-inch (f_r = 2 ksi)
	77,919 kip-inch (f_r = 3 ksi)
	103,892 kip-inch (f_r = 4 ksi)

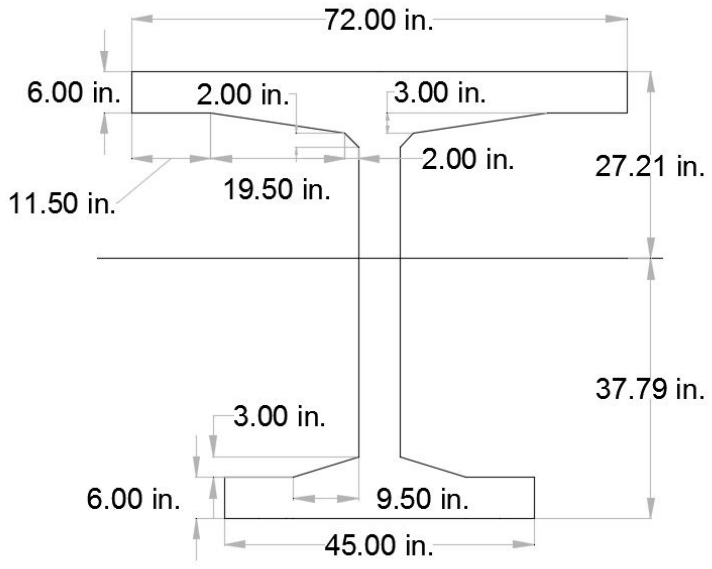

Deck BT 65 M24

Area, A	1,123 $in.^2$
Moment of Inertia, I	722,301 $in.^4$
Y_t	27.21 in.
Y_b	37.79 in.
S_t	26,545 $in.^3$
S_b	19,114 $in.^3$
wt	1,170 lb/ft
M_{cr}	38,228 kip-inch (f_r = 2 ksi)
	57,342 kip-inch (f_r = 3 ksi)
	76,456 kip-inch (f_r = 4 ksi)

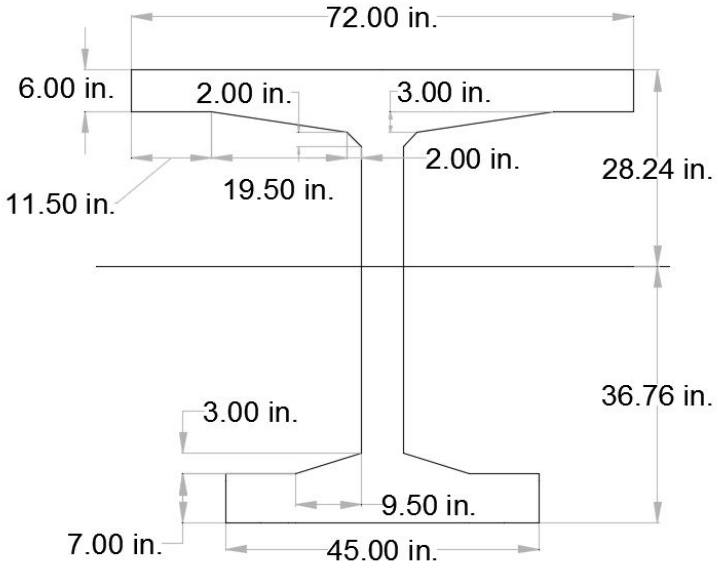

Deck BT 65 M25

Area, A	1,162 $in.^2$
Moment of Inertia, I	757,528 $in.^4$
Y_t	28.24 in.
Y_b	36.76 in.
S_t	26,825 $in.^3$
S_b	20,607 $in.^3$
wt	1,210 lb/ft
M_{cr}	41,214 kip-inch (f_r = 2 ksi)
	61,821 kip-inch (f_r = 3 ksi)
	82,428 kip-inch (f_r = 4 ksi)

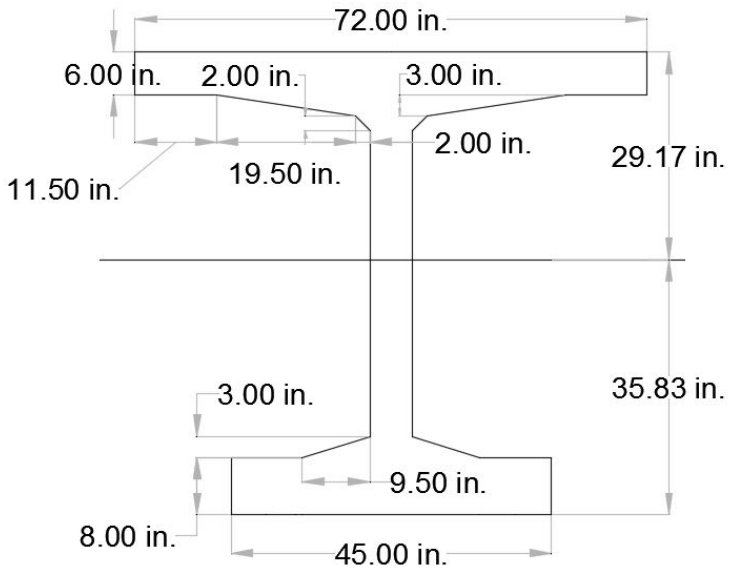

Deck BT 65 M26

Area, A	1,201 $in.^2$
Moment of Inertia, I	788,279 $in.^4$
Y_t	29.17 in.
Y_b	35.83 in.
S_t	27,024 $in.^3$
S_b	22,000 $in.^3$
wt	1,251 lb/ft
M_{cr}	44,000 kip-inch (f_r = 2 ksi)
	66,000 kip-inch (f_r = 3 ksi)

	88,000 kip-inch (f_r = 4 ksi)

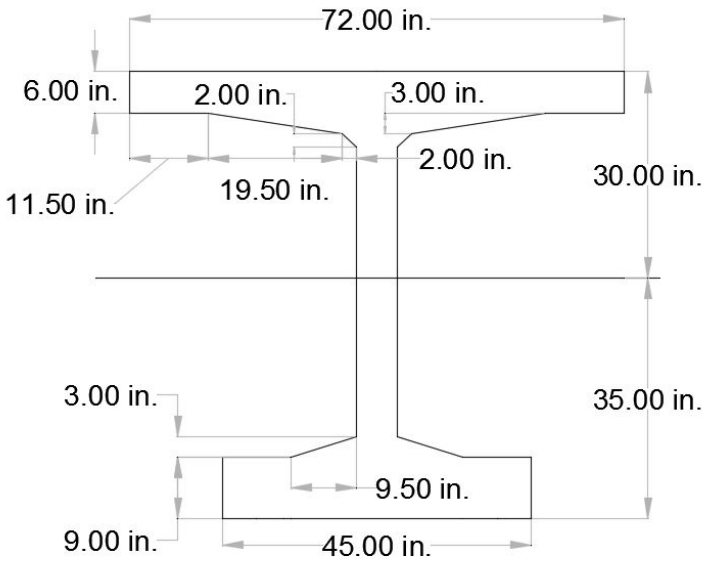

Deck BT 65 M27

Area, A	1,240 in.^{2}
Moment of Inertia, I	815,050 in.^{4}
Y_t	30.00 in.
Y_b	35.00 in.
S_t	27,168 in.^{3}
S_b	23,287 in.^{3}
wt	1,292 lb/ft

M_{cr}	46,574 kip-inch (f_r = 2 ksi)
	69,861 kip-inch (f_r = 3 ksi)
	93,148 kip-inch (f_r = 4 ksi)

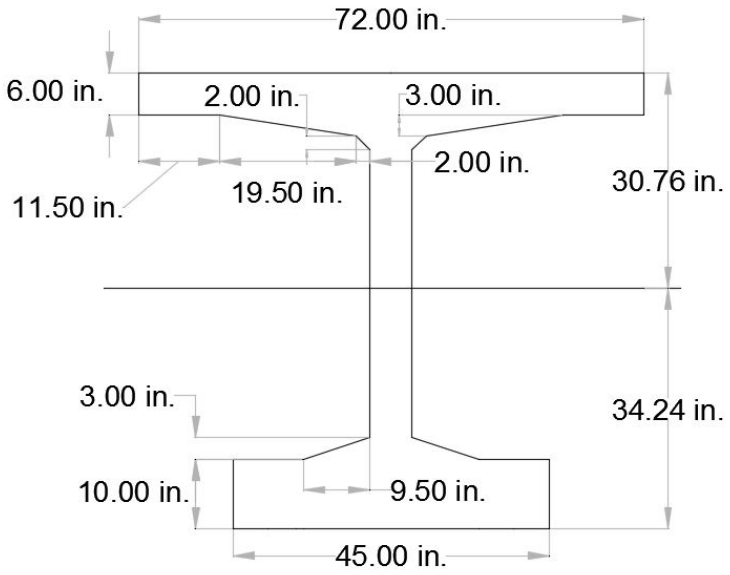

Deck BT 65 M28

Area, A	1,279 in.^{2}
Moment of Inertia, I	838,281 in.^{4}
Y_t	30.76 in.
Y_b	34.24 in.
S_t	27,252 in.^{3}

S_b	24,483 in.^{3}
wt	1,332 lb/ft
M_{cr}	48,966 kip-inch (f_r = 2 ksi)
	73,449 kip-inch (f_r = 3 ksi)
	97,932 kip-inch (f_r = 4 ksi)

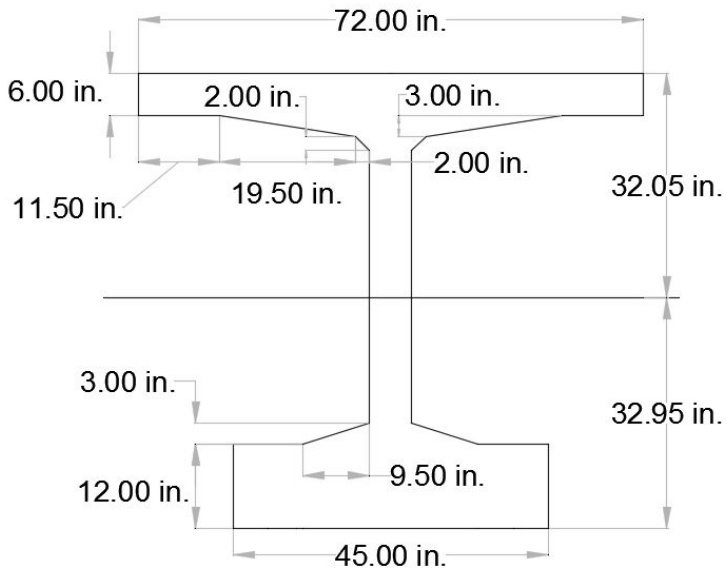

Deck BT 65 M29

Area, A	1,357 in.^{2}
Moment of Inertia, I	875,632 in.^{4}
Y_t	32.05 in.

Y_b	32.95 in.
S_t	27,321 in.^{3}
S_b	26,575 in.^{3}
wt	1,414 lb/ft
M_{cr}	53,150 kip-inch (f_r = 2 ksi)
	79,725 kip-inch (f_r = 3 ksi)
	106,300 kip-inch (f_r = 4 ksi)

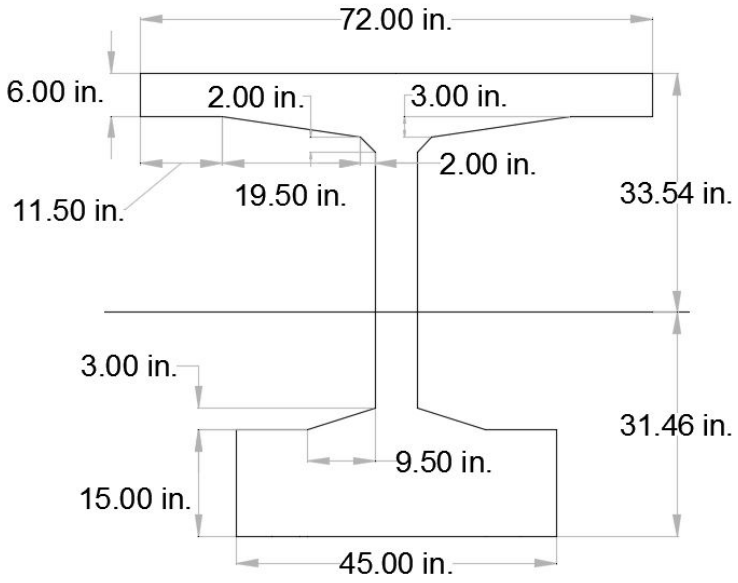

Deck BT 65 M30

Area, A	1,474 in.^{2}

Moment of Inertia, I	913,562 in.^{4}
Y_t	33.54 in.
Y_b	31.46 in.
S_t	27,238 in.^{3}
S_b	29,039 in.^{3}
wt	1,535 lb/ft
M_{cr}	58,078 kip-inch (f_r = 2 ksi)
	87,117 kip-inch (f_r = 3 ksi)
	116,156 kip-inch (f_r = 4 ksi)

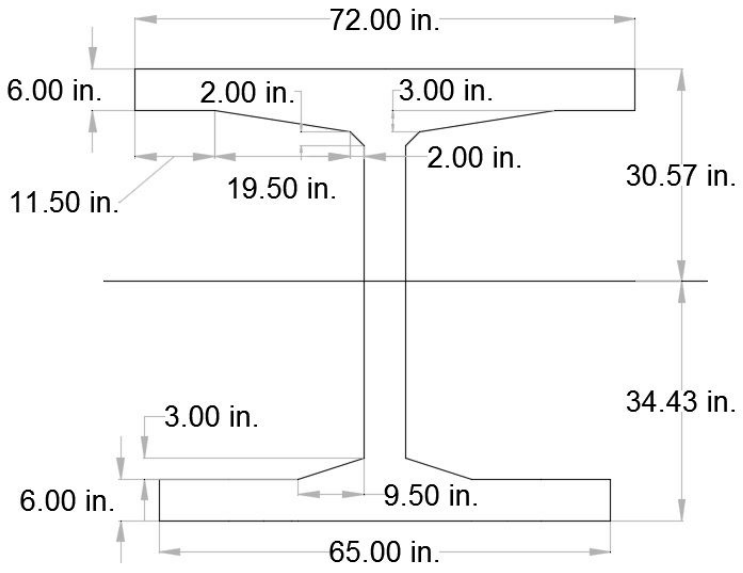

Deck BT 65 M31

Area, A	1,243 $in.^2$
Moment of Inertia, I	853,845 $in.^4$
Y_t	30.57 in.
Y_b	34.42 in.
S_t	27,931 $in.^3$
S_b	24,807 $in.^3$
wt	1,295 lb/ft
M_{cr}	49,614 kip-inch (f_r = 2 ksi)
	74,421 kip-inch (f_r = 3 ksi)
	99,216 kip-inch (f_r = 4 ksi)

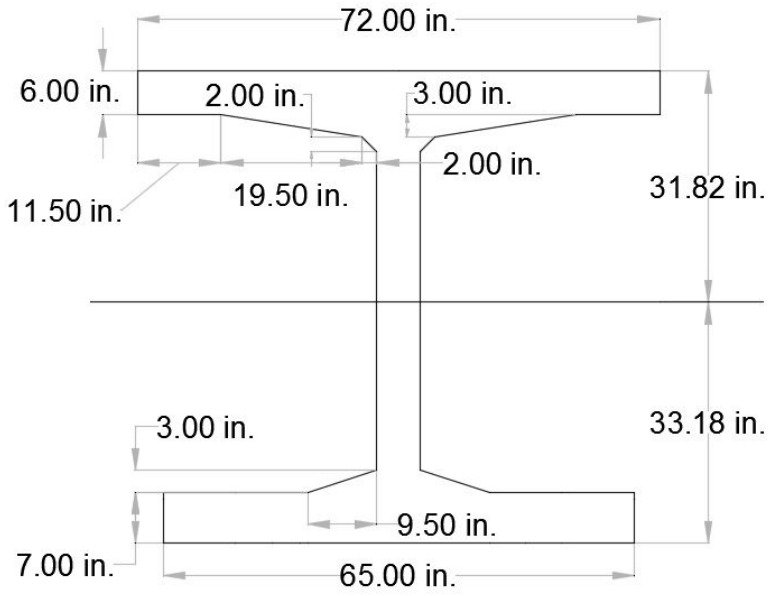

Deck BT 65 M32

Area, A	1,302 $in.^2$
Moment of Inertia, I	896,316 $in.^4$
Y_t	31.82 in.
Y_b	33.18 in.
S_t	28,168 $in.^3$
S_b	27,014 $in.^3$
wt	1,356 lb/ft
M_{cr}	54,028 kip-inch (f_r = 2 ksi)
	81,042 kip-inch (f_r = 3 ksi)
	108,056 kip-inch (f_r = 4 ksi)

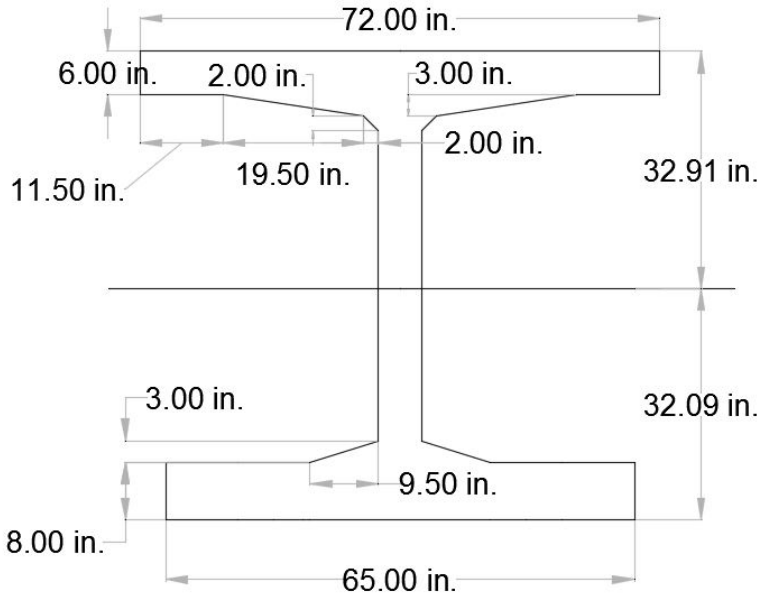

Deck BT 65 M33

Area, A	1,361 in.^{2}
Moment of Inertia, I	932,209 in.^{4}
Y_t	32.91 in.
Y_b	32.09 in.
S_t	28,326 in.^{3}
S_b	29,050 in.^{3}
wt	1,418 lb/ft
M_{cr}	58,100 kip-inch (f_r = 2 ksi)
	87,150 kip-inch (f_r = 3 ksi)

	116,200 kip-inch (f_r = 4 ksi)

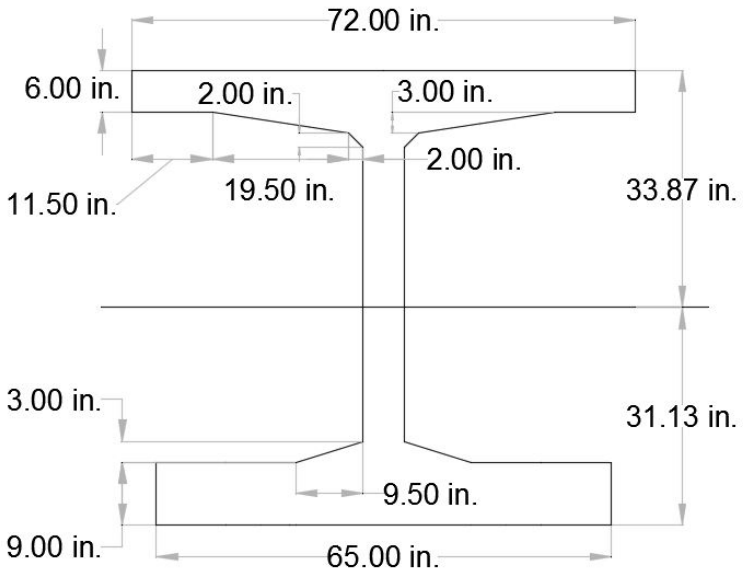

Deck BT 65 M34

Area, A	1,420 in.^{2}
Moment of Inertia, I	962,453 in.^{4}
Y_t	33.87 in.
Y_b	31.13 in.
S_t	28,416 in.^{3}
S_b	30,917 in.^{3}
wt	1,479 lb/ft

M_{cr}	61,834 kip-inch (f_r = 2 ksi)
	92,751 kip-inch (f_r = 3 ksi)
	123,668 kip-inch (f_r = 4 ksi)

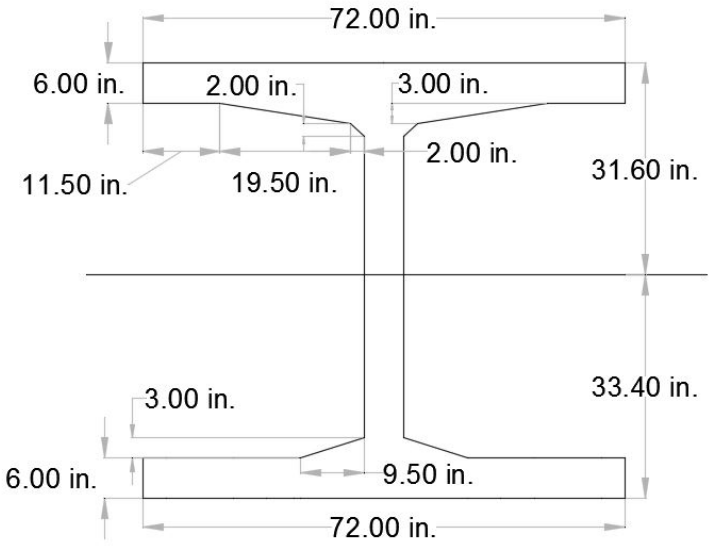

Deck BT 65 M35

Area, A	1,285 in.^{2}
Moment of Inertia, I	894,097 in.^{4}
Y_t	31.60 in.
Y_b	33.40 in.
S_t	28,294 in.^{3}

S_b	26,769 in.^{3}
wt	1,339 lb/ft
M_{cr}	53,538 kip-inch (f_r = 2 ksi)
	80,307 kip-inch (f_r = 3 ksi)
	107,076 kip-inch (f_r = 4 ksi)

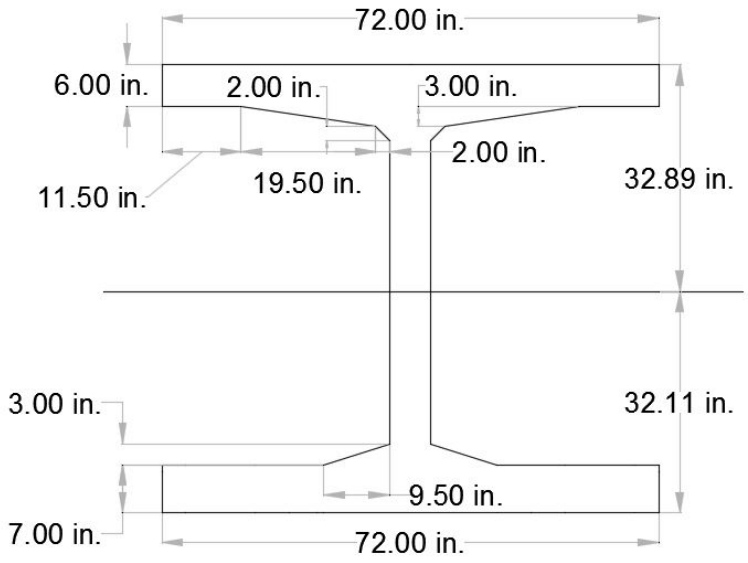

Deck BT 65 M36

Area, A	1,351 in.^{2}
Moment of Inertia, I	938,125 in.^{4}
Y_t	32.89 in.

Y_b	32.11 in.
S_t	28,523 in.^{3}
S_b	29,216 in.^{3}
wt	1,407 lb/ft
M_{cr}	58,432 kip-inch (f_r = 2 ksi)
	87,648 kip-inch (f_r = 3 ksi)
	116,864 kip-inch (f_r = 4 ksi)

Deck bulb Tee design		Pre-stressed			UHP-FRC		
Height (in.)	Length of girder (in.)	Number of strands	Mn (kip-inch)	Mcr (kip-inch)	Number of bars	Mn (kip-inch)	Mcr (kip-inch)
53	95	20-0.6" strands	51,146	40,317	7-#11	55,249	19,426 (fr = 2 ksi)
							29,139 (fr = 3 ksi)
	120	30-0.6" strands	73,302	57,501	10-#11	78,656	19,426 (fr = 2 ksi)
							29,139 (fr = 3 ksi)
65	95	18-0.6" strands	59,385	47,306	7-#11	68,353	26,668 (fr = 2 ksi)
							40,000 (fr = 3 ksi)
	120	23-0.6" strands	73,143	56,863	8-#11	78,046	26,668 (fr = 2 ksi)
							40,000 (fr = 3 ksi)

Appendix B

Double Tee

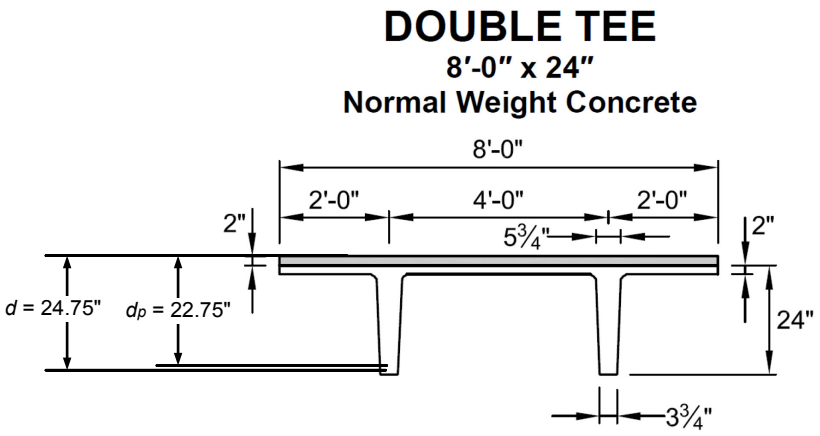

Section Properties

		Untopped		Topped	
A	=	401	$in.^2$	–	
I	=	20,985	$in.^4$	27,720	$in.^4$
y_b	=	17.15	in.	19.27	in.
y_t	=	6.85	in.	6.73	in.
S_b	=	1,224	$in.^3$	1,439	$in.^3$
S_t	=	3,064	$in.^3$	4,119	$in.^3$
wt	=	418	plf	618	plf
DL	=	50	psf	77	psf
V/S	=	1.41	in.		

Given:

- f'_c = 5000 psi and normal weight concrete for both the precast section and topping.
- Twelve (six in each stem) 0.5 in.-diameter 270 ksi low-relaxation strands; all strands are straight.
- All strands are bonded.
- f_{se} = 160 ksi.
- Mild steel reinforcement: two No. 6 bars (one in each stem). f_y = 60 ksi.
- Assume that each of the stems has a uniform width of 4.75 in. along the height.
- Span = 30 ft.

DESIGN OF PRESTRESSED DOUBLE-TEE WITH TOPPING:

Section properties:

- $d = 24.75\,in.$
- $d_p = 22.75\,in.$
- $\gamma_p = 0.28\,(low-relaxation\,strands)$
- $\rho_p = \dfrac{A_{ps}}{bd_p} = \dfrac{12\times 0.153}{8\times 12\times 22.75} = 0.00084$

- $\rho = \frac{A_s}{bd} = \frac{2 \times 0.44}{8 \times 12 \times 24.75} = 0.00037$

$$f_{ps} = f_{pu}\left(1 - \frac{\gamma_p}{\beta_1}\left(\rho_p \frac{f_{pu}}{f_c^{'}} + \frac{d}{d_p}\left(\omega - \omega^{'}\right)\right)\right)$$
$$= 270\left(1 - \frac{0.28}{0.8}\left(0.00084 \times \frac{270}{5} + \frac{24.75}{22.75} \times \frac{60}{5} \times 0.00037\right)\right)$$
$$= 265.3\,ksi$$

Assuming rectangular section behavior

$$A_s = 2 \times 0.44 = 0.88\,in^2, A_s^{'} = 0$$

$$0.85 f_c^{'} ab + A_s^{'} f_y^{'} = A_{ps} f_{ps} + A_s f_y$$
$$a = \frac{A_{ps} f_{ps} + A_s f_y}{0.85 f_c^{'} b}$$
$$= \frac{12 \times 0.153 \times 265.3 + 2 \times 0.44 \times 60}{0.85 \times 5 \times 96}$$
$$= 1.32 in. < h_f$$
$$c = \frac{a}{\beta_1}$$
$$= \frac{1.32}{0.8}$$
$$= 1.65\,in. < h_f$$

Design nominal moment capacity

$$M_n = A_{ps} f_{ps}\left(d_p - \frac{a}{2}\right) + A_s f_y\left(d - \frac{a}{2}\right) - A_s^{'} f_y^{'}\left(d^{'} - \frac{a}{2}\right)$$
$$= 12 \times 0.153 \times 265.3 \times \left(22.75 - \frac{1.32}{2}\right) + 2 \times 0.44 \times 60\left(24.75 - \frac{1.32}{2}\right)$$
$$= 12,032\,kip - in.$$

Check for Tension-controlled section

Pre-stressing steel:

$c = 1.65\,in.$

$d_p = 22.75\,in.$

$\varepsilon_{cu} = 0.003$

$$\frac{c}{d_p} = \frac{\varepsilon_{cu}}{\varepsilon_{cu} + \varepsilon_t}$$

$$\frac{1.65}{22.75} = \frac{0.003}{0.003 + \varepsilon_t}$$

$\varepsilon_t = 0.038 > 0.005$

Mild steel:

$c = 1.65\,in.$

$d = 24.75\,in.$

$\varepsilon_{cu} = 0.003$

$$\frac{c}{d} = \frac{\varepsilon_{cu}}{\varepsilon_{cu} + \varepsilon_t}$$

$$\frac{1.65}{24.75} = \frac{0.003}{0.003 + \varepsilon_t}$$

$\varepsilon_t = 0.042 > 0.005$

Tension controlled

Initial Cracking Moment

Weight of composite, $W_{dnc} = 618\,lb/ft$

$$M_{dnc} = \frac{W_{dnc} l^2}{8}$$

$$= \frac{0.618 \times 30^2}{8}$$

$$= 834,300\,lb - in.$$

$$P_e = A_{ps} f_{pe}$$
$$= 12 \times 0.153 \times 160$$
$$= 293.76\, kips$$
$$A_c(non-composite) = 401\, in^2$$
$$S_b(non-composite) = 1224\, in^3$$
$$S_c(composite) = 1439\, in^3$$
$$e(non-composite) = d_p - 2 - y_t = 22.75 - 2 - 6.85 = 13.9\, in.$$
$$f_r = -7.5\sqrt{f_c'}$$
$$= -7.5\sqrt{5000}$$
$$= -0.530\, ksi$$
$$M_{cr} = \left(-f_r + \frac{P_e}{A_c} + \frac{P_e e}{S_b} \right) S_c - M_{dnc} \left(\frac{S_c}{S_b} - 1 \right)$$
$$= \left(530 + \frac{293.76 \times 10^3}{401} + \frac{293.76 \times 10^3 \times 13.9}{1224} \right) 1439 - 834300 \left(\frac{1439}{1224} - 1 \right)$$
$$= 6470792.4\, lb - in.$$
$$= 6471\, kip - in.$$

Serviceability

Assuming a superimposed live load of 2,500 *lb/ft*

$$W_l = 0.2083\, kip / in$$
$$W_d = 0.0515\, kip / in$$
$$Factored\ load, W = 1.4W_d + 1.6W_l$$
$$= 1.4 \times 0.0515 + 1.6 \times 0.2083$$
$$= 0.40538\, kip / in$$

Camber due to prestressing force:

$$E_c = 57,000\sqrt{f_c'}$$
$$= 57,000\sqrt{5000}$$
$$= 4030\,ksi$$
$$\Delta_{prestress} = -\frac{P_e e l^2}{8EI}$$
$$= -\frac{293.76 \times 13.9 \times (30 \times 12)^2}{8 \times 4030 \times 27720}$$
$$= -0.59\,in.$$

Deflection due to loading:

$$\Delta_{load} = \frac{5wl^4}{384EI}$$
$$= \frac{5 \times 0.40538 \times (30 \times 12)^4}{384 \times 4030 \times 27720}$$
$$= 0.794\,in.$$

Net deflection at service:

$$\Delta_{net} = \Delta_{prestress} + \Delta_{load}$$
$$= -0.59 + 0.794$$
$$= 0.204\,in.$$

DESIGN OF PRESTRESSED DOUBLE-TEE WITH OUT TOPPING:

Section properties:

- $d = 22.75\,in.$
- $d_p = 20.75\,in.$
- $\gamma_p = 0.28\,(low - relaxation\ strands)$
- $\rho_p = \frac{A_{ps}}{bd_p} = \frac{12 \times 0.153}{8 \times 12 \times 20.75} = 0.00092$
- $\rho = \frac{A_s}{bd} = \frac{2 \times 0.44}{8 \times 12 \times 22.75} = 0.0004$

$$f_{ps} = f_{pu}\left(1-\frac{\gamma_p}{\beta_1}\left(\rho_p\frac{f_{pu}}{f_c^{'}}+\frac{d}{d_p}\left(\omega-\omega^{'}\right)\right)\right)$$

$$= 270\left(1-\frac{0.28}{0.8}\left(0.00092\times\frac{270}{5}+\frac{22.75}{20.75}\times\frac{60}{5}\times 0.0004\right)\right)$$

$$= 264.8\,ksi$$

Assuming rectangular section behavior

$$A_s = 2\times 0.44 = 0.88\,in^2,\ A_s^{'} = 0$$

$$0.85 f_c^{'} ab + A_s^{'} f_y^{'} = A_{ps} f_{ps} + A_s f_y$$

$$a = \frac{A_{ps} f_{ps} + A_s f_y}{0.85 f_c^{'} b}$$

$$= \frac{12\times 0.153\times 264.8 + 2\times 0.44\times 60}{0.85\times 5\times 96}$$

$$= 1.32 in. < h_f$$

$$c = \frac{a}{\beta_1}$$

$$= \frac{1.32}{0.8}$$

$$= 1.65\,in. < h_f$$

Design nominal moment capacity

$$M_n = A_{ps} f_{ps}\left(d_p-\frac{a}{2}\right)+A_s f_y\left(d-\frac{a}{2}\right)-A_s^{'} f_y^{'}\left(d^{'}-\frac{a}{2}\right)$$

$$= 12\times 0.153\times 264.8\times\left(20.75-\frac{1.32}{2}\right)+2\times 0.44\times 60\left(22.75-\frac{1.32}{2}\right)$$

$$= 10{,}933\,kip-in.$$

Check for Tension-controlled section

Pre-stressing steel:

$c = 1.65\,in.$

$d_p = 20.75\,in.$

$\varepsilon_{cu} = 0.003$

$$\frac{c}{d_p} = \frac{\varepsilon_{cu}}{\varepsilon_{cu} + \varepsilon_t}$$

$$\frac{1.65}{20.75} = \frac{0.003}{0.003 + \varepsilon_t}$$

$\varepsilon_t = 0.035 > 0.005$

Mild steel:

$c = 1.65\,in.$

$d = 22.75\,in.$

$\varepsilon_{cu} = 0.003$

$$\frac{c}{d} = \frac{\varepsilon_{cu}}{\varepsilon_{cu} + \varepsilon_t}$$

$$\frac{1.65}{22.75} = \frac{0.003}{0.003 + \varepsilon_t}$$

$\varepsilon_t = 0.038 > 0.005$

Tension controlled

<u>Transformed moment of Inertia</u>

$$n = \frac{E_s}{E_c} = \frac{29000}{4030.5} = 7.195$$

Transformed areas of strands:

$(n-1)A_{ps} = (7.195-1)\times 12 \times 0.153 = 11.374, d = 20.75\,in.$

Centroid of transformed section:

Part	**Area (in^2)**	**y_{top} ($in.$)**	**Ay_{top} ($in.^3$)**
Concrete	401	6.85	2746.85
Strands	11.374	20.75	236.01
	$\sum A = 412.374$		$\sum Ay_{top} = 2982.86$

$$y_{top} = \frac{\sum Ay_{top}}{\sum A} = \frac{2982.86}{412.374} = 7.23\,in.$$

$$y_{bottom} = 24 - y_{top} = 24 - 7.23 = 16.77\,in.$$

Uncracked transformed moment of Inertia:

Part	Area (in^2)	$\bar{y}$ ($in.$)	$I_{own\ axis}$ ($in.^4$)	Ay^2 ($in.^4$)
Concrete	401	-0.38	20,985	57.9
Strands	11.374	13.52	–	2079.06
				I = 23,122 $in.^4$

$I_{transformed} = 23{,}122\ in.^4$

Initial Cracking Moment

$$P_e = A_{ps} f_{pe}$$
$$= 12 \times 0.153 \times 160$$
$$= 293.76\,kips$$

$$A_c(non-composite) = 401\,in^2$$

$$S_b(non-composite, transformed) = 1378.77\,in^3$$

$$e(non-composite) = d_p - 2 - y_t = 22.75 - 2 - 6.85 = 13.9\,in.$$

$$f_r = -7.5\sqrt{f_c'}$$
$$= -7.5\sqrt{5000}$$
$$= -0.530\,ksi$$

$$M_{cr} = \left(-f_r + \frac{P_e}{A_c} + \frac{P_e e}{S_b}\right) S_b$$
$$= \left(530 + \frac{293.76 \times 10^3}{401} + \frac{293.76 \times 10^3 \times 13.9}{1378.77}\right) 1378.77$$
$$= 5824055\,lb - in.$$
$$= 5824\,kip - in.$$

Serviceability

Assuming a superimposed live load of 2,500 *lb/ft*

$$W_l = 0.2083\,kip/in$$
$$W_d = 0.0515\,kip/in$$
$$Factored\ load, W = 1.4W_d + 1.6W_l$$
$$= 1.4\times 0.0515 + 1.6\times 0.2083$$
$$= 0.40538\,kip/in$$

Camber due to prestressing force:

$$E_c = 57,000\sqrt{f_c'}$$
$$= 57,000\sqrt{5000}$$
$$= 4030\,ksi$$
$$\Delta_{prestress} = -\frac{P_e e l^2}{8EI}$$
$$= -\frac{293.76\times 13.9\times (30\times 12)^2}{8\times 4030\times 23122}$$
$$= -0.71\,in.$$

Deflection due to loading:

$$\Delta_{load} = \frac{5wl^4}{384EI}$$
$$= \frac{5\times 0.40538\times (30\times 12)^4}{384\times 4030\times 23122}$$
$$= 0.95\,in.$$

Net deflection at service:

$$\Delta_{net} = \Delta_{prestress} + \Delta_{load}$$
$$= -0.71 + 0.95$$
$$= 0.24\,in.$$

DESIGN OF NON-PRESTRESSED DOUBLE-TEE WITH UHP-FRC (UNTOPPED):

- Self-weight = 418 *lb/ft*
- Live load = 2,500 *lb/ft*
- f_c' = 22,000 *psi*
- E_c = 7,000 ksi
- 4-#11, 100 *ksi* steel
- d_t = 21 *in.*
- f_r = 2 *ksi*
- β_l = 0.65

Section properties

- A_C = 401 in^2
- I_g = 20,985 in^2
- y_b = 17.15 *in.*
- y_t = 6.85 *in.*
- S_b = 1,224 in^3
- S_t = 3,064 in^3

Transformed moment of Inertia

$$n = \frac{E_s}{E_c} = \frac{29000}{7000} = 4.143$$

Transformed areas of steel:

Layer1: $(n-1)A_{s1} = (4.143-1)\times 2\times 1.56 = 9.806, d_1 = 22\,in.$

Layer2: $(n-1)A_{s2} = (4.143-1)\times 2\times 1.56 = 9.806, d_2 = 20\,in.$

Centroid of transformed section:

Part	**Area (in^2)**	**y_{top} (*in.*)**	**Ay_{top} ($in.^3$)**
Concrete	401	6.85	2746.85
Steel layer 1	9.806	22	215.72
Steel layer 2	9.806	20	196.11
	$\sum A = 420.61$		$\sum Ay_{top} = 3158.68$

$$y_{top} = \frac{\sum Ay_{top}}{\sum A} = \frac{3158.68}{420.61} = 7.51 in.$$

$$y_{bottom} = 24 - y_{top} = 24 - 7.51 = 16.49 in.$$

Uncracked transformed moment of Inertia:

Part	**Area (in^2)**	**$\bar{y}$ ($in.$)**	**$I_{own\ axis}$ ($in.^4$)**	**Ay^2 ($in.^4$)**
Concrete	401	-0.66	20,985	174.68
Steel layer 1	9.806	14.49	–	2058.87
Steel layer 2	9.806	12.49	–	1529.74
				I = 24,748 $in.^4$

$I_{transformed} = 24{,}748\ in.^4$

Assuming rectangular section behavior

$$a = \frac{A_s f_y}{0.85 f_c^{'} b}$$

$$= \frac{4 \times 1.56 \times 100}{0.85 \times 22 \times 96}$$

$$= 0.348 in.$$

$$c = \frac{a}{\beta_1} = \frac{0348}{0.65} = 0.535 in.$$

Design nominal moment capacity

$$M_n = A_s f_y \left(d - \frac{a}{2} \right)$$

$$= 4 \times 1.56 \times 100 \left(21 - \frac{0.348}{2} \right)$$

$$= 12{,}995 kip - in.$$

Check for tension-controlled section

$$c = 0.535\,in.$$
$$d_t = 22\,in.$$
$$\varepsilon_{cu} = 0.015$$
$$\frac{c}{d_t} = \frac{\varepsilon_{cu}}{\varepsilon_{cu} + \varepsilon_t}$$
$$\frac{0.535}{22} = \frac{0.015}{0.015 + \varepsilon_t}$$
$$\varepsilon_t = 0.6 \gg 0.009$$

Initial cracking moment

$$S_b = \frac{I_{transformed}}{y_b} = \frac{24748}{16.49} = 1500$$
$$M_{cr} = f_r S_b$$
$$= 2 \times 1500$$
$$= 3000\,kip - in.$$

Serviceability

Assuming a superimposed live load of 2,500 *lb/ft*

$$W_l = 0.2083\,kip/in$$
$$W_d = 0.0515\,kip/in$$
$$Factored\ load, W = 1.4W_d + 1.6W_l$$
$$= 1.4 \times 0.0515 + 1.6 \times 0.2083$$
$$= 0.40538\,kip/in$$

$$\Delta = \frac{5wl^4}{384EI}$$
$$= \frac{5 \times 0.40538 \times (30 \times 12)^4}{384 \times 7000 \times 24748}$$
$$= 0.51\,in.$$

8'-0" × 24"
Normalweight Concrete

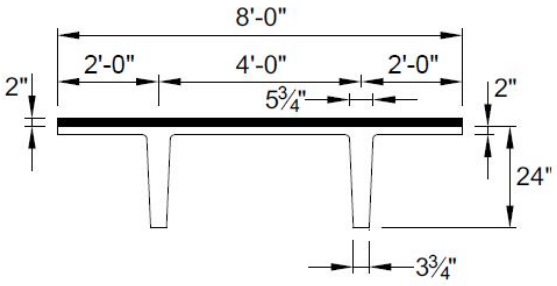

f'_c = 5000 psi

f_{pu} = 270,000 psi

½-in.-diameter regular strand

Section Properties

		No Topping		2 in. Topping	
A	=	401	in.^{2}	–	
I	=	20,985	in.^{4}	27,720	in.^{4}
y_b	=	17.15	in.	19.27	in.
y_t	=	6.85	in.	6.73	in.
S_b	=	1224	in.^{3}	1439	in.^{3}
S_t	=	3064	in.^{3}	4119	in.^{3}
wt	=	418	lb/ft	618	lb/ft
DL	=	52	lb/ft^2	77	lb/ft^2
V/S	=	1.41	in.		

8DT24

Double-Tee (No Topping)					
	Strand pattern	**Y_s (end) in.**	**Y_s (center) in.**	**M_n Kip-inch**	**M_{cr} Kip-inch**
8DT24	68-S	4.00	4.00	4838	3029
	88-S	5.00	5.00	6069	3626
	108-S	6.00	6.00	7109	4126
	128-S	7.00	7.00	7960	4527
	128-D1	11.67	3.25	9816	5629
	148-D1	12.86	3.50	11219	6373

Double-Tee (2 in. Topping)						
8DT24+2						
Strand pattern	48-S	68-S	88-S	108-S	128-S	128-D1
Y_s (end), in.	3.00	4.00	5.00	6.00	7.00	11.67
Y_s (center), in.	3.00	4.00	5.00	6.00	7.00	3.25

M_n, Kip-inch	3747	5334	6730	7935	8950	10807
Span, ft	**M_{cr}, kip-inch**					
28	2977	3916	4741	5450	6044	7339
30	2975	3915	4739	5449	6043	7338
32	2974	3913	4738	5447	6041	7336
34	2972	3911	4736	5445	6039	7334
36	2970	3909	4734	5443	6037	7332
38	2968	3907	4732	5441	6035	7330
40	2966	3905	4730	5439	6033	7328
42	2964	3903	4728	5437	6031	7326
44	2961	3901	4725	5434	6029	7324
46	2959	3898	4723	5432	6026	7321
48	2956	3896	4720	5429	6024	7319
50	2954	3893	4718	5427	6021	7316
52	2951	3890	4715	5424	6018	7313
54	2948	3887	4712	5421	6015	7310
56	2945	3884	4709	5418	6012	7307
58	2942	3881	4706	5415	6009	7304
60	2939	3878	4703	5412	6006	7301
62	2935	3875	4699	5409	6003	7298
64	2932	3871	4696	5405	5999	7294
66	2928	3868	4692	5402	5996	7291
68	2925	3864	4689	5398	5992	7287
70	2921	3861	4685	5394	5988	7283

Modified section properties for design with UHP-FRC:

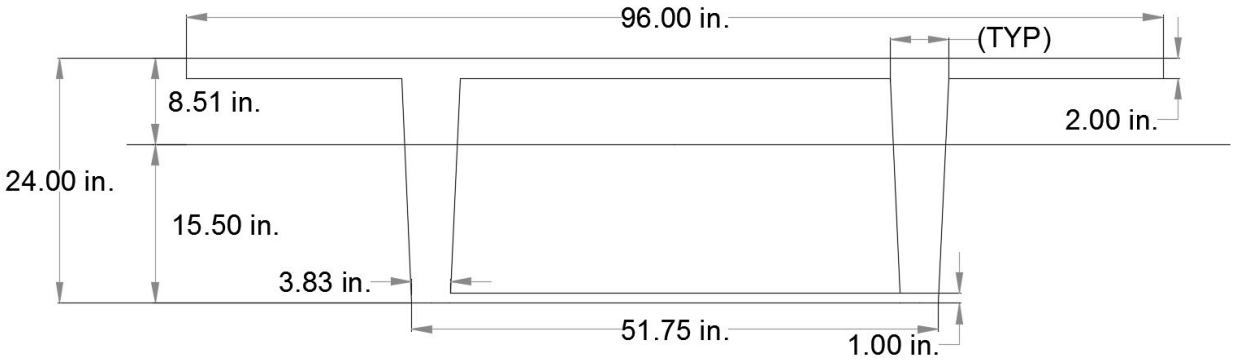

8DT24M1

Area, A	445.205 in.^{2}
Moment of Inertia, I	32,024 in.^{4}
Y_t	8.51 in.
Y_b	15.50 in.
S_t	3,763 in.^{3}
S_b	2,066 in.^{3}
wt	464 lb/ft
M_{cr}	4132 kip-inch (f_r = 2 ksi)
	6198 kip-inch (f_r = 3 ksi)
	8264 kip-inch (f_r = 4 ksi)

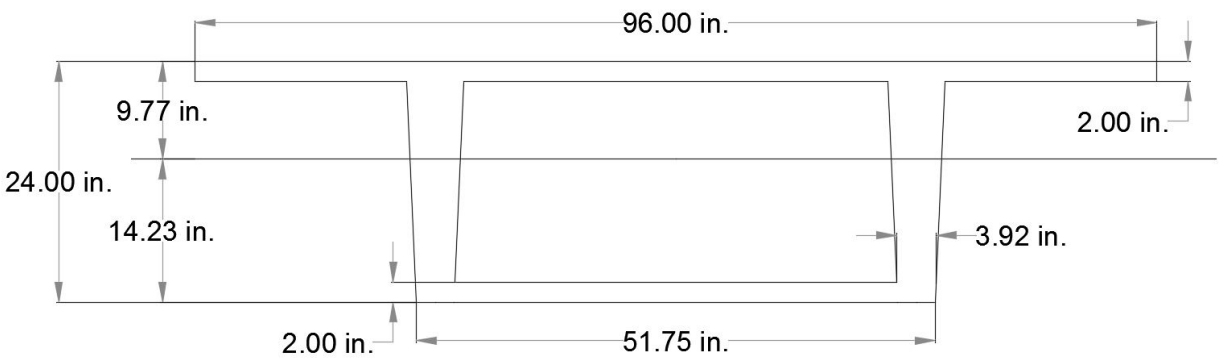

8DT24M2

Area, A	489.318 in.^{2}
Moment of Inertia, I	39,889 in.^{4}
Y_t	9.77 in.
Y_b	14.23 in.
S_t	4,083 in.^{3}
S_b	2,803 in.^{3}
wt	510 lb/ft
M_{cr}	5,606 kip-inch (f_r = 2 ksi)
	8,409 kip-inch (f_r = 3 ksi)
	11,212 kip-inch (f_r = 4 ksi)

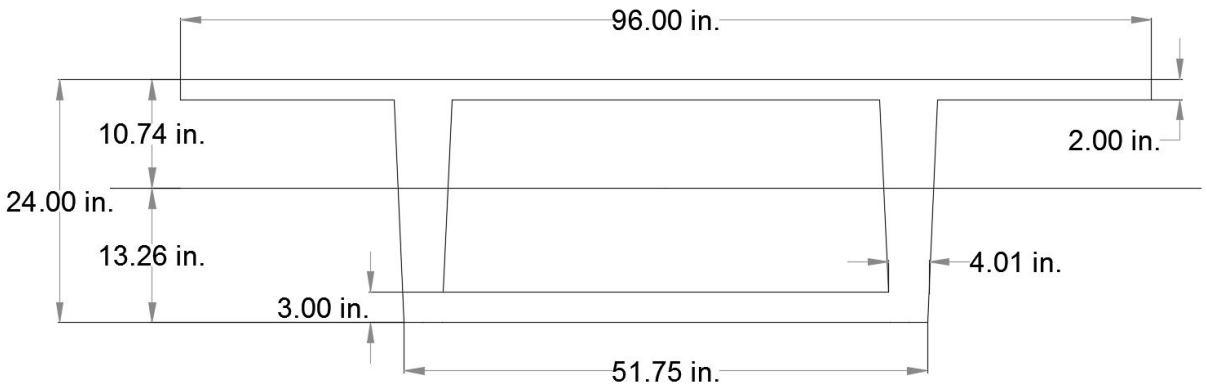

8DT24M3

Area, A	533.341 in.^{2}
Moment of Inertia, I	45,453 in.^{4}
Y_t	10.74 in.
Y_b	13.26 in.
S_t	4,232 in.^{3}
S_b	3,428 in.^{3}
wt	556 lb/ft
M_{cr}	6,856 kip-inch (f_r = 2 ksi)
	10,284 kip-inch (f_r = 3 ksi)
	13,712 kip-inch (f_r = 4 ksi)

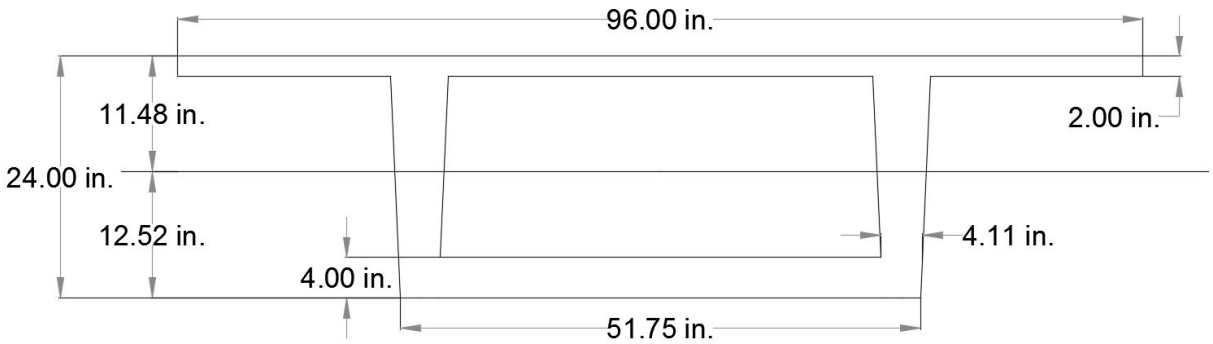

8DT24M4

Area, A	577.273 in.^{2}
Moment of Inertia, I	49,327 in.^{4}
Y_t	11.48 in.
Y_b	12.52 in.
S_t	4,297 in.^{3}
S_b	3,940 in.^{3}
wt	601 lb/ft
M_{cr}	7,880 kip-inch (f_r = 2 ksi)
	11,820 kip-inch (f_r = 3 ksi)
	15,760 kip-inch (f_r = 4 ksi)

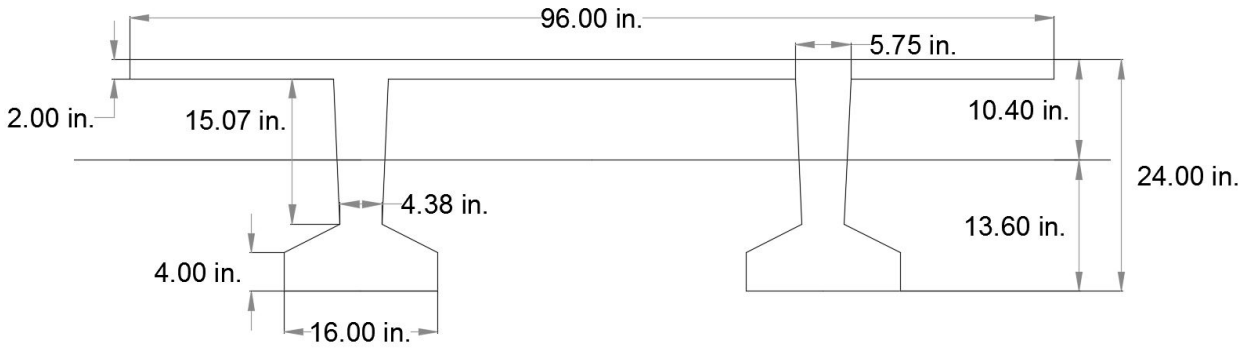

8DT24M5

Area, A	532.405 in.^{2}
Moment of Inertia, I	41,783 in.^{4}
Y_t	10.40 in.
Y_b	13.60 in.
S_t	4,018 in.^{3}
S_b	3,072 in.^{3}
wt	555 lb/ft
M_{cr}	6,144 kip-inch (f_r = 2 ksi)
	9,216 kip-inch (f_r = 3 ksi)
	12,288 kip-inch (f_r = 4 ksi)

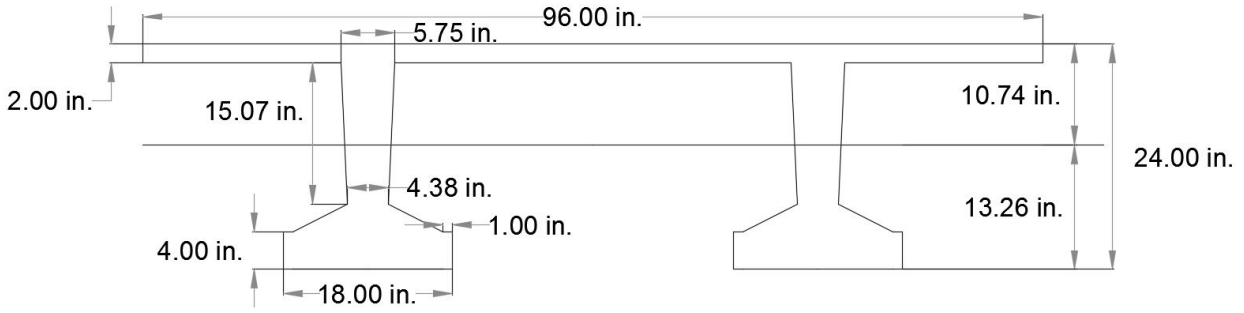

8DT24M6

Area, A	548.405 in.^{2}
Moment of Inertia, I	43,896 in.^{4}
Y_t	10.74 in.
Y_b	13.26 in.
S_t	4,087 in.^{3}
S_b	3,310 in.^{3}
wt	571 lb/ft
M_{cr}	6,620 kip-inch (f_r = 2 ksi)
	9,930 kip-inch (f_r = 3 ksi)
	13,240 kip-inch (f_r = 4 ksi)

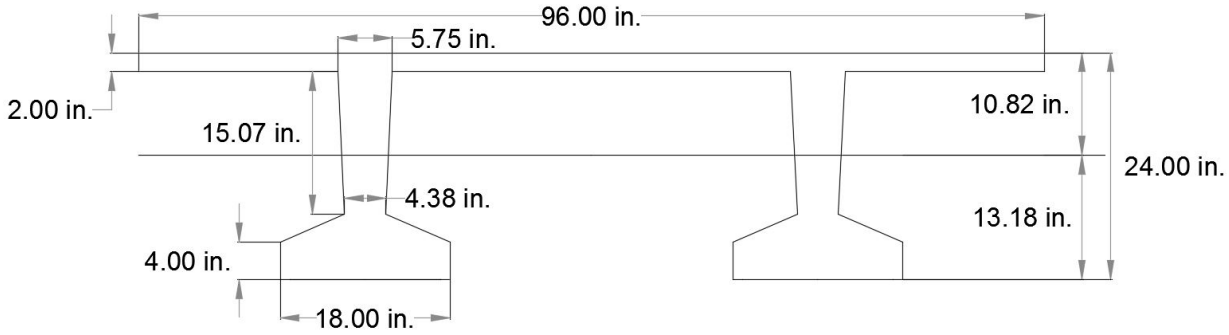

8DT24M7

Area, A	554.27 in.^{2}
Moment of Inertia, I	44,297 in.^{4}
Y_t	10.82 in.
Y_b	13.18 in.
S_t	4,094 in.^{3}

S_b	3,361 in.^{3}
wt	577 lb/ft
M_{cr}	6,722 kip-inch (f_r = 2 ksi)
	10,083 kip-inch (f_r = 3 ksi)
	13,444 kip-inch (f_r = 4 ksi)

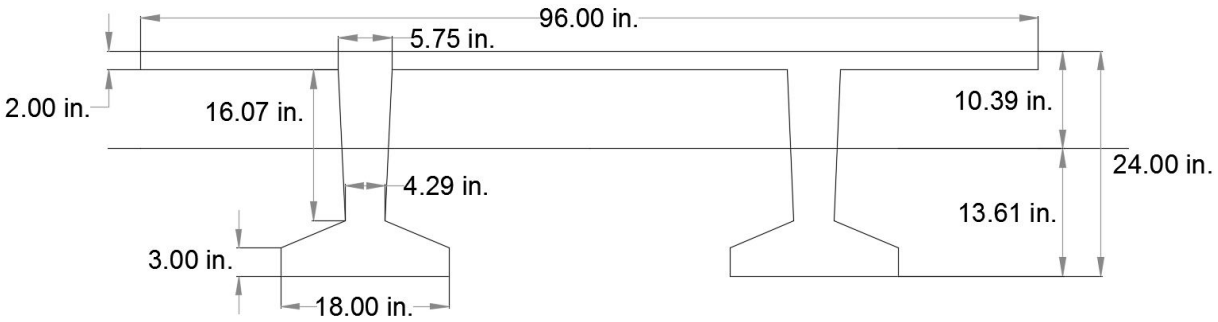

8DT24M8

Area, A	548.405 in.^{2}
Moment of Inertia, I	43,896 in.^{4}
Y_t	10.74 in.
Y_b	13.26 in.
S_t	4,087 in.^{3}
S_b	3,310 in.^{3}
wt	571 lb/ft
M_{cr}	6,620 kip-inch (f_r = 2 ksi)
	9,930 kip-inch (f_r = 3 ksi)

	13,240 kip-inch (f_r = 4 ksi)

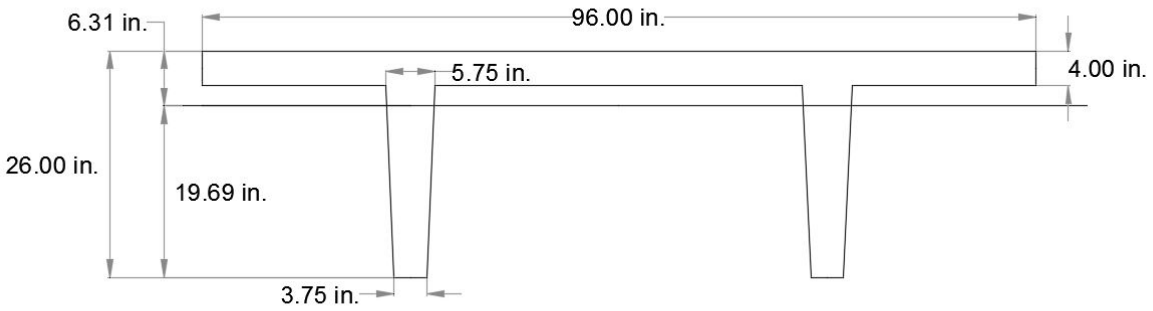

8DT26

Area, A	593.0 in.^{2}
Moment of Inertia, I	29,054 in.^{4}
Y_t	6.31 in.
Y_b	19.69 in.
S_t	4,604 in.^{3}
S_b	1,476 in.^{3}
wt	618 lb/ft
M_{cr}	2,952 kip-inch (f_r = 2 ksi)
	4,428 kip-inch (f_r = 3 ksi)
	5,904 kip-inch (f_r = 4 ksi)

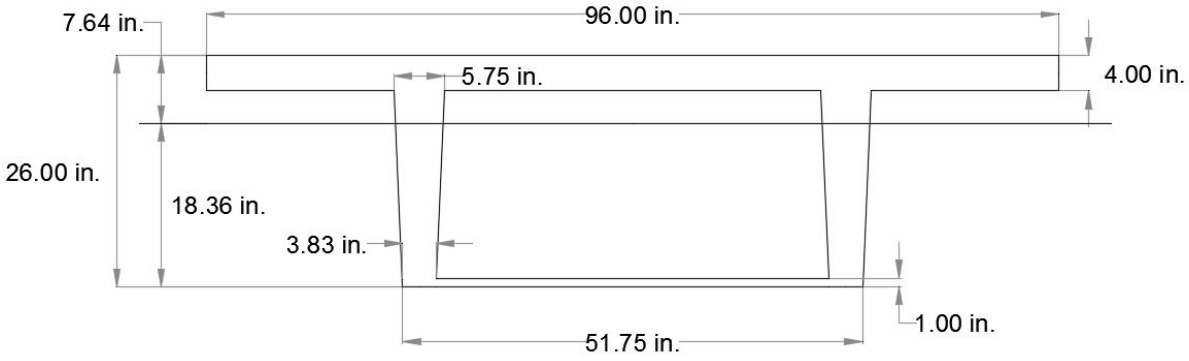

8DT26M1

Area, A	637.205 in.^{2}
Moment of Inertia, I	44,208 in.^{4}
Y_t	7.64 in.
Y_b	18.36 in.
S_t	5,786 in.^{3}
S_b	2,408 in.^{3}
wt	664 lb/ft
M_{cr}	4,816 kip-inch (f_r = 2 ksi)
	7,224 kip-inch (f_r = 3 ksi)
	9,632 kip-inch (f_r = 4 ksi)

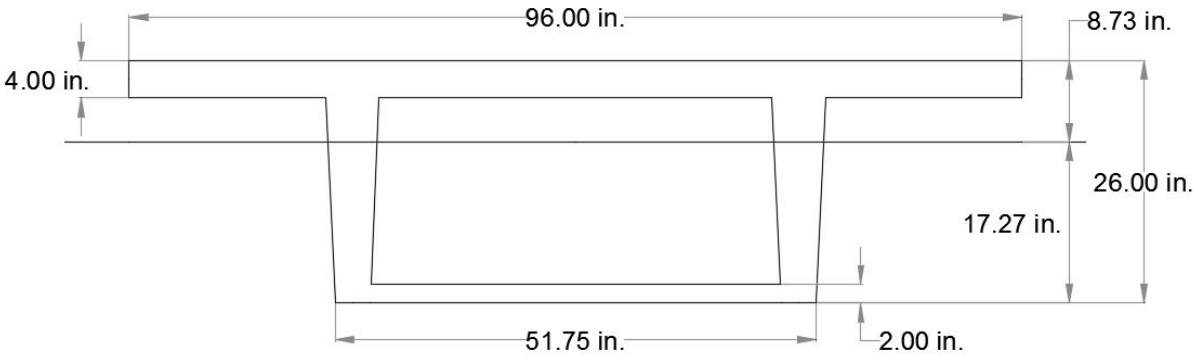

8DT26M2

Area, A	681.318 in.^{2}
Moment of Inertia, I	55,938 in.^{4}
Y_t	8.73 in.
Y_b	17.27 in.
S_t	6,408 in.^{3}
S_b	3,239 in.^{3}
wt	710 lb/ft
M_{cr}	6,478 kip-inch (f_r = 2 ksi)
	9,717 kip-inch (f_r = 3 ksi)
	12,956 kip-inch (f_r = 4 ksi)

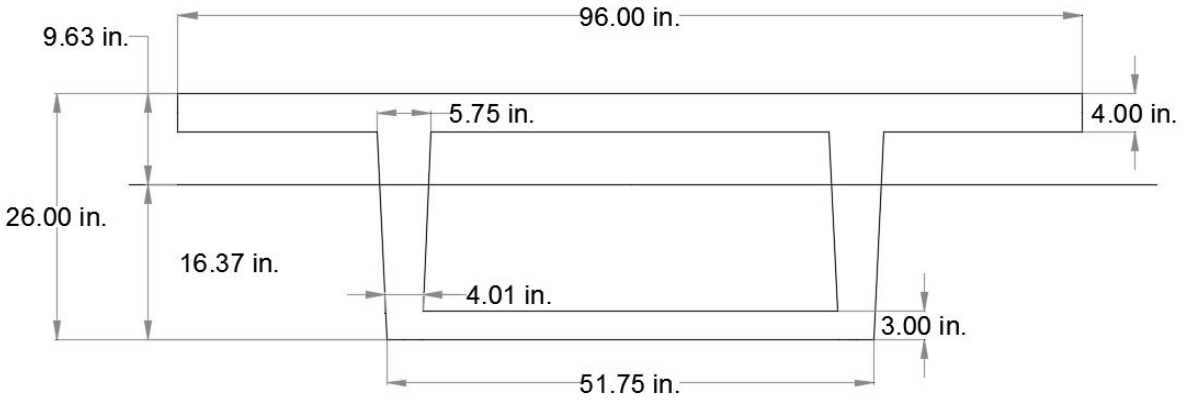

8DT26M3

Area, A	725.341 in.^{2}
Moment of Inertia, I	64,959 in.^{4}
Y_t	9.63 in.
Y_b	16.37 in.
S_t	6,745 in.^{3}
S_b	3,968 in.^{3}
wt	756 lb/ft
M_{cr}	7,936 kip-inch (f_r = 2 ksi)
	11,904 kip-inch (f_r = 3 ksi)
	15,872 kip-inch (f_r = 4 ksi)

8'-0" in. × 32" Normalweight Concrete

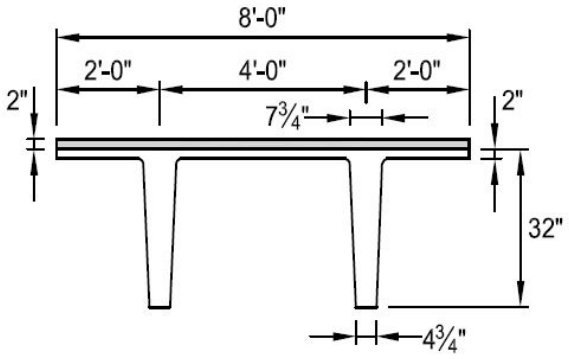

f'_c = 5000 psi

f_{pu} = 270,000 psi

1/2-in.-diameter regular strand

Section Properties

	No Topping	2 in. Topping
A	567 in.^{2}	—
I	55,464 in.^{4}	71,886 in.^{4}
y_b	21.21 in.	23.66 in.
y_t	10.79 in.	10.34 in.
S_b	2615 in.^{3}	3038 in.^{3}
S_t	5140 in.^{3}	6952 in.^{3}
wt	591 lb/ft	791 lb/ft
DL	74 lb/ft^2	99 lb/ft^2
V/S	1.79 in.	

8DT32

Double-Tee (No Topping)					
	Strand pattern	**Y_s (end) in.**	**Y_s (center) in.**	**M_n Kip-inch**	**M_{cr} Kip-inch**
8DT32	128-S	7.00	7.00	11921	6916
	148-S	8.00	8.00	13241	7495
	168-S	9.00	9.00	14370	7976
	188-S	10.00	10.00	15311	8359
	188-D1	14.39	4.00	19765	11002
	208-D1	15.50	4.25	21629	11948

Double-Tee (2 in. Topping)						
8DT32+2						
Strand pattern	128-S	148-S	168-S	188-S	188-D1	208-D1
Y_s (end), in.	7.00	7.00	8.00	9.00	14.39	15.50

Y_s (center), in.	7.00	7.00	8.00	9.00	4.00	4.25
M_n, Kip-inch	12912	14396	15691	16795	21251	23279
Span, ft	M_{cr}, kip-inch					
42	8843	9654	10352	10937	14008	15247
44	8840	9652	10350	10934	14005	15244
46	8837	9649	10347	10931	14003	15241
48	8834	9646	10344	10928	14000	15238
50	8831	9643	10341	10925	13996	15235
52	8828	9639	10337	10922	13993	15232
54	8824	9636	10334	10918	13990	15228
56	8821	9632	10330	10915	13986	15225
58	8817	9629	10327	10911	13983	15221
60	8813	9625	10323	10907	13979	15217
62	8809	9621	10319	10903	13975	15213
64	8805	9617	10315	10899	13971	15209
66	8801	9613	10311	10895	13967	15205
68	8797	9609	10307	10891	13962	15201
70	8792	9604	10302	10887	13958	15196
72	8788	9600	10298	10882	13953	15192
74	8783	9595	10293	10877	13949	15187
76	8778	9590	10288	10873	13944	15182
78	8774	9585	10283	10868	13939	15177
80	8768	9580	10278	10863	13934	15172
82	8763	9575	10273	10857	13929	15167
84	8758	9570	10268	10852	13924	15162
86	8753	9564	10262	10847	13918	15156
88	8747	9559	10257	10841	13913	15151
90	8741	9553	10251	10835	13907	15145

92	8735	9547	10245	10830	13901	15139

10'-0" × 24"
Normalweight Concrete

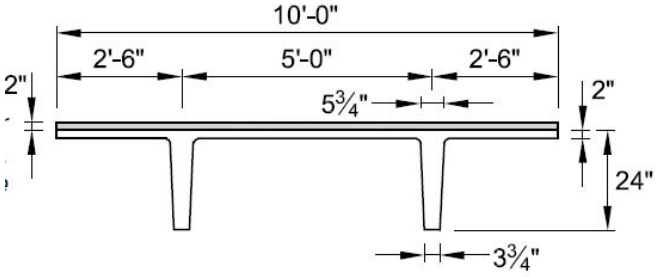

f'_c = 5000 psi

f_{pu} = 270,000 psi

$^1/_2$-in.-diameter regular strand

Section Properties

		No Topping		2 in. Topping	
A	=	449	in.^{2}	–	
I	=	22,469	in.^{4}	29,395	in.^{4}
y_b	=	17.77	in.	19.89	in.
y_t	=	6.23	in.	6.11	in.
S_b	=	1264	in.^{3}	1478	in.^{3}
S_t	=	3607	in.^{3}	4812	in.^{3}
wt	=	468	lb/ft	718	lb/ft
DL	=	47	lb/ft^2	72	lb/ft^2
V/S	=	1.35	in.		

10DT24

Double-Tee (No Topping)					
	Strand pattern	**Y_s (end) in.**	**Y_s (center) in.**	**M_n Kip-inch**	**M_{cr} Kip-inch**
10DT24	68-S	4.00	4.00	4862	3106
	88-S	5.00	5.00	6110	3723
	108-S	6.00	6.00	7173	4241
	128-S	7.00	7.00	8051	4661
	128-D1	11.67	3.25	9909	5763
	148-D1	12.86	3.50	11344	6526

Double-Tee (2 in. Topping)						
10DT24+2						
Strand pattern	68-S	88-S	108-S	128-S	128-D1	148-D1
Y_s (end), in.	4.00	5.00	6.00	7.00	11.67	12.86

Y_s (center), in.	4.00	5.00	6.00	7.00	3.25	3.50
M_n, Kip-inch	5358	6771	7999	9042	10899	12499
Span, ft	**M_{cr}, kip-inch**					
30	3983	4825	5552	6165	7453	8466
32	3981	4823	5550	6163	7451	8465
34	3979	4821	5548	6161	7449	8463
36	3977	4819	5546	6159	7447	8460
38	3974	4816	5544	6157	7445	8458
40	3972	4814	5541	6154	8456	7442
42	3970	4811	5539	6152	7440	8453
44	3967	4809	5536	6149	7437	8451
46	3964	4806	5533	6146	7434	8448
48	3961	4803	5531	6143	7432	8445
50	3958	4800	5528	6140	7429	8442
52	3955	4797	5525	6137	7425	8439
54	3952	4794	5521	6134	7422	8436
56	3949	4791	5518	6131	7419	8433
58	3945	4787	5514	6127	7415	8429
60	3942	4784	5511	6124	7412	8425
62	3938	4780	5507	6120	7408	8422
64	3934	4776	5503	6116	7404	8418
66	3930	4772	5499	6112	7400	8414

10'-0" × 32" Normalweight Concrete

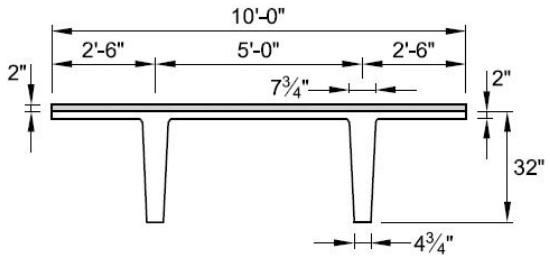

f'_c = 5000 psi

f_{pu} = 270,000 psi

½-in.-diameter regular strand

Section Properties

	No Topping	2 in. Topping
A	= 615 in.^{2}	—
I	= 59,720 in.^{4}	77,118 in.^{4}
y_b	= 21.98 in.	24.54 in.
y_t	= 10.02 in.	9.46 in.
S_b	= 2717 in.^{3}	3143 in.^{3}
S_t	= 5960 in.^{3}	8152 in.^{3}
wt	= 641 lb/ft	891 lb/ft
DL	= 64 lb/ft^2	89 lb/ft^2
V/S	= 1.69 in.	

10DT32

Double-Tee (No Topping)					
	Strand pattern	**Y_s (end) in.**	**Y_s (center) in.**	**M_n Kip-inch**	**M_{cr} Kip-inch**
10DT32	128-S	7.00	7.00	12014	7139
	148-S	8.00	8.00	13366	7746
	168-S	9.00	9.00	14533	8255
	188-S	10.00	10.00	15515	8666
	188-D1	14.39	4.00	19972	11310
	208-D1	15.50	4.25	21883	12285

Double-Tee (2 in. Topping)						
10DT32+2						
Strand pattern	128-S	148-S	168-S	188-S	188-D1	208-D1
Y_s (end), in.	7.00	8.00	9.00	10.00	14.39	15.50
Y_s (center), in.	7.00	8.00	9.00	10.00	4.00	4.25
M_n, Kip-inch	13005	14522	15854	17001	21458	23534

Span, ft	M_{cr}, kip-inch					
44	9095	9942	10676	11296	14355	15627
46	9092	9939	10673	11293	14352	15624
48	9088	9935	10669	11290	14348	15620
50	9085	9932	10666	11287	14345	15617
52	9081	9928	10662	11283	14341	15613
54	9078	9925	10659	11279	14338	15610
56	9074	9921	10655	11275	14334	15606
58	9070	9917	10651	11271	14330	15602
60	9066	9913	10647	11267	14326	15598
62	9061	9909	10642	11263	14321	15593
64	9057	9904	10638	11259	14317	15589
66	9052	9900	10634	11254	14312	15584
68	9048	9895	10629	11249	14308	15580
70	9043	9890	10624	11245	14303	15575
72	9038	9885	10619	11240	14298	15570
74	9033	9880	10614	11235	14293	15565
76	9028	9875	10609	11229	14288	15560
78	9022	9869	10603	11224	14282	15554
80	9017	9864	10598	11218	14277	15549
82	9011	9858	10592	11213	14271	15543
84	9005	9852	10586	11207	14265	15537
86	8999	9847	10580	11201	14259	15531
88	8993	9840	10574	11195	14253	15525

12'-0" × 28"
Normalweight Concrete

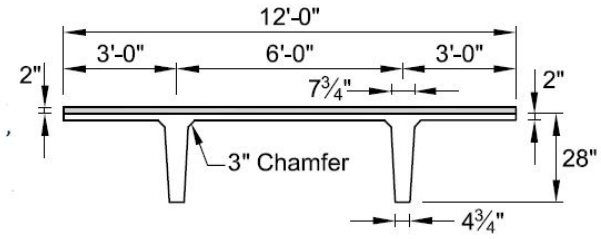

f'_c = 5000 psi

f_{pu} = 270,000 psi

½-in.-diameter regular strand

Section Properties

		No Topping		2 in. Topping	
A	=	640	in.^{2}	—	
I	=	44,563	in.^{4}	57,323	in.^{4}
y_b	=	20.01	in.	22.47	in.
y_t	=	7.79	in.	7.53	in.
S_b	=	2227	in.^{3}	2551	in.^{3}
S_t	=	5577	in.^{3}	7613	in.^{3}
wt	=	677	lb/ft	977	lb/ft
DL	=	56	lb/ft^2	81	lb/ft^2
V/S	=	1.62	in.		

12DT28

Double-Tee (No Topping)					
	Strand pattern	**Y_s (end) in.**	**Y_s (center) in.**	**M_n Kip-inch**	**M_{cr} Kip-inch**
12DT28	108-S	6.00	6.00	8868	5463
	128-S	7.00	7.00	10094	6025
	148-S	8.00	8.00	11139	6490
	168-S	9.00	9.00	12001	6856
	168-D1	13.00	3.75	15468	8913
	168-D1	14.39	4.00	17139	9769

Double-Tee (2 in. Topping)						
12DT28+2						
Strand pattern	108-S	128-S	148-S	168-S	168-D1	188-D1
Y_s (end), in.	6.00	7.00	8.00	9.00	13.00	14.39
Y_s (center), in.	6.00	7.00	8.00	9.00	3.75	4.00
M_n, Kip-inch	9694	11086	12295	13322	16790	18625

Span, ft	M_{cr}, kip-inch					
40	6919	7701	8371	8929	11285	12403
42	6916	7698	8368	8926	11282	12401
44	6913	7695	8365	8923	11279	12398
46	6909	7692	8362	8920	11275	12394
48	6906	7688	8359	8917	11272	12391
50	6903	7685	8355	8913	11269	12388
52	6899	7681	8352	8910	11265	12384
54	6895	7678	8348	8906	11261	12380
56	6891	7674	8344	8902	11257	12376
58	6887	7670	8340	8898	11253	12372
60	6883	7665	8336	8894	11249	12368
62	6879	7661	8331	8889	11245	12364
64	6874	7657	8327	8885	11240	12359
66	6870	7652	8322	8880	11236	12355
68	6865	7647	8317	8875	11231	12350
70	6860	7642	8313	8871	11226	12345
72	6855	7637	8307	8865	11221	12340

12'-0" × 32"
Normalweight Concrete

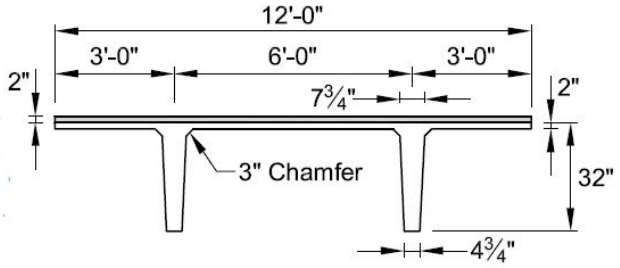

f'_c = 5000 psi

f_{pu} = 270,000 psi

½-in.-diameter regular strand

Section Properties

		No Topping		2 in. Topping	
A	=	690	in.^{2}	—	
I	=	64,620	in.^{4}	82,413	in.^{4}
y_b	=	22.75	in.	25.50	in.
y_t	=	9.25	in.	8.75	in.
S_b	=	2840	in.^{3}	3232	in.^{3}
S_t	=	6986	in.^{3}	9696	in.^{3}
wt	=	719	lb/ft	1019	lb/ft
DL	=	60	lb/ft^2	85	lb/ft^2
V/S	=	1.70	in.		

12DT32

Double-Tee (No Topping)					
	Strand pattern	**Y_s (end) in.**	**Y_s (center) in.**	**M_n Kip-inch**	**M_{cr} Kip-inch**
12DT32	128-S	7.00	7.00	12077	7342
	148-S	8.00	8.00	13451	7972
	168-S	9.00	9.00	14643	8504
	188-S	10.00	10.00	15653	8938
	208-D1	15.50	4.25	22054	12579
	228-D1	16.41	4.50	23938	13552

Double-Tee (2 in. Topping)						
12DT32+2						
Strand pattern	128-S	148-S	168-S	188-S	208-D1	228-D1
Y_s (end), in.	7.00	8.00	9.00	10.00	15.50	16.41
Y_s (center), in.	7.00	8.00	9.00	10.00	4.25	4.50

M_n, Kip-inch	13068	14607	15964	17139	23705	25754
Span, ft	**M_{cr}, kip-inch**					
40	9247	10117	10875	11523	15819	17079
42	9244	10114	10872	11520	15816	17076
44	9241	10111	10869	11517	15813	17073
46	9237	10108	10866	11513	15810	17070
48	9234	10104	10863	11510	15807	17067
50	9231	10101	10859	11507	15803	17064
52	9227	10097	10856	11503	15800	17060
54	9223	10094	10852	11499	15796	17056
56	9220	10090	10848	11496	15792	17052
58	9216	10086	10844	11492	15788	17048
60	9211	10081	10840	11487	15784	17044
62	9207	10077	10836	11483	15780	17040
64	9203	10073	10831	11479	15775	17035
66	9198	10068	10827	11474	15771	17031
68	9193	10063	10822	11469	15766	17026
70	9189	10059	10817	11465	15761	17021
72	9184	10054	10812	11460	15756	17016
74	9178	10049	10807	11454	15751	17011
76	9173	10043	10802	11449	15746	17006
78	9168	10038	10796	11444	15740	17001
80	9162	10032	10791	11438	15735	16995
82	9156	10027	10785	11432	15729	16989
84	9151	10021	10779	11427	15723	16983

10'-0" × 26"

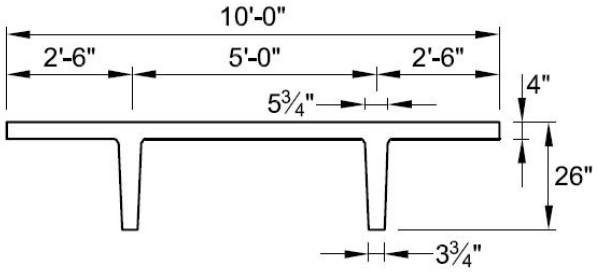

Section Properties

		Normalweight		Lightweight	
A	=	689	in.^{2}	689	in.^{2}
I	=	30,716	in.^{4}	30,716	in.^{4}
y_b	=	20.29	in.	20.29	in.
y_t	=	5.71	in.	5.71	in.
S_b	=	1514	in.^{3}	1514	in.^{3}
S_t	=	5379	in.^{3}	5379	in.^{3}
wt	=	718	lb/ft	550	lb/ft
DL	=	72	lb/ft^2	55	lb/ft^2
V/S	=	2.05	in.	2.05	in.

f'_c = 5000 psi

f_{pu} = 270,000 psi

$^1/_2$-in.-diameter regular strand

10DT26

Pretopped Double-Tee					
	Strand pattern	**Y_s (end) in.**	**Y_s (center) in.**	**M_n Kip-inch**	**M_{cr} Kip-inch**
10DT26	68-S	4.00	4.00	5358	3518
	88-S	5.00	5.00	6771	4228
	108-S	6.00	6.00	7999	4839
	128-S	7.00	7.00	9042	5352
	128-D1	11.67	3.25	10899	6454
	148-D1	12.86	3.50	12499	7310

10'-0" × 34"

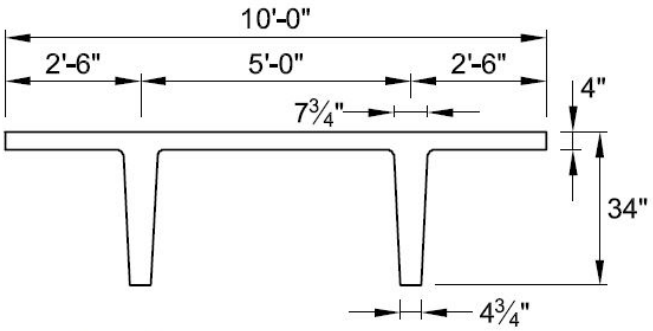

Section Properties

		Normalweight		Lightweight	
A	=	855	in.^{2}	855	in.^{2}
I	=	80,780	in.^{4}	80,780	in.^{4}
y_b	=	25.07	in.	25.07	in.
y_t	=	8.93	in.	8.93	in.
S_b	=	3222	in.^{3}	3222	in.^{3}
S_t	=	9046	in.^{3}	9046	in.^{3}
wt	=	891	lb/ft	683	lb/ft
DL	=	89	lb/ft^2	68	lb/ft^2
V/S	=	2.32	in.	2.32	in.

f'_c = 5000 psi

f_{pu} = 270,000 psi

$^1/_2$-in.-diameter regular strand

10DT34

Pretopped Double-Tee					
	Strand pattern	**Y_s (end) in.**	**Y_s (center) in.**	**M_n Kip-inch**	**M_{cr} Kip-inch**
10DT34	128-S	7.00	7.00	13005	8124
	148-S	8.00	8.00	14522	8850
	168-S	9.00	9.00	15854	9479
	188-S	10.00	10.00	17001	10010
	188-D1	14.39	4.00	21458	12654
	208-D1	15.50	4.25	23534	13747

12'-0" × 30"

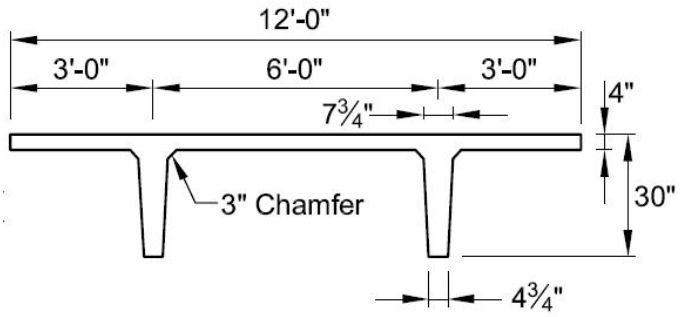

f'_c = 5000 psi

f_{pu} = 270,000 psi

½-in.-diameter regular strand

Section Properties

		Normalweight		Lightweight	
A	=	928	in.²	928	in.²
I	=	59,997	in.⁴	59,997	in.⁴
y_b	=	22.94	in.	22.94	in.
y_t	=	7.06	in.	7.06	in.
S_b	=	2615	in.³	2615	in.³
S_t	=	8498	in.³	8498	in.³
wt	=	967	lb/ft	741	lb/ft
DL	=	81	lb/ft²	62	lb/ft²
V/S	=	2.30	in.	2.30	in.

12DT30

Pretopped Double-Tee					
	Strand pattern	**Y_s (end) in.**	**Y_s (center) in.**	**M_n Kip-inch**	**M_{cr} Kip-inch**
12DT30	128-S	7.00	7.00	11086	6897
	148-S	8.00	8.00	12295	7473
	168-S	9.00	9.00	13322	7951
	188-S	10.00	10.00	14167	8330
	188-D1	14.39	4.00	18625	10974
	208-D1	15.50	4.25	20402	11917

12'-0" × 34"

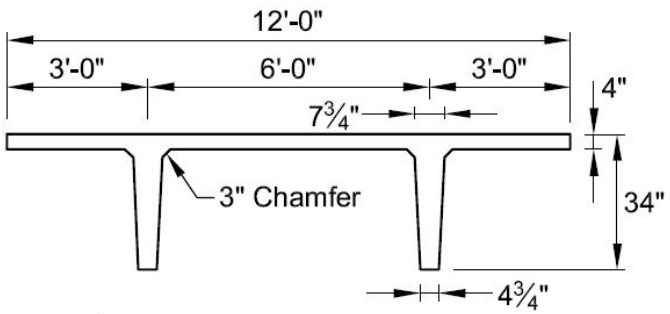

f'_c = 5000 psi

f_{pu} = 270,000 psi

½-in.-diameter regular strand

Section Properties

		Normalweight		Lightweight	
A	=	978	in.^{2}	978	in.^{2}
I	=	86,072	in.^{4}	86,072	in.^{4}
y_b	=	25.77	in.	25.77	in.
y_t	=	8.23	in.	8.23	in.
S_b	=	3340	in.^{3}	3340	in.^{3}
S_t	=	10,458	in.^{3}	10,458	in.^{3}
wt	=	1,019	lb/ft	781	lb/ft
DL	=	85	lb/ft^2	65	lb/ft^2
V/S	=	2.39	in.	2.39	in.

12DT34

Pretopped Double-Tee					
	Strand pattern	**Y_s (end) in.**	**Y_s (center) in.**	**M_n Kip-inch**	**M_{cr} Kip-inch**
12DT34	128-S	7.00	7.00	13068	8288
	148-S	8.00	8.00	14607	9032
	168-S	9.00	9.00	15964	9677
	188-S	10.00	10.00	17139	10225
	188-D1	14.39	4.00	21598	12869
	208-D1	15.50	4.25	23705	13980

15'-0" × 26"

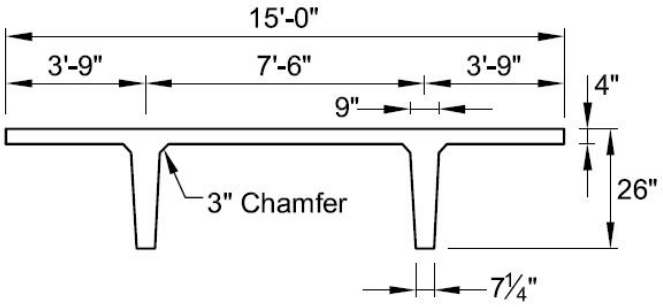

Section Properties

		Normalweight		Lightweight	
A	=	1078	in.^{2}	1078	in.^{2}
I	=	53,280	in.^{4}	53,280	in.^{4}
y_b	=	19.82	in.	19.82	in.
y_t	=	6.18	in.	6.18	in.
S_b	=	2688	in.^{3}	2688	in.^{3}
S_t	=	8618	in.^{3}	8618	in.^{3}
wt	=	1122	lb/ft	861	lb/ft
DL	=	75	lb/ft^2	57	lb/ft^2
V/S	=	2.38	in.	2.38	in.

f'_c = 5000 psi

f_{pu} = 270,000 psi

$^1/_2$-in.-diameter regular strand

15DT26

Pretopped Double-Tee					
	Strand pattern	**Y_s (end) in.**	**Y_s (center) in.**	**M_n Kip-inch**	**M_{cr} Kip-inch**
15DT26	88-S	7.00	7.00	6166	4425
	128-S	5.83	5.83	9746	6268
	168-S	5.69	5.69	12976	7937
	208-S	5.95	5.95	15868	9437
	248-S	6.42	6.42	18413	10763

15'-0" × 30"

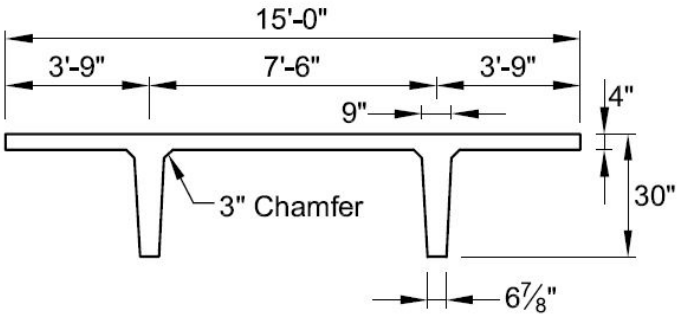

Section Properties

		Normalweight		Lightweight	
A	=	1133	in.^{2}	1133	in.^{2}
I	=	78,625	in.^{4}	78,865	in.^{4}
y_b	=	22.75	in.	22.75	in.
y_t	=	7.25	in.	7.25	in.
S_b	=	3457	in.^{3}	3457	in.^{3}
S_t	=	10,838	in.^{3}	10,838	in.^{3}
wt	=	1180	lb/ft	905	lb/ft
DL	=	79	lb/ft^2	60	lb/ft^2
V/S	=	2.42	in.	2.42	in.

f'_c = 5000 psi

f_{pu} = 270,000 psi

$^1/_2$-in.-diameter regular strand

15DT30

Pretopped Double-Tee					
	Strand pattern	**Y_s (end) in.**	**Y_s (center) in.**	**M_n Kip-inch**	**M_{cr} Kip-inch**
15DT30	88-S	7.00	7.00	7488	5515
	128-S	5.83	5.83	11728	7700
	168-S	5.69	5.69	15619	9711
	208-S	5.95	5.95	19170	11552
	248-S	6.42	6.42	22374	13220

15'-0" × 34"

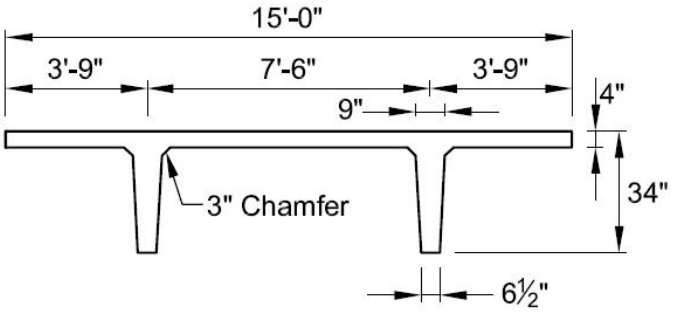

Section Properties

		Normalweight	Lightweight
A	=	1185 in.^{2}	1185 in.^{2}
I	=	109,621 in.^{4}	109,621 in.^{4}
y_b	=	25.65 in.	22.65 in.
y_t	=	8.35 in.	8.35 in.
S_b	=	4274 in.^{3}	4274 in.^{3}
S_t	=	13,121 in.^{3}	13,121 in.^{3}
wt	=	1234 lb/ft	946 lb/ft
DL	=	82 lb/ft^2	63 lb/ft^2
V/S	=	2.45 in.	2.45 in.

f'_c = 5000 psi

f_{pu} = 270,000 psi

$^1/_2$-in.-diameter regular strand

15DT34

Pretopped Double-Tee					
	Strand pattern	**Y_s (end) in.**	**Y_s (center) in.**	**M_n Kip-inch**	**M_{cr} Kip-inch**
15DT34	88-S	7.00	7.00	8810	6625
	128-S	5.83	5.83	13710	9148
	168-S	5.69	5.69	18262	11497
	208-S	5.95	5.95	22473	13678
	248-S	6.42	6.42	26337	15684

Appendix C

Tx 54 Girder

- f'_c = 5000 psi and normal weight concrete for the precast section
- f'_c = 4000 psi and normal weight concrete for the topping.
- Thirty-six 0.5 in.-diameter 270 ksi low-relaxation strands.
- e at center = 19.34 *in.*
- e at ends = 17.34 *in.*
- All strands are bonded.
- f_{se} = 160 ksi.
- Width of the topping, b_e = 9 *ft*
- Thickness of the topping, t_{top} = 8 *in.*
- Span = 100 *ft*

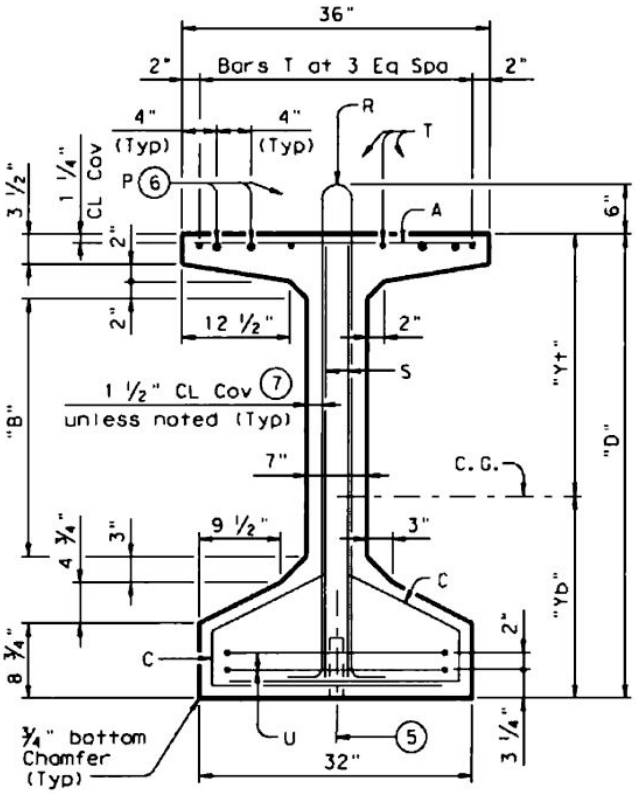

TYPE Tx46 & Tx54

GIRDER DIMENSIONS AND SECTION PROPERTIES								
Girder Type	"D" (in.)	"B" (in.)	"Yt" (in.)	"Yb" (in.)	Area ($in.^2$)	"Ix" ($in.^4$)	"Iy" ($in.^4$)	Weight (plf)
Tx46	46	22	25.90	20.10	761	198,089	46,478	793
Tx54	54	30	30.49	23.51	817	299,740	46,707	851

DESIGN OF PRESTRESSED Tx54 WITH TOPPING:

Section properties:

- $d = d_p = t_{top} + y_t + e_{cl} = 8 + 30.49 + 19.34 = 57.83\,in.$
- $\rho_p = \dfrac{A_{ps}}{bd_p} = \dfrac{36 \times 0.153}{9 \times 12 \times 57.83} = 0.00088$

$$k = 2\left(1.04 - \frac{f_{py}}{f_{pu}}\right)$$
$$= 2 \times (1.04 - 0.9)$$
$$= 0.28\,(low\,relaxation\,strands)$$
$$f_{ps} = f_{pu}\left(1 - k\frac{c}{d_p}\right)$$
$$= 270\left(1 - 0.28 \times \frac{c}{57.83}\right)$$

Assuming rectangular section behavior

$$c = \frac{A_{ps} f_{pu} + A_s f_s - A_s^{'} f_s^{'}}{0.85 f_c^{'} \beta_1 b + k A_{ps} \frac{f_{pu}}{d_p}}$$

$$= \frac{36 \times 0.153 \times 270}{0.85 \times 5 \times 0.8 \times 9 \times 12 + 0.28 \times 36 \times 0.153 \times \frac{270}{57.83}}$$

$$= 3.97\, in. < h_f$$

$$f_{ps} = 270 \times \left(1 - 0.28 \times \frac{3.97}{57.83}\right)$$

$$= 264.8\, ksi$$

$$a = \beta_1 c$$

$$= 0.8 \times 3.97$$

$$= 3.18\, in. < h_f$$

Design nominal moment capacity

$$M_n = A_{ps} f_{ps} \left(d_p - \frac{a}{2}\right) + A_s f_y \left(d - \frac{a}{2}\right) - A_s^{'} f_y^{'} \left(d^{'} - \frac{a}{2}\right)$$

$$= 36 \times 0.153 \times 264.8 \times \left(57.83 - \frac{3.18}{2}\right)$$

$$= 82,027\, kip - in.$$

Check for Tension-controlled section

Pre-stressing steel:

$$c = 3.97\, in.$$

$$d_p = 57.83\, in.$$

$$\varepsilon_{cu} = 0.003$$

$$\frac{c}{d_p} = \frac{\varepsilon_{cu}}{\varepsilon_{cu} + \varepsilon_t}$$

$$\frac{3.97}{57.83} = \frac{0.003}{0.003 + \varepsilon_t}$$

$$\varepsilon_t = 0.04 > 0.005$$

Tension controlled

Initial Cracking Moment

Weight of topping, $W_{topping} = 9 \times \frac{8}{12} \times 150 = 900\, lb/\, ft$

$W_{girder} = 851\, lb/\, ft$

Weight of composite, $W_{dnc} = W_{topping} + W_{girder} = 1751\, lb/\, ft$

$$M_{dnc} = \frac{W_{dnc} l^2}{8}$$
$$= \frac{1.751 \times 100^2}{8}$$
$$= 26,265\, kip - in.$$

$$P_e = A_{ps} f_{pe}$$
$$= 36 \times 0.153 \times 160$$
$$= 881.28\, kips$$
$$A_c(non-composite) = 817\, in^2$$
$$S_{nc}(non-composite) = 12,749\, in^3$$
$$I_x(composite) = 413,212\, in^4$$
$$y_t(composite) = 20.76\, in.$$
$$y_b(composite) = 41.24\, in.$$
$$S_c(composite) = \frac{792412}{41.24} = 19,214\, in^3$$
$$e(non-composite) = 19.34 in.$$
$$f_r = 7.5\sqrt{f_c'}$$
$$= 7.5\sqrt{5000}$$
$$= 0.530\, ksi$$
$$f_{cpe} = \frac{P_e}{A_c} + \frac{P_e e}{S_{nc}}$$
$$= \frac{881.28}{817} + \frac{881.28 \times 19.34}{12749}$$
$$= 2.42\, ksi$$
$$\gamma_1 = 1.6$$
$$\gamma_2 = 1.1$$
$$\gamma_3 = 1.0$$
$$M_{cr} = \gamma_3 \left(\left(\gamma_1 f_r + \gamma_2 f_{cpe} \right) S_c - M_{dnc} \left(\frac{S_c}{S_{nc}} - 1 \right) \right)$$
$$= 1.0 \left(\left(1.6 \times 0.530 + 1.1 \times 2.42 \right) \times 19214 - 26265 \times \left(\frac{19214}{12749} - 1 \right) \right)$$
$$= 54,122\, kip - in$$

DESIGN OF PRESTRESSED Tx54 WITH OUT TOPPING:

Section properties:

- Equivalent thickness of flange, $h_f = 4.5\ in.$
- $d_p = y_t + e_{cl} = 30.49 + 19.34 = 49.83\,in.$
- $\gamma_p = 0.28\,(low - relaxation\ strands)$
- $\rho_p = \dfrac{A_{ps}}{bd_p} = \dfrac{36 \times 0.153}{36 \times 49.83} = 0.003$

$$k = 2\left(1.04 - \frac{f_{py}}{f_{pu}}\right)$$
$$= 2 \times (1.04 - 0.9)$$
$$= 0.28\,(low\,relaxation\ strands)$$
$$f_{ps} = f_{pu}\left(1 - k\frac{c}{d}\right)$$
$$= 270\left(1 - 0.28 \times \frac{c}{49.83}\right)$$

Assuming rectangular section behavior

$$c = \frac{A_{ps}f_{pu} + A_s f_s - A_s^{'} f_s^{'}}{0.85 f_c^{'} \beta_1 b + kA_{ps}\dfrac{f_{pu}}{d_p}}$$
$$= \frac{36 \times 0.153 \times 270}{0.85 \times 5 \times 0.8 \times 36 + 0.28 \times 36 \times 0.153 \times \dfrac{270}{49.83}}$$
$$= 11.37\,in. > h_f$$

T-Section behavior

$$c = \frac{A_{ps}f_{pu} + A_s f_s - A_s^{'} f_s^{'} - 0.85 f_c^{'}\left(b - b_w\right)h_f}{0.85 f_c^{'}\beta_1 b_w + kA_{ps}\dfrac{f_{pu}}{d_p}}$$

$$= \frac{36 \times 0.153 \times 270 - 0.85 \times 5 \times \left(36 - 7\right) \times 4.75}{0.85 \times 5 \times 0.8 \times 7 + 0.28 \times 36 \times 0.153 \times \dfrac{270}{49.83}}$$

$$= 28.04\,in. > h_f$$

$$a = \beta_1 c$$

$$= 0.8 \times 28.04$$

$$= 22.43\,in. > h_f$$

$$f_{ps} = f_{pu}\left(1 - k\frac{c}{d}\right)$$

$$= 270\left(1 - 0.28 \times \frac{28.04}{49.83}\right)$$

$$= 227.46\,ksi$$

Design nominal moment capacity

$$M_n = A_{ps}f_{ps}\left(d_p - \frac{a}{2}\right) + A_s f_y\left(d - \frac{a}{2}\right) - A_s^{'} f_y^{'}\left(d^{'} - \frac{a}{2}\right) + 0.85 f_c^{'}\left(b - b_w\right)h_f\left(\frac{a}{2} - \frac{h_f}{2}\right)$$

$$= 36 \times 0.153 \times 227.46 \times \left(49.83 - \frac{22.43}{2}\right) + 0.85 \times 5 \times \left(36 - 7\right) \times 4.75 \times \left(\frac{22.43}{2} - \frac{4.75}{2}\right)$$

$$= 53,554\,kip - in.$$

Check for Tension-controlled section

Pre-stressing steel:

$c = 28.04\,in.$

$d_p = 49.83\,in.$

$\varepsilon_{cu} = 0.003$

$$\frac{c}{d_p} = \frac{\varepsilon_{cu}}{\varepsilon_{cu} + \varepsilon_t}$$

$$\frac{28.04}{49.83} = \frac{0.003}{0.003 + \varepsilon_t}$$

$\varepsilon_t = 0.0023 < 0.005$

Transformed moment of Inertia

$$n = \frac{E_s}{E_c} = \frac{29000}{4030.5} = 7.195$$

Transformed areas of strands:

$(n-1)A_{ps} = (7.195-1)\times 36 \times 0.153 = 34.12, d_p = 49.83\,in.$

Centroid of transformed section:

Part	Area (in^2)	y_{top} ($in.$)	Ay_{top} ($in.^3$)
Concrete	817	30.49	24,910.33
Strands	34.12	49.83	1700.2
	$\sum A = 851.12$		$\sum Ay_{top} = 26610.53$

$$y_{top} = \frac{\sum Ay_{top}}{\sum A} = \frac{26,610.53}{851.12} = 31.265\,in.$$

$y_{bottom} = 54 - y_{top} = 54 - 31.26 = 22.73\,in.$

Uncracked transformed moment of Inertia:

Part	Area (in^2)	$\bar{y}$ ($in.$)	$I_{own\ axis}$ ($in.^4$)	Ay^2 ($in.^4$)
Concrete	817	-0.775	299,740	490.71
Strands	34.12	18.565	–	11759.77
				I = 311,990 $in.^4$

$I_{transformed}$ = 311,990 $in.^4$

Initial Cracking Moment

$$P_e = A_{ps} f_{pe}$$
$$= 36 \times 0.153 \times 160$$
$$= 881.28\, kips$$
$$A_c = 817\, in^2$$
$$S_{nc} = 13,726\, in^3$$
$$I_x = 311,990\, in^4$$
$$y_t = 31.265\, in.$$
$$y_b = 22.73\, in.$$
$$e(non-composite) = 19.34 in.$$

$$f_r = 7.5\sqrt{f_c'}$$
$$= 7.5\sqrt{5000}$$
$$= 0.530\, ksi$$
$$f_{cpe} = \frac{P_e}{A_c} + \frac{P_e e}{S_{nc}}$$
$$= \frac{881.28}{817} + \frac{881.28 \times 19.34}{13726}$$
$$= 2.32\, ksi$$
$$\gamma_1 = 1.6,\ \gamma_2 = 1.1,\ \gamma_3 = 1.0$$
$$M_{cr} = \gamma_3 \left(\left(\gamma_1 f_r + \gamma_2 f_{cpe} \right) S_{nc} \right)$$
$$= 1.0\left(\left(1.6 \times 0.530 + 1.1 \times 2.32 \right) \times 13726 \right)$$
$$= 46,675\, kip - in$$

DESIGN OF NON-PRESTRESSED Tx54 WITH UHP-FRC (WITH DECK):

- Self-weight (girder) = 851 *lb/ft*
- Live load = 2,500 *lb/ft*
- f_c' = 22,000 *psi*
- E_c = 7,000 ksi
- 9-#11, 100 *ksi* steel
- f_r = 3 *ksi*
- β_1 = 0.65

Composite Section properties

- A_C = 1681 in^2
- I_g = 599,105 in^2
- y_b = 45.13 *in.*
- y_t = 16.87 *in.*
- S_b = 13,275 in^3
- S_t = 35,513 in^3

Transformed moment of Inertia

$$n = \frac{E_s}{E_c} = \frac{29000}{7000} = 4.143$$

Transformed areas of steel:

Steel: $(n-1)A_s = (4.143-1)\times 9\times 1.56 = 44.12, d = 62\,in.$

Centroid of transformed section:

Part	Area (in^2)	y_{top} (*in.*)	Ay_{top} ($in.^3$)
Concrete	1681	16.87	28366.33
Steel	44.12	60	2647.5
	$\sum A = 1725.12$		$\sum Ay_{top} = 31013.83$

$$y_{top} = \frac{\sum Ay_{top}}{\sum A} = \frac{31013.83}{1725.12} = 17.98\,in.$$

$$y_{bottom} = 62 - y_{top} = 62 - 17.98 = 44.02\,in.$$

Uncracked transformed moment of Inertia:

Part	Area (in^2)	$\bar{y}$ (*in.*)	$I_{own\ axis}$ ($in.^4$)	Ay^2 ($in.^4$)

Concrete	1681	-1.103	599,015	2045
Steel	44.12	42.02	–	77920
				I = 678,981 $in.^4$

$I_{transformed} = 678{,}981\ in.^4$

Assuming rectangular section behavior

$$a = \frac{A_s f_y}{0.85 f_c' b}$$
$$= \frac{9 \times 1.56 \times 100}{0.85 \times 22 \times 108}$$
$$= 0.698\,in. < h_f$$
$$c = \frac{a}{\beta_1} = \frac{0.695}{0.65} = 1.07\,in. < h_f$$

Design nominal moment capacity

$$M_n = A_s f_y \left(d - \frac{a}{2} \right)$$
$$= 9 \times 1.56 \times 100 \left(60 - \frac{0.695}{2} \right)$$
$$= 83{,}752\,kip - in.$$

Check for tension-controlled section

$c = 1.07\,in.$

$d_t = 22\,in.$

$\varepsilon_{cu} = 0.015$

$$\frac{c}{d_t} = \frac{\varepsilon_{cu}}{\varepsilon_{cu} + \varepsilon_t}$$
$$\frac{1.07}{60} = \frac{0.015}{0.015 + \varepsilon_t}$$
$$\varepsilon_t = 0.8 > 0.008\,(Tension - controlled \lim it\ for\ 100\,ksi\ steel\ by\ AASHTO)$$

Initial cracking moment

$$S_b = \frac{I_{transformed}}{y_b} = \frac{678981}{44.02} = 15,424\,in^3$$

$$M_{cr} = f_r S_b$$
$$= 3 \times 15424$$
$$= 46,273\,kip - in. < M_{cr}\ from\ prestressed\ girder$$

Increasing reinforcement from 9-#11 to 22-#11, $S_b = 18{,}403\ in^3$

$$M_{cr} = f_r S_b$$
$$= 3 \times 18403$$
$$= 55,209\,kip - in. > M_{cr}\ from\ prestressed\ girder$$

Moment capacity with 22-#11

$$a = \frac{A_s f_y}{0.85 f_c^{'} b}$$
$$= \frac{22 \times 1.56 \times 100}{0.85 \times 22 \times 108}$$
$$= 1.7\,in. < h_f$$

$$c = \frac{a}{\beta_1} = \frac{1.7}{0.65} = 2.61 in. < h_f$$

$$M_n = A_s f_y \left(d - \frac{a}{2} \right)$$
$$= 22 \times 1.56 \times 100 \left(59.5 - \frac{1.7}{2} \right)$$
$$= 202,286\,kip - in.$$

DESIGN OF NON-PRESTRESSED Tx54 WITH UHP-FRC (UNTOPPED):

- Self-weight = 851 *lb/ft*
- $f_c' = 22{,}000\ psi$
- E_c = 7,000 ksi
- 9-#11 and 22-#11, 100 *ksi* steel
- $f_r = 2\ ksi$
- $\beta_1 = 0.65$

Section properties

- $A_C = 817\ in^2$
- $I_g = 299{,}740\ in^2$
- $y_b = 23.51\ in.$
- $y_t = 30.49\ in.$
- $S_b = 12{,}749\ in^3$
- $S_t = 9{,}830\ in^3$

Design with 9-#11:

Transformed moment of Inertia

$$n = \frac{E_s}{E_c} = \frac{29000}{7000} = 4.143$$

Transformed areas of steel:

Layer1: $(n-1)A_s = (4.143-1)\times 2\times 1.56 = 9.806, d_1 = 22\,in.$

Centroid of transformed section:

Part	Area (in^2)	y_{top} ($in.$)	Ay_{top} ($in.^3$)
Concrete	817	30.49	24910.33
Steel	44.125	60	2647.54
	$\sum A = 861.125$		$\sum Ay_{top} = 27{,}557.87$

$$y_{top} = \frac{\sum Ay_{top}}{\sum A} = \frac{27557.87}{861.125} = 32.0\,in.$$

$$y_{bottom} = 62 - y_{top} = 54 - 32.0 = 22.0\,in.$$

Uncracked transformed moment of Inertia:

Part	Area (in^2)	$\bar{y}$ ($in.$)	$I_{own\ axis}$ ($in.^4$)	Ay^2 ($in.^4$)
Concrete	817	-1.512	299,740	1868.15
Steel	44.125	27.99	–	34589.25
				I = 336,197 $in.^4$

$I_{transformed} = 336{,}197\ in.^4$

Assuming rectangular section behavior

$$a = \frac{A_s f_y}{0.85 f_c' b}$$
$$= \frac{9 \times 1.56 \times 100}{0.85 \times 22 \times 36}$$
$$= 2.09\,in. < h_f$$
$$c = \frac{a}{\beta_1} = \frac{2.09}{0.65} = 3.21\,in. < h_f$$

Design nominal moment capacity

$$M_n = A_s f_y \left(d - \frac{a}{2} \right)$$
$$= 9 \times 1.56 \times 100 \left(52 - \frac{2.09}{2} \right)$$
$$= 71{,}541\,kip - in. > M_n\ for\ non - prestressed$$

Check for tension-controlled section

$$c = 3.21\,in.$$
$$d_t = 60\,in.$$
$$\varepsilon_{cu} = 0.015$$
$$\frac{c}{d_t} = \frac{\varepsilon_{cu}}{\varepsilon_{cu} + \varepsilon_t}$$
$$\frac{3.21}{60} = \frac{0.015}{0.015 + \varepsilon_t}$$
$$\varepsilon_t = 0.26 > 0.009\,(ACI)$$
$$> 0.008\,(AASHTO)$$

Initial cracking moment

$$S_b = \frac{I_{transformed}}{y_b} = \frac{336197}{22} = 15822$$

$$M_{cr} = f_r S_b$$
$$= 3 \times 15282$$
$$= 45,845\, kip - in. \simeq M_{cr}\ prestressed\ untopped\ girder$$

Design with 22- #11:

Transformed moment of Inertia

$$n = \frac{E_s}{E_c} = \frac{29000}{7000} = 4.143$$

Transformed areas of steel:

Layer1: $(n-1)A_s = (4.143-1) \times 22 \times 1.56 = 107.87, d = 59.5\, in.$

Centroid of transformed section:

Part	**Area (in^2)**	**y_{top} ($in.$)**	**Ay_{top} ($in.^3$)**
Concrete	817	30.49	24910.33
Steel	107.86	59.5	6417.84
	$\sum A = 921.86$		$\sum Ay_{top} = 31,328$

$$y_{top} = \frac{\sum Ay_{top}}{\sum A} = \frac{31328}{921.86} = 33.98\, in.$$

$$y_{bottom} = 54 - y_{top} = 54 - 33.98 = 20.0\, in.$$

Uncracked transformed moment of Inertia:

Part	**Area (in^2)**	**$\bar{y}$ ($in.$)**	**$I_{own\ axis}$ ($in.^4$)**	**Ay^2 ($in.^4$)**
Concrete	817	-3.38	299,740	9352.05
Steel	107.86	25.62	–	70836.45
				I = 379,928 $in.^4$

$I_{transformed}$ = 379,928 $in.^4$

Assuming rectangular section behavior

$$a = \frac{A_s f_y}{0.85 f_c^{'} b}$$

$$= \frac{22 \times 1.56 \times 100}{0.85 \times 22 \times 36}$$

$$= 5.09\,in. > h_f$$

$$c = \frac{a}{\beta_1} = \frac{5.09}{0.65} = 7.84\,in. > h_f$$

T-section behavior

$$A_{sf} f_y = 0.85 f_c^{'} h_f \left(b - b_w\right)$$

$$A_{sf} = \frac{0.85 f_c^{'} h_f \left(b - b_w\right)}{f_y}$$

$$= \frac{0.85 \times 22 \times 4.75 \times \left(36 - 7\right)}{100}$$

$$= 25.76\,in^2$$

$$\left(A_s - A_{sf}\right) f_y = 0.85 f_c^{'} b_w a$$

$$a = \frac{\left(A_s - A_{sf}\right) f_y}{0.85 f_c^{'} b_w}$$

$$= \frac{(22 \times 1.56 - 25.76) \times 100}{0.85 \times 22 \times 7}$$

$$= 6.53\,in. > h_f$$

$$c = \frac{a}{\beta_1} = \frac{6.53}{0.65} = 10.06\,in. > h_f$$

Design nominal moment capacity

$$M_n = A_{sf} f_y \left(d - \frac{h_f}{2}\right) + \left(A_s - A_{sf}\right) f_y \left(d - \frac{a}{2}\right)$$

$$= 25.76 \times 100 \left(59.5 - \frac{4.75}{2}\right) + \left(22 \times 1.56 - 25.76\right) \times 100 \times \left(59.5 - \frac{6.53}{2}\right)$$

$$= 195,291\,kip - in. > M_n\ for\ non - prestressed$$

Check for tension-controlled section

$c = 10.06\,in.$

$d_t = 59.5\,in.$

$\varepsilon_{cu} = 0.015$

$$\frac{c}{d_t} = \frac{\varepsilon_{cu}}{\varepsilon_{cu} + \varepsilon_t}$$

$$\frac{10.06}{59.5} = \frac{0.015}{0.015 + \varepsilon_t}$$

$$\varepsilon_t = 0.74 > 0.009\,(ACI)$$
$$> 0.008\,(AASHTO)$$

Initial cracking moment

$$S_b = \frac{I_{transformed}}{y_b} = \frac{379928}{20.12} = 18883.1$$

$$M_{cr} = f_r S_b$$
$$= 3 \times 18883.1$$
$$= 56,649\,kip - in. > M_{cr}\,of\ \ prestressed\ untopped\ girder$$

References

ACI Committee 318, 2013, "Building Code Requirements for Structural Concrete (ACI 318-14) and Commentary (ACI 318R-14)," American Concrete Institute, Farmington Hills, MI, 519 pp.

AFGC, 2013, “Béton fibrés à ultra-hautes performances, (Ultra high performance fiber-reinforced concretes)”, recommendations, France.

Aghdasi, P.; Palacios, G.; Heid, A.E.; and Chao, S.-H., 2015, 'Mechanical properties of a highly flowable ultra-high-performance fiber-reinforced concrete mixture considering large-size effects,' High Performance Fiber Reinforced Cement Composites (HPFRCC 7), International Workshop, Stuttgart, Germany.

Aoyama, H., 2001, “Design of Modern Highrise Reinforced Concrete Structures,” Imperial College Press, London, United Kingdom.

Bakis, C.E.; Bank, L.C.; Brown, V.L.; Cosenza, E.; Davalos, J.F.; and Lesko, J.J., Machinda, A., Rizkalla, S.H., Triantafillou, T.C., 2002, “Fiber-reinforced polymer composites for construction state-of-the-art review,” Journal of Composites for Construction, ASCE, V.6, No. 2, pp. 73-87.

Bache, H.H., 1981, “Densified cement/ultrafine particle-based materials,” In: 2nd int. conference on superplasticizers in concrete, Ottawa.

Cho, J. S., 2011, “Shear behavior of steel fiber reinforced prestressed concrete beams without shear reinforcement.” Doctoral dissertation, Dept. of Civil and Environmental Engineering, Univ. of Texas at Arlington.

Davila, R. S., 2007, “Recommendations for the design of ultra-high performance concrete structures.” Doctoral dissertation, Massachusetts Institute of Technology.

Graybeal, B. A., and Davis, M., 2008, “Cylinder or Cube: Strength Testing of 80 to 200 MPa (11.6 to 29 ksi) Ultra-High Performance Fiber-Reinforced Concrete,” ACI Materials Journal, V. 105, No. 6, pp. 603-609.

Graybeal, B., 2015, “Tensile Mechanical Response of Ultra-High-Performance Concrete,” Advances in Civil Engineering Materials, V. 4, No. 2, pp. 62-74.

Benmokrane, B.; Chaallal, O.; Masmoudi, R., 1996. “Flexural Response of Concrete Beams Reinforced with FRP Reinforcing Bars,” ACI Structural Journal, V. 93, No. 1, pp. 46-55.

Benyus, J., “Biomimicry: Innovation Inspired by Nature,” 1997.

Bischoff, P., 2005, "Reevaluation of Deflection Prediction for Concrete Beams Reinforced with Steel and Fiber-Reinforced Polymer Bars,” Journal of Structural Engineering, V. 131, No. 5, May, pp. 752-767. Doi: 10.1061/(ASCE)0733-9445(2005)131:5(752)

Bell, B.; Essary, J.; and Arevalo, H., 2016, “High Performance Concrete Facades UHP-FRC in Precast Sandwich Panel Design,”

Brown, V.L.; Bartholomew, C.L., 1993, “FRP Reinforcing Bars in Reinforced Concrete Members,” ACI Materials Journal, V. 90, No. 1, pp. 34-39.

Brunauer, S.; Yudenfreund, M.; Odler, I.; and Skalny, J., 1973a, “Hardened Portland Cement Pastes of Low Porosity, VI. Mechanism of the Hydration Process,” Cement and Concrete Research, V. 3, No. 2, pp 129-147.

Brunauer, S.; Skalny, J.; Odler, I.; and Yudenfreund, M., 1973b, “Hardened Portland Cement Pastes of Low Porosity, VII. Further Remarks about Early Hydration, Composition and Surface Area of Tobermorite Gel. Summary,” Cement and Concrete Research, V. 3, No. 3, pp. 279-293.

Ceccato, C., 2012, “Material Articulation: Computing and Constructing Continuous Differentiation,” Architectural Design: Material Computation: Higher Integration in Morphogenetic Design Volume 82, Issue 2, pp. 96–103, Wiley Press.

De Larrard, F.; and Sedran, T., 1994, “Optimization of Ultra-High-Performance Concrete by the Use of a Packing Model,” Cement and Concrete Research, V. 24, No. 6, pp. 997-1009.

Desimone, M.V., 2009, "Deflections of Continuous GFRP-Reinforced Concrete Beams,” MSCE thesis, Department of Civil and Environmental Engineering, Villanova University, Villanova, PA.

Fehling, E.; Bunje, K.; and Leutbecher, T., 2004, “Design relevant properties of hardened Ultra High Performance Concrete,” Proceedings of the International Symposium on Ultra High Performance Concrete, University of Kassel, pp. 327-338, Kassel, Germany.

Fehling, E.; Schmidt, M.; Teichmann, T.; Bunje, K.; Bornemann, R.; Middendorf, B., 2005, “Entwicklung, Dauerhaftigkeit und Berechnung – Ultrahochfester Beton (UHPC),” Forschungsbericht DFG FE 497/1-1, Schriftreihe Baustoff- und Massivbau, Band 1, p. 132, Kassel.

Jungwirth, J.; Muttoni, A., 2005, “Versuche zum Tragverhalten von ultra hochfestem Beton,” IS-BETON, Bericht 00.02.R8, Lausanne.

Kendall, K.; Howard, A. J.; and Birchall, J. D., 1983, “The Relation between Porosity, Microstructure and Strength, and the Approach to Advanced Cement-Based Materials,” Philosophical Transactions of the Royal Society of London, A 310, London, UK, pp. 139-153.

Koleravic, B., “Architecture in the digital age,” p. 32, Spon Press, London.

Li, Victor C.; and Fischer, G., 2002, "Reinforced ECC-An evolution from materials to structures." In Proceedings of the first FIB congress, Osaka, Japan, pp. 105-122.

Michaluk, C. R.; Rizkalla, S.; Tardros, G.; and Benmokrane, B., 1998, “Flexural Behavior of One-Way Concrete Slabs Reinforced by Fiber Reinforced Plastic Reinforcement,” ACI Structural Journal, V.95, No. 3, pp. 353-364.

Mielenz, R. C., 1984, “History of chemical admixtures for concrete”, Concrete International, Vol. 6, Issue 4, p. 40-54.

Naaman, A. E.; Reinhardt H. W., 2006, “Proposed classification of HPFRC composites based on their tensile response,” Materials and Structures, 39, pp. 547-555.

Nagasaka, T.; Fukuyums, H.; and Tanigaki, M., 1993, "Shear Performance of Concrete Beams Reinforced with FRP Stirrups,” Fiber-Reinforced -Plastic Reinforcement for Concrete Structures-International Symposium, SP-138, American Concrete Institute, Farmington Hills, MI, pp. 789-811.

Nanni, A., 1993, “Flexural behavior and design of RC members using FRP reinforcement,” Journal of Structural Engineering, V.119, No.11, pp. 3344–3359.

NEHRP Consultants Joint Venture, 2014, “Use of High-Strength Reinforcement in Earthquake-Resistant Concrete Structures,” National Institute of Standards and Technology.

Odler, I.; Yudenfreund, M.; Skalny, J.; and Brunauer, S., 1972a, “Hardened Portland Cement Pastes of Low Porosity, III. Degree of Hydration. Expansion of Paste, Total Porosity,” Cement and Concrete Research, V. 2, No. 4, pp. 463-480.

Odler, I.; Hagymassy, J.; Bodor, E. E.; Yudenfreund, M.; and Brunauer, S., 1972b, “Hardened Portland Cement Pastes of Low Porosity, IV. Surface Area and Pore Structure,” Cement and Concrete Research, V. 2, No. 5, pp. 577-589.

PCI Committee on Precast Sandwich Wall Panels., 2011, “State of the Art of Precast/Prestressed Concrete Sandwich Wall Panels,” Chicago, IL, PCI.

Ranade, R.; Li, V.C.; Stults, M.D.; Heard, W.F.; and Rushing, T.S., 2013, “Composite Properties of High-Strength, High-Ductility Concrete,” ACI Materials Journal, V. 110, No. 4, pp. 413-422.

Reineck, K.-H.; Greiner, S., 2004, “Entwurf und Konstruction dichter Heisswasser-Wärmespeicher aus ultrahochfestem Faserfeinkornbeton,” Abschlussbericht BMU 0329606V, Institut für Leichtbau Entwerfen und Konstruieren, Universität Stuttgart, Germany, March.

Richard, P.; and Cheyrezy, M., 1995, “Composition of Reactive Powder Concretes,” Cement and Concrete Research, V. 25, No. 7, Oct., pp. 1501-1511.

Richart, F.E.; and Brown, R.L., 1934, “An Investigation of Reinforced Concrete Columns: A Report of an Investigation,” The Engineering Experiment Station, University of Illinois, in cooperation with the American Concrete Institute, University of Illinois, Urbana, Illinois.

Roy, D. M.; and Gouda, G. R., 1973, “High Strength Generation in Cement Pastes,” Cement and Concrete Research, V. 3, No. 6, pp. 807-820.

Roy, D. M.; Gouda, G. R.; and Bobrowsky, A., 1972, “Very High Strength Cement Pastes Prepared by Hot Pressing and other High Pressure Techniques,” Cement and Concrete Research, V. 2, No. 3, pp. 349-366.

Sonobe, Y.; Fukuyama, H.; Okamoto, T.; Kani, N.; Kimura, K.; Kobayashi, K.; Masuda, Y.; Matsuzaki, Y.; Mochizuki, S.; Nagasaka, T.; Shimizu, A.; Tanano, H.; Tanigaki, M.; and Tenshigawara, M., 1997, “Design Guidelines of FRP Reinforced Concrete Building Strcutures,” Journal of Composites for

Construction, V. 1, No. 3, pp.90-115. Doi: 10.1061/(ASCE)1090-0268(1997)1:3(90)

Spasojevic, A., 2008, “Structural implications of ultra-high performance fibre-reinforced concrete in bridge design,” École Polytechnique Fédérale de Lausanne, Switzerland.

“SP Systems Guide to Composites,” Composite Engineering Materials - Systems

Stang, H.; Li, V. C., 2004, “Classification of Fibre Reinforced Cementitious Materials for Structural Applications,” 6th RILEM Symposium on fibre reinforced concrete (FRC), - BEFIB 2004, Varenna, Italy, pp. 197-218.

Tracy, K.; Bell, B.; Yogiaman, C.; Tessmer, L.; McClellan, K.; Vrana, A.; Verboon, E., 2014, “Plastic- Cast Concrete: Fabrication as Applied Research. Fabricate: Negotiating Design and Making FABRICATE,” pp. 240-247. Editors: Fabio Gramazio, Matthias Kohler and Silke Langenberg editors. Publishers: gta, Vertag, Zurich.

Tue, N. V.; Simsch, G.; Schneider, H.; Schmidt, D., 2004, “Bearing Capacity of Stub Columns made of NSC, HSC and UHPC confined by a Steel Tube,” Proceedings of the International Symposium on Ultra High Performance Concrete, University of Kassel, pp. 339-350, Kassel, Germany, September.

Tureyen, A. K.; and Frosch, R. J., 2002, “Shear Tests of FRP Reinforced Concrete Beams without Stirrups,” ACI Structural Journal, V. 99, No. 4, July-Aug., pp. 427-434.

Wille, K.; Naaman, A.E., and El-Tawil, S., 2011, “Optimizing Ultra-High-Performance Fiber-Reinforced Concrete: Mixtures with Twisted Fibers Exhibit Record Performance under Tensile Loading,” Concrete International, V. 33, No. 9, pp.35-41.

Wille, K.; Naaman, A.E.; El-Tawil, S.; and Parra-Montesinos, G.J., 2012, “Ultra-High Performance Concrete and Fiber Reinforced Concrete: Achieving Strength and Ductility without Heat Treatment,” Materials and Structures, V. 45, No. 3, pp. 309-324.

Yudenfreund, M.; Odler, I.; and Brunauer, S., 1972a, “Hardened Portland Cement Pastes of Low Porosity, I. Materials and Experimental Methods,” Cement and Concrete Research, V. 2, No. 3, May, pp. 313-330.

Yudenfreund, M.; Skalny, J.; Mikhail, R. S.; and Brunauer, S., 1972b, “Hardened Portland Cement Pastes of Low Porosity, II. Exploratory Studies. Dimensional Changes,” Cement and Concrete Research, V. 2, No. 3, May, pp. 331-348.

Yudenfreund, M.; Hanna, K. M.; Skalny, J.; Odler, I.; and Brunauer, S., 1972c, “Hardened Portland Cement Pastes of Low Porosity, V. Compressive Strength,” Cement and Concrete Research, V. 2, No. 6, pp. 731-743.

Zhishen, W.; Xin, W.; and Gang, W., 2012, “Advancement of structural safety and sustainability with basalt fiber reinforced polymers,” CICE2012, Rome, 13, 15-29.

Biographical Information

Venkatesh Babu Kaka was born in Guntur, India on November 21, 1990. After obtaining a Bachelor of Science in Civil Engineering from Bapatla Engineering College (BEC), Bapatla in 2012, he worked as a lecturer in BEC for a few months. In June of 2013, he enrolled in the Graduate School at The University of Texas at Arlington.

During his Graduate studies working with Dr. Shih-Ho Chao, he involved in several projects including NSF NEESR-RC project “Full-Scale RC and HPFRC Frame Sub assemblages Subjected to Collapse-Consistent Loading Protocols for Enhanced Seismic Safety and Performance”, NSF project “Establishing Manufacturing and Large-Scale Casting Process and Structural Design Criteria for Ultra-High-Performance Fiber-Reinforced Concrete (UHP-FRC)” and “The Effect of Fiber Corrosion on Shear Capacity of Steel Fiber Reinforced Concrete Beams.” He also co-founded a startup named GKC (Gamarra Kaka Chao) Archstructural with Dr. Shih-Ho Chao and Jean Carlos Gamarra during his Graduate program.

After receiving his M.S in Structural Engineering and Applied, Venkatesh plans to work as a Structural Engineer and gain design experience working towards his P.E. license. He is a member of several professional organizations such as American Concrete Institute (ACI), American Society of Civil Engineers (ASCE), Precast/Prestressed Concrete Institute (PCI) and Earthquake Engineering Research Institute (EERI).